ONE-POT MICROWAVE CONVERSION OF OIL PALM MESOCARP FIBRE TO LEVULINIC ACID USING LIGNIN-DERIVED CRYOGEL INCORPORATED WITH PHOSPHOTUNGSTIC ACID-NIOBIUM (V) OXIDE

NADIAH SYAFIQAH BINTI MOHD AZLAN

THESIS SUBMITTED TO
THE UNIVERSITY OF NOTTINGHAM FOR THE
DEGREE OF DOCTOR OF PHILOSOPHY
MAY 2024

Abstract

Levulinic acid is an important platform chemical with wide applications, and it can be produced from lignocellulosic biomass. In this study, a finely tuned method was developed to produce levulinic acid from oil palm mesocarp fibre using microwave-assisted synthesis in a lignin-derived carbon cryogel incorporated with phosphotungstic acid and niobium oxide, coupled with a gamma-valerolactone/water biphasic system. This catalytic system addresses challenges in producing levulinic acid from recalcitrant biomass, which can hinder the cellulose hydrolysis process due to the low selectivity of solid bifunctional acid catalysts in breaking down the tightly packed crystalline cellulose structure. These catalysts are often easily deactivated, difficult to recycle, and have poor thermal tolerance. The biphasic gamma-valerolactone/water system efficiently removed 95% lignin and 55% hemicellulose, making the cellulose substrate available for the conversion reaction. Meticulously tailored carbon cryogels, synthesised from lignin and xanthan gum crosslinked hydrogel under gentle sol-gel-hydrothermal conditions, offered desirable properties including a swelling ratio of 10.3 g g^{-1}, compressive strength of 0.82 MPa at 90% strain, crosslinking yield of 71.7%, surface area of 57.41 m^2 g^{-1}, and porosity of 0.13 cm^3 g^{-1}. These cryogels, incorporated with phosphotungstic acid and niobium oxide, provided bifunctional Brønsted-Lowry and Lewis acidity at a ratio of 1.48 and acid sites of 12.50 mmol g^{-1}, fostering a synergistic effect in catalysing tandem reactions with a synergy factor of 2.15. The cryogel catalyst exhibited a balanced distribution of micropores, mesopores, and macropores, enhancing thermal

conductivity and allowing the diffusion of biomass particles. This resulted in an impressive conversion of oil palm mesocarp fibre to levulinic acid with 97.4% efficiency in a one-pot conversion. The final levulinic acid yield surged to 22.1% under optimal parameters for microwave power (388 W), catalyst loading (0.13 g), biomass loading (0.07 g), and the gamma-valerolactone to water ratio (8.41), approaching the theoretical maximum of 22.7%. The cryogel catalyst reduced energy requirements, resulting in low activation energies of 98.7 kJ mol^{-1} for cellulose conversion to glucose and 62.3 kJ mol^{-1} for glucose conversion to levulinic acid. The predominant conversion pathway presumably involves the direct conversion of glucose to levulinic acid, bypassing the HMF intermediate. The carbon cryogel catalyst exhibited robustness with an 85% efficiency after four cycles, declining to 52% by the eighth cycle, due to humin formation that may persist. The production cost of the cryogel catalyst is estimated at RM 5.23 per gram. This study proposes a technically and economically feasible, sustainable production of levulinic acid from biomass with potential for scale-up. Future work could focus on optimising the catalyst's cost reduction for scaling-up production, exploring alternative humin utilisation to upgrade by-products to value-added products in addition to levulinic acid production, and conducting computational chemistry to understand and optimise the microenvironments around active catalytic sites for better performance.

Keywords: Lignin cryogel; phosphotungstic acid; niobium oxide; biomass conversion; levulinic acid; microwave-assisted

List of Publications

Journal Papers

1) **Azlan, N.S.M.**, Yap, C.L., Gan, S., Rahman, M.B.A. 2022. Effectiveness of various solvents in the microwave-assisted extraction of cellulose from oil palm mesocarp fiber. Materials Proceedings, 59, 583-590.
   DOI: 10.1016/j.matpr.2021.12.086
2) **Azlan, N.S.M.**, Yap, C.L., Gan, S., Rahman, M.B.A. 2022. Recent advances in the conversion of lignocellulosic biomass and its degraded products to levulinic acid: A synergy of Brønsted-Lowry acid and Lewis acid. Industrial Crops and Products, 181, 114778.
   DOI: 10.1016/j.indcrop.2022.114778
3) **Azlan, N.S.M.**, Yap, C.L., Tiong, Y.W., Gan, S., Rahman, M.B.A. 2023. The interplay of Brønsted-Lowry and Lewiss acid sites in bifunctional catalyst for the biomass conversion to levulinic acid. Journal of Biomimetics, Biomaterials and Biomedical Enginering, 61, 71-76.
   DOI: https://doi.org/10.4028/p-RNTv04
4) **Azlan, N.S.M.**, Yap, C.L., Tiong, Y.W., Gan, S., Rahman, M.B.A. 2024. Enhanced microwave conversion of oil palm mesocarp fiber to levulinic acid using $H_3PW_{12}O_{40}$-Nb_2O_5 functionalized carbon cryogel derived from lignin hydrogel. Bioresource Technology Reports, 25, 101750.
   DOI: https://doi.org/10.1016/j.biteb.2023.101750

List of Attended Conferences

1) 3rd International Conference on Recent Advances in Materials and Manufacturing (ICRAMM 2021)
2) 8th International Conference on Composite Materials and Material Engineering (ICCMME 2023) – Best Presentation Award

Acknowledgements

I extend my deepest gratitude to my supervisor, Dr. Yap Chiew Lin, and co-supervisors, Prof. Gan Suyin and Prof. Mohd Basyaruddin Abdul Rahman, for their unwavering support and invaluable guidance throughout this research journey. Their expertise and encouragement have been instrumental in shaping the trajectory of this study. A special acknowledgment goes to the dedicated lab technicians, including Mr. Fareez, Ms. Khairani, Ms. Fatihah, Ms. Fathiah, Ms. Siti, Mr. Ashraf, and Mr. Aidil, whose technical expertise and assistance significantly contributed to the success of this project. Their commitment to excellence has been a constant source of inspiration. Gratitude is also extended to all research officers from the Centre for Research and Instrumentation Management (*i*-CRIM), Universiti Kebangsaan Malaysia (UKM), Nanotechnology and Catalysis Research Centre (NanoCat), Universiti Malaya (UM), and Malaysian Nuclear Agency.

I am profoundly grateful to my parents and family members for their continuous support and encouragement. Despite the challenges encountered along the way, their unwavering belief in me has been a driving force, enabling me to overcome obstacles and complete this academic journey. I would also like to acknowledge the financial support from the Ministry of Higher Education (MOHE), Malaysia, for the Fundamental Research Grant Scheme (FRGS) provided. Thank you to everyone who has played a role in this endeavour, contributing to the realisation of this research. Your support has been invaluable, and I am sincerely thankful for each person who has been a part of this academic odyssey.

Table of Contents

List of Tables

List of Figures

List of Abbreviations

BET	Brunauer–Emmett–Teller
sp^3 C	A carbon atom that is sp^3 hybridised
Zeolite β	Microporous, crystalline aluminosilicate materials
(–C(O)CH_3)	Pyruvate molecules in xanthan gum
$(C_5H_8O_4)_n$	Polysaccharide-derived from hemicellulose
[BMIM][Cl]	1-Butyl-3-methylimidazolium chloride
$[C_2C_1im]Cl$	1-Ethyl-3-methylimidazolium chloride
$[C_4C_1im]Cl$	1-Butyl-3-methylimidazolium chloride
[EMIM][Ac]	1-Ethyl-3-methylimidazolium acetate
$[HMIM][HSO_4]$	1-Hexyl-3-methylimidazolium hydrogen sulphate
[I]s	Activity of acid species in Hammett acidity function
$[IH^+]_s$	Activity of the solvated proton in Hammett acidity function
$[MIMPSH]H_2PW$	Heteropoly acid ionic liquid
ΔG	Gibbs free energy
ΔH	Change in enthalpy
ΔS	Change in entropy
1/T	The reciprocal of the absolute temperature (in Kelvin)
A	Pre-exponential factor
AC	Activated carbon
$Al_2(SO_4)_3$	Aluminium sulphate
AlCl3	Aluminium chloride
Amberlyst 36	A bead form, macroreticular, sulphonic acid ion exchange resin
B/L	Ratio of Bronsted-Lowry to Lewis acid
BJH	Barrett-Joyner-Halenda
L/C	Ratio of catalyst to lignin
C=C	Carbon-carbon double bond
C-3	A side chain that contains three carbon atoms
C-6	A side chain that contains six carbon atoms
C9 monomers	A group of aromatic hydrocarbons
C–C	Carbon-carbon bond
CCD	Central composite design
CF_3SO_3H	Trifluoromethanesulphonic acid
C–H	Carbon-hydrogen bond
CH_2	Methylene
CH_2OH	Methanediol
CIr	Crystallinity index
CO_2	Carbon dioxide
C–O–C	Carbon-oxygen-carbon bond found in ether
COO^-	Carboxylate ion

COOH	Carboxyl group
Cr^{3+}	Chromium (III) ion
$CrCl_3$	Chromium (III) chloride
Cs	Caesium
Cs^+	Caesium ion
Cu^{2+}	Copper (II) ion
$CuCl_3$	Copper (III) chloride
CuO	Copper oxide
Cα-Cβ	The bond between the alpha (α) and beta (β) carbon atoms in a molecule. The alpha carbon (Cα) is the first carbon atom that attaches to a functional group, such as a carbonyl. The beta carbon (Cβ) is the second carbon atom next to the functional group.
DES	Deep eutectic solvent
DFT	Density functional theory
DMF	Dimethyl formamide
DMSO	Dimethyl sulphoxide
DOPMF	Dewaxed oil palm mesocarp fibre
DSC	Differential scanning calorimetry
DTG	Derivative thermogravimetry
E_a	Activation energy
EDTA	Ethylenediaminetetraacetic acid
EDX	Energy dispersive X-ray
EHL	Enzymatic hydrolysis lignin residue
ETP	Economic Transformation Programme
FA	Formic acid
FDCA	2,5-furandicarboxylic acid
Fe^{3+}	Fe (III) ion
$FeCl_3$	Fe (III) chloride
Fe-NbP	A ternary system of Iron (Fe), Niobium (Nb), and Phosphorus (P)
FTIR	Fourier-transform infrared spectroscopy
G	Coniferyl alcohol
GC-MS	Gas chromatography mass spectrometry
GVL	γ-valerolactone
H	*p*-coumaryl alcohol
H^+	Hydrogen ion
H_2	Hydrogen molecule
H_2O	Water
H_2O_2	Hydrogen peroxide
H_2SO_4	Sulphuric acid
H_3PO_4	Phosphoric acid

$H_3PW_{12}O_{40}$	Phosphotungstic acid
$H_4SiW_{12}O_{40}$	Silicotungstic acid
$H_5AlW_{12}O_{40}$	Aluminotungstic acid
$H_5BW_{12}O_{40}$	Borotungstic acid
HCl	Hydrochloric acid
He	Helium
HF	Hierarchical factor
HMF	Hydroxymethylfurfural
H-Nb_2O_5	Monoclinic structure of Nb_2O_5
HNO_3	Nitric acid
HOMO	Highest energy occupied molecular orbital
HPLC-VWD	High-performance-liquid chromatography- variable wavelength
HTSACFs	Hydrothermal sulphonated activated carbon fibres
I_{002}	Intensity of the diffraction peak corresponding to the (002) plane of the crystal lattice in cellulose
I_{am}	Intensity of the diffraction peak corresponding to the amorphous portion
IL	Ionic liquid
IUPAC	International Union of Pure and Applied Chemistry
KCl	Potassium chloride
L225-SO_3H	Sulphonic acid derivative
LA	Levulinic acid
LC_{50}	Lethal concentration
LCA	Life cycle assessment
L-CA	Carbon-based solid acid catalyst
LCC	Lignin-derived carbonaceous catalyst
LD_{50}	Lethal dose
LF-A	Lignosulphonate-based heterogeneous sulphonic acid catalyst by direct polymerisation
LF-B	Lignosulphonate-based heterogeneous sulphonic acid catalyst by templated with silica
LF-C	Lignosulphonate-based heterogeneous sulphonic acid catalyst by silica
LIG-FUR	Lignin-furfural
LIG-PEGDE	Lignin-polyethylene glycol diglycidyl ether
LIG-XG	Lignin-xanthan gum
LUMO	Lowest energy unoccupied molecular orbital
LXCC1	Lignin-xanthan gum carbon cryogel with ratio of water to lignin at 1:1
LXCC5	Lignin-xanthan gum carbon cryogel with ratio of water to lignin at 5:1

$M_3/nPW_{12}O_{40}$	Heteropolyacid where M represents a metal ion
MIBK	Methyl isobutyl ketone
MLC-SO_3H	Magnetic lignin-derived carbonaceous catalyst
Mn_3O_4/ZSM-5	Manganese oxide incorporated with Zeolite Socony Mobil–5 (aluminosilicate zeolite)
MoO_3	Molybdenum trioxide
MTHF	Methyltetrahydrofuran
N	Nitrogen atom
N_2	Nitrogen molecule
Na^+	Sodium ion
Na_2CO_3	Sodium carbonate
NaCl	Sodium chloride
NaOH	Sodium hydroxide
Nb_2O_5	Niobium oxide
Nb^{5+}	Niobium (V) ion
Nb_{5c}	Band structure of Nb_2O_5
NbAlS-1	Hetero-atomic MFI-type zeolite incorporated simultaneously niobium(v) and aluminium(iii) centres
NBMA	N,N'-methylenebis(acrylamide)
Nb-O	A chemical bond between niobium (Nb) and oxygen (O)
NbO_6	A niobium (Nb) atom surrounded by six oxygen (O) atoms, forming an octahedral coordination geometry
$NbOPO_4$	Niobium phosphate
NbOx	Niobium oxides, where 'x' stands for the number of oxygen atoms bonded to each niobium atom
Nb-P	Niobium phosphide
NFPA	National Fire Protection Association
N–H	Nitrogen-hydrogen bondd
NH_3-TPD	Ammonia thermo desorption
Ni	Nickel
Ni-HMETS-10	A hierarchically structured zeolite catalyst that incorporates nickel (Ni) into the ETS-10 zeolite
NMR	Nuclear magnetic resonance
O(2)–H···O(6)	A hydrogen bond where a hydrogen atom attached to the oxygen atom labeled as "2" is interacting with the oxygen atom labeled as "6"
O(3)···H–O(6)	Interchain of hydrogen boond
O(3)–H···O(5)	A hydrogen bond where a hydrogen atom attached to the oxygen atom labeled as "3" is interacting with the oxygen atom labeled as "5
O_2	Oxygen
OH	Hydroxide

OPEFB	Oil palm empty fruit bunch
OPMF	Oil palm mesocarp fibre
P/P_0	Relative pressure
Pd	Palladium
PEG-200	Polyethylene glycol with an average molecular weight of 200
PEG-400	Polyethylene glycol with an average molecular weight of 400
PEGDE	Polyethylene glycol diglycidyl ether
pH	Logarithmic scale to specify the acidity or basicity of an aqueous solution
pK_a	Strength of an acid in solution
PKS	Palm kernel shell
Pt	Platinum
R/C	Ratio of resorcinol to catalyst
R/F	Ratio of resorcinol to formaldehyde
R/W	Ratio of resorcinol to water
R^2	Coefficient of determination
RF	Resorcinol-formaldehyde
RSM	Response surface methodology
Ru	Rubidium
S	Sinapyl alcohol
SBA-15	Santa Barbara Amorphous-15, a highly stable mesoporous silica sieve
S_{BET}	Surface area based on Brunauer–Emmett–Teller method
Sc	Scandium
$Sc(OTf)_2$	Scandium (III) trifluoromethanesulphonate
SDG	Sustainable development goal
SEM	Scanning electron microscope
SF	Synergy factor
SG	Sol-gel
SGH	Sol-gel-hydrothermal
SiO2	Silicon dioxide
Sn	Tin
Sn^{4+}	Tin (IV) oxide
SO_3H	Sulphonic group
SQX	Standardless quantitative X-ray analysis
TA	Texture analyser
tanδ	Loss tangent
TCD	Thermal conductivity detector
TGA	Thermogravimetric analysis
THF	Tetrahydrofuran
Ti^{4+}	Titanium (IV) ion
TiO_2	Titanium oxide

T_m	Melting temperature
T-Nb_2O_5	Orthorhombic structure of Nb_2O_5
TPA	Tungstophosphoric acid
TT- Nb_2O_5	Pseudohexagonal structure of Nb_2O_5
UHV	Ultra High Vacuum
UN	United Nation
USA	United States
V_2O_5	Vanadium (V) oxide
V_{mac}	Volume of macropores
V_{meso}	Volume of mesopores
V_{micro}	Volume of micropores
W/L	Ratio of water to lignin
W_a	Weight of hydrogel before soaking
W_d	Weight of dry hydrogel
W_e	Equilibrium weight for hydrogel
WO_3^-	Tungsten trioxide
W–O–W	The bond between tungsten (W) and oxygem (O)
W_s	Weight of wet hydrogel
XG/L	Ratio of xanthan gum to lignin
XPS	X-ray photoelectron spectroscopy
XRD	X-ray diffraction
XRF	X-ray fluorescence spectroscopy
Zeolite Y	Aluminosilicate molecular sieve that belongs to the family of faujasite-type structures
Zn^{2+}	Zinc (II) ion
$ZnBr_2$	Zinc (II) bromide
Zr^{4+}	Zirconium (IV) ion
ZSM-5	Zeolite Socony Mobil–5 (aluminosilicate zeolite that belongs to the pentasil family of zeolites)
α–O–4	A linkage in lignin that connects a phenylpropane unit to a phenyl ring
β-1,4-glucan	Polysaccharide composed of glucose units linked by β-1,4-glycosidic bonds
β–O–4	A bond that connects a phenylpropane unit to a phenyl ring
ϵ'	Dielectric constant
ϵ''	Loss factor
η	Cross-linking reaction

List of Units

µL	Microlitre	kV	Kilovolt
µm	Micrometre	M	Molar
µmol m^{-2}	Micromole per metre square		
sen/kWh	Sen per kilo Watt hour	m^2 g^{-1}	Square metre per gram
$	United States dollar	metric t/yr	Metric tonne per year
$/kg	United States dollar per kilogram	mg	Milligram
%	Percentage	mg g^{-l}	Milligram per gram
°C	Degree Celcius	min	Minute
°C min^{-1}	Degree Celcius per minute	mL	Millilitre
CFU mL^{-1}	Colony Forming Unit per millilitre	mL min^{-1}	Millilitre per minute
cm^{-1}	Per centimetre	mm	Millimetre
cm^3 g^{-1}	Cubic centimetre per gram	mM	Millimolar
Da	Dalton	mm s^{-1}	Millimetre per second
eV	Electronvolt	mmol g^{-l}	Millimole per gram
g	Gram	mol L^{-1}	Mole per litre
g g^{-1}	Gram per gram	MPa	Megapascal
g L^{-1}	Gram per litre	mPa·s	Millipascal-second
g mL^{-1}	Gram per millilitre	MΩ·cm	Megaohm-centimetre
g mol^{-1}	Gram per mole	nm	Nanometre
g cm^{-3}	Gram per cubic centimetre	particulate mL^{-1}	Particle per millilitre
h	hour	RM	Ringgit Malaysia
J mol^{-1} K^{-1}	Joule per mole per Kelvin	rpm	Revolution per minute
K	Kelvin	s	Second
kJ mol^{-1}	Kilojoule per mole	t	Tonne
kJ mol^{-1} K^{-1}	Kilojoule per mole per Kelvin	W	Watt
km	Kilometre		

Chapter 1

Introduction

1.1 Research background

Levulinic acid (LA) has been recognised by the US Department of Energy as one of the top 12 platform chemicals due to its diverse applications such as fuel additives, plasticisers, pharmaceuticals, and solvents. It also serves as a precursor for the synthesis of herbicides and food additives [1]. Presently, LA is primarily synthesised from the conventional petrochemical route, specifically derived from maleic anhydride or furfuryl alcohol [2]. However, the cost remains relatively high, ranging from $5 to 8 per kilogram in 2013 [3–4], making it less conducive for large-scale production given the lower yield from this production route. Despite this, LA consumption was anticipated to rise, potentially reaching 3,820 tonnes in 2020 [3]. The consumption of LA was estimated to gradually increase to 19,710 tonnes in 2022 and 28, 800 tonnes in 2024. The global LA market size was valued at USD 80.0 million in 2023 and is projected to grow at a CAGR of 6.13% from 2024 to 2030 [5] . This market growth is primarily driven by the increasing preference for LA derivatives over synthetic counterparts due to their superior properties.

Biomass conversion, known as the Biofine process, has emerged as a viable avenue for reducing the cost of LA, achieving a range of $0.09–0.22 per kilogram [6]. This technology involves two key steps: (i) biomass depolymerisation to monosaccharides and hydroxymethylfurfural (HMF) at a temperature of 210–220

°C with ~12 s reaction time, and (ii) LA production from HMF at a temperature of 190–200 °C with a reaction time of 15–30 min [3].

Several commercial-scale plants utilising the Biofine process have been established for LA production, which include GFBichemicals at Italy, Segetics, Inc. and Incitor at USA [7]. Noteworthy, Incitor is currently upgrading a plant that will have the capacity to process 160,000–240,000 metric tonnes of biomass per year to variety commodity chemicals, including levulinic acid [3].

To date, the global agricultural industry, which exploits 47 million square kilometres of land, is dominated by oil palm plantations [8]. Malaysia, the second-largest oil palm producer [9], possesses 280,000 square kilometres of oil palm plantations and produces 400 million tonnes of oil palm fruit [10]. In Malaysia, the oil palm industry generated approximately 83 million dry tonnes of solid biomass waste per year in 2012, but only 10% was used for downstream applications [10]. This amount was projected to rise to 100 million tonnes by 2020 [11]. According to the Malaysian Palm Oil Board, Malaysia currently generates more than 90.53 million dry tonnes of solid oil palm biomass in various forms, including empty fruit bunches, palm kernel shells, mesocarp fibres, oil palm trunks, and oil palm fronds [12]. These lignocellulosic biomass wastes, rich in lignin, cellulose, and hemicellulose, hold significant potential for conversion into high-value products such as LA platform chemicals [8].

The production of LA from biomass involves complex reactions involves sugar and HMF intermediates. Potent acid catalysts are crucial for selective production of LA and avoid reaction stoppage at intermediate stages [3]. Heterogeneous catalysis gaining attention for its environmental friendliness,

stability, recyclability, and ease of product recovery compared to the conventional homogeneous catalysis [7–9]. Despite its high activity and selectivity, homogeneous catalysis poses challenges in material corrosion and recycling [13–15].

The field of heterogeneous catalysts is diverse, with zeolites, metal salts, polyoxometalates, and carbon-based solid acid catalysts [16–17]. Carbon-based solid acid catalysts stand out due to their high acidic density and cost-effectiveness, making them potent for biomass conversion into LA. Carbon-based solid acid catalyst has evolved from sulphonated carbon-based solid acids [18–19], a viable alternative to conventional homogeneous sulphuric acid, which produced through incomplete carbonisation of microcrystalline cellulose followed by a sulphonation process. The catalysts feature $–SO_3H$, –COOH, and phenolic–OH groups, have shown promise in cellulose hydrolysis with an effective $–SO_3H$ density one-tenth that of sulphuric acid [20], while ensuring the use of renewable a carbon source such as biomass lignin.

Lignin, the second most abundant natural organic material after cellulose, stands out as the primary aromatic organic biopolymer. Its substantial carbon content renders it a valuable precursor for activated carbon in the production of carbon-based solid catalysts [21]. Activated carbon shares distinctive properties with other types of heterogeneous, featuring a large surface area, unique structure, and notable reactivity [22]. However, the process of producing activated carbon requires high-energy. The alternative strategy is proposed via lignin-derived cryogel. Unlike conventional solid acid catalysts, lignin cryogel, which is prepared via a sol-gel method at milder temperatures (70–180 °C), provides a unique three-dimensional network structure with a satisfactory surface area [23–24]. This allows

for better interactions with reactants of various sizes from biomass. However, lignin-derived cryogel needs to be functionalised with other types of solid acid catalysts to enhance its reactivity and selectivity for biomass conversion to LA.

The emergence of superacid solid catalysts, polyoxometalates (or heteropoly acids), has garnered attention due to their unique physicochemical properties. Notably, aqueous solutions containing $H_3PW_{12}O_{40}$ and $H_4SiW_{12}O_{40}$ exhibit higher acidity than conventional mineral acids such as H_2SO_4, HNO_3, and HCl, positioning them as key players in catalytic systems for biomass conversion [25]. Polyoxometalates demonstrate exceptional performance in cellulose hydrolysis to glucose and are recyclable, despite the extraction process needed for catalyst regeneration from homogeneous solutions. In addition to polyoxometalates, niobium-based catalysts have exhibited effective catalytic activity as solid acid catalyst for converting biomass or biomass derivatives into biofuels and bio-based chemicals over the past few decades [26]. Some studies have proven that modified Nb-based catalysts potentially contribute to LA selectivity [27–28]. Notably, the combination of polyoxometalates and Nb-based catalyst on lignin-derived cryogel can boost the synergistic effect of the catalyst. This is due to their possession of Brønsted and Lewis acid sites, which exhibit superior catalytic activity and stability [26].

Lignin cryogel functionalised with acid catalysts provide versatility to be designed to possess high stability and numerous strong protonic acid sites, which able to maintain strong acidity even in the aqueous reaction medium. Despite its potential as a catalyst carrier for biomass conversion, research into the use of lignin as a catalyst support for biomass conversion to LA remains limited. To date, only

three significant studies (**Table 1.1**) have delved into the development of lignin-based solid acid catalysts for cellulose conversion to LA, revealing its potential for further exploration. The results show excellent catalyst properties such as mesoporous structure, high thermal stability, well-distributed active sites, and proper texture for swift mass transport are essential to achieve high LA yield.

Table 1.1 Literature studies on lignin-based catalysts for cellulose conversion to LA.

Ref.	Feedstock	Catalyst	Reaction medium	Characteristics	LA yield (%)
[21]	Microcrystalline cellulose	Lignin-based catalyst doped with FeS (impregnation method)	185 °C, 120 min in GVL (monophasic system)	S_{BET}: 21.61 $m^2 g^{-1}$, V_{pores}: 0.04 $cm^3 g^{-1}$, *x*: 4.13 nm	35.6
[29]	Cellulose residue	Phosphoric acid-activated lignin-based solid acid catalysts (impregnation method)	190 °C, 150 min in MIBK/H_2O-NaCl (biphasic system	S_{BET}: 583.1 $m^2 g^{-1}$, V_{pores}: 0.66 $cm^3 g^{-1}$, *x*: 4.74 nm	67.9
[30]	Cellulose from sugarcane	Lignin-based solid acid catalyst	140 °C, 6 h in water (monophasic system)	-	38.6

*Note: The literature search is based on Scopus and is not restricted by any specific time period. *x* refers to size of pores.

Although biomass is cheap and readily available, but it is hard to dissolve in water [31]. Biphasic systems have been proposed, where the organic solvent with high solubility of cellulose is mixed with the aqueous phase to ensure the consistency of catalytic performance through tandem reactions in one-pot conversion. Nonetheless, the efficient conversion of biomass to LA requires not only

an efficient catalyst and production technology, but a thorough optimisation of operational reaction parameters [32]. Solvent molecules in biphasic system also able to increase dielectric constant reactants, allows lower operating temperatures [33].

Akin with other traditional methods, various carbon-based solid acid catalysts were reported to produce 50–60% LA yield via conventional heating over at least 10 h at 180 °C [32, 34–35]. This excessive reaction times produce thick product that hard to be isolated, as well as prompting undesirable decomposition of catalyst [36]. Alternatively, researchers have explored the use of a microwave-assisted method in the conversion reaction. Microwaves offer a swift (3–15 min) and energy-efficient process. These helps rapid activation of reactants, enhances selectivity, as well as preserve the catalyst, enhancing its recyclability [37] Nonetheless, in the one-pot conversion of biomass to LA, the optimisation of microwave energy, catalyst properties, and operating conditions such as reaction time and temperature is essential to achieve high LA yield with minimal cost and waste generation [38–39]

A recent kinetic examination of LA production from starch employing the microwave-assisted method revealed an activation energy of 91–101 kJ mol^{-1} for glucose dehydration to HMF, significantly lower than the 228–246 kJ mol^{-1} observed under conventional oil bath heating [40]. The lower activation energy values signify a more facile HMF formation at lower energy levels, contributing to the observed variations in LA product formation between microwave and conventional heating methods. Therefore, it is crucial to acknowledge that unconventional heating methods may yield distinct product profiles in comparison to conventional heating [41–42].

1.2 Problem statement

Levulinic acid (LA) synthesis is a critical process in various industries. However, it often faces challenges due to the cost and availability of feedstock like chemicals, cellulose, or sugars [43–46], as well as the non-robust catalytic systems that can influence efficiency and productivity. The petrochemical route for producing levulinic acid, such as via maleic anhydride, poses environmental and safety risks due to the use of hazardous chemicals that can cause severe irritation to the skin, eyes, and respiratory system [47]. In contrast, the Biofine process, which utilises biomass, offers a greener and more eco-friendly alternative [47].

This study explores the use of oil palm mesocarp fibre, an abundant agricultural resource, as a sustainable alternative [48]. However, the complex structure of biomass, characterised by tightly packed chains of crystalline cellulose [49–50], makes it difficult to fractionate, hindering the cellulose hydrolysis process. Currently, sophisticated solvents, such as organic solvents and ionic liquids (ILs), are used to deconstruct the rigid structure of lignocellulose biomass. The conversion process to LA indirectly involves a tandem step of reaction (intermediates). Conventional homogeneous acids like hydrochloric acid and sulphuric acid are commonly used to catalyse LA production from biomass-derived materials [31]. However, these pose an environmental risk due to the acidic and toxic waste generated [51]. Alternatively, heterogeneous catalysts [51–57], including carbon-based solid acid catalysts, have emerged for biomass conversion to LA. Despite advancements, a persistent challenge is low selectivity [58], affecting the overall yield of LA.

Hence, this study proposes the use of bifunctional catalysts that consist of both Brønsted and Lewis acid sites to boost the synergistic effect of the catalytic system. However, the use of bifunctional catalysts has its drawbacks as they are easily deactivated, difficult to recycle, and have poor thermal tolerance [53, 59–60]. To address this, the catalyst support has been introduced by using lignin to act as a carrier for the supported catalyst. A new strategy via the sol-gel-hydrothermal method in preparing a final working catalyst was used to produce lignin-derived carbon cryogel incorporated with bifunctional catalysts.

Lignin cryogels can help in dispersing the active catalytic sites more uniformly, which minimises the chances of catalyst deactivation. The homogeneous distribution of active species ensures consistent catalytic performance over multiple cycles [61]. The porous structure of lignin cryogels allows for better diffusion of reactants and products. This means that reactants can easily reach the catalyst sites, and products can be removed efficiently, reducing the likelihood of catalyst deactivation [62]. Hence, this facilitates easier recovery and reuse of the bifunctional catalysts, making the process more sustainable and cost-effective. Additionally, lignin-derived carbon cryogels provide a robust support structure that can improve the thermal stability of bifunctional catalysts. This helps in maintaining the catalyst's activity at higher temperatures, reducing the risk of deactivation due to thermal degradation.

Despite the advantages of lignin cryogel, there is a need for improvement in synthesising high-yield cryogel. Therefore, the right precursor used as a cross-linker is important to form a strong cross-linking with lignin moieties, leading to higher stability and yield of cryogels [63]. The strong cross-linking within lignin cryogels

provides excellent mechanical strength, which helps in maintaining the integrity of the catalyst under various reaction conditions. This reduces the wear and tear of the catalyst, further extending its lifespan. Detailed process optimisation related to synthesis conditions is necessary to control the properties of lignin-derived cryogels and maximise their performance.

The field of LA production has seen considerable progress over the years with the emergence of various heterogeneous catalysts tested for improving the yield. However, the traditional method of LA synthesis via conventional heating is time and energy-consuming [64–65]. This study suggests using a household microwave as an alternative approach, which can reduce time and energy consumption, indirectly lower the operational cost, and potentially extend the catalyst's shelf life by reducing the exposure time of the catalyst to harsh reaction conditions [66].

This work focuses on addressing the challenges in LA production by solving the issues of expensive and dangerous feedstock, fractionation of biomass components (using γ-valerolactone (GVL)), low selectivity and deactivation of catalysts (optimising properties of lignin-based cryogel incorporated with $H_3PW_{12}O_{40}$-Nb_2O_5), and energy-efficient microwave conversion (a fully operational and kinetically optimised microwave process). It also emphasises sustainable LA production through recyclability and cost studies.

1.3 Research significance

This study explores the underutilised conversion of oil palm mesocarp fibre (OPMF) to LA, using pre-treated OPMF to enhance catalyst accessibility and improve LA yield. The complex structure of agricultural biomass often hinders contact with acid sites on carbon-based solid acids during biomass conversion. However, utilising OPMF can produce carbon-neutral and even carbon-negative energy [67–69], aligning with the "Waste-to-energy" framework.

The study employs a biphasic solvent system, consisting of an aqueous and an organic phase (GVL), to enhance biomass component deconstruction. This setup allows for in-situ fractionation of LA product during the reaction, preventing further degradation of the products and formation of humin [20], a byproduct that can negatively impact yield and quality.

The research introduces a novel lignin-derived cryogel incorporated with $H_3PW_{12}O_{40}$ and Nb_2O_5. This lignin cryogel, synthesised at a low operation temperature via the sol-gel process, can resist high temperatures or harsh conditions for many cycles of the biomass conversion process. The incorporation of bifunctional catalysts to the lignin cryogel enhances the reactivity of the newly developed catalysis, forming a meso-to-nanostructure of the catalysts that is easily tuneable according to the size of biomass particles [70] .

The study also explores the conversion of biomass to LA using a modified microwave, which saves time and energy, leading to cleaner conversion products, lower energy costs, and a smaller environmental footprint [71]. The combination of microwave-assisted method with the biphasic solvent system and the mesoporous

structure of the catalyst can help improve reactant penetration to catalyst sites [72–73].

The research emphasises the importance of balancing product yield, selectivity, and associated costs. It includes detailed optimisation studies for synthesis conditions of lignin-based cryogel, properties of the catalyst, and reaction conditions for biomass-conversion-to-LA. The efficiency of the catalytic system employed was assessed through kinetic studies on biomass-to-LA conversion via microwave-assisted method. The study also evaluates the reusability of the lignin cryogel catalyst over multiple cycles, supporting its economic viability.

Overall, this study contributes significantly to achieving the Sustainable Development Goals (SDGs) directed by the United Nations, particularly SDG 7 (affordable, reliable, sustainable, modern, and clean energy for all) [74], SDG 12 (sustainable consumption and production) [22], and SDG 13 (climate change mitigation efforts).

1.4 Research aim and objectives

The present study aims to enhance the conversion of OPMF to LA by developing a cost-effective, efficient, and sustainable catalyst that utilises biomass-derived materials for the feedstock, catalyst support, and reaction medium. The specific objectives of the study are outlined as follows:

1) To identify the OPMF components and the solvent effects on components deconstruction.
2) To develop a lignin-derived carbon cryogel incorporated with $H_3PW_{12}O_{40}$-Nb_2O_5.
3) To optimise the performance of the catalytic system for converting OPMF to LA.
4) To model the reaction kinetics and establish thermodynamic data for OPMF conversion to LA catalysed by the lignin-derived carbon cryogel incorporated $H_3PW_{12}O_{40}$-Nb_2O_5 via a microwave-assisted biphasic system.
5) To propose a reaction pathway for the microwave-assisted conversion of OPMF to LA catalysed by the lignin-derived carbon cryogel incorporated with $H_3PW_{12}O_{40}$-Nb_2O_5.
6) To assess the reusability of the lignin-derived carbon cryogel incorporated with $H_3PW_{12}O_{40}$-Nb_2O_5.
7) To conduct a cost analysis of the microwave conversion of OPMF to LA using the lignin-derived carbon cryogel incorporated with $H_3PW_{12}O_{40}$-Nb_2O_5.

Chapter 2

Literature review

2.1 Overview

The yield of LA from biomass conversion is highly dependent on the efficiency of the catalytic system used. Carbon-based solid acids, known for their exceptional stability, reactivity, and versatility, have been widely used in catalytic conversion applications, including the biomass conversion to LA. These catalysts are particularly effective due to their high surface area and strong acidity, which provides ample active sites for the reaction. Their reactivity can be significantly enhanced, and side reactions suppressed by incorporating Brønsted-Lowry and Lewis acid as the active components. The Brønsted or Lewis acids can donate protons or accept electrons during the reaction, facilitating the conversion of biomass to LA. The creation of these multifunctional catalysts depends on optimising the synergistic effect between the active components and the proportion and distribution of acid sites on the surface of catalyst support.

Using a biphasic solvent system is another strategy to enhance the performance of carbon-based catalysts. This system, consisting of two immiscible solvents, can help separate the product from the reactants, reducing the chances of side reactions and improving the yield of LA. Applying microwave heating is another technique that can enhance the reactivity of carbon-based catalysts. The rapid and uniform heating provided by microwaves can accelerate the reaction, leading to a higher yield of LA in a shorter time.

To address the challenge of cellulose hydrolysis, researchers are seeking new active components to enhance catalyst activity and exploring alternative feedstocks for LA conversion. This literature review aims to provide a comprehensive examination of the catalytic system used for biomass conversion to LA (**Figure 2.1**). It focuses on key aspects such as understanding the state of the art of LA, exploring the properties and availability of oil palm biomass feedstock, the synthesis process of lignin-derived carbon cryogel incorporated with $H_3PW_{12}O_{40}$-Nb_2O_5 and its associated factors, and keeping up with the latest developments in microwave-assisted biphasic systems for biomass conversion to LA.

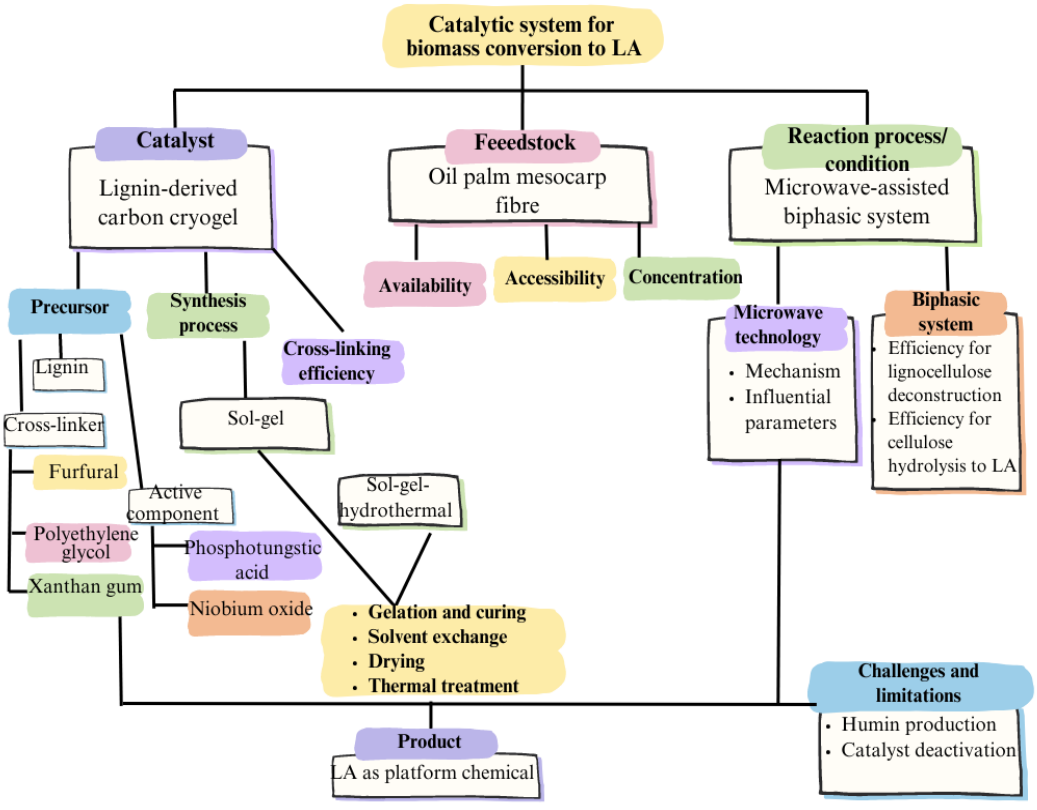

Figure 2.1 Overview of literature review for the catalytic system for biomass conversion to LA.

2.2 LA as platform chemical

LA also known as 4-oxopentanoic acid, β-acetylpropionic acid, and γ-ketovaleric acid, is a concise yet multifaceted compound. It is characterised by a ketone carbonyl and an acidic carboxyl group [33, 75].

2.2.1 Route for biomass to LA

In literature, there are two main routes that are often reported for biomass conversion to LA, which involves cellulosic and hemicellulose pathway (**Figure 2.2**). The conversion of biomass to LA involves a tandem step of reaction involving intermediate stages in which each step is importantly catalysed by different acid sites, either Brønsted-Lowry or Lewis acid [3, 31]. The hydrolysis of biomass via cellulose involves its degradation to hexose sugars while via hemicellulose involves degradation to pentose sugar.

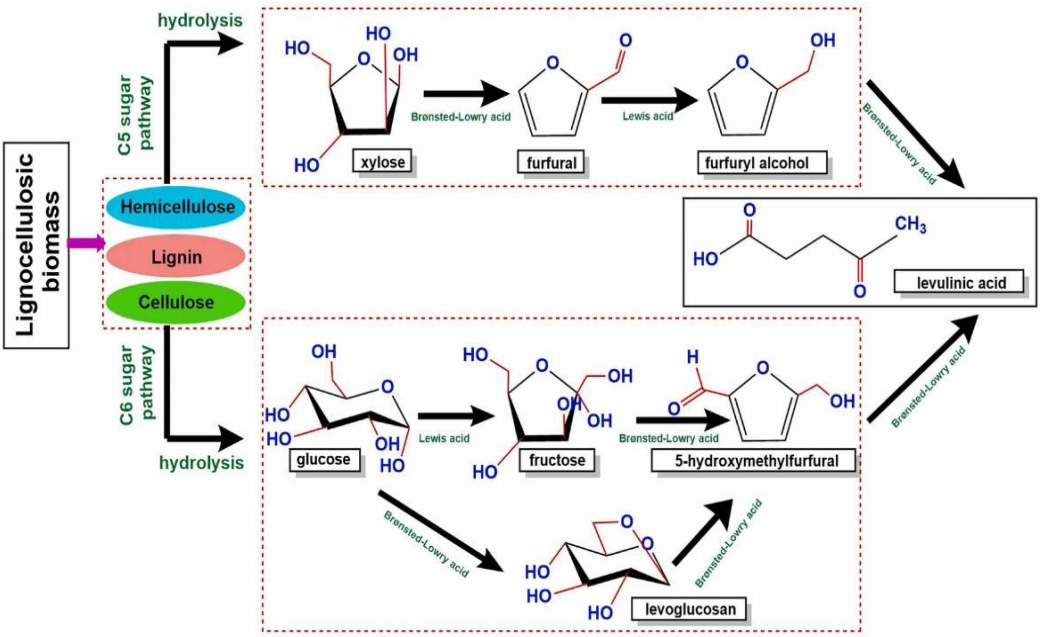

Figure 2.2 Mechanisms for LA synthesis via cellulose and hemicellulose hydrolysis.

To date, the conversion of biomass through cellulose pathway (C6 sugar) is more dominant than hemicellulose pathway (**Figure 2.3**). The cellulose route is often preferred for biomass conversion due to several reasons. Firstly, cellulose is the largest component of biomass, usually about half by weight [76]. Secondly, its conversion to sugar accounts for about a quarter of the total projected cost of producing a platform chemical from biomass [76]. Therefore, cost-effective cellulose conversion processes are essential to the commercialisation of biomass-to-LA technology [76]. Lastly, the conversion of hemicellulose to LA is less efficient due to the formation of furfural from the C5 sugar substrates under the same conditions [77].

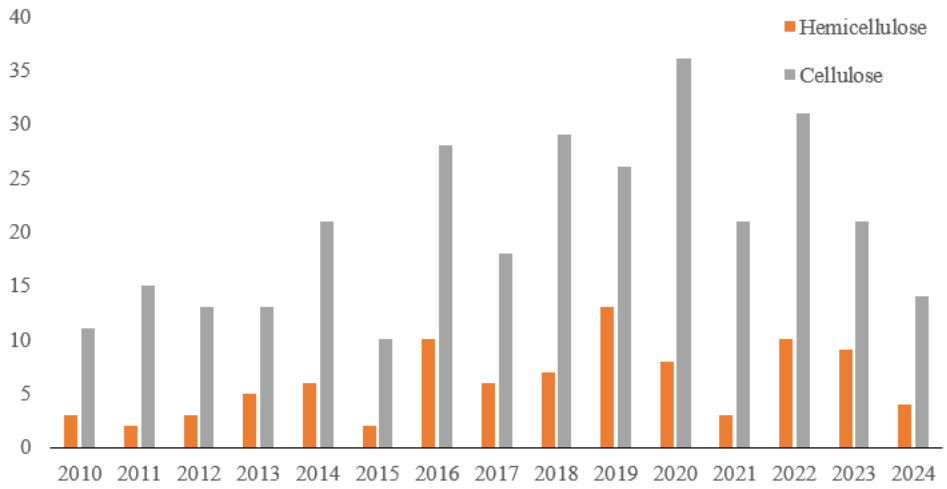

Figure 2.3 Distribution of lignocellulose conversion to LA via hemicellulose or cellulose pathway from 2010-2024, which is extracted from Scopus Database.

HMF is a major intermediate product formed during the dehydration process of hexose sugars. However, HMF is unstable under acidic conditions and can be further converted into other products, such as 2-methylfuran and 2,5-dimethylfuran [78–80], or oxidised to form functional monomers like 2,5-furandicarbaldehyde and 2,5-furandicarboxylic acid (FDCA) [81–82]. These side reactions can reduce the amount of HMF available for conversion into LA, thereby affecting the overall yield of LA. Meanwhile, an efficient catalytic system with strong acidity can cause instability of HMF as acidic conditions promote hydration of HMF, which is a key step in its conversion to LA. Liu *et* al. demonstrated the process of HMF hydration to LA (**Figure 2.4**), which involves the hydration of the C=C bond in HMF to form an intermediate compound (IC1), dehydration of IC1 to form IC2, cleavage of the C-O bond in IC2 to produce 1,2-dicarbonyl structure (IC3), decarboxylation of IC3 to produce IC4 and formic acid (FA), and a hydration-negative hydrogen-transfer

reaction to LA [83]. This demonstration has shown that the efficiency of the catalyst can greatly influence LA yield and selectivity.

The formation of FA can compete with the formation of LA, potentially reducing the yield of LA [3]. However, FA itself has various applications and can be used in the production of formaldehyde, rubber, plasticisers, pharmaceuticals, and textiles. It can also be used in fuel cells [84], as a feed source for hydrogen storage and production [85], or in the transfer hydrogenation of LA to yield higher value products [86–89]. Therefore, while the production of FA may reduce the yield of LA, it does not necessarily represent a loss in terms of overall product value.

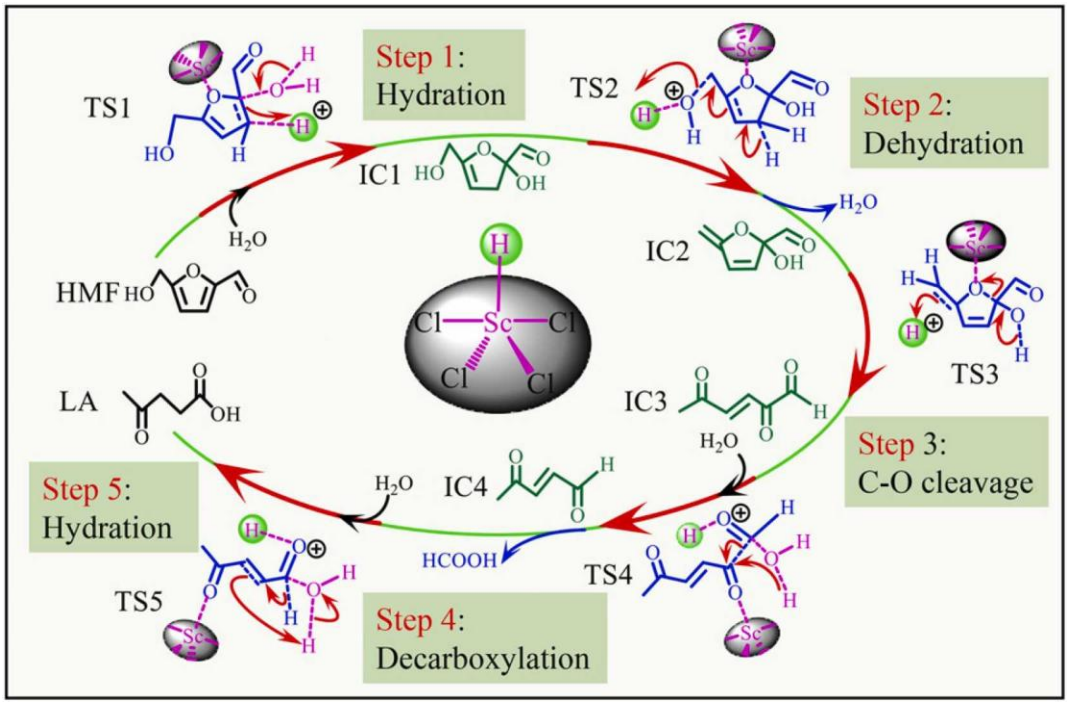

Figure 2.4 Conversion of HMF to LA via $HScCl_4$ catalytic system and the transition states involved. Reproduced with permission from Liu *et* al. [83].

2.2.2 Key properties of LA for broad applications

LA, with the chemical formula $C_5H_8O_3$, is a versatile compound with wide-ranging applications. It features a five-carbon backbone, a carbonyl group (C=O) at one end, and a carboxyl group (COOH) at the other [90]. LA is a colourless to pale yellow crystalline solid with a caramel-like aroma. It is stable with a boiling point of 245–246 °C and a melting point of 33 °C [91]. Its density is 1.1335 g cm^{-3}, and it has a refractive index of approximately 1.4396 [92].

LA is known for its reactivity, making it suitable for various reactions such as esterification and amidation. These reactions produce LA derivatives (**Figure 2.5**) with diverse functional groups [33]. LA is highly soluble, dissolving readily in water, alcohols, acids, and certain organic solvents [33]. Its mild acidity, with a pK_a value of approximately 4.76 [88], allows it to release a proton, forming levulinate salts, which have a range of applications [33].

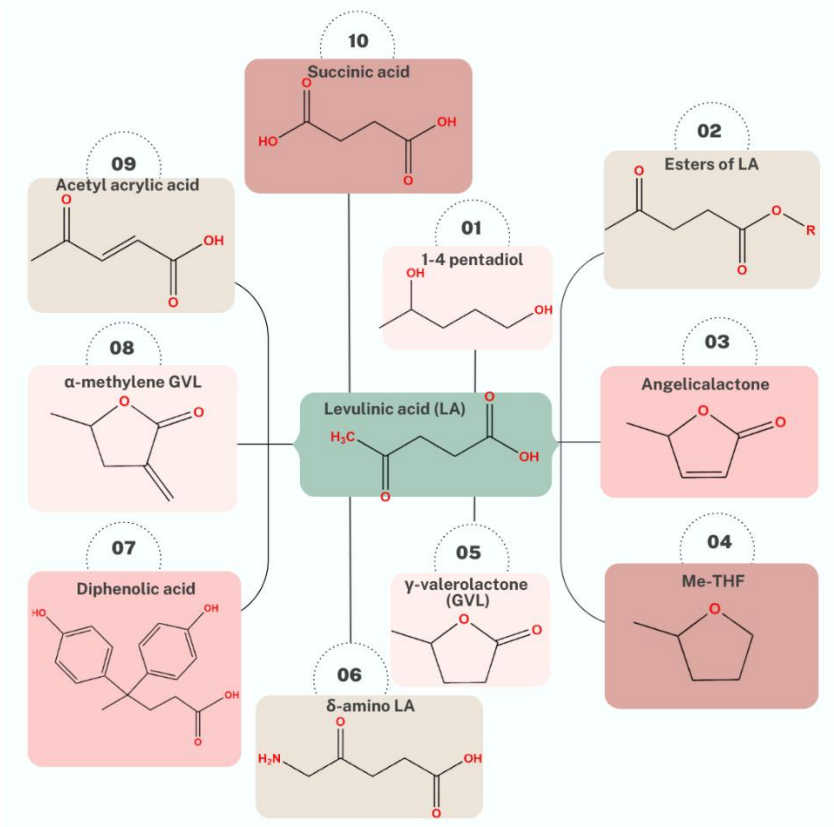

Figure 2.5 LA derivatives.

The demand for LA has been growing due to global population growth and the increased need for various products (**Figure 2.6**), including pharmaceuticals, petroleum fuel, cosmetics, tobacco, flavours, and food, which makes it a crucial building block [93–94]. In particular, the demand for LA in sectors like food, pesticides, pharmaceuticals, and agriculture has been continuously growing, with a projected increase of 6% from 2014 to 2020 [94] . LA is also recognised as a key commodity chemical and is often used as a precursor in the rubber and plastic industry.

Figure 2.6 Applications of LA in various industries.

LA is identified by the US Department of Energy as a top value-added chemical. It is a promising and sustainable material for synthesising other valuable chemicals like GVL, methyltetrahydrofuran (MTHF), hydroxymethylfurfural (HMF), ethyl levulinate, succinic acid, 2-pentanol, 2-butanol, among others [95–96]. As a member of the gamma-keto acids, LA is a versatile platform chemical capable of producing biofuel derivatives that can be blended with petroleum products, offering cleaner-burning fuels without the risk of phase separation [6].

Specifically, GVL can undergo esterification to form pentanoate esters [97], or it can be hydrogenated to produce pentanoic acid. The latter can then undergo

catalytic upgrading to yield 5-nonanone through ketonisation and subsequent hydrogenation, producing either alkanes or alcohols, depending on the catalyst employed. The resulting alcohols can be further dehydrated to form alkenes, allowing for oligomerisation and facilitating the production of C6-C27 hydrocarbon fuels [86, 98–99]. Another noteworthy development is the recently introduced thermal deoxygenation process, which can convert LA into energy dense cyclic and aromatic products characterised by a low oxygen-to-carbon ratio. These products can be easily refined to yield hydrocarbon fuels [100].

2.3 Oil palm biomass as an initial substrate

Biomass, which is essentially hydrocarbon-based, comprises elements such as carbon, hydrogen, oxygen, and nitrogen, along with trace amounts of sulphur and other inorganic substances [101]. Solid biomass waste from oil palm industry is generated in two primary ways: from oil palm plantations and palm oil extraction mills (**Figure 2.7**). The plantations produce waste in the form of harvested trunks and pruned fronds. The extraction mills generate waste such as oil palm empty fruit bunches (OPEFB), oil palm mesocarp fibre (OPMF), and palm kernel shells (PKS) [11]. The empty fruit bunches are a byproduct of the oil extraction process, which involves subjecting the fresh fruit bunches to pressurised cooking and stripping. OPMF, a fibrous material, is what remains after the extraction of palm oil from the mesocarp, the fleshy fruit pulp that surrounds the palm kernel [8]. Palm kernel shells are obtained through a process that separates the nut from its kernel [11].

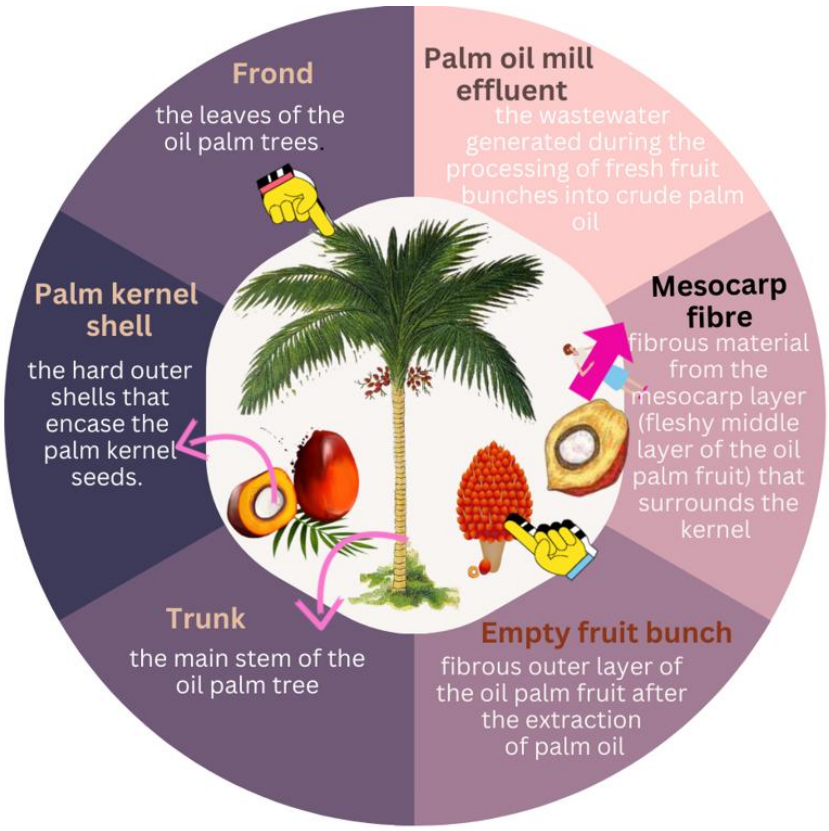

Figure 2.7 Types of oil palm (*Elaeis guineensis*) biomass.

2.3.1 Current availability

In Malaysia, OPMF is a significant component of the total oil palm waste, accounting for 11.6 million tonnes of dry weight [11]. Despite its abundance, OPMF is often left to decompose naturally [102]. This underutilisation, coupled with the lack of technology to fully exploit the remaining waste, exacerbates the problem of biomass overload.

Recognising the increasing amount of oil palm biomass waste, the Malaysian government launched the Economic Transformation Programme (ETP) in 2010. The ETP aims to transform Malaysia into a high-income nation by 2020 [103], with one of its critical factors being the improvement in the utilisation of oil palm biomass and its related industries [11].

OPMF, like other biomass wastes, is a form of lignocellulosic biomass consisting of significant organic components such as lignin, cellulose, hemicelluloses, extractives, and ash [104–106]. Although extractives and ash are minor components compared to the other three (**Figure 2.8**), they have their own important benefits. Extractives include fatty acids, proteins, waxes, and minerals [107]. In biomass, extractives are non-structural components that can be removed using solvents like water or ethanol [108]. Fats and waxes, which are long-chain hydrocarbons that can be saturated or unsaturated, are typically found in the outer layers of plant cells and can be used to produce valuable chemicals and materials such as adhesives, coatings, and bioplastics [108]. Extractives generally have lower thermal stability compared to the main structural components of biomass like cellulose and lignin, and they can volatilise or decompose at relatively low temperature [109].

Ash is an important component of non-combustibles in biomaterials. It helps predict and determine the distribution of yield percentages into solid, liquid, and gaseous products [110]. It has been proven that an increase in the ash content of biomass will increase the yield percentage of solid and gaseous products, while the liquid yield percentage will decrease [111]. Abnisa *et* al. [110] observed that oil palm leaves with higher ash content produced a lower bio-oil yield percentage and higher char and gaseous products. All these components are formed during photosynthesis, where CO_2 and sunlight are converted into chemical energy [112]. This chemical composition of OPMF, illustrated in **Figure 2.8**, differs from other types of oil palm biomass and can be influenced by factors such as topography, management practices, climate, and disturbances [113].

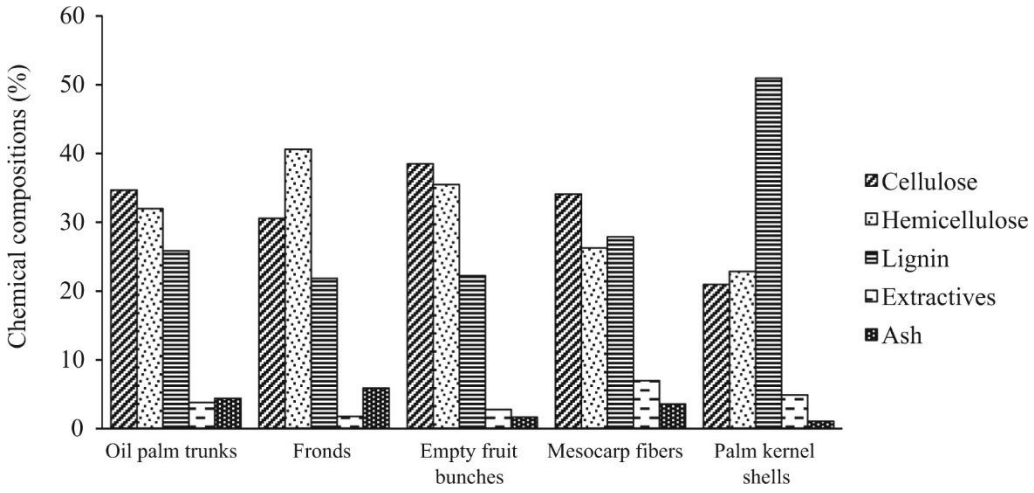

Figure 2.8 Chemical compositions of oil palm biomass. Reproduced with permission from Awalludin *et* al. [11].

OPMF is an appealing feedstock for large-scale production of LA due to its unique properties, sustainable characteristics, and relatively low costs [58]. The lower hemicellulose and lignin content in OPMF facilitates the selective conversion of cellulose to LA. Lignin acts as a chemical binder, impeding the separation of cellulose from hemicellulose and hindering the conversion of crystalline cellulose to amorphous cellulose [114]. In oil palm biomass, such as fronds and trunks, lignin has a higher content of guaiacyl (G) and syringyl (S) units [115], linked by various chemical bonds, including ether and carbon-carbon bonds. Lignin contains functional groups like methoxy, hydroxyl, and carbonyl, which influence its reactivity and interaction with other materials [116]. The molecular weight of lignin in palm biomass ranges from a few hundred to several thousand Daltons [117]. Lignin exhibits good thermal stability, suitable for high-temperature applications, with thermal degradation occurring between 200–500 °C [116]. It also has a relatively high glass transition temperature (T_g), usually between 90–180 °C [118],

depending on its purity and source. The efficient and eco-friendly utilisation of OPMF for LA production is a promising avenue that combines the goals of waste reduction, sustainability, and chemical production.

2.3.2 Surface accessibility

Cellulose-derived biomass accessibility is a challenge without pretreatment due to the dense packing of cellulose and hemicellulose by layers of lignin, caused by hydrogen bonding and chemical linkages [119–120]. This restricts catalyst access to cellulose, inhibiting the chemical conversion of biomass to LA [121].

α-cellulose and hemicelluloses together form holocellulose, the total polysaccharide fraction. α-cellulose, an insoluble polysaccharide, has a linear structure composed of β-D-glucopyranose units linked by β (1-4) glycosidic bonds [122]. It is divided into crystalline and amorphous regions, as depicted in **Figure 2.9**. The crystalline region, highly organised with tightly packed chains forming intermolecular hydrogen bonds, gives cellulose its high tensile strength [123], makes it water-insoluble [124], and provides resistance to degradation [125–126]. Each glucose unit in cellulose contains three hydroxyl (–OH) groups: two on one side (2–OH and 3–OH) and one on the opposite side (6–OH).

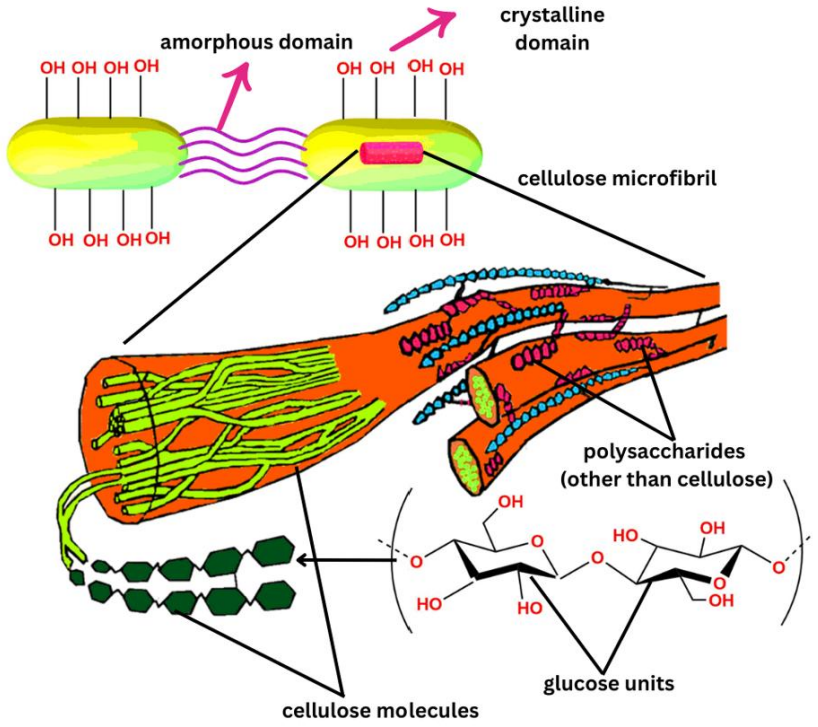

Figure 2.9 Structure of cellulose microfibrils.

Surface accessibility significantly influences cellulose hydrolysis. The amorphous regions, though linked to cellulose crystals, lack lateral stabilisation through H-bonding, making them more accessible for bonding with other molecules, including water, and increasing accessibility to acid catalysts or chemicals [127]. Meanwhile, hemicellulose (**Figure 2.10**), unlike cellulose, consists of various sugar units, including arabinose, xylose, mannose, glucose, and galactose [112]. It has a complex, branched structure of polysaccharides with a general formula of $(C_5H_8O_4)_n$ (**Figure 2.10)**. Despite its complexity, hemicellulose, which includes beta (β) and gamma (γ) cellulose [128], is more readily hydrolysed compared to cellulose due to its shorter and less rigid structure in the amorphous region [129–130].

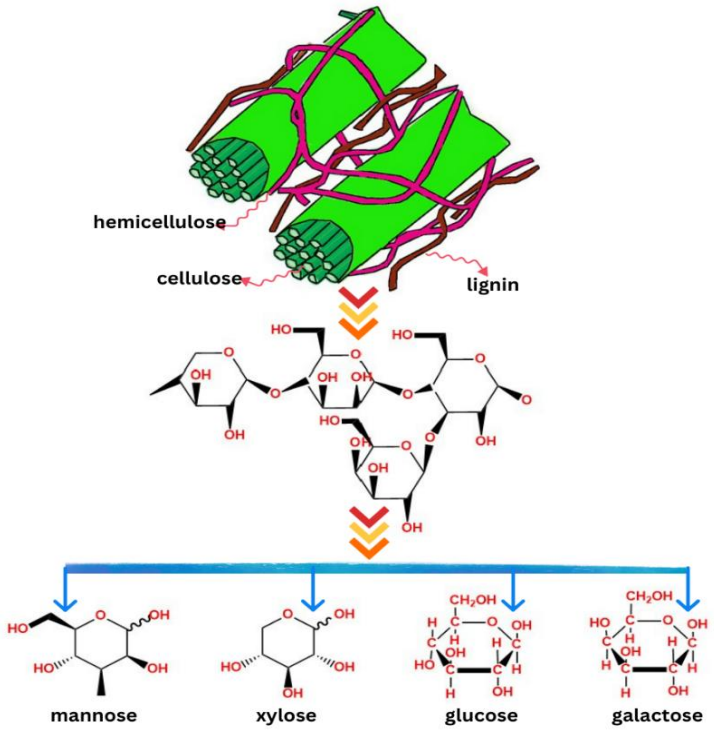

Figure 2.10 Repeatable sugar units that are mostly found in the hemicellulose.

Hemicellulose, due to its branching nature, serves as a “glue” that binds cellulose fibres together, thereby enhancing the overall strength and cohesion of the cell wall. Isolating hemicellulose from cellulose becomes crucial for enhancing cellulose hydrolysis. A variety of pretreatment methods are employed to facilitate this process, which involves increasing cellulose accessibility by removing hemicellulose and lignin. These methods encompass physical, mechanical, and chemical approaches such as milling, grinding, alkali treatment, oxidising agents, and the use of organic solvents, extending beyond the conventional use of dilute or concentrated acid [131–133].

Comminution, involving chipping, grinding, dry, wet, and vibratory ball milling, as well as compression milling, is utilised to facilitate material handling in

subsequent processing steps [134]. The dimensions of materials typically range from 10 to 30 mm after chipping and decrease to 0.2 to 2 mm after milling or grinding [135]. The energy consumption for size reduction during mechanical comminution depends on the final particle size, and it has been suggested that maintaining a particle size range of 3−6 mm can keep the energy input below 30 kWh per tonne of biomass [136]. Another technology using γ-ray irradiation has been tested for cleaving β-1,4-glycosidic bonds of cellulose, resulting in a larger surface area and lower crystallinity [137], making cellulose more accessible, but it is considered too expensive for full-scale processes [138].

Microwave pretreatment is a technique that is commonly employed in contemporary research and is often integrated with various other treatment methods [139–142]. This technique efficiently converts electromagnetic energy into heat, causing the fibres to rupture and facilitating the degradation of lignin, loss of hemicellulose, and disruption of cellulose ultrastructure. This process allows solvent particles to penetrate the innermost parts of the fibres, thereby enhancing biomass digestibility [130].

Table 2.1 provides a summary of the current state of oil palm biomass treatment using solvolysis in combination with microwave technologies. Solvolysis breaks down lignocellulosic components (lignin, cellulose, and hemicellulose) into low molecular weight compounds [11]. This process can be conducted in organic solvents at temperatures ranging from 120–180 °C with the presence of a catalyst (base or acid), or at higher temperatures ranging from 180 to 250 °C without a catalyst. These relatively low-temperature conditions are energy-efficient, produce fewer pollutants, and are more cost-effective compared to other thermochemical

processes like pyrolysis or conventional heating. Depending on the end yield requirements, solvolysis can be carried out under atmospheric pressure or higher [143–144]. As Liu and Zhang [145] have noted, conducting solvolysis at relatively low temperatures can prevent the formation of tar compounds that result from cross-linking between hydrocarbon and aromatic compounds.

With technology advancements, novel solvents such as ionic liquid and deep eutectic solvents have been explored for biomass dissolution. It is important to identify the best solvent properties for biomass dissolution without compromising economic viability. As indicated in **Table 2.1**, most oil palm biomass is commonly treated either with acid or NaOH for product isolation. However, when cellulose is extracted from biomass in a separate pot before its hydrolysis to simple sugars, the crystallinity of cellulose may increase [146–147]. This is because the extraction process often involves the removal of amorphous regions of cellulose, leaving behind the more crystalline regions [148–149]. This can enhance the purity of the cellulose [146–147]. But losing amorphous cellulose during the pretreatment step could reduce the conversion rate of cellulose to glucose and limit LA yield. Furthermore, using extracted pure cellulose requires more effort to break down the recalcitrant structure of cellulose in the second step of conversion process. Instead, combining the pretreatment strategies with the conversion process in a one-pot reaction could potentially facilitate in-situ fractionation and bond loosening, concurrently aiding in the hydrolysis of both amorphous and crystalline cellulose [150–152].

Table 2.1 Lignocellulosic components of oil palm biomass are extracted following alkaline or acid pretreatment using a microwave-assisted method.

Feedstock	Reaction conditions	Size of biomass particles	Solvent to biomass ratio	Solvent	Cellulose (%)	Hemicellulose (%)	Lignin (%)	Reference
OPT	80 °C, 60 min	< 1 mm	10:1	2.5 M NaOH	71.88	11.77	15.13	[153]
OPF	80 °C, 60 min	< 1 mm	10:1	2.5 M NaOH	68.86	11.84	16.94	[153]
OPEFB	12 min, 180 W	1-2 mm	10:1	3 % NaOH (*w/v*)	24.50[a]	24.50[a]	74.00	[154]
OPEFB	110 °C, 80 min, 900 W	< 1 mm	10:1	Soaked in 8% H_2SO_4 (*v/v*), 2.5 N NaOH	85.40	3.50	5.30	[155]
OPF	80 °C, 60 min, 700 W	< 1 mm	10:1	2.5 M NaOH	42.86	54.54	0.90	[156]
OPEFB	12.5 min, 550 W	40-60 mesh	20:1	Glycerol + 1 % H_2SO_4 (*v/v*)	43.75	26.22	17.35	[157]
OPEFB	180 °C, 2.5 min, 195 rpm	40-60 mesh	10:1	1 % oxalic acid (*w/v*)	13.88	72.06	25.26	[158]
OPEFB	190 °C, 3 min	40-60 mesh	10:1	1.1 % oxalic acid	41.23	26.55	23.62	[159]

[a] The percentage of cellulose or hemicellulose are counted as a part of holocellulose component.

2.3.3 Low concentration

In an aqueous solution, the concentration of raw biomass used for LA production typically ranges from 100 to 200 g L^{-1}. However, due to the presence of lignin and hemicellulose, the initial concentration of hexoses (derived from cellulose) in the reaction solution is lower, usually between 50 to 100 g L^{-1} [3].

One LA molecule (with a molecular weight of 116 g mol^{-1}) is produced from one hexose molecule (with a molecular weight of 180 g mol^{-1}). This means that the theoretical yield of LA from hexoses is 64.4 wt%. However, the actual yield of LA from raw biomass typically only reaches 50 to 60% of this theoretical yield [160–162]. After the reaction, the LA concentration is approximately 16 to 40 g L^{-1}, regardless of any changes in solvent volume.

Zheng *et* al. reported that LA concentration achieved through the $FeCl_3$ catalytic conversion of corn stalk was 16.14 g L^{-1} [163]. The low LA concentration leads to relatively higher costs in downstream processing. This suggests that direct hydrolysis of raw biomass may not be the most efficient method. However, the use of an improved catalytic system can enhance the yield of LA. Specifically, the properties of an acid catalyst, such as surface area, porosity, acidity, chemical changes [24, 164], as well as its potential for efficient recycling over multiple cycles, can significantly maximise the catalytic activity and improve the yield, thereby contributing to cost efficiency. Therefore, a comprehensive study of the performance of solid acid catalysts is crucial. This includes a critical examination of their efficiency, reusability, kinetic and thermodynamic properties. Additionally, a thorough analysis of the economic and environmental costs associated with these

catalysts is necessary. The ultimate goal is to optimise the conversion of biomass to LA, making it not only more favourable but also scalable for industrial applications.

2.4 Catalytic system for biomass conversion to LA

Biomass conversion to LA without a catalyst gave feeble LA yield (1–7%) and selectivity (10–16%) under mild conditions (130–180 °C, 3–8 h) [160, 165–167]. Therefore, the addition of acid catalysts is a mandatory step to feasibly convert the biomass to LA.

2.4.1 Emergence of solid bifunctional catalyst

Bifunctional catalysts, which catalyse two distinctive reactions simultaneously, are created by incorporating Lewis acids into Brønsted-Lowry acids [31]. These catalysts can exist in both homogeneous and heterogeneous systems. However, heterogeneous bifunctional solid acid catalysts are particularly promising for sustainable LA production. Their properties can be tailored to specific needs, and they can be more easily recovered upon recycling.

The formation of a bifunctional catalyst through the coupling of Brønsted-Lowry and Lewis acids not only combines two distinctive reactions but also technically alters the structural properties of the two acid centres. This significantly affects the catalytic behaviour of the system. Moreover, this coupling provides a rich amount of pronucleophiles and electrophiles in the reaction medium [168], initiating a vast amount of polar addition reactions (**Figure 2.11**), such as in isomerisation and hydration steps, which are beneficial for the catalysis.

Despite the wide range of total acidity that can be obtained from different types of bifunctional catalysts, there is a lack of critical discussion in the literature on the interplay between Brønsted-Lowry and Lewis acids [31]. This interplay is linked to the synergistic effect of the catalyst during biomass conversion to LA. It is crucial to find a suitable concentration ratio of Brønsted-Lowry acid to Lewis acid that provides a selective amount of acid sites sufficient for effectively catalysing the tandem reactions. It is important to note that the resulting synergistic efficiencies greatly depend on the nature of the catalyst [31]. This includes the ratio of Brønsted-Lowry acid to Lewis acid, the individual and total acidity strengths, and the physicochemical properties of the catalysts, such as surface area, volume of porosity, and size of pores [31, 168].

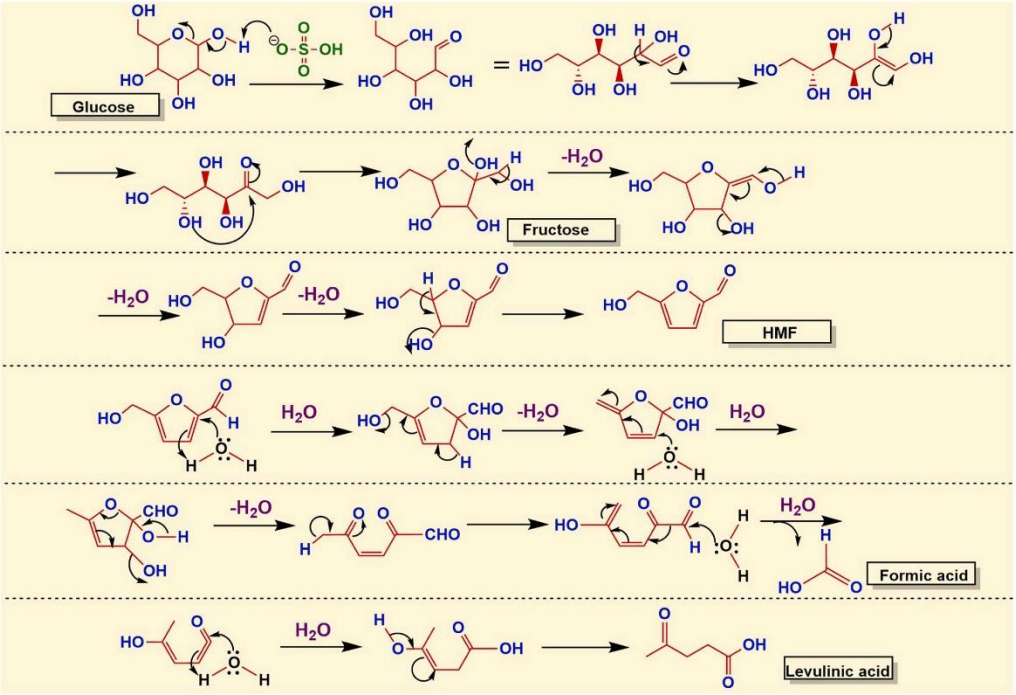

Figure 2.11 Polar addition reactions. Reproduced with permission from Badgujar *et* al. [168].

2.4.1.1 Phosphotungstic acid

Heteropolyacids (HPAs), including tungsten-based heteropolyacids, are novel catalysts possessing both Brønsted and Lewis acid sites [169–170]. They are often preferred for acid-catalysed reactions due to their exceptional acidic strength and thermal stability, especially among the Keggin-type HPAs [170]. Key tungsten based HPAs, each with different central heteroatoms, include phosphotungstic acid ($H_3PW_{12}O_{40}$), silicotungstic acid ($H_4SiW_{12}O_{40}$), borotungstic acid ($H_5BW_{12}O_{40}$), and aluminotungstic acid ($H_5AlW_{12}O_{40}$).

$H_3PW_{12}O_{40}$ is widely used commercially due to its high-water solubility, which allows for a high concentration of H^+ ions in an aqueous medium. These ions interact with the oxygen atoms on the ether linkage of cellulose to initiate the reaction (**Figure 2.12**). However, practical reaction conditions of high temperature and prolonged time can lead to by-reactions, such as the production of humins, which significantly reduce the LA yield and deactivate the catalyst. To address this, HPAs can be transformed into heterogeneous catalysts by exchanging protons with metal ions [171–172] or by supporting them on suitable materials like zeolites, metal oxides (e.g., Nb_2O_5, MoO_3), clay, and resin. This enhances their thermal stability, surface area, and acidity, generating more active and selective catalytic sites [173].

Although a specific combination of phosphotungstic acid with metal oxide like niobium oxide for hydrolysis of biomass to LA has not yet been explored, its effectiveness in the selective conversion of alpha and beta-pinenes into valuable terpenes [174] was proven. The niobium oxide coated on superparamagnetic iron oxide nanoparticles (SPION) impregnated with phosphotungstic acid demonstrated

high conversion efficiency (80–100%) and selectivity (50% for camphene and limonene) with low production of polymeric byproducts (18–28%) [174]. The catalyst could be easily recovered with a magnet and reused for up to five cycles while maintaining similar activity and distribution of products [174]. The SPION covered with 30 wt% of Nb_2O_5 gave the best performance when impregnated with $H_3PW_{12}O_{40}$ as co-catalyst [174].

Following this, the combination of phosphotungstic acid and niobium oxide could potentially be a strong candidate for enhancing the conversion of biomass to LA. This is despite their already proven success in other reactions, including the preparation of indole derivatives, benzylation, Friedel–Crafts acylation, regioselective ring opening of epoxides, esterification, and hydroamination [173, 175–179]. These synergistic effect of these catalysts in these reactions could potentially be leveraged for biomass conversion to LA.

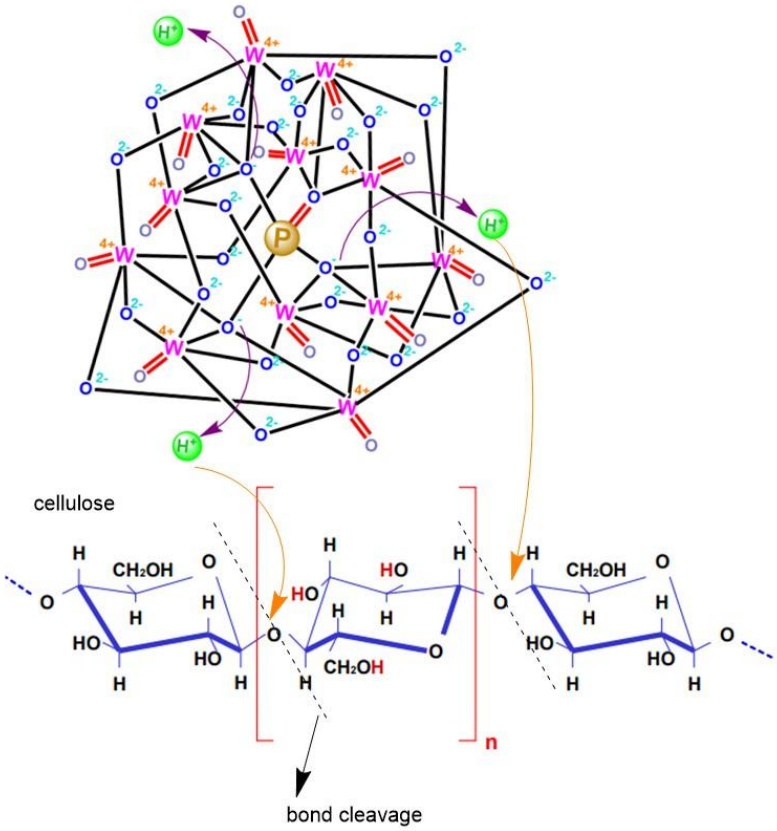

Figure 2.12 Structure of phosphotungstic acid. High concentrations of H^+ ions attack the glycosidic bonds of cellulose.

Metal-exchanged HPAs can be divided into two groups: Group A includes HPAs with protons exchanged with small metal ions like Na^+ and Cu^{2+}, which have low surface area, high water solubility, and the ability to absorb polar or basic molecules in the solid bulk. In contrast, Group B comprises HPAs containing large metal ions like Cs^+, characterised by high surface area, water insolubility, and an inability to absorb molecules [170]. Certain HPA salts of metal ions (M^{n+}) of $PW_{12}O_{40}^{-3}$ ($M_{3/n}PW_{12}O_{40}$) exhibit Lewis acidity (**Figure 2.13**), originating from the metal cation as an electron pair acceptor, in addition to the characteristic Brønsted

acidity of HPAs generated from the dissociation of coordinated water under the polarising effect of the cation [180–184].

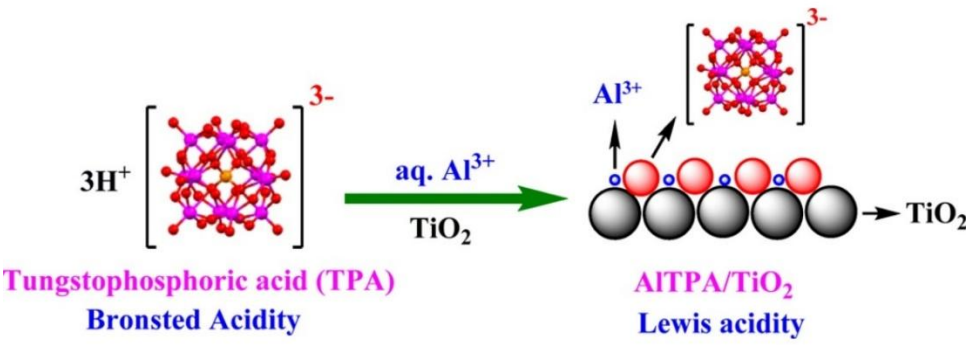

Figure 2.13 The incorporation of TiO_2 Lewis acid into tungstophosphoric acid. Reproduced with permission from Kumar *et* al. [170].

$H_3PW_{12}O_{40}$ has been modified with organic groups to improve its amphiphatic characteristic. As Brønsted-Lowry acidity is associated with hydrophobicity and Lewis acidity is associated with hydrophilicity, the tuning of amphiphatic characteristic is expected to produce a synergistic effect, enhancing the selectivity to LA. In particular, the amphiphatic characteristic is associated with a temperature-responsive property, which can enhance cellulose solubility in a homogeneous system, ease the catalyst separation in accordance with its changes in physical state, and improve catalytic power [167, 185–187].

In recent studies, several types of surfactants, such as quaternary ammonium salt and ionic liquid, have been added to $H_3PW_{12}O_{40}$ to promote its amphiphatic characteristic. Cheng *et* al. introduced the amphiphatic $[C_{16}H_{33}N(CH_3)_3]H_2PW_{12}O_{40}$ catalyst, derived from $H_3PW_{12}O_{40}$ and the quaternary ammonium surfactant (cetrimonium bromide), for starch conversion [185]. This

catalyst boosted the glucose yield up to 82.4% and could be separated from starch directly after washing with hot water and undergoing filtration, reflecting its temperature-responsive property. The catalyst also maintained its catalytic activity over several cycles.

In another study, Sun *et* al. developed the amphiphile [MIMPSH]H_2PW catalyst, formed from the combination of MIMPSH ionic liquid and $H_3PW_{12}O_{40}$, for cellulose conversion [186]. However, only 36.0% of glucose yield was obtained. The authors claimed that more glucose could have been converted to LA with extended reaction time, as a high LA yield of 63.1% was evident. Recently, Li *et* al. [188] improved the $H_3PW_{12}O_{40}$ catalytic system by employing both cellulose and glucose conversions in a green emerging DES (γ-valerolactone, GVL) solvent, producing an excellent LA yield of > 85%. However, when combined with ionic liquid groups, the $H_3PW_{12}O_{40}$ catalyst did not show its recycling behaviour corresponding to temperature-sensitive conditions, so separation of the catalyst from the products was employed by alcoholic solvent (such as ethanol) extraction.

On the other hand, the acidity of $H_3PW_{12}O_{40}$ can be tailored by integrating O_2- species in the polyanion with a metal Lewis acid or supported metal Lewis acid. The addition of Lewis metal ions promotes the uniform distribution of Lewis acid sites throughout the surface of the catalyst, improving the accessibility of substrate to the catalyst for glucose isomerisation. Furthermore, substitution of one proton of $H_3PW_{12}O_{40}$ by a solid acid cation (such as Cs and Sn) has improved their performance over several cycles without losing catalytic activity [189] and promoted cellulose conversion. Nonetheless, this modified $H_3PW_{12}O_{40}$ is not selective for LA [190]. Zhang *et* al. investigated the conversion of cellulose to LA

in the MIBK/water system (9:1) via $H_3PW_{12}O_{40}$ coupled with Lewis metal cations, including Ti^{4+}, Cu^{2+}, Sn^{4+}, Zr^{4+}, Zn^{2+}, Fe^{3+} and Cr^{3+} cations [167]. The Lewis acidity increases in the order of $H_3PW_{12}O_{40}$ (0.03 mmol g^{-1}) < $ZnH_3PW_{12}O_{40}$ (0.21 mmol g^{-1}) < $ZrH_3PW_{12}O_{40}$ (0.25 mmol g^{-1}) < $SnH_3PW_{12}O_{40}$ (0.32 mmol g^{-1}) < $CrH_3PW_{12}O_{40}$ (0.40 mmol g^{-1}) < $CuH_3PW_{12}O_{40}$ (0.41mmol g^{-1}) < $TiH_3PW_{12}O_{40}$ (0.56 mmol g^{-1}) < $FeH_3PW_{12}O_{40}$ (0.58 mmol g^{-1}), while the Brønsted-Lowry acidity decreases in the order of $H_3PW_{12}O_{40}$ (1.75 mmol g^{-1}) > $TiH_3PW_{12}O_{40}$ (1.59 mmol g^{-1}) > $CuH_3PW_{12}O_{40}$ (1.52 mmol g^{-1}) > $SnH_3PW_{12}O_{40}$ (1.22 mmol g^{-1}) > $ZrH_3PW_{12}O_{40}$ (1.14 mmol g^{-1}) > $ZnH_3PW_{12}O_{40}$ (1.12 mmol g^{-1}) > $FeH_3PW_{12}O_{40}$ (0.57 mmol g^{-1}) > $CrH_3PW_{12}O_{40}$ (0.54 mmol g^{-1}). Among the couplings, $FeH_3PW_{12}O_{40}$ and $CrH_3PW_{12}O_{40}$ gave exceptionally low LA yields (29.9% and 28.5%, respectively) owing to their low Brønsted-Lowry acidity and the resulting low total acidity (0.15 mmol $g^{-1}$and 0.94 mmol g^{-1}, respectively) [167]. It is also noted that all the LA yields obtained (28.5–65.6%) were higher than those from parent HPAs such as $H_3PW_{12}O_{40}$ (11.3%), $H_4SiW_{12}O_{40}$ (18.6%) and $H_5BW_{12}O_{40}$ (17.2%) as well as H_2SO_4 (18.4%), indicating that modifications of HPAs-type catalyst with extrinsic Lewis acid also influence the amphiphatic factor. Excess addition of Lewis acid decreases the Brønsted-Lowry acidity, altering the ratio of Brønsted-Lowry acidity to Lewis acidity (B/L), and decreases the total acidity significantly, thereby reducing the overall performance. Brønsted-Lowry acid still plays a primary role in dictating the overall catalytic performance.

2.4.1.2 Niobium oxide

Niobium-based catalysts, specifically $Nb_2O_5 \cdot nH_2O$ (NbO) and $NbOPO_4 \cdot nH_2O$ (NbP), are renowned for their efficiency as solid acid catalysts. They exhibit water tolerance and strong acidity, making them ideal for various acid-catalysed reactions [191]. Both NbO and NbP feature Brønsted and Lewis acid sites, but NbP has a higher ratio of Brønsted acid sites to Lewis acid sites compared to NbO [192–193]. In niobic acid, the surface Nb-OH functions as Brønsted acid sites, while unsaturated coordinated Nb^{5+} serves as Lewis acid sites [194].

Unlike typical solid acids, niobium-based catalysts maintain operational Lewis acid sites on their surface even in an aqueous medium [193]. Their robust acid properties and unique water tolerance make them ideal for water-involved reactions, particularly in sugar and polysaccharide conversions [195–196]. Recently, there has been a surge in interest in niobium compounds and related materials for catalysis, especially as solid acids, demonstrating effectiveness in heterogeneous reactions involving water, such as hydration, hydrolysis, isomerisation, epoxidation, or esterification [197].

Amorphous Nb_2O_5, known for its high surface acidity and numerous surface defects, is frequently studied. However, it is susceptible to fragility and changes in temperature and pressure [198–199]. The crystalline phases of Nb_2O_5 (**Figure 2.14**), formed by distorted octahedra (NbO_6) connected by edges and corners, exhibit varied textural and structural stabilities due to polymorph structure-dependent distortion [198, 200–201].

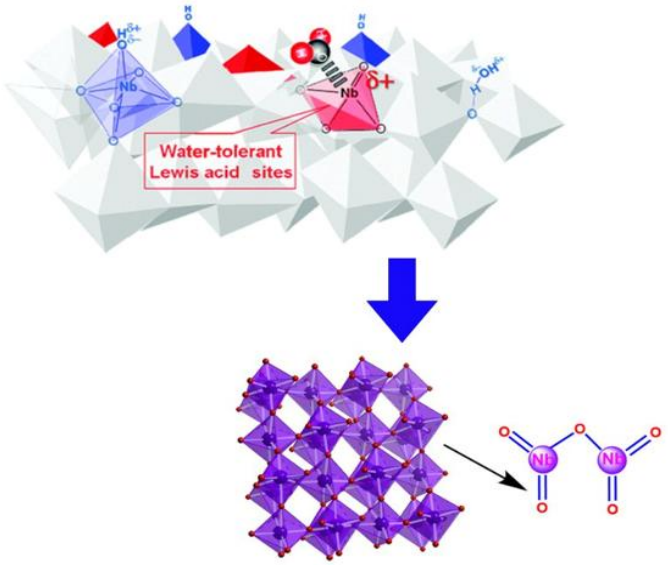

Figure 2.14 Structure of niobium oxide in crystallite form.

In hydrothermal synthesis, elevating both temperature and pressure initiates a sequential transformation of Nb_2O_5 phases: from the amorphous Nb_2O_5 state to TT-Nb_2O_5 (**Figure 2.15)**, further transitioning to T-Nb_2O_5, and ultimately resulting in the formation of H-Nb_2O_5 [198, 201–202]. Among these phases, TT-Nb_2O_5 presents the highest number of oxygen vacancies, leading to significant polyhedral distortion, which translates into highly polarised and disordered surface rich in Lewis and Brønsted acid sites, crucial for superior hydrodeoxygenation catalyst performance [203].

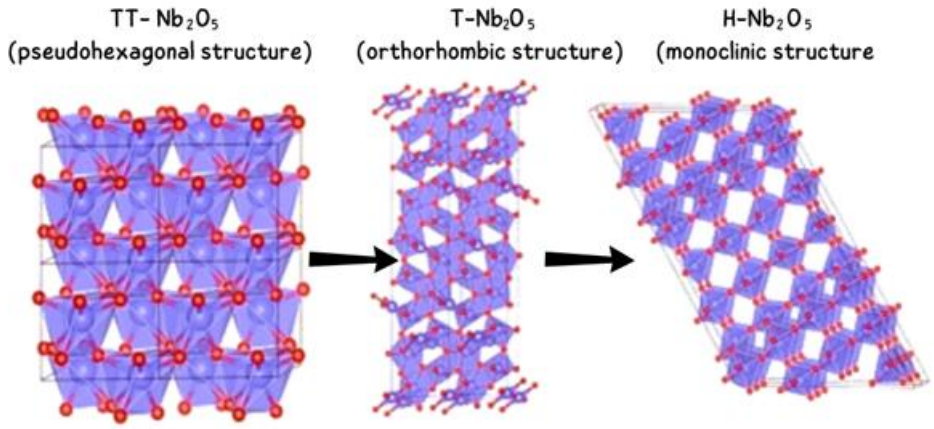

Figure 2.15 Different phases of Nb_2O_5 that can undergo transformations during chemical reaction.

Recent research has highlighted the significance of Nb-based solid acids, such as Nb_2O_5 [193], Nb_2O_5-supported metals (Ru, Pd, Pt, Ni) [203–207], niobium phosphate ($NbOPO_4$) [208], and NbAlS-1 [209], in catalytic cleavage of C–O bonds in lignin or lignin model compounds. These catalysts, particularly NbOx species, facilitate C–O bond cleavage and dehydration due to the unique electronic and energy band structure of Nb_{5c} [210]. In Nb_2O_5, niobium adopts a d^0 configuration, where the d-electrons are transferred to the O 2p-orbital, rendering the d-orbital empty. The highest metal ion oxidation state features unoccupied d-orbitals, fostering metal binding to an electron in a localised state akin to O 2s [210].

A detailed study by Liu *et* al. compared the performance of Fe-NbP (Fe-doped niobium phosphate) with Nb_2O_5 in the production of LA and HMF [211]. They found that Fe-NbP, boasting higher total acid density (3.59 mmol g^{-1}) and an appropriate Brønsted/Lewis acid ratio (1.32), exhibited superior activity, yielding 64.2% LA and 11.8% HMF at 180 °C in 3 h. In contrast, Nb_2O_5 produced only 17.7% LA and 26.8% HMF, attributed to its lack of Brønsted acid sites (B/L molar

ratio: 0.08), rendering it inactive for glucose-fructose isomerisation and fructose dehydration [64].

Yang *et* al. explored a mixed acid catalyst using H_3PO_4-modified Nb_2O_5 (NA-p) in a biphasic water/2-butanol system, achieving a 49.0% HMF yield at high temperature [212]. Nowak *et* al. studied glucose dehydration over various catalysts and found that HMF selectivity depended on the ratio of Brønsted and Lewis acid sites. Despite niobium-based materials being explored in water-tolerant solid acid catalysis, detailed reports on tuning acid types and surface distribution are lacking [202].

Additionally, the choice of feedstock materials can influence LA selectivity. Wang *et* al. achieved 100% conversion at 120 °C for 120 min in DMSO, yielding 86% HMF when fructose was directly dehydrated to HMF over Nb_2O_5 [28]. Gao *et* al. increased niobic acid's surface area by preparing ordered mesoporous carbon doped with Nb_2O_5 (OMCN), obtaining complete fructose conversion and 76.5% selectivity to HMF in DMSO at 120 °C for 2 h [213]. García-Sancho *et* al. discovered that Nb_2O_5 supported on SBA-15 efficiently catalysed the dehydration of D-xylose to furfural, with 93% selectivity after reacting at 160 °C for 24 h in a water/toluene biphasic system [214].

Considering recent studies, Nb_2O_5 exhibits high selectivity to HMF, suggesting the potential to increase LA selectivity if sufficient Brønsted acid sites are available to rehydrate HMF to LA. Therefore, a promising approach for LA synthesis involves combining an acid catalytic system by adding more Brønsted acid sites to Nb_2O_5.

2.4.2 Carbon-based catalyst support

Carbon-based catalyst supports have emerged as a significant component in the development of bifunctional catalysts, such as heteropoly acid and niobium oxide. These supports enhance the performance of the catalysts by providing a high surface area for the active sites, improving the dispersion of the active species, and facilitating electron transfer [215–216].

Recently, carbon-based catalysts derived from graphene oxide (GO) have been sulphonated with sulphonic acid to form SO_3H functionalised carbon catalysts for the conversion of sugar to LA [217]. In the first version, GO, which has a high density of hydrophilic functional groups including hydroxyl, carboxyl, and epoxy groups, was sulphonated to incorporate Brønsted-Lowry acid sites, forming GO–SO_3H. The synergistic effects arise from the interaction between surface hydroxyl groups of GO and Brønsted-Lowry acid sites in the GO–SO_3H. This interaction resulted in a significantly higher LA yield of 78% than that of GO alone (13%) under mild reaction conditions (200 °C, 2 h), implying higher activities of hydrolysis of glucan to glucose, glucose isomerisation and fructose decomposition.

To improve upon GO–SO_3H, sulphonated activated carbon (AC–SO_3H) was designed to impart higher total acidity (3.8 mmol g^{-1}), higher SO_3H density (2.5 mmol g^{-1}), and larger BET surface area (753 $m^2 g^{-1}$) [217]. However, AC–SO_3H yielded an unexpectedly low LA yield of 4.2%, apparently due to the unfavourable structures and inappropriate ratio of Brønsted-Lowry acid sites to Lewis acid sites. AC–SO_3H exhibited lower hydrophobicity index (1.64) than that of GO–SO_3H (2.54), implying fewer Brønsted-Lowry acid sites for the adsorption of substrates

amenable for the catalytic reaction [217]. Excessive Lewis acid sites in the AC–SO_3H catalyst also may aggravate the activity of Brønsted-Lowry acid sites that are essential for the formation of HMF and LA, thereby reducing the LA yield.

On the other hand, the cellulase-mimetic catalyst (CMC) derived from a sucralose precursor is an emerging solid acid catalyst. It contains superlative binding domains (−Cl) that can effectively attack the glycosidic bonds [34] of carbohydrates feedstock, as well as SO_3H groups that allow the synergistic effects of the subsequent tandem catalytic system. The catalyst is particularly designed for cellulose conversion to LA in a pure water system, which is otherwise limited by the insolubility of both substrate and catalyst. CMC possesses an excellent mesoporous structure with a high BET surface area ($482\ m^2\ g^{-1}$) and large mesoporous volumes ($0.47\ cm^3\ g^{-1}$), producing a moderate LA yield of 46% (at 180 °C, 15 h) [34]. Meanwhile, the CMC catalyst derived from the sucrose precursor showed a slightly lower total surface area ($459\ m^2\ g^{-1}$) and the volume of mesopores ($0.40\ cm^3\ g^{-1}$), which was consistent with the lower LA yield obtained (only 11%) [34]. This suggests that the presence of −Cl groups as the binding domain plays an important role in the conversion reaction, presumably by facilitating the access of hydrolysed intermediates to the inner catalytic sites for the reaction to occur.

2.4.3 Evolution of carbon-based catalyst support: carbon cryogel

Carbon supports offer promising advantages in maintaining the structure of catalysts and enhancing their performance. However, several challenges need to be overcome when using carbon-based catalyst supports. One of the main issues is the oxidation of carbon at low potential, leading to the corrosion of the carbon support under

oxygen evolution conditions [218]. This corrosion is a significant cause of catalyst failure.

Another challenge is the high selectivity for carbon monoxide (CO) at high operating temperatures in bifunctional catalytic systems [219]. Addressing this issue is crucial to enhance the yield and selectivity of LA. Furthermore, carbon-based catalysts often exhibit poor stability, low activity, and selectivity [220], which need to be tackled to improve their efficiency.

To address these problems concurrently, carbon cryogel, with its tuneable properties, has been introduced. Carbon at low potential can be overcome by using special precursors like lignin, which is resistant to both biotic and abiotic stresses [221]. It is resistant to strong acids, making plant cell walls durable and impermeable to harsh conditions [222]. Carbon cryogel also exhibits a high crosslinking density, which can help resist oxidation, such as being crosslinked with xanthan gum, due to its stable double helix structure.

Meanwhile, preparing carbon cryogel with certain additives can help reduce selectivity for CO at high temperatures. For instance, niobium-based alloys have been shown to have high-temperature oxidation resistance [223]. The higher the niobium content, the better the high-temperature oxidation resistance [224]. This suggests that the incorporation process can alter the reaction pathways and improve the selectivity towards the desired LA product.

Carbon cryogels, with their high cross-linking density and stable carbon-carbon bonds, are robust and resistant to structural collapse under reaction conditions [62]. Their stability can be further improved by introducing heteroatoms like phosphorus, strengthening the carbon framework [225]. The activity of these

catalysts can be enhanced by increasing the number of active sites, achievable through defect creation or heteroatom incorporation. These modifications improve the overall catalytic activity [220]. The selectivity of these catalysts can be improved by controlling the reaction environment, tuning the pore structure, and adjusting surface chemistry. For instance, creating a hierarchical pore structure enhances mass transfer and selectivity [62]. Incorporating phosphorus into tungsten-phosphoric acid can alter the catalyst's electronic properties and influence reaction pathways, thereby improving selectivity [220].

2.4.4 Insight into lignin-derived carbon cryogel

Lignin, is an ideal candidate for catalyst support due to its phenolic character, accessibility, biodegradability, and cost-effectiveness. It has been effectively utilised as a renewable carrier material for producing both metal-free solid catalysts [13, 21, 226–228] and lignin-immobilised metal catalysts. These lignin-derived catalysts offer several advantages, including high product efficiency, continuous operation, environmental cleanliness, and ease of separability [14, 229–232]. Unlike metal catalysts, which can be difficult to recover due to their small particle size and tendency to agglomerate, lignin supports offer an effective and recoverable platform for immobilising metal catalysts [233–236], thereby limiting the leaching of catalyst particles.

There is growing interest in lignin-derived catalysts, leading to extensive research into a specialised category of porous carbon materials known as carbon cryogels. These materials, which can exist as highly porous monolithic structures or powders (**Figure 2.16**), have garnered significant attention due to their well-

developed and controllable mesoporosity [237]. The typical structure of cryogels, as depicted in **Figure 2.17**, is obtained through the sol-gel method. This method involves the polycondensation of resorcinol with formaldehyde. It is a cost-effective and reproducible synthesis method initially introduced by Pekala [238] and has since been widely adopted by researchers [239–240]. This method enables the production of highly porous carbon cryogels with consistent characteristics, which are crucial for their practical use on a larger scale.

Carbon cryogels exhibit great potential for various applications, including catalyst supports [241–244], due to their customisable meso-nanostructure. However, their use for biomass hydrolysis remains limited. To date, only a few studies, such as those by Zainol and co-workers [164, 243–245], have attempted to use lignin-based cryogel for catalysing the esterification process. These studies used lignin-furfural and lignin-ILs precursors, demonstrating that a variety of other polymers can be crosslinked with lignin to form a 3D network gel.

Therefore, this study aims to review the synthesising parameters for carbon cryogel, taking into account the different precursors used. These precursors exhibit different properties and undergo chemical changes to form a strong crosslinking carbon cryogel. A more detailed understanding of theses parameters is particularly needed for lignin carbon cryogel, especially when it undergoes polycondensation with other types of polymers.

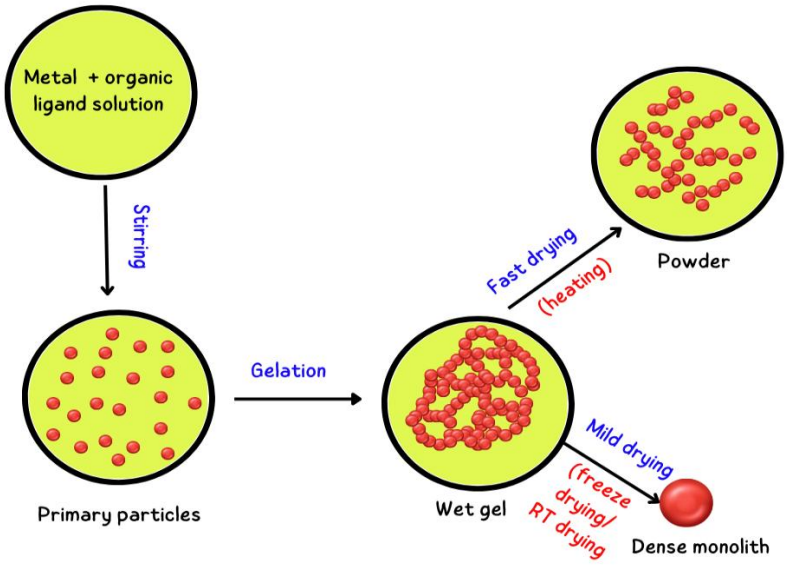

Figure 2.16 The existence of carbon cryogel in different forms.

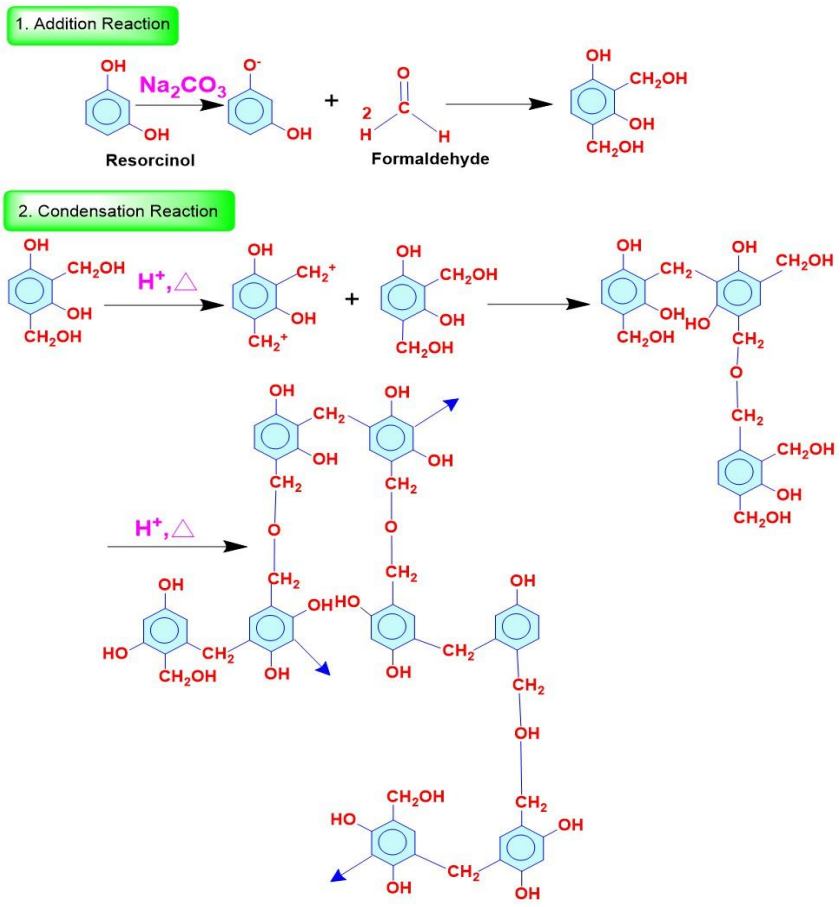

Figure 2.17 An example of the molecular mechanism that underlies the polymerisation of resorcinol with formaldehyde to form a cryogel. Reproduced with permission from Lin *et* al. [246].

2.4.4.1 Main precursors for cryogel formation

Lignin, a major precursor for cryogel formation, is used in the context of lignin-derived carbon cryogel as a catalyst support. The synthesis of carbon cryogel involves a wide range of precursors, including monomers, polymers, small molecules, biomacromolecules, nanostructures, and metal/ligand units [247]. These precursors bond with other monomers to initiate the growth of building blocks/polymers [248], forming interconnected 3D network structures (**Figure 2.18**)

and open channels for mass/charge transport. This structure is promising for catalytic applications, including carbons, oxides, and metals [248].

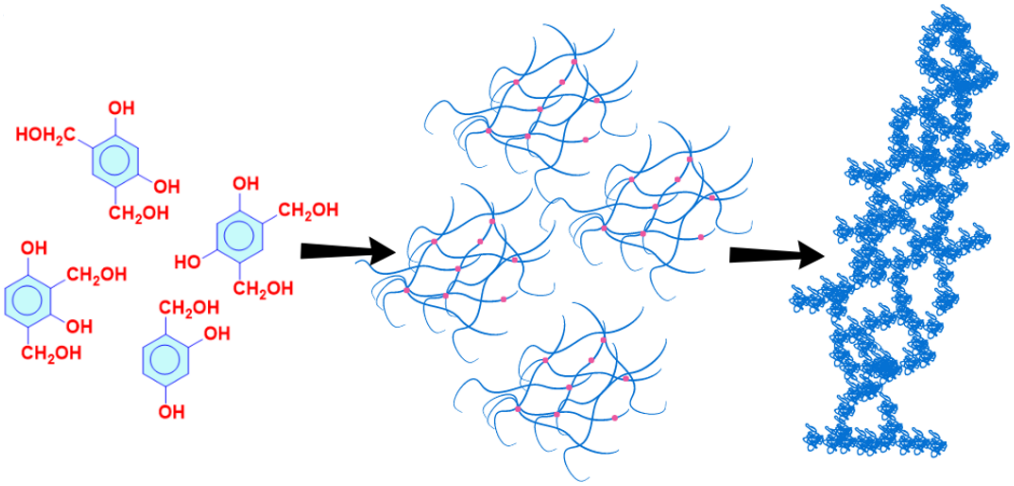

Figure 2.18 An example of cluster growth of resorcinol-formaldehyde monomers.

Despite being the second most abundant material in lignocellulose after cellulose [249–251], lignin has been underutilised in catalysis. Its applications have mainly focused on its role as a carrier or functional polymer in specific catalytic processes [21, 24, 29, 226]. This underutilisation may be due to its complex structure and heterogeneous characteristics. Lignin's heterogeneity arises from the presence of numerous functional groups, including aliphatic and aromatic phenols, carboxyl, ketones, and hydroxymethyl, among others [53]. These groups contribute to lignin's biocompatibility and hydrophobicity [252–253].

Lignin, the primary source of bio-polyphenols within lignocellulose (**Figure 2.19**), is composed of three phenylpropane units: coniferyl alcohol (G), sinapyl alcohol (S), and *p*-coumaryl alcohol (H). These units act as monomers in the lignin polymerisation process [254]. The arrangement and abundance of these phenylpropanoid units during lignin polymerisation determine the resulting lignin

type, structure and properties [254], with specific compositions varying depending on the plant species and tissue type. These units form a randomised 3D network structure through various bonds such as ether, ester, carbon-carbon, and methylene bridges [255–256]. The choice of lignin type is pivotal for gel synthesis, considering the availability of functional groups (**Table 2.2**) in lignin and its solubility [257].

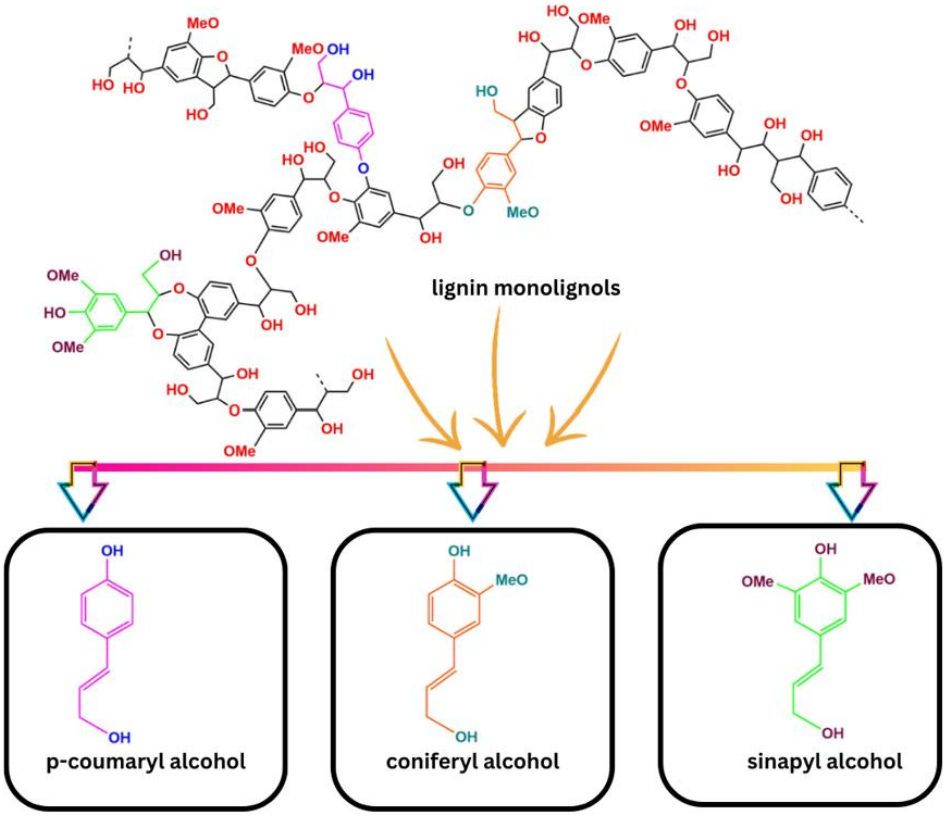

Figure 2.19 The complex structure of lignin that consists of repeatable units of monolignols.

Table 2.2 Characteristics of lignin.

Source	Pulp process	Lignin (%)	COOH (mmol g^{-1})	Phenolic OH (mmol g^{-1})	Total sugars
Softwood lignin	Sulphur-free	64.7	Nd	Nd	1.77
Softwood lignin (Curan 100)	Sulphate (Kraft)	96.8	2.00	2.50	0.71
Pine wood lignin	Sulphate (Kraft)	90.0	2.50	1.80	2.06
Aspen wood lignin	Steam explosion	>40.0	5.43	0.47	Nd
Lignin from annual plants	Sulphate (Kraft)	24.0-26.0	Nd	2.43	Nd

*Note: Nd = not detected

Technical lignin, mainly sourced from industries, includes various types such as kraft lignin, hydrolysis lignin, organosolv lignin, and pyrolytic lignin. These variants differ in composition and molecular weight based on the extraction methods employed [257]. Technical lignin is a valuable resource for various chemical productions. It contains essential aliphatic and aromatic hydroxyl groups, making it suitable for direct use as polyols in polyurethane production, with the potential to replace up to 30% of petroleum-based polyols [258]. However, its reactivity is somewhat limited compared to lignin fragments due to its complex structure. In contrast, depolymerised lignin fragments offer enhanced reactivity and can substitute up to 50% of petroleum-based polyols, thereby increasing availability and reactivity [259–260]. Depolymerisation can effectively reduce the branching and molecular weight of lignin, enhancing lignin solubility and biodegradability. This

process facilitates the creation of a more homogeneous lignin polymer network, which can further promote gelation.

Among technical lignin, Kraft lignin, also known as alkaline lignin, is a significant component for polymerisation due to its abundant and hydrophobic nature [261]. This lignin is approximately produced for 27,000 tonnes yearly [262]. Hydrophobic interactions can drive the self-assembly of monomers, leading to the formation of larger branched polymers. As the linking continues, at a certain extent of the reaction, links between the polymers result in the formation of a single macroscopic molecule [263–264]. This point in the reaction is defined as the gel point, where the system loses fluidity and viscosity becomes very large [263–264]. Therefore, high hydrophobicity can facilitate the formation of these cross-links and contribute to the polymerisation process during gelation, leading to the development of materials with solid-like mechanical properties [265–266].

The degree of condensation and the presence of aromatic ring structures in lignins are indicated by the number of double bond equivalents (DBE). Kraft lignin has a slightly higher DBE count than other technical lignins, which suggests a greater likelihood of severe cracking during the kraft pulping process [254]. This cracking is due to reactions between hydroxide, hydrosulphide, and lignin, leading to an increased number of double bonds in the structure of kraft lignin. The multiple carbon double bonds in kraft lignin can trigger the formation of a hydrogel in monomers by quickly spreading active sites [267].

Lignin monomers alone often form relatively weaker covalent bonds, making it challenging to achieve stable crosslinking [248]. As a result, previous studies have primarily focused on chemically modifying lignin with other polymers

as cross-linkers [260, 268–270]. To enhance mechanical strength, a dual approach that combines physical and chemical cross-linking within a single network has been adopted [271].

The addition of cross-links between polymer chains can significantly affect the physical properties of the polymer. Generally, there are 3 types of cross-linkers that have been tested, including natural and synthetic biopolymers as well as building block. Natural polymers present a compelling alternative to synthetic polymers in bio-catalysis due to their exceptional biocompatibility and biodegradability [272]. These polymers, characterised by high molecular weight compounds with linear long chains formed by repeating units, are abundant in various organisms, including polypeptides, proteins, chitin, alginic acid, starch, and agar [273–278].

In practical applications, cryogels must not only support their own weight but also withstand external forces [279–281]. However, conventional methods of preparing natural polymer-based cryogels often yield structures with poor mechanical properties, thus limiting their potential applications [282–283]. Consequently, enhancing the mechanical performance of these cryogels is imperative, driving recent efforts towards developing strategies to improve their stiffness, strength, and stretchability [284–287].

One noteworthy natural polymer is xanthan gum, also known as corn sugar gum, produced by the bacterium *Xanthomonas campestris* [288]. It is a high molecular weight and branched polysaccharide consisting of linear long chains composed of repeating units of mannose and glucose, with approximately 1.25% pyruvic acid content [289]. Structurally, xanthan gum features a main chain of

cellobiose duplicate units, stabilised against pH, temperature, and shear stress changes [290]. Additionally, its polymer backbone, like cellulose, includes β-d, 1,4 anhydroglucose repeat units, adorned with trisaccharide side chains that are affixed to C-3 on alternating rings [288]. These side chains include a D-glucuronic acid unit sandwiched between two D-mannose units [291], imparting a polyanionic character to the polysaccharide (**Figure 2.20**)

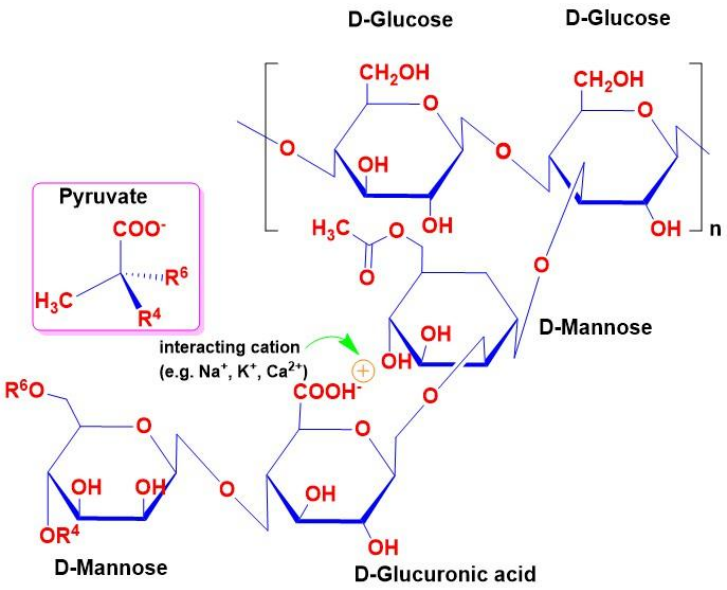

Figure 2.20 Structure of xanthan gum.

Other than natural biopolymer, synthetic polymers, derived from chemical reactions of small organic monomers, have been widely utilised in constructing cryogels. While these cryogels demonstrate strong water absorption and exceptional mechanical properties, their limited biodegradability and potential toxicity impose significant constraints on their applications. Among synthetic biopolymers, polyethylene glycol presents a more appealing alternative to dialdehydes due to their lower toxicity levels [292–293]. The molecular formula of polyethylene glycol is

$(C_2H_4O)_nH_2O$, where n denotes the average number of oxyethylene groups. The molecular weight can range from 200 to several million, corresponding to the number of oxyethylene groups [294].

The emergence of furfural as a potential building block and cross-linker has introduced an innovative approach for a poly-condensation reaction that yields furan resin, resulting in the formation of complex polymeric structures [295]. The interaction between lignin and furfural generates unique compounds, leveraging their abundance as biomass byproducts. This method enhances the sustainability of gel synthesis and broadens the potential applications of resulting materials.

Furfural, derived from agricultural products like crops and sugarcane, is a furan derivative with a highly reactive aldehyde group and conjugated double bond system [296–299]. This versatility allows furfural to participate in ring opening in its structure [300–302], making it useful in synthetic bio-composite materials with tannin [303–304] and lignin [305]. Additionally, furfural can participate in synthesising furan resin through poly-condensation reactions with lignin [24]. This results in linear oligomers with furan rings connected by methylene and methylene-ether bridges, forming intricate polymeric structures [295]. As a renewable resource derived from biomass, furfural offers sustainable solutions for gel synthesis, contributing to the development of eco-friendly materials and processes [306].

Zainol *et* al. synthesised carbon cryogels from lignin and furfural, demonstrating promising materials for esterification reactions [24]. These compounds, obtained from biomass processing, offer greener alternatives to more toxic chemicals historically used in gel synthesis, such as phenol or resorcinol and formaldehyde. By employing lignin and furfural, researchers aim to develop carbon

cryogels that can replace strong acid catalysts like H_2SO_4 in esterification reactions. This approach aligns with the growing emphasis on renewable resources and environmentally friendly practices in material science and engineering.

2.4.4.2 The role of cross-linking in carbon cryogel

Cross-linking strategies play a crucial role in shaping the molecular structures, morphologies, and properties of cryogels for catalytic applications. These strategies, which fall into two broad categories - noncovalent (physical) and covalent bonding (chemical), often involve a combination of multiple cross-linking methods to create functional cryogels. This allows for tailored interactions for specific catalytic applications [248]. Cross-linked polymer networks within hydrogels provide a unique morphology with hierarchical pores, serving as templates for diverse micro-/nanostructures of cryogel [248]. These interconnected mesoporous materials enhance catalytic binding sites, with the resulting high surface area facilitating surface reactions, including chemical reactions.

Multiple crosslinking methods can form either semi-interpenetrating networks or double network hydrogels [286, 307–308]. Unlike single networks derived from a single polymer, double network hydrogels comprise two interconnected polymeric networks [248]. The interpenetrating network hydrogel, a subtype of double network hydrogel, forms when a pre-cross-linked component with a linear molecular structure penetrates another cross-linked network. This interlocked structure results in a dense and compact matrix, significantly enhancing mechanical strength [309].

Table 2.3 describes the efficiency of lignin polymer as both a cross-linked unit and a cross-linker for various hydrogel applications. Catalyst application is the least explored area. Phenylpropane units of lignin linked by irregular C–C and C–O bonds possess charged functional groups like hydroxyl groups—both phenolic and aliphatic [310]. These groups enable lignin to bind water and other soluble substances through physical crosslinking driven by interactions like ionic interactions, hydrogen bonds, hydrophobic forces, or Van Der Waals forces, without requiring a crosslinking agent [311–312]. Relying solely on physical crosslinking can result in poor mechanical properties of cryogels, hindering their widespread applications [313]. Therefore, the emergence of double network or semi-interpenetrating network introducing cross-linking agent aims to establish a chemical crosslinking network with lignin monomers. This enhances the strength of covalent bonding and improves the strength of the initial hydrogel, subsequently enhancing the desirable properties and performance of cryogels. Furthermore, chemical crosslinking increases cryogel structure homogeneity [314].

Table 2.3 Role of lignin as biomass, a crosslinked unit and a crosslinking agent involve numerous types of crosslinking reactions.

Lignin role	Cross-linking type	Crosslinker	Lignin interaction	Matrix	Methods	Applicability	Ref.
Lignin as biomass	Non-covalent (physical)	N,N'-methylenebis(acrylamide) (NBMA)	H-bonding	Polymerised acrylamide	Copolymerisation	Water treatment for heavy metals	[315]
		-	H-bonding	Polyurethane	Sol-gel	Toughening component for cell culture studies	[316]
		Borax	H-bonding	Hydroxyethyl cellulose and polyvinyl alcohol	Sol-gel	Removal of heavy metals and dyes	[317]
Lignin as crosslinked unit	Non-covalent (physical)	Lignin	Electrostatic	Chitosan	Gelation, freeze drying	Scaffold in tissue engineering	[318]
	Covalent	Formaldehyde	Chemical	Phenol/lignin/ formaldehyde Lignin-tannin-formaldehyde	Self-crosslinking by blending	Not stated	[319]
		Glutaraldehyde	Chemical	Lignin-phenol-resorcinol	Copolymerisation	Catalysts, adsorbents	[320]
		Polyamine	Chemical	Lignin and epoxy resin	Self-crosslinking by blending, thermal treatment	Not stated	[321]
		Epichlorohydrin	Chemical	Lignin	Gelation	Not stated	[322]

		Epichlorohydrin	Chemical	Cellulose and lignin	Thawing, thermal treatment	Controlled release systems	[323–324]
		Epichlorohydrin	Chemical/H-bonding	Polyvinyl alcohol and lignin or lignin-epoxy	Copolymerisation	Dyes adsorption	[325–326]
		Poly (ethylene) glycol diglycidyl ether	Chemical	Lignin	Self-crosslinking by blending, freeze-dried	Supercapacitors	[327–329]
		-/NMBA	Chemical	Acrylamide-polyvinyl alcohol-graft-lignin copolymers	Radical polymerisation	Water treatment	[330–331]
		Epichlorohydrin	Chemical	Xanthan and lignin	Copolymerisation	Adsorbent	[332]
Lignin as crosslinking agent	Non-covalent (physical)	Lignin	H-bonding /electrostatic	Chitosan and polyvinyl alcohol	Thermal treatment, thawing	Wound dressing	[333]
	Covalent	Lignin	Chemical	Polymerised acrylic acid and poly (vinyl pyrrolidone)	Radical polymerisation	Drug delivery	[270]
		Aminated lignin	Chemical	Polyvinyl alcohol	Copolymerisation	Antibacterial	[334]
		Lignin/lignin and NMBA	Chemical	Polymerised acrylic acid	Copolymerisation	Absorbent in personal care products	[335–336]
		Lignin	Chemical	Polymerised N-isopropylacrylamide	Thermal treatment/ copolymerisation	Tissue repair, drug release and water purification	[337]
		Lignin/lignin and PEG	Chemical	Poly (methyl vinyl ether co-maleic acid) (GRANTEZ)	Copolymerisation/thermal treatment	Dye removal, antimicrobial coatings	[338–339]

However, the effectiveness of these strategies in enhancing the mechanical performance of cryogels remains to be fully explored and validated.

The physical properties of the polymer, such as elasticity, viscosity, and solubility, are significantly affected by the degree of crosslinking and the presence or absence of crystallinity [340]. While crosslinking can enhance the elasticity of polymers, allowing them to stretch and return to their original form, an increase in the number of cross-links can make the polymer more rigid, less elastic, and even brittle [340]. This could limit the potential applications of the resulting cryogels.

The combination of precursors in hydrogel formulation determines the average molecular weight of polymer chains between crosslinks [313]. A low average weight results in highly stretched hydrophilic polymer chains between crosslinks, making them prone to fracture and leading to a fragile/brittle nature [313]. This suggests that careful adjustment of the crosslink density or precursor concentration is crucial, but achieving the optimal balance can be challenging.

Furthermore, while the formation of lignin-derived carbon cryogel provides a prominent strategy involving radical polymerisation that can improve the efficiency of the crosslinked network of cryogel, the incorporation of acid catalyst on lignin catalyst support acts as radicals that initiate the growth of the hydrogel network through polymer chain termination occurring via combination, disproportionation, or transfer [341–342]. This process, while promising, is complex and requires careful control of reaction conditions to ensure successful polymerisation. **Figure 2.21** illustrates that the phenolic hydroxyls of lignin form

radicals when initiators are present. These radicals react with monomers to create lignin grafted copolymers within a polymerised network, leading to the formation of interpenetrating polymer network hydrogels [343].

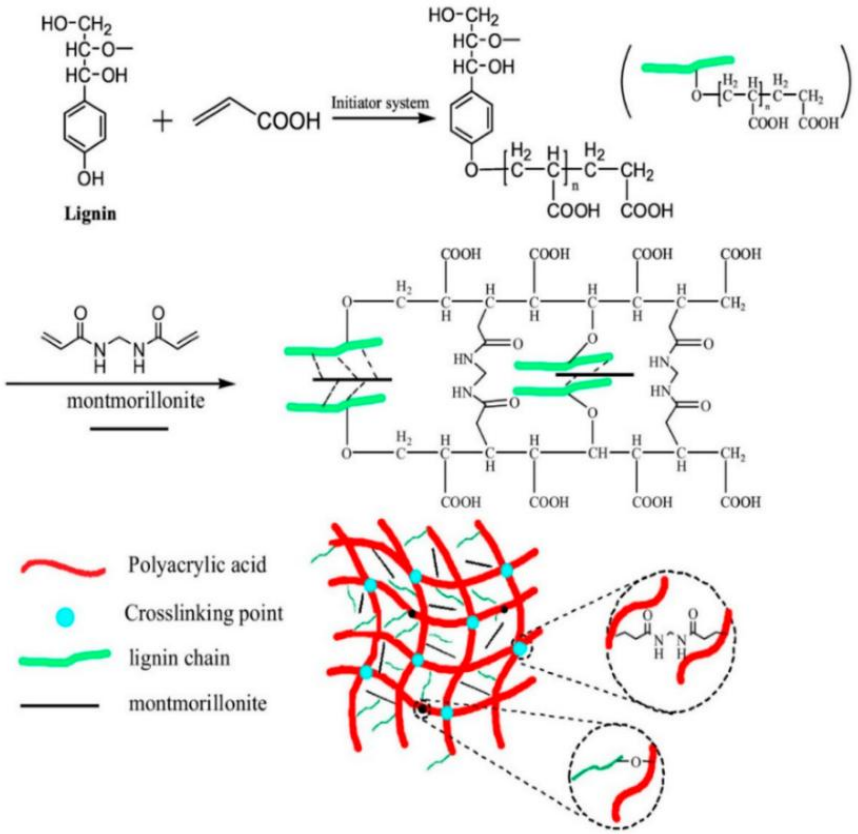

Figure 2.21 A model to simulate the cross-linking reaction between lignin and montmorillonite (cross-linker) involving an initiator system (polyacrylic acid) to form carbon cryogel. Reproduced with permission from Sun *et* al. [336].

2.4.4.3 Sol-gel

Sol-gel polycondensation first involves producing a hydrogel through polymerisation network. This hydrogel becomes a cryogel when freeze-dried (**Figure 2.22**). Sols are colloidal particles dispersed in a liquid, with diameters ranging from 1 to 100 nm. Gels, on the other hand, form interconnected, rigid networks with pores of submicrometric-size [344]. During gel synthesis, fine

particles of acid catalysts can be dispersed within the well-defined pores of a support to achieve high catalytic activity [345].

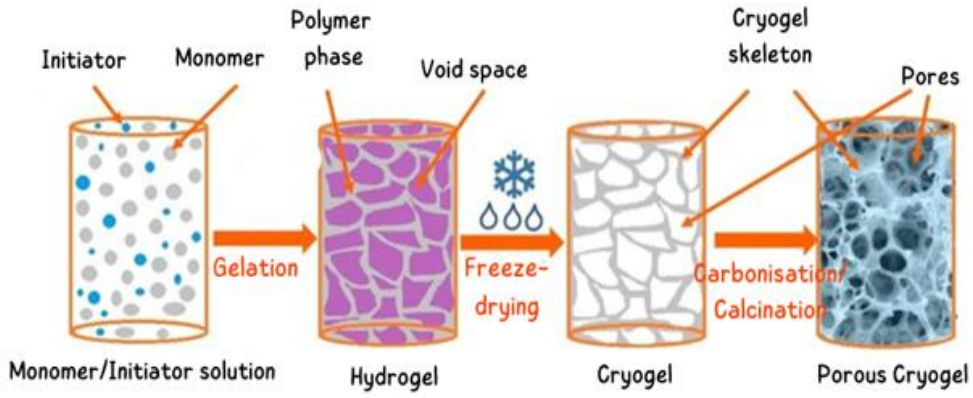

Figure 2.22 The sol-gel polycondensation process involves the transformation of a hydrogel to cryogel.

Sol-gel polycondensation offers an alternative to a traditional catalyst preparation method, such as impregnation, for enhancing chemical or template activation for lignin-derived catalyst support under milder conditions (**Figure 2.23**). Incorporating acid catalysts into the gel network structure during sol-gel polycondensation produces immobilising catalysts that can enhance biomass hydrolysis in cascade reactions. This approach can replace impregnation, which often results in an uneven distribution of active species at the support's grain boundary, especially at higher concentrations, leading to larger particle sizes [346]. Another method, ion-exchange can potentially stabilise metal species on the catalyst support [347], promoting better dispersion compared to wet impregnation. However, its widespread use is hindered by low loading due to the limited number of terminals OH groups on the support's surface [347].

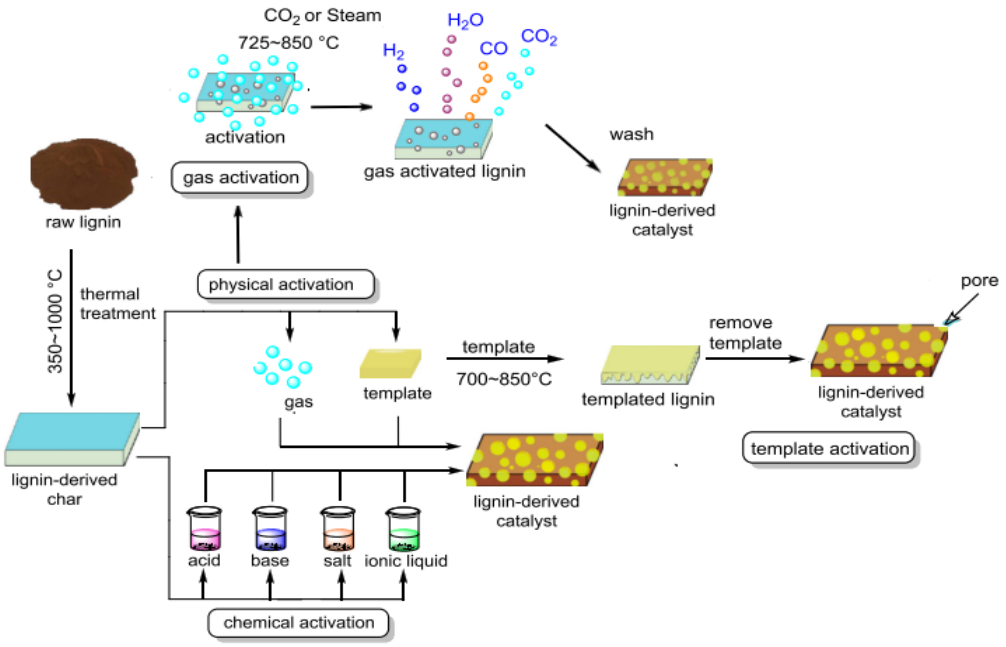

Figure 2.23 Activation of lignin-derived catalyst. Reproduced with permission from Zhu *et* al. [348].

Template activation, conventionally employed through pyrolysis at temperature above 500 °C, introduces porosity into lignin-derived char, yielding activated carbons with well-ordered pore sizes and distributions [348]. Like chemical activation, it plays a crucial role in transforming raw lignin into catalysts with ample porosity and abundant catalytic active sites. **Table A.1** summarises various lignin-based catalysts produced via impregnation (see in **Appendix 1** for detailed data). These catalysts show promise with well-developed pore structures after high thermal treatment, but they often face challenges related to catalyst leaching [349]. Meanwhile, the sol-gel technique, which provides versatility in final catalytic material properties [350–352], such as high purity, homogeneity, and tuneable processing temperatures and porosity due to accessible synthesis parameters, remains limited in literature, with no examples of catalysing biomass conversion to LA. Despite this, the properties of

lignin-based catalysts and their synthesis methods in general are worth reviewing in this study to develop lignin-based cryogels with optimal functionalities.

Despite the milder operational conditions of sol-gel processing compared to the impregnation method, the properties of lignin-based catalysts are almost similar for both methods. For instance, Fierro *et* al. produced a mesopore-dominated porous activated carbon (AC) from kraft lignin using template activation, yielding a high specific surface area and mesopore volume [353]. The process involved carbonising a mixture of kraft lignin and silicon colloids at 180 °C for 5 h and then at 850 °C for 2 h. The use of silicon colloids with an average nanoparticle size of 20 nm as template precursors resulted in lignin-derived AC with a surface area of 200 $m^2\ g^{-1}$ and a total pore volume of 0.55 $cm^3\ g^{-1}$, with mesopores accounting for approximately 96.4% of the total pore volume. In comparison, Zainol *et* al. demonstrated the efficacy of lignin-furfural carbon cryogels doped with H_2SO_4 for biodiesel production [24] and ionic liquid-furfural carbon cryogels doped with H_2SO_4 for ethyl levulinate synthesis [164]. These studies underscore the reusability and durability of carbon cryogels across multiple cycles, with minimal reduction in product yield. The lignin-derived carbon cryogel from this study exhibited significant surface area and porosity (139–570 $m^2\ g^{-1}$ and 0.31–0.62 $cm^3\ g^{-1}$) via the preparation method of 30 min of gelation, 8 h of freeze-drying, and 2 h of calcination at 400 °C [164]. This sol-gel approach via milder conditions is comparable to lignin-derived catalysts prepared by impregnation.

2.4.4.4 Sol-gel-hydrothermal

In sol-gel synthesis, metal species are incorporated into an ionic oxide network more efficiently due to the homogeneity and high dispersion of metal oxides [354], resulting in catalysts that are more stable compared to those produced by impregnation. However, encapsulation may decrease the activity of some sol-gel catalysts by limiting the accessibility of the catalyst's active sites [355]. The forms of metal species on catalyst surfaces can vary due to different preparation techniques and experimental conditions (i.e., precursor formulation, temperature), which can impact catalytic reactions [356–357].

The sol-gel method allows control over the textural and surface properties of composite oxides. This is achieved by regulating the hydrolysis and polycondensation of metal alkoxides, which yield hydroxides or oxides under specific conditions. To produce qualified nanomaterials in sol-gel processing, it is essential to achieve homogeneous macromolecular oxide networks [358]. These methods typically yield amorphous precipitates that require calcination in air to transform them from amorphous to crystalline phases. However, the calcination process often leads to particle agglomeration, grain growth, reduced surface area, and phase transformation, all of which decrease catalytic activity.

Hydrothermal processing, an alternative to calcination, allows for catalyst crystallisation under milder temperatures. It is widely used in the synthesis of zeolites and the production of advanced ceramic powders with ultrafine particle sizes. This method provides control over grain size, particle morphology, crystalline phase, and surface chemistry through various processing variables.

Enhancing the crystalline phase improves the surface area and creates active surface sites. This facilitates the adsorption and immobilisation of catalyst species onto the surface, anchoring the catalyst and preventing it from leaching into the reaction mixture. The crystalline phase of lignin-based catalyst supports can form strong chemical bonds with catalyst species through surface functional groups or defects, enhancing stability. Moreover, the hydrothermal process releases free radicals that actively propagate through monomer bonds to form polymer chains [359]. This controls the chemistry of precursor molecules and their interactions with the solvent and catalyst, driving the gelation process and enhancing the kinetics of hydrolysis and condensation reactions in sol-gel processes.

However, developing stable lignin gels presents challenges due to the long incubation times required for gelation, typically ranging from 1 to 5 days or more [23, 319, 360–361]. It is paramount to find mild synthesis and processing conditions that preserve biocompatibility and the integrity of encapsulated compounds [362]. Additionally, cost considerations drive the exploration of alternatives to expensive starting materials, such as resorcinol-formaldehyde, which contribute to 80% of the total cost of traditional sol-gel processes. Therefore, the integration of sol-gel processing with a hydrothermal approach emerges as a solution. This method offers numerous advantages over other growth processes, including operational simplicity, low energy consumption, and the potential for large-scale industrialisation [363].

Li *et* al. found that carbon cryogels synthesised via sol-gel hydrothermal (SGH) methods exhibited slower decreases in surface area during calcination compared to sol-gel (SG) approaches [358]. This indicates better thermal stability for SGH-prepared materials. The study also revealed that TiO_2 catalysts formed

stronger interactions with SiO_2 supports via SGH routes than SG, leading to better thermal stability [358]. Meanwhile, Costa *et* al. demonstrated the effectiveness of the sol-gel-hydrothermal process for synthesising crystalline hydroxyapatite with micro- and nanowire morphologies [364]. Particle diameter ranged from 25 to 800 nm and decreased with increasing solution pH, while both particle length and diameter increased with prolonged hydrothermal processing [364].

2.4.4.5 Determinant factors for cryogel formation

The formation and performance of carbon cryogels as catalyst supports are significantly influenced by the initial formulation of the hydrogel and its preparation conditions [365]. The polymeric hydrogel network, which can manipulate the structure and properties of porous carbon gels, is extensively applied in both wet and dried gel forms. The initial formulation of hydrogel precursors, such as water, lignin, crosslinkers, and acid catalysts, plays a crucial role in this process [366]. The properties of hydrogels, including swelling behaviour, water absorption capacity, mechanical strength, and porosity, are influenced by the preparation conditions for each step involved in the sol-gel process as stated in **Table 2.4.** These properties further impact the behaviour of the cryogel, reflecting its overall performance for catalysing biomass conversion to LA.

Manipulating the length of polymer chains between crosslinks and controlling the interaction between polymer chains and water can enhance the hydrogel's flexibility and resistance to fracture. This involves adjusting the ratio of hydrophilic to hydrophobic moieties within individual polymer chains, allowing for the dissipation of energy when force or stress is applied to the network [142]. The

adjustment of phenol concentration plays a crucial role in polymer formation. Higher concentrations result in rapid hydrophilicity loss, resembling phenolic resins that precipitate in water, while lower concentrations hinder polymerisation. Careful adjustment yields gel-like materials within a narrow concentration range, expandable with increased catalyst concentration [208]. The physicochemical properties, rheological behaviour, and mechanical performance of lignin-based gels are notably enhanced by the high cure and crosslinking of lignin with the pristine gel matrix [266].

Table 2.4 Factors influencing the synthesis of robust hydrogels at various stages of the sol-gel process. Resorcinol-formaldehyde (RF) is used as a model precursor.

Stage 1: Gelation and curing	
Factor	**Effect**
Decreasing reactant concentrations (equivalent to reducing R/F, R/W, or R/C ratios	Smaller particles and pore sizes
	Less compaction (less voids) of gel structure
	Increase surface areas of carbon gels
	Either reduce or increase pore volumes of carbon gels, depending on pH
	Depending on pyrolysis temperature and gel pH
Acidic catalyst solution	At low RF concentrations: small, smooth, fractal aggregates of particles with wide pore size distributions
	At high RF concentrations: no fractal aggregates, very narrow pore size distributions may reduce gelation time
Alkaline catalyst solutions	High concentrations: polymeric gels (small polymer particles interconnected with large necks, high surface areas, high mechanical strengths), reduces gelation time
	Low concentrations: colloidal gels (large particles interconnected with narrow necks, low surface areas, low mechanical strengths)
	Increase surface areas and pore volumes of carbon gels
Increasing gel pH	Insignificant effect on surface area of carbon gels
	Increase pore volume of carbon gels at high density of reactants

	Required for improving the crosslinking of polymer particles
Stage 2 : Solvent exchange and drying	
Solvent exchange	Necessary for supercritical drying with CO_2 or freeze-drying
	Facilitates replacement with drying media
	Reduction of surface tensions upon subcritical evaporation
Subcritical drying	Production of dried dense polymers called “xerogels”
	Causes significant shrinkage of especially wide pores
	Effects can be significant if gels were synthesised with high mechanical strength
Supercritical drying with CO_2	Production of dried light polymers called “aerogel”
	Insignificant shrinkage of pore structure
	High surface areas, pore volumes
	Requires high pressures, long times for exchanging solvent with CO_2
Supercritical drying with acetone	Like supercritical drying with CO_2 but with lower pressures
	Eliminates necessity for exchanging solvent with CO_2, shortens processing time significantly.
	Requires high temperatures to shift acetone to supercritical conditions
	May cause partial thermal decomposition of dried gels
Freeze-drying	Production of dried light polymers called “cryogels” based on sublimation of frozen solvents
	Cryogels mostly mesoporous
	Density of solvents must be invariant with freezing
Stage 3: Pyrolysis	
Increasing pyrolysis temperature	Reduces oxygen content
	Reduces surface area of carbon gels
	Reduces pore volumes of carbon gels
	Increases macropore size distributions
	Increase micropore size distributions when very low R/C ratios are used

During gelation, monomers undergo addition and condensation reactions, forming polymer chains and releasing small molecules like water or alcohol [246, 368]. Achieving the right monomer-to-catalyst ratio is crucial for initiating gelation.

Studies on RF gels highlight the importance of the catalyst in initiating R anions during the addition reaction to facilitate subsequent condensation reaction, leading to highly crosslinked clusters (7 to 10 nm in diameter) [369], followed by particle aggregation [370]. Crosslinkers play a crucial role in covalently bonding with lignin monomers in the presence of catalysts [371], while water facilitates swelling behaviour and provides a medium for acid dissociation, initiating polymerisation and leading to the formation of a crosslinked network and hydrogel (**Figure 2.24**).

The proportion of the precursors can vary depending on the nature of polymeric materials (as detailed in **Table A.2** in **Appendix 2)** and obtaining the right ratio can be challenging [372–373]. The catalyst concentration in the sol [374–375] can also influence the final properties of gels, impacting their particle size and density. Stirring for a brief period (between 5 [376] and 30 min [377]) creates a sol, with caution needed when adding additives like carbon cloths to avoid negative impacts on gelation [378]. Solvent choice and temperature also play vital roles, with acetone lowering heating requirements (from ~80 to ~40 °C) [379] and water enabling polymerisation at lower temperatures (30 °C) [379].

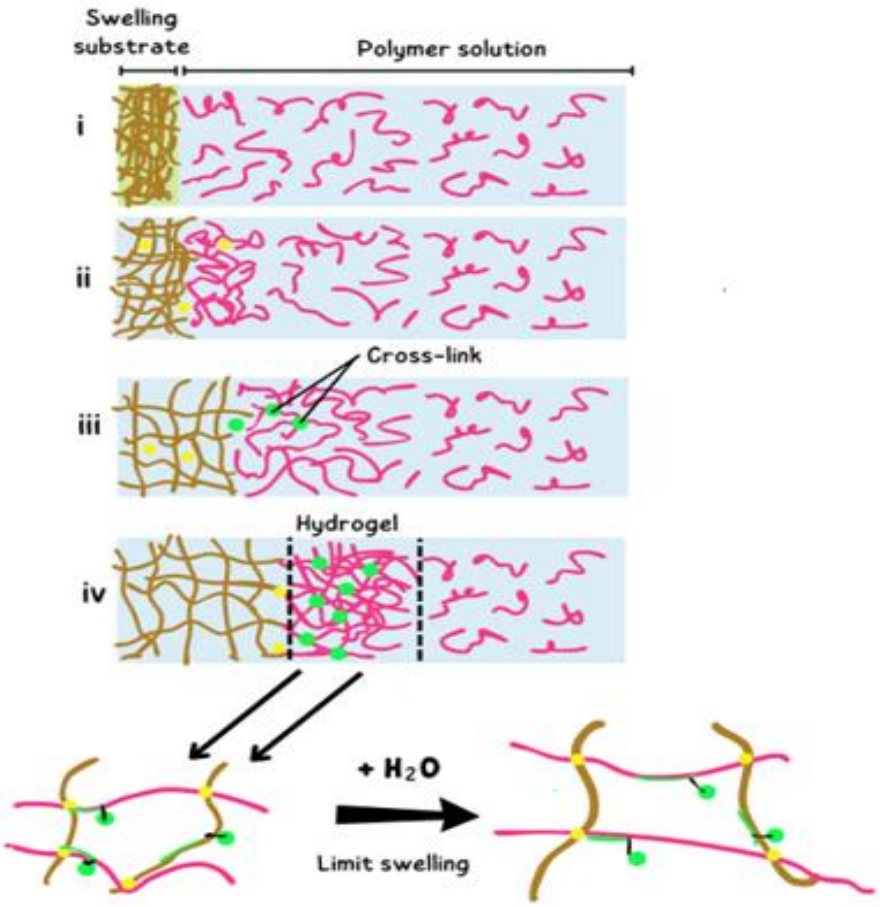

Figure 2.24 Initiation of polymerisation that shows crosslinking activities in a hydrogel.

Gelation occurs within days, influenced by reactant ratios, densities, and temperatures [246, 380]. Initial cluster formation takes about an hour [370], followed by slow crosslinking [370], accelerated by adjusting pH < 6.8 [246]. A temperature program is applied, followed by curing to crosslink polymer clusters into a solid gel shape [370, 381]. The curing step, taking about a week at elevated temperatures (80 to 90 °C), may require prolonged times to ensure sufficient completion of crosslinking reactions, preventing swelling during subsequent stages

of exchanging the aqueous solution with an organic solution [370]. Aging in a dilute acid solution enhances crosslinking density without shrinkage, improving mechanical strength [382–383]. This aging step is crucial for handling fragile gel monoliths without breakage.

Upon completing the final crosslinked gel, removing the aqueous solvent, often used as the reaction medium, becomes crucial. The method chosen significantly impacts carbon gel properties. Typically, aqueous solvents are replaced with organic counterparts (e.g., methanol, acetone, isopropanol, or amyl acetate) [238] through repetitive washing, often accelerated by heating to expedite diffusion and exchange [238]. Solvent exchange with t-butanol improves carbon cryogel porosity by preventing ice volume expansion from collapsing the mesopore structure [372]. This step could streamline subcritical drying, reducing time and temperature requirements for evaporation and minimising surface tension on wet gel pore walls, thus reducing shrinkage.

In the transition of hydrogel to cryogel, the drying method is implied. The drying process of gels can yield large, fully dense monoliths [384]. Various methods are available for producing carbon gels, including subcritical drying, supercritical drying, and freeze-drying or a natural drying process (evaporation) at ambient temperature and pressure without manipulation [385]. Although air-drying emerges as a simpler and cost-effective method, freeze-drying is proposed as a cost-effective alternative for creating mesoporous carbon cryogels [386]. This process involves freezing the liquid solvent and then removing it by sublimation, eliminating the formation of a vapour-liquid interface. Although freeze-drying is expected to minimise vapour-liquid interfaces, some gel

shrinkage may still occur. Therefore, freeze-drying smaller samples is considered more practical for producing mesoporous cryogels. Carbon cryogels also exhibit substantial BET surface areas and significant mesopore volumes, which can be controlled by adjusting the quantities of reactants, catalysts, and water in the sol–gel polycondensation process [387]. Comparatively, the surface areas and mesopore volumes of carbon cryogels are smaller than those of carbon aerogels produced by supercritical drying, but pyrolysis facilitates easier micropore formation. The potential synthesis of carbon cryogels in the form of microspheres could significantly enhance their manageability in catalytic applications.

Freeze-drying is generally considered more feasible than subcritical and supercritical drying. Subcritical drying involves solvent evaporation at atmospheric conditions to produce a dense polymer, known as a xerogel. This process can cause significant alterations in surface tension, leading to the collapse of the pore structure. It is important to note that shrinkage in carbon xerogels is most pronounced for pore sizes exceeding 10 Å [370].

On the other hand, supercritical drying with CO_2, has advantages such as preserving the aerogel's structure and enhancing the surface area and total pore volume. However, it can also present drawbacks, such as high pressures and extended drying times for solvent exchange. To shorten the process time, method improvements have been made by implementing supercritical drying with an organic solvent, such as acetone. However, gel textures resulting from supercritical drying with acetone differ from those with CO_2, showing increased shrinkage and density [388]. The shrinkage ratio is sensitive to the rate of depressurisation, with very high depressurisation rates leading to larger

shrinkage ratios [368]. Polymeric carbon aerogels, characterised by their small particle size, high surface area, and high compressive modulus, exhibit substantial shrinkage during supercritical drying [370].

Following drying, the organic gel undergoes pyrolysis, or carbonisation, to achieve a pure carbon structure. This process eliminates remaining oxide and hydrogen groups at elevated temperatures. These carbonised structures, known as carbon gels, are typically produced in a tube furnace under inert gas flow (N_2, argon, or He). Pyrolysis temperatures range from 600 to 2100 °C and are gradually approached using temperature programming [389].

As outlined in **Table 2.4**, variations in pyrolysis conditions significantly impact the properties of carbon gels. The pyrolysis step, marked by endothermic reactions, reduces macropores while increasing micropores and mesopores, thereby enhancing surface area [390]. According to Zhang *et* al., minor surface area reduction occurs above ~600 °C, while lower temperatures may increase surface area [391]. Subcritical drying typically results in a 20% shrinkage and 50% mass reduction due to pyrolysis [370]. Although pore sizes and volumes decrease, the surface area of the carbon gel may increase post-pyrolysis, especially with dilute sols and low catalyst to water or reactant to catalyst ratios [392]. Shrinkage and mass reduction decrease with higher reactant to catalyst ratios [393]. Additionally, the inclusion of organic fibres in the gel solution may mitigate shrinkage during pyrolysis [394].

Despite effective carbonisation, calcination outperformed in forming carbon cryogels derived from acidic lignin-furfural mixtures through sol-gel polycondensation [245]. Characterisation using a surface area analyser and NH_3-TPD showed higher surface area and acidity in calcined cryogels (426.5 $m^2 g^{-1}$

and 16.1 mmol g^{-1}) compared to carbonised cryogels (214.2 m^2 g^{-1} and 11.3 mmol g^{-1}) [245]. The results indicate that the calcination process under ambient air can possibly enhance the thermal stability and acids sites of the cryogel.

2.5 Microwave-assisted biphasic system

In the early years, the integration of microwave heating with acids and alkaline compounds was suggested to enhance hydrolysis efficiency [140]. Microwave pretreatment, when combined with chemical hydrolysis, effectively removes lignin and hemicellulose from biomass, thereby making cellulose more accessible [33, 395].

Alkaline solutions effective in removing lignin, while acidic solutions target hemicellulose within lignocellulosic biomass [396]. Dilute acid is particularly efficient in converting hemicellulose into soluble sugars, which facilitates the subsequent hydrolysis of cellulose. Notably, acids such as H_2SO_4 and HCl have been applied in organosolv pretreatment within a temperature range of 180–210 °C. These acids play a catalytic role in dissolving biomass components, facilitating the separation of lignin and hemicellulose from cellulose, and introducing a biphasic system. The presence of these acids also acts as a pH regulator, neutralising hydroxide ions (OH^-) that might impede the pretreatment process due to increased water dissociation at elevated temperatures.

Due to safety concerns about inorganic acids, research has explored the use of organic acids, such as maleic and oxalic acid, as additives to organosolv pretreatments. These organic acids exhibit higher catalytic efficiency under equivalent severity conditions and prevent the production of inhibitors, unlike

sulphuric acid. Notably, they selectively hydrolyse β-(1,4) bonds [397] and minimise sugar degradation [398–399].

2.5.1 Efficiency of microwave technology

Microwave dielectric heating introduces microwave energy directly into the chemical reactor, allowing direct access to the reaction vessel. This method heats only the reactants and solvent, not the vessel itself, promoting uniform temperature distribution for the entire sample volume (**Figure 2.25**). This results in increased stability of monosaccharides, shorter processing times, reduced energy input [400], and decreased formation of by-products or decomposition products [401–402]. Pressurised systems can achieve temperatures significantly above the conventional boiling point of the solvent, creating internal pressure that can disrupt the biomass structure [403].

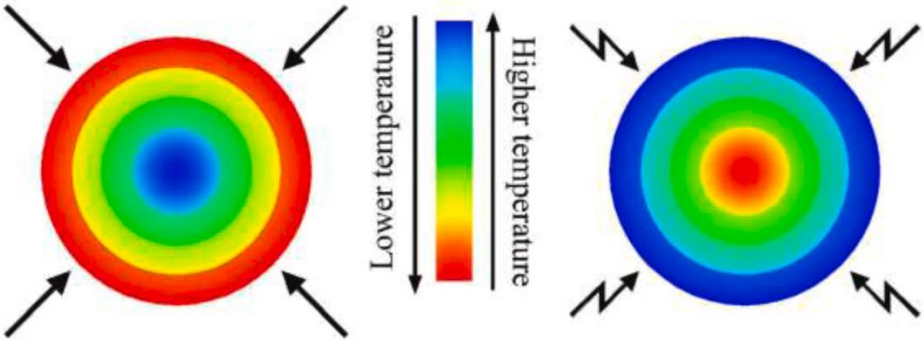

Figure 2.25 The difference in the distribution mechanism of temperature between conventional and microwave heating. Reproduced with permission from Mushtaq *et* al. [404].

Microwave radiation, particularly in low-loss materials like biomass, leads to higher core temperatures compared to surface temperatures, promoting effective disruption of lignin and cell walls for enhanced hydrolysis [405]. The thermal effects induced by microwaves involve the alignment of dipoles with the oscillating electric field, breaking hydrogen bonds [406]. Selective heating by

microwaves allows direct biomass heating without the need for hot gases or ablative surfaces in a cool setting. Volumetric heating overcomes traditional heat transfer limits, offering increased heating rates, smaller device sizes, and large particle processing capabilities [407]. While microwave heating maintains similar energy requirements to traditional processes, it exhibits great potential for reducing operating costs and increasing production capacity. Furthermore, microwave-assisted methods demonstrate a substantial, up to 85-fold, energy saving, as indicated by research findings [408].

Venturing into higher temperatures strategically equips the system with the energy required to accelerate the rupture of C–C and C–O bonds, thereby reducing reaction times. Remarkable findings demonstrate that at 260 °C within just 10 min, researchers achieved a high lignin yield (61.4 wt. %) coupled with low molecular phenol [409]. This tactful reduction in reaction time serves as a safeguard against undesired reactions that yield side products and the formation of recalcitrant structures, such as $sp^3C–sp^3C$ linkages. These hindrances cast a shadow on biomass deconstruction, arising from an excessive surge in movement among reactive species, including free radicals and charged entities. The manifestation of these undesirable linkages gains traction with the cleavage of ether bonds from lignin and hemicellulose during prolonged deconstruction processes. Extended reaction times also give rise to fused ring structures and aromatisation, leading to the emergence of side products such as char-like structures and polymers, ultimately diminishing the overall yield of LA products [410].

Table 2.5 provides an overview of the current state-of-the-art in microwave-assisted biomass conversion to LA. This approach not only

accelerates conversion reactions but also enhances product selectivity, as evidenced by studies [411–412]. Duan *et* al. utilised metal salt catalysts (ferric sulphide) and compared microwave-assisted depolymerisation to traditional heating. Results showed that microwaves could specifically cleave condense linkages Cα-Cβ at temperatures below 160 °C, increasing the ratio of the soluble fraction from 67% to 86% [413].

Most reported chemistry experiments have utilised domestic microwave ovens due to their widespread availability and cost-effectiveness. However, this practice has hindered the broader adoption of microwave-assisted organic synthesis due to the challenges outlined earlier. The inherent lack of control in domestic microwave ovens during microwave-assisted synthesis has resulted in numerous incidents, including explosions. One strategy to mitigate this risk has been to exclude solvents from reactions, conducting them on solid supports like clays, aluminium oxides, and silica [414–415]. Many noteworthy syntheses have been achieved using this solvent-free technique, emphasising its environmental friendliness by eliminating solvents and simplifying workup procedures. However, the environmental impact should be further scrutinised, considering the frequent use of solvents for pre-absorption of substrates onto the solid support and washing of products.

Table 2.5 LA production via microwave-assisted conversion at different reaction conditions.

Ref.	Feedstock	Mode	Reaction conditions	LA yield (%)
[38]	*Miscanthus x Giganteus*	Microwave reactor, 2.45 GHz	160 °C, 80 min, sulphated zirconium dioxide catalyst + 10 mM HCl, 2:1 catalyst-to-biomass ratio	63.8
[416]	Mandarin peel	Microwave reactor, 250 W, 220 psi, medium stirring	180 °C, 38 min, 2 M maleic acid, 0.1 g $Al_2(SO_4)_3$ and 1:22 biomass: maleic acid ratio (g mL^{-1}).	86.7
[417]	Pine wood cellulose	Microwave digestion system, 1200 W, 225 psi	20 min, 2%, *v*/*v* H_2SO_4, biomass concentration 3.3%	25.0
[418]	Glucose solution	Modified domestic microwave (output power 1200 W)	363 K, 6 min, 0.5 g $ZnBr_2$ + 1M HCl	53.0
[419]	*Cortinarius armillatus*.	Microwave reactor, 90 W	180 °C, 40 min, 0.5 M H_2SO_4 + 0.0075 M $CrCl_3$	62.0
[420]	Microcrystalline cellulose	Microwave reactor, 800 W	160 °C, 30 min, SO_3H functionalised ionic liquid	55.0
[421]	Cellulose	Microwave reactor, 400 W, 800 rpm	200 °C, 3.32 min, 1.37 M HCl	43.1
[422]	Cellulose	Monomode microwave reactor	170 °C, 50 min, 2 M H_2SO_4	34.2
[423]	Orange peel	-	170 °C, 30 min, 2 M H_2SO_4	71.0
[423]	Potato peel	-	170 °C, 30 min, 2M H_2SO_4	20.4

Modifying the characteristics of solid supports can significantly influence reaction outcomes, making various clays and other supports popular in both solvent-free and solution-phase techniques. Achieving precise temperature control at the surface of solids in solvent-free techniques may be challenging. This poses potential issues related to reaction predictability, reproducibility, and controllability. Nevertheless, solvent-free approaches offer benefits, such as enhanced safety by avoiding the use of low-boiling solvents that could lead to undesirable pressure increases during heating.

2.5.1.1 Comparison in operational mechanism

Like all electromagnetic radiation, microwave radiation comprises an electric field component and a magnetic field component. The electric field component is responsible for dielectric heating, which operates through two key mechanisms. The first mechanism, dipolar polarisation, involves the alignment of dipoles, such as water molecules, with an external electric field, resulting in rotation. This rotation is rapid in gases but hindered in liquids due to molecular spacing and collisions. Under microwave radiation, the dipolar re-orientation generates a phase difference, leading to dielectric heating. Notably, substances lacking dipole characteristics, like dioxane, do not heat, while water, with a large dipole moment, heats readily. Gases also remain unheated due to the precise alignment of rotating molecules with the electric field [403].

When microwaves enter a cavity, they undergo reflections by the walls, eventually forming a three-dimensional stationary pattern of standing waves, known as modes. Domestic microwave ovens are typically designed with three to six modes to ensure a uniform heating pattern for general food items. However, this multi-mode technique can introduce 'hot and cold spots' in the

field pattern, leading to varying heating efficiencies for small loads. For well-defined heating patterns in small loads, a microwave apparatus with a single-mode cavity is ideal. This type of apparatus allows only one mode, preventing the formation of 'hot and cold spots' and ensuring a uniform heating pattern. In organic chemistry, where microwave technology is prevalent, controlling the heating pattern is crucial for small samples, enhancing reproducibility and predictability. This capability enhances reproducibility and predictability and is especially beneficial for optimising yields in synthetic processes, which can be challenging in domestic microwave ovens. Single-mode systems offer higher field strengths, enabling more rapid heating.

The second major interaction of the electric field component is the conduction mechanism. In a single-mode microwave cavity with fixed radiation power and time, this mechanism results in tap water exhibiting a higher final temperature than distilled water. This phenomenon stems from ions in the sample moving through the solution under the influence of the electric field, resulting in increased collision rates and heat generation (**Figure 2.26**). The conductivity mechanism, stronger than the dipolar mechanism, contributes to a higher final temperature in tap water due to the presence of ions.

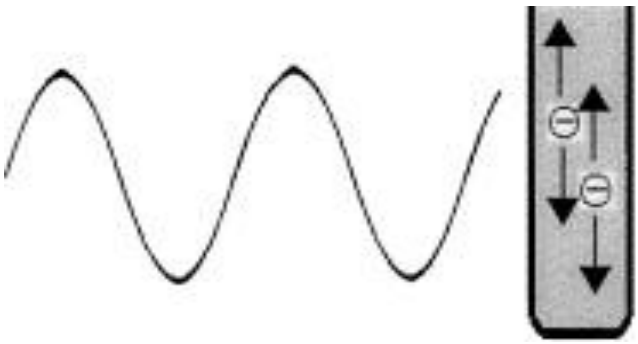

Figure 2.26 Charged particles in a solution will follow the applied electric field.

2.5.1.2 Influential parameters for microwave conversion

The effectiveness of microwave heating in various solvents depends on their dielectric polarisation, which is influenced by the ability of dipoles to reorient. Solvents with higher dielectric constants (**Figure 2.27**), generally polar in nature, tend to absorb microwave irradiation more efficiently. However, it is crucial to consider the conversion of absorbed energy into heat, as this can lead to solubility issues and the formation of heterogeneous mixtures. The loss angle, denoted as tan δ, emerges as a pivotal parameter in this context. Solvents like ethanol exhibit superior coupling with microwave irradiation owing to their higher loss tangent. This insight underscores the significance of selecting solvents that not only absorb microwave energy effectively but also translate it into uniform heating, avoiding the pitfalls associated with solubility challenges and heterogeneous mixtures.

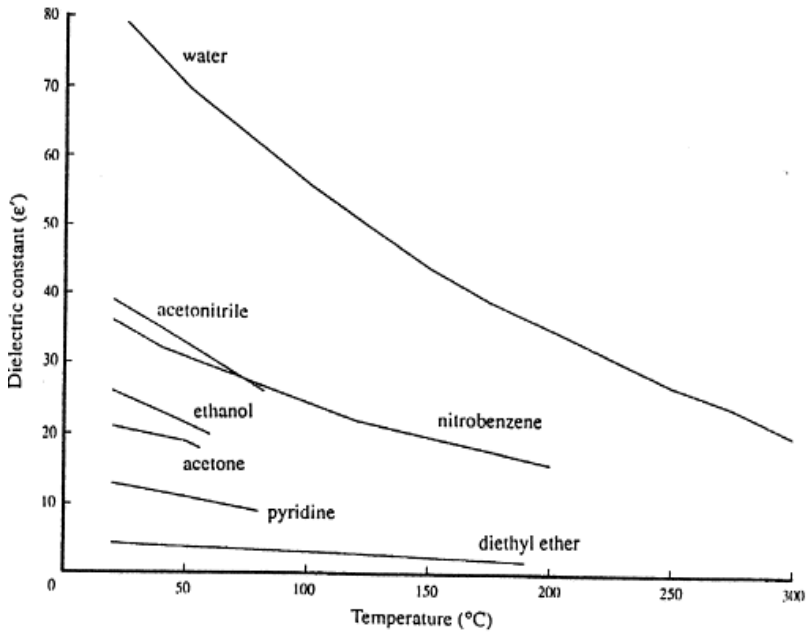

Figure 2.27 Plots of dielectric constants against temperature for various solvents. Reproduced with permission from Dean [424].

The re-orientation of dipoles and charge displacement, equivalent to an electric current, results in dielectric loss when a dielectric does not precisely follow the electric field. The relationship between tanδ, dielectric constant (ϵ') and loss factor (ϵ'') is intricate [414], explaining the dielectric loss phenomenon. Physical properties, volume, and geometry of the reaction vessel play a role in achieving uniform and reproducible heating [425]. Temperature-induced changes in the dielectric constant, especially in water, and the addition of polar solvents or salts can enhance heating rates, providing effective means for microwave-assisted organic synthesis.

Non-polar solvents do not absorb microwave irradiation efficiently. However, the energy transfer between polar molecules and the non-polar solvent bulk becomes rapid, enabling the effective use of non-polar solvents in microwave organic synthesis. ILs have emerged as novel alternatives to dipolar aprotic solvents for organic synthesis. These liquids, despite being salts, dissolve appreciably in water and various organic solvents including alcohols, offering excellent dielectric properties for microwave-assisted organic synthesis [426]. Some ILs are even soluble in non-polar organic solvents, allowing them to serve as microwave coupling agents when transparent solvents are employed [403, 424]. The dielectric advantages of ILs contribute to their efficiency and environmental friendliness in microwave-assisted organic synthesis. However, the practical application of microwave pretreatment at a commercial scale faces challenges, as it demands specialised knowledge and incurs high initial costs for large-scale machinery [427].

Fatriasari *et* al. studied the impact of microwave pretreatment conditions—specifically temperature, irradiation time, and maleic acid

concentration—on the enzymatic hydrolysis performance of OPEFB [397]. Notably, the pretreatment temperature emerged as the primary factor influencing the product yield, overshadowing the effects of irradiation time and maleic acid concentration. Microwave pretreatment was carried out within the temperature range of 160 to 200 ℃ with a fixed irradiation time of 2.5 min. An increase in irradiation temperature led to reduction in pulp recovery, attributed to the loss of chemical components during pretreatment. Specifically, OPEFB pretreated at 190 ℃ exhibited the highest cellulose composition (57.5%). Microwave irradiation induced disruption in oil palm biomass fibres, resulting in the removal of lignin and hemicellulose content. However, severe pretreatment conditions beyond 190 ℃ led to a decline in cellulose content (44.0%) due to cellulose degradation.

2.5.2 Biphasic system

While biomass and cellulose feedstock offer cost-effectiveness and widespread availability, dissolving insoluble raw biomass and cellulose in an aqueous medium poses a challenge. This is especially due to the phenomenon of autoionisation of water at elevated temperatures, which results in high concentrations of H^+ and OH^- ions. The low solubility of cellulose in water can hinder mass transfer between the substrate and solvent, thereby slowing down the reaction process. Studies by Chiappe *et* al. have reported low yields of LA in monophasic water systems [428], even under optimal conditions, demonstrating the limitations of this approach.

However, water is essential for protecting free radicals and facilitating the rehydration of HMF into LA. As a solution, biphasic systems have been

proposed as an alternative. In these systems, an organic solvent with high cellulose solubility is combined with an aqueous phase to ensure consistent catalytic performance through tandem reactions. Various organic solvents, such as dimethyl sulphoxide (DMSO), methyl isobutyl ketone (MIBK), tetrahydrofuran (THF), γ-valerolactone (GVL), methylbenzene, and ionic liquids (ILs), have been extensively investigated for their catalytic performances.

Among these, GVL offers several advantages, including efficient biomass-derived product, high cellulose solubility, high recyclability, and high thermal stability. These properties make it for large-scale LA production at a reasonable cost. GVL's capability to improve the partitioning coefficient helps prevent co-product deposition induced by bifunctional solid acid catalysts. Maximum LA yields produced in GVL/aqueous systems have ranged between 70% and 96.8% [167, 188].

Cellulose can be completely solubilised in at least 50%wt of GVL [429–431], with LA yields reaching 69% when the GVL composition increases up to 90%wt. However, further increment beyond the optimum value slightly reduces LA yield due to water deficiency for HMF rehydration [432].

2.5.2.1 Efficiency for lignocellulose deconstruction

To enhance cellulose hydrolysis, increasing lignin solubility is advantageous. Lignin, a complex polymer present in plant cell walls alongside cellulose and hemicellulose, forms a protective barrier around cellulose fibres. While this barrier shields the cellulose, it can impede the access of hydrolytic enzymes or chemical catalysts, thus slowing down the hydrolysis process.

High lignin solubility means that lignin molecules are better dispersed or dissolved in the reaction medium, such as during pretreatment (**Figure 2.28**), promoting bond scission and facilitating the deconstruction of lignocellulosic components. Consequently, the lignin barrier around cellulose fibres becomes more permeable or disrupted, allowing enzymes or catalysts to penetrate and access cellulose more readily. This enhanced access boosts cellulose hydrolysis efficiency by facilitating the breakdown of cellulose into sugars like glucose or fructose.

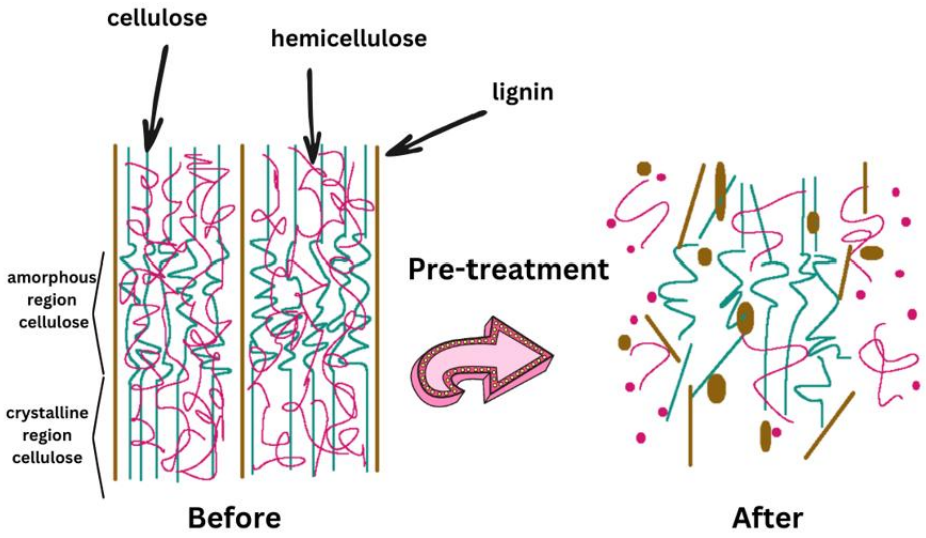

Figure 2.28 Recalcitrant biomass structure is deconstructed after pre-treatment.

Various solvent systems have been developed for lignin dissolution, including ionic liquids (ILs) [433–435], ILs–water mixtures [436], and liquid ammonia [437]. ILs play a crucial role in biomass deconstruction, serving both as solvents and catalysts, in addition to common organic solvents. However, achieving an optimal outcome requires careful selection of imidazolium side groups and anions within the ILs for pretreatment. This choice significantly influences cellulose crystallinity, necessitating a delicate balance to reduce

crystallinity without compromising cellulose stability. Imidazolium cations' side groups tend to be attracted to anions like chloride, acetate, and formate, enhancing cellulose solvation and disrupting its hydrogen bonding network, thereby reducing crystallinity [438]. Certain ILs, like [C_4C_1im]Cl and [C_2C_1im]Cl, demonstrate remarkable solubility for carbohydrates [439]. [BMIM]Cl, with its imidazolium cations and chloride ions, effectively disrupts hydrogen bonds within cellulose [440]. High-viscosity ILs contribute to enhanced cellulose solubility due to increased interactions between the IL and cellulose chains, preventing their reassociation and averting reprecipitation.

While ILs exhibit diminished lignin solubility compared to cellulose and hemicellulose, the addition of water introduces a transformative "cosolvency effect" [441–442]. Water disrupts hydrophobic interactions among lignin molecules, enhancing its dispersion within the IL [251]. However, water's addition may reduce cellulose solubility as imidazolium cations compete with water molecules for binding sites on the cellulose surface [443]. Achieving optimal efficiency in biomass deconstruction requires precise control of factors such as temperature, time, ILs concentration, composition, and the presence of co-solvents or additives. Maintaining a delicate equilibrium in water content enhances lignin solubility and disrupts cellulose crystallinity, facilitating biomass conversion into LA. The infusion of water also reduces the cost of using ILs and aids in the recovery of less concentrated IL.

However, these solvents have drawbacks. ILs, for instance, are expensive and viscous, limiting their industrial use [444]. Meanwhile, liquid ammonia systems require high pressure and low temperature, making long-term lignin handling challenging [437]. Additionally, the structure and properties of lignin

vary based on plant type and preparation method, making one solvent effective for some lignins but not others [445–447]. Finding green, robust, and cost-effective solvents for different lignins remains crucial. Ideal solvents should be cheap, nontoxic, non-volatile, less viscous, highly efficient, and easily adaptable to various lignin types. While GVL-based solvents derived from carbohydrate-based biomass, proposed by Horváth *et* al. [448], offer several advantages, including inertness toward oxygen and water, high boiling and flash points, low melting point, and low vapour pressure [449–450], further research is needed to explore and expand GVL's applications as a sustainable solvent. Xue *et* al. discovered that the solubility of dealkaline lignin reached 53.9% at 343 K in the GVL/water biphasic system [451], surpassing its solubility in other biphasic systems such as GVL/DMSO (44.1%), GVL/DMF (17.6%), and GVL/ILs (13.9–28.2%).

2.5.2.2 Efficiency for cellulose hydrolysis to LA

In biphasic systems, the bifunctional catalyst can more easily attack the glycosidic bonds of cellulose due to the prior disruption by the superior solvent. This partially breaks down the recalcitrant cellulosic structure, which is characterised by numerous intra- and intermolecular hydrogen bonds [32]. Additionally, biphasic systems allow for lower operating temperatures, facilitated by the higher dielectric constant of reactants resulting from solvent molecules [33]. Faba *et* al. investigated the role of carbon materials as facilitators of mass transfer in the selective conversion of cellulose to HMF within a biphasic solvent system, resulting in an enhancement of extraction kinetics by over 3.7 times [452].

The aqueous phase is also crucial for integrating active Lewis acid centres, particularly for the isomerisation of glucose to fructose [187]. Moreover, the addition of water may slow the formation of HMF due to stronger interaction between water and acidic protons compared to the interaction between water and the 2–OH of glucose [428]. This can minimise the production of undesirable humin polymers [453]. Li *et* al. proposed that the integration of the $H_3PW_{12}O_{40}$ catalyst into the GVL biphasic system plays a crucial role in minimising the generation of by-products throughout the conversion process [188]. This system acts as both a solvent and acid catalyst in LA production, suggesting that GVL possesses organic groups capable of altering the amphiphilic properties of the $H_3PW_{12}O_{40}$ catalyst. This alteration improves cellulose solubility and promotes its conversion to LA.

However, soluble Lewis acid in water initiates a homogeneous system, necessitating an additional recycling step. Therefore, integrating biphasic systems into the catalytic activity can reduce the solubility of Lewis acid while maintaining surface wettability for efficient substrate-catalyst binding in heterogeneous systems, facilitating catalyst recycling. Furthermore, the two-layer formation of biphasic systems ensures easy product isolation, promoting the mass transfer of HMF into the organic phase and LA into the aqueous phase.

Other polar solvents such as DMSO and THF were also applied to catalyse cellulose hydrolysis with the HPAs-based acid catalyst ($ChH_4AlW_{12}O_{40}$), resulting in high HMF selectivity and low LA formation [187]. This is due to the strong polar solvents such as DMSO and THF, which could potentially stabilise HMF because of their solvating ability towards positively charged intermediates [454]. However, DMSO was only prevalent for

fructose conversion to HMF, and a high boiling point of DMSO raised concerns associated with its high energy usage in the conversion process [33]. In the MIBK/water system (10:1, *v/v*), the LA yield achieved was 74.8% [187], and no further increase was observed as the MIBK increased. Contrastingly, ratios below 9:1 caused a decreasing LA yield of < 60%.

2.6 Strategies for challenges and limitations in catalytic system

The challenges and limitations in catalytic systems for biomass conversion to LA primarily revolve around humin production and catalyst deactivation. Although it is challenging to completely avoid these problems due to the complex nature of the biomass feedstocks and the reaction process, these issues can be managed and mitigated by minimising humin production and extending the lifespan of the catalyst.

2.6.1 Humin production

The formation of humin byproducts during biomass conversion to LA presents a significant challenge and is a topic of future research interest. Humin compounds are complex, high-molecular-weight polymeric substances that can accumulate in reaction mixtures, leading to reduce LA yields and catalyst deactivation. Understanding and controlling humin formation is crucial for improving the overall efficiency and economics of LA production from biomass. Future perspectives in this area include elucidating the mechanistic pathways of humin formation, identifying key factors influencing its production, and developing effective strategies to minimise its generation. Various catalysts, solvents, and reaction conditions are being explored to mitigate humin formation, with the aim of designing more selective and stable processes.

Humin formation is influenced by various factors, including reaction conditions, substrate species, and concentration. Li *et* al. observed that biomass with a complex structure, compared to saccharides solution, tended to promote more side reactions, and decrease the recycling lifespan of catalysts [455]. At high temperatures (100–200 °C), condensation reactions occurred between carbohydrates and C–O and C–C bonds, leading to humin formation. Treatment in compressed hot water at different temperatures (150, 200, and 225 °C) resulted in a decrease in $–SO_3H$ density from 0.58 mmol g^{-1} to 0.35, 0.30, and 0.20 mmol g^{-1}, respectively. Interestingly, when the reaction was conducted in non-aqueous organic solvents like DMSO and MIBK, minimal deactivation of acidic carbon was observed, while rapid deactivation occurred in aqueous solvent systems. The swift deactivation in aqueous solvents was primarily attributed to re-ionisation or polymerisation of dehydrated products on the catalyst surface, leading to humin deposition in the catalyst pores. Addition of salt (e.g., NaCl or KCl) was suggested as a possible approach to promote HMF production and inhibit humin formation.

Researchers have suggested the use of H_2O_2 solution for removing humin deposited on the surface of solid catalysts [32, 432, 456]. Shen *et* al. observed the catalyst turning black after five cycles of use, indicating potential humin deposition [34]. The total surface area of the fresh catalyst was 482 $m^2 g^{-1}$, whereas after five cycles, it reduced to 302 $m^2 g^{-1}$. Following five cycles, the catalyst underwent washing with a 30 wt % H_2O_2 solution at room temperature for 12 h, resulting in a colour change from black to brown. Subsequently, the total surface area of the regenerated $SA–SO_3H$ catalyst increased to 419 $m^2 g^{-1}$. Interestingly, the yield of LA improved post-regeneration, resembling that of the

fresh SA–SO_3H catalyst. Similarly, Deng *et* al. employed a sequential washing method with hot deionised water, ethanol, and acetone after each cycle [457]. They observed an increase in humin deposition on the catalyst with each cycle, and the –SO_3H content of the catalyst exhibited a linear relationship with the amount of humin formation.

Advanced analytical techniques and in-situ monitoring will play a vital role in unravelling the complexities of humin formation during biomass conversion, providing valuable insights for the development of efficient and sustainable LA production processes. Ultimately, addressing the challenge of humin byproduct formation holds the potential to enhance the viability and scalability of biomass-to-LA conversion technologies, promoting the sustainable production of this valuable platform chemical.

2.6.2 Catalyst deactivation

Catalyst deactivation during the conversion of biomass into LA presents a significant hurdle in achieving efficient and economically viable processes. This deactivation often manifests as a gradual decline in the catalyst's activity over time, resulting from various factors inherent to the complex nature of biomass feedstocks. One primary contributor to catalyst deactivation is coking, where carbonaceous deposits accumulate on the catalyst's surface, blocking active sites and reducing the catalyst's ability to facilitate the desired chemical transformations.

Another issue is catalyst poisoning, where impurities or unwanted compounds present in the biomass, such as sulphur and nitrogen compounds, bind to the catalyst's active sites, rendering them inactive. Sintering, a process in

which catalyst particles agglomerate and lose their high surface area, can also lead to deactivation.

Several strategies are employed to address these challenges and overcome catalyst deactivation. One approach is catalyst regeneration, where deactivated catalysts can be restored to their original activity by removing carbonaceous deposits or poisons through techniques like calcination or washing the catalyst with water or organic solvents such as methanol, acetone, and propanol [457–458]. Immobilising the catalyst onto a support material can enhance its stability and make it easier to recover and reuse. Using promoters in the catalyst formulation can improve stability and resistance to poisons or coking.

Moreover, the presence of cations in the aqueous substrate solution can lead to catalyst deactivation through proton exchange (proton leaching) with the sulphonic acid group. Typically, this deactivation is reversible since the deactivated sulphonic group can undergo secondary ion exchange with a stronger Brønsted acid (i.e., pK_a-regenerated Brønsted acid) compared to the pK_a of the immobilised sulphonic acid. Scholz *et* al. utilised microporous water to flush out the matrix after each catalytic reaction, followed by treatment at room temperature with a 0.2 M CF_3SO_3H solution for regeneration [459]. With a high pK_a value (pK_a = -20) of CF_3SO_3H, the cationic exchange sulphonic group was regenerated through secondary ion exchange. Subsequently, the reactor was flushed with microporous water until the outlet solution reached a pH of 7. This process demonstrated that treating the used catalyst with a strong Brønsted acid could restore its activity via a reversible ion exchange process. Given the low pK_a value of CF_3SO_3H and its non-sulphonating nature or involvement in

oxidation-reduction reactions during regeneration, it proved to be a suitable choice as the catalyst regenerator.

However, the use of strong Brønsted acid posed significant technical safety challenges. Consequently, alternative methods to stabilise the catalyst and prevent ion exchange process deactivation were explored. Crown ether and ethylenediamine tetraacetic acid (EDTA) were introduced into the liquid feedstock. EDTA can form stable chelating compounds with divalent metal cations, inhibiting their ion exchange ability with the sulphonic acid matrix. Similarly, crown ethers can form stable complexes with various small cations, thereby inhibiting the proton exchange capacity of the cation with the $–SO_3H$ group without compromising the activity and stability of the catalyst.

Catalyst engineering allows for the design of catalysts with tailored structures and compositions to reduce deactivation susceptibility. Optimising reaction conditions, including temperature, pressure, and solvent composition, can influence deactivation rates. Continuous catalyst monitoring, often through in-situ spectroscopy, enables real-time assessment and intervention when deactivation is detected. Selecting the right catalyst for area specific biomass feedstock and conversion process is also crucial, as some catalysts inherently resist deactivation better than others. Additionally, bifunctional catalysts with multiple active sites can help prevent the build-up of undesirable intermediates. In some cases, continuous catalyst addition during the reaction can maintain catalytic activity more stably over time. These strategies collectively offer solutions to mitigate catalyst deactivation, ensuring more efficient and cost-effective biomass conversion processes for LA production.

2.7 Concluding remarks

In conclusion, LA is a crucial platform chemical in sustainable biorefinery production, yet its large-scale synthesis is hindered by the complex nature of lignocellulosic biomass and the potential for undesired side reactions. This review emphasises the necessity for a robust catalytic system that can efficiently and selectively facilitate tandem reactions such as depolymerisation, isomerisation, and hydration within a single-pot setup.

Key considerations include understanding the components of biomass and the influence of solvents on their breakdown, both of which are essential for successful biomass conversion. The development of a lignin-derived carbon cryogel catalyst, incorporating $H_3PW_{12}O_{40}$ and Nb_2O_5, addresses the demand for enhanced reaction efficiency and selectivity. This bifunctional catalyst capitalises on the synergistic effects of Brønsted-Lowry and Lewis acids to improve conversion rates and product yields.

Tailoring catalyst properties by optimising the proportion of Brønsted-Lowry and Lewis acids is essential for maximising efficiency. The influence of these acid types on surface area, acidity, porosity, and functional group modifications is critical for enhancing catalyst performance. Evaluating the synergistic effects of the carbon cryogel can be achieved through analysis of either the synergy factor, kinetic data, frontier orbital energy, or structure-activity relationships.

Optimisation of the catalytic system is further supported by insights into reaction kinetics and thermodynamic data, which are vital for modelling the conversion process and proposing a reaction pathway, particularly within the context of a microwave-assisted biphasic system. The review also highlights the

significance of catalyst reusability and economic considerations, emphasising the need to assess catalyst stability, recyclability, and overall cost-effectiveness.

Overall, this literature review not only provides valuable insights into research methodologies for designing carbon cryogel catalysts that optimise performance but also underscores the importance of addressing biomass recalcitrance, identifying suitable reaction conditions, and ensuring economic viability in terms of material costs, operational expenses, and catalyst reusability. Advancements in these areas are paramount for achieving the goal of sustainable and scalable LA production. A collective effort and a deeper understanding of catalyst mechanisms are essential for overcoming existing challenges and facilitating commercial-scale applications. By focusing on these critical aspects, we can enhance the efficiency and sustainability of biomass conversion processes, ultimately paving the way for innovative and cost-effective solutions in the production of LA from biomass.

Chapter 3

Research Materials and Methodology

This chapter outlines the structured research methodologies aimed at achieving specific objectives, as illustrated in the accompanying mind map in **Figure 3.1**. The study commenced with an analysis of oil palm mesocarp fibre (OPMF) to quantify its components, providing essential baseline data on the composition of cellulose, lignin, and hemicellulose. Given the challenging nature of lignocellulosic biomass, the characterisation of cellulose was conducted to assess its accessibility for cellulose hydrolysis to produce LA. In this phase, various solvents were evaluated to identify the most suitable option for biomass valorisation.

Following this, the synthesis of carbon cryogel was undertaken. During this process, the properties of the material in its hydrogel state were assessed prior to its conversion into cryogel. The optimal cross-linker for creating a robust carbon cryogel was determined from several candidates, including lignin-polyethylene glycol, lignin-xanthan gum, and lignin-furfural. The selected carbon cryogel was then subjected to optimisation for hydrogel formulation, where the ratios of precursor components were found to significantly influence the final performance of the cryogel. Subsequent phases of the research focused on determining the optimal conditions for carbon cryogel preparation and reaction parameters to maximise LA yield. Response Surface Methodology (RSM) was employed in all optimisation studies to systematically identify the best parameters.

Kinetic and thermodynamic studies were conducted to evaluate the activity of the lignin-derived carbon cryogel in a one-pot conversion process facilitated by microwave assistance. A proposed reaction pathway for this catalytic system was developed using kinetic parameters and gas chromatography-mass spectrometry (GC-MS) screening. Lastly, the research included an assessment of catalyst recycling and cost estimation to evaluate the economic viability of the process for sustainable LA production. This involved examining the durability and reusability of the catalyst to ensure consistent performance, as well as evaluating the overall cost-effectiveness of the method for large-scale applications.

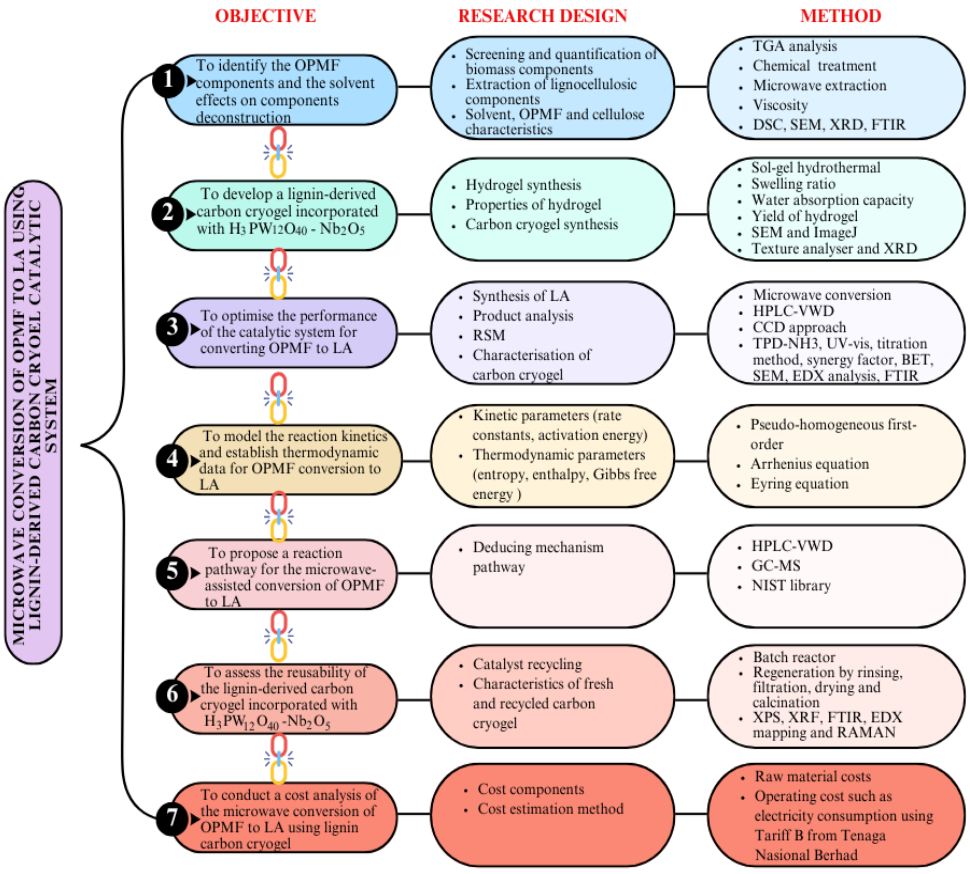

Figure 3.1 Research methodologies throughout the study on the microwave conversion of OPMF to LA using a catalytic system of lignin-derived carbon cryogel incorporated with $H_3PW_{12}O_{40}$-Nb_2O_5.

3.1 Materials and chemicals

OPMF was obtained from Palong Palm Oil Mill, which is about 40 km away from Bahau, Negeri Sembilan, Malaysia. The collected sample was in the form of pressed fibrous strands.

γ-valerolactone (99%), polyethylene glycol diglycidyl ether (M_{n500}), levulinic acid (99%), hydroxymethyl furfural (99%), formic acid (98%), D-glucose, fructose and [HMIM][HSO_4] (98%) were purchased from Sigma Aldrich (Darmstadt, Germany). Acetone, ethanol, toluene, ethyl acetate, ethyl lactate, and 2-butoxyethanol, sulphuric acid (98%), t-butanol and [BMIM][Cl]

(95%) were purchased from Thermo Fisher Scientific (Pittsburgh, USA) whereas [EMIM][Ac] (95%) was purchased from Ionic Liquid Technologies (GmbH, Germany). Phosphotungstic acid ($H_3PW_{12}O_{40}$), niobium oxide (Nb_2O_5), furfural (99 %), and 2-methoxyethanol (as internal standard) were purchased from Nacalai Tesque (Kyoto, Japan). Alkaline lignin and xanthan gum were purchased from Tokyo Chemical (Japan). All reagents were of AR grade and used without further purification. Pure sodium hydroxide pellets were used for alkaline fractionation. Ultrapure water (18.2 MΩ·cm, <0.01 $CFUmL^{-1}$, <1 particulate mL^{-1}) was treated in a Milli-Q water purification system from Merck (Darmstadt, Germany).

3.2 Preparation of dewaxed sample

The raw OPMF (**Figure 3.2**) was first prepared following Chieng *et* al. [460]. The OPMF sample was soaked in distilled water for 24 h, then rinsed with hot water (60 °C) and acetone prior to drying at 60 °C in an oven to remove any soil organisms. The dried OPMF was cut small and milled using an ultra-centrifugal mill. The sample was sieved into a particle size of <200 µm and dewaxed with a mixture of toluene and ethanol (2:1, *v/v*) at 80 °C for 6 h, to remove any extractives [461].

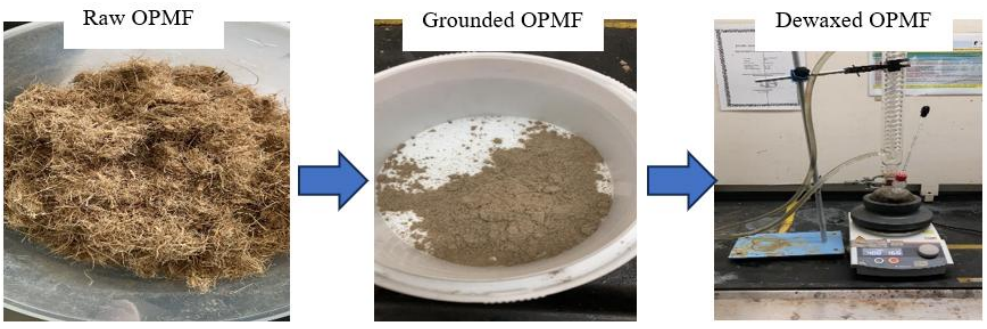

Figure 3.2 Oil palm mesocarp fibre was ground and dewaxed before proceeding to sample preparation.

3.3 Screening and quantification of biomass components

Thermogravimetric analysis (TGA) was used to measure the weight change of the samples as a function of temperature and/or time. The thermo-stability property of the sample was analysed using Perkin Elmer Thermal Analyser (Waltham, MA, USA). About 10 mg of sample was heated at a rate of 10 °C min^{-1} with nitrogen gas as a carrier at the flow rate of 20 mL min^{-1}. The degradation of the samples was tracked by monitoring the percentage of weight loss across a range of temperatures. Further insights into the composition of cellulose and hemicellulose, derived from the holocellulose content, were quantified through chemical analysis, as outlined in **Appendix 3**.

3.4 Extraction of lignocellulosic components

Figure 3.3 represents the detailed process of lignocellulosic components extraction. The methods were adapted and modified from Lan *et* al. [462] and Monteil-Rivera *et* al. [463]. Dewaxed OPFM (DOPMF) was mixed with γ-valerolactone (GVL) at a ratio of 1:50 (*v/v*) and heated at 180 °C (450 W) for 2 min, followed by 1 min of holding time. The heated sample was cooled down and then regenerated with a mixture of acetone and water at 1:1 (*v/v*). The mixture was stirred at 1200 rpm for 50 min and centrifuged. The supernatant was decanted while the solid residue (carbohydrate precipitate) was collected to undergo extraction with 4% NaOH at 50 °C and a solid: liquid ratio of 1:25 (g mL^{-1}) for 45 min. The mixture was then centrifuged to separate the cellulose fraction and the remaining supernatant was adjusted to pH 6.8 and precipitated with 3 volumes of 95% ethanol. Hemicellulose fractionation was collected after centrifugation at 7000 rpm for 10 min. The supernatant was concentrated under 60 °C and regenerated with 50 mL of acidified water at pH 2.0 to precipitate

lignin. Both cellulose and hemicellulose precipitates were dried in the oven at 70 °C while lignin precipitate was freeze-dried at -40 °C. The whole process of extraction described above was repeated and tested on other solvents, including a series of ionic liquids (i.e., [HMIM][HSO_4], [BMIM][Cl], and [EMIM][Ac]), ethyl acetate, ethyl lactate, and 2-butoxyethanol.

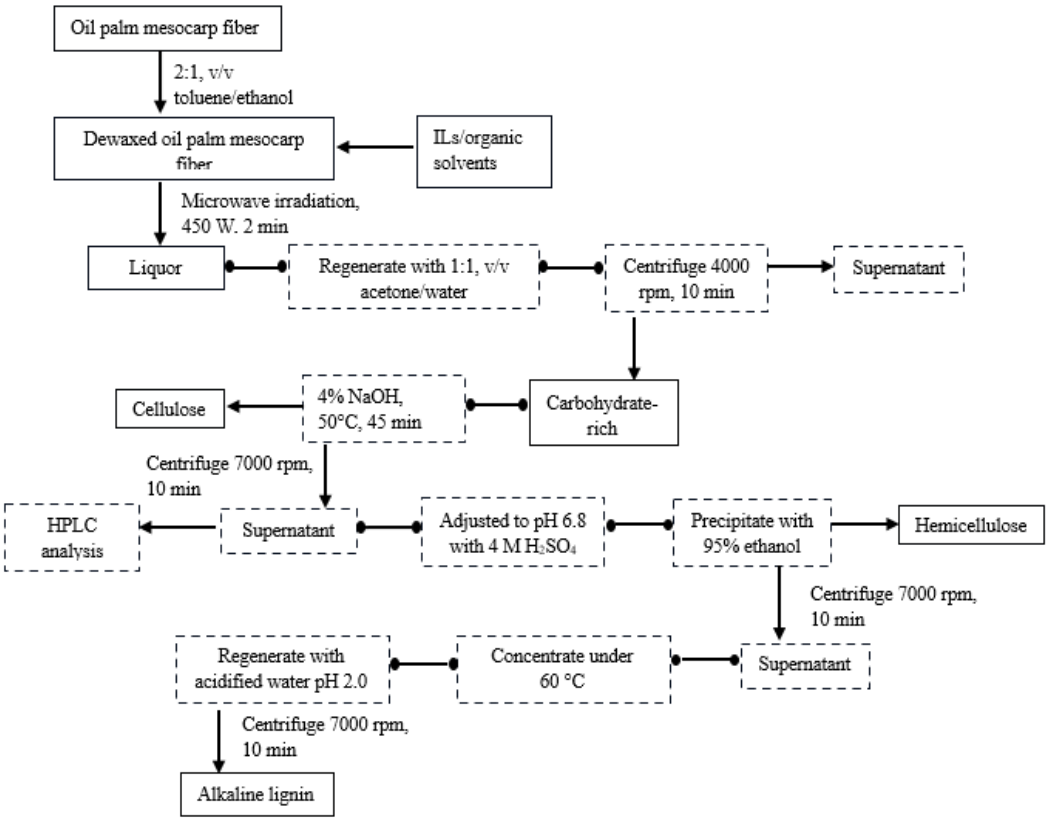

Figure 3.3 The flow process of lignocellulosic components extraction.

The calculation for extracted cellulose, hemicellulose and lignin was adapted from the prior study [464] as shown in **Eq. 3.1**:

$$\text{Percentage of extracted components (cellulose/hemicellulose/lignin)} = \frac{\text{Obtained residue mass}}{\text{initial sample mass}} \times 100 \quad (3.1)$$

Meanwhile, the removal of lignin and hemicellulose can be computed using **Eq. 3.2**, and the recovery of cellulose can be assessed through **Eq. 3.3**, both derived from the preceding study [465].

$$\text{Lignin/hemicellulose removal (\%)} = \frac{M_0 - M_1}{M_0} \times 100 \quad (3.2)$$

where M_0 = Lignin/hemicellulose before pretreatment;

M_1 = Lignin/hemicellulose after pretreatment

$$\text{Cellulose recovery (\%)} = \frac{C_1}{C_0} \times 100 \quad (3.3)$$

where C_0 = Cellulose before pretreatment; C_1 = Cellulose after pretreatment

3.5 Viscosity of solvent

The viscosity of ionic liquids (ILs) solutions was measured using a Brookfield AMETEK viscometer (LVDVE230, USA) at a temperature of 293.15 K. The spindle speed was selected according to the viscosity of the ILs.

3.6 Characterisation of cellulose

Differential scanning calorimetry (DSC) analysis was employed using equipment DSC Q2000 (Mettler Toledo, Ohio, USA) from 30 °C to 400 °C at a heating rate of 5 °C min^{-1}. The N_2 flow was 20 mL min^{-1}.

FTIR was used to examine the functional group change of the samples. The FTIR spectra were recorded on an attenuated total reflection Fourier transform-infrared spectroscopy (ATR-FTIR, Perkin Elmer Frontier FT Mid-IR/Far-IR, USA). The spectral analysis was performed within the range of 400–4000 cm^{-1}.

Scanning electron microscope (SEM) was used to study the morphology change of the samples. The SEM micrographs were recorded by using a Fei

Quanta 400F (Hillsboro, OR, USA) scanning electron microscope operating at 20 kV accelerating voltage. The samples were prepared by placing them on platinum and coating them with a Sputter coating system for 3 min to ensure good conductivity prior to analysis.

The crystallinity index of samples was obtained via XRD patterns. The samples were scanned at 2° min^{-1} with a 2θ angle range from 3° to 60° by using an X-ray diffractometer (Philips/X'Pert Pro PANAnalytical-PW 3040/60 MPD, Almelo, The Netherlands). The crystallinity index value was computed to quantify the crystallinity of the samples. The crystallinity index (CIr) is defined by **Eq. 3.4**, where I_{002} is the peak intensity corresponding to the crystalline region and I_{am} is the peak intensity of the amorphous region.

$$\text{CIr (\%)} = \frac{I_{002} - I_{am}}{I_{002}} \times 100 \quad (3.4)$$

3.7 Statistical analysis

The mean differences among fractions of lignocellulosic biomass components, hemicellulose and lignin removal, and cellulose recovery using different extracting solvents were evaluated through one-way ANOVA paired with the Tukey test. This analysis was conducted using IBM SPSS Statistics 23.

3.8 Hydrogel synthesis

Lignin-derived hydrogels were synthesised using the sol-gel-hydrothermal method. Three different cross-linkers including xanthan gum, furfural, and polyethylene glycol (PEGDE) were used to screen their crosslinking with the lignin moieties, forming hydrogels. Lignin (2 g) was dissolved in 3.2 mL of deionised water for 30 min with constant stirring at 25 °C and 350 rpm. Then,

2 mL of deionised water was slowly added, and the mixture was continuously stirred at 750 rpm for 4 h until a homogeneous solution was achieved. The ratio of water to lignin was set to 1:1 (*w/w*) considering the amount of water added for the second time. Acid catalysts ($H_3PW_{12}O_{40}$ and Nb_2O_5) were added to the mixture with 0.08 mmol each (1:1, *w/w*). The crosslinker was added to the lignin mixture at a fixed concentration of 0.5 mmol g^{-1} lignin. The mixture was heated to 70 °C for 30–45 min until a sol-gel was formed. **Table 3.1** shows that lignin mixtures were treated differently for polymerisation to occur, according to different types of crosslinkers.

Table 3.1 The lignin hydrogels that are cross-linked to furfural and xanthan gum are subjected to hydrothermal process at respective curing conditions.

Cross-linkers	**Mass (g)**	**Curing conditions**	
		Temperature (°C)	**Time (h)**
Xanthan gum	0.934	180	1.0
Furfural	0.096	180	1.5
PEGDE	0.531	25	24.0

3.9 Testing properties of hydrogel

3.9.1 Swelling ratio

Lignin-derived hydrogels were tested for their swelling degree gravimetrically using the following relation in **Eq. 3.5**. The dry hydrogel was initially determined by weighing the hydrogel (W_d) prior soaking process. The weighted hydrogel (W_s) was then soaked in clean distilled water for the interval of 2, 4, 10, 20, 40 min, 1 h, 2 h, and 24 h.

$$\text{Swelling ratio (g g}^{-1}) = \frac{W_s - W_d}{W_d} \quad (3.5)$$

3.9.2 Water absorption capacity

The ability of hydrogel to absorb water was calculated by weighing the hydrogel (W_a) prior soaking process. The weighted hydrogel was then soaked in clean distilled water until it attained its equilibrium weight (W_e). So, the water absorption capacity was calculated based on **Eq. 3.6**.

$$\text{Water absorption (\%)} = \frac{W_e - W_a}{W_a} \times 100 \quad (3.6)$$

3.9.3 Yield of the hydrogel

The yield of hydrogel was determined with respect to the total amount of reactants used for the polycondensation. The form of hydrogel reflects the degree of cross-linking. The amount of the hydrogel obtained after crosslinking and the amount of reactants brought into the reaction were represented by values of m_h and m_r, respectively. Hence, the yield of cross-linking reaction, η, can be calculated using **Eq. 3.7**.

$$\eta\ (\%) = \frac{m_h}{m_r} \times 100 \quad (3.7)$$

3.9.4 Porosity

The porous structure of the lignin hydrogels was observed through SEM as described in **Section 3.6**. The captured micrographs from SEM were transferred to ImageJ for measuring the pore size diameter and the distribution of pore size was further analysed using OriginLab 2023.

3.9.5 Compressive strength

Lignin-derived hydrogels were measured for their strength using a texture analyser (TA.XTplus, Stable Micro Systems, Surrey, UK) with a probe size of P/75 (**Figure 3.4**). Each hydrogel sample was prepared in different shapes and

sizes according to the mould used. The parameters used for texture analysis included pre-test speed, test speed, post-test speed, and trigger force which were set to 1 mm s^{-1}, 2 mm s^{-1}, 10 mm s^{-1}, and 5 N, respectively.

Figure 3.4 Compression test on the hydrogels.

3.10 Carbon cryogel synthesis

A lignin-gum-derived (LIG-XG) hydrogel was first synthesised as explained in **Section 3.8** and was rinsed with water to remove any unreacted monomers that might be present in the hydrogel after its initial synthesis. The hydrogel was soaked in t-butanol for 3 h for solvent exchange, facilitating the freeze-drying process. The hydrogel was pre-frozen overnight and freeze-dried at -40 °C for 12 h to form a cryogel. The carbon cryogel was subsequently calcined at 400 °C for 1 h, with these parameters being adopted based on optimisation studies conducted in a previous study [24].

During the initial testing of carbon cryogel performance, LIG-XG hydrogels were formulated with different ratios of water to lignin (1:1 and 5:1)

and various concentrations (0.04, 0.08, and 0.12 mmol) of acid catalysts ($H_3PW_{12}O_{40}$ and Nb_2O_5).

3.11 Synthesis of levulinic acid

The DOPMF (0.1 g) was added into a borosilicate reactor containing 5 mL of GVL and 0.5 mL of water. A carbon cryogel catalyst (0.2 g) was added to the reactor. The reaction was carried out via microwave irradiation (SAMSUNG, Model ME711K, 230 V/50 Hz) at 450 W for 2 min. Infrared IR Laser thermometer and laboratory thermometer were used determine the temperature of the solvent after the effect of heating. Upon heating, the reaction mixture was quickly quenched with iced water to stop the side reactions. The supernatant of the product sample was extracted from the reactor and measured for its final volume and then diluted in the 100 mL volumetric flask. The sample (1 mL) was filtered through a 0.22 μm PTFE syringe filter into a 2 mL vial, and 0.2 mL of internal standard was injected into the same vial. The sample mixture was vortexed for 1 min and ready for product quantification.

3.12 Product analysis

The LA product was quantified using a high-performance liquid chromatography coupled with a variable wavelength detector (HPLC-VWD, Agilent Series 1210, USA). The peak of LA in the chromatogram was detected using the Aminex HPX-87H column (BioRad, 300 x 7.8 mm) via an isocratic run of the 5mM sulphuric acid at 60 °C with the flow rate of 0.6 mL min^{-1}, the injection volume of 20 μL and λ = 190 nm. Method validation was carried out (refer to **Appendix 4**) to check the precision, linearity and sensitivity of analytical method used. The final percentage of LA was

calculated using **Eq. 3.8**. The theoretical maximum yield of LA from cellulose conversion was determined using **Eq. 3.9**. LA efficiency was calculated using **Eq. 3.10**.

$$\text{Actual LA yield (\%)} = \frac{\text{Amount of LA (g)}}{\text{Initial biomass loading (g)}} \times 100 \quad (3.8)$$

$$\text{Theoretical LA yield (\%)} = \frac{\text{Cellulose content in biomass (g)} \times 0.71}{\text{Initial biomass loading (g)}} \times 100$$

$$\text{where} \quad \frac{\text{Molecular weight of LA (g mol}^{-1})}{\text{Molecular weight of cellulose (g mol}^{-1})} = \frac{116}{162} = 0.71 \quad (3.9)$$

$$\text{Efficiency of LA (\%)} = \frac{\text{Experimental yield}}{\text{Theoretical yield}} \times 100\% \quad (3.10)$$

3.13 Response surface methodology

A RSM employing a central composite design (CCD) approach was utilised to devise the experimental layout for optimising (i) hydrogel formulation, (ii) attributes of carbon cryogels, and (iii) reaction conditions for biomass conversion to LA, facilitated by Design Expert Version 13 software. Each optimisation stage was carried out sequentially. **Table 3.2** delineates the parameters for hydrogel formulation, encompassing the ratios of lignin to water (W/L), lignin to xanthan gum (XG/L), and lignin to acid catalysts (C/L). **Table 3.3** outlines the parameter ranges for carbon cryogel attributes, including the ratios of $H_3PW_{12}O_{40}$ to Nb_2O_5, solvent exchange conditions, and calcination time and temperature. Meanwhile, **Table 3.4** delineates the parameter ranges for microwave conversion, encompassing microwave power, catalyst loading, biomass loading, and the ratio of GVL to water. All parameters were examined

at five levels. The experimental yields were computed based on the experimental trials and validated with triplicate data using **Eq. 3.11**.

Table 3.2 Parametric studies: Hydrogel formulations.

Factors	**Symbol**	**Levels**				
		-∝	**-1**	**0**	**+1**	**+∝**
Ratio of water to lignin	A	0.32	1.00	2.00	3.00	3.68
Ratio of xanthan gum to lignin	B	0.08	0.25	0.50	0.75	0.92
Ratio of catalyst to lignin	C	0.01	0.06	0.13	0.20	0.25

Table 3.3 Parametric studies: Carbon cryogel attributes.

Factors	**Symbol**	**Levels**				
		-∝	**-1**	**0**	**+1**	**+∝**
Calcination temperature (°C)	A	100	200	300	400	500
Calcination time (min)	B	15	30	45	60	75
Ratio of $H_3PW_{12}O_{40}$ to Nb_2O_5	C	1	2	3	4	5
Solvent exchange (h)	D	2	8	14	20	26

Table 3.4 Parametric studies: Reaction conditions for conversion process.

Factors	**Symbol**	**Levels**				
		-∝	**-1**	**0**	**+1**	**+∝**
Microwave power (W)	A	150	300	450	600	750
Catalyst loading (g)	B	0.02	0.08	0.14	0.20	0.26
Biomass loading (g)	C	0.01	0.04	0.07	0.10	0.13
Ratio of GVL to water	D	4	6	8	10	12

$$\text{Error} = \frac{|\text{Validation result} - \text{CCD result}|}{\text{CCD result}} \times 100 \quad (3.11)$$

For the parametric studies on hydrogel formulations, the CCD entailed 8 factorial points, 6 axial points, and 6 replicates at the centre points, totalling 20 experiments. Meanwhile, the parametric studies on carbon cryogel attributes and reaction conditions for biomass conversion to LA comprised 16 factorial points, 8 axial points, and 6 replicates, resulting in 30 experiments. The number of experiments for each stage was determined according to **Eq. 3.12**. The quadratic equation model, aimed at forecasting the optimal conditions, can be formulated to fit a second-degree polynomial design, as depicted in **Eq. 3.13**.

$$N = 2^n + 2n + n_c \quad (3.12)$$

where N is the number of experiment, n is the number of factor and n_c is the number of replicate at the centre point.

$$Y = \beta_0 + \sum_{i=1}^{n} \beta_i X_i + \sum_{i=1}^{n} \beta_{i\,i} X_i^{\,2} + \sum_{i=1}^{n} \sum_{j>1}^{n} \beta_{i\,j} X_i X_j \quad (3.13)$$

where Y is the predicted response, n is the number of experiments, β_0 , β_i , β_{ii} , β_{ij} are regression coefficients for constant, linear , quadratic and interaction terms, accordingly, X_i and X_j are coded independent factors.

Analysis of variance (ANOVA) was utilised to evaluate the model's goodness of fit. The quality of the predicted model was assessed through the correlation coefficient (R^2), while its statistical significance was determined by Fisher's F test. The significance of model terms was assessed based on the *p*-value (probability) at a 95% confidence level. Three-dimensional plots and corresponding contour plots were generated to visualise the interactive effects of independent variables across all optimisation stages. Additionally, a response surface equation was optimised numerically to maximise the LA yield, determining the optimal hydrogel formulations, carbon cryogel attributes, and

operating conditions. The models were developed with the assumption of equal variance.

3.14 Characterisation of carbon cryogel

In the second phase of the optimisation studies, a thorough assessment was conducted to understand the impact of carbon cryogel characteristics on LA yield. This evaluation focused on a representative subset of samples, specifically 2O1, 2O8, 2O11, 2O15, 2O21, 2O22, and OPT2. These samples were carefully selected to cover the spectrum of variations observed throughout the optimisation process.

3.14.1 Total acidity

Total acidity was determined through two distinct methods. Initially, temperature-programmed desorption of ammonia (NH_3-TPD, TPDRO 1100 series, Thermo Electron) was employed. The instrument underwent a cleaning process with a 20 mL min^{-1} nitrogen flow for 5 min. Subsequently, a 500 mg catalyst sample was degassed at 150 °C for 30 min under a constant nitrogen flow (20 mL min^{-1}). The sample was then cooled to 50 °C, and ammonia was adsorbed for 1 h. Once saturation was achieved, nitrogen purging was conducted for 30 min at 20 mL min^{-1} to eliminate excess ammonia from the catalyst's surface. Finally, the catalyst sample was subjected to heating from 50 to 800 °C for 1 h under a constant helium flow (20 mL min^{-1}), with a ramping rate of 10 °C min^{-1}. The concentration of desorbed ammonia was quantified using a thermal conductivity detector (TCD).

Subsequently, total acidity, representing acid density, was determined using the acid-base titration method, following the procedure outlined by Namchot *et* al. [466]. Here, 100 mg of the catalyst was mixed with 100 mL of

0.1 M NaOH solution and stirred at 145 rpm at room temperature overnight. Following this, 10 mL of the solution was back-titrated with 0.5 M HCl until a neutral pH was achieved. These measurements were conducted in triplicate for accuracy.

3.14.2 Hammett acidity

The Hammett acidity function (H_0) was utilised to assess the Brønsted-Lowry acidities of carbon cryogels incorporated with $H_3PW_{12}O_{40}$-Nb_2O_5. In this study, 4-nitroaniline, possessing a $pK(I)_{aq}$ value of 0.99, was chosen as the basic indicator. Water was selected as the solvent due to its ability to dissolve a wide range of substances and its relative chemical inertness.

A 100 mg sample of the catalyst and a portion of Hammett indicator (3.07×10^{-1} mmol L^{-1}) were dissolved in 20 mL of distilled water. This mixture was stirred for 12 h in the sealed beaker at room temperature, after which the solid was isolated through filtration. Subsequently, the absorbance of the mixture was measured using a Cary 500 UV/Vis/NIR spectrophotometer at 360 nm.

The Hammett value was determined using the calculation described in **Eq. 3.14**, as detailed elsewhere [187, 467]. In this equation, $pK(I)_{aq}$ represents the pK_a value of the aqueous indicator solution, while $[IH^+]_s$ and $[I]_s$ denote the respective molar concentrations of the protonated and unprotonated forms of the indicator in the solvent. The maximal absorbance was obtained from the unprotonated form of the indicator and decreased upon the addition of the carbon cryogel catalyst to the indicator solution.

$$H_o = pK(I)_{aq} + \log\left(\frac{[I]_s}{[IH^+]_s}\right) \quad (3.14)$$

3.14.3 Lewis acid content

Lewis acid sites were quantified by calculating the difference between the total acidity acquired through the titration method (**Section 3.14.1**) and the Brønsted-Lowry acid sites determined using the Hammett acidity function (**Section 3.14.2**). Hence, the ratio of Brønsted-Lowry to Lewis acid sites can be deduced.

3.14.4 Synergy factor

The synergy factor (**Eq. 3.15**) of the carbon cryogel catalyst was calculated to assess its overall catalytic performance using **Eq. 3.16** and **Eq. 3.17** particularly in situations where the catalyst contains multiple active sites or components. This factor helps to understand whether the combination of different catalytic components or sites in the carbon cryogel results in a synergistic effect, which means that the acid functionalised carbon cryogel, is more effective in promoting a chemical reaction than the individual components would be on their own.

$$\text{Synergy factor} = \frac{A}{B} \tag{3.15}$$

A represents selectivity of LA in the mixed acid system

B represents the theoretical selectivity of LA in the mixed-acid system (ratio of Brønsted-Lowry acid × selectivity of LA catalysed by pure Brønsted-Lowry acid) + (ratio of Lewis acid × selectivity of LA catalysed by pure Lewis acid)

$$\text{Selectivity (\%)} = \frac{\text{yield of LA}}{\text{LA conversion}} \times 100\% \tag{3.16}$$

$$\text{Conversion (\%)} = \frac{\text{mass of cellulose reacted}}{\text{initial mass of cellulose}} \times 100\% \tag{3.17}$$

3.14.5 Surface area and pore distribution

The surface area, pore size and volume of catalyst samples were evaluated according to the standard N_2 physisorption using a Micromeritics ASAP2020 analyser. The catalyst samples were outgassed in vacuum at 300 ℃ for 10 h before N_2 physisorption. The surface area of the catalyst was determined using the Brunauer–Emmet–Teller (BET) method. The distributions of the micropores and mesopores were estimated using the t-plot and Barrett, Joyner & Halenda (BJH) methods, respectively.

3.14.6 Porosity and element analysis

SEM, as described in **Section 3.6**, was utilised to examine the distribution of the porous structure in the carbon cryogels. Energy-Dispersive X-ray Spectroscopy (EDX) was used to check the elemental analysis and its distribution. The sample was prepared similarly to the one used for SEM analysis, involving coating with a conductive layer. Specific regions of interest were then selected for EDX mapping using the X-Max detector at a 35° angle, with an accelerating voltage set at 20 kV.

3.14.7 Chemical changes in functional group

FTIR analysis, as detailed in **Section 3.6**, was performed to observe any alterations in the functional groups present in carbon cryogels incorporated with $H_3PW_{12}O_{40}$-Nb_2O_5. The identification of these functional groups was based on comparison with an IR spectrum table (refer to **Appendix 5**). .

3.15 Determination of kinetic and thermodynamic parameters

Experiments targeting the conversion of OPMF to LA were conducted using a 14 mL borosilicate reactor (FAVORIT, 20.75 × 70.00 mm). The procedure

outlined in **Section 3.11**, was followed, incorporating the optimised reaction conditions employed in **Section 3.13**. This involved a carbon cryogel catalyst loading of 0.131 g, biomass loading of 0.074 g, and a GVL-to-water ratio of 8.414. Simultaneously, microwave power was set at five different levels: 100 W, 150 W, 200 W, 250 W, and 300 W to investigate the kinetics of the conversion process at intervals of 20 s, 40 s, 60 s, 80 s, 100 s, and 120 s. To ensure accuracy and reliability, triplicate samples were prepared for each level of microwave power, and the product yields including LA produced were determined under varied power conditions using HPLC-VWD analysis described in **Section 3.12**.

3.16 Deducing mechanism pathway

A simple mechanism pathway was proposed based on the product analysis obtained based on method specified in **Section 3.12**. Due to complex reaction of biomass conversion to LA, possible unknown products were expected to produce. The GC analysis (Perkin Elmer Clarus 680, USA) equipped with an MS detector and a fused silica capillary column (Agilent HP-FFAP, 30 m length x 0.32 mm diameter x 0.25 μm film thickness, USA) was conducted using helium as a carrier gas to screen products with unknown concentrations from the product analysis obtained via HPLC-VWD. The unknown analysis by GC-MS was relied on compound identification using spectral matches against mass spectral libraries according to NIST library guidelines (**Table 3.5**) that shows highest similarity score. The oven temperature was initially set at 90 °C and maintained for 3 min, after which it was increased at a rate of 10 °C min^{-1} until reaching 230 °C, where it was held for an additional 10 min. The auto injector (InjBauto) temperature was set at 240 °C, and a solvent delay of 2 min was implemented. The injection volume and split ratio were set at 1.0 μL and 50:1, respectively.

Both the transfer and source temperatures were set at 200 °C. The mass spectrometer was configured to scan from 35 to 350 Da.

Table 3.5 NIST library guidelines [468].

Match Factor (SI) or Reverse Match Factor (RSI) Thresholds	Mass Spectral Match
900 and above	Excellent
800–900	Good
700–800	Fair
<600	Poor

3.17 Catalyst recycling

The biomass conversion experiments to produce LA through microwave irradiation were conducted using a fresh catalyst—carbon cryogel, following the procedures outlined in **Section 3.11**. The optimised reaction conditions, as obtained in **Section 3.13**, were employed. Upon completing the microwave heating process, the resulting product was extracted from the reactor using a 10 mL glass pipette. The catalyst underwent three rinses with distilled water, followed by drying in an oven at 60 ℃ for 12 h. Subsequently, it was calcined at 100 ℃ to regenerate active sites. This catalyst regeneration process enabled its reuse for subsequent cycles, and this cycle repetition was continued up to the 8^{th} iteration. For each catalytic conversion cycle, triplicate samples were prepared to ensure consistency and reliability of the results.

3.18 Characteristics of fresh and recycled catalysts

3.18.1 X-ray photoelectron spectroscopy (XPS)

The fresh and recycled carbon cryogel samples, each cut to dimensions of 1 × 1 cm, were subjected to analysis. The analysis instrument was purged with an Ultra High Vacuum (UHV) environment to prevent surface contamination and ensure precise sample analysis. The XPS (Kratos/Shimadzu Axis Ultra DLD) instrument was utilised to irradiate the material's surface with X-rays, inducing the emission of photoelectrons. The resulting XPS spectra, detailing the energy and intensity of emitted photoelectrons, were meticulously analysed to identify peaks corresponding to targeted elements and reveal their chemical states. The kinetic energy of photoelectrons was directly correlated with the binding energy of electrons within the sample.

3.18.2 X-ray fluorescence spectroscopy (XRF)

Carbon cryogel sample was ground into a fine powder and pressed into a pellet using a hydraulic press. This ensures a homogeneous representation of the sample. Calibration was performed using certified reference materials, employing SQX calculations to ascertain known elemental compositions. This calibration generated a curve that establishes a correlation between the X-ray intensity recorded by the detector and the concentration of elements in the sample. Subsequently, the prepared sample was introduced into the XRF instrument (Rigaku, ZSX Primus IV), and the X-ray tube was activated to emit X-rays. Upon interaction with the sample, X-rays induced the emission of characteristic fluorescent X-rays. The intensity and energy of these emitted X-rays were measured by the detector, and the data were analysed to identify the

peaks corresponding to targeted elements. The intensities of these peaks were then utilised to quantify the elemental concentrations. Comparisons between the intensities of characteristic X-ray peaks and the calibration curve enabled the determination of element concentrations in the sample. The results were reported as a comprehensive list of elemental concentrations present in the sample. The elemental concentrations of both the fresh carbon cryogel and the recycled carbon cryogel were assessed.

3.18.3 Raman spectroscopy

Carbon cryogel samples were prepared and exposed to monochromatic light. Raman spectroscopy (Thermo Scientific, DXR2xi) with a 532 nm laser and a 50 μm slit was used to examine the light scattered by the sample. The Raman effect, observed through the inelastic scattering of monochromatic light, enabled the measurement of frequency changes in photons interacting with the sample. This shift yielded valuable information about the carbon defects in the carbon cryogel, facilitating a comparison between the fresh and recycled catalysts.

3.19 Cost components

The materials and chemicals utilised in both the carbon cryogel process and the microwave conversion of biomass to LA are detailed in **Table 3.6.** Prices were updated based on 2023 rates obtained from the Evergreen supplier.

Table 3.6 Current price of materials or chemicals used for carbon cryogel synthesis.

Entry	Materials/ Chemicals	Price (RM)
1	Alkaline lignin	70 / 100 g
2	Phosphotungstic acid	412 / 100 g
3	Niobium oxide (CAS Number 1313-96-8)	430 / 100 g
4	Xanthan gum (CAS Number 11138-66-2)	423 / 100g
5	t-butanol	8.60 /100 mL
6	γ-valerolactone	169/ 100 mL

3.20 Cost estimation method

The expenses associated with the catalytic conversion of biomass to LA employing carbon cryogel incorporated with $H_3PW_{12}O_{40}$-Nb_2O_5 were initially assessed by considering the cost of raw materials and the electricity consumption of the equipment utilised during the catalytic process. The power consumption of the equipment was determined using the power ratings specified in the instrument manuals. This power consumption was then multiplied by the duration of usage, and the electricity rate was based on Tariff B (Low Voltage Commercial Tariff) provided by Tenaga Nasional Berhad, which stands at 32 sen/kWh for a single unit of usage.

Chapter 4

Identification of Oil Palm Mesocarp Fibre Main Components and The Solvent Effects on Components Deconstruction

4.1 Introduction

The choice of solvent is crucial in enhancing cellulose extraction as it influences biomass deconstruction, improves cellulose solubility to promote hydrolysis, disrupts biomass structure, and affects lignin and hemicellulose removal or fragmentation [469]. The successful breakdown of lignocellulosic biomass into its constituent components heavily depends on solvent properties including the thermal stability of the solvent used. Solvent extraction typically involves subjecting the biomass to high temperatures to facilitate the dissolution of these components. A thermally stable solvent can withstand these elevated temperatures without degrading or losing its efficacy, ensuring efficient dissolution and solvation of various biomass components [441]. As a result, it can effectively fractionate cellulose, hemicellulose, and lignin from the biomass matrix.

Microwave treatment significantly influences cellulose crystallinity, a key factor affecting its susceptibility to hydrolysis. Crystallinity refers to the organisation and packing of cellulose chains within microfibrils. Microwave irradiation disrupts this crystalline structure by breaking hydrogen bonds and reducing crystallinity [153], making cellulose more accessible to acids during subsequent hydrolysis. A less crystalline cellulose structure is more receptive to

breakdown, leading to improved hydrolysis rates and yields [470]. The crystallinity index (CrI) is crucial in assessing the balance between crystalline and amorphous regions, especially after microwave treatment with the solvent.

In addition to its impact on crystallinity, microwave treatment plays a vital role in altering the functional groups and structural characteristics of cellulose [141]. This treatment can introduce or modify functional groups on the cellulose surface, such as carboxyl, aldehyde, or ketone groups. These new functional groups act as catalytic sites for hydrolysis reactions, enhancing the reactivity of cellulose with hydrolytic agents. As a result, microwave treatment facilitates the breakdown of cellulose into its constituent glucose molecules, a critical step in the hydrolysis process. These functional groups also enhance the compatibility of cellulose with various hydrolysis catalysts or solvents, providing additional support to the overall efficiency of the hydrolysis process.

This chapter of the thesis focuses on several key areas: (1) the identification of the primary components of biomass, (2) the evaluation of lignin and hemicellulose removal processes, (3) the assessment of cellulose recovery, (4) the study of how solvent properties affect biomass deconstruction, and (5) the investigation of the impact of microwave treatment on the characteristics of cellulose.

4.2 Identification of biomass components

Based on **Figure 4.1**, TGA analysis shows the weight loss profile, reflecting the decompostion of different components present in the biomass, such as cellulose, hemicellulose, lignin, and other organic matter. Overall, the thermal decompositon of components for OPMF and DOPMF was slightly different.

Despite lower moisture content < 10% for both OPMF and DOPMF at Stage I (30–130 °C), the TGA curve illustrated that decomposition of components in OPMF was slightly faster than DOPMF. It was obvious at Stage II, between 250–290 °C, the weight loss of biomass components in OPMF at the respective temperature range was slightly greater than DOPMF, representing holocellulose contents that comprised cellulose and hemicellulose. This may presumably because of the presence of impurities in the raw bioamass material such as waxes, oils, and other extractives, leading to an earlier onset of decomposition of OPMF.

Furthermore, the difference can also be attributed to difference in cellulose and hemicellulose compositions between OPMF and DOPMF before and after dewaxing process. Based on additional chemical analysis (**Appendix 3**), the quantification of cellulose and hemicellulose is presented as in **Table 4.1**. After dewaxing process, hemicellulose contents slightly decreased (from 19.7 to 17.7%) while cellulose contents slightly increased (from 30.0 to 32.0%). This may be caused to the natural behaviour of amorphous hemicellulose that is more susceptible to degradation or removal during dewaxing pretreatment at 80 °C [471] , resulting in its lower content in DOPMF. This is in agreement with the previous study which reported that hemicellulose has a slightly lower temperature of starting thermal degradation at 190–230 °C than that of cellulose

at 210 °C and higher [472]. Hence, dewaxing can be additional step to carry out selective removal of hemicellulose.

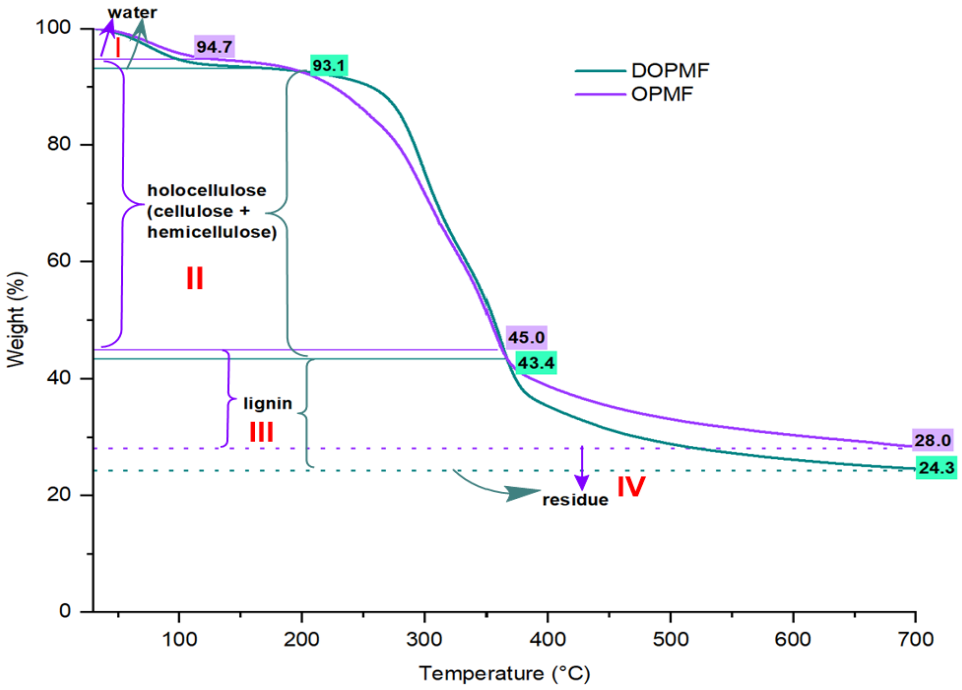

Figure 4.1 TGA curves representing main biomass components composition.

Table 4.1 Compositions of lignocellulosic components.

Cellulose (%)	Hemicellulose (%)	Lignin (%)	Ref.
32.0	17.7	19.1	This study
25.5–43.0	25.3–33.0	16.3–32.4	[141, 473–476]

Meanwhile, lignin at Stage III showed the highest thermal stability among the three components which started to degrade only at 360 °C, owing to its recalcitrant nature that is not easily disrupted. The results showed that a slightly higher lignin content in DOPM (19.1%) than OPMF (17.0%). While the primary aim of the dewaxing process is to eliminate waxes and lipids from biomass, it does not directly affect lignin content. However, there may be situations where TGA analysis suggests a higher weight percentage of lignin in dewaxed biomass. This can occur because some residual lignin remains within the biomass, despite challenges in lignin removal that result in incomplete

separation from other components like cellulose and hemicellulose. As a result, lignin can be retained within the biomass matrix.

At stage IV (below the dotted line), the percentage of residue remained in OPMF (28.0%) was slightly higher than DOPMF (24.3%), following the presence of waxes in biomass that can affect its thermal behaviour. Waxes are long-chain hydrocarbons that have higher melting points and are more stable compared to other biomass components. In this study, the degradation of residues began above 700 °C. Meanwhile, Yasim-Anuar *et* al. reported that the stage of heating for the degradation of residues was above 550 °C. The residues are often referred as char that contain non-volatile components like ash, inorganic minerals, and carbonaceous materials [475]. The difference in starting temperature of degradation of residues could be attributed to variations in the nitrogen flow rate employed during TGA analysis. Nitrogen serves to carry away volatile decomposition products and maintain a consistent environment. A higher nitrogen flow rate can enhance heat transfer and more efficiently remove volatile decomposition products, resulting in faster degradation. However, it is important to note that regardless of the different flow rates tested in the range of 20–100 mL min^{-1}, the percentage change in the remaining residues remained relatively constant at approximately 20%.

It is important to note that undewaxed biomass has a protective wax layer that impedes heat penetration to underlying components like cellulose and hemicellulose. However, when biomass is dewaxed, these components are exposed to direct heat transfer. This exposure facilitates faster thermal degradation, breaking down cellulose and hemicellulose into smaller fragments and volatile compounds. Thus, dewaxed biomass allows for more efficient heat

transfer during thermal processes such as pyrolysis or other biomass conversions. In this study, the TGA analysis of OPMF aligns with the findings in **Table 4.1**. Any minor variations could be due to differences in quantification methods, plantation areas, planting batches, and maturity levels of the sourced samples.

4.3 Efficient removal of lignin and hemicellulose

Figure 4.2 reveals that all tested organic solvents, including GVL, ethyl acetate, 2-butoxyethanol, and ethyl lactate, demonstrated superior lignin removal compared to a selection of ionic liquids (ILs) – BMIM IL, EMIM IL, HMIM IL, and a mixture of HMIM/GVL. These organic solvents achieved at least 85% lignin removal, while HMIM IL and HMIM/GVL showed lower removal rates. These results align with the findings of Long *et* al., who reported a delignification rate of 67.2% at 180 °C, increasing to 90% at 200 °C, when using the acidic ionic liquid [$C_4H_8SO_3$Hmim] HSO_4 on sugarcane bagasse [477]. This suggests that reaction temperature significantly influences the efficiency of solvents in depolymerising lignin.

Yuan *et* al. proposed that organic solvents can effectively remove lignin at lower temperatures due to their ability to break ether linkages in lignin [478]. Additionally, the strong hydrogen bond interactions between the solvent and the free hydroxyl groups in lignin aid in its dissolution [479]. Conversely, ionic liquids require higher temperatures to efficiently remove lignin. This is attributed to their ability to disrupt lignin's complex structure, a naturally occurring aromatic cross-linked polymer [480]. Above 400 °C, radical reactions predominate, leading to an extensive rearrangement of the lignin structure and

cleavage of C–C bonds [481]. This results in the formation of oligomers and monomers, facilitating these radical reactions and overcoming the recalcitrant nature of lignin [480].

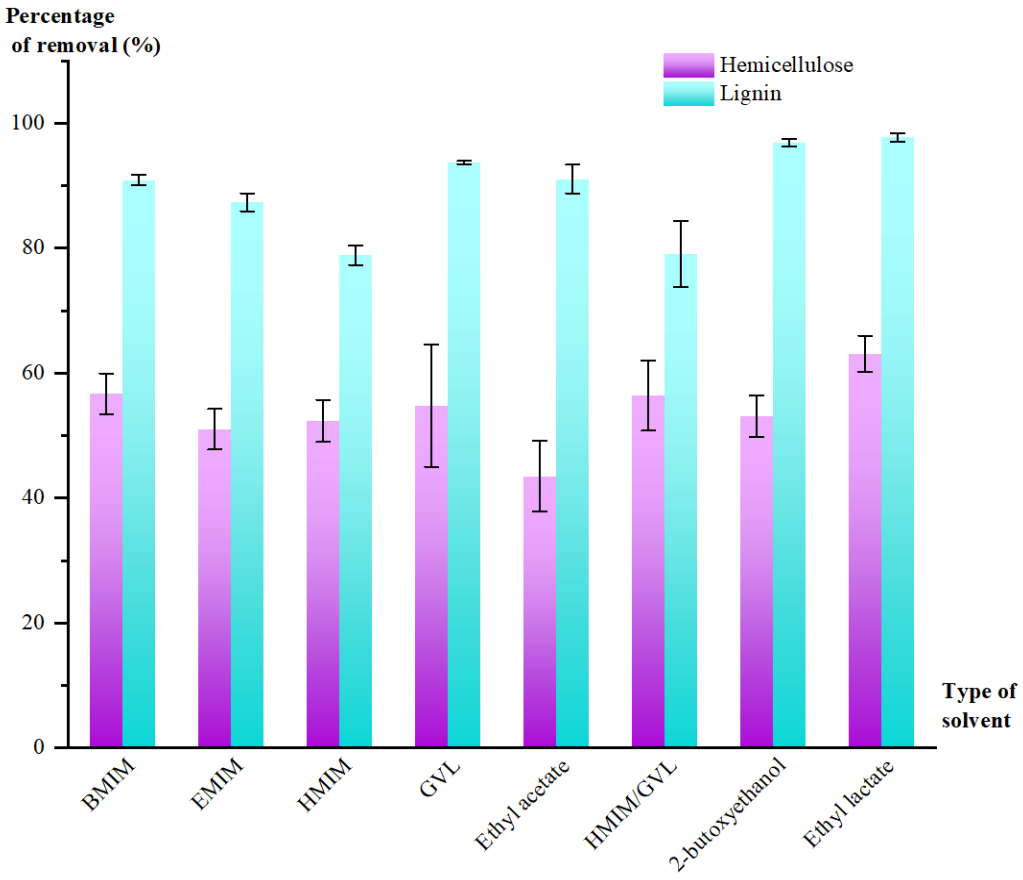

Figure 4.2 Post-microwave extraction: Organic solvents outperform ionic liquids in lignin and hemicellulose removal.

As depicted in **Figure 4.2**, both ILs and organic solvents can remove 55–60% of hemicellulose under microwave conditions (450 W, 2 min). This is because the amorphous and naturally branched structure of hemicellulose makes it more susceptible to deconstruction [482]. Consequently, both organic solvents and ILs can disrupt the hydrogen bonds in hemicellulose, facilitating its solubility and making it easier to extract. The consistent removal of hemicellulose by the tested solvents is also reflected in its extracted percentage, as reported in **Appendix 6**.

However, ethyl acetate was an exception, resulting in less than 50% hemicellulose removal. This could be attributed to its specific interactions with hemicellulose. Factors such as the solvent's polarity, hydrogen bond capacity, and the specific conditions of the extraction process can influence the efficiency of hemicellulose removal [483]. Under the conditions used, ethyl acetate might not interact as effectively with hemicellulose, leading to lower removal rate.

High removal of lignin and hemicellulose can create conditions that are more favourable for the hydrolysis of cellulose. By removing these components, the cellulose becomes more accessible [484]. This is due to the increase in the surface area of the cellulose fibres, which allows for better contact between the cellulose and the hydrolytic agents [485]. This improved accessibility makes it easier for hydrolysis to occur, leading to higher glucose yields and further promoting LA yield. The efficient removal of lignin and hemicellulose also increases the porosity of the biomass material [486] . This enhanced porosity can facilitate the penetration of water, solvent particles, and catalyst into the material, further promoting cellulose hydrolysis.

4.4 Recovery of cellulose

Figure 4.3 illustrates the increasing order of cellulose recovery via solvent-extraction: BMIM IL < HMIM IL < HMIM/GVL < EMIM IL < ethyl acetate < ethyl lactate < 2-butoxyethanol < GVL. Both GVL and 2-butoxyethanol demonstrated nearly 100% cellulose recovery, indicating their effectiveness in separating cellulose from other components such as lignin and hemicellulose. The amount of recovered cellulose is a key determinant of its readiness for hydrolysis [487]. The recovery of cellulose is indicative of the rate at which the biomass structure is disrupted. As cellulose is a primary component of

lignocellulosic biomass and maintains its physical integrity [488], its recovery reflects this disruption.

Among the solvents, GVL is expected to favour the production of LA due to its strong extraction capability. This enhances biomass deconstruction, making the loosened cellulose microfibrils more amenable for subsequent conversion to LA. Wettstein *et* al. investigated cellulose breakdown at 428 K in two-phase reaction setups with GVL and water-based solutions containing HCl (0.1–1.25 M) and an additional substance like salt or sugar. This dual-phase system yielded significant levulinic and formic acid (approximately 70%) and completely dissolved cellulose [489].

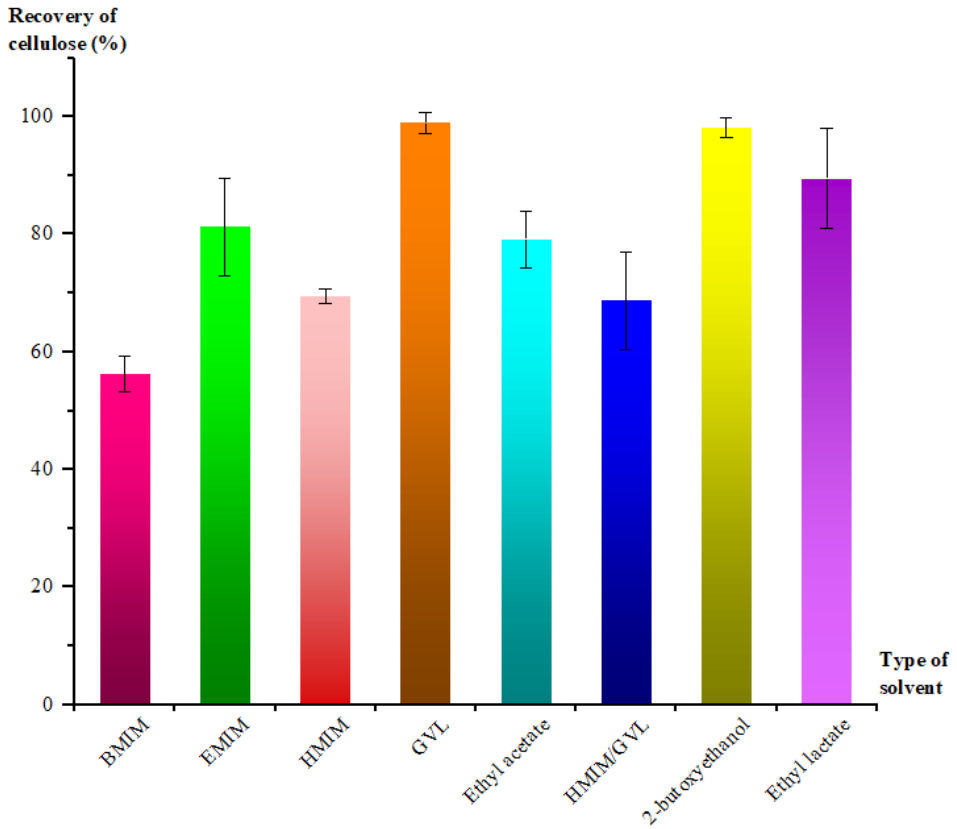

Figure 4.3 Cellulose recovery via solvent extraction: GVL leads with the highest yield, while BMIM IL lags at a mere ~22%.

4.5 The influence of solvent properties in biomass deconstruction

Variations in recovery of cellulose and lignin and hemicellulos removal are primarily driven by solvent parameters related to polarity, viscosity, thermal stability, and solubility.

Polarity plays a pivotal role in determining the solubility of lignocellulosic components. The percentage of recovered cellulose can be influenced by the high electric dipole moment of polar protic solvents [490], due to the presence of hydroxyl (O–H) and amine (N–H) groups. Polar protic solvents, such as 2-butoxyethanol and ethyl lactate, can form strong hydrogen bonds with the hydroxyl groups in cellulose. This bonding promotes the dissolution of cellulose in the extracting solvent, making it more amenable to extract.

On the flip side, polar aprotic solvents like GVL and ethyl acetate exhibit weaker hydrogen bonding but possess a larger dielectric constant and dipole moment due to oxygen double-bound carbon, allowing them to attack cellulose's glycosidic bonds through reactive nucleophile species [488]. This, in turn, makes the hydrolysis of cellulose into glucose and further conversion to LA products feasible. Given that GVL itself is derived from lignocellulosic biomass, it naturally exhibits high compatibility with lignocellulosic biomass solubilisation.

The slightly higher hemicellulose removal achieved by protic polar solvents like GVL and ethyl lactate in comparison to ethyl acetate (**Figure 4.2**) can be attributed to their capability of forming hydrogen bonds with polar functional groups present in hemicellulose, making them effective in hemicellulose removal [483]. The interaction between polar solvents and

hemicellulose molecules helps to break the hydrogen bonds holding hemicellulose in the biomass matrix.

Cellulose's high solubility in GVL can also be attributed to its relatively low viscosity (2.18 mPa·s at 25 °C) compared to the tested ILs, 2-butoxyethanol, and ethyl lactate (**Table 4.2**). This lower viscosity allows for more efficient mass transfer during dissolution. On the contrary, ethyl acetate, with its extremely low viscosity and boiling point (77 °C) (**Table 4.2**), indicates weaker intermolecular forces that require less energy to overcome. As a result, more vigorous attacks on cellulose occur, subsequently influencing the recovery of cellulose.

The extraction capability of ILs for cellulose follows the inverse order of their viscosity trend (**Table 4.2**), specifically [BMIM][Cl] < [HMIM][HSO_4] < [EMIM][Ac]. [EMIM][Ac], with its shorter alkyl chain length, lower hydrophobicity, and reduced viscosity, creates favourable conditions for dissolving hydrophilic cellulose containing large hydroxyl groups. Conversely, [HMIM][HSO_4], with a monoalkylated structure and longer chain, has the opposite effect. The increasing viscosity of ILs leads to a decrease in density and surface tension, resulting in lower extraction power [491]. Additionally, ILs, with their poorly coordinated delocalised charge (anion) and organic ion (cation), can prevent the formation of a stable crystal lattice in cellulose. The disruption of the crystal lattice could lead to a breakdown of the cellulose structure, potentially reducing the amount of intact cellulose that can be recovered after the treatment.

Table 4.2 Viscosity of imidazolium-based ILs and organic solvents.

Temperature (K)	Solvent	Viscosity (mPa·s)	Ref.
293.15	[BMIM][Cl]	4134.33	This study
	[HMIM][HSO_4]	1669.67	This study
	[EMIM][Ac]	181.53	This study
	[HMIM][HSO_4]/GVL	149.23	This study
	Ethyl lactate	2.71	[492]
298.15	2-butoxyethanol	2.90	[493]
	GVL	2.18	[494]
	Ethyl acetate	0.46	[495]

GVL boasts a high boiling point (205 °C), low vapour pressure, and exceptional thermal stability even at operating temperatures as high as 180 °C (450 W), ensuring it maintains its solubilising power over extended periods. To broaden the understanding of solvent capabilities in the deconstruction of biomass components using a combination of organic solvents and ILs, a study was conducted. This study examined the simultaneous removal of hemicellulose and lignin, along with the recovery of cellulose, using a 1:1 (*v/v*) mixture of [HMIM][HSO_4] and GVL. [HMIM][HSO_4] was selected due to its ability to extract all three components and its potential cost-effectiveness compared to other ILs.

In comparison, [EMIM][Ac] was considered too expensive, while [BMIM][Cl] raised safety concerns, limiting their practicality. Additionally, [HMIM][HSO_4] displayed superior thermal stability compared to other ILs, as demonstrated in the TGA thermogram (**Figure 4.4**), thus offering a broader range of operating temperatures for potential improvements.

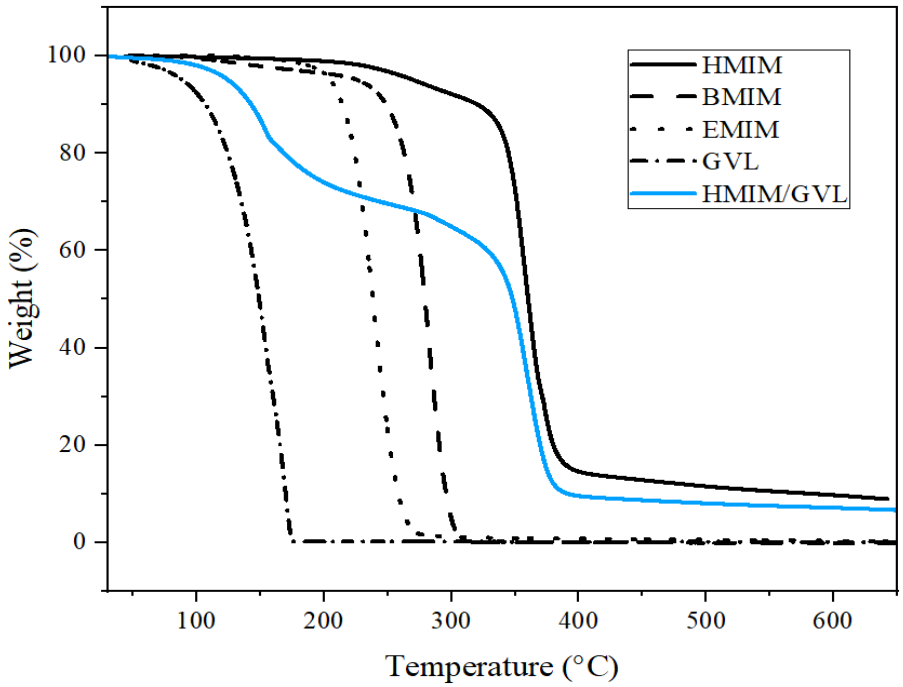

Figure 4.4 Thermal stability of different types of ILs and GVL.

However, the [HMIM][HSO_4]/GVL (1:1, *v/v*) mixture did not significantly enhance the removal of lignin and hemicellulose as well as the regeneration of cellulose to pure [HMIM][HSO_4] (**Figure 4.2 & 4.3, Section 4.3 & 4.4**). The addition of GVL to the ILs system did not yield the expected increase in regenerated cellulose, likely due to the interruption of the non-polar hydrocarbon chain from [HMIM][HSO_4], which limited cellulose solubility. Nonetheless, the mixture allowed for a reduction in [HMIM][HSO_4] consumption without compromising its decent performance in extracting all biomass components. This presents a cost-saving option since GVL (3.88 $/kg) [496] is approximately three times cheaper than [HMIM][HSO_4] (10 $/kg) [497].

4.6 Effects of microwave treatment on cellulose characteristics

From the initial screening, GVL appeared to have greater potential than other solvents for enhancing the deconstruction of biomass. This corresponds to its ability to recover a high percentage of cellulose while simultaneously removing significant amounts of hemicellulose and lignin, thus facilitating the hydrolytic process. Given this, it is important to observe the behaviour of cellulose as it undergoes microwave irradiation treatment in conjunction with GVL solvent extraction. Microwave treatment is a versatile and efficient method for modifying cellulose characteristics, which ultimately influences its propensity for hydrolysis. This treatment can significantly impact the purity, crystallinity, and functional group properties of cellulose, all of which play a crucial role in determining its reactivity during hydrolysis.

4.6.1 Structural purity

DTG thermograms (**Figure 4.5a**) reveal two peaks around 300 °C and 350 °C in both OPMF and DOPMF, corresponding to the decomposition of hemicellulose and cellulose, respectively. This observation aligns with Diez *et* al., who suggested that hemicellulose decomposes first between 200–300 °C, followed by cellulose between 250–380 °C [498] . The disappearance of a broad peak in the lower degradation temperature range (200–300 °C) in the extracted cellulose indicates the successful removal of thermally unstable hemicellulose during the microwave extraction process using GVL.

Figure 4.5a shows that the DTG curve of the cellulose sample has a greater derivative weight regarding its deconvoluted peak area compared to cellulose in OPMF and DOPMF (as detailed in **Appendix 7**). This indicates that the extracted cellulose has a higher purity (83%) compared to DOPMF (46%)

and OPMF (41%). Higher purity means fewer impurities like hemicellulose and lignin, which can interfere with cellulose hydrolysis. Pure cellulose has a more crystalline structure following the removal of amorphous regions from both hemicellulose and cellulose, increasing the crystallinity and intermolecular hydrogen-bonded domains [499]. This crystallinity makes it less susceptible to hydrolysis because catalysts or enzymes find it harder to break down the tightly packed cellulose fibres. Conversely, the pretreated biomass from DOPMF may have more amorphous cellulose than crystalline, indicating its lower purity compared to extracted cellulose. DOPMF is preferable over OPMF for extraction as the wax and cuticles are removed, leaving a greater amount of amorphous and crystalline components for subsequent dissolution and hydrolysis. This is supported by a higher derivative weight change in DOPMF as shown in the DTG thermogram (**Figure 4.5a**).

Despite the higher purity of cellulose obtained by microwave extraction, the thermal degradation of cellulose (**Figure 4.5a**) shifts slightly to a lower range of 200–300 °C. This shift could be due to the substitution of cellulose hydroxyl groups by GVL carboxyl groups, forming carboxylate esters that graft onto the cellulose surface through a transesterification reaction. This process reduces the sample's resistance to pyrolysis, initiating cellulose dehydration, releasing water, and leading to cellulose decomposition [500]. The reduced thermal stability can also be attributed to the smaller dimensions of crystalline cellulose, which provide a larger surface area for heat conditions.

The DSC curve of regenerated cellulose from DOPMF (**Figure 4.5b**) shows a melting temperature (T_m) at 164 °C, corresponding to the crystalline part of cellulose. The small peaks at lower temperatures (130–150 °C) are

presumably attributed to the endothermic transition of some remaining amorphous components. The sharpness of the peak at 164 °C confirms the crystallinity of the obtained cellulose and the effectiveness of GVL in fractionating hemicellulose and cellulose and removing the amorphous components during microwave extraction.

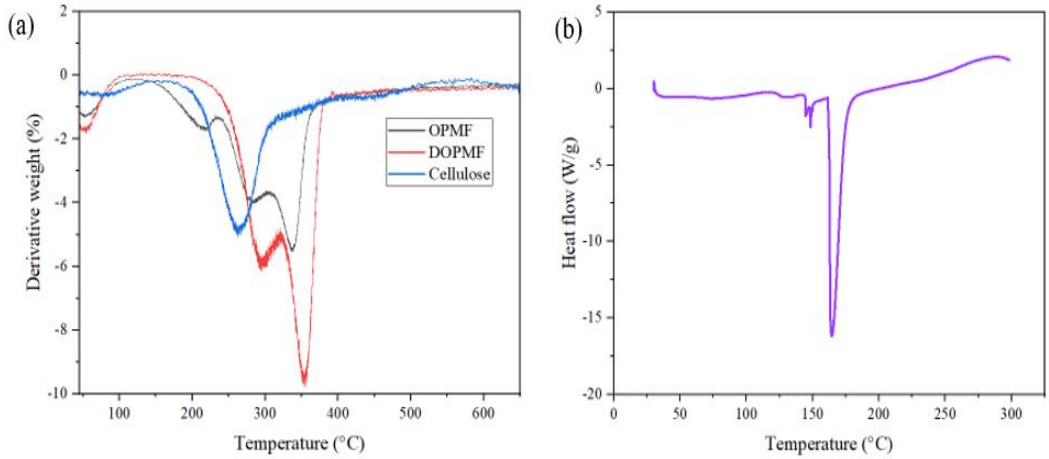

Figure 4.5 (a) Derivative thermogravimetric (DTG) curves of OPMF, DOPMF, and regenerated cellulose; (b) DSC curve of regenerated cellulose. The regenerated cellulose was obtained by dewaxing followed by GVL-microwave extraction.

4.6.2 Structural crystallinity

The XRD patterns in **Figure 4.6** display the characteristic peaks of the cellulose I structure around 22°, with less intense peaks at approximately 18°. These peaks correspond to the amorphous regions of cellulose, as detailed in **Table 4.3**. In the XRD pattern of oil palm biomass, a peak at 28° is often associated with the presence of minerals [501]. Dewaxing can expose or concentrate mineral components within the fibre, such as silica or other inorganic compounds, which can produce sharp diffraction peaks [502]. These minerals are often present in

small amounts in plant materials and can become more prominent after dewaxing [501].

During the extraction process, the structural arrangement of the fibres is altered, and many of the mineral components present in the raw fibre are removed, causing the intensity of the peak at 28° to decrease [503]. The extraction process focuses on isolating cellulose, which reduces the presence of other components like lignin and minerals. This purification results in a more defined cellulose structure, typically showing peaks around 22°, while reducing the intensity of peaks associated with other materials [504]. However, the second peak, likely contributed by silica minerals appearing in the cellulose component (**Figure 4.6**), is probably due to the extraction process using GVL and the isolation of cellulose with NaOH. This process removes organic and amorphous components, concentrating and exposing different phases of silica that were not as prominent in the raw fibre [502, 505].

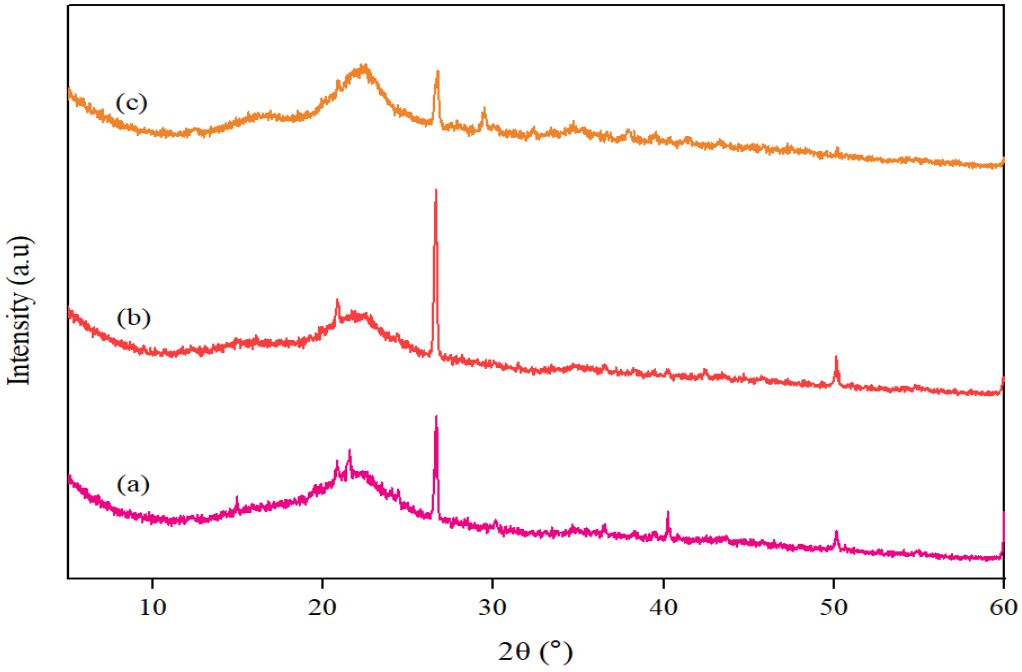

Figure 4.6 XRD patterns of (a) OPMF; (b) DOPMF; (c) cellulose.

Table 4.3 The crystallinity index of OPMF samples throughout dewaxing and GVL-microwave extraction.

Ref.	Samples	2θ (Amorphous) (°)		2θ (002) (°)		CrI (%)
		Degree	Intensity (I_{am})	Degree	Intensity (I_{002})	
This study	OPMF	18.54	733.08	21.92	965.37	24.06
This study	DOPMF	18.75	640.10	21.86	972.97	34.21
This study	Cellulose	18.25	633.07	22.50	1190.21	46.81

Following the dewaxing process, the CrI increases due to the removal of wax and cuticle, which allows better solvent access to the cellulose structure. The highest CrI observed, 46.81%, results from microwave extraction in GVL. This high CrI is attributed to the removal of lignin and hemicellulose from cellulose fibrils and the dissolution of the amorphous cellulose region.

It is important to note that the CrI obtained in this study indicates a higher proportion of amorphous regions compared to crystalline ones. This suggests that the cellulose is more likely to undergo hydrolysis. The balance between crystalline and amorphous regions can significantly vary depending on factors such as the source of cellulose, processing conditions, and treatment methods used.

GVL effectively penetrates the amorphous regions of cellulose, leading to the hydrolytic cleavage of glycosidic bonds and the release of individual crystallites. This is evident in the narrower XRD diffraction peaks (see **Figure 4.6c**). The increase in CrI suggests that microwave extraction with GVL produces relatively pure crystalline cellulose. A higher CrI indicates improved mechanical properties of crystalline cellulose, such as stiffness, rigidity, and durability, which is suitable for those involving high-temperature processes. However, in this case, cellulose with lower CrI is preferable to allow cellulose

accessibility to chemicals that break down cellulose structure. These regions are less tightly packed than the crystalline regions, allowing for easier penetration and breakdown.

The results suggests that microwave technologies can more effectively break down the crystalline structure compared to other pretreatment methods such as alkaline or acid hydrolysis, and steam explosion. These methods yield a higher crystallinity index of extracted cellulose, which is not favourable for biomass conversion studies, even though it may be useful for various demanding industrial applications.

4.6.3 Functional groups and structural changes

Through FTIR analysis, the structural transformations and functional group alterations from raw OPMF to dewaxed OPMF, and finally to extracted cellulose are meticulously examined, as depicted in **Figure 4.7**. Initially, OPMF contained a variety of compounds, including alkanes, esters, aromatics, ketones, and alcohols. Significant changes were observed in the O–H stretching region, specifically at the peak of 3285 cm^{-1}, associated with phenolic and aliphatic groups. Both OPMF and DOPMF samples showed hydrophilic behaviour, as indicated by the O–H stretching peaks. However, GVL extraction reduced the intensity of this peak in the cellulose sample, suggesting disrupted hydrogen bonding and a broader peak (ranging from 3000 to 3328 cm^{1}) corresponding to residual carbohydrate. This suggests that GVL-microwave extraction could initiate cellulose hydrolysis.

Further evidence of lignin and amorphous region removal was obtained by analysing changes in C–H stretching before and after GVL-microwave extraction. The C–H vibration peak at 2918 cm^{-1}, attributed to methyl and

methylene groups of lignin, was present in both OPMF and DOPMF samples but disappeared in the cellulose sample, signifying the successful removal of lignin. After GVL-microwave extraction, the peak around 2851 cm^{-1} related to C–H stretching in the amorphous region of cellulose, disappeared, indicating the removal of the amorphous cellulose structure. The peak around 1377 cm^{-1}, related to C–H in the crystalline region of cellulose, showed a slight reduction, suggesting decreased crystallinity.

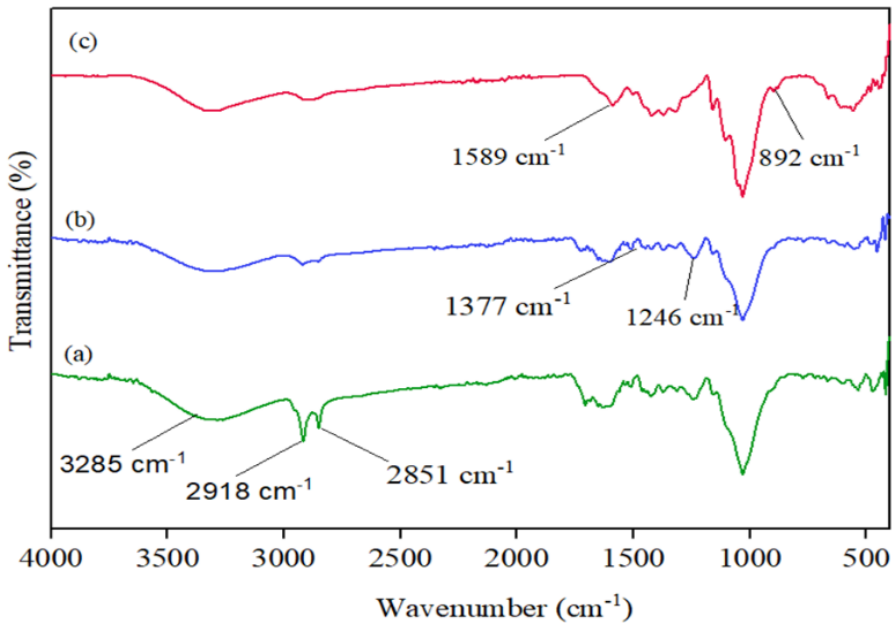

Figure 4.7 FTIR spectra of **(a)** OPMF; **(b)** DOPMF; **(c)** cellulose.

The impact of GVL on cellulose extraction was evident in the C=O stretching region, associated with carbonyl functional groups. This band was notably present in the cellulose sample at the peak of 1589 cm^{1}, indicating the substitution of cellulose hydroxyl groups by highly reactive keto-lactone and carboxylic groups from the GVL solvent. The syringyl ring and C–O stretching peak at 1246 cm^{-1}, observed in the spectra of OPMF and DOPMF, gradually disappeared in the cellulose spectrum, indicating the removal of lignin and a

portion of hemicellulose via GVL-microwave extraction. The purity of crystalline cellulose was confirmed by the presence of β-glycosidic linkages in the glucose ring of the cellulose chain, a feature absents in the OPMF and DOPMF samples.

Surface morphology changes were meticulously examined through SEM analysis, from OPMF to dewaxed OPMF (DOPMF), and ultimately to the extracted cellulose (**Figure 4.8**). The initial state of raw OPMF (**Figure 4.8a**) had a notably rough surface, characterised by impurities, wax, fatty substances, and globular protrusions [506]. The dewaxing process effectively removed these rough and irregular surface features, resulting in a smoother surface (**Figure 4.8b**). This smoother surface post-dewaxing primed the material for more efficient GVL-microwave extraction of cellulose (**Figure 4.8c**), as the prior removal of non-cellulosic components enhanced accessibility.

The microwave-based extraction within GVL disrupted the lignocellulosic complex, leading to the shortening of the long fibres and generating more fragments and wrinkles (**Figure 4.8c**). It facilitated the solubilisation of lignin and hemicellulose, resulting in the exposure of a higher porosity and a wider surface area within the concealed cellulose structure (**Figure 4.8d**), as previously reported by Chieng *et* al. [460].

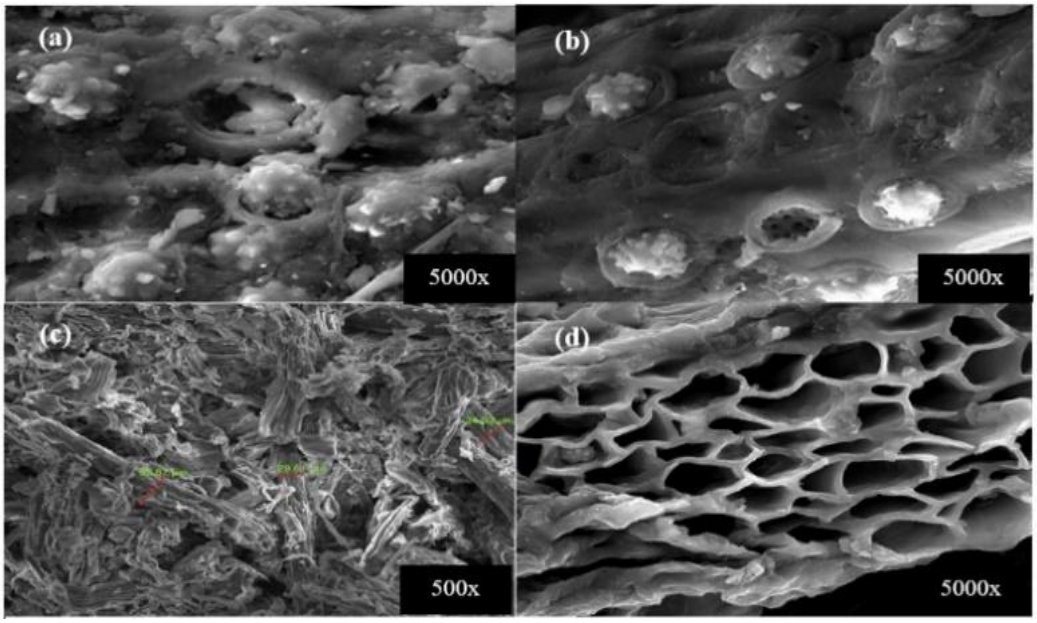

Figure 4.8 SEM represents morphology of **(a)** raw biomass (OPMF); **(b)** DOPMF (dewaxed); **(c)** cellulose (size fraction: 29.61–52.87 μm); **(d)** porous structure of cellulose after GVL-microwave extraction.

4.7 Concluding remarks

The study revealed several key insights into the effects of various treatments on the deconstruction of biomass components. The results demonstrated that the TGA analysis showed a decrease in hemicellulose content and an increase in cellulose content after dewaxing, highlighting the natural susceptibility of amorphous hemicellulose to degradation. Organic solvents exhibited superior lignin removal capabilities compared to ionic liquids (ILs), with the reaction temperature playing a significant role in solvent efficiency. Both ILs and organic solvents achieved 55–60% hemicellulose removal under microwave conditions, attributed to the amorphous structure of hemicellulose. Ethyl acetate was less effective, removing less than 50% of hemicellulose due to its specific interactions and solvent properties. A high removal rate of lignin and hemicellulose improved cellulose hydrolysis conditions, enhancing cellulose accessibility by increasing surface area and porosity.

Among the solvents, GVL favoured LA production due to its strong extraction capability, improving biomass deconstruction and making cellulose microfibrils more amenable to conversion. Solvent parameters such as polarity, viscosity, thermal stability, and solubility influenced variations in cellulose recovery and lignin and hemicellulose removal. The structural purity and crystallinity of cellulose was examined post-microwave extraction in GVL, showing a 46.81% CrI, suggesting GVL's effectiveness in penetrating amorphous cellulose regions for hydrolytic cleavage. FTIR analysis indicated GVL reduced the O–H stretching peak in cellulose, suggesting disrupted hydrogen bonding and a broader carbohydrate peak, initiating cellulose hydrolysis. SEM analysis showed that the dewaxing process smoothed the cellulose surface, enhancing GVL-microwave extraction efficiency by disrupting the lignocellulosic complex, shortening fibres, and increasing porosity and surface area.

These findings provide valuable insights into biomass treatment effects and underscore the importance of selecting an appropriate solvent to optimise catalyst performance. As explored in the subsequent chapter, the choice of solvent not only influences the deconstruction of biomass but also plays a pivotal role in the functionality of catalysts derived from lignin. The effective removal of hemicellulose and lignin creates a more favourable environment for catalyst interactions, thereby enhancing the overall efficiency of biomass conversion processes to LA. This connection between solvent efficiency and catalyst performance lays the groundwork for future investigations into the integration of solvent properties with catalytic systems, ultimately aiming for more effective biomass conversion strategies.

Chapter 5

Synthesis of Lignin-derived Carbon Cryogel Incorporated with $H_3PW_{12}O_{40}$-Nb_2O_5

5.1 Introduction

Building on the insights from the first chapter regarding biomass deconstruction and solvent efficiency, this chapter delves into the role of lignin, a natural macromolecule abundant in aliphatic and phenolic hydroxyls [507]. These hydroxyls can provide significant rigidity and resistance, contributing to the structural integrity of materials. Furthermore, they serve as potential cross-linking sites [507], which are crucial for forming stable networks within materials. This cross-linking capability makes lignin an excellent candidate for supporting catalysts used in biomass conversion processes. Previous research studies have focused on chemically modifying lignin with polymers, exploiting the weaker covalent bonding in lignin monomers [260, 268–270]. A dual approach, combining physical and chemical cross-linking [271], enhances mechanical strength and significantly impacts polymer properties based on the degree of crosslinking [340].

This study evaluates the effectiveness of three crosslinkers—natural and synthetic biopolymers and building blocks—in forming strong and stable lignin-derived hydrogels. The robust hydrogels are crucial for upgrading to carbon cryogels that can improve the thermal stability of catalyst supports. Hydrogel precursors, which may include small molecules, biomacromolecules, nanostructures, and metal/ligand units [260], bond to other monomers to initiate

the growth of building blocks or polymers [272]. The effectiveness of the crosslinkers depends on their unique properties:

- **Xanthan Gum**: A natural biopolymer from *Xanthomonas campestris*, is highly hydrophilic and resists dispersity in the reaction medium [508].
- **Polyethylene Glycol Diglycidyl Ether (PEGDE)**: A strong and durable synthetic biopolymer that has a moderate degradation rate [509], which might impact catalytic activity and stability [510].
- **Furfural**: A building block acting as a crosslinker, contains reactive aldehyde groups that form covalent bonds with lignin's phenolic groups [511].

The crosslinking reaction (**Figure 5.1)** is influenced by operating conditions such as temperature, pH, and reaction time. Different sol-gel conditions and methods are employed (as detailed in **Chapter 3, Section 3.8, Table 3.1**) to investigate the effects of crosslinkers.

The chapter explores how crosslinkers affect hydrogel properties, including swelling behaviour, water absorption capacity, yield, mechanical strength, and porosity, indicating crosslinking density. The upgrading of lignin-derived hydrogel to carbon cryogel is investigated using acid catalysts like $H_3PW_{12}O_{40}$-Nb_2O_5. This comprehensive study provides valuable insights into the potential of lignin-derived hydrogels in biomass conversion, continuing the exploration of biomass treatment and conversion methods introduced in the first chapter.

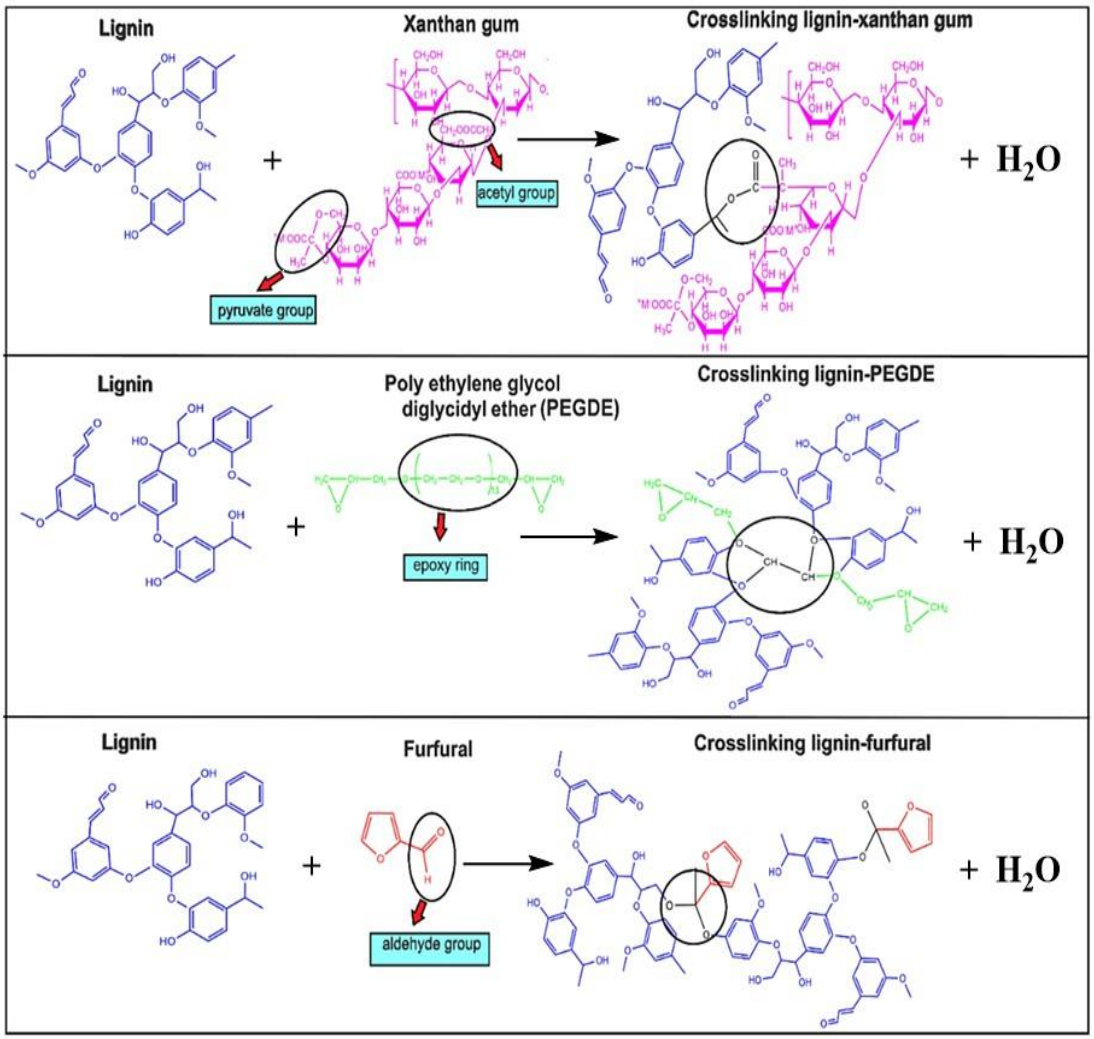

Figure 5.1 Crosslinking reaction between lignin and different types of crosslinkers: (a) xanthan gum, (b) PEGDE, and (c) furfural.

5.2 Properties of lignin-derived hydrogels

5.2.1 Swelling capacity and water absorption capacity

Figure 5.2a depicts the swelling behaviour of three lignin-derived hydrogels: lignin-gum (LIG-XG), lignin-glycol (LIG-PEGDE), and lignin-furfural (LIG-FUR). LIG-PEGDE exhibited the highest swelling ratio (27.4 g g^{-1}), followed by LIG-XG (10.3 g g^{-1}) and LIG-FUR (8.9 g g^{-1}). The swelling ratio of LIG-PEGDE significantly differed (p-value<0.05) from the other two hydrogels. The lignin hydrogel's water absorption ability is demonstrated in **Figure 5.2b**, influenced by the chemical structure of the polymer chains and cross-linkers. The high

swelling of LIG-PEGDE is attributed to epoxy rings reacting with lignin's phenolic groups, enhancing the nucleophilic attack of the strong phenoxide nucleophile, and promoting ring-opening polymerisation [512]. As the hydrogel swells, hydrophobic groups (e.g. $–CH_2$) interact with water to form hydrophobically bound water [513], enhancing water absorption capacity and catalytic activity during LA production. However, excessive swelling has drawbacks, including water backflow, larger macropores on the hydrogel interface, and reduced crosslinking at equilibrium.

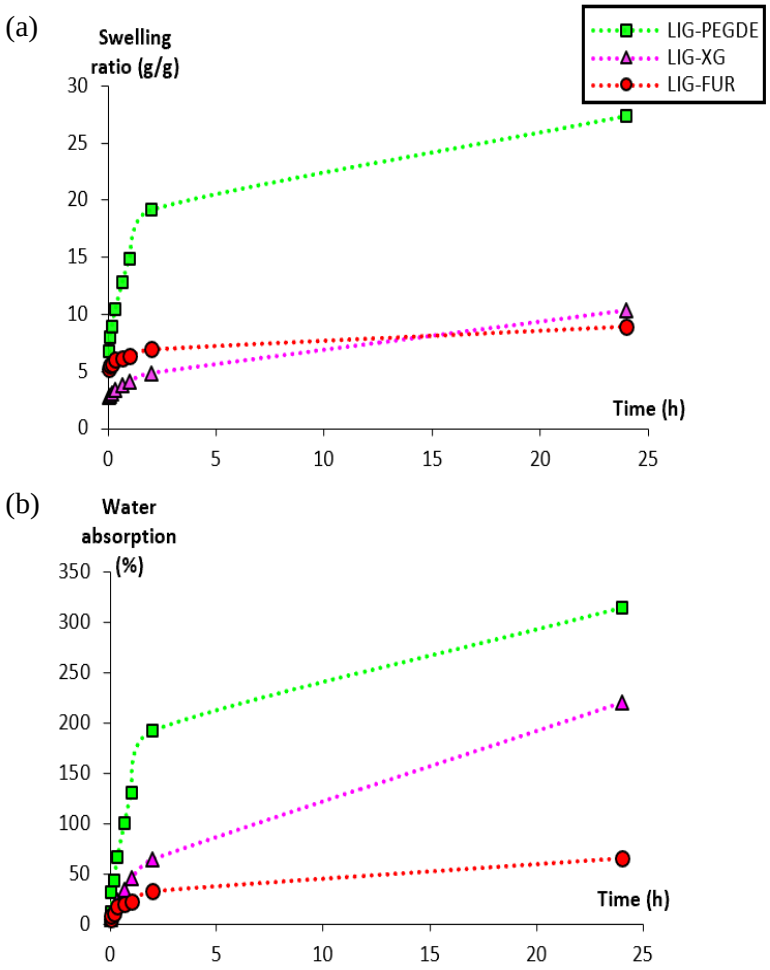

Figure 5.2 (a) Swelling ratio; (b) Water absorption of different types of hydrogels.

In contrast, LIG-XG exhibited moderate swelling, indicating higher crosslinking activity between polymer chains. It maintained its shape and showed controlled swelling with a high-water absorption capacity (220%), significantly different (p-value <0.05) from LIG-PEGDE (314%) and LIG-FUR (66%). Xanthan gum's unique chemical structure, with carboxylic functional groups (pyruvic and glucuronic acid) capable of ionisation in the presence of water, facilitates strong electrostatic attractions and crosslinking reactions, resulting in a well-crosslinked gel to overcome bulk water solely imbibed in capillary pores [514].

LIG-FUR displayed the poorest swelling behaviour and the lowest absorption capacity due to hydrophobic furan rings and alkyl chains [515]. The abundance of hydrophobic groups in LIG-FUR hindered water attraction, affecting ideal hydrogel formation, and leading to a brittle hydrogel with reduced crosslinking density that might disperse in the reaction medium [514]. The weak crosslinking of LIG-FUR is influenced by the longer bond length of the carbonyl group in furfural's aldehyde functional group (−RCHO), weakening the covalent bond strength [516]. Weak acidic functional groups in furfural further disrupt the crosslinking process, affecting gelation at higher pH levels.

5.2.2 Yield of the hydrogel

The yield of the hydrogel is a significant parameter to assess the efficiency of the synthesis process and the density of cross-linking. In **Figure 5.3**, LIG-XG gives the highest yield at 71.7%, indicating a stronger crosslinking reaction compared to LIG-FUR (23.8%) and LIG-PEGDE (21.4%). The yield of LIG-XG was significantly different (p-value<0.05) from the other two hydrogels. In comparison to other studies, a lignin-based hydrogel crosslinked with polyvinyl

alcohol (PVA) exhibited a higher swelling ratio (1278 g g^{-1}) but a lower yield of 50% [517], while using the same alkaline lignin with PVA [326], resulted in a yield of 70% and a lower swelling ratio (146 g g^{-1}), similar to LIG-XG in this study. The difference in yield may be attributed to the concentration of NaOH used in the hydrogel synthesis, which affected the osmotic pressure, water uptake, and hydrophilicity.

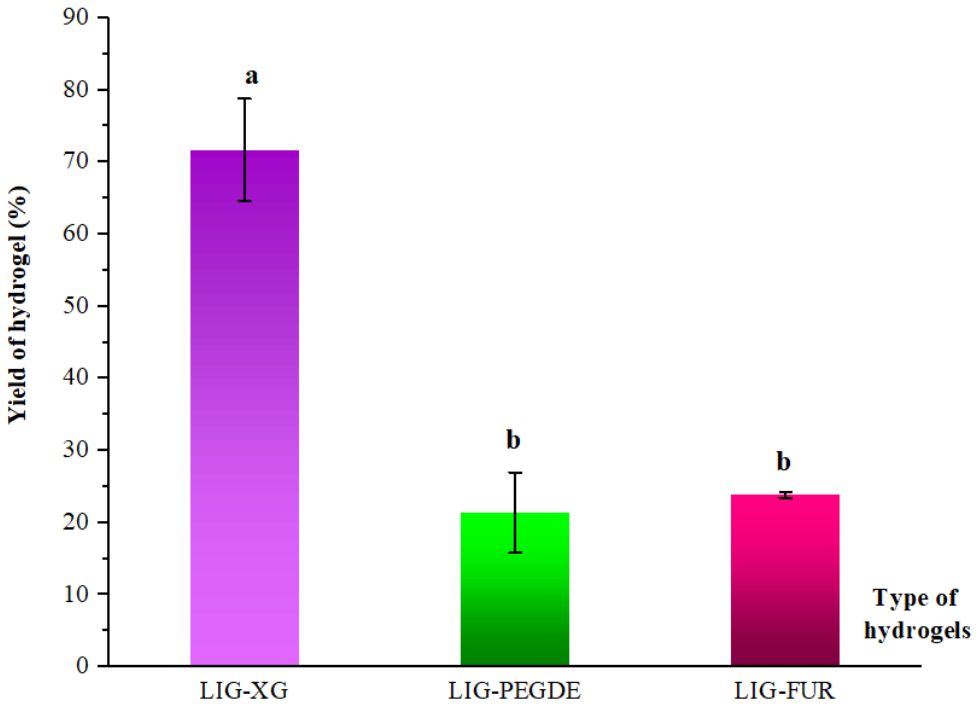

Figure 5.3 LIG-XG outperforms, yielding approximately three times more than both LIG-PEGDE and LIG-FUR.

Various factors, such as precursors, polymerisation conditions (reaction time and temperature), and the type of crosslinker, can influence the hydrogel yield. The high yield of LIG-XG can be attributed to its high molecular weight, leading to more reactive sites available for cross-linking. In contrast, inappropriate proportions of PEGDE to lignin in LIG-PEGDE can result in PEGDE-clustering, reducing the yield. LIG-FUR's low molecular weight (< 100 g mol^{-1}) and low solubility in water contribute to a lower crosslinking density

and yield due to incomplete crosslinking [24]. The polymerisation temperature at the curing stage also plays a role, as higher temperatures may affect the crosslinking activity of LIG-PEGDE molecules. This can be seen when the LIG-PEGDE was cured only at 25 °C for an extended period (as mentioned in **Chapter 3, Section 3.8, Table 3.1**) to avoid polymer melting, which could break C–C or C–O bonds [518]. Therefore, selecting the appropriate crosslinker is crucial to ensure compatibility at higher temperatures, resulting in a more densely crosslinked hydrogel network with less space for free unreacted monomers or polymers.

5.2.3 Porosity

Figure 5.4 illustrates the pore size distribution of different lignin-derived hydrogels: LIG-FUR, LIG-XG, and LIG-PEGDE. LIG-FUR exhibited a smaller range of average pore sizes (0.5–1.0 µm) compared to LIG-XG (2.5–4.5 µm) and LIG-PEGDE (3.0–4.0 µm). Interestingly, LIG-XG showed a wider range of pore sizes (0.1–28 µm) with a higher distribution of smaller pores, making it favourable for interactions with both large and small reactant particles in biomass. Additionally, hydrogels composed of 70% xanthan gum and 30% lignin consistently showed an average pore size of 0.5–1.0 µm [332], which aligns with the typical range of pore sizes found in biomass at the micron scale [519].

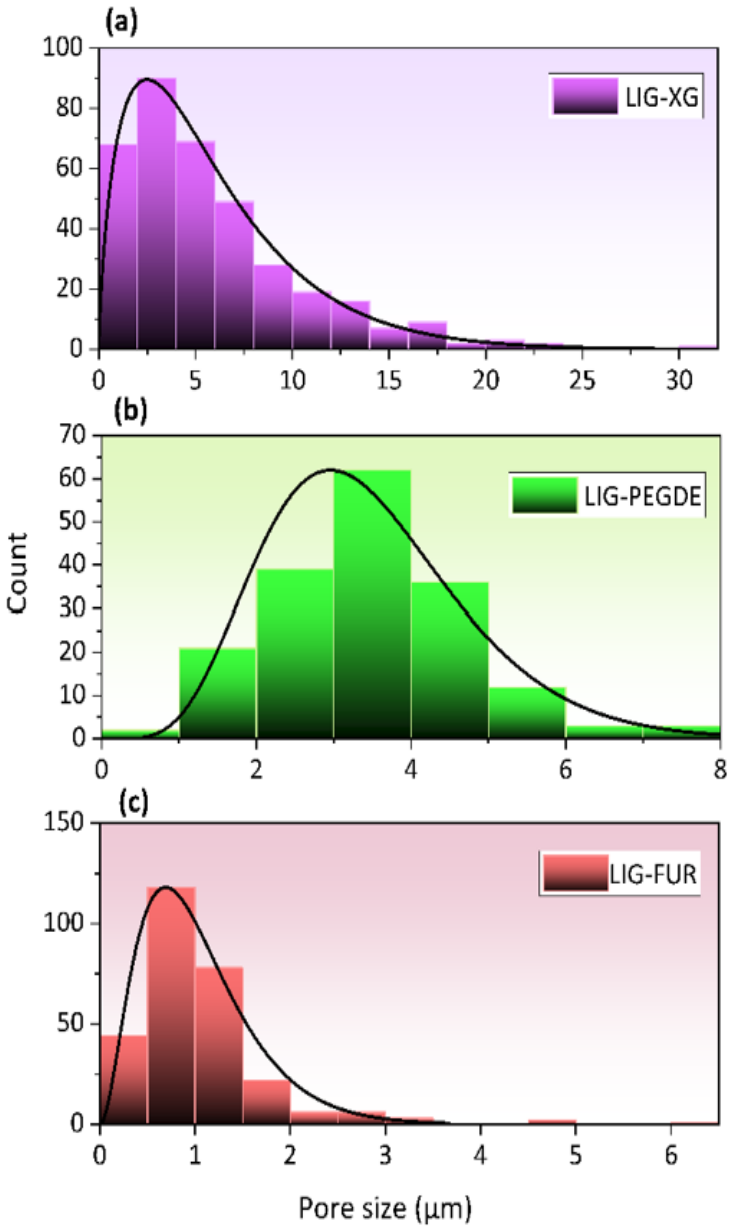

Figure 5.4 Pore distributions among different types of hydrogel. LIG-PEGDE stands out with its even pore sizes, as evidenced by the bell-curve shape of its distribution.

The SEM micrographs in **Figure 5.5** confirm that LIG-XG has a larger surface area with a diverse range of pore sizes. The porosity of a hydrogel is intricately linked to its swelling behaviour. When lignin-derived hydrogels come into contact with a solvent like water, they undergo swelling and expansion, leading to the opening of pores between polymer chains [520]. This increased

porosity enables enhanced interaction with the biomass. Furthermore, microwave irradiation, driven by the high dielectric constant, induces physical changes in the DOPMF biomass [153]. Specifically, under high temperature or microwave power, the structure undergoes damage, cleaving the condensed linkages Cα-Cβ [257]. This process exposes more cellulose, facilitating its release and aiding in the conversion of biomass to LA. However, the interaction between the cryogel catalyst and DOPMF biomass can be influenced by different microwave settings. These settings can alter the energy of electromagnetic radiation transferred to both the lignin-derived cryogel and the biomass molecules, potentially causing uneven heating during LA conversion. Factors such as chemical composition, crosslinking density, solvent properties, and environmental conditions influence the degree of swelling and porosity.

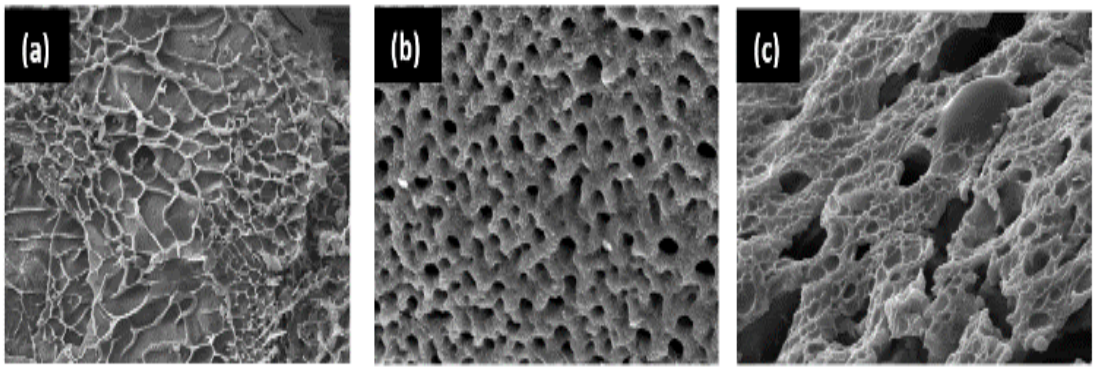

Figure 5.5 Morphology of lignin hydrogels under scanning electron microscope (SEM) for (a) LIG-XG; (b) LIG-PEGDE; and (c) LIG-FUR.

LIG-FUR demonstrates lower porosity due to reduced space for solvent expansion, resulting in a lower degree of swelling and smaller voids within the hydrogel. The porosity of LIG-FUR is perturbed with the formation of lump within the gel structure showing incomplete crosslinking between polymer chains. In contrast, the highly branched polymer in LIG-XG promotes strong physical interactions [513] with water molecules, retaining more water and

creating larger pores when more water is present. This condition allows larger biomass or cellulose particles to pass through the catalytic sites during biomass conversion.

The smaller pores in LIG-PEGDE, compared to LIG-XG, result from its high swelling capacity, which leads to the formation of smaller pore volumes when the hydrogel is swollen. Size of pores of LIG-XG falls within a wider range, forming a greater surface area while LIG-PEGDE has a uniform pore size distribution with smaller surface area for catalytic activity to occur. Although LIG-PEGDE exhibits superior swelling behaviour, it can also damage the hydrogel matrix and reduce pore size [521]. The porosity of the hydrogel significantly affects its catalytic efficiency, mechanical properties, permeability, and diffusivity. To achieve target properties, such as the degree of swelling, chemical composition, crosslinking density, and stability, it is essential to tune the porosity of the hydrogel by selecting the appropriate crosslinker and adjusting parameters such as polymer concentration, water content, and environmental conditions during hydrothermal synthesis. This will create a well-balanced porous structure that includes both macropores and mesopores, closely resembling the natural structure of the biomass, and facilitating the conversion process.

5.2.4 Mechanical properties

Figure 5.6 illustrates that LIG-XG exhibits high elasticity, reaching 0.81 MPa at 90% strain, comparable to a lignin hydrogel prepared with 0.5% xanthan gum that produces 1.5 MPa at 90% strain [522]. This indicates that both hydrogels were strong and deformed only when the strain was close to 100%. The high

elasticity of LIG-XG is the reason for its lower swelling ratio compared to LIG-PEGDE.

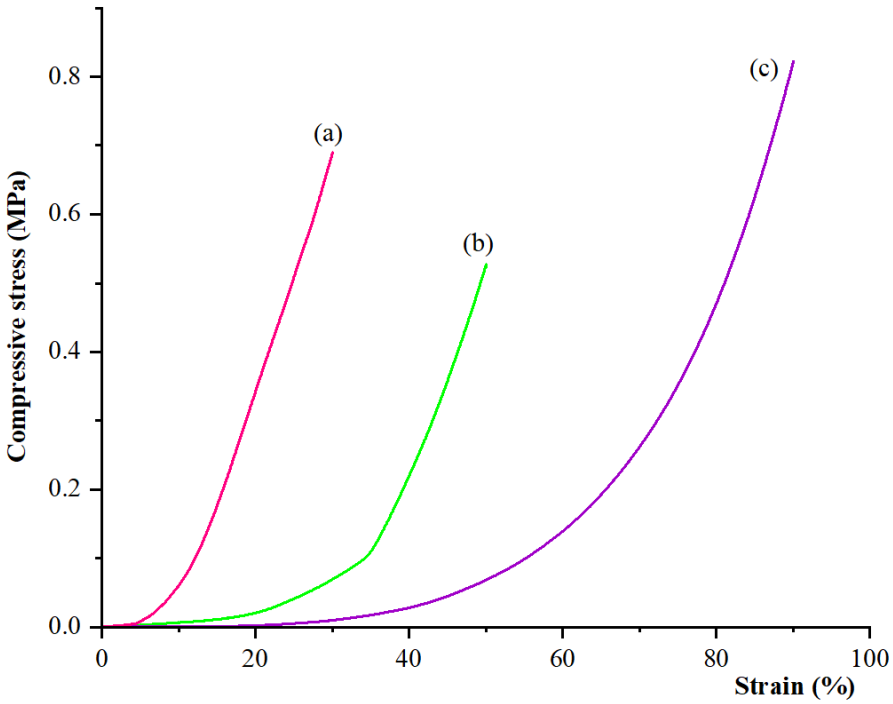

Figure 5.6 Compressive stress for **(a)** LIG-FUR; **(b)** LIG-PEGDE and **(c)** LIG-XG hydrogels.

On the other hand, the stress-strain curve (**Figure 5.6**) shows that the LIG-PEGDE hydrogel reaches 0.52 MPa at 50% strain. Beyond 50% strain, the shape of the LIG-PEGDE hydrogel slightly distorts. Similar to LIG-FUR, the stress can be retained up to 30% strain at 0.7 MPa, but at this point, the structure of the hydrogel breaks, altering its original shape and affecting its morphology and mechanical properties. The lower yield of LIG-FUR can contribute to a brittle and fragile hydrogel network, and the degree of crosslinking and furfural concentration can cause shape distortion upon reaching the limits.

The degree of crosslinking can vary under different polymerisation conditions. At higher temperatures, the polymerisation reaction typically proceeds faster and can result in a more crosslinked network with smaller pores. This leads to a hydrogel with higher compressive stress, as the smaller pores

provide more points of contact between the polymer chains, making it more resistant to deformation [523]. This explains the higher stress-strain curve of LIG-FUR compared to LIG-PEGDE. However, the presence of ether (–O–) linkages in the PEGDE polymer chain leads to the formation of a soft and flexible hydrogel, allowing it to be compressed up to 50% strain. Nevertheless, LIG-PEGDE may not be suitable as catalyst support in biomass conversion due to its significant loss of weight at high temperatures [510] and the handling of potentially toxic or harmful by-products [509].

In contrast, LIG-XG shows more favourable properties with its unique polymer backbone, non-toxicity, and biodegradability. It can withstand a broad range of temperatures and pH scales in the presence of ions, facilitating the sol-gel process without forfeiting the environment [524]. During high-temperature hydrothermal treatment, the formation of covalent bonds and intermolecular interactions between the monomers or polymers occurs, leading to the creation of a stronger and more stable hydrogel network with optimal mechanical strength and stability. Additionally, the good mechanical properties of LIG-XG are relatively connected to its porosity. The high elasticity and flexibility of XG-based materials allow LIG-XG to withstand deformation, thereby forming larger pores within the hydrogel matrix and increasing the overall porosity. The flexible LIG-XG hydrogel can expand and contract in response to external stimuli such as changes in temperature or pH.

5.3 Upgrading lignin-derived hydrogel to carbon cryogel

Following a meticulous screening process outlined in **Figure 5.7**, LIG-XG was chosen for further development into a carbon cryogel. This selection aimed to assess its effectiveness in catalysing the conversion of biomass to LA. The carbon cryogel was then incorporated with $H_3PW_{12}O_{40}$-Nb_2O_5, a choice informed by a preliminary study [525] focused on identifying a bifunctional catalyst with high selectivity towards yielding a greater amount of LA (refer to **Appendix 8** for details).

The successful incorporation of $H_3PW_{12}O_{40}$-Nb_2O_5 into the LIG-XG hydrogel was evidenced by XRD patterns (**Appendix 9**). Notable crystallinity phases, found at 28° and 25°, correspond to $H_3PW_{12}O_{40}$ and Nb_2O_5, respectively, in the raw catalyst. The Keggin-type structure of phosphotungstic acid, denoted as $[PW_{12}O_{40}]^{3-}$, is characterised by distinct peaks in the XRD pattern, indicating a well-ordered crystalline structure. Nb_2O_5 typically exists in several polymorphs, with the orthorhombic phase being the most common, identified by unique diffraction peaks indicative of specific atomic arrangements in their crystal lattices. However, when $H_3PW_{12}O_{40}$ and Nb_2O_5 are incorporated into a hydrogel, the XRD pattern often shows less intense and reduced peaks. This change suggests a reduction in crystallinity, implying that the catalysts are more dispersed or have a less ordered structure within the hydrogel matrix. Hydrogels, being highly hydrated networks, can swell significantly, causing the catalysts to become more dispersed and less ordered, disrupting the regular crystal lattice of $H_3PW_{12}O_{40}$ and Nb_2O_5, leading to broader and less intense peaks in the XRD patterns.

These structural insights set the foundation for performance analysis of the carbon cryogels. The initial screening involved LXCC1 and LXCC5 carbon cryogels, as shown in **Figure 5.8a,** with different water-to-lignin (W/L) ratios. LXCC5, with a W/L ratio of 5:1, yielded 5.9% LA, while LXCC1, with a W/L ratio of 1:1, produced 9.2% LA. Subsequent testing, depicted in **Figure 5.8b**, explored LXCC1 cryogels with varying catalyst-to-lignin (C/L) ratios. LXCC1/0.08 demonstrated a slightly higher yield compared to LXCC1/0.04 and LXCC1/0.12. These findings underscore the importance of catalyst concentrations and reactant amounts during hydrogel formulation, as they significantly impact the performance of carbon cryogel in catalysing oil palm mesocarp fibre to LA, as evidenced by the final yield. Therefore, it is crucial to carefully consider the proportions of reactants and catalysts in hydrogel formulation to achieve the desired properties, while also accounting for how reactants respond to changes in environmental factors. This careful balance ensures optimal performance of the carbon cryogel catalysts in biomass conversion processes.

Figure 5.7 Initial screening for the properties of hydrogel.

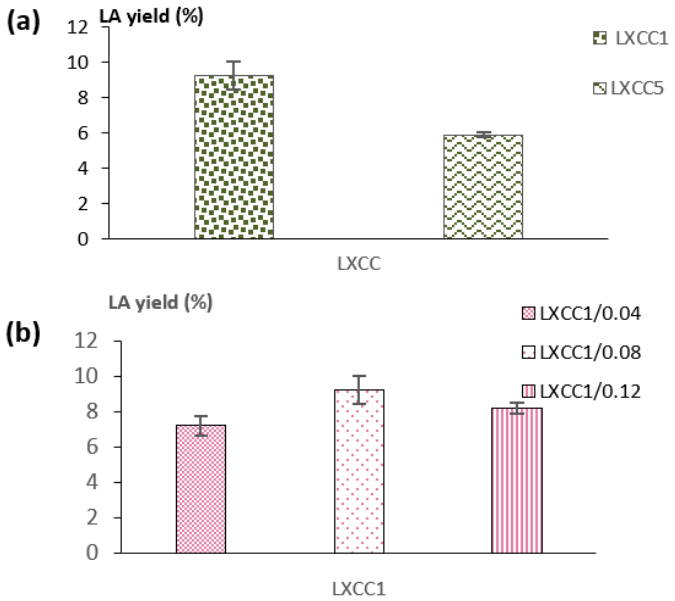

Figure 5.8 (a) LXCC1 and LXCC5 are prepared at different ratios of W/L, implying a constant concentration of xanthan gum (0.5 mmol g^{-1} lignin) and 0.08 mmol for each acid catalyst; and **(b)** LXCC1 hydrogels are prepared with different concentrations of acid catalysts while maintaining a fixed ratio of $H_3PW_{12}O_{40}$ and Nb_2O_5 at 1:1.

5.4 Concluding remarks

In conclusion, the study meticulously examined three types of lignin-derived hydrogels: LIG-XG, LIG-PEGDE, and LIG-FUR. LIG-PEGDE demonstrated the highest swelling ratio, which could lead to potential issues like water backflow and reduced crosslinking at equilibrium. Meanwhile, LIG-XG exhibited moderate swelling, indicating higher crosslinking activity between polymer chains and maintained its shape with a high-water absorption capacity. LIG-FUR displayed the poorest swelling behaviour and lowest absorption capacity due to its hydrophobic furan rings and alkyl chains.

The yield of the hydrogels, an important parameter for assessing synthesis efficiency and cross-linking density, was highest in LIG-XG, indicating a stronger crosslinking reaction. Hydrogel porosity, closely linked to swelling behaviour, is crucial for enhanced interaction with biomass. LIG-FUR showed lower porosity due to reduced space for solvent expansion, while LIG-XG, with its highly branched polymer, promoted strong physical interactions with water molecules, creating larger pores when more water is present. Mechanical properties were also examined, with LIG-XG showing high elasticity and LIG-PEGDE reaching 0.52 MPa at 50% strain. After careful screening, LIG-XG was chosen for upgrading to carbon cryogel to test its efficacy in catalysing biomass to LA. Initial screening involved LXCC1 and LXCC5 carbon cryogels, with LXCC1 producing a higher yield of LA.

These findings underscore the importance of catalyst concentrations and reactant amounts during hydrogel formulation, impacting the performance of carbon cryogels in catalysing oil palm mesocarp fibre to LA. Thus, the study provides valuable insights into optimising hydrogel formulations, cryogel

properties, and reaction conditions, as discussed in the preceding chapter, to maximise LA yield from biomass conversion. These insights highlight the potential of these hydrogels in biomass conversion, paving the way for more sustainable and efficient production methods.

Chapter 6

Optimisation Studies on the Performance of Catalytic System in the Conversion of Oil Palm Mesocarp Fibre to Levulinic Acid

6.1 Introduction

Drawing upon the insights from the previous chapter concerning the successful development of stable and strong lignin-derived carbon cryogels, this chapter focuses on the formulation and optimisation of carbon cryogels derived from lignin for biomass conversion. It emphasises improving the efficiency of the cryogel's crosslinked network, which is essential for its role as a catalyst support in biomass hydrolysis, despite its limited application in this field [24, 243–245, 526]. This efficiency is achieved through the incorporation of acid catalysts onto the lignin support in the right proportion, which triggers the formation of the hydrogel network via polymer chains [343].

In the presence of initiators, the phenolic hydroxyl groups in lignin generate radicals that react with monomers, resulting in the formation of lignin-grafted copolymers within a polymerised matrix. Acid promoters enhance polymerisation by enabling both chemical and physical crosslinking through redox initiators that produce free radicals [341–342]. For example, the successful copolymerisation of acrylic acid with lignin, utilising NMBA as an external crosslinker and montmorillonite as an inorganic filler, leads to the creation of superabsorbent composites [336].

The ratios of reactants play a crucial role in determining the properties of the resulting gel. An excess of crosslinker can result in a dilution effect and an

increase in particle size near the gelation limit. This is further affected by a decrease in reactant density due to an increase in solvent volume, which in turn impacts the properties of the carbon cryogel [394]. The development of lignin-derived carbon cryogels that are incorporated with bifunctional catalysts yields a high surface area, strong acidity, and good thermal, mechanical, and chemical stability—qualities that are advantageous for effective catalysis [226, 348, 527]. As a catalyst support, carbon cryogels can immobilise catalysts [233–236], enhancing catalytic systems by minimising the leaching of catalyst molecules and providing reactive sites for the catalytic process [53].

However, using microwaves can present challenges if samples overheat, resulting in rapid moisture loss and uneven heat distribution [528–529], which diminishes the efficiency of microwave pretreatment. Thus, an effective catalytic system necessitates careful selection of feedstock, appropriate choice of catalyst, suitable design of catalyst support, and control of the reaction medium. Employing a multivariate approach, Response Surface Methodology (RSM) serves as a valuable mathematical model for optimising complex processes with multiple variables that affect the yield of LA. This chapter investigates optimisation studies related to the carbon cryogel synthesis process, influencing both the performance of carbon cryogels and the conditions for biomass conversion to LA. The optimisation strategies are organised into three distinct phases: hydrogel formulation, properties of the carbon cryogel, and conditions for the catalytic system reaction. Through these sequential optimisation phases, the goal is to enhance the efficiency of LA production and ensure the overall effectiveness of the catalytic system.

6.2 Parametric studies on hydrogel formulations

RSM, employing a CCD approach, optimised the hydrogel precursors (as shown in **Chapter 3, Section 3.13, Table 3.2**), thereby influencing their properties to produce a stable carbon cryogel. It is crucial to maintain proportional balance among all components with lignin, as it forms the backbone of the carbon cryogel. The reactant parameters included the ratios of water to lignin (W/L), xanthan gum to lignin (X/L), and catalyst to lignin (C/L). The optimisation studies involved 20 experimental runs (as detailed in **Table 6.1**), which reflect the interactions between process variables during hydrogel formation, indirectly evaluating the LXCC catalytic system's overall performance and optimising the LA yield.

Table 6.1 Design of experiments by RSM-CCD approach.

Sample (run)	Point type	Parameters			Response
		A	B	C	Y_i
		Ratio of water to lignin (W/L)	Ratio of gum to lignin (X/L)	Ratio of catalyst to lignin (C/L)	LA yield (%)
1O1	Factorial	1.00(-1)	0.25(-1)	0.06(-1)	16.27
1O2	Factorial	3.00(+1)	0.25(-1)	0.06(-1)	14.94
1O3	Factorial	1.00(-1)	0.75(+1)	0.06(-1)	11.12
1O4	Factorial	3.00(+1)	0.75(+1)	0.06(-1)	7.48
1O5	Factorial	1.00(-1)	0.25(-1)	0.20(+1)	15.59
1O6	Factorial	3.00(+1)	0.25(-1)	0.20(+1)	16.19
1O7	Factorial	1.00(-1)	0.75(+1)	0.20(+1)	12.71
1O8	Factorial	3.00(+1)	0.75(+1)	0.20(+1)	15.07
1O9	Axial	0.32(-∝)	0.50(0)	0.13(0)	14.33
1O10	Axial	3.68(+∝)	0.50(0)	0.13(0)	11.06
1O11	Axial	2.00(0)	0.08(-∝)	0.13(0)	17.14
1O12	Axial	2.00(0)	0.92(+∝)	0.13(0)	9.16
1O13	Axial	2.00(0)	0.50(0)	0.01(-∝)	13.56
1O14	Axial	2.00(0)	0.50(0)	0.25(+∝)	18.38
1O15	Centre	2.00(0)	0.50(0)	0.13(0)	16.24
1O16	Centre	2.00(0)	0.50(0)	0.13(0)	17.29
1O17	Centre	2.00(0)	0.50(0)	0.13(0)	17.66
1O18	Centre	2.00(0)	0.50(0)	0.13(0)	18.57
1O19	Centre	2.00(0)	0.50(0)	0.13(0)	17.62
1O20	Centre	2.00(0)	0.50(0)	0.13(0)	16.55

Replicated centre points (Sample 1O5–1O20) showed small standard deviations (0.03–1.25%) for the mean LA yield, indicating high repeatability, reproducibility, and reliability of the optimised conditions. The RSM numerical optimisation revealed the maximum LA yield (18.4%) at W/L, X/L, and C/L ratios of 2.14, 0.40, and 0.20, respectively. These optimal conditions were identified by locating process variables close to the design space, as observed in the response 3D contour plots. Deviations from these values resulted in reduced LA yields. The obtained yield (18.4%) was comparable to other studies (**Table 6.2**). The quadratic model suggested by the software correlated data to the LA yield and was validated with triplicate data (**Table 6.3**), showing an error of <5% and an experimental LA yield of 18.7% with a standard deviation of 0.52.

Table 6.2 Comparisons in LA yield from biomass conversion via various solid acid catalytic systems.

Catalyst	Feedstock	Reaction conditions	LA yield (%)	LA efficiency (%)	Reference
Sulphonated carbonaceous (0.25 g)	Corn straw (0.5 g)	200 °C, 1 h in aqueous, hydrothermal	6.6	–	[530]
20%Nb/Al oxide	Kiwifruit waste	190 °C, 15 min in aqueous, conventional heating	14.7	–	[531]
Amberlyst 36	Vegetable waste	150 °C, 5 min in aqueous, microwave heating	17.0	–	[532]
Sulphonated carbonaceous solid/lignin-based solid (0.84 g)	Sugarcane (1 g)	140 °C, 6 h in aqueous, water bath heating	38.6	59.8	[30]

Table 6.3 Optimisation of hydrogel formulations and validation for LA yields.

Experiment	Ratio W/L	Ratio X/L	Ratio C/L	Response (%)	Error (%)
				LA yield	
CCD	2.14	0.40	0.20	18.4	
Validation (Trial 1)	2.14	0.40	0.20	19.1	
Validation (Trial 2)	2.14	0.40	0.20	18.1	
Validation (Trial 3)	2.14	0.40	0.20	19.0	
Validation[a]	2.14	0.40	0.20	18.7	1.81

[a]Mean for triplicate data

6.2.1 RSM contour plots

The 3D surface contour plots in **Figure 6.1** depict interactions between two independent variables while keeping the third constant at its optimum value. **Figure 6.1a** suggests that changing W/L consistently impacts LA yield regardless of X/L, possibly due to different mechanisms affecting LA yield.

Figure 6.1b indicates that the ratio of C/L has a stronger influence on LA yield than W/L, and there is a significant interaction between C/L and W/L. **Figure 6.1c** shows a greater influence of C/L than X/L on LA yield, with a significant interaction between C/L and X/L. This can be attributed to the acid catalysts ($H_3PW_{12}O_{40}$ and Nb_2O_5), which enhance the thermal stability of the hydrogel matrix by forming strong interactions with the polymer chains and creating a more compact hydrogel structure that retains its integrity at elevated temperatures.

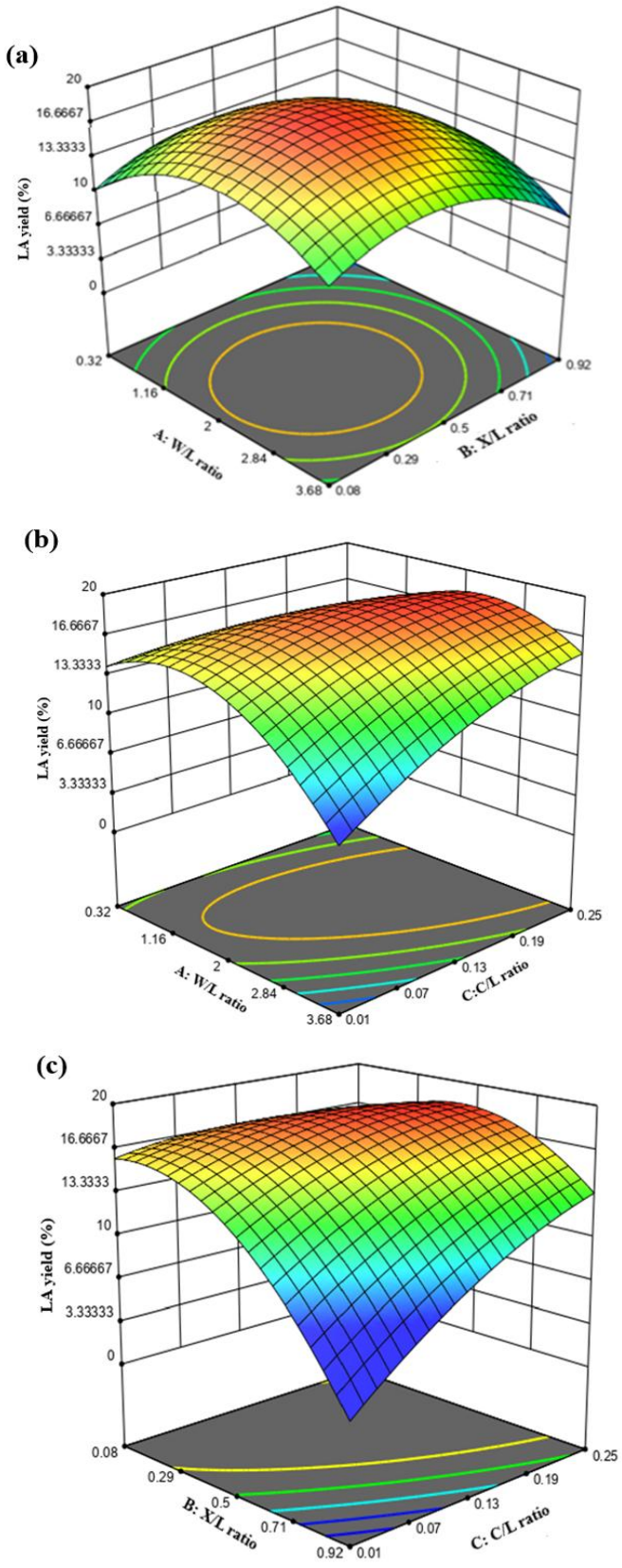

Figure 6.1 The 3D surface when the parameters are set to optimum (a) C/L = 0.20; (b) X/L = 0.40; and (c) W/L = 2.14.

Careful optimisation is required for xanthan gum concentration during hydrogel formulation, especially under harsh conditions, to avoid slower reaction rates and lower LA yields. Higher temperatures during hydrothermal treatment promote stronger crosslinked networks between xanthan gum and lignin, increasing thermal energy for a higher rate of molecular motion and enhancing the likelihood of crosslinking reactions. This improvement in crosslinking leads to enhanced water retention and mechanical stability, making it ideal for biomass conversion to LA. Additionally, LXCC shows high thermal stability (**Figure 6.2**), beginning to decompose at 400 °C and retaining 75% of its weight beyond 700 °C. It is noteworthy that Ingtipi *et* al. found that LIG-XG offered three times more protection than conventional hydrogels derived from synthetic polymers, displaying self-flame-retardant properties [533]. This finding supports the results of present study, confirming LXCC's ability to withstand higher temperatures.

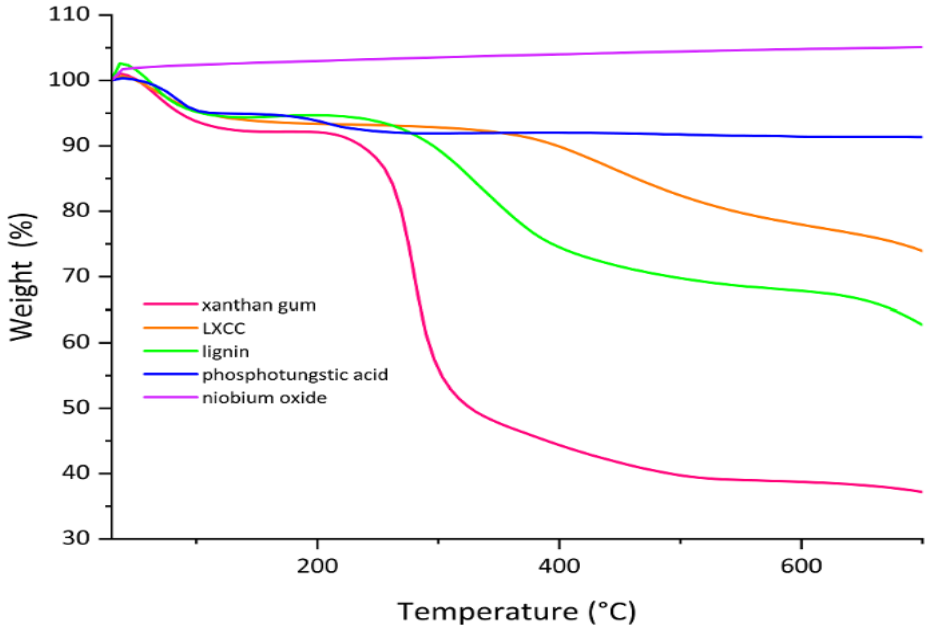

Figure 6.2 TGA curves represent the thermal decomposition of LXCC and its single precursors (xanthan gum, lignin, and catalysts).

6.2.2 RSM statistical analysis

The proposed model for LA yield in terms of coded factors is represented by **Eq. 6.1**.

$$\text{Yield} = 17.32 - 0.55A - 2.20B + 1.31C - 0.07AB + 0.99AC + 1.07BC - 1.65A^2 - 1.49B^2 - 0.49C^2 \quad (6.1)$$

The proposed model demonstrated high accuracy with an R^2 value of 0.96, indicating that 96% of the variation in LA yield can be attributed to the process variables explained by the model. The coefficient of variation of 5.94% further supported the reliability of the responses within the range of process conditions. The adjusted R^2 (0.92) and predicted R^2 (0.78) showed good agreement between the experimental and predicted LA yield, reinforcing the model's reliability.

ANOVA analyses are performed for each response model, as shown in **Table 6.4**, to assess the significance of interactions between process variables and individual factors. The linear and quadratic terms significantly influenced LA yield, except for C^2. Among these terms, the linear term of B was identified as the most important variable affecting LA yield, with a high F-value of 84.97 and a small *p*-value of <0.01. The interaction terms AC and BC also showed significant effects on LA yield, indicating the quadratic effect of the respective variables.

Table 6.4 Statistical analysis for the reaction terms (linear, quadratic, and cross-product).

Source	Sum of squares	Degree of freedom	Mean of square	F-value	Prob>F	Standard error	Remark
Model	176.02	9	19.56	25.17	<0.0001		Significant
A – W/L ratio	4.13	1	4.13	5.32	0.0438	0.24	
B – X/L ratio	66.04	1	66.04	84.97	<0.0001	0.24	
C – C/L ratio	23.37	1	23.37	30.07	0.0003	0.24	
A^2	39.17	1	39.17	50.41	<0.0001	0.23	
B^2	31.91	1	31.91	41.06	<0.0001	0.23	
C^2	3.48	1	3.48	4.47	0.0605	0.23	
AB	0.04	1	0.04	0.05	0.8251	0.31	
AC	7.87	1	7.87	10.13	0.0098	0.31	
BC	9.24	1	9.24	11.88	0.0063	0.31	
Residual	7.77	10	0.78				
Lack of Fit	4.25	5	0.85	1.21	0.4202		Not significant
Pure error	3.52	5	0.70				
Cor total	183.79	19					

The statistical analysis confirmed the significance of the model, with <0.01% chance that the F-value of the model could occur due to noise. The lack of fit F-value (1.21) relative to the pure error was found to be insignificant, indicating a good fit of the proposed model for predicting LA yield. The adequate precision, with a signal-to-noise ratio of 17, suggested that the ratio was >4, which was desirable for navigating the design space suggested by the CCD approach.

The additional diagnostic plots (**Figure 6.3**) were used to assess the adequacy of the quadratic model. The normal probability plot of the residuals demonstrated an approximately linear pattern, suggesting that the error terms were normally distributed and independent. The scattered studentised residuals

ranged between -3 and +3, indicating a constant error and satisfactory prediction of the experimental data using the quadratic model. This confirms that the plot behaved well, with no significant deviations from the random pattern of the other residuals. The plot of the actual response (experimental LA yield) versus the predicted response (predicted LA yield) resulted in a high R^2 value of >0.9, indicating a strong correlation between the two. The externally studentised residuals were scattered between -4.15 and +4.15, and no outliers were observed throughout the 20 runs, showing a good fit of the data. All experimental runs fell below the maximum value on the leverage plot (leverage is 1), indicating that no observations deviated significantly from the assumption of normally distributed errors. The leverage plot also provided insights into influential observations that could significantly affect LA yield and helped in understanding the relationship between the analysed parameters. Finally, Cook's distance confirmed the absence of outliers in the experimental runs, with all data points having a value of <1, thereby affirming the accuracy of the analysis and the limited influence of individual observations on the regression results.

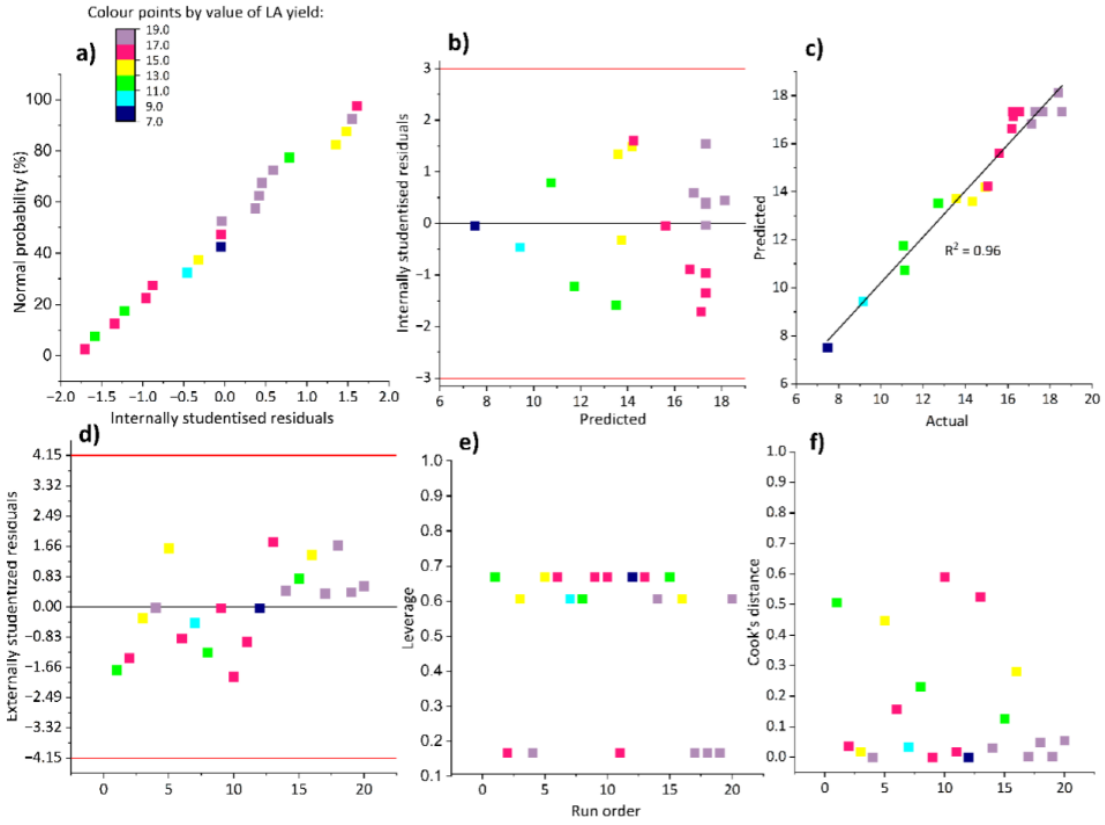

Figure 6.3 Diagnostic plots for **(a)** normal probability plot of residuals; **(b)** studentised residuals; **(c)** actual vs. predicted; **(d)** good fit of the data; **(e)** leverage plot; and **(f)** Cook's distance.

6.3 Factors affecting carbon cryogel performance

The RSM models were used to examine the changes in LA yield resulting from variations in the ratios of W/L, X/L, and C/L. Understanding the behaviour and presence of each precursor in hydrogel formulation is crucial for designing an efficient carbon cryogel that can achieve higher LA yields from the conversion of oil palm mesocarp fibre. While the numerical optimisation indicated an optimum yield of 18.4%, the LXCC catalytic system currently demonstrated a high LA efficiency of 81% based on theoretical LA yield calculated from cellulose conversion of the oil palm mesocarp fibre (see **Chapter 3**, **Eq. 3.10** in **Section 3.12**). Therefore, it is important to investigate how changes in the ratios

of W/L, X/L, and C/L (**Figure 6.4**) can be incorporated to improve the LA yield using the LXCC catalytic system.

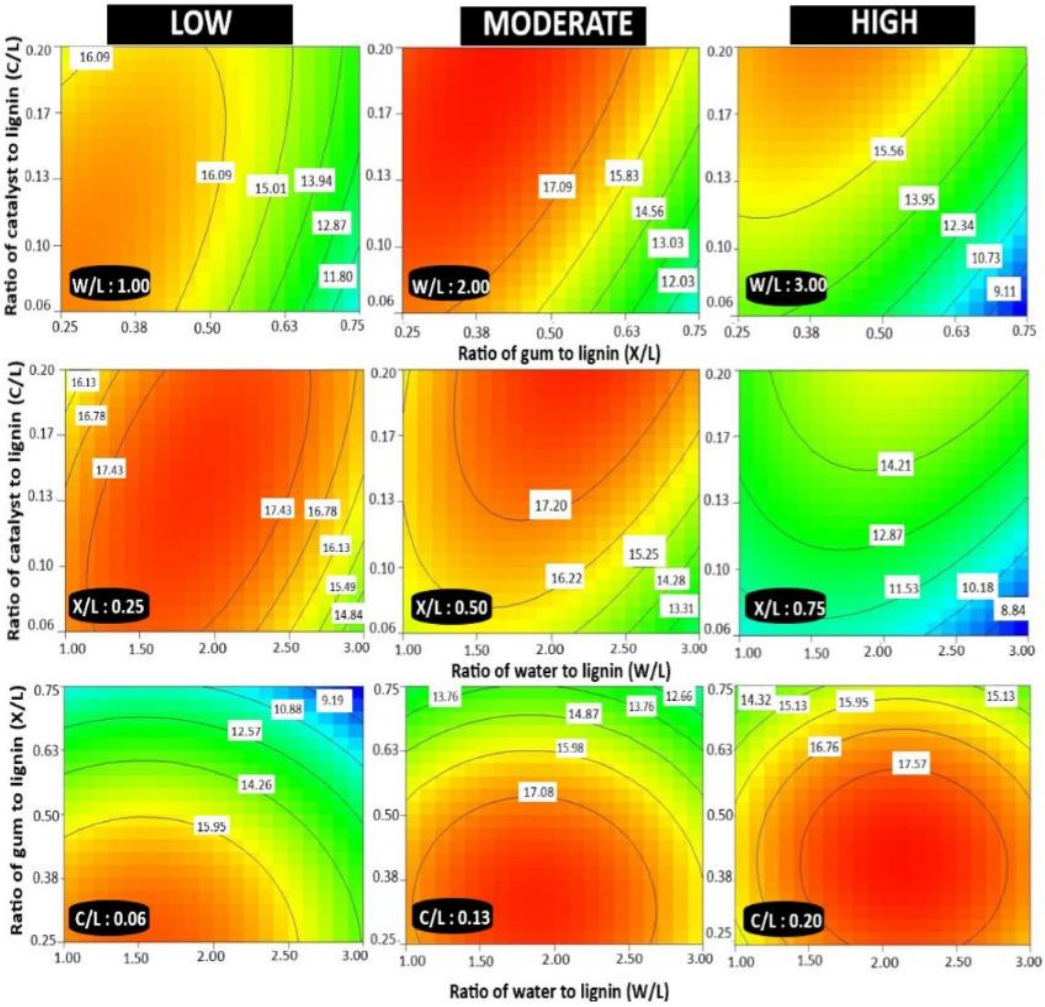

Figure 6.4 The effects of changing the two parameters on LA yield while one parameter is kept constant and observed at three different levels (low, moderate, and high). The parameters involved are W/L, X/L, and C/L.

6.3.1 Water to lignin ratio

The W/L ratio is critical as it affects the degree of crosslinking in the hydrogel. Lower ratios of W/L resulted in a decreased yield as xanthan gum and catalyst concentrations increased (**Figure 6.4** in **Section 6.3**). Several factors contribute to this trend. Firstly, lignin has low solubility (0.625 g mL^{-1}) in water [310], which can lead to insufficient water content and difficulty in achieving a

homogeneous mixture with xanthan gum. At moderate W/L ratios, the LA yield increased and reached an optimum at an X/L ratio of 0.40. However, a further increase in xanthan gum concentration led to a gradual decrease in LA yield (11.8%). Similarly, at high W/L ratios (3:1), an increase in xanthan gum proportion resulted in a decrease in LA yield. The LA yield was negligibly affected by changes in acid concentration at moderate water content, but significant effects were observed at high W/L ratios. In a high-water content medium, increasing acid concentration improves the LA yield by ensuring a balanced proportion of water and catalyst, enabling the acid to dissolve and react effectively with the LA precursor. It is crucial to control the water content during hydrogel formation to manage catalyst activity and gelation.

6.3.2 Xanthan gum to lignin ratio

The contour plot (**Figure 6.4** in **Section 6.3**) revealed that higher LA yields were achieved at low ratios of X/L, while slightly decreased yields were observed with increasing W/L and C/L ratios. Although at moderate and high ratios of X/L, the yield of LA did not improve when excessive water was added to a hydrogel formulation with a high W/L ratio, diluting the pyruvate molecules ($–C(O)CH_3$) derived from pyruvic acid acetal groups at the C–3 position of the mannose units of xanthan gum, affecting the overall hydrophobicity of the molecule and its interaction with lignin. Additionally, the excessive addition of water to a high concentration of xanthan gum can cause the hydrogel to swell and become hydrated. Both aforementioned conditions can reduce the mechanical strength of the hydrogel by spreading out the chains of the polymer network, weakening its overall structure and making it more susceptible to tearing or breaking and eventually impacting the carbon cryogel performance. Meanwhile, increasing

xanthan gum concentration led to a decrease in LA yield at medium and high ratios, limiting the diffusion of reactants and reducing contact between the catalyst and lignin. This is because the excessively high concentration of xanthan gum can promote the formation of a composite or "crosslinked solid" that interferes with the gelation process. The resulting crosslinked solid possesses a rigid and compact structure, lacking the characteristic properties of a hydrogel such as high-water content, flexibility, and swelling capacity. Otherwise, a sufficient amount of water mixed with xanthan gum can form a stable and viscous sol-gel as even distribution of the polymer chains supported with high water affinity. On the other hand, a high acid concentration would affect the properties of xanthan gum, as low pH values promote the protonation of xanthan gum molecules, reducing its ability to form hydrogen bonds and interact with water, thereby decreasing hydrogel stability. At high X/L ratios, the high concentration of acid catalysts in the hydrogel matrix can cause saturation of catalyst particles and form clusters, impacting the mechanical properties of the resulting hydrogel.

6.3.3 Catalyst to lignin ratio

The ratio of C/L plays a crucial role in achieving a selective reaction for biomass conversion to LA. Variations in LA yields could be seen at low (0.06), medium (0.13), and high (0.20) C/L ratios. When the C/L ratio was low, the addition of more water to the lignin mixture resulted in decreased LA yields. Excessive water dilutes the acid catalyst, reducing its effectiveness in catalysing the hydrolysis reaction. On the other hand, when the C/L ratio was within the medium to high range, the addition of water was more significant for achieving higher LA yields. Sufficient water is required to accommodate the high number

of active sites on the acid catalyst, thereby increasing the rate of the chemical reaction that converts hexoses to LA. Meanwhile, excessively acidic conditions and low water content can lead to the degradation or modification of the lignin structure. Therefore, controlling the amount of water during formulation is crucial to balance the pH and maximise the activity of the acid catalyst, thereby improving the efficiency of the LA production process.

As the C/L ratio increases, the pH value decreases, allowing the protonation of carboxylic acid and phenolic hydroxyl groups in the lignin molecules. This leads to a more polar structure and increased solubility of lignin in the gel mixture. Crosslinking is further enhanced in an acidic medium as gelation may occur within a few hours if the pH is <6.8, whereas it may take two days to form a gel if the initial solution pH is >7.0 [370]. Achieving the desired cryogel that is thermally stable and reactive for LA production from biomass requires a balance between xanthan gum and acid concentrations to lignin. The acid catalysts ($H_3PW_{12}O_{40}$ and Nb_2O_5) employed in this study not only exhibited selectivity for LA conversion but also enhanced the thermal stability of the hydrogel as initiators or free radicals, due to strong interfacial bond formation [534] to withstand high temperatures (>180 °C). Therefore, maintaining balanced concentrations of these catalysts is crucial for hydrogel formulations.

6.4 Parametric studies on factors affecting carbon cryogel characteristics

During the second stage of optimisation, the 30 experimental runs, as outlined in **Table 6.5**, revealed that the performance of the carbon cryogel varied based on the extended factors observed throughout the synthesis process. These factors include the ratio of $H_3PW_{12}O_{40}$ to Nb_2O_5, calcination time and temperature, as well as solvent exchange. Notably, during runs 25–30, the centre points were

replicated, and the small standard deviations (ranging from 0.10 to 0.52) from the mean LA yield indicated high repeatability and reproducibility of the results. This confirmed the reliability of the optimised conditions.

Based on the numerical optimisation using RSM, the maximum LA yield (20.1%) was achieved by setting the calcination temperature and time, the ratio of $H_3PW_{12}O_{40}$ to Nb_2O_5, and solvent exchange time at 336 °C, 51.4 min, 3.02, and 9.2 h, respectively. The model was validated with triplicate data (**Table 6.6**), resulting in an error of <5%. The experimental LA yield was 20.2%, with a standard deviation of 0.36. **Eq. 6.2** represents the proposed model for LA yield in terms of coded factors.

$$\text{Yield} = 19.44 + 1.23A + 0.45B + 0.72C - 0.88D - 0.08AB - 0.01AC - 0.23AD + 0.02BC - 0.81BD + 0.85CD - 1.93A^2 - 1.25B^2 - 1.68C^2 - 0.82\,D^2 \quad (6.2)$$

Table 6.5 Parametric studies on factors affecting carbon cryogel properties throughout the synthesis process.

Run	Point type	Parameters				Response
		A	**B**	**C**	**D**	**Y_i**
		Calcination temperature (°C)	**Calcination time (min)**	**Ratio of $H_3PW_{12}O_{40}$ to Nb_2O_5**	**Solvent exchange time (h)**	**LA yield (%)**
2O1	Factorial	200(-1)	30(-1)	2(-1)	8(-1)	12.40
2O2	Factorial	400(+1)	30(-1)	2(-1)	8(-1)	15.40
2O3	Factorial	200(-1)	60(+1)	2(-1)	8(-1)	13.40
2O4	Factorial	400(+1)	60(+1)	2(-1)	8(-1)	17.15
2O5	Factorial	200(-1)	30(-1)	4(+1)	8(-1)	11.67
2O6	Factorial	400(+1)	30(-1)	4(+1)	8(-1)	15.23
2O7	Factorial	200(-1)	60(+1)	4(+1)	8(-1)	13.98
2O8	Factorial	400(+1)	60(+1)	4(+1)	8(-1)	16.52
2O9	Factorial	200(-1)	30(-1)	2(-1)	20(+1)	11.19
2O10	Factorial	400(+1)	30(-1)	2(-1)	20(+1)	13.13
2O11	Factorial	200(-1)	60(+1)	2(-1)	20(+1)	9.43
2O12	Factorial	400(+1)	60(+1)	2(-1)	20(+1)	11.85
2O13	Factorial	200(-1)	30(-1)	4(+1)	20(+1)	13.89
2O14	Factorial	400(+1)	30(-1)	4(+1)	20(+1)	16.44
2O15	Factorial	200(-1)	60(+1)	4(+1)	20(+1)	12.82
2O16	Factorial	400(+1)	60(+1)	4(+1)	20(+1)	14.47
2O17	Axial	100(-∝)	45(0)	3(0)	14(0)	9.67
2O18	Axial	500(+∝)	45(0)	3(0)	14(0)	13.97
2O19	Axial	300(0)	15(-∝)	3(0)	14(0)	12.08
2O20	Axial	300(0)	75(+∝)	3(0)	14(0)	17.01
2O21	Axial	300(0)	45(0)	1(-∝)	14(0)	11.08
2O22	Axial	300(0)	45(0)	5(+∝)	14(0)	14.51
2O23	Axial	300(0)	45(0)	3(0)	2(-∝)	18.27
2O24	Axial	300(0)	45(0)	3(0)	26(+∝)	14.24
2O25	Centre	300(0)	45(0)	3(0)	14(0)	18.78
2O26	Centre	300(0)	45(0)	3(0)	14(0)	18.40
2O27	Centre	300(0)	45(0)	3(0)	14(0)	20.52
2O28	Centre	300(0)	45(0)	3(0)	14(0)	20.73
2O29	Centre	300(0)	45(0)	3(0)	14(0)	18.51
2O30	Centre	300(0)	45(0)	3(0)	14(0)	19.69

Table 6.6 Optimisation of carbon cryogel attributes and validation for LA yields.

Experiment	Calcination temperature (°C)	Calcination time (min)	Ratio of $H_3PW_{12}O_{40}$ to Nb_2O_5	Solvent exchange time (h)	Response (%)	Error (%)
					LA yield	
CCD	336	51.4	3.02	9.2	20.10	
Validation (Trial 1)	336	51.4	3.02	9.2	19.99	
Validation (Trial 2)	336	51.4	3.02	9.2	20.00	
Validation (Trial 3)	336	51.4	3.02	9.2	20.62	
Validation[a]	336	51.4	3.02	9.2	20.20	0.50

[a]Mean for triplicate data.

6.4.1 RSM contour plots

Figure 6.5 illustrates that all 3D surface plots exhibit a curved shape while maintaining two variables constant. The curvature indicates interactions or higher-order effects between the factors, suggesting that a linear model may not adequately capture the relationship. This implies that the impact of the factors on the response is not constant and changes with variations in factor levels. There might be a combined effect of both factors that differ from the sum of their individual effects, a hypothesis to be further validated through statistical analysis in **Section 6.4.2**.

Each 3D surface plot in **Figure 6.5** presents a distinct pattern in response to its RSM. In **Figure 6.5a**, the contour indicates a consistent influence of changing calcination temperature and time on LA yield, signifying that an increase in both factors results in an increased yield of LA. The behaviour of the catalyst system, particularly during calcination, is complex. Factors beyond calcination time and temperature, such as catalyst composition, surface properties, and other reaction conditions, may have a more pronounced impact

on LA yield. These factors could overshadow the specific interaction effect between calcination time and temperature.

In **Figure 6.5b**, the simultaneous increase in calcination temperature and the ratio of Brønsted-Lowry to Lewis acid promotes the yield of LA, reaching an optimum point where the value starts to decrease. **Figure 6.5c** demonstrates an increasing LA yield with rising calcination temperature, in contrast to decreasing solvent exchange**. Figure 6.5d** indicates that the increasing pattern of calcination time aligns with an increasing ratio of Brønsted-Lowry to Lewis acid, meaning both factors affect LA yield in the same direction. Meanwhile, the interactions between factors B and D and between factors C and D in **Figure 6.5e** and **6.5f**, respectively, show an opposite direction as LA yield increases or decreases.

(a)

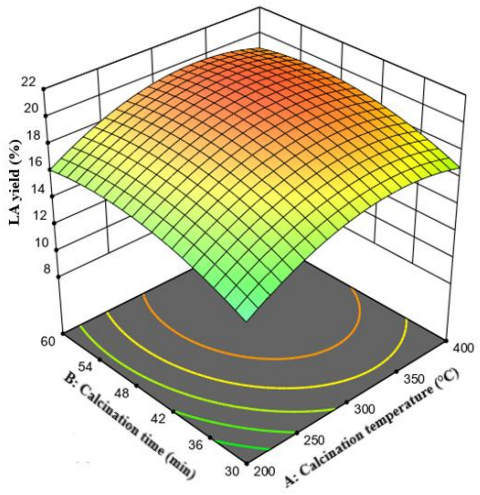

(b)

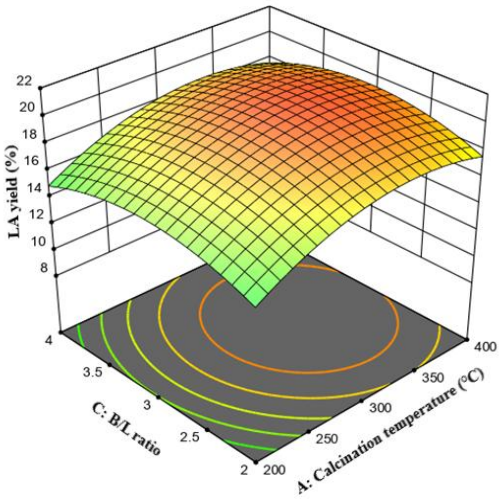

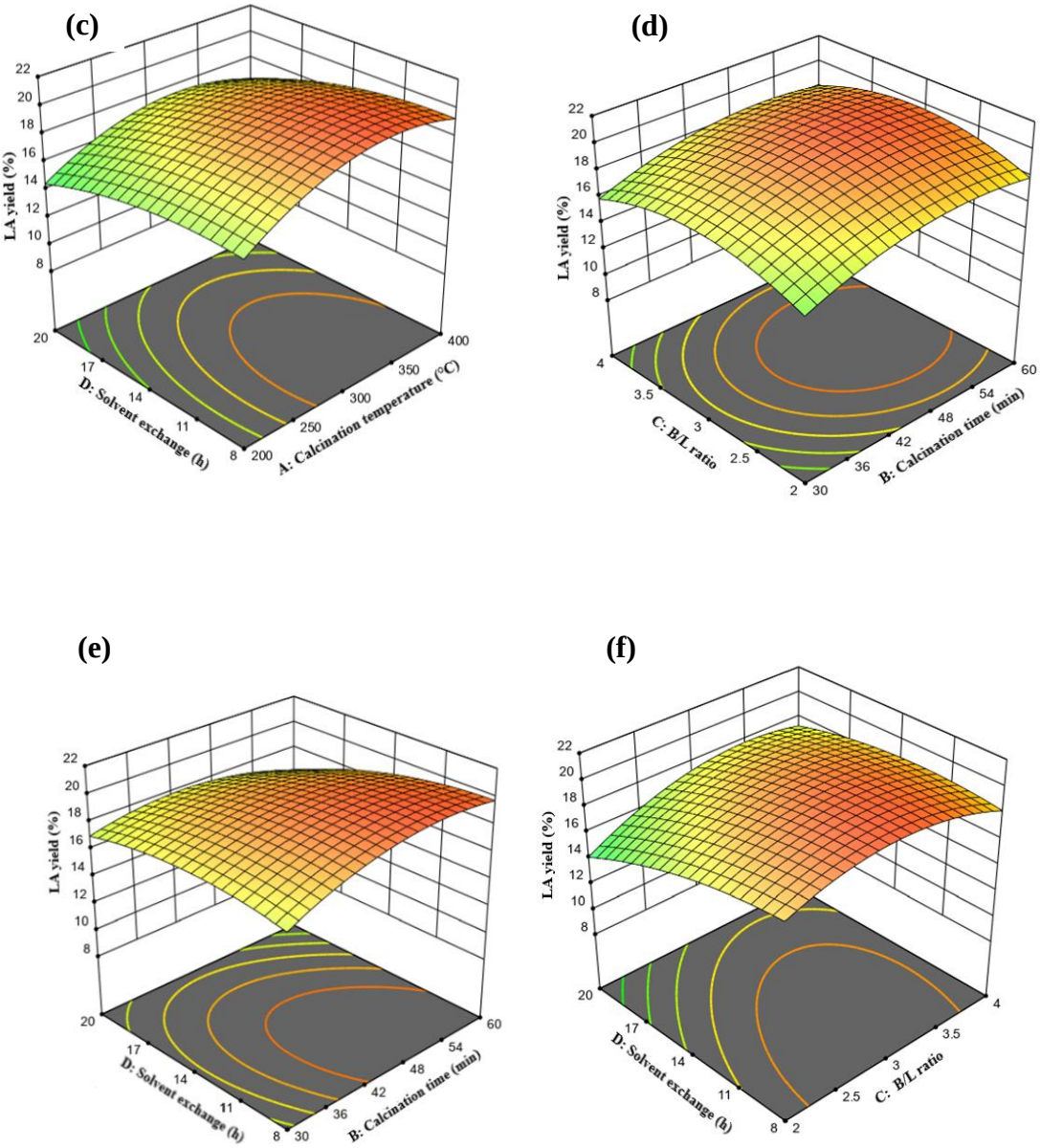

Figure 6.5 RSM surface plots for different interactions between (a) calcination temperature and calcination time; (b) calcination temperature and ratio of Brønsted-Lowry to Lewis acid; (c) calcination temperature and solvent exchange; (d) calcination time and ratio of $H_3PW_{12}O_{40}$ to Nb_2O_5; (e) calcination time and solvent exchange; and (f) ratio of $H_3PW_{12}O_{40}$ to Nb_2O_5 and solvent exchange.

6.4.2 RSM statistical analysis

The proposed model demonstrates exceptional accuracy, as evidenced by an R^2 value of 0.95, indicating that 95% of the variation in LA yield can be attributed to the model-explained process variables. The coefficient of variation, at 6.46%, further emphasises the reliability of responses within the range of process conditions. A commendable agreement between experimental and predicted LA yield is evident in the adjusted R^2 (0.90) and predicted R^2 (0.80). ANOVA analyses were conducted for each response model (refer to **Table 6.7)** to assess the significance of interactions between process variables and individual factors. Linear and quadratic terms significantly influenced LA yield, with quadratic terms A (F-value=109.94) and C (F-value=83.81) emerging as crucial variables. The Model F-value of 21.02 indicates the model's significance, and the lack of fit F-value of 0.82 affirms a good fit. The adequate precision, with a signal-to-noise ratio of 14.92, suggests that the ratio is >4, which is desirable for navigating the design space suggested by the CCD approach.

Interaction effects between factors such as AB, AC, AD, and BC may reach saturation at extreme factor levels in a CCD design, potentially reducing their significance. Quadratic terms, however, capture curvature and non-linear behaviour, resulting in higher F-values. Interaction terms BD and CD demonstrated significant effects, indicating synergy between factors. Solvent exchange time may be a prime factor controlling catalytic kinetics, influencing overall performance, while calcination temperature and time may have limited sensitivity to detect small changes in LA production due to their interaction. This could be due to the range of temperatures and time tested in the experimental

design, which might compromise the sensitivity of the catalyst towards other influential factors.

Due to the complex behaviour of derived catalysts like carbon cryogel, factors beyond calcination temperature and time, such as catalyst composition, surface area, pore size distribution, and acidity strength, may play significant roles. These factors could overshadow specific interaction effects, making the diffusivity of reactants and products in and out of the catalyst, along with side reactions caused by catalytic activity, key factors in determining overall efficiency. The exchange rate between water molecules and solvent particles can influence the movement of the immobilising catalyst in and out of the system, thus affecting overall performance. Factors like the ratio of $H_3PW_{12}O_{40}$ to Nb_2O_5 and solvent exchange time may induce changes in the catalyst structure or surface properties, influencing catalytic activity in ways not easily explained by a simple interaction model. Subsequently, selected samples (2O1, 2O8, 2O11, 2O15, 2O21, 2O22, and 2O28) were further analysed for carbon cryogel properties influencing LA yield concerning the variability of changes in significant parameters.

Table 6.7 Statistical analysis for each response variable and the interaction terms.

Source	Sum of squares	Degree of freedom	Mean of square	F-value	*p*-value	Std error	Remark
Model	272.580	14	19.470	21.0200	<0.0001		Significant
A – Calcination temperature (°C)	36.100	1	36.100	38.9700	<0.0001	0.20	
B – Calcination time (min)	4.760	1	4.760	5.1400	0.0386	0.20	
C – Ratio of $H_3PW_{12}O_{40}$ to Nb_2O_5	12.580	1	12.580	13.5800	0.0022	0.20	
D – Solvent exchange (h)	18.660	1	18.660	20.1400	0.0004	0.20	
A^2	101.850	1	101.850	109.9400	<0.0001	0.18	
B^2	42.530	1	42.530	45.9100	<0.0001	0.18	
C^2	77.640	1	77.640	83.8100	<0.0001	0.18	
D^2	18.330	1	18.330	19.7900	0.0005	0.18	
AB	0.105	1	0.105	0.1130	0.7412	0.24	
AC	0.004	1	0.004	0.0040	0.9521	0.24	
AD	0.860	1	0.860	0.9280	0.3506	0.24	
BC	0.005	1	0.005	0.0050	0.9452	0.24	
BD	10.570	1	10.570	11.4100	0.0041	0.24	
CD	11.490	1	11.490	12.4100	0.0031	0.24	
Residual	13.900	15	0.926				
Lack of Fit	8.640	10	0.864	0.8219	0.6310		Not significant
Pure Error	5.260	5	1.050				
Cor Total	286.480	29					

6.5 Effects of carbon cryogel properties on LA production

Understanding carbon cryogel properties is crucial for optimising LA production and improving catalyst performance. Catalyst properties, such as acidity, surface area, porosity, and specific functional groups, are key determinants of effectiveness. The intricate nature of these properties significantly influences LA production, emphasising the importance of active site availability and effective

mass transport facilitated by porosity. Non-linear relationships between these properties highlight the necessity of incorporating quadratic terms in statistical models to capture nuances and understand their interactions. Hence, the pivotal roles of both experimental data and earlier-discussed statistical analyses in elucidating relationships and refining the catalyst for optimal LA production become evident. The fine-tuning of carbon cryogel properties is achievable when a delicate balance among acidity, surface characteristics, and porosity is unlocked.

In this study, selected samples from 2O1, 2O8, 2O11, 2O15, 2O21, 2O22, and OPT2 were further analysed for their properties to investigate the effects of cryogel properties on LA yield. Among them, four were from factorial points, two were from axial points, and OPT2 was the optimised sample.

6.5.1 Acid strength

Figure 6.6 illustrates the TPD-NH_3 analysis of the carbon cryogel catalyst incorporated with $H_3PW_{12}O_{40}$-Nb_2O_5, highlighting a distribution of weak (100–350 °C), medium (350–600 °C), and strong (600–800 °C) acid sites. Notably, samples 2O1, 2O11, and 2O15 exhibit the highest densities of weak acid sites, measuring 9.356, 7.632, and 7.651 mmol g^{-1}, respectively. Desorption of NH_3 on weak sites at 100–350 °C corresponds to non-acidic –OH groups of Brønsted acid [535], while higher temperatures relate to active Brønsted and Lewis acid functions [536]. Typically, Brønsted acids provide medium acid strength, whereas Lewis acid sites are the strongest [537].

The distribution of acidic sites significantly affects the reaction rate and selectivity in LA production. The spatial arrangement of these sites on the catalyst surface is crucial, as it impacts reactant accessibility and promotes

efficient catalysis. The presence of weak acid sites in samples 2O1, 2O11, and 2O15 is notably impacted by the lower calcination temperature of 200 °C used during the synthesis of carbon cryogels. In contrast, samples subjected to calcination temperatures exceeding 300 °C (as shown in **Figure 6.6**) exhibit fewer weak acid sites. This difference is attributed to the retention of more original functional groups at lower calcination temperatures, which promotes the formation of weak acid sites.

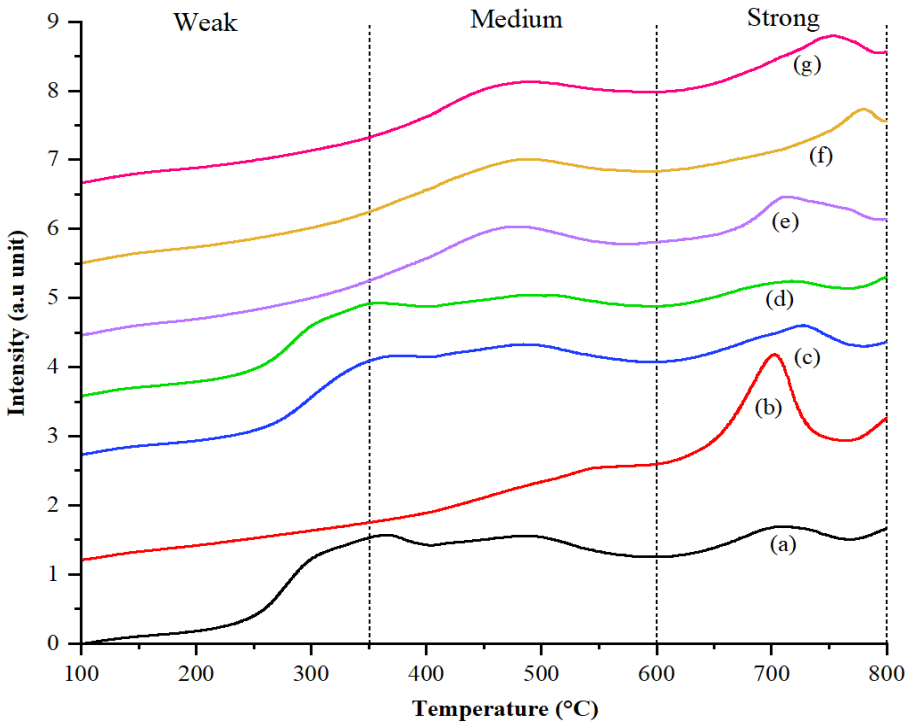

Figure 6.6 Acid density by TPD-NH_3 for samples (a) 2O1; (b) 2O8; (c) 2O11; (d) 2O15; (e) 2O21; (f) 2O22 and (g) OPT2.

In sample 2O1, a shorter solvent exchange duration (8 h) might not suffice to remove all residual species, contributing to the higher formation of weak acid sites. The solvent t-butanol, essential in the exchange process, might participate in surface reactions and modifications, with the shorter duration limiting interaction time and affecting the incorporation of t-butanol-derived

species. Specific surface functional groups, particularly hydroxyl (–OH) groups within mesopores, may also contribute to weak acid site formation [538].

Sample 2O8 reveals remarkable performance, primarily attributed to its high concentration of strong acid sites. This is due to the formulation's increased ratio of Brønsted acid compared to Lewis acid, achieved by a higher ratio of $H_3PW_{12}O_{40}$ to Nb_2O_5 (4:1), combined with a high calcination temperature of 400 °C. This temperature is critical in enhancing the catalyst's acid strength and density, as it accelerates the decomposition of oxygen-containing groups associated with medium acid sites. Consequently, the concentration of medium acid sites is reduced, thereby lowering their density.

The transformation is validated by the TPD-NH_3 curve (**Figure 6.6**), which shows that medium acid sites are active within the temperature range of 350–600 °C. These sites play a pivotal role in balancing the reactivity provided by strong acid sites and the selectivity offered by weak acid sites, thus significantly contributing to the overall acidity profile of the catalyst surface. As a result, sample 2O8, which exhibited a higher density of strong acid sites, achieved a higher LA yield of 16.5% compared to other tested samples such as 2O1, 2O11, and 2O15, as well as some axial points in the CCD approach (samples 2O21 and 2O22).

In contrast, sample 2O22 demonstrated a lower LA yield of 14.5%, despite having a higher ratio of $H_3PW_{12}O_{40}$ to Nb_2O_5 (5:1). This discrepancy can be attributed to the lower calcination temperature (300 °C) and shorter duration (45 min) for sample 2O22. The duration of calcination profoundly influences the formation and stability of acid sites in the catalyst. Short calcination times may not provide sufficient energy for the complete decomposition of precursor

materials and the formation of well-defined acid sites, leading to a higher proportion of weak acid sites due to incomplete transformations. Meanwhile, prolonged calcination times enhance the stability and strength of acid sites, as extended exposure to high temperatures allows for more thorough dehydration and condensation reactions. This enhances the interaction between active components, $H_3PW_{12}O_{40}$ and Nb_2O_5, and the lignin-derived carbon support. However, an extended solvent exchange (14 h) process could over-remove stabilising agents or functional groups that contribute to the formation of strong acid sites, thereby diminishing their presence and altering their strength. This can result in a decrease in the number of accessible strong acid sites, which may become embedded within the dense structure or even deactivated due to thermal degradation.

The results from sample 2O8 underscore the significant interaction between calcination time (B factor) and solvent exchange (C factor) effects, as detailed in **Table 6.7**. This analysis highlights the importance of optimising these variables to maximise catalyst performance and achieve higher LA yields. The optimised sample (OPT2) presents a higher proportion of medium acid sites compared to strong acid sites relative to 2O8, resulting in higher LA yields of 20.2%. Excessively high calcination temperatures, as seen in sample 2O8, diminish crucial medium acid site presence. The optimal temperature at 336 °C for 51.4 min results in a twofold increase in medium acid site density compared to 2O8.

Table 6.8 Strength of acid sites of different conditions of carbon cryogel synthesis.

Sample	Acid Density (mmol g^{-1})			
	Weak	**Medium**	**Strong**	**Total**
2O1	9.356	5.815	1.967	17.138
2O8	0.581	3.129	4.577	8.287
2O11	7.632	5.708	2.522	15.862
2O15	7.651	5.379	1.999	15.029
2O21	1.186	9.200	2.634	13.020
2O22	1.150	8.347	2.417	11.914
OPT2	1.556	7.867	3.234	12.657

Overall, the incorporation of $H_3PW_{12}O_{40}$ and Nb_2O_5 into the carbon cryogel has proven to be highly effective, providing robust acid sites due to the well-defined Brønsted acidity from the protons (H^+) of phosphotungstic acid and the strong acid sites from Nb_2O_5. The NbOx species play a crucial role in cleaving C–O bonds and catalysing dehydration, due to the unique electronic and energy band structure of Nb5c, which contributes significantly to the overall acidity profile [539]. This synergy between Brønsted and Lewis acid sites enhances catalytic activity and selectivity, particularly in isomerisation reactions, thereby influencing product distribution.

In this study, the optimised carbon cryogel (LXCC catalytic system) demonstrated a total acidity of 12.66 mmol g^{-1}, outperforming previous successful catalysts like HY zeolite (2.68 mmol g^{-1}) [538], pure $H_3PW_{12}O_{40}$ (2.46 mmol g^{-1}) [540], and sulphonated activated carbon fibre (2.43 mmol g^{-1}) [541]. When compared to other solid acid catalysts such as HY zeolite, which produced a maximum of 1.58 mmol g^{-1} acid sites—and slightly increased to 2.81 mmol g^{-1} with 5% Fe impregnation—the evidence suggests that Fe successfully diffused into HY zeolite [538], thereby inducing new acid sites. This supports

the notion that metal oxides like Fe, Al, and Nb enhance LA yield by strengthening acidity. According to Zainol *et* al., the carbon cryogel's total acidity was notably high, ranging from 9.34 to 20.38 mmol g^{-1} [164].

Strong acid sites are essential during the conversion of biomass to LA, as they activate reactant molecules and create the necessary acidic environment for breaking chemical bonds and initiating catalytic reactions. They also facilitate dehydration reactions, transforming intermediates into LA, stabilising catalytic activity, and reducing the risk of deactivation over time. However, an excess of strong acid sites can lead to undesirable side reactions such as humin formation, which can ultimately reduce the overall LA yield. Despite this risk, the study's utilisation of a microwave-assisted method successfully shortened reaction times and potentially mitigated deactivation rates.

6.5.2 Distribution of acid sites

The acid site distribution in carbon cryogel catalysts was thoroughly examined using the Hammett acidity function and acid-titration methods. Although NH_3-TPD is a valuable tool for analysing the total acid content and intensity in solid acid catalysts, it falls short in distinguishing between Brønsted-Lowry and Lewis acid sites. In this study, the Hammett acidity function (**Figure 6.7**) was employed to specifically characterise the Brønsted acidity in various carbon cryogel catalyst formulations. Lower Hammett acidity (H_0) values indicate stronger acidity [187], and the results, as detailed in **Table 6.9**, show a decreasing order of acidity strength: 2O8 > 2O22 > OPT2 > 2O15 > 2O1 > 2O21 > 2O11.

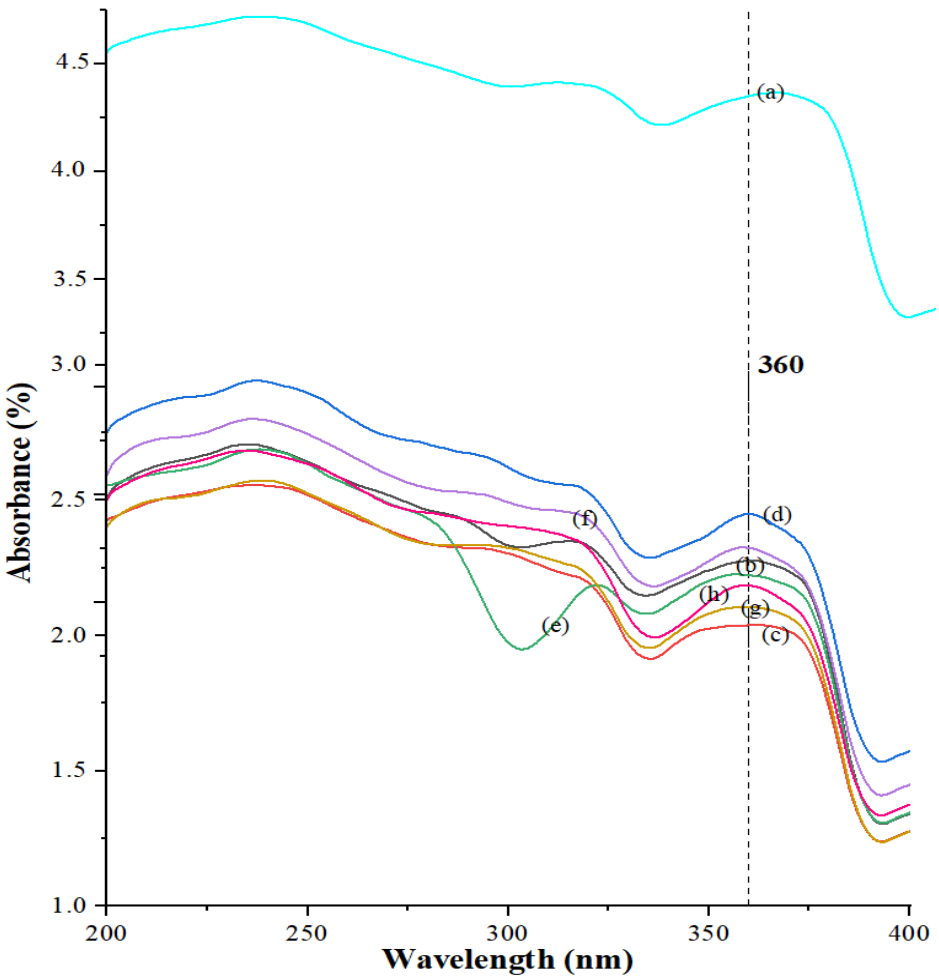

Figure 6.7 UV-Vis spectra represents Hammett acidity function for selected carbon cryogel samples (a) blank, (b) 2O1, (c) 2O8, (d) 2O11, (e) 2O15, (f) 2O21, (g) 2O22 and (h) OPT2.

Table 6.9 Hammett acidity function for cryogel samples.

Sample	**A_{max}**	**[I] %**	**[IH] %**	***H_0***
Blank	4.388	100.00	0.00	–
2O1	2.281	52.91	47.09	1.041
2O8	2.167	50.26	49.74	0.995
2O11	2.449	56.81	43.19	1.109
2O15	2.277	52.81	47.19	1.039
2O21	2.286	53.03	46.97	1.043
2O22	2.193	50.87	49.13	1.005
OPT2	2.213	51.32	48.68	1.013

The H_0 values obtained align with findings by Sun *et* al. [187], who reported a range of 0.41 to 0.63 for other types of heteropoly acid-derived catalysts. Lower H_0 values are attributed to potent Brønsted-Lowry acid sites originating from $H_3PW_{12}O_{40}$, which readily donate protons (H^+). This is associated with Nb_2O_5 loading, suggesting the presence of a super acidic system. The hydrogen bond between the cation (Nb) and the anion (WO_3^-) enhances acidity, resulting in double the acidity of combined catalysts [542]. Additionally, Brønsted acid sites are likely generated at the boundaries between two niobic oxide monolayer domains, thereby augmenting catalytic activity [543].

Calcination temperature plays a significant role in catalytic activity, with the optimum temperature identified as 336 °C. This temperature reflects the intricate relationship between catalyst physicochemical properties, including crystalline and molecular structure, and the density and strength of acid sites. Lopez *et* al. conducted studies on esterification and transesterification rates [544], focusing on near-saturation W surface densities [545], which resulted in a satisfactory product yield. The formation of crystalline WO_3 at 800 °C did not immediately compromise the catalyst's activity, suggesting that higher temperatures, where heteropolyoxotungstate clusters still appear, serve as catalytically active sites facilitating biomass conversion.

In this study, both $H_3PW_{12}O_{40}$ and Nb_2O_5 exhibited sustained catalytic activity at 400 °C (refer to **Figure 6.2, Section 6.2.1**). However, it is important to note that xanthan gum itself showed limited thermal stability, especially above 220 °C. Excessive calcination temperatures may alter the cryogel structure, leading to the leaching of the incorporated acid catalyst and consequently lowering overall catalytic activity. This underscores the critical balance required

in optimising calcination conditions to preserve the catalyst's effectiveness in biomass conversion.

Sample 2O8 exhibited the second-highest LA yield after OPT2, attributed to its higher $H_3PW_{12}O_{40}$ loading and reduced solvent exchange duration. The increased catalyst loading in 2O8 compensates for the removal of functional groups lost during template combustion, effectively preventing structural damage caused by exothermic hot spots [546]. These findings underscore the intricate interplay of various factors, including catalyst loading, solvent exchange duration, and calcination temperature, in determining the performance of carbon cryogel catalysts for biomass conversion.

Table 6.10 illustrates the variations in the distribution of Brønsted-Lowry and Lewis acid sites across all samples, highlighting OPT2 as having the optimal ratio for achieving the highest LA yield. The total acidity observed in this study surpassed values reported in other studies [187, 538, 541], typically ranging below 9 mmol g^{-1}, with the minimum LA yield found in sample 2O11. Maintaining the appropriate balance between Brønsted-Lowry and Lewis acid sites within the carbon cryogel is crucial for influencing the LA yield. An excess of Lewis acid may overshadow the role of strong Brønsted acid in facilitating the breakage of β-1,4 glycosidic bonds in cellulose, ultimately enhancing catalytic efficiency. Nevertheless, an adequate number of Lewis acid sites may be required to promote subsequent reactions while limiting the formation of intermediates.

Table 6.10 Distribution of Brønsted-Lowry and Lewis acid sites in carbon cryogel prepared at different conditions of calcination, acid treatment and solvent exchange duration.

Sample	Brønsted-Lowry acid sites (mmol g^{-1})	Lewis acid sites (mmol g^{-1})	Total acidity (mmol g^{-1})	Ratio of Brønsted-Lowry to Lewis	Synergy factor
2O1	6.99	10.01	17.00	0.70	1.26
2O8	7.77	1.33	9.10	5.85	1.88
2O11	5.97	10.53	16.50	0.57	0.94
2O15	7.02	8.48	15.50	0.83	1.31
2O21	6.96	7.64	14.60	0.91	1.14
2O22	7.58	4.72	12.30	1.61	1.55
OPT2	7.45	5.05	12.50	1.48	2.15

The study by Kitano *et* al. unveiled insights into hydrolysis activities regulated by Brønsted acidity [543]. An increase in the number of Brønsted acid sites was observed up to a calcination temperature of 1123 K, followed by a reduction beyond this temperature. Intriguingly, Brønsted acid sites persist even at calcination temperatures exceeding 1100 K, indicating that high-temperature calcination plays a role in generating these acid sites. In contrast, the number of Lewis acid sites shows a monotonic decrease as calcination temperature rises. This explains why, in this study, higher Lewis acid sites were obtained on samples (2O1, 2O11 and 2O15) at a lower calcination temperature of 200 °C. This discrepancy can be attributed to the reduction of Lewis acid sites on the cryogel surface in proportion to the fraction of the surface occupied by the deposited Nb_2O_5.

Assessing the synergic activity of a catalysis system involves defining a synergy factor, with the resulting complexities summarised in **Table 6.10**. A synergy factor exceeding 1 indicates positive synergic catalytic activity within the mixed-acid system. In the findings, most synergy factors surpassed 1,

affirming the effectiveness of most mixed-acid systems ($H_3PW_{12}O_{40}$-Nb_2O_5 carbon cryogel) in decomposing glucose into LA in a one-pot conversion and showcasing robust synergic catalytic activity. Notably, sample 2O11 exhibited a slightly lower synergy factor of 0.94. While OPT2 displayed the most potent synergic catalytic activity, boasting a synergy factor of 2.15.

6.5.3 Surface area and pore distribution

Figure 6.8 illustrates the low-pressure N_2 adsorption isotherms for the examined samples. These isotherms exhibit a convex shape relative to the P/P_0 axis, with the adsorbed amount rapidly increasing as P/P_0 approaches 1. The N_2 adsorbed volumes for the samples range from 3 to 100 $cm^3\ g^{-1}$. According to the IUPAC classification, all carbon cryogel samples demonstrate Type III isotherms [547], characteristic of mesoporous materials. Type III isotherms are marked by a hysteresis loop caused by capillary condensation in mesopores [548]. The desorption branch of the hysteresis loop features a steep region associated with the closure of the loop (see **Figure 6.8**). The IUPAC classification identifies the hysteresis loops of the N_2 adsorption isotherms as Type H_3, indicating the presence of heterogeneous slit-shaped pores in the samples.

The Type III isotherm lacks a flat portion, indicating the absence of typical monolayer formation seen in other isotherms. This suggests that adsorbate molecules are not confined to a single layer on the surface, where the adsorbate-adsorbate interaction is significant compared to adsorbate-sorbent interaction [549]. Instead, multiple layers form, leading to the upward trend in the isotherm. This behaviour may result from the surface characteristics of xanthan gum, known for its low surface area and pore radius. Kaur *et* al.

observed a similar trend when investigating XG grafted copolymers [550], finding that the surface area of XG did not significantly change after grafting with acrylic acid as the acid initiator (0.220 to 0.798 $m^2 g^{-1}$ after grafting). This aligns with this study, where the surface area of the cryogel sample did not exhibit enhancement. At low pressures, some samples (2O1, 2O8, 2O11, 2O21, and 2O22) displayed negative volume adsorbed, resulting in a very low surface area (<0.8 $m^2 g^{-1}$), indicating the absence of distinct monolayer formation in this region as micropores start filling. As the pressure increases, the adsorption process continues without exhibiting a plateau, distinguishing it from Type I or Type II isotherms and indicating multilayer adsorption.

Despite this, sample 2O15 exhibited a slightly higher surface area of 1.29 $m^2 g^{-1}$, significantly increasing to 57.41 $m^2 g^{-1}$ for sample OPT2. This highlights the importance of the precise proportion of precursors, including lignin, xanthan gum, and acid initiators, in achieving successful lignin-XG grafted copolymers. The results are summarised in **Table 6.11**, which provides an overview of the surface area, pore size, and pore distribution for the studied samples. The pore size distribution within carbon cryogels was assessed by BJH analysis, identifying micropores (<2 nm), mesopores (2–50 nm), and macropores (>50 nm), which were not captured by BET analysis [551].

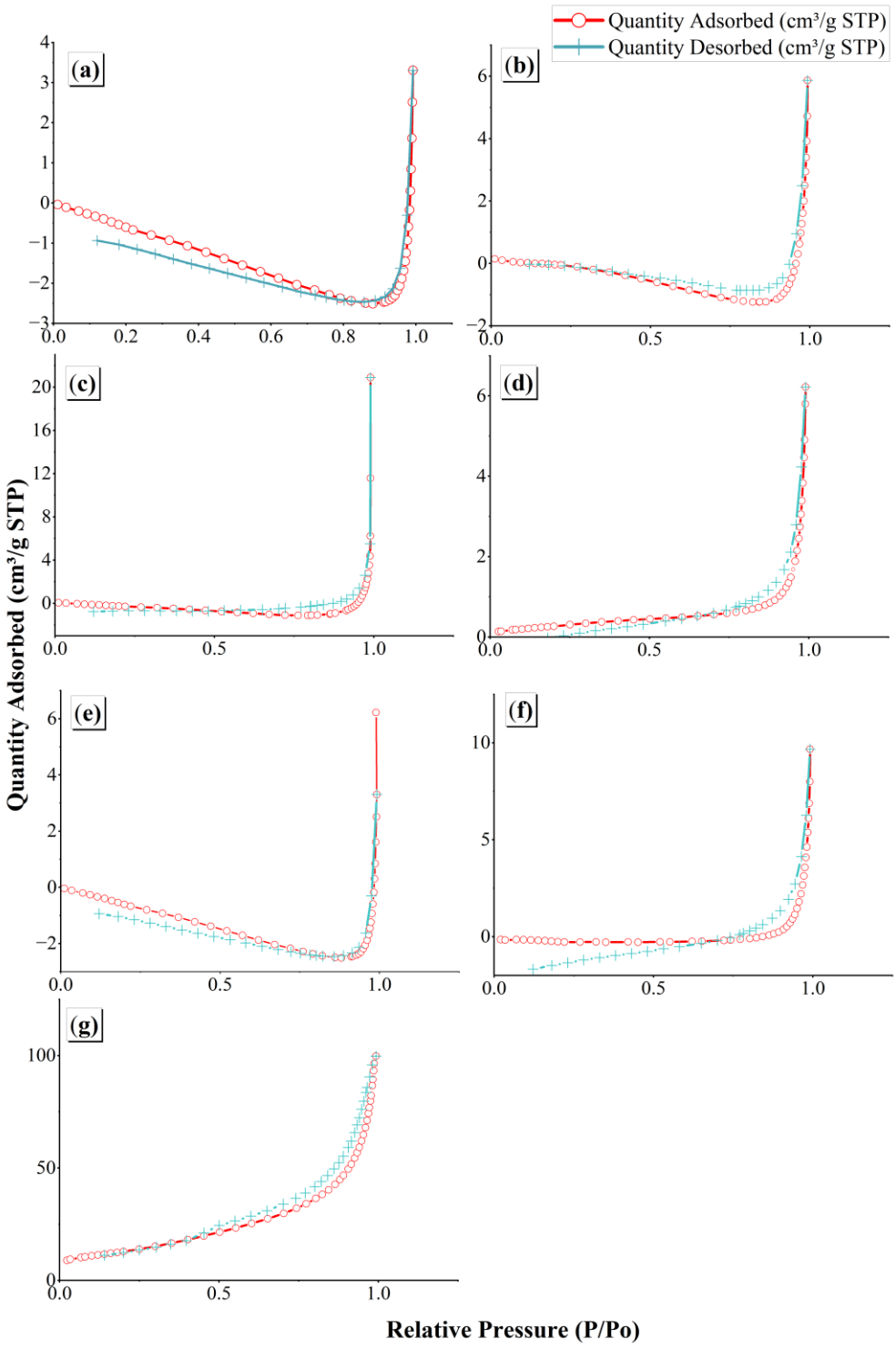

Figure 6.8 N_2 adsorption-desorption isotherm for (a) 2O1; (b) 2O8; (c) 2O11; (d) 2O15; (e) 2O21; (f) 2O22; and (g) OPT2.

While the surface area of the cryogel sample in this study was comparatively lower than that of some catalysts in other research (refer to **Table 6.11**), it is noteworthy that mesopores dominated the pore size distribution. The design of the carbon cryogel aims to enhance the mesoporous surface area [46, 48], thereby improving transport within the catalyst pores. This optimisation becomes particularly relevant when cellulose undergoes hydrolysis into glucose, as it facilitates the subsequent decomposition of glucose—especially given its smaller size—into LA.

Additionally, the lower surface area of the carbon cryogel corresponds to a larger pore diameter, attributed to the presence of metal oxides and high oxygen-containing groups in $H_3PW_{12}O_{40}$, effectively blocking the micropores. This observation aligns with the findings of Zakaria *et* al. [552], who reported a similar increase in pore diameter in Fe/HY zeolite catalysts due to metal oxides causing an excess of mesopores. In a related study, Kumari *et* al. specified that the use of tungstophosphoric acid (TPA) supported on mesoporous niobium oxophosphate (NbP) caused alterations in textural properties compared to the parent materials, particularly with an increased bulk TPA dispersion on NbP [553]. This change was attributed to the deposition of TPA species within the pores of the NbP support, leading to a fine dispersion on the support surface. Consequently, this partial blockage of adsorption sites on the catalyst support resulted in a decrease in surface area with an increasing TPA loading on the NbP support. However, despite this reduction, it was explicitly mentioned that both surface area of the support and the prepared TPA/NbP exhibited a higher surface area than bulk TPA (S_{BET} = 8.5 m^2 g^{-1}), overcoming a recognised disadvantage of heteropolyacid-type catalysts.

Table 6.11 Textural properties of studied carbon cryogels and other types of catalyst.

Ref.	Catalyst (Feedstock)	Single point ($m^2 g^{-1}$)	Langmuir ($m^2 g^{-1}$)	t-plot ($m^2 g^{-1}$)	S_{BET} ($m^2 g^{-1}$)	S_{micro} ($m^2 g^{-1}$)	S_{meso} ($m^2 g^{-1}$)	S_{macro} ($m^2 g^{-1}$)	Acid sites (μmol m^{-2})	Pore size (nm)	LA yield (%)
This study	$H_3PW_{12}O_{40}$	4.80	6.53	1.77	3.52	0.10	3.03	0.20	1.243	16.36	8.40
This study	Nb_2O_5	0.81	1.10	0.31	0.36	0.04	0.26	0.06	0.077	31.55	10.90
This study	LXCC-2O1 (DOPMF)	–	–	–	0.29	–	0.03	0.26	58.620	111.93	12.40
This study	LXCC-2O8 (DOPMF)	0.01	0.01	1.25	0.30	–	–	0.30	30.330	123.46	16.52
This study	LXCC-2O11 (DOPMF)	–	–	–	0.87	–	0.07	0.80	18.970	149.11	9.43
This study	LXCC-2O15 (DOPMF)	0.92	1.60	1.61	1.29	0.21	0.83	0.26	12.020	29.72	12.82
This study	LXCC-2O21 (DOPMF)	–	–	–	0.11	–	–	0.11	132.730	176.31	11.08
This study	LXCC-2O22 (DOPMF)	–	–	–	0.52	–	0.43	0.09	23.650	71.45	14.51
This study	LXCC-OPT2 (DOPMF)	44.72	63.90	44.85	57.41	1.85	53.11	2.45	0.220	10.88	20.20
[211]	Fe-NbP (Cellulose)	–	–	–	305.41	–	–	–	0.012	6.82	64.20
[538]	10% Fe/HY zeolite (Glucose)	–	–	–	549.30	133.60	415.80	–	0.005	1.89	62.00
[35]	Multifunctional sulphonated humins (Bamboo)	–	–	–	1.90	–	–	–	2.110	1.00	45.60

[554]	Carbon foam supported $H_5AlW_{12}O_{40}$ (Cellulose)	–	–	–	5.60	–	–	–	0.131	668.40	61.90
[554]	Carbon foam (Cellulose)	–	–	–	7.30	–	–	–	–	1220.00	8.90

*Note: S_{BET} for DOPMF is 0.12 $m^2 g^{-1}$ and its average pore size is 161.47 nm.

The preparation method of the carbon cryogel may also influence the resulting surface area. The acid catalyst was added before XG was grafted to lignin polymer backbones via sol-gel polycondensation, assuming that the acid catalysts were entrapped in the XG-lignin copolymer templates. Consequently, the surface and density of acid sites become co-factors with surface area, influencing LA yield.

6.5.4 Porosity

In this study, the porosity of selected carbon cryogel samples (**Table 6.12**) varied significantly based on preparation conditions, primarily influenced by calcination effects and acidity. Among the samples, OPT2 stood out with the largest pore volume, showcasing a hierarchical porous structure that facilitated effective interaction with biomass particles of various sizes. This adaptable pore structure is crucial for enhancing catalytic activity, as it influences the accessibility and efficiency of acid sites for biomass conversion.

Table 6.12 Volume of pores of carbon cryogel samples compared to other catalysts.

Ref.	Catalyst sample	V_{pores} ($cm^3 g^{-1}$)	V_{micro} ($cm^3 g^{-1}$)	V_{meso} ($cm^3 g^{-1}$)	V_{macro} ($cm^3 g^{-1}$)	HF
This study	2O1	0.008	–	–	0.008	–
This study	2O8	0.009	–	–	0.009	–
This study	2O11	0.033	–	0.0007	0.032	–
This study	2O15	0.010	0.0001	0.0005	0.009	0.006
This study	2O21	0.005	–	–	0.005	–
This study	2O22	0.015	–	0.0030	0.012	–
This study	OPT2	0.156	0.0060	0.1000	0.050	0.035
[211]	Fe-NbP	0.520	–	–	–	–
[538]	HY zeolite	0.265	0.1670	0.0980	–	0.163
[554]	Carbon foam supported $H_5AlW_{12}O_{40}$	0.900	–	–	–	–

The presence of macropores is critical for enabling larger biomass particles to access catalyst pores, enhancing cellulose conversion and subsequent LA formation. However, the impact of pore size extends beyond simple accessibility. Most samples with larger macropore sizes showed decreased LA yields due to conditions that can lead to unwanted side reactions, such as fragmentation and polymerisation [555–556], highlighting the complexity of optimising pore structure for catalytic efficiency. Therefore, hierarchical porous structure offers benefits for tandem steps, as cellulose-derived biomass hydrolyses at macropore surface, and glucose dehydration catalytically occurs at mesopore and micropore surfaces [556–557]. Larger mesopore sizes can foster the formation of hydronium ions in aqueous solutions, increasing local protonic acidity, which is beneficial for catalytic activity.

Interestingly, the catalytic performance is not solely determined by the number of acid sites (refer to **Table 6.11**). Sample OPT2, despite having fewer acid sites (0.220 μmol m^{-2}) than 2O15 (12.02 μmol m^{-2}), achieved a higher LA yield due to its superior mesoporous surface area. Excessive acid sites, as seen in sample 2O15, can lead to over-reactions and by-product formation [554], negating the benefits of a high acid site density. Even with fewer active sites, sample OPT2 may consist of highly efficient active sites that lead to a more selective catalytic process, focusing on the desired reaction pathway and reducing side reactions, thus increasing the yield of LA. With fewer active sites, there is a lower risk of catalyst deactivation due to fouling or blockage, ensuring more consistent catalytic activity over extended periods.

The efficient active sites are driven by their well-balanced and structured porous catalyst, related to the hierarchical factor (HF). HF provides valuable

insights into the catalyst's structure, relating to its porosity. It is expressed as the product of relative mesoporosity (S_{meso}/S_{BET}) and relative microporosity (V_{micro}/V_{total}) [558]. HF can assess catalytic performance by indicating transport efficiency within catalyst pores that can be improved [559–560]. Sample OPT2 has a higher HF (0.035) than 2O15 (0.006), indicating a high relative ratio of mesoporous to microporous structures. However, sample OPT2 exhibited a comparable HF to high hierarchical Fe/HY zeolites (0.163) [538], showing that tuning mesoporous properties should comply with the condition of the feedstock, where a lower HF in this study is significant for biomass conversion while higher HF in other studies [538] is relevant for glucose conversion to LA. This means the significant balance between macropores, mesopores, and micropores is important as bulky particles from biomass need to be successfully hydrolysed in macropores.

Sample 2O8 provided an interesting case with its uneven distribution of mesopores, possibly leading to their negligible presence on the catalyst surface. Despite this, the sample achieved a notable LA yield of 16.5%. This outcome may be attributed to its effect on altering the acidity ratio between $H_3PW_{12}O_{40}$ and Nb_2O_5 to 4:1. This suggests that the increased loading of $H_3PW_{12}O_{40}$ in the 2O8 sample facilitated cellulose hydrolysis, thereby enhancing the LA yield. However, the sample also suffered a loss in micropore volume and exhibited a very low total pore volume. This could be attributed to the activity of phosphorus at higher loadings of $H_3PW_{12}O_{40}$, leading to the formation of water-soluble (poly)phosphate species, which can cause dealumination [561], resulting in the partial blockage of channels by phosphorus. Such blockage alters diffusion characteristics by decreasing pore dimensions and openings, consequently

leading to longer diffusion pathways for reactants and products [562]. These findings align with previous studies that reported phosphorus forming monolayer islands throughout the H-ZSM-5 channel system, which reduce the detection of micropores by conventional physisorption methods [563–564]. This consistent evidence underscores the complex interplay between phosphorus loading and pore structure in catalytic systems.

The BJH adsorption analysis in **Figure 6.9** reveals an intriguing trend in sample 2O11: despite having a higher pore volume (**Figure 6.9a**), it yielded the lowest LA percentage (9.43%) among the samples tested. This indicates that while the material may possess a higher total pore volume and surface area compared to others, the distribution of pore sizes might not be conducive to efficient adsorption or diffusion of reactants and products during LA production. This is because sample 2O11 exhibits a deficiency in micropores and contains fewer mesopores compared to macropores. This imbalance limits the mass transfer of reactants during the degradation of cellulose into sugar intermediates. As a result, the overall catalytic activity is affected. This observation aligns with the lower pore volume for pore widths of less than 50 nm (mesoporous), as shown in **Figure 6.9a**. Consequently, there is a reduced specific surface area (S_{BET}), as illustrated in **Table 6.11**. Understanding the complex interplay between pore volume, surface area, and LA yield in carbon cryogels is essential. This relationship often defies simple explanations, highlighting the importance of detailed morphological and textural analysis for optimising catalytic performance.

As illustrated in **Figure 6.9b**, a larger surface area does not necessarily equate to a larger pore volume. This is evident in sample 2O11 as it has a larger total pore volume than other tested samples (2O1, 2O8, 2O15, 2O21 and 2O22) due to its larger volume of macropores despite its total surface area being lower than sample 2O15. Sample 2O15 has a larger surface area due to its mesopores and some micropores, indicating its higher proportion of smaller pores, contributing to its overall surface area due to their higher surface-to-volume ratio. Nonetheless, samples 2O8 and 2O22 showed higher LA yields than sample 2O15 despite their lower surface area. This may be due to higher acid sites in those samples (**Table 6.11** in **Section 6.5.3**) lead to surface shrinkage in carbon cryogels, affecting the overall surface area, but larger acid sites can increase pore volume, creating more extensive networks of channels and voids within the material. This expanded porous structure allows for a greater volume of reactants to access and interact with the active sites, thereby enhancing the overall catalytic efficiency.

The pore size of carbon cryogels plays a significant role in determining catalytic efficiency, as larger pore sizes generally mean a reduction in the total surface area available for catalytic reactions. This can be seen when the average pore size for sample 2O1 (111.93 nm) and 2O21 (176.31 nm) showed larger macropores, which can sometimes overshadow the contribution of micropores to the total pore volume. While micropores contribute significantly to the surface area due to their small size and high density of active sites, their impact on the total pore volume is less pronounced when larger pores are present. This is because micropores contribute more to the surface area than to the volume, whereas larger pores contribute more to the volume. This is also related to HF

values that are negligible due to most samples following their disappearing micropores. Larger pores provide more space for byproducts to be trapped or retained, hindering their desorption from the catalyst surface. As byproducts accumulate, they may block active sites, impeding the adsorption of reactants and reducing the overall turnover rate of the catalytic reaction.

(a)

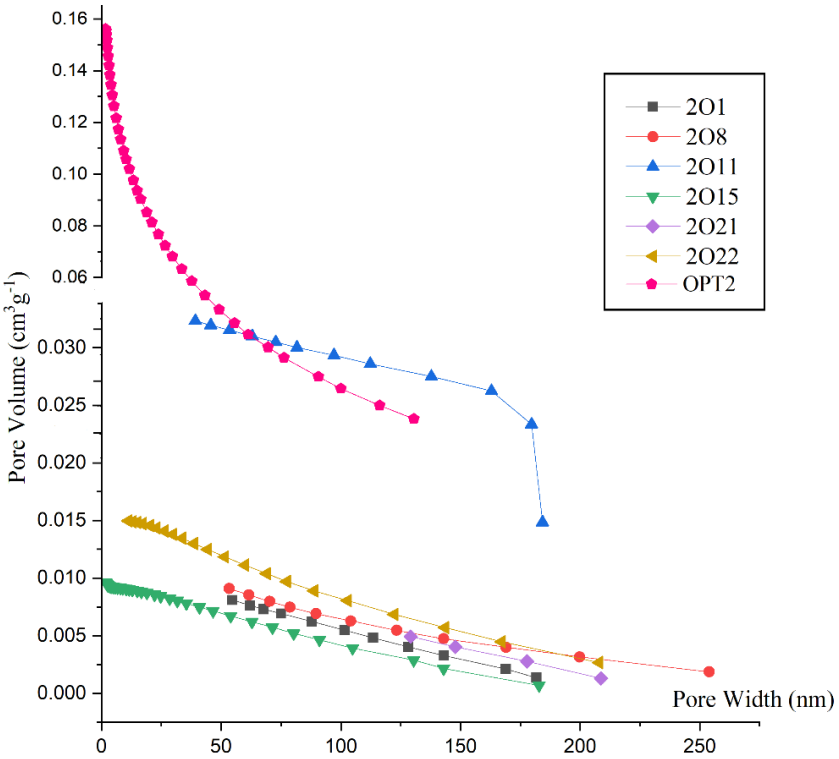

(b)

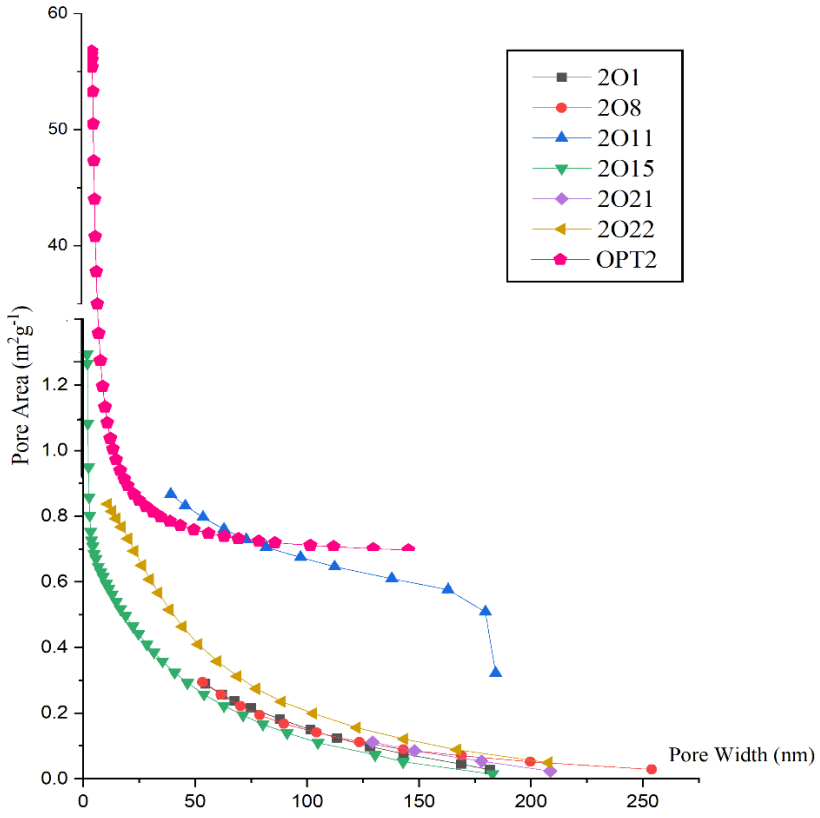

Figure 6.9 BJH adsorption isotherm for assessing pore distribution across (a) pore volume; (b) pore area.

The morphology of lignin-derived carbon cryogel, as depicted in **Figure 6.10**, reveals critical insights into its transformation from precursors to the final structure, highlighting the inherent porosity of lignin, a biomass-derived biopolymer, alongside the sol structure of xanthan gum, which serves as a gelling agent in the cryogel formation process. Each acid catalyst used in the process contributes distinctive structural features, with $H_3PW_{12}O_{40}$ exhibiting a rough and flat appearance and Nb_2O_5 presenting a diamond-like structure. Scanning Electron Microscopy (SEM) analysis plays a crucial role in examining the morphology of both the precursors and the resulting carbon cryogel, enabling researchers to observe surface characteristics and structural evolution during the cryogel's formation, thereby enhancing the understanding of the material's properties and its potential applications.

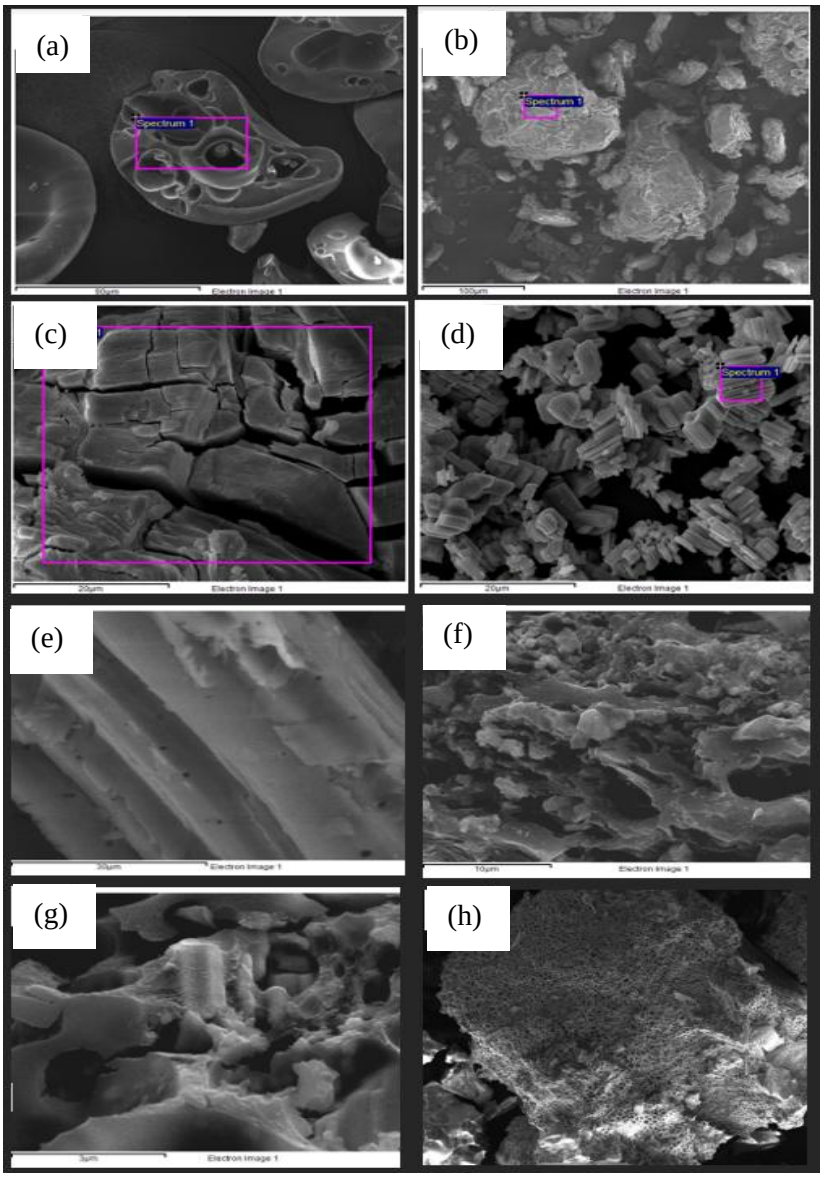

Figure 6.10 SEM images for raw materials (a) lignin; (b) xanthan gum; (c) $H_3PW_{12}O_{40}$; (d) Nb_2O_5; (e) DOPMF; and carbon cryogel sample for (f) cross section; (g) internal surface; (h) outer surface.

Precise measurements of biomass particles, catalyst size, and reactants for cryogel formation (**Table 6.13**) were carefully considered to tailor the desired porous structure. The SEM images in **Figure 6.11** vividly depict the extensive range of pore sizes in the materials. The feedstock sizes, ranging from micro to nano scale, necessitate the design of a carbon cryogel within that specific size

range. This diversity in pore size distribution, encompassing both mesopores and macropores, is evident. The formation of the macropore structure is influenced by the biomass feedstock.

Table 6.13 Size of particles (materials used for cryogel synthesis) based on SEM visualisation and ImageJ analysis.

Material	Range of size
DOPMF	400 nm – 40 µm
Lignin	4 – 30 µm
Xanthan gum	0.3 – 0.6 cm
$H_3PW_{12}O_{40}$	80 – 1000 µm
N_b2O_5	60 – 180 µm
LXCC	10 nm – 180 µm

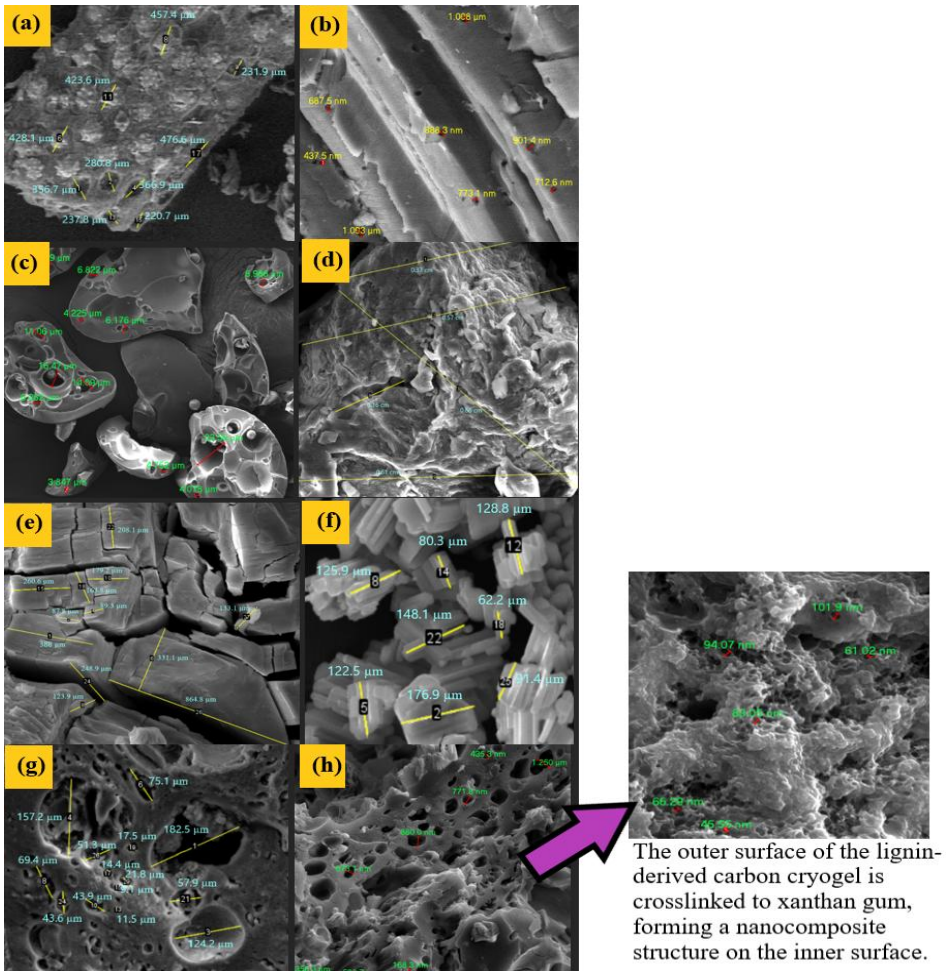

Figure 6.11 FESEM images for sizes of raw materials: (a) DOPMF at micro scale; (b) DOMF at nano scale; (c) lignin; (d) xanthan gum; catalysts for (e) $H_3PW_{12}O_{40}$ and (f) Nb_2O_5; and synthesised carbon cryogel at (g) micro-scale and (h) nanoscale.

Based on the FESEM analysis, the carbon cryogel exhibits irregular pores with variations in size, creating sites with different acidities, as depicted in **Figure 6.6** (in **Section 6.5.1**), showcasing weak, medium, and strong acid sites. To further understand the relationship between pore sizes, structures, and surface heterogeneity, EDX analysis was conducted to observe changes in single elements within the optimised carbon cryogel. This analysis provides insights into the distribution of acid sites and main precursors (**Table 6.14**), influencing the structure of the catalyst surface. The consistent carbon content post-calcination indicates that the chosen calcination temperature effectively preserves the main component and structure of the carbon cryogel. Meanwhile, the reduction in oxygen content post-calcination suggests the removal of non-carbon components, driven off as carbon dioxide or other volatile oxides. The lower oxygen content signifies the formation of a more porous structure.

Sample OPT2 achieves the optimum LA yield due to a homogeneous distribution of acid sites, as shown in **Figure 6.12**, with minimal impact from catalyst loss. In contrast, other samples, such as 2O8, experience an uneven distribution of acid sites, leading to leaching of phosphorus from $H_3PW_{12}O_{40}$ and niobium from Nb_2O_5. The leaching is attributed to calcination effects, where oversaturated of active components at high temperatures causes them to detach from the catalyst structure. Notably, the agglomeration of Nb at specific locations proves an exceptionally high peak of strong acid sites at 700 °C, as illustrated in **Figure 6.6**. The localised concentration of acidic components can exacerbate structural weaknesses, making the catalyst more susceptible to degradation during calcination, further promoting leaching. This leaching diminishes the activity of the acid sites and subsequently reduces the LA yield.

Therefore, maintaining a uniform distribution of acid sites is crucial for preserving catalyst integrity and achieving optimal performance.

Table 6.14 EDX analysis of elements present in carbon cryogels, with the total amount of acid catalyst integrated into all the carbon cryogel samples is 0.216 mmol. This total comprises both $H_3PW_{12}O_{40}$ and Nb_2O_5, indicating the overall density of active acidic components. Specific ratios of $H_3PW_{12}O_{40}$ to Nb_2O_5 for each sample are detailed in the footnotes.

Sample	**Element (%)**							
	C	**O**	**Na**	**K**	**P**	**W**	**Nb**	**S**
Lignin	53.48	34.10	7.02	–	–	–	–	5.40
Xanthan gum	50.16	46.98	1.94	0.54	–	–	–	–
DOPMF	56.94	41.20	–	0.20	–	–	–	–
$H_3PW_{12}O_{40}$	7.55	27.46	–	–	1.11	63.42	–	–
Nb_2O_5	9.27	26.49	–	–	–	–	64.24	–
2O1[a]	55.16	28.55	4.03	0.72	0.11	9.97	1.46	2.94
2O8[b]	50.91	19.54	4.07	0.78	0.28	19.31	1.52	1.03
2O11[a]	48.10	25.72	8.25	0.69	0.13	11.78	0.34	1.96
2O15[b]	46.73	23.48	5.54	0.94	0.29	22.68	0.81	1.32
2O21[c]	54.67	22.50	4.98	0.63	0.09	8.01	0.66	1.33
2O22[d]	52.45	22.06	1.92	0.58	0.32	14.12	0.81	1.49
OPT2[e]	53.88	24.41	3.64	0.76	0.44	18.90	5.31	0.49

[a]2:1

[b]4:1

[c]1:1

[d]5:1

[e]3.02:1

The impact of solvent exchange time on the surface area is noteworthy. Prolonged exposure to t-butanol can lead to shrinkage, causing contraction and saturation of pores. This physical blockage reduces the overall pore volume and surface area, thereby limiting the space available for reactants. Optimising solvent exchange time is crucial to prevent excessive leaching, preserve active sites, and maximise surface area. This is exemplified by the lower LA yield of sample 2O11 (9.4%). The relatively low surface area observed in some carbon

cryogel samples (**Table 6.11**) underscores the complexity of multiple determinants influencing surface catalysts. For instance, the lowest surface areas in samples 2O1 and 2O21 were due to insufficient or excessive solvent exchange periods combined with low calcination conditions and catalyst modification. Therefore, achieving optimal parameters during carbon cryogel synthesis is pivotal for improving surface area, reaching up to 57.41 $m^2 g^{-1}$, and creating the desired hierarchical porous structure necessary for catalytic activity in biomass conversion. Striking a balance ensures the ideal surface area is complemented by a sufficient acidic environment for optimal catalyst efficiency.

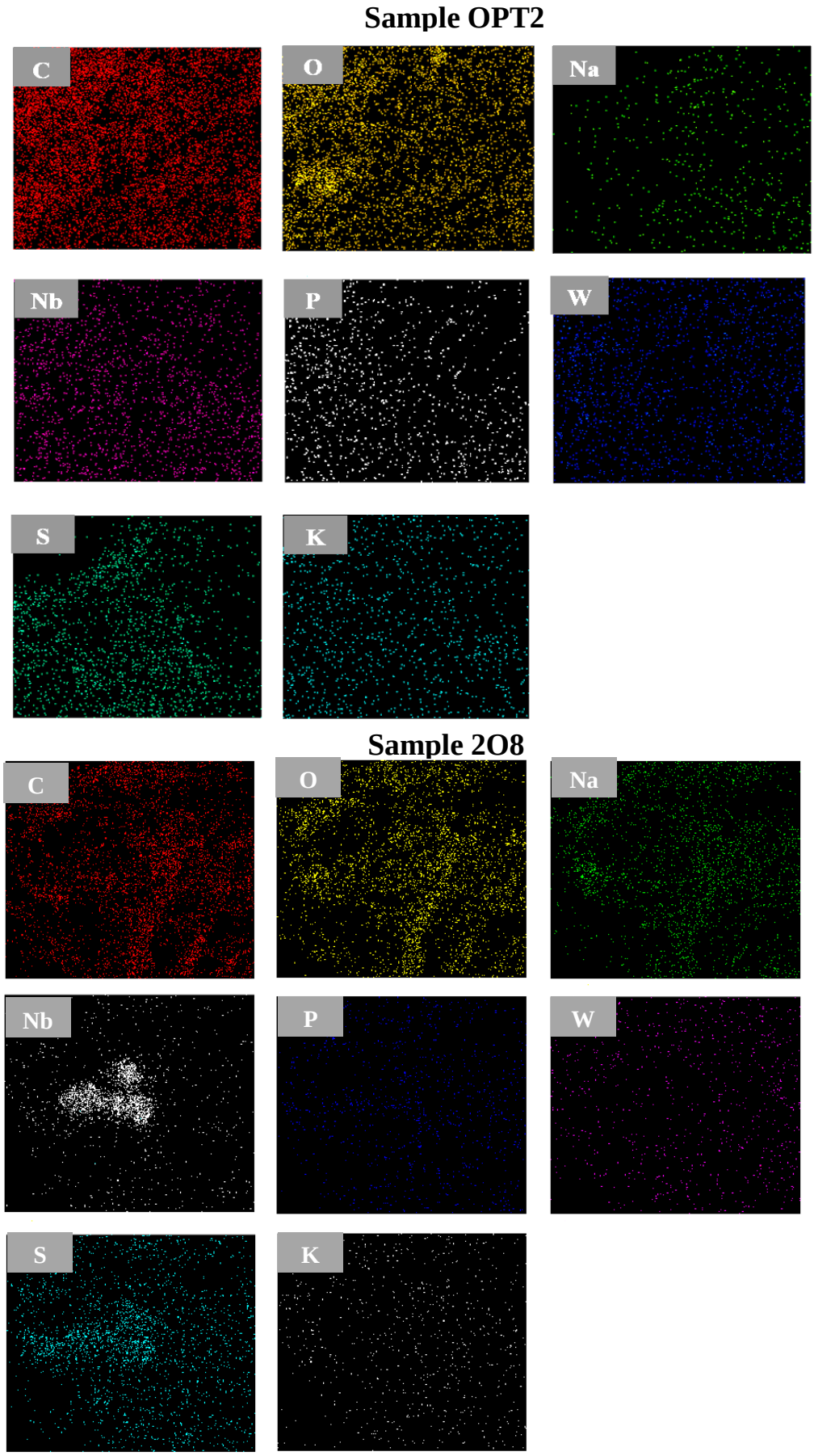

Figure 6.12 EDX mapping for distribution of elements within the carbon cryogel of OPT2 and 2O8 samples.

6.5.5 Functional groups

In **Figure 6.13**, the FTIR spectra illustrate the variations in functional groups as the carbon cryogel undergoes different preparation conditions, including changes in calcination temperature, duration, the ratio of Brønsted-Lowry to Lewis acids, and solvent exchange time. These functional groups can either enhance or hinder the catalytic activity within the carbon cryogel. Higher calcination temperatures lead to extensive removal of organic moieties, impurities, and templates within the carbon cryogel. This may transform functional groups, creating more active sites and increasing the LA yield, as observed in sample 2O8. At 400 °C, C–H peaks at 624 and 834 cm^{-1} shifted, indicating changes in the C–H functional groups. The shift is attributed to calcination, a process that promotes the formation of new chemical bonds within the composite material resulting from the interaction between $H_3PW_{12}O_{40}$, Nb_2O_5, and lignin polymers. This interaction directly impacts C–H bonding patterns.

The Nb–O bands in the Nb_2O_5 catalyst exhibit two intense and broad features centred around 640 and 990 cm^{-1} [565]. Meanwhile, the characteristic IR bands of $H_3PW_{12}O_{40}$ typically appear at 1082, 972 and 890 cm^{-1} [170]. These bands correspond to the asymmetric stretching vibrations of P–O, W = Ot and W–O–W within the primary Keggin structure [565]. The presence of these bands suggests the Keggin structure's stability even after its dispersion on Nb_2O_5 and lignin precursors. Notably, the synergistic effect of $H_3PW_{12}O_{40}$ and Nb_2O_5 results in a vibrational band at 1132 cm^{-1} [197], arising from the merging of the P–O band in $H_3PW_{12}O_{40}$ with the Nb–O band in Nb_2O_5 [553]. The intensity of

the band at 1132 cm^{-1} varies with the different ratios of $H_3PW_{12}O_{40}$ to Nb_2O_5 added to the carbon cryogel.

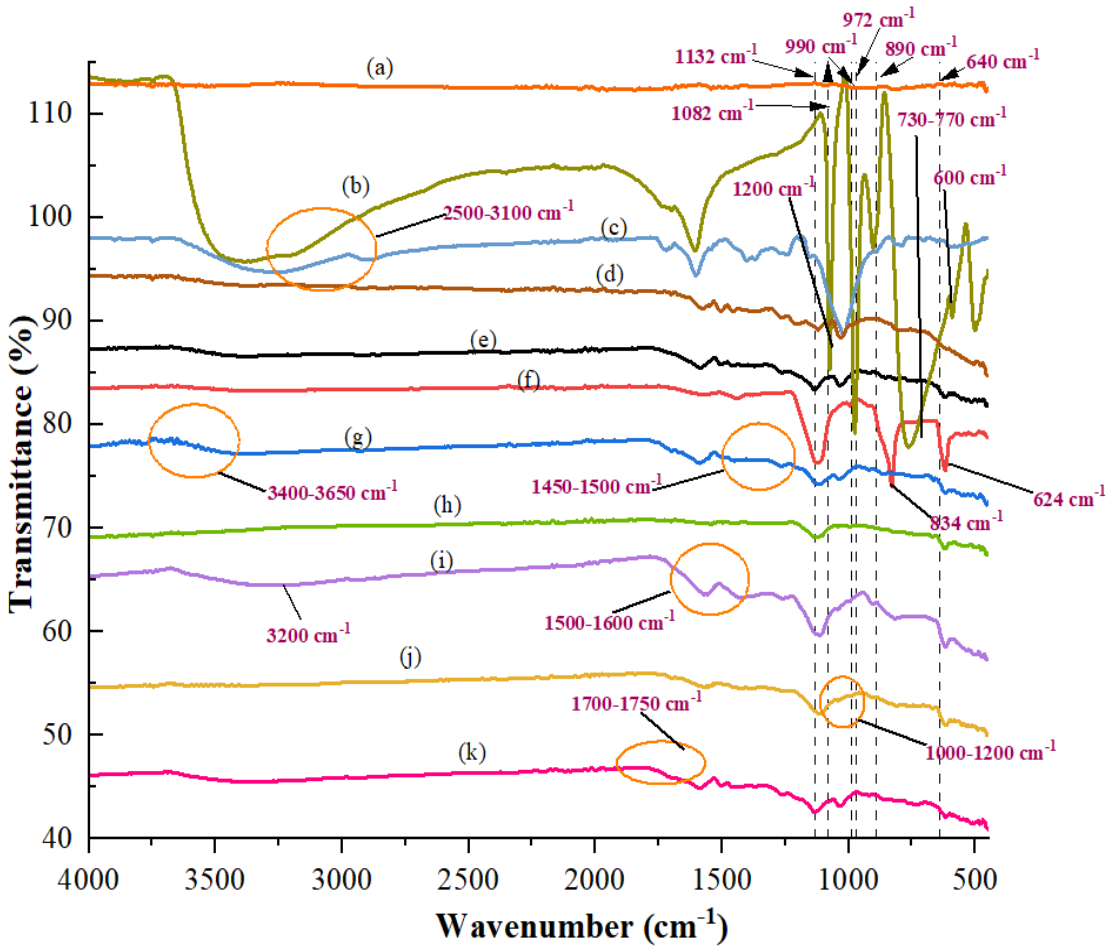

Figure 6.13 FTIR spectra for carbon cryogel samples and raw precursor materials: (a) Nb_2O_5; (b) $H_3PW_{12}O_{40}$; (c) xanthan gum; (d) lignin; (e) 2O1; (f) 2O8; (g) 2O11; (h) 2O15; (i) 2O21; (j) 2O22; and (k) OPT2.

Sample OPT2 produced the highest LA yield due to retention of strong aromatic rings at the optimal calcination temperature (336 °C), preventing deconstruction of the lignin-derived carbon cryogel. C–H stretching and vibrations at 1450–1500 cm^{-1} indicated the template preservation [254], while C=C stretching at 1500–1600 cm^{-1} suggested the presence of carbon-carbon double bonds. Compared to samples OPT2 and 2O8, other tested samples

displayed notable C=C stretching, likely due to incomplete combustion of organic precursors during calcination at 200 °C. These C=C bonds may form part of the carbon backbone structure in the form of conjugated systems, contributing to the overall stability and rigidity of the carbon structure. Within the cryogel context, the presence of C=C bonds suggests the retention of some original carbon-carbon double bonds from the precursor materials (lignin and xanthan gum).

The 1700–1750 cm^{-1} range showed broad peaks, indicating C=O bonds formed during crosslinking between lignin and xanthan gum [332]. These carbonyl groups impact the reactivity and surface chemistry of carbon materials. The duration of calcination influences functional group stability, with extended calcination altering groups and reducing catalytic activity. For example, sample 2O11, calcined at 200 °C for up to 60 min, showed reduced C–H (1450–1500 cm^{-1}) and C–O–C (1000–1200 cm^{-1}) stretching, resulting in a lower LA yield. Additionally, the presence of sulphonic acid functional groups ($–SO_3H$), originating from the alkaline lignin content used in the cryogel, is evident in the structure. This is observed through specific band spectra, including the S–O stretching vibration at around 1150 cm^{-1} [245] and S–O stretching at approximately 1050 cm^{-1} [24, 566–567].

O–H functional groups at 2500–3100 cm^{-1}, 3200 cm^{-1}, and 3400–3650 cm^{-1} suggest the presence of acidic, phenol, and alcohol groups, respectively, as detailed in the FTIR bands and assignments table (**Appendix 5**). The ratio of Brønsted-Lowry to Lewis acids influences these groups, as demonstrated by samples 2O8, 2O15, 2O22, and OPT2. The vibration of O–H groups is also affected by the duration of solvent exchange, which plays a crucial role in

preserving and making functional groups accessible. Prolonged solvent exchange, lasting 20 h, tends to remove more organic precursors and solvents, resulting in the development of larger pores. Conversely, a shorter exchange time may retain more materials, potentially leading to smaller pores. Optimal solvent exchange avoids the collapse of the porous structure and the leaching of active sites. Specifically, the XG spectrum exhibits two absorption peaks at 3431 cm^{-1} and 2922 cm^{-1}, corresponding to the stretching vibration of hydroxyl (–OH) groups and sp^3 hydrocarbon (C–H) groups, respectively [568–569]. The decrease in peak intensities at these bands suggests the elimination of O–H groups after calcination, resulting in the formation of a porous structure in the carbon cryogel templates [245]. According to Yamamoto *et* al. [386], the pore surface of the carbon cryogel is expected to become more hydrophobic, with the degree of hydrophobicity intensifying as the calcination temperature rises. This heightened hydrophobicity proves advantageous, particularly in restraining the direct conversion of glucose to LA.

6.6 Parametric studies on reaction conditions for microwave conversion to LA

In the final stage of optimisation, a series of 30 experiments (refer to **Table 6.15**) were conducted to evaluate the performance of the carbon cryogel under various conditions, including microwave power, catalyst and biomass loading, and the GVL-to-water ratio. Samples 25–30 were deliberately replicated, and the minor discrepancies in the experimental yield, ranging from 0.20 to 2.32, underscored the reliability and consistency of the results, thereby validating the optimised conditions.

This conclusive optimisation phase becomes imperative to methodically enhance the efficiency of the overall catalytic system. The optimisation of reaction conditions extends beyond the laboratory scale, encompassing considerations of resource utilisation, including solvent medium, catalyst, biomass, and energy consumption. Identifying conditions that yield high LA products while minimising resource consumption holds both economic and environmental significance.

In the domain of numerical optimisation employing RSM, the highest LA yield (~22.1%) was attained with a microwave power of 388 W, catalyst loading of 0.131 g, biomass loading of 0.074 g, and a GVL-to-water ratio of 8.414. The model's precision was affirmed through triplicate data (see **Table 6.16**), with the error falling below 5%. Across the experiments, a 22.49% LA yield was achieved, accompanied by a standard deviation of 1.29. **Eq. 6.3** outlines the proposed model for LA yield in terms of coded factors.

$$\text{Yield} = 21.90 - 1.88A - 0.53B + 0.67C + 1.16D - 0.71AB + 0.73AC - 0.07AD - 0.70BC + 0.17BD - 0.24CD - 2.03A^2 - 1.09B^2 - 1.42C^2 - 2.72D^2 \quad (6.3)$$

Table 6.15 Parametric studies for reaction conditions affecting LA yield.

Sample (Run)	Point type	Parameters				Response
		A	**B**	**C**	**D**	**Y_i**
		Microwave power (W)	**Catalyst loading (g)**	**Biomass loading (g)**	**GVL-to-water ratio**	**LA yield (%)**
3O1	Factorial	300(-1)	0.08(-1)	0.04(-1)	6.00(-1)	14.35
3O2	Factorial	600(+1)	0.08(-1)	0.04(-1)	6.00(-1)	10.24
3O3	Factorial	300(-1)	0.20(+1)	0.04(-1)	6.00(-1)	16.27
3O4	Factorial	600(+1)	0.20(+1)	0.04(-1)	6.00(-1)	9.24
3O5	Factorial	300(-1)	0.08(-1)	0.10(+1)	6.00(-1)	16.29
3O6	Factorial	600(+1)	0.08(-1)	0.10(+1)	6.00(-1)	15.35
3O7	Factorial	300(-1)	0.20(+1)	0.10(+1)	6.00(-1)	15.23
3O8	Factorial	600(+1)	0.20(+1)	0.10(+1)	6.00(-1)	10.27
3O9	Factorial	300(-1)	0.08(-1)	0.04(-1)	10.00(+1)	17.14
3O10	Factorial	600(+1)	0.08(-1)	0.04(-1)	10.00(+1)	13.87
3O11	Factorial	300(-1)	0.20(+1)	0.04(-1)	10.00(+1)	20.42
3O12	Factorial	600(+1)	0.20(+1)	0.04(-1)	10.00(+1)	11.42
3O13	Factorial	300(-1)	0.08(-1)	0.10(+1)	10.00(+1)	19.15
3O14	Factorial	600(+1)	0.08(-1)	0.10(+1)	10.00(+1)	15.55
3O15	Factorial	300(-1)	0.20(+1)	0.10(+1)	10.00(+1)	16.79
3O16	Factorial	600(+1)	0.20(+1)	0.10(+1)	10.00(+1)	14.53
3O17	Axial	150(-∝)	0.14(0)	0.07(0)	8.00(0)	15.99
3O18	Axial	750(+∝)	0.14(0)	0.07(0)	8.00(0)	11.03
3O19	Axial	450(0)	0.02(-∝)	0.07(0)	8.00(0)	18.54
3O20	Axial	450(0)	0.26(+∝)	0.07(0)	8.00(0)	16.04
3O21	Axial	450(0)	0.14(0)	0.01(-∝)	8.00(0)	14.53
3O22	Axial	450(0)	0.14(0)	0.13(+∝)	8.00(0)	17.44
3O23	Axial	450(0)	0.14(0)	0.07(0)	4.00(-∝)	9.21
3O24	Axial	450(0)	0.14(0)	0.07(0)	12.00(+∝)	12.29
3O25	Centre	450(0)	0.14(0)	0.07(0)	8.00(0)	22.24
3O26	Centre	450(0)	0.14(0)	0.07(0)	8.00(0)	20.17
3O27	Centre	450(0)	0.14(0)	0.07(0)	8.00(0)	21.96
3O28	Centre	450(0)	0.14(0)	0.07(0)	8.00(0)	20.53
3O29	Centre	450(0)	0.14(0)	0.07(0)	8.00(0)	21.79
3O30	Centre	450(0)	0.14(0)	0.07(0)	8.00(0)	22.19

Table 6.16 Optimisation of reaction conditions and validation for LA yields.

Experiment	Microwave power (W)	Catalyst loading (g)	Biomass loading (g)	GVL-to-water	Response (%)	Error (%)
					LA yield	
CCD	388	0.131	0.074	8.414	22.49	
Validation (Trial 1)	388	0.131	0.074	8.414	22.28	
Validation (Trial 2)	388	0.131	0.074	8.414	22.21	
Validation (Trial 3)	388	0.131	0.074	8.414	21.91	
Validation[a]	388	0.131	0.074	8.414	22.13	1.60

[a]Mean for triplicate data.

6.6.1 RSM contour plots

Figure 6.14 illustrates that all 3D surface plots display a curved shape while holding two variables constant. This curvature suggests interactions or higher-order effects between the factors, hinting that a linear model may inadequately capture the relationship. It implies that the impact of the factors on the response is not constant and changes with variations in factor levels. There might be a combined effect of both factors that differs from the sum of their individual effects, a hypothesis to be further validated through statistical analysis in **Section 6.6.2**.

Each 3D surface plot in **Figure 6.14** reveals a distinct pattern in response to its RSM. In **Figures 6.14a** and **6.14b**, the contour indicates that changes in catalyst or biomass loading, with increasing microwave power, would cause a decrease in LA yield. Meanwhile, the contour plot in **Figure 6.14c** shows a slightly different pattern, where the contour colours for both sides of the factors (microwave power and GVL-to-water ratio) contrast with each other. This signifies that changes occurring in one of them would not affect another factor to influence the LA yield. Given the complexity of the catalytic system with its

components, it is crucial to verify the interaction between catalyst loading and biomass loading. Based on **Figure 6.14d**, both factors move in the same direction, meaning any increase in biomass loading and catalyst loading simultaneously affects the yield of LA. However, **Figure 6.14e** and **6.14f** indicate that the high yields of LA are concentrated at the centre of the curvature, but the directions of both factors, either between factor B and D or between factor C and D, move oppositely.

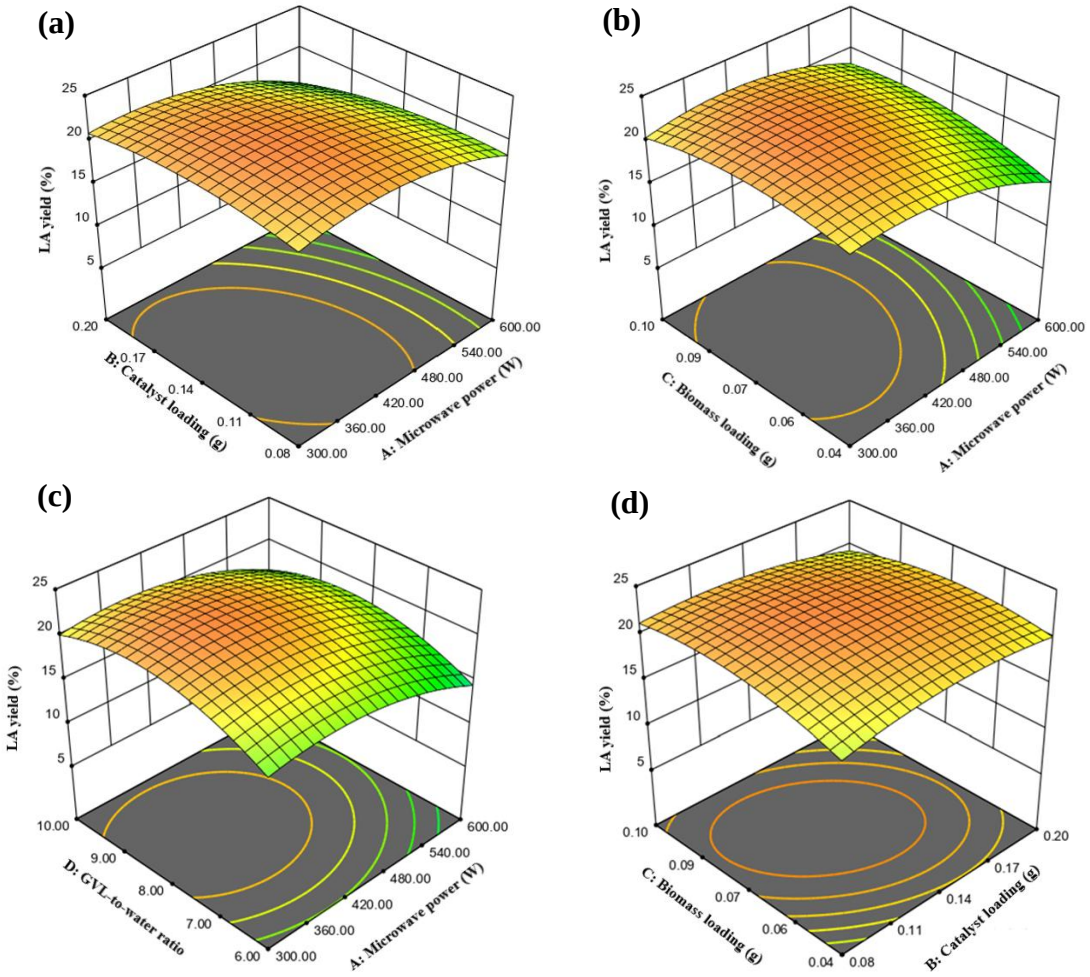

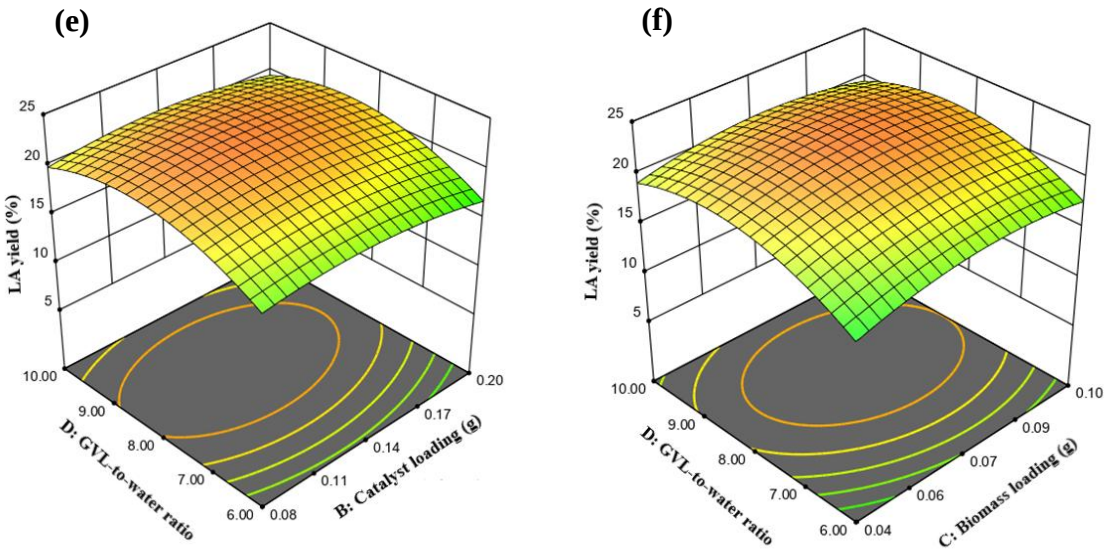

Figure 6.14 RSM surface plots for different interactions between (a) microwave power and catalyst loading; (b) microwave power and biomass loading; (c) microwave power and ratio of GVL to water; (d) catalyst loading and biomass loading; (e) catalyst loading and ratio of GVL to water; and (f) biomass loading to ratio of GVL to water.

6.6.2 RSM statistical analysis

The proposed model exhibits high accuracy, with an R^2 value of 0.95, signifying that 95% of the variation in LA yield can be ascribed to the process variables explained by the model. The coefficient of variation, at 8.00%, further underscored the reliability of the responses within the range of process conditions. The adjusted R^2 (0.90) and predicted R^2 (0.79) showcased a commendable agreement between the experimental and predicted LA yield, fortifying the model's reliability.

ANOVA analyses were conducted for each response model (refer to **Table 6.17**) to evaluate the significance of interactions between process variables and individual factors. The linear and quadratic terms exerted substantial influence on LA yield. Specifically, the quadratic terms showed the

most crucial variables affecting LA yield compared to linear terms and interaction terms, boasting high F-values up to 122.90, with a small *p*-value of <0.0001. This proves that the relationship between the factors and the response is not strictly linear. The significant quadratic terms represent the curvature or nonlinearity in the relationship, indicating that the effect of a factor on the response changes as the level of the factor varies. Quadratic terms are especially useful to explain an important factor like catalyst loading that did not represent any changes in concentration towards LA yield when tested individually, implying that changing the catalyst loading alone does not have a strong, direct impact on the LA yield. Meanwhile, it became significant when involving quadratic terms, signifying the relationship between catalyst loading and LA yield is not a simple straight line, and the linear terms were not dominant factor affecting the final yield. The model suggested that there is a more complex relationship between catalyst loading and the LA yield where too little or too much catalyst loading is less effective than a moderate amount. Moreover, the interaction terms that showcased a significant combined effect of two factors (catalyst loading and other factors) implied that the influence of catalyst loading is not independent of other factors. So, the effect of changing catalyst loading depends on the levels of microwave power and biomass loading, showing any synergistic or antagonistic effects.

The Model F-value of 19.98 implied the model's significance, with less than a 0.0001% chance that the F-value could occur due to noise. The lack of fit F-value of 0.76 implied that the lack of fit was not significant relative to pure error, affirming a good fit of the proposed model for predicting LA yield. There was a 67.00% probability that a lack of fit F-value of this magnitude could occur

due to noise. The adequate precision, with a signal-to-noise ratio of 14.52, suggests that the ratio is greater than 4, which is desirable for navigating the design space suggested by the CCD approach.

Based on **Table 6.17**, there are three interaction terms that were significantly different: A and B, A and C, and B and C. While factor D representing GVL-to-water ratio was only significant for linear and quadratic terms. This shows the direct, linear effect of changing the GVL-to-water ratio on the LA yield. As the GVL-to-water ratio increased or decreased, the LA yield changes in a predictable linear manner. The significant quadratic term of the GVL-to-water ratio suggested that there might be an optimal GVL-to-water ratio associated with maximum or minimum values of the LA yield. The lack of significance in the interaction terms involving the GVL-to-water ratio suggests that the influence of this ratio is relatively independent of other factors, whereby its changes did not interact strongly with changes in other factors to impact the LA yield differently (see contour plots in **Figure 6.14**).

Table 6.17 Statistical analysis for the optimisation on reaction conditions.

Source	Sum of Squares	Degree of freedom	Mean Square	F-value	*p*-value	Remark
Model	463.42	14	33.10	19.98	<0.0001	Significant
A-Microwave power	84.74	1	84.74	51.16	<0.0001	
B-Catalyst loading	6.79	1	6.79	4.10	0.0611	
C-Biomass loading	10.68	1	10.68	6.45	0.0227	
D-GVL to water ratio	32.10	1	32.10	19.38	0.0005	
AB	8.03	1	8.03	4.85	0.0438	
AC	8.49	1	8.49	5.13	0.0388	
AD	0.07	1	0.07	0.04	0.8362	
BC	7.94	1	7.94	4.80	0.0447	
BD	0.44	1	0.44	0.27	0.6133	
CD	0.94	1	0.94	0.57	0.4631	
A^2	113.48	1	113.48	68.51	<0.0001	
B^2	32.55	1	32.55	19.65	0.0005	
C^2	54.99	1	54.99	33.20	<0.0001	
D^2	203.57	1	203.57	122.90	<0.0001	
Residual	24.85	15	1.66			
Lack of Fit	14.98	10	1.50	0.76	0.67	Not significant
Pure Error	9.87	5	1.97			
Cor Total	488.27	29				

The relationship between the mean and median in a boxplot provides valuable insights into the distribution of the data. In **Figure 6.15**, variations in LA yield were observed as individual factors were tested at five different levels. In most cases, the mean values were consistently lower than the median lines. This discrepancy indicates a left-skewed distribution, suggesting that a few low values are influencing the median to shift leftward. The left (lower) tail of the distribution appeared longer and fatter, with the box shifted to the right. This configuration indicates that most of the data is concentrated on the right side, causing the median to be closer to the upper quartile. Consequently, for each factor, including microwave power, catalyst loading, biomass loading, and

GVL-to-water ratio, the median values (e.g., 450 W, 0.14 g, 0.07 g, and 8.00, respectively) corresponded to the highest distributions of LA yields.

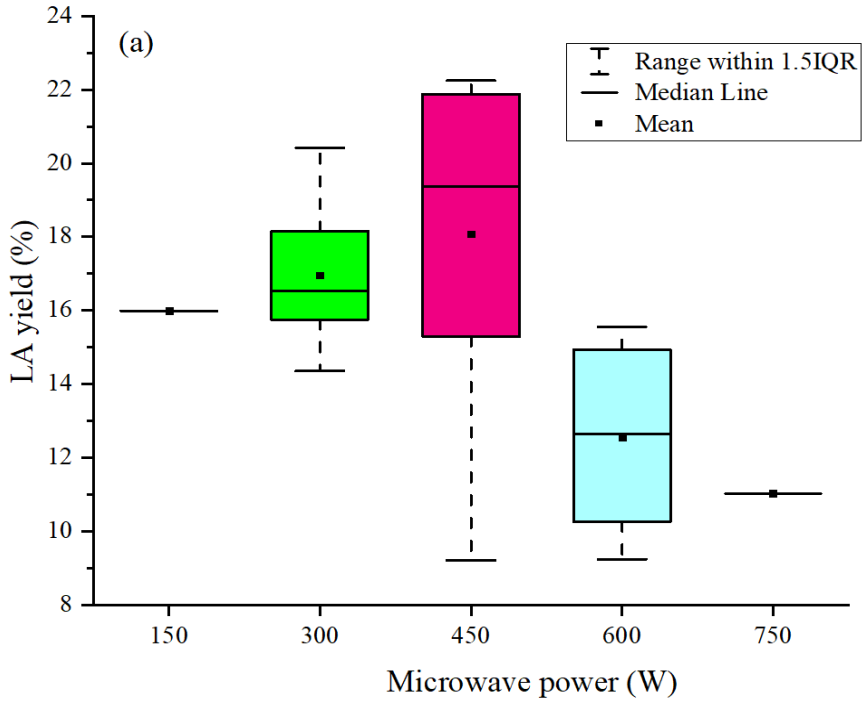

.

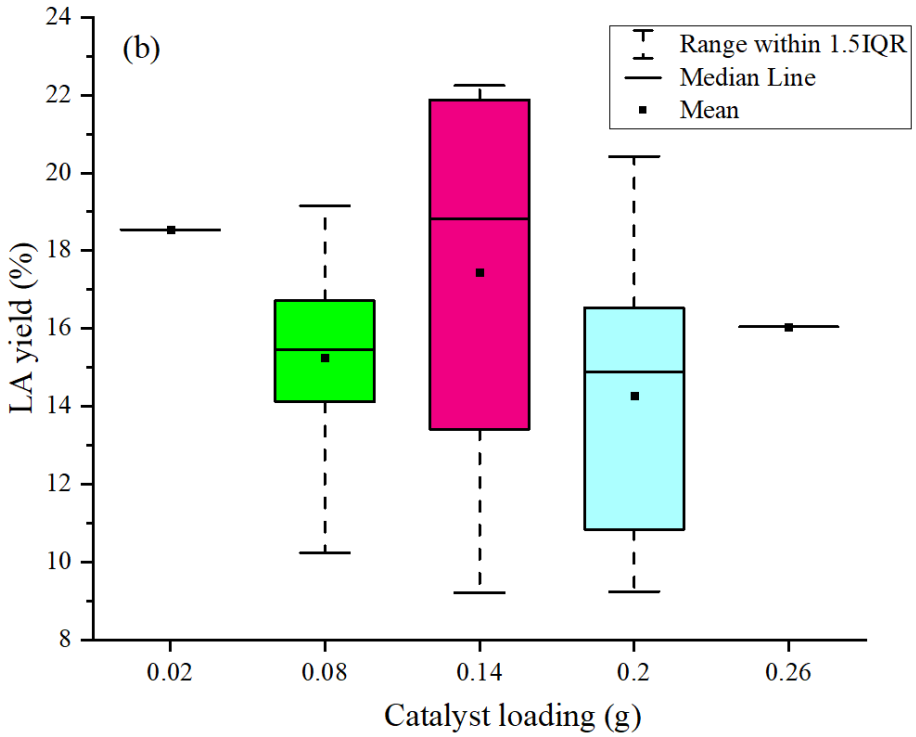

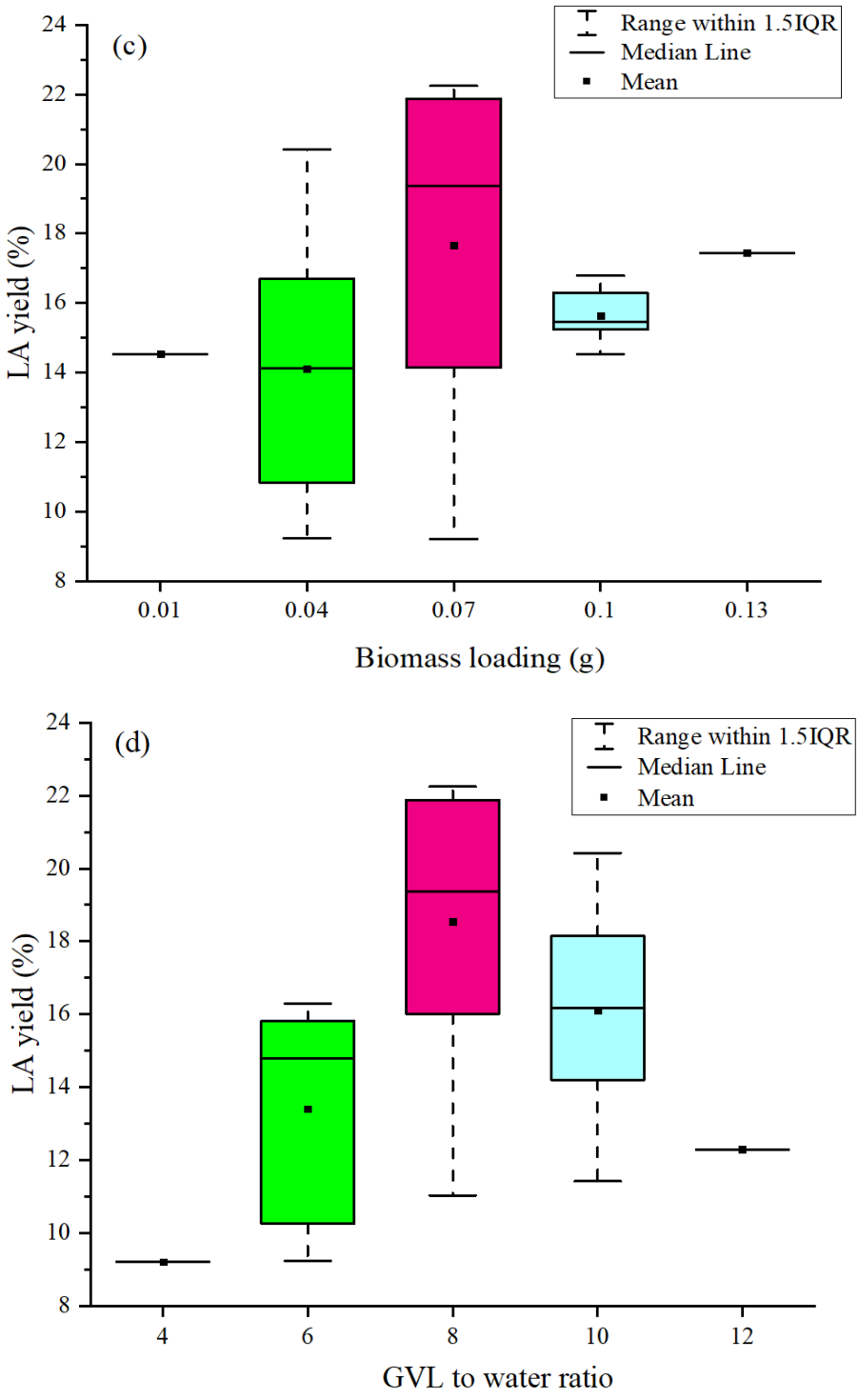

Figure 6.15 Box plots for each factor that influence the LA yield during reaction conditions: (a) microwave power; (b) catalyst loading; (c) biomass loading and (d) GVL to water ratio.

6.6.3 Factors affecting efficient reaction conditions

In this study, the LA yield pattern, as shown in **Table 6.15** in **Section 6.6**, was lower at a microwave power of 600 W compared to 300 W, while keeping other conditions constant (catalyst loading, biomass loading, and GVL-to-water ratio). This finding indicates that microwave power is a crucial factor in determining chemical reactivity, as it closely correlates with the reaction temperature. Both temperature and time significantly affect reaction yield and conversion [83, 540]. Higher temperatures, associated with increased microwave power, enhance catalytic activity, leading to improved yield and conversion. According to Zainol *et* al., the yield and conversion increase gradually as the temperature rises from 78 to 150°C, but they begin to decrease beyond this point [245].

In this study, the reaction time was minimised to 2 min, with the assumption that other influential factors were at play. The decision for a short reaction time is based on the premise that fast reactions can occur rapidly, assuming a high rate of catalytic activity within a short duration [525]. It is important to note that the solvent media temperature should not exceed 170 °C, as excessively acidic conditions can lead to reduced yield. Excessive temperature or high microwave power may trigger the formation of intermediates rather than the desired products, especially with high catalyst loading, as observed in sample 3O4. This sample, with a catalyst loading of 0.2 g and microwave power of 600 W, produced a 9.2% LA yield. The low yield is attributed to the aggregation or clustering of catalyst particles, which leads to uneven heating and localised overheating.

This study found that a lower ratio of catalyst to biomass, such as 0.8 and 0.28, resulted in slightly higher LA yields of 16.3% and 18.5%, respectively. In

contrast, higher ratios, equivalent to 0.20 g and 0.04 g of catalyst and biomass respectively, produced LA yields of less than 14%. The study suggests that higher catalyst loading (0.20 g) can lead to oversaturation of active sites when the temperature or microwave power is increased up to approximately 210 °C or 600 W. This oversaturation, due to the strong acidity of the calcined cryogel, can result in the blocking of active sites by the product. This blockage could subsequently reduce yield and conversion as the reaction slowly reaches equilibrium, suggesting that LA selectivity may be influenced by side reactions. These findings highlight the significant role of catalyst loading in enhancing selectivity. This is supported by Zainol *et* al. [245], who reported that calcined cryogel enhanced product yield due to esterification reactions at temperatures up to 150 °C. Therefore, the chosen microwave power setting should be compatible with the catalyst loading to optimise LA yield.

This study observed that an increase in microwave power (600 W) and biomass loading (0.10 g) resulted in a lower LA yield of less than 15.5%. This decrease in yield could be attributed to biomass particle clustering, similar to the effect observed with catalyst loading. Such clustering can create denser regions, potentially causing mass transfer limitations and reducing the available surface area for catalytic interaction [570–571]. The interplay of microwave power and biomass loading appears to influence mass transfer within the reaction mixture, extending beyond mere heating effects. A balanced biomass loading can facilitate favourable mass transport conditions, thereby positively impacting LA production. While higher microwave power can enhance synergy with catalyst and biomass loading, the trade-off with increased energy consumption necessitates careful consideration. Striking a balance is crucial, where the

benefits of elevated energy input are justified by a significant improvement in LA yield. Lu *et* al. observed a significant influence of substrate concentration on LA yield. As the substrate concentration increased, the LA yield exhibited a gradual decline from 87.7% to 45.9% [540]. This trend suggests that elevated substrate concentrations may promote side reactions, leading to a reduction in LA yield. These insights underscore the importance of carefully managing microwave power, biomass loading, and substrate concentration to optimise LA yield.

The solvent composition significantly influences product distribution and the degradation process in catalytic dehydration reactions. In the context of cellulose conversion using carbon cryogel, the impact of varying GVL additions was evident. As the GVL-to-water ratio increased from 4 to 8 (**Table 6.17**), the LA yield consistently increased from 14.4% to 21.9%, with a catalyst to biomass loading at 2 and microwave power ranging from 300 to 450 W. However, the yield slightly decreased when the GVL-to-water ratio reached 10. This observation aligns with the findings of Lu *et* al. [540], where reducing the GVL addition to 85% resulted in increased LA yields (87.7%) via silicotungstic acid (HSiW), indicating a promoting effect of water on selectivity. A higher GVL-to-water ratio is crucial due to GVL's higher boiling point than water, contributing to better temperature control and stability of reaction intermediates. Lower GVL addition can limit reactant accessibility to adsorb on the catalyst site [572], affecting cellulose solubility for hydrolysis and creating a less conducive environment for inhibiting byproduct formation.

Efficiency is evident in the biphasic system compared to other solvents. Liu *et* al. demonstrated that the water–MIBK biphasic system efficiently

separates LA [83], minimising side reactions by obtaining 1.6% humins and enhancing the LA yield. This aligns with Lu's findings [540], supporting the idea that the biphasic system minimises side reactions and improves product yield compared to a single-phase system. Sun *et* al. also highlighted solvent effects across different polarities [187], where strongly polar solvents, such as DMSO, and specific solvent-to-water ratios, at least 8, achieved higher LA yields, reaching ~70% through glucose conversion. The study noted the benefits of polar solvents in stabilising HMF [573] and favoured THF for HMF production with minimal LA formation [574].

6.7 Concluding remarks

The study utilised RSM with a CCD approach to optimise the hydrogel precursors and produce a stable carbon cryogel under optimal reaction conditions. Key parameters included the ratios of water to lignin (W/L), xanthan gum to lignin (X/L), and catalyst to lignin (C/L). The maximum LA yield was 18.4% at W/L, X/L, and C/L ratios of 2.14, 0.40, and 0.20, respectively. The 3D surface contour plots indicated that the C/L ratio had a stronger influence on the LA yield than the other ratios, with significant interactions between the C/L ratio and the others. As the C/L ratio increased, the pH value decreased, allowing the protonation of carboxylic acid and phenolic hydroxyl groups in the lignin molecules. This led to a more polar structure and increased solubility of lignin in the gel mixture.

The second stage of optimisation revealed that the performance of the carbon cryogel varied based on factors such as the ratio of $H_3PW_{12}O_{40}$ to Nb_2O_5, calcination time and temperature, and solvent exchange time. The maximum LA

yield of 20.1% was achieved under specific settings of these factors. The optimised sample exhibited a higher proportion of medium acid sites to strong acid sites compared to other samples, resulting in a higher LA yield. Excessively high calcination temperatures reduced the presence of crucial medium acid sites. The carbon cryogel, incorporating $H_3PW_{12}O_{40}$ and Nb_2O_5, is a key source of strong acid sites during biomass conversion to LA. However, an excess of strong acid sites can lead to undesired side reactions, reducing the overall LA yield.

The study found that the surface area (57.41 $m^2\ g^{-1}$) and porosity (0.13 $cm^3\ g^{-1}$) of the optimised cryogel were comparatively lower than those of some catalysts in other research. However, mesopores dominated the pore size distribution. The design of the carbon cryogel aims to enhance the mesoporous surface area, thereby improving transport within the catalyst pores. This optimisation is particularly relevant when cellulose undergoes hydrolysis into glucose, facilitating the subsequent decomposition of glucose into LA.

Interestingly, the optimised carbon cryogel showed a homogeneous distribution of acid sites, suggesting minimal impact from catalyst loss after the calcination and solvent exchange period. Higher calcination temperatures led to the extensive removal of organic moieties, impurities, and templates within the carbon cryogel, transforming functional groups and resulting in more active sites and increased LA yield. Notably, the synergistic effect of $H_3PW_{12}O_{40}$ and Nb_2O_5 resulted in a vibrational band at 1132 cm^{-1}, arising from the merging of the P–O band in $H_3PW_{12}O_{40}$ with the Nb–O band in Nb_2O_5. This vibrational band supports the synergy factor achieved by the working carbon cryogel, with the highest value obtained by the optimised sample at 2.15.

The final stage of optimisation evaluated the performance of the carbon cryogel under diverse conditions, including microwave power, catalyst and biomass loading, and the GVL-to-water ratio. The highest LA yield of approximately 22.1% was attained with a microwave power of 388 W, catalyst loading of 0.131 g, biomass loading of 0.074 g, and a GVL-to-water ratio of 8.414. The study determined that factors such as microwave power, catalyst loading, biomass loading, substrate concentration, and solvent composition influence the yield of LA from biomass.

In summary, this study highlights the critical importance of balancing acidity, surface characteristics, and porosity to optimise the properties of carbon cryogels. Establishing ideal reaction conditions is vital to mitigate potential shortcomings within the overall catalytic system. These optimised properties lay the groundwork for the next phase of the study, which will focus on the kinetic and thermodynamic evaluation of the catalytic system. Notably, while the optimisation model did not explicitly incorporate microwave reaction time, understanding how these optimised cryogel attributes interact with both kinetics and thermodynamics in the next chapter is essential. As microwave power increases, the reactivity of carbon cryogels is expected to be influenced by the extended reaction time. Higher microwave power often leads to increased thermal energy, enhancing the mobility of reactants and potentially accelerating reaction rates. This interaction can significantly affect the cryogel's structural and chemical properties, influencing not only the speed at which reactions occur but also the energy profiles associated with the production process.

Chapter 7

Kinetic and Thermodynamic Studies on the Conversion of Oil Palm Mesocarp Fibre to Levulinic Acid Using Lignin-Derived Cryogel Incoporated with $H_3PW_{12}O_{40}$-Nb_2O_5

7.1 Introduction

The previous chapter highlighted the optimisation of the carbon cryogel formulation and properties, emphasising the significance of balancing acidity, surface characteristics, and porosity to achieve enhanced LA yields. These optimised properties serve as a foundation for the next stage of the study, where the focus shifts to investigating the kinetic and thermodynamic aspects of the catalytic system. Exploring the interplay of these factors will provide a deeper understanding of the cryogel's performance under microwave irradiation. By examining how variations in microwave power and reaction time influence LA production efficiency, this comprehensive evaluation is critical for assessing the viability and effectiveness of the carbon cryogel in real-world applications.

Understanding the kinetic and thermodynamic properties will illuminate how the cryogel's structural and chemical characteristics respond to increased thermal energy and enhanced reactant mobility. This will influence not only the speed of reactions but also the energy profiles and equilibrium states associated with the production process [575], ensuring the successful application of the optimised carbon cryogel in biomass conversion to LA.

Microwave irradiation has emerged as a powerful tool in catalysis due to its ability to penetrate deep into cellulose layers [576]. It can disrupt the crystal

structure and enhance the interaction between carbon cryogel-incorporated $H_3PW_{12}O_{40}$-Nb_2O_5 catalysts and the solid substrate, expediting the hydrolysis process. This is attributed to the volumetric and selective heating capabilities of microwaves, which allow for rapid and efficient heating of the catalytic system [577]. Microwave irradiation significantly impacts the kinetics of catalytic reactions, enhancing catalyst activity and increasing reaction rates [576]. This is because polar reactant molecules under microwave irradiation rotate faster and enter the transition state more rapidly than in conventional heating systems [576].

From a thermodynamic perspective, microwave irradiation can influence the energy profiles of reactions. The rapid and selective heating provided by microwaves can decrease activation energy, making reactions more thermodynamically favourable [578]. Additionally, microwave heating can lead to variations in kinetic parameters, such as reaction rate constant, activation energy, frequency factor, and reaction order [579]. The efficiency of microwave irradiation in catalytic systems is evident in its energy-saving potential. The volumetric heating of materials by microwaves requires a relatively short processing time compared to conventional heating, leading to energy savings [577]. Furthermore, the selective heating of catalysts enhances catalytic performance, making the process more efficient [401].

Several studies have demonstrated the effectiveness of microwave irradiation in catalytic systems. For instance, the greatest impact on LA yield was observed when the synergistic effect of H_2SO_4 and $CrCl_3$ was analysed, showing clear influences on reaction kinetics due to variations in reaction driving force and resistance under microwave irradiation [419]. Another study on the

valorisation of rice straw revealed that microwave heating led to a decrease of 40–150 kJ mol^{-1} in activation energy at the end of the conversion process compared with conventional pyrolysis [580].

This chapter provides a comprehensive examination of the kinetic factors governing the catalytic conversion of biomass into LA using carbon cryogel-incorporated $H_3PW_{12}O_{40}$-Nb_2O_5 catalysts. Understanding reaction kinetics is vital as it offers insights into the speed of cellulose hydrolysis to glucose and glucose decomposition to LA, enhancing yields and ensuring the viability of large-scale applications. The carbon cryogel, enriched with thermally stable acid catalysts ($H_3PW_{12}O_{40}$-Nb_2O_5), facilitates the evaluation of the rate at which reactants are consumed and products are generated. Beyond the kinetic model, this study also delves into thermodynamic considerations, quantifying data to calculate the Gibbs free energy (ΔG). This parameter is crucial in determining the spontaneity of the chemical reaction involved in the one-pot microwave irradiation process used to convert oil palm mesocarp fibre into LA.

Understanding and predicting system behaviour is of utmost importance. Analysing thermodynamic quantities such as enthalpy (ΔH) and entropy (ΔS) provides insights into a system's equilibrium state. This is essential for enhancing the feasibility of chemical reactions to achieve desired outcomes. Such understanding not only maximises efficiency but also minimises energy consumption and reduces costs, making the process more sustainable and economically viable.

7.2 Effect of microwave treatment on cellulose hydrolysis

This section explores the impact of varying microwave powers, which correspond to different temperatures, on the process of converting cellulose into sugar. As depicted in **Figure 7.1**, the conversion of cellulose was initially low at a microwave power of 100 W, equivalent to 110 °C, with a conversion rate of approximately 2.8% in 2 min. However, when the temperature rose to 150 °C (equivalent to a microwave power of 300 W), the conversion rate significantly increased to around 41.1%. This substantial increase suggests that the carbon cryogel-$H_3PW_{12}O_{40}$-Nb_2O_5 catalyst, due to its strong acidity, effectively catalyses the hydrolysis of cellulose into oligosaccharides, such as sugars.

As the conversion of cellulose increased with the rise in reaction temperature from 110 to 150 °C, it indicates that the cellulose partially dissolves in water, leading to the formation of long-chain oligomers. The solubilised cellulose chains are adsorbed onto the carbon cryogel through hydrogen bonds formed between the hydroxyl groups (–OH) of cellulose and the highly electronegative groups (O atoms) of the carbon cryogel. These chains are then hydrolysed into oligosaccharides by the adjacent H^+ ions from $H_3PW_{12}O_{40}$, which can enter the mesopores of the carbon cryogel and undergo further hydrolysis to form glucose. Consequently, the yield of glucose increased almost linearly to 11.6% at 300 W.

The influence of microwave power is significant in driving the carbon cryogel catalyst in the hydrolysis of cellulose, enhancing glucose yields and selectivity (up to 21% and 75% respectively), as depicted in **Figure 7.1**. This is in comparison to conventionally heated non-catalytic processes, as confirmed by Fan *et* al. [41]. This is due to the activation of the amorphous region of cellulose

at significantly lower temperatures than possible under conventional conditions. However, the glucose yield in this study was slightly lower than the 21% achieved in another study [41]. This was correlated with its high selectivity of 94.8% at 100 W, which substantially decreased to 34.2% at 300 W within a few seconds. This suggests that the strong acidity can further dehydrate glucose into other degraded products such as fructose, HMF and LA as the reaction time increases.

Figure 7.1 clearly shows that the effect of microwave power is tuneable, as the hydrolysis of cellulose to glucose was very fast in the first seconds of reaction times, while the glucose simultaneously decomposes rapidly to secondary products at longer times. This discrepancy may be attributed to the efficiency of the carbon cryogel, which is expected to contain a sulphonic acid (SO_3H) functional group based on prior elemental analysis in **Chapter 6**. This group acts as a co-catalyst, doubling the action of the catalytic system, thereby facilitating the conversion process while minimising energy consumption under 2 min of reaction. This finding is comparable to the work of Shen *et* al., who achieved a 10% yield of glucose using a carbon-based catalyst derived from sucralose under reaction conditions of 140 °C for 15 h of hydrothermal treatment [34].

The type of cellulose, which is derived from biomass, can influence its hydrolysis due to the varying degrees of crystallinity it exhibits. In this study, a slightly higher rate of cellulose conversion, reaching 41% at 300 W can be attributed to a high ratio of the amorphous region to the crystalline region (66% to 34% respectively) in the cellulose derived from biomass. This finding aligns with the results obtained in the DSC curve (**Figure 4.6b**) for the cellulosic

structure treated under microwave-GVL reaction (**Chapter 4, Section 4.5.1**). The curve presents only small peaks at lower temperatures (130–150 °C), indicating that the amorphous components degraded to sugars under this reaction condition at 300 W (150 °C). The crystalline structure was not involved throughout the process, as major structural changes in this region only occur well above 170 °C due to the melting temperature, T_m at 164 °C, which corresponds to the crystalline part of cellulose. As noted by Fan *et* al., the total depolymerisation of cellulose in the microwave was limited to 14%, suggesting that only a small fraction of the cellulose is available for hydrolysis. This is particularly true when using microcrystalline cellulose, which consists of both amorphous (13%) and crystalline regions (87%), each with significantly different structural and thermal properties.

In this study, a fibrous sample was used, taking into account the higher crystallite size that corresponds to the low surface area of oil palm mesocarp fibre at 0.12 $m^2 g^{-1}$. This suggests that a strong acidity, associated with the resulting carbon cryogel, is needed to cleave the β-1,4-glycosidic bonds of the polymeric structure. This cleavage is an essential step for the conversion of cellulose into oligosaccharides. Morales-delaRosa *et* al. indicated that different types of cellulose, specifically microgranular and fibrous, showed different concentrations of glucose [581]. The concentration is lower for fibrous samples within a 2-h reaction time. The higher acidity of the catalyst plays a crucial role in lowering the reaction temperature to milder conditions (<160 °C), thereby reducing harsh conditions for operating conditions. This is important because when the hydrolysis temperature is high, the occurrence of pyrolysis and other side reactions become significant, and the amount of tars and other difficult-to-

handle by-products increases as the temperature is raised above the optimum temperatures.

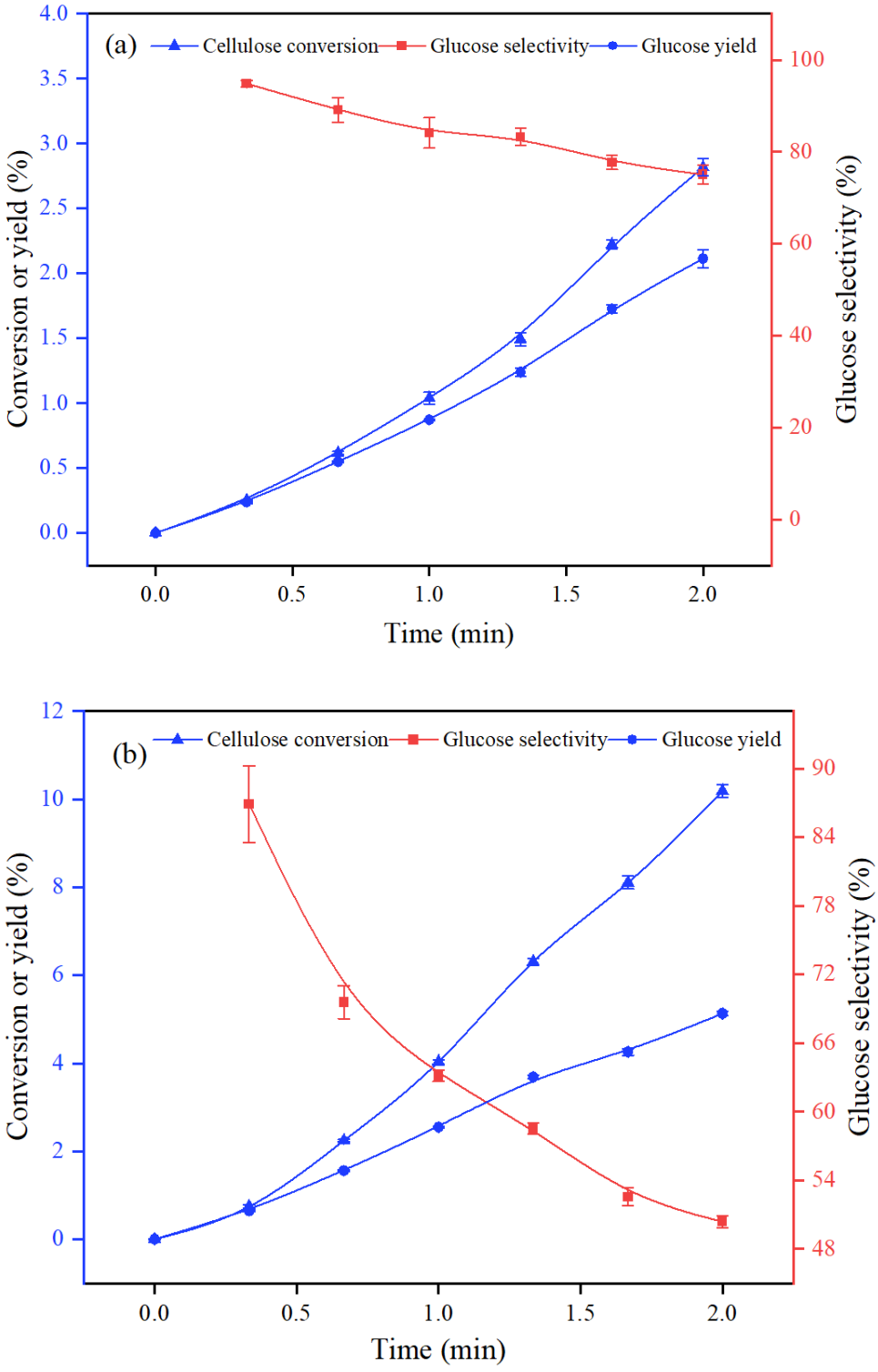

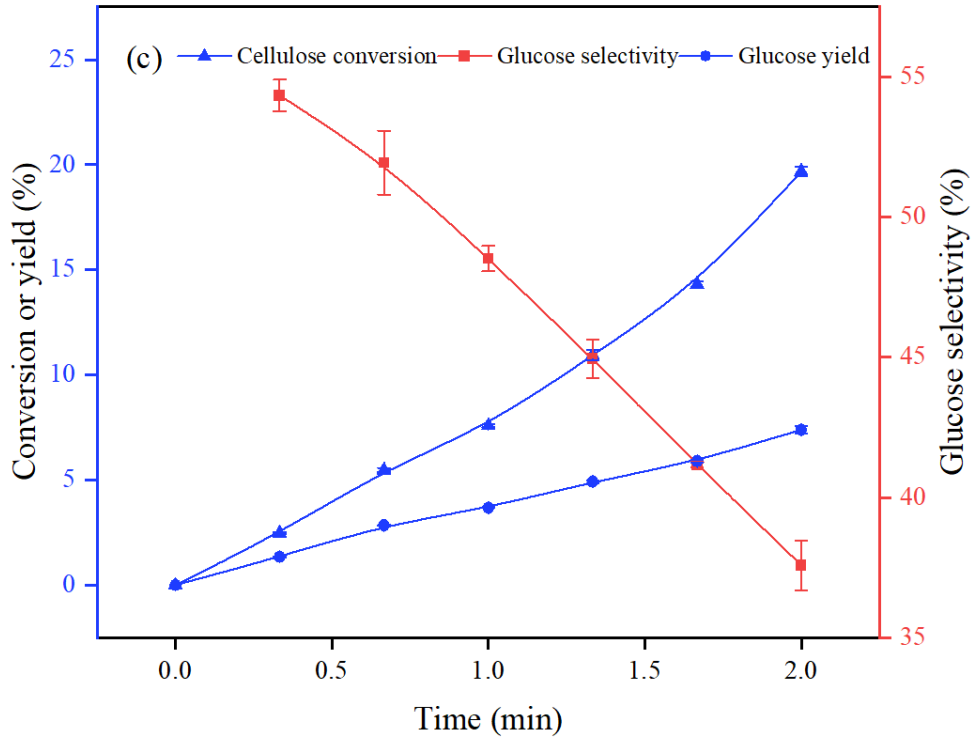
(c)
Cellulose conversion
Glucose selectivity
Glucose yield
Conversion or yield (%)
Glucose selectivity (%)
Time (min)
0
5
10
15
20
25
35
40
45
50
55
0.0
0.5
1.0
1.5
2.0

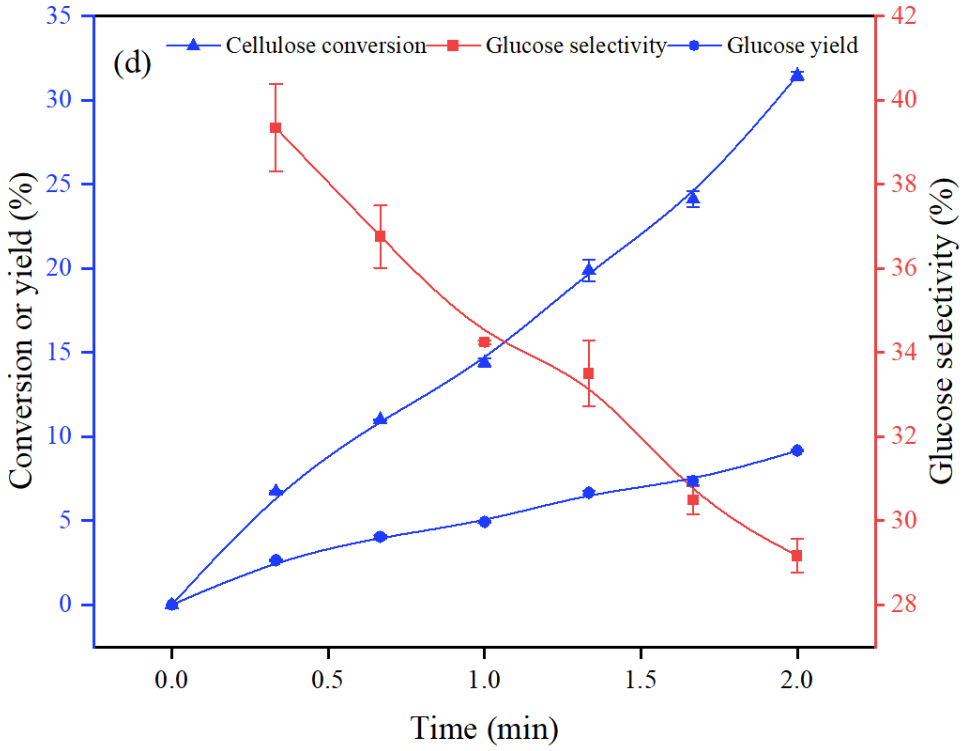
(d)
Cellulose conversion
Glucose selectivity
Glucose yield
Conversion or yield (%)
Glucose selectivity (%)
Time (min)
0
5
10
15
20
25
30
35
28
30
32
34
36
38
40
42
0.0
0.5
1.0
1.5
2.0

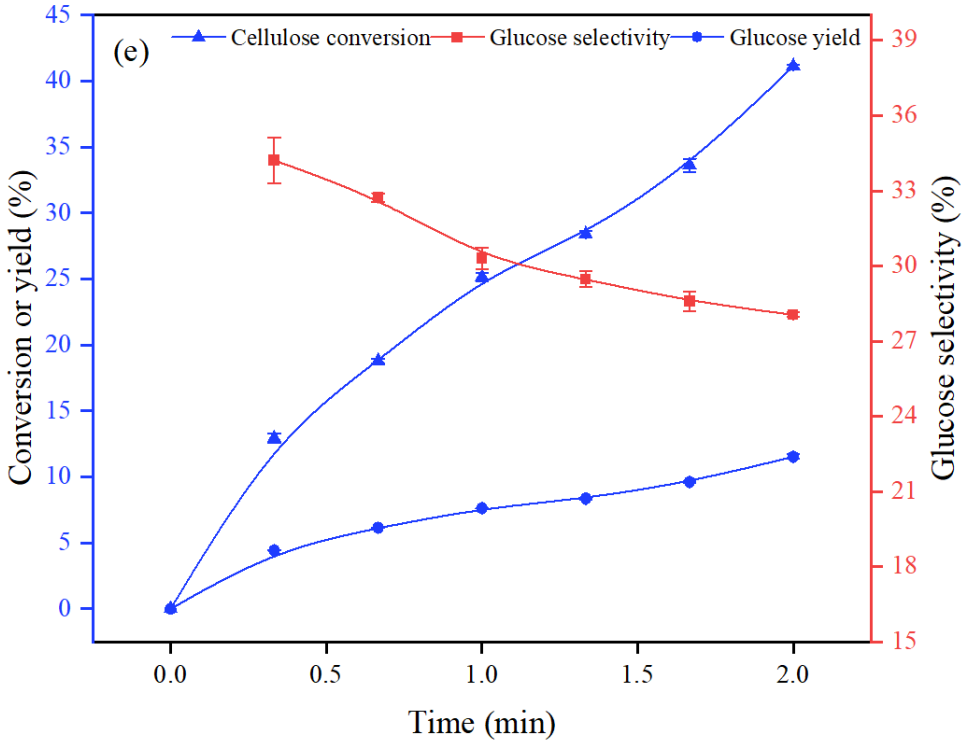

Figure 7.1 Cellulose conversion, glucose selectivity, and glucose yield at (a) 100 W; (b) 150 W; (c) 200 W; (d) 250 W and (e) 300 W. The conversion of cellulose is determined by the percentage of cellulose that is converted to LA. Meanwhile, the selectivity of glucose is determined by the ratio of glucose conversion to glucose yield.

7.3 Effect of microwave treatment on glucose decomposition to LA

Figure 7.2 illustrates how the decomposition of glucose influences both the yield and selectivity of LA. In this study, HMF was not a focus due to its minimal concentration, which even vanished in some samples as temperature increased to 150 °C. The low HMF concentration resulted from the hydrolysis reaction conducted in an aqueous medium, coupled with simultaneous secondary reactions that promoted the rehydration of HMF to LA, a phenomenon also noted by other researchers under similar conditions [582].

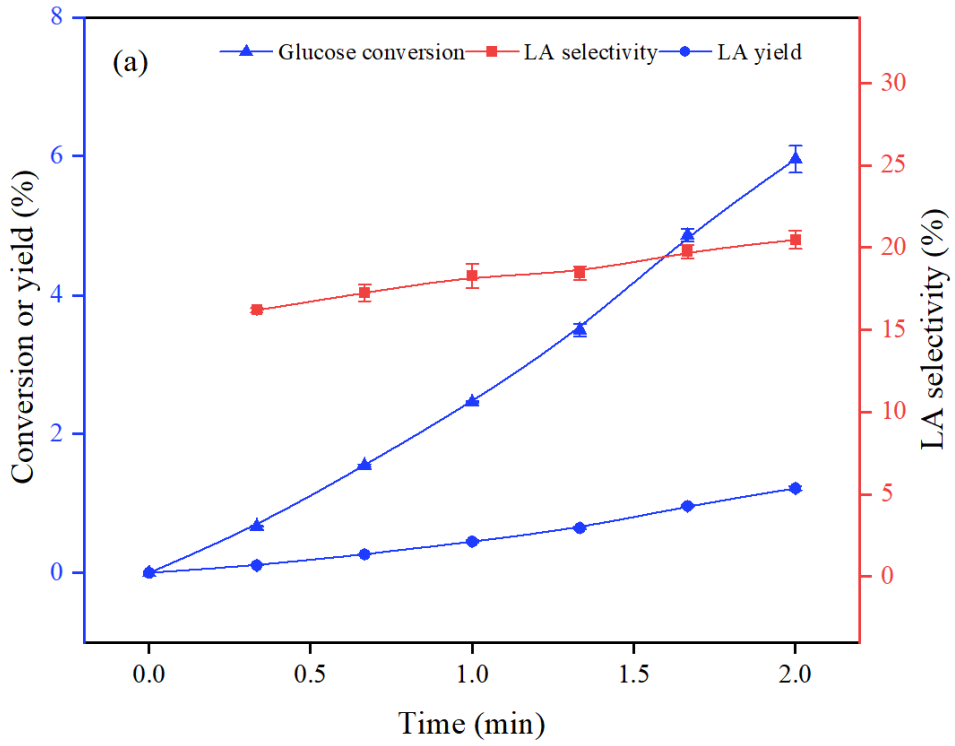
(a)
Glucose conversion
LA selectivity
LA yield
Conversion or yield (%)
LA selectivity (%)
Time (min)
0
2
4
6
8
0
5
10
15
20
25
30
0.0
0.5
1.0
1.5
2.0

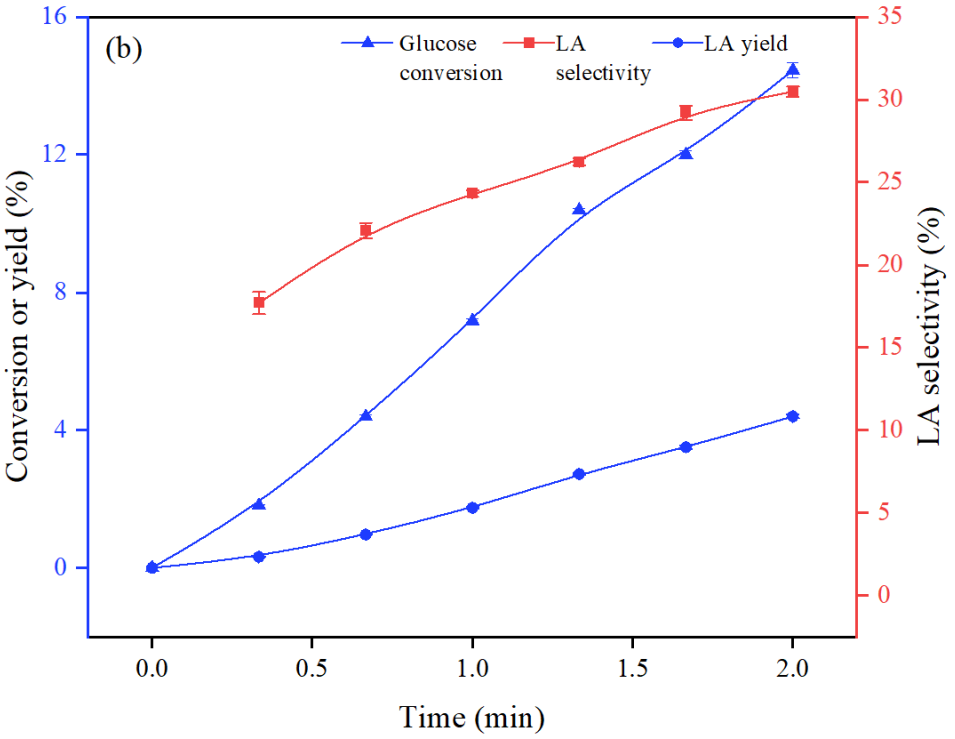
(b)
Glucose conversion
LA selectivity
LA yield
Conversion or yield (%)
LA selectivity (%)
Time (min)
0
4
8
12
16
0
5
10
15
20
25
30
35
0.0
0.5
1.0
1.5
2.0

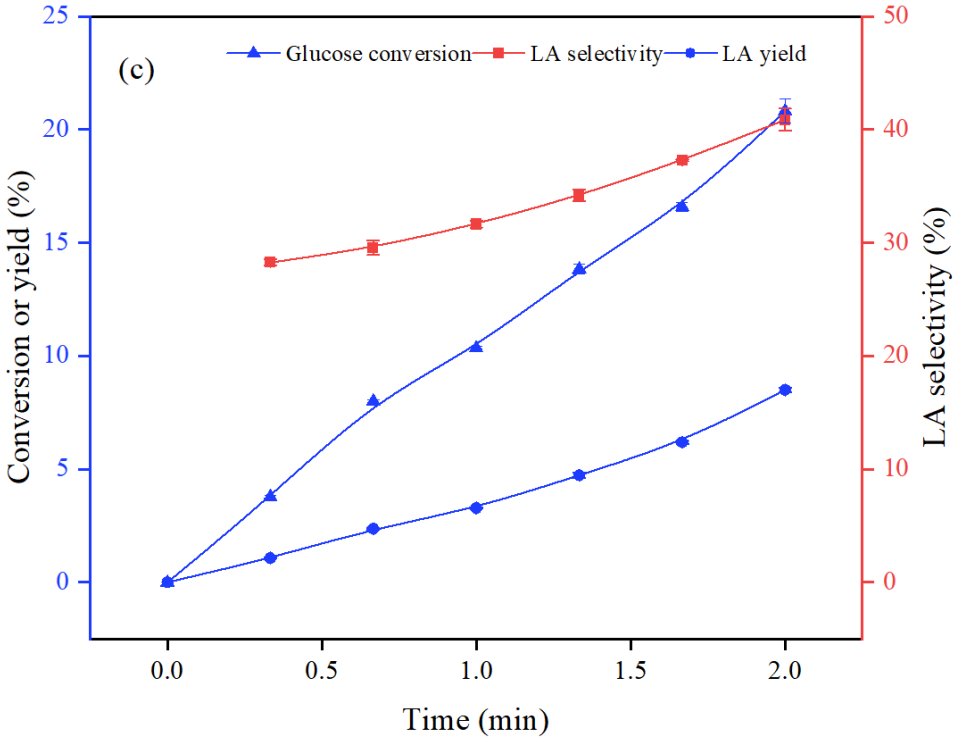
(c)
Glucose conversion
LA selectivity
LA yield
Conversion or yield (%)
LA selectivity (%)
Time (min)
0
5
10
15
20
25
0
10
20
30
40
50
0.0
0.5
1.0
1.5
2.0

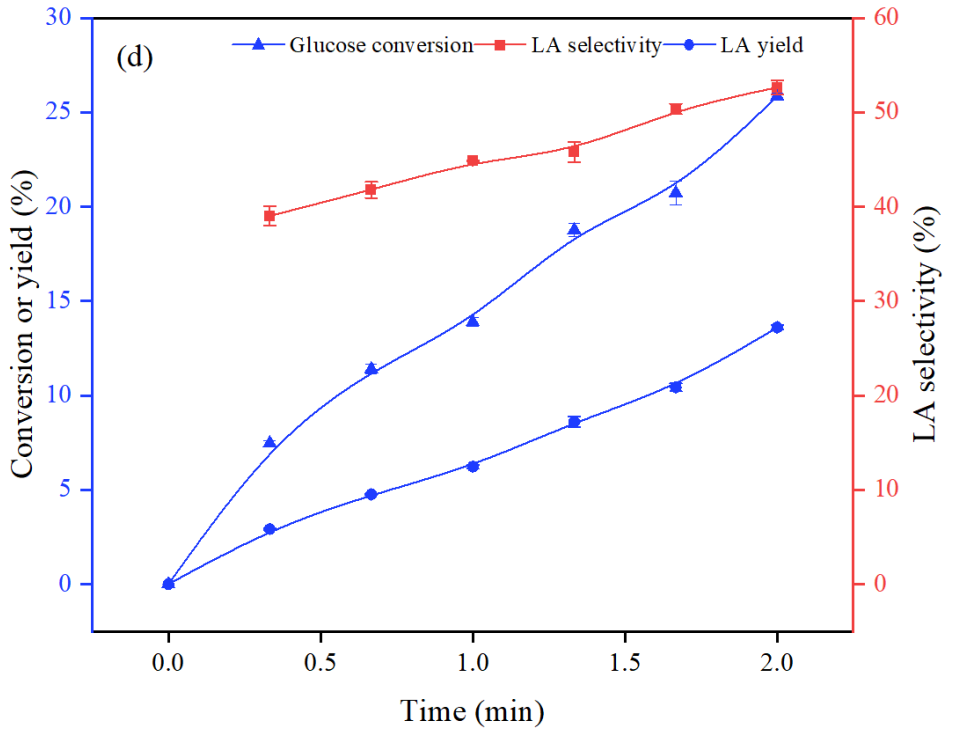
(d)
Glucose conversion
LA selectivity
LA yield
Conversion or yield (%)
LA selectivity (%)
Time (min)
0
5
10
15
20
25
30
0
10
20
30
40
50
60
0.0
0.5
1.0
1.5
2.0

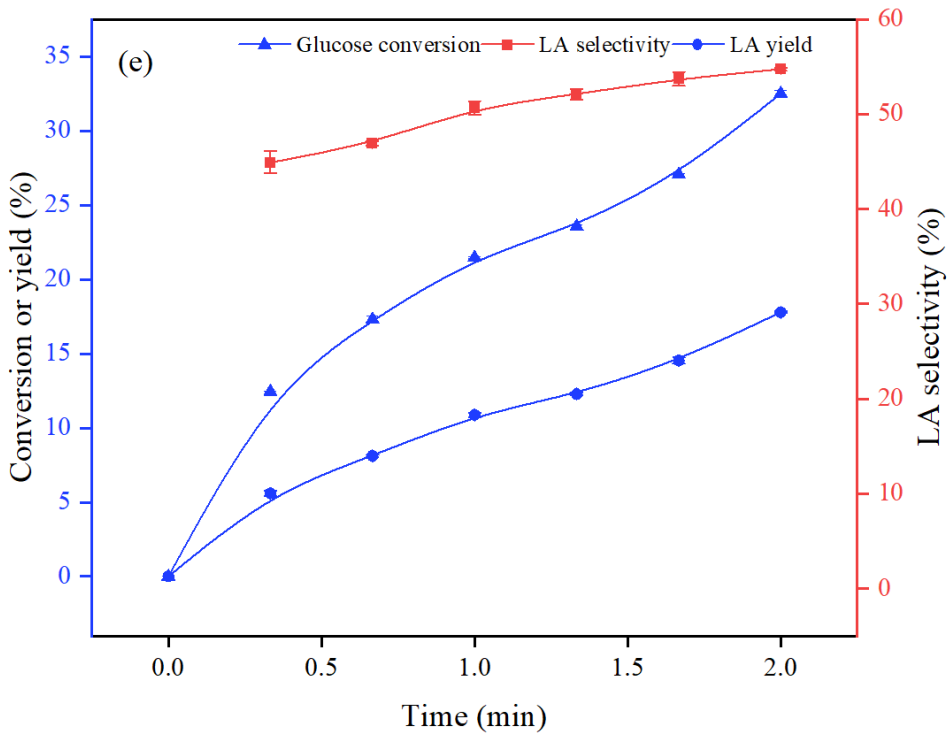

Figure 7.2 Glucose conversion, LA selectivity and LA yield at (a) **110 °C (**100 W); (b) **120 °C (**150 W); (c) **130 °C (**200 W); (d) **140 °C** (250 W) and (e) **150 °C** (300 W). The conversion of glucose is determined by the ratio of the amount of glucose converted to the theoretical yield of glucose, which is obtained from the cellulose conversion of the OPMF sample. The selectivity of LA is determined by the ratio of its conversion to the yield.

According to **Figure 7.2a–7.2e**, the reactions converting glucose to LA are in the kinetic limited regime. The yield and selectivity of LA increase with reaction temperature and time. While LA formation is generally low, it increases with reaction temperature. At a reaction temperature of 150 °C (300 W), the LA yield is moderate at short reaction times but increases rapidly at longer reaction times. **Figure 7.3** shows that as power increases over time, LA efficiency also increases significantly. This change in LA formation coincides with the slowing increase in glucose concentration. Morales-delaRosa *et* al. agreed that the change in LA formation occurs when glucose formation is higher because LA is a secondary product from glucose [581].

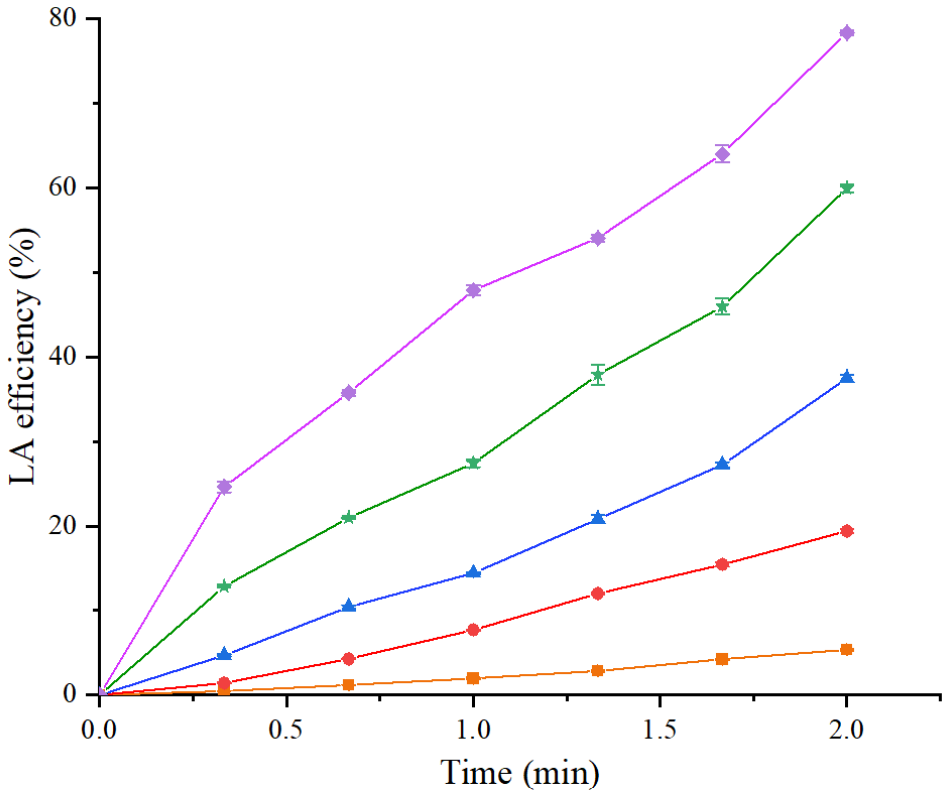

Figure 7.3 LA selectivity at different microwave powers:

As depicted in **Figure 7.2e**, the conversion of glucose increased to a peak of 32.5% when the microwave power was ramped up to 300W. This led to a significant increase in LA yield and selectivity to 17.8% and 54.7%, respectively. This can be attributed to the strong Brønsted acidity of $H_3PW_{12}O_{40}$, which is known to perform better in both homogeneous and heterogeneous acid-catalysed reactions than mineral acids [583–584]. This strong acid can disrupt the hydrogen bonds in the cellulose backbone, a critical factor in polysaccharide structures. It is well established that the depolymerisation of cellulose is heavily dependent on the structure of the hydrogen bond network [585].

Cellulose structure involves intersheet, interchain, and intrachain hydrogen bonds, which provide rigidity and stability but can be disrupted at high temperatures [586]. However, the use of a strong acid leads to a more

deconstructed polymeric precursor, making it more susceptible to acid attack without the need for high reaction temperatures. This inhibits consecutive reactions leading to LA. Fan *et* al. found that weakening the hydrogen bond network within the molecular cellulose matrix at temperatures above 180 °C allows the polar CH_2OH groups to act as "molecular radiators", initiating the cleavage of the polysaccharide chain and selective formation of glucose [41]. The use of a strong acid can also enhance the glucose yield [41].

Within the structure of cellulose, microwave treatment can assist the intrachain O(2)–H···O(6) and interchain O(3)···H–O(6) bonds, making them more susceptible to proton/deuterium exchange than the intrachain O(3)–H···O(5) bond. This implies that after microwave-assisted heating, the protons associated with the $CH_2O(6)H$ group become more accessible. These groups can participate in localised rotation in the presence of microwaves, acting as "molecular radiators" and facilitating the transfer of microwave energy to their surrounding environment [587].

Morales-delaRosa *et* al. suggested that the superior strength of $H_3PW_{12}O_{40}$ not only boosts the depolymerisation of cellulose into glucose but also transforms the emerging monosaccharide into corresponding dehydration products, leading to a higher overall yield of solubilised products compared to other acids [581]. When comparing $H_3PW_{12}O_{40}$ with strong and moderate mineral acids H_2SO_4 and H_3PO_4, respectively, under the same effective acid concentration, the performance of cellulose hydrolysis under microwave irradiation shows that both the conversion and glucose yield after 3 h at 90 °C follow the order: $H_3PW_{12}O_{40} > H_2SO_4 > H_3PO_4$ [576]. This indicates the crucial

role of the strong Brønsted acid in enhancing the hydrolysis rate and glucose yield.

In the carbon cryogel catalytic system, the presence of Nb_2O_5 can speed up the isomerisation of glucose to fructose. This rapid conversion process could bypass the formation of fructose in the final product solution due to the strong acidity of Nb_2O_5 when combined with $H_3PW_{12}O_{40}$. Shimizu *et* al. reported that Nb_2O_5, a new heterogeneous Lewis acid catalyst, exhibits high catalytic performance and good reusability [172]. Interestingly, among the metal oxides, Nb_2O_5 shows the highest catalytic activity, outperforming TiO_2 and Al_2O_3 [172]. This remains true even when the activities are normalised by their BET specific surface areas. The activity of Nb_2O_5 is even higher than that of $Sc(OTf)_3$, a well-known homogeneous water-tolerant Lewis acid catalyst [588].

Under microwave conditions, the Nb-based catalyst can reduce its state after 1 min of reaction, facilitating the hydrolysis process and its conversion to LA [589]. Additionally, the use of GVL in a biphasic water system selectively increases the yield of LA over HMF. Prati *et* al. found that the hydrolysis of cellulose in the presence of Amberlyst 70 and GVL resulted in a selectivity to LA of 69%, compared with only 20% in water [589]. Therefore, strong properties of the acid catalyst support the finding in this study where the glucose conversion to fructose and HMF can be skipped, leading directly to LA formation and facilitating the process. However, Ren *et* al. suggested that variations in LA selectivity across different levels of microwave power and time indicate that the catalytic process targeting LA production involves intermediate stages of glucose and HMF [420]. This is observed under conditions of incomplete cellulose conversion. The implied reaction pathway likely involves

the initial depolymerisation of cellulose to glucose, which then transforms to HMF, and subsequently dehydrates to form LA and FA [420]. This multistep process towards LA requires efficient catalytic systems for selective LA formation.

7.4 Establishing a kinetic model

A kinetic study was conducted to delve deeper into the depolymerisation of cellulose to LA, catalysed by carbon cryogel incorporated with $H_3PW_{12}O_{40}$-Nb_2O_5. Numerous studies have been conducted on the systematic kinetic analysis of biomass hydrolysis to LA. In this study, a simplified kinetic model for the carbon cryogel-catalysed depolymerisation of cellulose to LA in the GVL-water system was proposed, as shown in **Figure 7.4**. This model includes the depolymerisation of cellulose to glucose and the subsequent conversion of glucose to LA and humins. Given that fructose and HMF were not observed in most of kinetics experiments due to its instant degradation under high-power microwave irradiation conditions employed for LA synthesis [590], hence the formation reaction of HMF and its subsequent decomposition reactions were not included in the kinetic model.

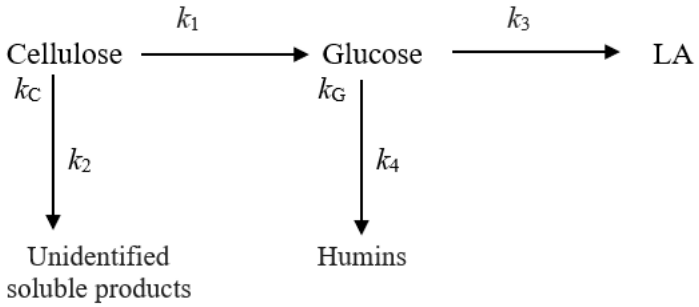

Figure 7.4 A proposed kinetic model for OPMF conversion to LA.

The kinetic model is constructed based on certain assumptions, which are detailed below, and these assumptions are supported by findings from previous studies referenced in this work [590–593]:

(1) The kinetic models are based on the pseudo homogeneous first-order approach.
(2) All reactions are irreversible.
(3) The formation of fructose and HMF intermediates is negligible, and the hydrolysis of cellulose and dehydration reaction of glucose form LA through a series of irreversible reaction.
(4) All humins and other soluble products are by-products.
(5) LA is the primary product from glucose decomposition, and other possible reactions are negligible.

Based on these assumptions and the reaction network, the reaction rates for the depolymerisation of cellulose and decomposition of glucose were defined as **Eqs. (7.1), (7.2)**, respectively.

$$R_C = (k_1 + k_2)C_C \tag{7.1}$$

$$R_G = (k_3 + k_4)C_G \tag{7.2}$$

From these reaction rates, the following set of differential equations were derived as **Eqs. (7.3), (7.4), (7.5)**:

$$\frac{-dC_C}{dt} = (k_1 + k_2)C_C = k_C C_C \tag{7.3}$$

$$\frac{dC_{GLU}}{dt} = k_1 C_C - (k_3 + k_4)C_G = k_1 C_C - k_G C_G \tag{7.4}$$

$$\frac{dC_{LA}}{dt} = k_3 C_G \tag{7.5}$$

Here, the rates of cellulose depolymerisation and glucose decomposition were simplified as **Eqs. (7.6) and (7.7)**, respectively.

$$k_C = k_1 + k_2 \quad (7.6)$$

$$k_G = k_3 + k_4 \quad (7.7)$$

By solving the differential equations (7.3), (7.4), and (7.5), analytical expressions for the concentrations of cellulose, glucose, and LA were derived, as detailed in **Eqs. (7.8), (7.9),** and **(7.10)**, respectively.

$$C_C = C_{C_0} e^{-k_C t} \quad (7.8)$$

$$C_G = \frac{k_1 C_{C_0}}{k_G - k_C} (e^{-k_C t} - e^{-k_G t}) \quad (7.9)$$

$$C_{LA} = \frac{k_1 k_3 C_{C_0}}{k_G - k_C} \left[\frac{k_G (1-e^{-k_C t}) - k_C (1-e^{k_G t})}{k_C k_G}\right] \quad (7.10)$$

The nomenclature for **Eqs. (7.1)** through **(7.10)** is as follows: R_C and R_G denote the reaction rates of cellulose depolymerisation and glucose decomposition, respectively. C_C, C_G, C_{LA}, and C_{C_0} represent the concentration of cellulose, glucose, LA and the initial concentration of cellulose, respectively. The kinetic constants of cellulose depolymerisation, glucose decomposition, and Reactions 1,2,3, and 4 are represented by k_C, k_G, k_1, k_2, k_3, and k_4, respectively. The reaction rate constants for both kinetic studies were computed in the following manner:

(1) The cellulose depolymerisation rate constant (k_C) was determined from the plot of -ln(1-*X*) versus reaction time, where *X* is the cellulose conversion.

(2) The glucose decomposition rate constant (k_G) was determined from the plot of -ln(1-*X*) versus reaction time, where *X* is the glucose conversion.

(3) k_1 was obtained from the plot of -ln(1-*X*) versus reaction time, where *X* is the glucose formation.

(4) k_3 was obtained from the plot of -ln(1-*X*) versus reaction time, where *X* is the LA formation.

(5) The constants k_2 and k_4 were calculated from the differences between k_C and k_1, and between k_G and k_3, respectively.

(6) All the differential equations were used to fit the experimental data.

The linearity observed in **Figure 7.5** supports the first-order dependence of cellulose depolymerisation, glucose decomposition, glucose formation, and LA formation. **Table 7.1** confirms the validity of the selected kinetic model, enabling the calculation of reaction rate constants. **Table 7.2** illustrates that at lower microwave power levels (100-200 W), the rate constant for cellulose

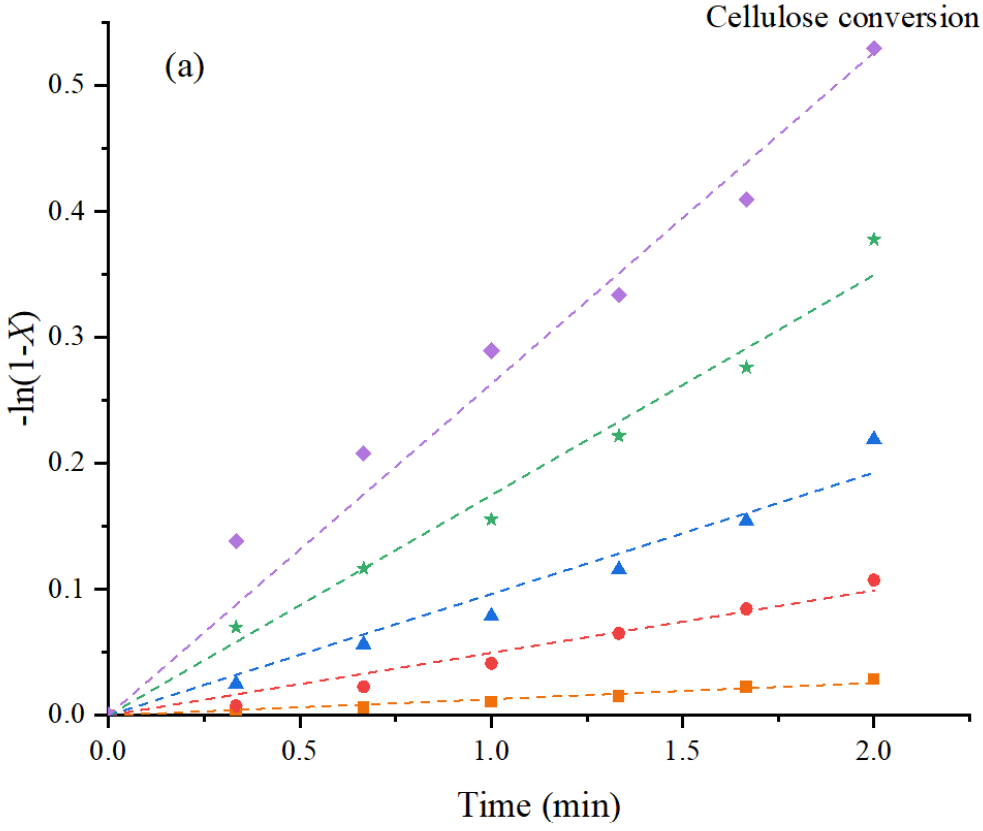

hydrolysis surpasses that of glucose decomposition. However, when the microwave power reaches 250 W, the rate constant for cellulose depolymerisation exceeds that of glucose decomposition.

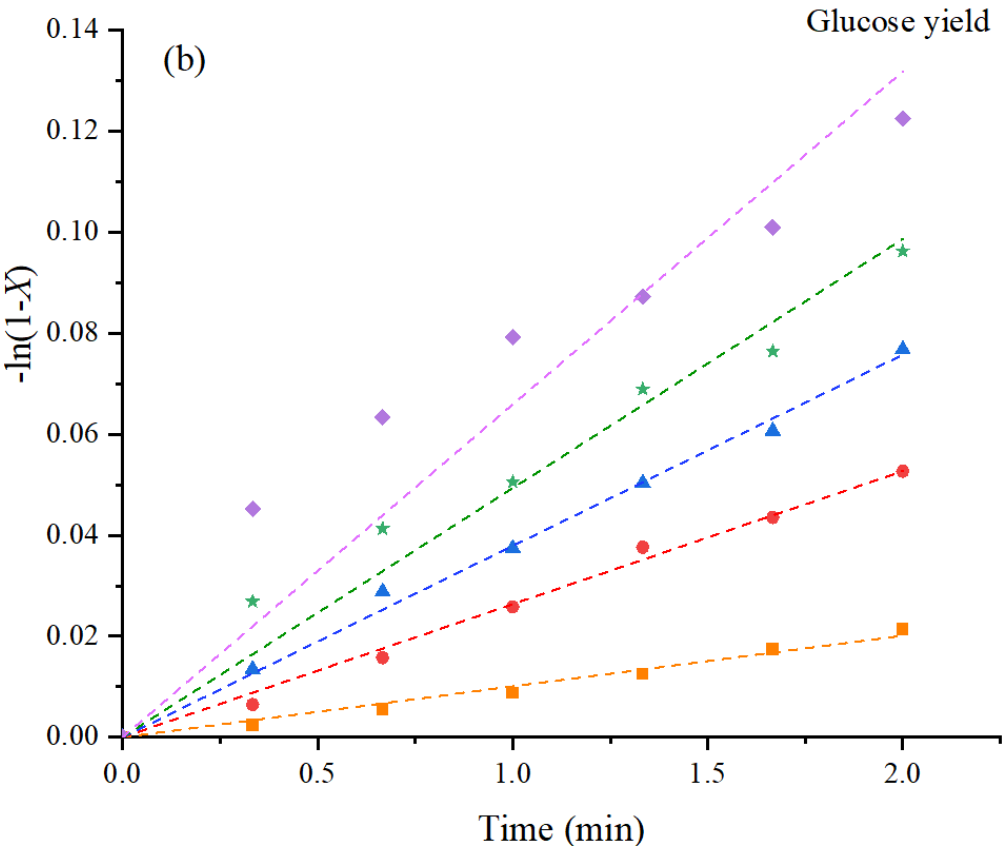
Glucose yield
(b)
0.14
0.12
0.10
0.08
0.06
0.04
0.02
0.00
-ln(1-X)
0.0
0.5
1.0
1.5
2.0
Time (min)

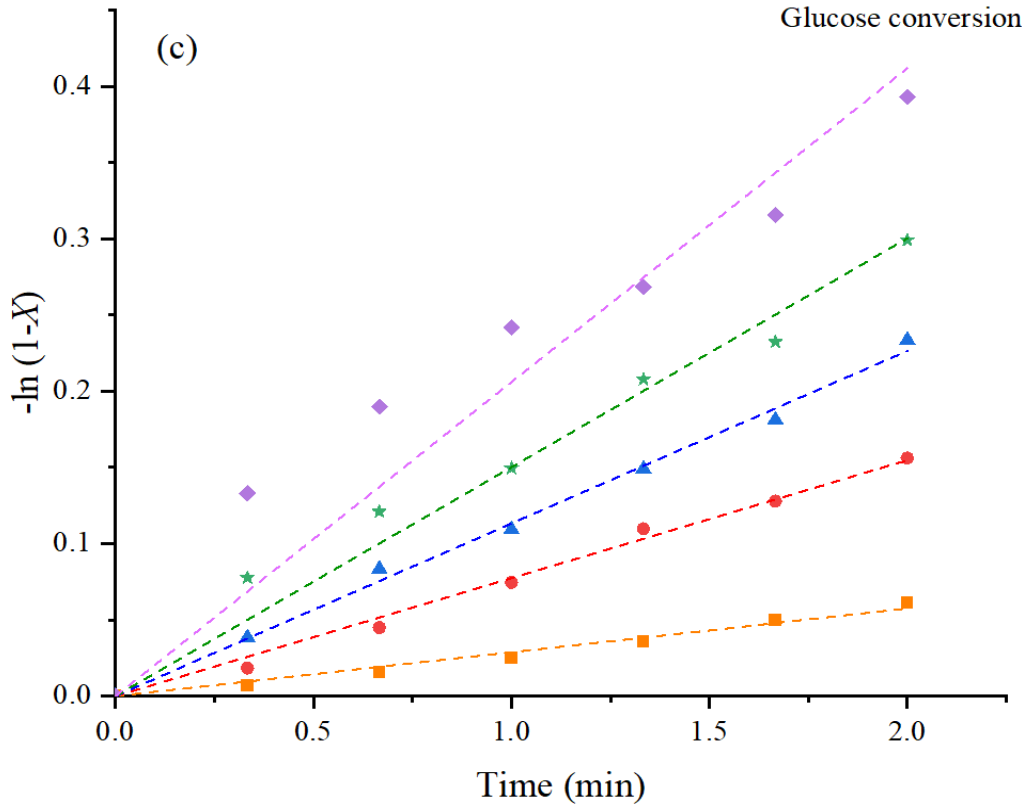
Glucose conversion
(c)
0.4
0.3
0.2
0.1
0.0
-ln (1-X)
0.0
0.5
1.0
1.5
2.0
Time (min)

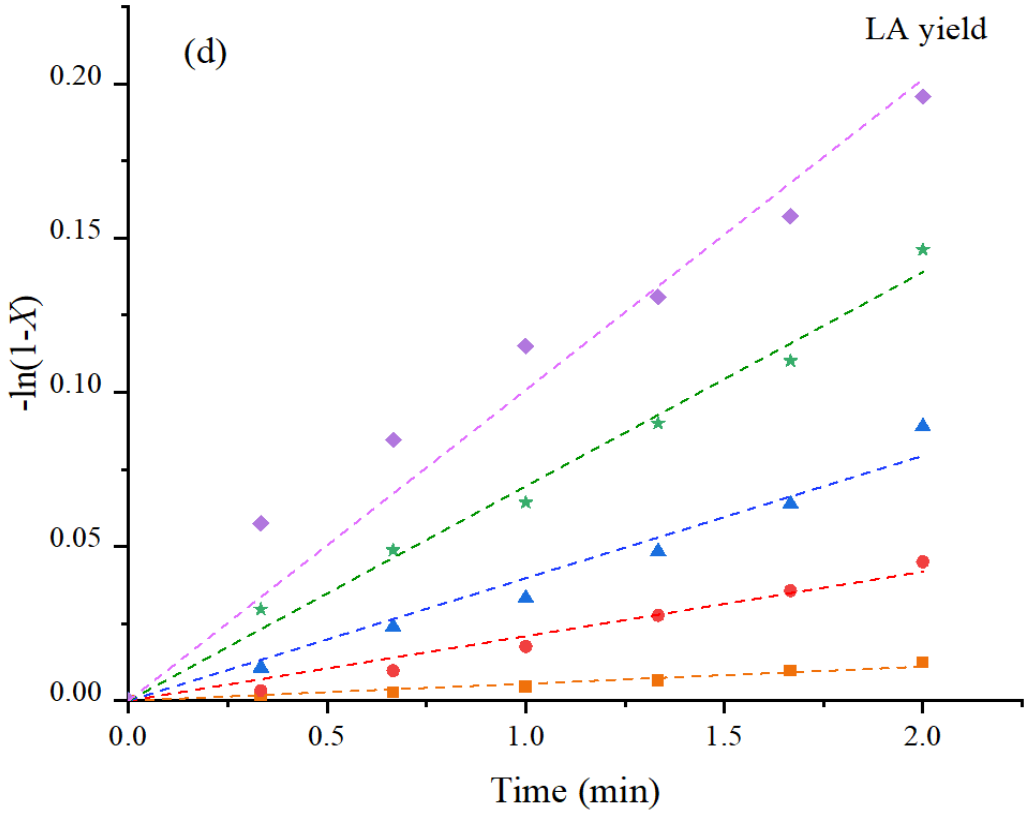

Figure 7.5 Kinetic profiles for (a) cellulose conversion – k_C; (b) glucose formation – k_1; (c) glucose conversion – k_G and (d) LA formation – k_3 via an LXCC catalytic system at different microwave powers (W): ■ 100 ● 150 ▲ 200 ★ 250 ◆ 300.

Table 7.1 The coefficient of determination for the pseudo-first-order reactions.

Microwave power (W) [a]	**R^2**			
	Cellulose conversion	**Glucose yield**	**Glucose conversion**	**LA yield**
100	0.983	0.993	0.993	0.984
150	0.987	0.998	0.997	0.988
200	0.986	0.999	0.999	0.989
250	0.995	0.991	0.993	0.997
300	0.992	0.972	0.979	0.988

[a]For each level of microwave power, the temperature of the final solution is measured immediately after the reaction using both an infrared thermometer and a lab thermometer.

Table 7.2 The reaction rate constant for each step in the tandem reaction process of biomass conversion to LA at various microwave power levels.

Microwave power (W)[a]	Reaction rate constant (min^{-1})					
	k_C	k_1	k_2	k_G	k_3	k_4
100	0.0129	0.0101	0.0028	0.0288	0.0055	0.0232
150	0.0496	0.0264	0.0232	0.0774	0.0209	0.0564
200	0.0963	0.0379	0.0585	0.1133	0.0397	0.0736
250	0.1749	0.0493	0.1255	0.1502	0.0695	0.0807
300	0.2633	0.0659	0.1974	0.2060	0.1008	0.1052

[a] Corresponding temperature for each microwave power level are as follows: 100 W corresponds to 110 °C, 150 W to 120 °C, 200 W to 130 °C, 250 W to 140 °C, and 300 W to 150 °C. These temperature profiles are utilised for fitting the data to the Arrhenius plot.

At lower power levels, the energy provided is insufficient to rapidly break down cellulose's complex structure, specifically the β-(1 → 4)-glycosidic bonds, into glucose. Cellulose, being a complex carbohydrate with strong intermolecular forces, requires substantial energy for hydrolysis. Conversely, glucose, a simpler molecule, decomposes more readily under these conditions, resulting in a lower rate constant for cellulose hydrolysis compared to glucose decomposition. When the microwave power is increased to 250 W, sufficient energy is available to overcome the energy barrier for cellulose depolymerisation. However, glucose decomposition, being an exothermic process, releases energy. At higher microwave power, the system might become overly energetic, potentially destabilising the reaction pathway, and favouring glucose conversion to LA, thereby slowing down the rate of glucose decomposition.

According to Kang *et* al., cellulose hydrolysis to glucose and glucose decomposition typically occurs simultaneously, but the reaction rates are significantly influenced by the reaction conditions [3]. This study aligns with

Sasaki *et* al.'s findings, which reported a faster glucose decomposition rate than its formation rate during hydrolysis at relatively low temperatures (290–350 °C). However, when the temperature exceeds 350 °C, the cellulose hydrolysis rate outpaces that of glucose decomposition [594–595]. Interestingly, the higher temperature used in this study was not even greater than the relatively low temperature used in the aforementioned study. This suggests that carbon cryogel incorporated with $H_3PW_{12}O_{40}$-Nb_2O_5 enhances energy efficiency, reacting at a faster rate at temperatures below 200 °C.

This study reveals that at 300 W, the rate of glucose decomposition (0.2060 min^{-1}) is marginally slower than that of cellulose depolymerisation (0.2633 min^{-1}). This suggests that glucose decomposition could be the rate-limiting step in the conversion of cellulose-derived biomass to LA. Contrastingly, Ren et al. observed the slowest reaction rate constant for the depolymerisation of cellulose to glucose (0.134 min^{-1}) via acidic IL at 170 °C, while the fastest reaction rate was for the conversion of glucose to LA (0.258 min^{-1}) [593]. Despite this, the rate of cellulose hydrolysis in this study was slightly higher than the fastest reaction in the previous study, indicating that carbon cryogel incorporated with $H_3PW_{12}O_{40}$-Nb_2O_5 enhances the reaction rate.

Moreover, as the microwave power increases, the rate constant for LA formation also increases, indicating a significant increase in LA yield at higher microwave temperatures, possibly above 140 °C. The slowest observed reaction rate constant was for LA formation when the low powers implied, compared to cellulose depolymerisation, glucose formation, and glucose yield. This rate increased from 0.0055 min^{-1} at 100 W to 0.1008 min^{-1} at 300 W (150 °C). This could be due to the bypassing of certain tandem steps in the process of enhancing

direct conversion from glucose to LA. These bypassed steps might have facilitated the conversion of glucose to LA. Consequently, the formation of HMF, an intermediate in LA production from glucose, might be limited, slowing down the overall rate of LA formation.

However, the catalytic system presented by the carbon cryogel catalyst was faster than the Fe/HY zeolite catalyst reported earlier [590], which achieved the highest rate constant for LA formation at 0.0432 min^{-1} at a higher temperature of 200 °C. The slower reaction rate for LA formation (k_3) than that for glucose decomposition (k_G), as per **Table 7.2**, is also likely because LA, being the final product in the biomass hydrolysis process, takes a longer time to form. It is generally protonated and can form a very stable protonated dihydro-5-hydroxy-5-methyl-2(3H)-furanone, as shown by quantum chemistry calculations using GAMESS [596].

Although LA can be converted to unidentified chemicals, the reaction rate is over 500 times lower than that of HMF conversion [3, 596]. However, under severe reaction conditions, such as higher catalyst concentration, temperature, and longer reaction time [162, 597–601], LA can also be converted to other byproducts, including gaseous products like H_2, CH_4, and CO, which can slower its formation [602]. It has been found that the crucial step for LA production from glucose is the dehydration process of protonated glucose, which involves several intermediate steps [603]. It has also been reported that these dehydration steps are highly endothermic, and the entire process from glucose to LA is dominated by these steps [604]. Meanwhile, glucose dehydration leads to the formation of byproducts, such as anhydroglucose and glucose oligomers, which can slow down the reaction rate for LA formation [605]. The presence of

Brønsted and Lewis acids, which catalyse multiple steps for glucose conversion to LA, can further slowdown the overall reaction rate for LA formation. Each step in the reaction pathway has its own rate, contributing to the overall reaction rate.

Overall, the increment in microwave power, leading to a rise in temperature, offers an efficient means of energy transfer to the reaction mixture. This heightened energy promotes faster molecular movement and collisions, consequently accelerating the reaction rate. Microwave irradiation enhances mass transfer by inducing convection currents and improving the movement of reactants to catalytic sites, contributing to increased reaction rates. Physical observations, such as examining the colour intensity of the final product, were made. **Figure 7.6** illustrates visual observations where a well-mixed single layer of solvent was formed after microwave-irradiation conversion. This suggests the absence of visible concentration gradients, stagnant regions, or boundary layers, enhancing the efficiency and safety of the process.

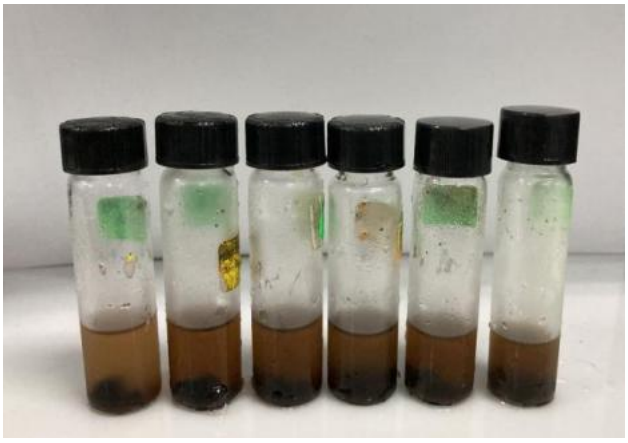

Figure 7.6 Colour intensity of final reaction products.

7.5 Kinetic and thermodynamics evaluation

Thermodynamic data can be acquired by fitting the experimental results to kinetic models. The Arrhenius equation is the starting point for relating kinetic and thermodynamic parameters. **Eq. 7.11** expresses the temperature dependence of the rate constant (*k*).

$$k = Ae^{-\frac{E_a}{RT}} \quad (7.11)$$

Here, E_a is the activation energy (kJ mol^{-1}), *R* is the gas constant (8.314 J mol^{-1}K^{-1}), T is the temperature (K) and *A* is the pre-exponential factor (min^{-1}).

By taking the natural logarithm of **Eq. 7.11, Eq. 7.12** is obtained to give the Arrhenius plot:

$$\ln k = -\frac{E_a}{R} \times \frac{1}{T} + \ln A \quad (7.12)$$

The values of E_a and *A* were determined from the slope and intercept of the Arrhenius plot of ln *k* versus 1/T.

Activation parameters for the depolymerisation of cellulose to LA were determined using an Arrhenius plot (**Figure 7.7**) with the natural logarithm of the rate constant (ln *k*) plotted against the inverse of temperature (1/T). The details of this analysis are provided in **Table 7.3**. The activation energy (E_a) for the depolymerisation of cellulose to glucose was calculated to be 98.72 kJ mol^{-1}, based on the slope of the Arrhenius plot. The pre-exponential factor (A), derived from the y-intercept, was found to be 5.04×10^{11} min^{-1}.

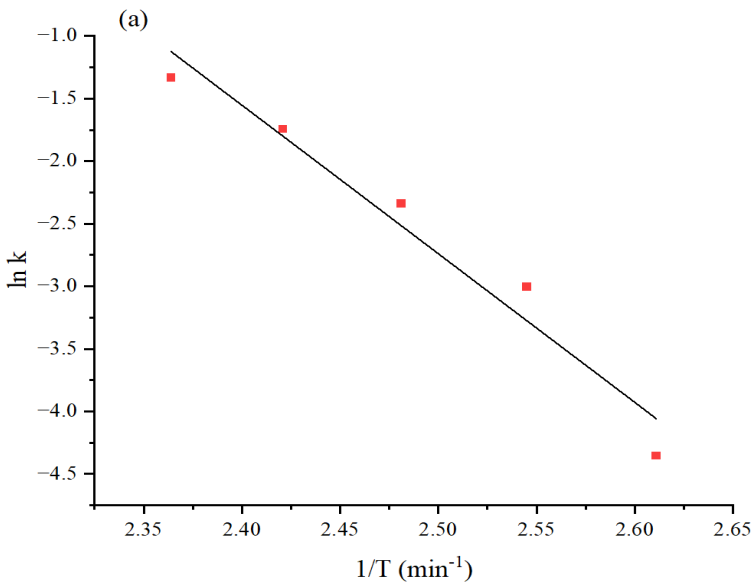
(a)
ln k
−1.0
−1.5
−2.0
−2.5
−3.0
−3.5
−4.0
−4.5
2.35
2.40
2.45
2.50
2.55
2.60
2.65
1/T (min-1)

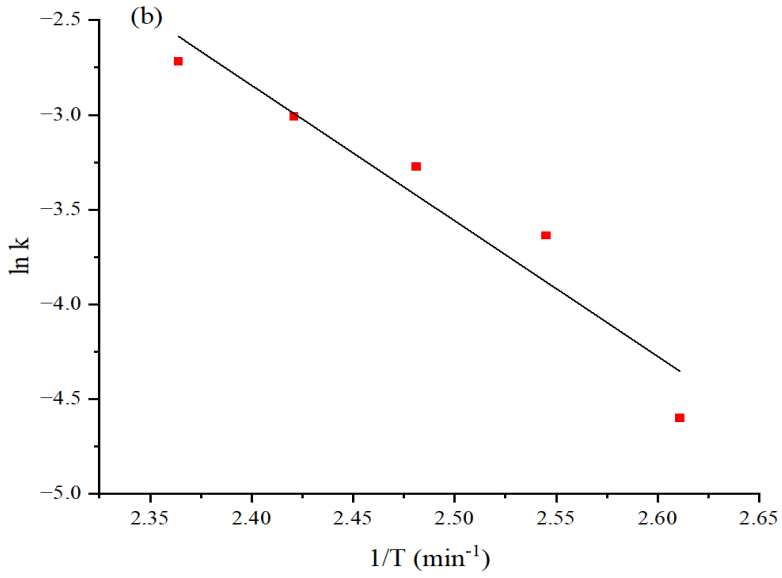
(b)
ln k
−2.5
−3.0
−3.5
−4.0
−4.5
−5.0
2.35
2.40
2.45
2.50
2.55
2.60
2.65
1/T (min-1)

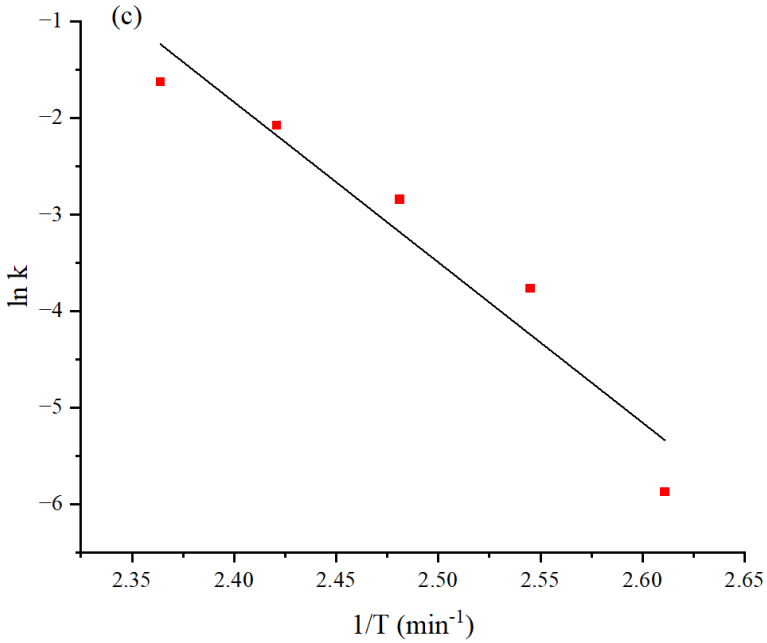
(c)
ln k
−1
−2
−3
−4
−5
−6
2.35
2.40
2.45
2.50
2.55
2.60
2.65
1/T (min-1)

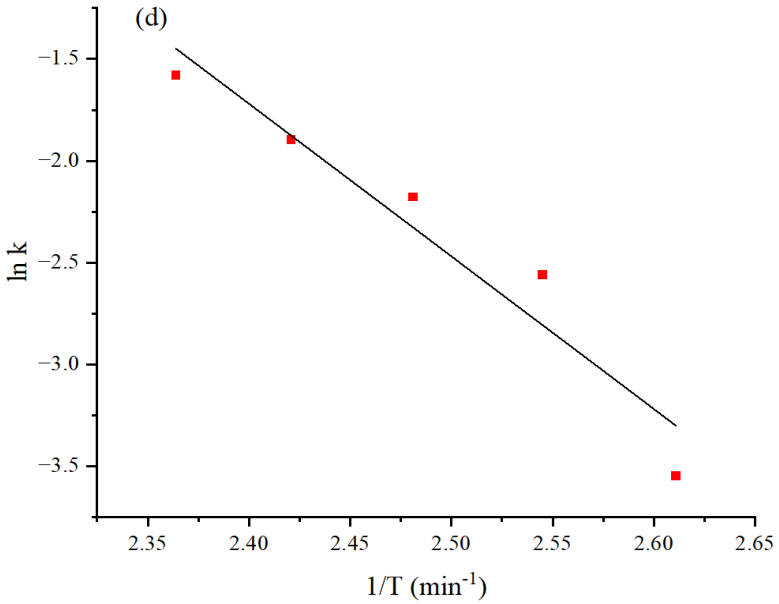

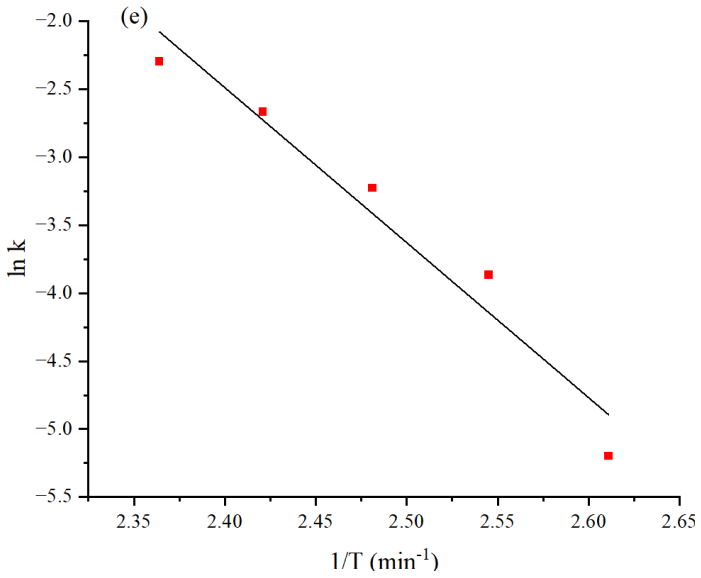

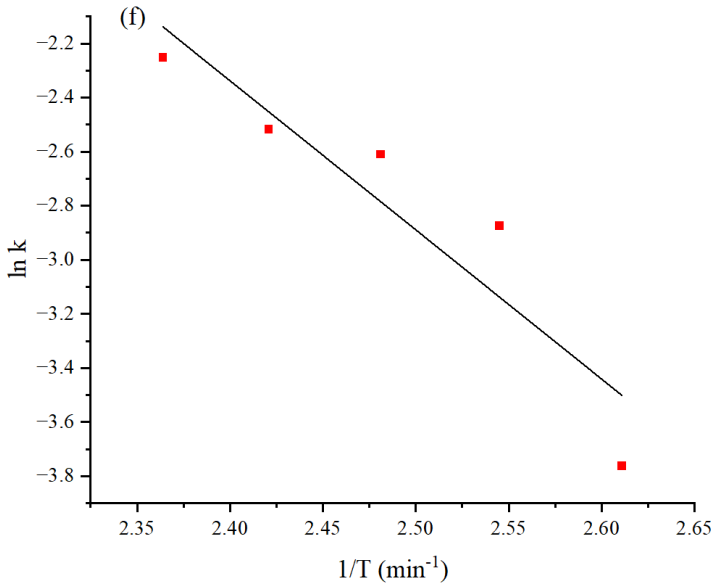

Figure 7.7 Arrhenius plots for (a) k_C; (b) k_1; (c) k_2; (d) k_G; (e) k_3 and (f) k_4.

Table 7.3 The activation energy for each reaction involved in the one-pot conversion of biomass to LA.

Parameter	Reaction					
	C	**1**	**2**	**G**	**3**	**4**
E_a (kJ mol^{-1})	98.72	59.47	138.03	62.31	94.82	45.87
A (min $^{-1}$)	5.04 x 10^{11}	1.66 x 10^{6}	3.22 x 10^{16}	1.16 x 10^{7}	6.42 x 10^{10}	5.43 x 10^{4}
R^2	0.958	0.924	0.930	0.930	0.952	0.863

The performance of the carbon cryogel catalyst used in this study was comparable to that of an IL catalytic system, which exhibited a higher E_a of 121.78 kJ mol^{-1} for the conversion of microcrystalline cellulose to LA [593]. Notably, Girisuta *et* al. reported an even higher E_a of 151.5 kJ mol^{-1} using a H_2SO_4 catalyst [606]. These results suggest that the carbon cryogel-catalysed depolymerisation of cellulose is energetically more favourable. The enhanced protonation of the glycosidic oxygen in cellulose by the strong acidity of $H_3PW_{12}O_{40}$ can promote the catalytic cleavage of cellulose [42, 607].

In contrast, the E_a for glucose decomposition was relatively low at 62.31 kJ mol^{-1}, compared to the 73.03 kJ mol^{-1} reported by Cheng *et* al. for a solid acid catalyst (CH_3-SBA-15-SO_3H) in a GVL reaction medium [608]. In the GVL system, a high concentration of GVL alters the mechanism of glucose decomposition from isomerisation to dehydration reactions [609]. The use of a solid Brønsted acid catalyst in a highly concentrated GVL solution enhances glucose adsorption compared to pure water, due to the microheterogeneity of the solution [610]. These factors, along with the previously mentioned proton instability, facilitate the conversion of glucose to HMF in the GVL system.

The E_a for the conversion of glucose to humins was the lowest among all reactions at 45.87 kJ mol^{-1}, suggesting that a carefully designed temperature

range (110 – 150 °C) is necessary for high-yield LA production, as it is least affected by variations in microwave power and temperature. This finding aligns with the report by Cheng *et* al., who found a similar E_a of 41.53 kJ mol^{-1} when using GVL as the solvent system [608], which limits humin formation. In contrast, Ramli *et* al. reported a higher E_a of 75.70 kJ mol^{-1} for the conversion of glucose to humins [590], which exceeds the E_a for glucose decomposition to LA (68.90 kJ mol^{-1}). This indicates that the former reaction is more sensitive to temperature conditions (120-200 °C), suggesting that higher temperatures promote the formation of humins from glucose. Therefore, excessively high temperatures may not be favourable for LA production due to the increased tendency for humin formation. **Table 7.4** summarises the comparison of kinetic models obtained in this study with those reported in the literature for different types of catalytic systems.

Table 7.4 E_a comparisons in different catalytic systems.

Ref.	Feedstock	Proposed model	Cellulose content (%)	Catalyst	Solvent	Temp. (°C)	E_a (kJ mol^{-1})	A (min^{1})
[591]	Wheat straw	Biomass $\xrightarrow{k_1}$ Sugar $\xrightarrow{k_2}$ HMF $\xrightarrow{k_3}$ LA; Sugar $\xrightarrow{k_4}$ Humic and unidentified soluble products; HMF $\xrightarrow{k_5}$ Humic and unidentified soluble products	40.4	H_2SO_4	Water (autoclave)	190–230	E_{a1} = 78.7 E_{a2} = 54.5 E_{a3} = 56.5	A_1 = 1.49 ×10^{10} A_2= 1.50 ×10^{5} A_3 = 1.43 ×10^{7}
[582]	Sugarcane bagasse[a]	(Glucan) Cellulose $\xrightarrow{k_1}$ Glucose $\xrightarrow{k_2}$ HMF $\xrightarrow{k_3}$ LA + FA; Glucose $\xrightarrow{k_4}$ Humins	43.3	H_2SO_4	Water (autoclave)	150–200	E_{a1} =144.8 E_{a2} =152.1 E_{a3} = 101.6 E_{a4} = 161.4	A_1 = 1.59 ×10^{18} A_2= 6.56 ×10^{18} A_3 = 2.71 ×10^{14} A_4 = 6.94 ×10^{19}
[40]	Corn starch	Starch $\xrightarrow{k_1}$ Glucose $\xrightarrow{k_2}$ HMF $\xrightarrow{k_4}$ LA; Glucose $\xrightarrow{k_3}$ Humins; HMF $\xrightarrow{k_5}$ Humins; LA $\xrightarrow{k_6}$ Decomposition products	NA	HCl	Water (microwave)	135–165	E_{a1} =39.9 E_{a2} =101.0 E_{a3} = 52.7 E_{a4} = 288.0 E_{a5} = 133.0 E_{a6} = 61.7	NA
[593]	Microcrystalline cellulose	Cellulose $\xrightarrow{k_1}$ Glucose $\xrightarrow{k_2}$ LA; Glucose $\xrightarrow{k_3}$ Humins	NA	[C_3SO_3 Hmim] HSO_4 IL	De-ionised water (autoclave)	160–180	E_{a1} =121.8 E_{a2} =202.6 E_{a3} = 166.9	NA
[601]	Corn stalk	(Glucan) Cellulose $\xrightarrow{k_1}$ LA $\xrightarrow{k_2}$ Decomposition products	41.5	$FeCl_3$	Salt bath water (conventional heating)	220–240	E_{a1} =133.0	A_1 = 7.10 ×10^{13}

[575]	Corncobs	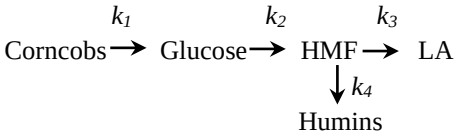	35.4	H_2SO_4	Water (conventional heating)	150–180	E_{a1} =135.3 E_{a2} = 134.4 E_{a3} = 96.5 E_{a4} = 101.6	$A_1 = 1.08 \times 10^{15}$ $A_2 = 9.90 \times 10^{14}$ $A_3 = 4.02 \times 10^{11}$ $A_4 = 1.24 \times 10^{12}$
[611]	OPMF		30.0	$InCl_3$-[HMIM][HSO_4]	Water (conventional heating)	135–175	E_{a1} = 56.5	$A_1 = 1.30 \times 10^{6}$
[612]	Corncob	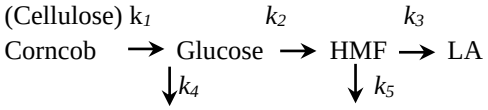	32.6	$SnCl_4$	Water (conventional heating)	170–190	E_{a1} = 48.2 E_{a2} = 46.0 E_{a3} = 57.0 E_{a4} = 76.3 E_{a5} = 67.3	$A_1 = 7.28 \times 10^{4}$ $A_2 = 4.20 \times 10^{4}$ $A_3 = 2.14 \times 10^{6}$ $A_4 = 1.03 \times 10^{7}$ $A_5 = 2.82 \times 10^{7}$
This study[b]	Dewaxed OPMF	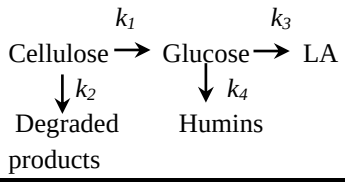	32.0	Lignin-derived carbon cryogel	GVL/water (microwave)	110–150	E_{a1} = 59.5 E_{a2} =138.0 E_{a3} = 94.8 E_{a4} = 45.9	$A_1 = 1.66 \times 10^{6}$ $A_2 = 3.22 \times 10^{16}$ $A_3 = 6.42 \times 10^{10}$ $A_4 = 5.43 \times 10^{4}$

[a]The unit of *A* is in s^{-1}; [b]The present study is conducted through microwave at 100-300 W.

Applying the transition theory, the Eyring equation (**Eq. 7.13**), is an extension of the Arrhenius equation that incorporates thermodynamic considerations. It is particularly useful for considering reactions in different phases (gas, condensed, and mixed). It allows for the determination of thermodynamic activation parameters, namely, activation enthalpy (ΔH) and activation entropy (ΔS). **Eq. 7.13** provides the Eyring plot of ln (*k*/T) versus 1/T for assessing both ΔH and ΔS from the slope and intercept (**Figure 7.8**), respectively. The Gibbs free energy of activation (ΔG) was calculated using **Eq. 7.14**,

where k_B is the Boltzmann's constant (1.381×10^{-23} J K^{-1}), h is the Plank's constant (6.626×10^{-34} J s), and R is the gas constant (8.314 J mol^{-1} K^{-1})

$$\ln\left(\frac{k}{T}\right) = -\frac{\Delta H}{R} \times \frac{1}{T} + \ln\left(\frac{k_B}{h}\right) + \frac{\Delta S}{R} \qquad (7.13)$$

$$\Delta G = \Delta H - T\Delta S \qquad (7.14)$$

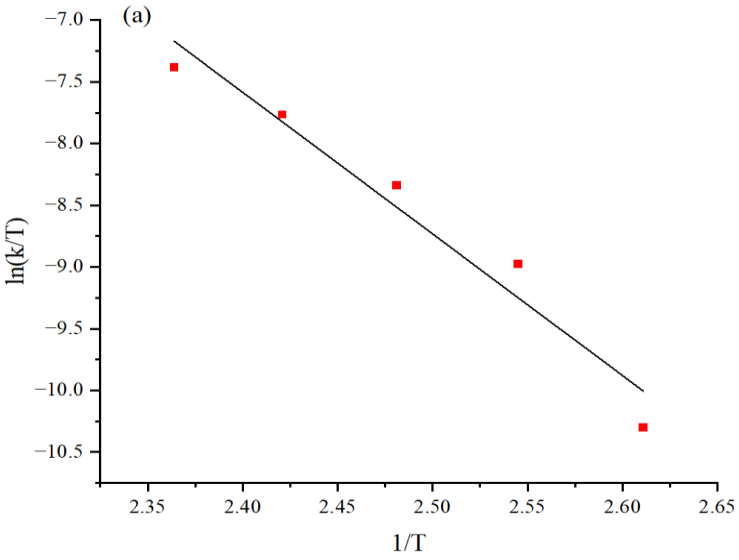
(a)
−7.0
−7.5
−8.0
−8.5
−9.0
−9.5
−10.0
−10.5
ln(k/T)
2.35
2.40
2.45
2.50
2.55
2.60
2.65
1/T

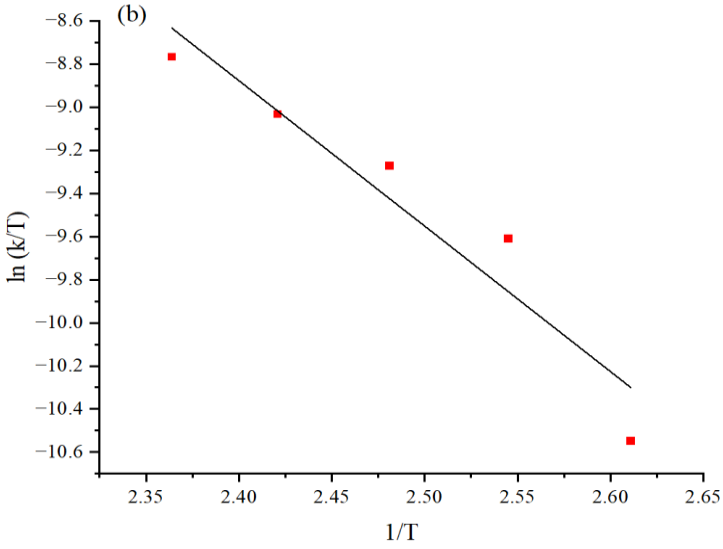
(b)
−8.6
−8.8
−9.0
−9.2
−9.4
−9.6
−9.8
−10.0
−10.2
−10.4
−10.6
ln (k/T)
2.35
2.40
2.45
2.50
2.55
2.60
2.65
1/T

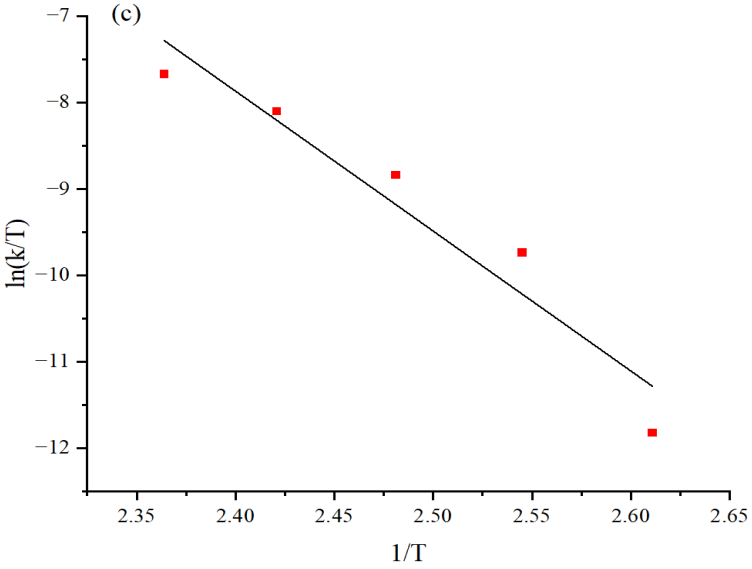
(c)
−7
−8
−9
−10
−11
−12
ln(k/T)
2.35
2.40
2.45
2.50
2.55
2.60
2.65
1/T

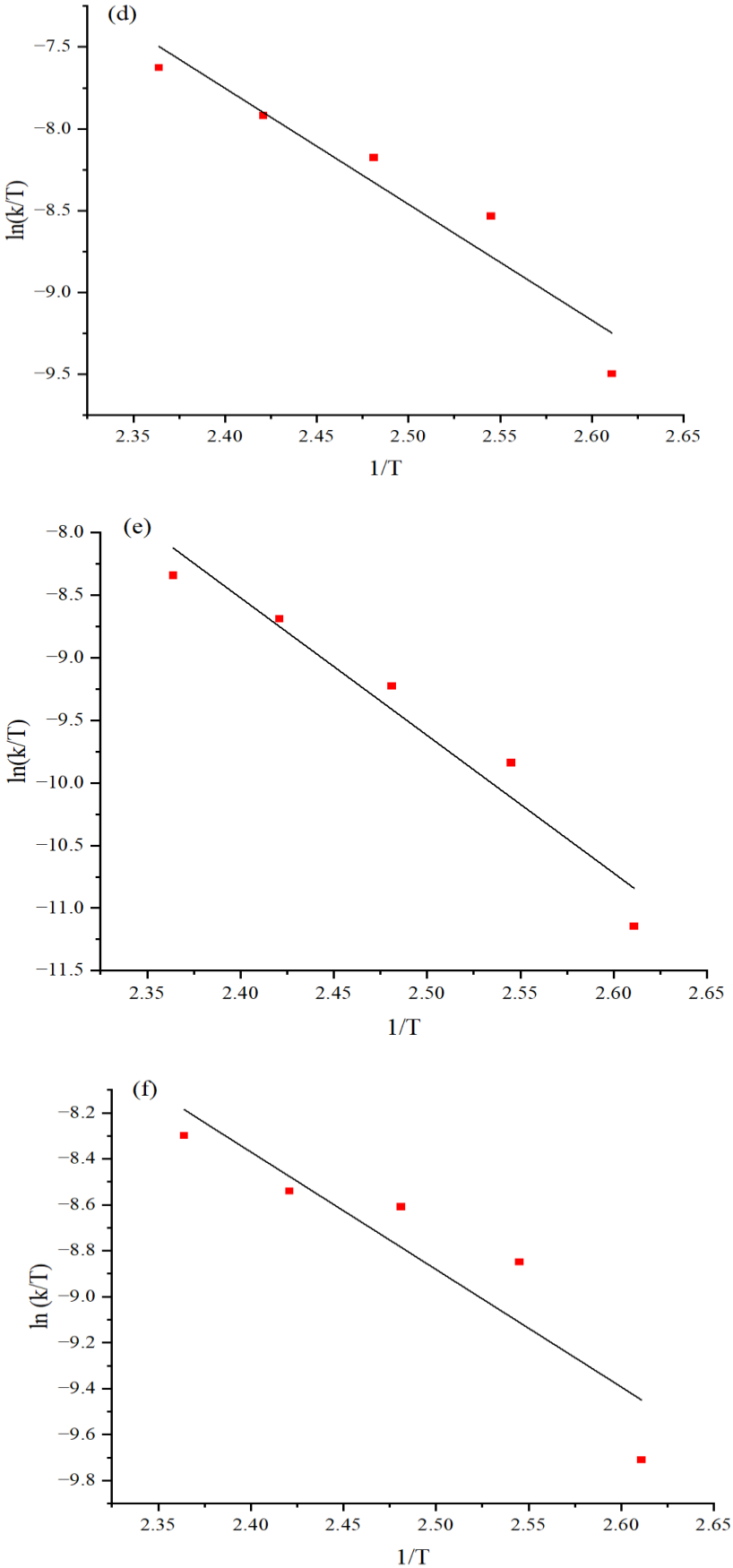

Figure 7.8 Eyring plots for (a) k_C; (b) k_1; (c) k_2; (d) k_G; (e) k_3 and (f) k_4.

In this study, positive ΔH values were observed for all reactions (**Table 7.5**), indicating that they were endothermic. The enthalpy change (ΔH) for the depolymerisation of cellulose is more positive and greater than that for the decomposition of glucose. This suggests that breaking down cellulose into its constituent parts requires more energy than breaking down glucose, as reflected by the higher activation energy (E_a) for cellulose depolymerisation compared to glucose decomposition (**Table 7.3**). This could be attributed to the complex structure of cellulose, which is composed of a long chain of glucose units. The bonds between these glucose units in cellulose are strong and require a significant amount of energy to break. Conversely, glucose, being a simple sugar, involves breaking fewer and less complex bonds during its decomposition [613] .

Table 7.5 Thermodynamic data for each reaction involved in the one-pot conversion of biomass to LA.

Parameter	**Reaction**					
	C	**1**	**2**	**G**	**3**	**4**
ΔH (kJ mol^{-1} K^{-1})	+95.38	+56.13	+134.69	+58.97	+91.48	+42.53
ΔS (J mol^{-1} K^{-1})	-31.68	-136.63	+60.31	-120.47	-48.82	-165.06
ΔG (kJ mol^{-1}) at 423 K	+108.78	+113.92	+109.18	+109.93	+112.13	+112.35
R^2	0.955	0.912	0.927	0.922	0.948	0.844

Notably, the highest ΔH (+134.69 kJ mol^{-1} K^{-1}) was observed for reaction 2, which involves cellulose depolymerisation to other unknown degraded products. The higher ΔH suggests that this degradation process might involve more complex reactions or the formation of products with stronger bonds, requiring more energy. For instance, thermal degradation of cellulose begins with depolymerisation via glycosidic bond cleavage, followed by ring

fragmentation reactions that lead to the formation of several lights oxygenates [614]. The positive entropy value (ΔS) for reaction 2 indicates an increase in disorder within the system, possibly because the products of the reaction (other degraded products) are more disordered than the reactants (cellulose) [615]. Meanwhile, other reactions showed negative ΔS values (**Table 7.5**), indicating that the transition state had a more ordered structure than the reactants in the ground state.

A more negative entropy of activation (ΔS) value of -136.63 J mol^{-1} K^{-1} was observed in reaction 1 compared to -120.47 J mol^{-1} K^{-1} in reaction 3. This suggests that the transition state in the depolymerisation of cellulose involves more components than in the decomposition of glucose, leading to a greater degree of disorder in the system [616]. This is further supported by the observation that the catalyst-substrate complex in the ground state occupies a wider range of conformational states, resulting in an increased entropy for this state [617].

Interestingly, the Gibbs free energy of activation (ΔG) value for cellulose depolymerisation (+108.78 kJ mol^{-1}) was slightly lower than that for glucose decomposition (+109.93 kJ mol^{-1}). This suggests that the initial breakdown of the cellulose structure is more energetically feasible, which could enhance the subsequent conversion of glucose to LA. Furthermore, the ΔG values obtained in this study were lower than those reported by Ramli and Amin [618], who found values of 128.2 kJ mol^{-1} and 128.4 kJ mol^{-1} for the conversion of glucose to HMF and HMF to LA, respectively, using [SMIM][$FeCl_4$] IL. All reactions exhibited positive ΔG as shown in **Table 7.5**, indicating that these reactions are endergonic and energetically unfavourable, and therefore, are not spontaneous.

Overall, the ΔG for humin formation is more positive than that for cellulose depolymerisation and glucose conversion, indicating that it is less spontaneous than these two reactions. This suggests that, under given temperature conditions and in the absence of external energy, humin formation is less likely to occur spontaneously compared to glucose and LA. Catalytic sites exhibit a temperature-dependent activation energy. Although the rate of reaction can increase at higher temperatures, due to more energetic collisions between the catalyst and reactant molecules, these conditions can also promote cross-polymerisation and condensation, leading to humin formation rather than glucose dehydration. Despite this, the LXCC catalytic system is conducive to LA formation under the tested reaction condition of 300 W (423 K), as evidenced by the ΔG value. This implies that the LXCC system can effectively control the reaction pathway, favouring LA production over humin formation at these conditions.

7.6 Concluding remarks

The incorporation of $H_3PW_{12}O_{40}$ and Nb_2O_5 in the carbon cryogel promotes biomass hydrolysis, showcasing higher conversion efficiency and demonstrating kinetic feasibility for OPMF conversion to LA. The acid functionalities in $H_3PW_{12}O_{40}$ and Nb_2O_5 enhance catalytic reactions, and these catalysts are fine-tuned to the carbon cryogel, improving surface interactions with biomass components. The higher surface area of carbon cryogels provides ample deposition sites for $H_3PW_{12}O_{40}$ and Nb_2O_5, increasing the number of active catalytic sites. Microwave irradiation significantly enhances the efficiency of the carbon cryogel catalyst in cellulose hydrolysis, leading to improved glucose yields and selectivity (up to 21% and 75%, respectively).

The porous structure of carbon cryogels, mimicking the size of biomass components, aids the diffusion of reactants and products, enhancing catalytic efficiency. Catalysts supported on carbon cryogels may stabilise reaction intermediates, favouring tandem steps in the reaction. This stabilisation reduces the activation energy by lowering the energy barrier for intermediate steps, resulting in 62.3 kJ mol^{-1} for glucose decomposition. The porous structure also allows effective adsorption of intermediates onto catalyst sites, stabilising them by holding them in proximity to catalytic sites. Interactions between the catalyst and substrate, involving the transfer of electrons or protons, reduce intermediate reactivity and prevent undesired side reactions, hence lowering the activation energy for glucose conversion to humins (45.9 kJ mol^{-1}).

Ultimately, this chapter highlights the importance of maintaining a balance between optimal temperature and microwave power conditions to promote LA formation while preserving the activity of the acid catalyst.

Achieving this balance is crucial to prevent the formation of undesirable by-products and ensure high selectivity towards LA. The interactions within this system significantly affect overall reaction kinetics, leading to a reduction in the activation energy required for converting biomass to LA. The subsequent chapter will explore the detailed mechanism of biomass conversion to LA, utilising a carbon cryogel incorporated with $H_3PW_{12}O_{40}$-Nb_2O_5. This exploration is vital for understanding how external factors significantly impact reaction kinetics. Through comprehensive kinetic and thermodynamic analyses, the reaction pathway can be elucidated, intermediate steps can be pinpointed, and the influence of various factors on the reaction mechanism can be comprehended. Such insights are indispensable for constructing predictive models and enhancing the catalytic process, ultimately advancing the optimisation of these reactions for practical applications.

Chapter 8

Reaction Pathway For the Conversion of Oil Palm Mesocarp Fibre to Levulinic Acid Using Lignin-Derived Cryogel Incorporated with $H_3PW_{12}O_{40}$-Nb_2O_5

8.1 Introduction

Building on the findings from the previous chapter, it is widely acknowledged that the pathways for producing LA and HMF via cellulose-derived biomass share similarities, with HMF serving as a vital intermediate in the biomass conversion process to LA [4, 96, 619]. This is in agreement with Kang et al. [3], as shown in **Figure 8.1**. This process typically unfolds through five sequential steps: (i) pretreatment of lignocellulosic biomass, (ii) hydrolysis of cellulose into glucose, (iii) isomerisation of glucose to fructose, (iv) dehydration of hexoses (glucose and fructose) to HMF, and (v) rehydration of HMF to LA.

According to Weingarten *et* al., higher temperatures and shorter reaction times favour the production of HMF during thermoconversion [620]. Other studies further clarified that the formation of HMF is an earlier step in the reaction pathway, occurring more readily and at lower temperatures than LA formation [621–623]. HMF is an important intermediate in the conversion of biomass to LA and other valuable chemicals. However, if the conditions favour HMF production too much, it could potentially reduce the yield of LA, as more of the available biomass gets converted into HMF instead of LA.

The isomerisation and ring-opening steps take place on the catalyst's surface and within its pores, where both Lewis and Brønsted acid sites are

present [624–626]. The isomerisation reaction is critical in forming HMF, especially when Lewis acids are employed in the catalytic conversion of glucose [627]. The linear molecule of 1,2-enediol is then dehydrated into HMF over Lewis acid sites. The simultaneous reaction of glucose formation and glucose decomposition importantly portrays the right balance of proportion between Brønsted and Lewis acid sites [3]. Brønsted acid sites can donate protons necessary for the protonation steps, while Lewis acid sites can accept electron pairs, stabilising the transition states during isomerisation [628]. The presence of Brønsted acid can facilitate Lewis acid-catalysed isomerisation and improve reaction selectivity [629].

This chapter delves into deducing the reaction pathway for biomass-to-LA conversion using carbon cryogel incorporated with $H_3PW_{12}O_{40}$-Nb_2O_5 in the GVL/water biphasic systems via microwave heating. Such insight helps identify side reactions that may produce unwanted byproducts, leading to strategies to suppress these side reactions and increase the selectivity of the desired product. A detailed understanding of the reaction mechanism can lead to the development of predictive models, which can be used to simulate the reaction under different conditions. Moreover, in a large-scale industrial setting, understanding the mechanism can help in better process control, predicting how changes in conditions will affect the overall rate and yield of the reaction.

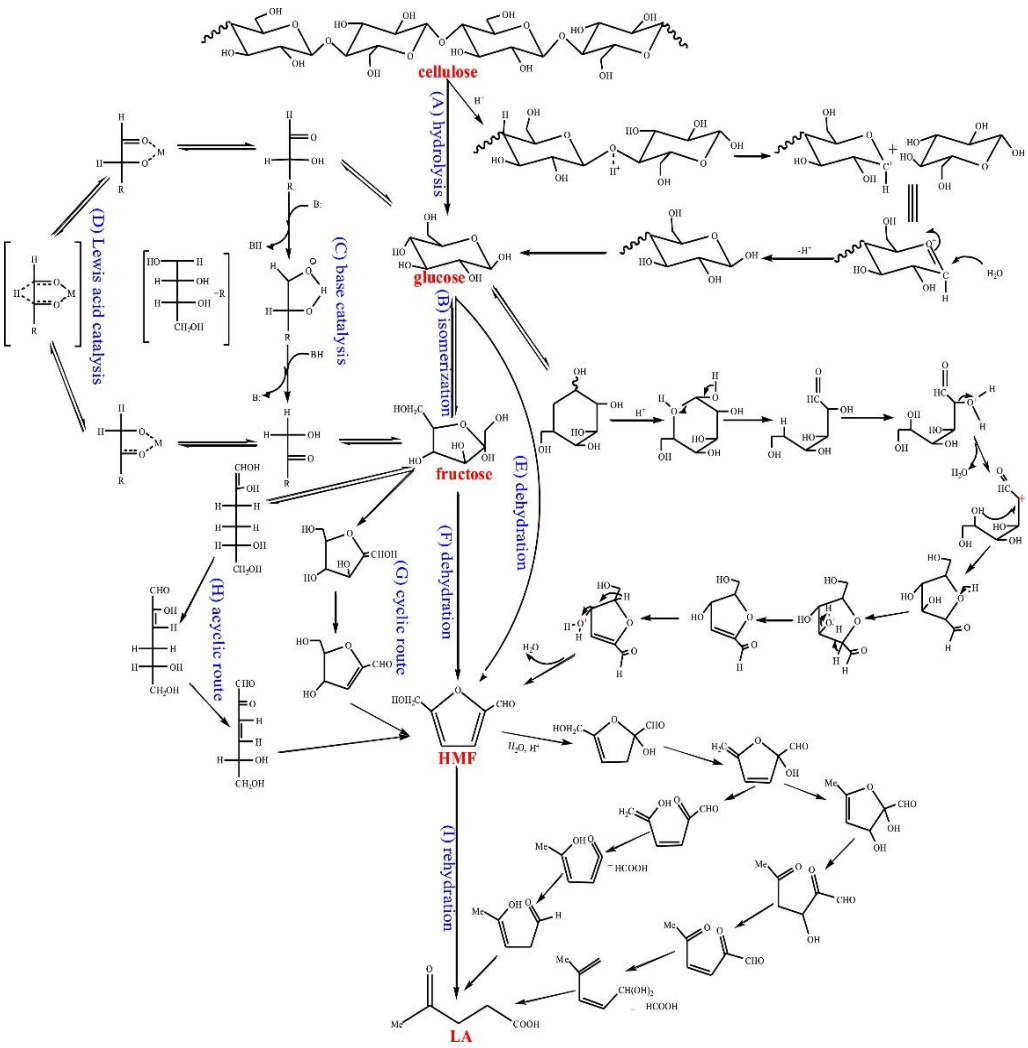

Figure 8.1 The mechanism from the conversion of cellulose to LA. Reproduced with permission from Kang *et* al. [3].

8.2 Identification of possible products

Drawing from the findings in **Chapter 7 on the kinetic studies**, the HPLC analysis (**Figure 8.2**) for the reactions at lower temperatures (110–130 °C) revealed the presence of glucose, fructose, LA, HMF and formic acid (FA). However, **Figure 8.2** shows that fructose, HMF and FA could not be detected in all samples in this study which was conducted at optimum temperature (168 °C). Instead, an unidentified product (peak 5) was significantly observed. This result predicts that the disappearance of HMF at higher temperatures may be due to presence of this unidentified product or HMF is favourable to LA formation.

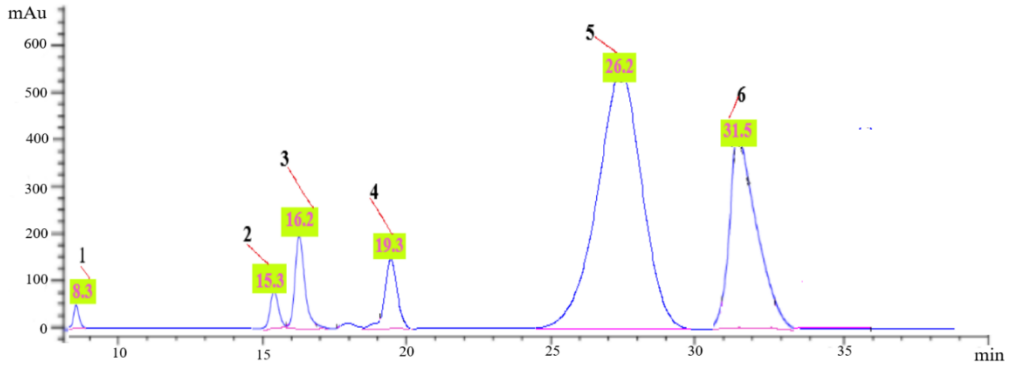

Figure 8.2 The HPLC chromatogram shows the products detected under the condition of 200 W (130 °C) for 2 min include (1) glucose, (2) formic acid, (3) levulinic acid, (4) 2-methoxymethanol (as an internal standard), (5) unknown, and (6) HMF, respectively.

To screen the possible unidentified product formed, the final product solution obtained from microwave conversion of biomass was further analysed through GC-MS. As depicted in **Figure 8.3**, a prominent peak appeared at a retention time of 3.68 min, constituting 94% of the total peak area. This suggested a possible different type of intermediate formed rather than HMF. **Figure 8.4** represents a list of possible products present in the GC-MS spectrum has been compiled, prioritising those with the highest match and reverse match factors as outlined in **Chapter 3, Section 3.16, Table 3.5**.

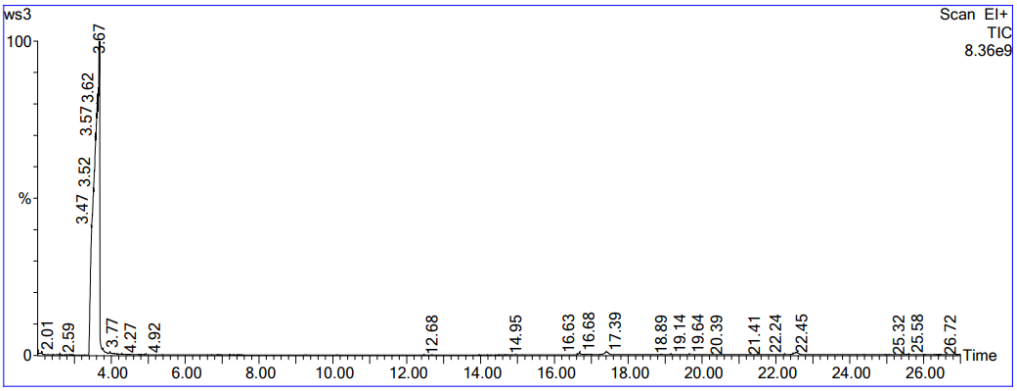

Figure 8.3 The chromatogram profile from the GC-MS analysis of the sample solution, as depicted in Figure 8.2.

Noteworthy, one of the detected compounds is 2(3H)-Furanone, dihydro-5-methyl-, which corresponds to the GVL solvent. This observation suggests that the solvent has been retained to some extent and could potentially be recycled for subsequent reaction cycles. However, it is worth noting that the presence of other by-products may also stem from the degradation induced by the GVL solvent [21].

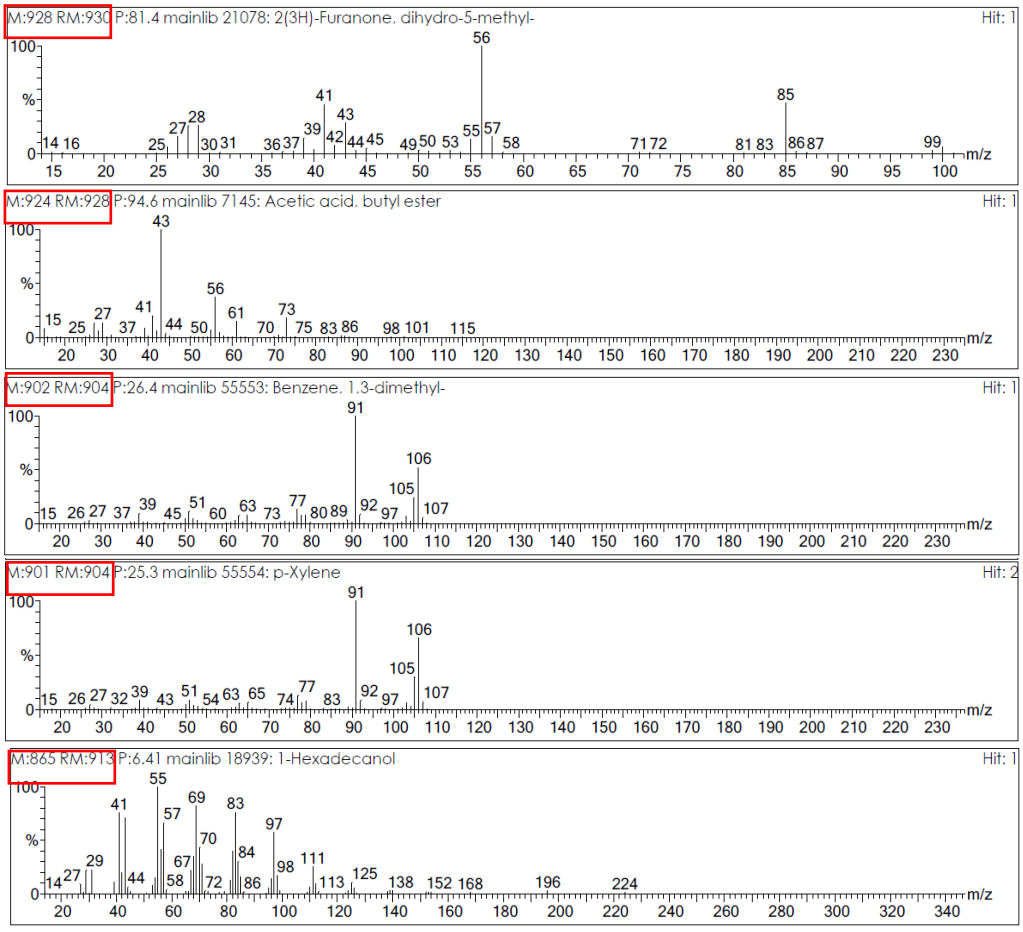

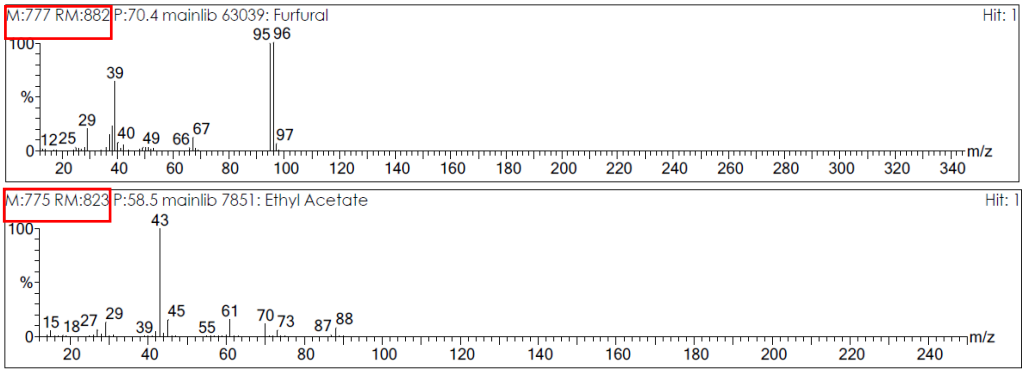

Figure 8.4 The total ion chromatogram spectrum obtained from GC-MS analysis reveals the composition of the hydrolysate produced through biomass conversion. Match (M) and rematch (RM) values are shown at the left corner of the spectrum.

Secondly, the formation of various acetate esters (**Figure 8.4**), such as butyl acetate and ethyl acetate, could possibly be derived from acetic acid, which is converted from furfural. As furfural is one of the detected products (**Figure 8.4**), its presence may come either from the cellulose or hemicellulose pathway as fructose can be detected in a few samples at lower temperatures (110–130 °C). This suggests that the fructose is favourable to HMF conversion at lower temperatures, otherwise, it can possibly be converted to furfural. This observation is consistent with the findings of Han *et* al. [21], who identified furfural and other additional co-products, like furfural, and 3-acetylprapanol during cellulose conversion to LA using a lignin-derived solid catalyst in a GVL solvent. Their research suggests that fructose leads to furfural production [21], and furfural undergoes several steps to ultimately yield acetic acid during the reaction, which is then further reduced to ethanol (see **Figure 8.5**).

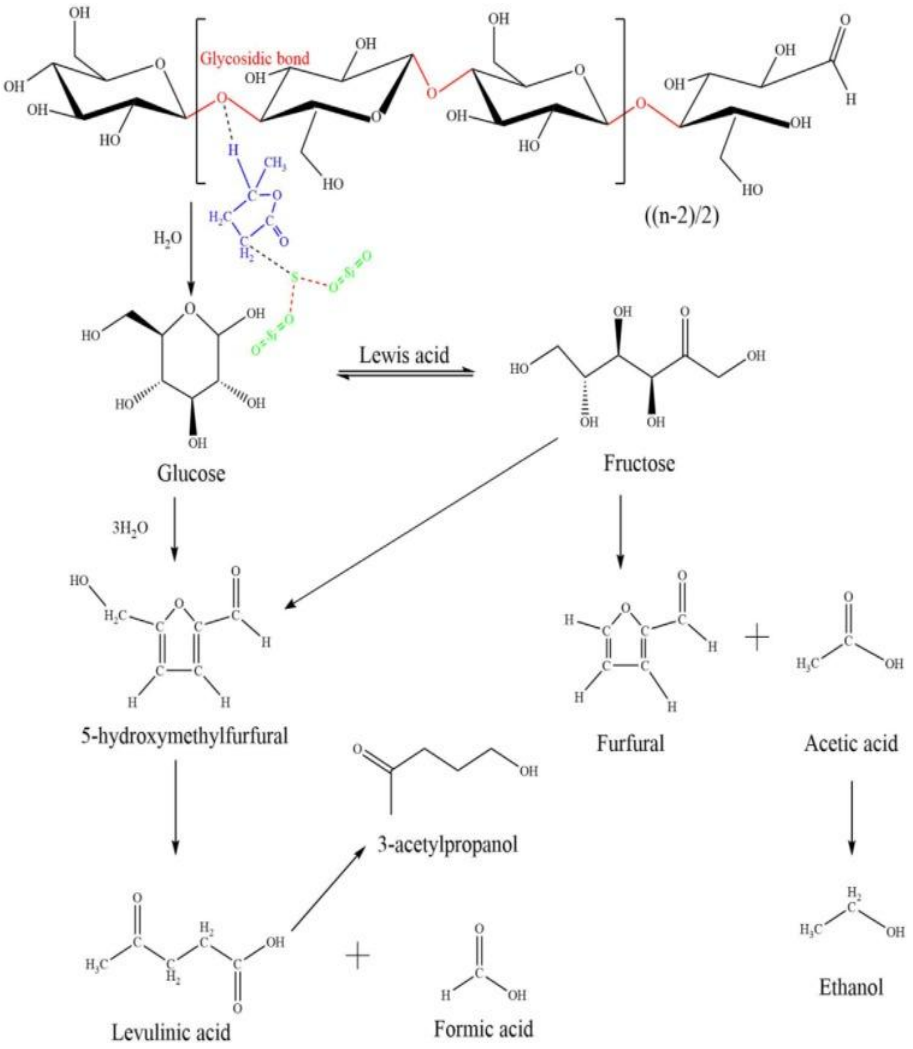

Figure 8.5 The reaction of cellulose hydrolysis. Reproduced with permission from Han *et* al. [21].

However, the presence of furfural through the hemicellulose pathway is possible as using GVL as a solvent medium, it has the power to remove lignin and hemicellulose significantly (as discussed in **Chapter 4**). Despite that, Xiang *et* al. indicated that formation of by-products from hemicellulose may not always interfere with the cellulose pathway reaction [630], depending on various factors including reaction conditions, catalyst selectivity, and the nature of the by-products formed [631–632]. Meanwhile, some studies conclude that furfural formation from xylose decomposition is inevitable during lignocellulosic

biomass hydrolysis, with furfural being highly unstable in acidic solutions and capable of forming humins when reacting with sugars [633–634].

In this study, the disappearance of HMF in some samples may not only be influenced by the temperature, but also by the strength of carbon cryogel incorporated with $H_3PW_{12}O_{40}$ and Nb_2O_5 that exhibited high acidity (12.66 mmol g^{-1}) favoured LA selectivity over HMF selectivity under highly acidic conditions [538, 619, 635]. This aligns with findings from Ya'aini *et* al. who used modified HY zeolite-$CrCl_3$ to form a hybrid catalyst which is able to catalyse multistep of biomass conversion to LA in one-pot reaction, due to enhanced acidity that limits the HMF production [557]. Meanwhile, Ren *et* al. found only trace amounts of HMF in another catalytic system of ionic liquids (SFIL) [420], suggesting faster dehydration of HMF to LA compared to glucose transformation to HMF, especially via hybrid catalysts. Runge and Zhang [636] and Yang *et* al. [637] suggested that the conversion of glucose to furan—based intermediate (such as HMF) gives low LA yield due to reactions between furfural and C5 sugars in a one-pot reaction system. So, direct conversion from glucose to LA found in this study could be beneficial.

Furthermore, the presence of *p*-xylene and 1,3-dimethyl benzene (**Figure 8.4**) in the reaction mixture suggested the degradation of HMF to these products rather than being converted to LA. This result has been aligned with the findings that a multifunctional solid acid catalyst allows deoxygenation of HMF to its key intermediate 2,5-dimethylfuran (DMF) before being upgraded to ethylene to produce 1,3-dimethyl benzene and *p*-xylene through a tandem Diels-Alder (dehydration) pathway [638–640]. Indirectly, this biomass conversion process to LA proves its complexity through tandem steps in one-pot reaction. Besides,

the presence of 1-hexadecanol (cetyl palmitic alcohol) can be assumed due to the application of oil palm biomass as a feedstock, but the use of GVL in a biphasic system can potentially enhance transesterification in addition to cellulose hydrolysis in the presence of carbon cryogel [641].

8.3 Brønsted-Lewis functionalities in hydrolysis of cellulose to LA

The literature suggested acid-catalysed hydrolysis of cellulose to produce glucose typically involves three main steps (**Figure 8.6**): (i) protonation of the glycosidic oxygen, (ii) cleavage of the glycosidic linkage, and (iii) nucleophilic attack by water [3, 44]. Upon protonation of the glycosidic oxygen, the adjacent anhydroglucose unit linked to the glycosidic oxygen at the C1 position undergoes a half-chair rotational conformational change. This conformational change is impeded by both intra- and inter-chain hydrogen bonds [3, 638]. Although the cleavage of β-1,4-glycosidic bonds in cellulose is a determining step in the reaction [642], the degree of crystallinity plays a crucial role in influencing the reaction rate. Higher crystallinity restricts the accessibility of the β-1,4-glycosidic bonds, resulting in a slower hydrolysis rate.

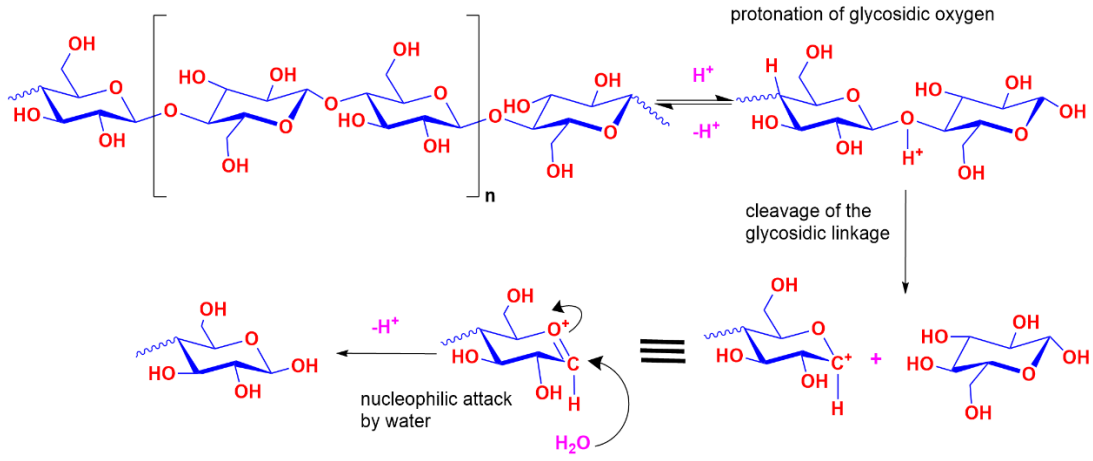

Figure 8.6 Cellulose hydrolysis to glucose.

In this study, as reported in **Chapter 4, Section 4.5.2, Table 4.3**, it was observed that the cellulose extracted from dewaxed oil palm mesocarp fibre (DOPMF) exhibited a higher crystallinity index of 46.81% compared to DOPMF's 34.21%. This suggests that biomass-derived cellulose is less amenable to biomass hydrolysis than DOPMF, thereby affecting the LA yield. Therefore, opting for DOPMF may be more advantageous due to its cost-effectiveness, requiring less treatment, and potentially leading to higher efficiency in direct conversion to LA. This aligns with Van de Vyver et al.'s recommendation to use ball-milled cellulose with a low crystallinity index as it offers a faster reaction rate by enhancing cellulose accessibility for hydrolysis compared to commercial cellulose substrates with higher crystallinity [642].

The catalytic mechanism of carbon cryogel incorporated with $H_3PW_{12}O_{40}$-Nb_2O_5 for cellulose hydrolysis to LA, is elucidated in **Figure 8.7**. This mechanism is pivotal in the context of biomass conversion, where the decomposition of glucose and its isomerisation to fructose typically occur alongside cellulose hydrolysis [643]. Notably, GVL is instrumental in enhancing cellulose hydrolysis and causing the carbon cryogel to swell [21], thus improving the diffusion of sugar intermediates through the catalyst's pores and boosting catalytic activity. This swelling phenomenon is similar to findings from studies utilising Amberlyst 70 within a GVL system [432].

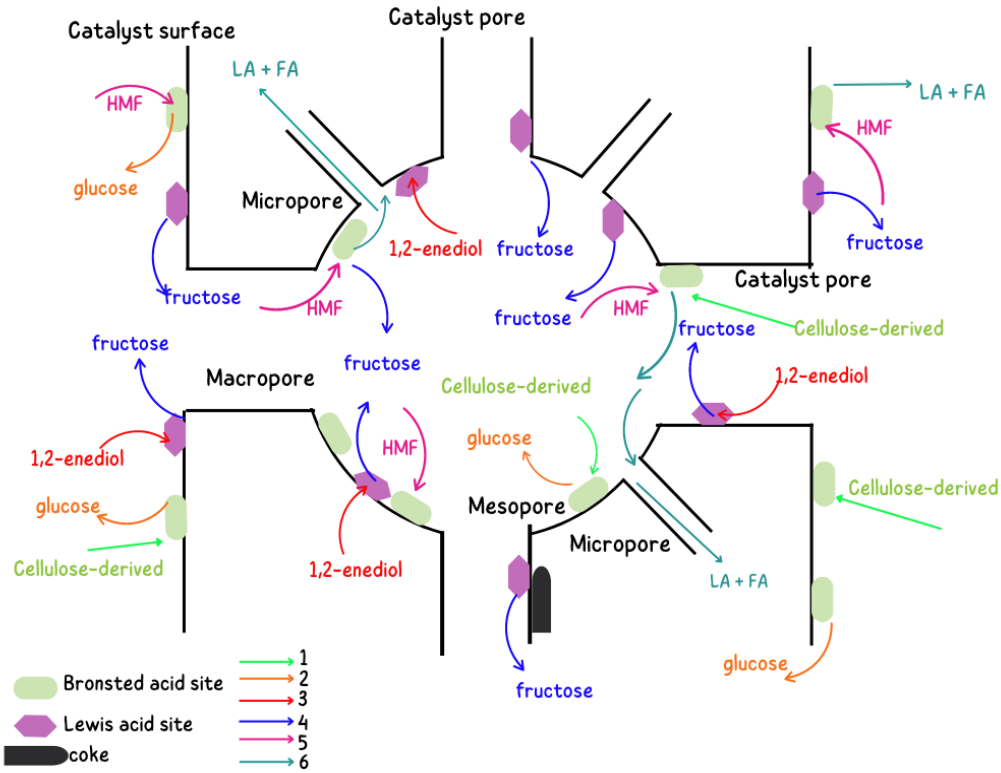

Figure 8.7 Mechanism of carbon cryogel catalyst for cellulose hydrolysis to LA.

The surface of Nb_2O_5, consisting of NbO_4 tetrahedra, represents the Lewis acid sites essential for glucose isomerisation [193]. These sites accept electron pairs, forming adducts, and facilitate an intramolecular hydride shift (**Figure 8.8**) that converts glucose to fructose [644–645]. This conversion occurs as glucose transitions from a ring structure to a linear chain, forming 1,2-enediol. Unlike base and enzyme catalysts, Lewis acids maintain their catalytic activity in the presence of strong Brønsted acids [3], as demonstrated by Yue *et* al. [646]. The combination of Lewis acidic transition metal oxides with weak Brønsted acid sites potentially enhances glucose isomerisation on the Lewis acid surface sites, particularly with WO_3. The substitution of Nb on the WO_3 surface facilitates sugar deprotonation and results in an overall lower activation barrier for isomerisation [646].

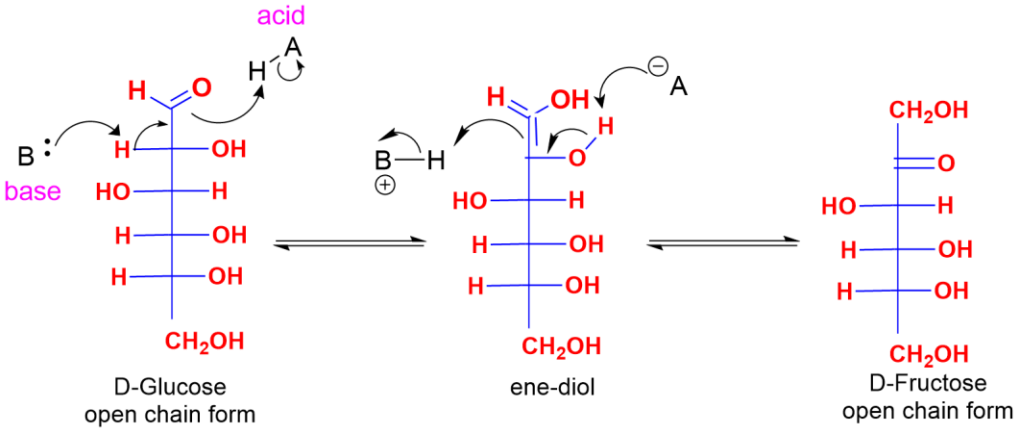

Figure 8.8 Isomerisation of glucose to fructose.

The study indicates that an average pore size of 10.88 nm, as detailed in **Chapter 6, Section 6.5.3**, is sufficient for HMF to pass through and move away from active sites. This minimises further reactions that could lead to unwanted by-products or coking. Conversely, smaller pores may impede HMF diffusion, causing its accumulation and potential degradation at active sites [647]. Research by Lourvanij and Rorrer highlights that a pore size exceeding 1.7 nm ensures efficient diffusion of HMF away from active sites [626], which enhances overall reaction efficiency. Pore size directly influences the diffusion of sugar molecules and smaller compounds like LA and FA within the catalyst. Studies by Kruger *et* al. [555] and Lourvanij and Rorrer [626] suggest that pores larger than 1 nm significantly enhance sugar diffusion. Linear molecules like LA and FA, being small enough, can diffuse through the micropores effectively [625]. Based on Taghavi's suggestion that LA molecules are approximately 0.5 nm [648], the carbon cryogel's average pore size is adequate for glucose molecules to access active sites and for smaller LA molecules to diffuse out after the reaction.

The mesoporous carbon cryogels are crucial in minimising congestion within the catalyst by allowing intermediate products and by-products to diffuse away [649], thereby reducing the risk of unwanted reactions or coking [650].

The study highlights the importance of a balanced ratio of Brønsted to Lewis acid sites (**Chapter 6, Section 6.5.2**) for optimal catalytic performance of mesoporous carbon. A maximum LA yield of 20.5% was achieved with a Brønsted to Lewis acid site ratio of 1.48. This finding aligns with research by Taghavi *et* al. on bifunctional catalysts, particularly MIL-101(Cr)–SO_3H, which indicates that a similar balance enhances catalytic activity with a molar ratio of Brønsted to Lewis acid sites of 1.1 [651]. Therefore, the catalytic conversion of biomass to LA is intricately linked to the acid sites, porous structure, and shape selectivity of the catalyst, especially its mesopores. An appropriate balance of these factors facilitates efficient sugar isomerisation and diffusion, ultimately maximising LA yield through the effective use of mesoporous carbon cryogel [149].

8.4 Proposed mechanism

This study suggests two main routes based on the non-detection of fructose and HMF in certain samples, which similar to Figure 8.5 [21] :

(1) Direct pathway, in which glucose may convert directly to HMF, which then rehydrates to form LA.

(2) Indirect pathway, in which glucose may first transform into fructose, which then dehydrates to HMF or preferentially degrades into other products than HMF.

For the direct pathway, a cyclic mechanism in a highly acidic environment could facilitate the conversion of glucose to HMF through an intermediate like 3-deoxyglucosane [3]. However, this route typically results in low HMF yields due to limited fructose involvement. Conversely, the indirect

pathway suggests that HMF forms during the glucose-to-fructose conversion, with 1-2, enediol as a crucial intermediate [645], indicating HMF's significant role as a precursor to LA.

The difficulty in detecting HMF highlights the challenges in selectively converting lignocellulosic biomass to HMF, presumably cause by cellulose's low reactivity and HMF's instability, which tends to quickly transform into LA and other by-products under hydrothermal conditions [652]. Previous research has shown that in the catalytic conversion to LA, cellulose first breaks down into glucose, which then forms HMF before dehydrating into LA and FA [653–656].

The high LA was achieved under optimal conditions (388 W, 0.131 g catalyst, 0.074 biomass, and 8.44 GVL:water ratio) This underscores the effectiveness of overall catalytic systems in achieving high selectivity of LA. Another study also proved that employing supercritical fluid ionic liquids (SFILs) combined with microwave irradiation has proven to be a highly selective method for producing LA from cellulose, bypassing the intermediate stages of glucose and HMF [657–658].

Several factors influence the selectivity of HMF and LA. Proper acidity adjustment is essential during HMF rehydration, especially when water interacts with the furan ring's C2-C3 bond. This prevents the dilution effect from reducing acid concentration, which is necessary for producing LA and FA as the final products [659]. Research indicates that acids with a $pK_a > 2$ are ineffective catalysts for converting HMF to LA, implying that this reaction does not catalyse itself [660]. Meanwhile, under more severe conditions—such as higher catalyst concentrations, increased temperatures, and longer reaction times—LA can break down into various byproducts [162, 597–601].

In this study, FA can be detected at low concentration (<5%) and gas bubbles were noticed after the microwave conversion in some of the samples conducted at higher temperature > 150 °C. This finding has been consistent with previous studies that found elevated acid levels can also cause LA gasification, yielding hydrogen (H_2), methane (CH_4), and carbon monoxide (CO) [602]. The often-lower yields were reported due to side reactions [598, 661–662], despite theoretically having the same molar yield as LA. Besides, the stability of FA is compromised under heat and acidic conditions [661], with Lewis acids significantly accelerating its degradation [193]. Above 180 °C, formic acid's thermal degradation can produce CO_2, CO, H_2, and water [661]. In acidic conditions, furfuryl alcohol may arise from HMF losing formaldehyde [663]. Additionally, a minor amount of levulinic acid carbonate could be produced through a Lewis acid-catalysed retro-aldol reaction [664]. From the findings in this study and supporting literature [21, 652], the reaction pathway for biomass conversion to LA through the hexose sugars pathway is inferred, as shown in **Figure 8.9**.

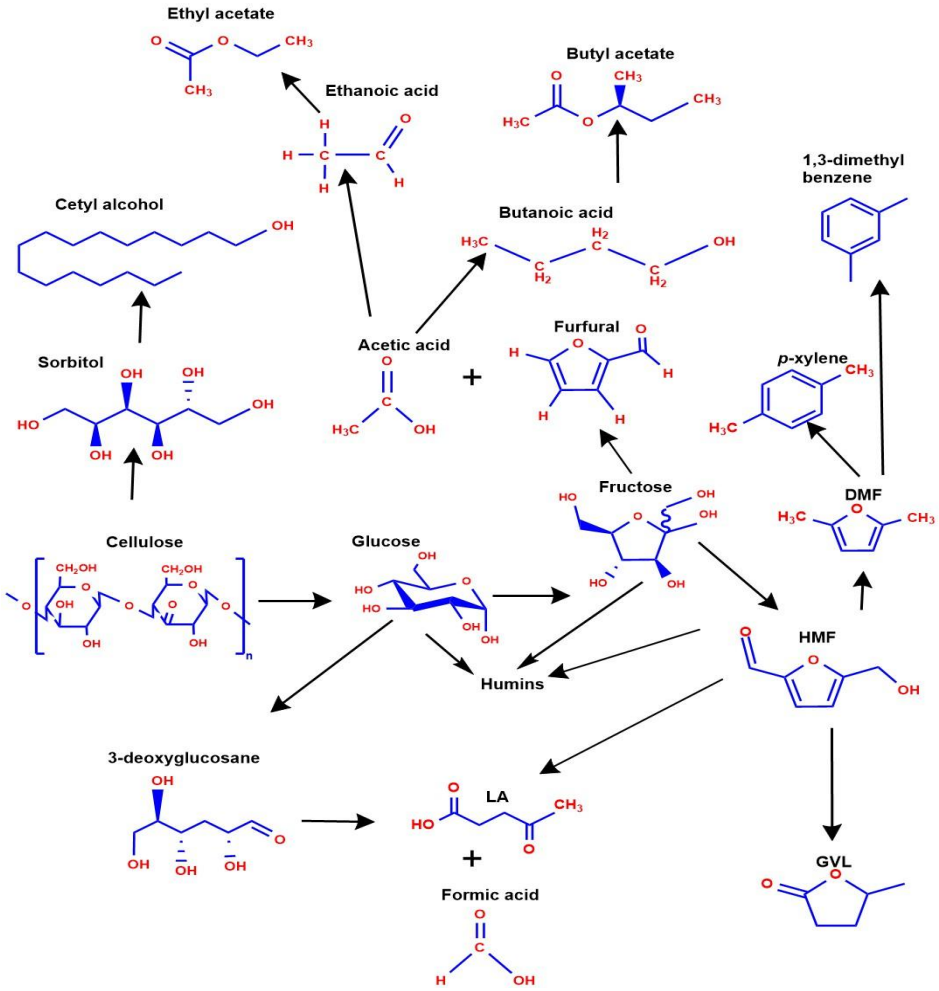

Figure 8.9 The proposed mechanism for cellulose hydrolysis to LA via carbon cryogel incorporated with $H_3PW_{12}O_{40}$-Nb_2O_5 in the GVL/water biphasic system.

8.5 Concluding remarks

In the carbon cryogel incorporated with the $H_3PW_{12}O_{40}$-Nb_2O_5 system and combined with the microwave-GVL treatment method, an operating temperature above 150 °C initiates a biomass conversion pathway highly favourable for LA formation. This pathway involves the hydrolysis of biomass to cellulose, the conversion of cellulose to glucose, and finally, glucose to LA. The process is influenced by the appearance of HMF at varying operating temperatures (110–150 °C), where the stability of HMF changes with temperature. At elevated temperatures, HMF can either favour LA formation or lead to the creation of other platform chemicals that deviate from the LA route. Additionally, HMF serves as an intermediate to DMF in the conversion process. This study, while aligning with established literature pathways, provides insights into a new intermediate formed due to microwave conversion. This is influenced by the rapid degradation of hemicellulose in the reaction medium and the potent GVL with microwave conversion, which can transform significant biomass components into valuable products such as *p*-xylene, furfural, 1,3-diethyl benzene, ethyl acetate, butyl acetate, and cetyl alcohol, alongside the targeted LA.

Understanding the mechanism of the carbon cryogel incorporated with $H_3PW_{12}O_{40}$-Nb_2O_5 is crucial as it highlights the importance of optimising acid properties and reaction conditions, such as temperature, to enhance LA selectivity. This catalytic system offers a novel alternative for biomass conversion to LA in a one-pot process, bypassing the conversion to HMF. Instead, a direct conversion from biomass to LA is preferred to maximise LA yield and selectivity, preventing interruptions at the HMF intermediate. The

carbon cryogel system also addresses the deactivation of Lewis acids, which is vital for glucose isomerisation. $Nb_2O_5.nH_2O$, providing major Lewis acid sites, retains its acidity even in the presence of water, advantageous for reactions requiring water for the rehydration of HMF to LA. This offers a solution to replace water-sensitive Lewis acids from metal chlorides and addresses the hydrothermal instability of zeolites commonly used for hydrolysis to LA.

The detailed study of the reaction pathway and mechanism of the carbon cryogel catalyst in this chapter sets the stage for the following chapter's focus on catalyst recycling studies. Understanding the optimal conditions and mechanisms for LA formation helps to identify challenges related to catalyst deactivation and by-product formation. This knowledge is essential for developing effective recycling strategies that maintain catalyst activity and selectivity over multiple cycles. By addressing these challenges, the study aims to enhance the sustainability and economic viability of the catalytic system, ensuring consistent benefits in large-scale applications.

Chapter 9

Recycling Studies on the Conversion of Oil Palm Mesocarp Fibre to Levulinic Acid Using Lignin-Derived Cryogel Incorporated with $H_3PW_{12}O_{40}$-Nb_2O_5

9.1 Introduction

Recycling studies of the $H_3PW_{12}O_{40}$ catalyst are essential for overcoming the challenges associated with its recovery from aqueous solutions [665]. A significant issue is its tendency to form a liquid-like phase, which complicates extraction and reuse. Addressing this challenge is vital for enhancing efficiency in large-scale production and promoting sustainable industry practices. Developing a robust catalytic system via carbon cryogel incorporated with $H_3PW_{12}O_{40}$-Nb_2O_5 that retains activity over multiple cycles is crucial to navigating these obstacles.

Catalyst recycling in biomass conversion to LA plays a central role in green chemistry, improving both economic efficiency and environmental sustainability [90]. The regeneration process involves removing impurities and restoring active sites, with specifics varying based on catalyst type, biomass, and reaction conditions such as temperature, pressure, and solvent [666]. Different biomass types can introduce varying impurities or structural components that impact catalyst interactions, thereby affecting catalyst performance and regeneration potential. Additionally, the acid strength and stability of the catalyst are critical for determining its recyclability without a loss in effectiveness.

A thorough understanding of these factors is vital for optimising the recycling process. A deep understanding of biomass conversion mechanisms to LA is key to enhancing catalyst recycling. By examining how catalysts interact with biomass components, researchers can design more effective regeneration processes. Insights into reaction intermediates and pathways help identify factors that lead to catalyst deactivation, which can be addressed during recycling to ensure prolonged efficacy.

Minimising humin formation, a by-product of biomass conversion, is closely linked to the recycling process [667]. Efficient recycling can significantly reduce humin production, leading to improved LA yields. By understanding mechanistic pathways, researchers can develop strategies to suppress humin production, thereby enhancing the overall efficiency of the system [668].

This chapter emphasises the evaluation of catalyst regeneration and reusability by characterising regenerated catalysts and comparing them with alternatives. Such studies are crucial for assessing the efficacy of the carbon cryogel system over multiple recycling cycles. By evaluating cost-effectiveness while maintaining LA yields, this research aims to ensure that advancements in reaction pathways are scientifically groundbreaking, economically viable, and environmentally sustainable.

9.2 Catalyst regeneration and reusability

One of the primary advantages of solid catalysts over liquid catalysts lies in their reusability. To assess the performance and stability of the former, an optimised carbon cryogel was chosen for LA production from dewaxed oil palm mesocarp fibre (DOPMF) at 388 W for 2 min, utilising 130 mg of catalyst (for the fresh cycle) and 70 mg of DOPMF following the optimised reaction conditions obtained in the previous objective (refer **Chapter 6, Section 6.6**). In **Figure 9.1**, the reusability of carbon cryogel incorporated with $H_3PW_{12}O_{40}$-Nb_2O_5 is examined over eight cycles, showcasing a gradual decrease in LA efficiency from 97.4% in the fresh cycle to 52.8% in the last cycle, equivalent to a 12% LA yield at the last cycle. It was observed that the LA yield decreased by approximately 8% after completing the last cycle.

However, despite this reduction in efficiency, **Figure 9.1** highlights the percentage of catalyst loss concerning mass loading from the fresh cycle. The data indicates that the catalyst loss reached 31.5% after eight cycles. The diminishing LA yield in each cycle may be attributed to the loss of catalytic activity during the washing and regenerating process, as suggested by previous studies [538, 554]. In this study, a batch reactor was employed, where after each catalytic cycle, the catalyst underwent a regeneration process involving washing (**Figure 9.2**) and calcination to remove adsorbed by-products before being reused in subsequent cycles. Despite the loss observed after eight cycles, the catalytic activity remains promising. Comparable to the first five cycles, the carbon cryogel retains 81.8% of its activity, with only an 18.2% loss. This performance is consistent with other studies [38, 635, 653], and is considered satisfactory for promoting the economic viability of its reuse.

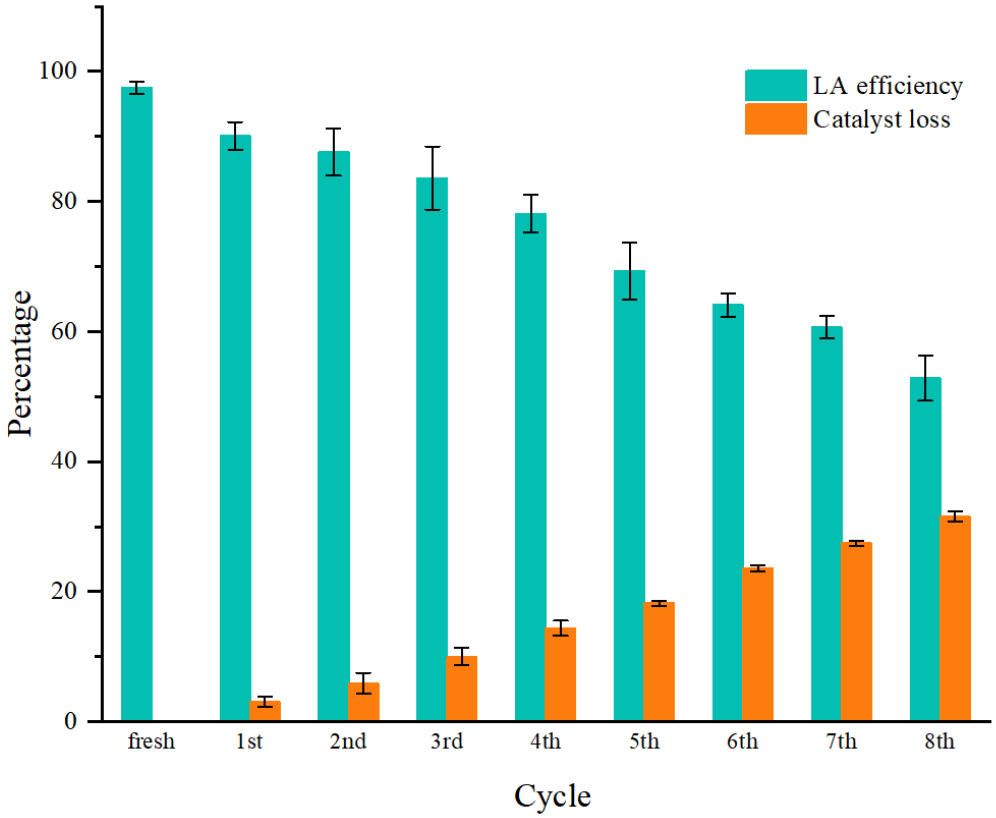

Figure 9.1 Recycling of carbon cryogel for eight consecutive cycles. After each cycle, the remaining catalyst was reused for the subsequent cycle without adding fresh catalyst.

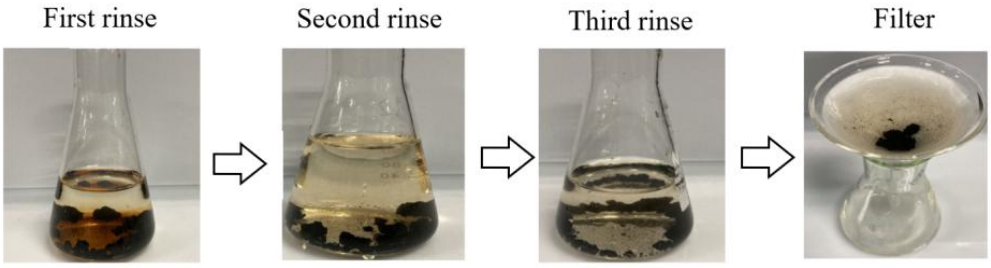

Figure 9.2 The washing steps for carbon cryogel are carried out until the water is clear to remove any impurities, including soluble humins, that may have deposited on the catalyst.

9.3 Characterisation of regenerated catalyst

Exploring the potential leaching of $H_3PW_{12}O_{40}$ and Nb_2O_5 from the carbon cryogel into the solution, the analysis focused on experimental samples. These samples utilised the optimised carbon cryogel discussed in **Chapter 6 (Section 6.4, Table 6.6)** and the recycled carbon cryogel employed after the eighth cycle. The objective was to assess any structural changes in the catalyst, both initially and after multiple recycling events.

Figure 9.3 presents the XPS spectrum, which shows a similarity in the surface functional groups and elements between the fresh and recycled carbon cryogels. **Figure 9.4a** depicts the high-resolution C 1s spectra for both cryogels, revealing three dominant peaks. The peak at roughly 285.4 eV is associated with C–C bonds (sp^2 hybridised carbon), the one near 286.9 eV with C–O bonds, and the peak close to 289.1 eV with C=O bonds. In the recycled carbon cryogel's C 1s spectra, there is a noticeable decrease in the C–C peak's intensity, while the C–O and C=O peaks' intensities have increased. This change is linked to the presence of inorganic metal salts such as potassium, calcium, magnesium, and sodium salts in natural biomass, which can leach into the aqueous solution. These metal ions, once leached, can lead to the deactivation of the catalyst during biomass hydrolysis by replacing the protons on the solid acid catalysts [655–656]. Accumulation of by-products or contaminants from the biomass sample during the conversion process may also interfere with the chemical structure of the catalyst.

Repeated calcination for recycling the catalyst can cause thermal breakdown of chemical species, leading to oxidation and changes in the C–C, C–O, and C=O bonds[654]. **Figure 9.4b** shows an increase in C=O and C–O

bond intensities at approximately 530.8 eV and 534.2 eV, suggesting that oxidation during recycling exposes reactive species on the carbon cryogel's surface, forming new chemical bonds [654, 657]. Changes in these bond peaks may result from interactions with oxidised metal species. Additionally, a slight rise in intensity at about 529.8 eV in **Figure 9.4b** could indicate the presence of metal oxides like niobium or tungsten oxide. The O 1s spectrum identifies peaks at 529.8 eV, characteristic of W–O–W or Nb–O bonds, and an additional peak at 530.8 eV, which intensifies post-recycling, indicative of C=O bonds. A pronounced peak at 535.5 eV corresponds to surface water molecules, mirroring the O1s binding energy in water-related deposits.

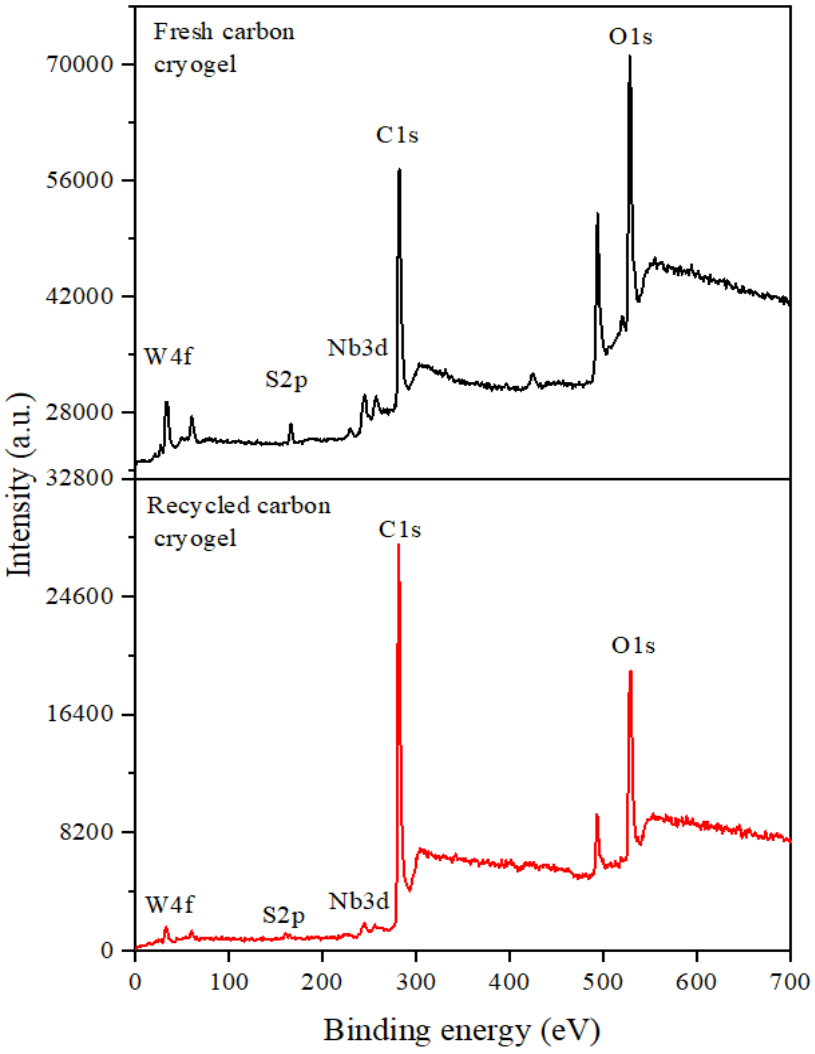

Figure 9.3 Full survey of XPS spectra of carbon cryogels.

Figures 9.4c, **d**, and **e** indicate a slight reduction in the primary elements of the acid catalyst ($H_3PW_{12}O_{40}$ and Nb_2O_5), hinting at minor leaching. Nonetheless, this does not greatly affect catalyst efficiency, which drops from 97.4% to 52.8% after eight cycles. The slight decline in the carbon cryogel's performance could be due to the loss of some tungsten, niobium, and phosphorus. Xu *et* al. observed similar leaching effects of active sites and pore blockages by hydrolysis residues during the washing process [554]. Still, the carbon cryogel outperforms the raw $H_3PW_{12}O_{40}$ catalyst in reusability, which easily disperses in the solvent, complicating recycling.

The detailed XPS analysis of W 4f in **Figure 9.4d** uncovers three distinct W 4f doublets, with the $4f_{7/2}$ peaks positioned at 31.4, 36.4, and 38.5 eV, consistent across both new and reused carbon cryogels. According to Jalil *et* al., the intensity of peaks within $HxWO_3$ is a measure of W–O bond covalency, with greater intensity signifying stronger bonds [658]. **Figures 9.4b** and **9.4d** demonstrate consistent peak intensity for both the original and the recycled carbon cryogel, suggesting the preservation of robust W–O covalency. This implies that the Keggin structure of the $H_3PW_{12}O_{40}$ molecule remains stable after multiple recycling processes. Additionally, the detection of Nb $3d_{5/2}$ and Nb $3d_{3/2}$ at 202.4 eV and 207.6 eV, respectively, reveals that C and O contributions predominantly arise from Nb–C and Nb–O bonds [669–670] . The enhanced Nb_2O_5 peak observed in the recycled cryogel may be attributed to a reduction in Nb–C bonding caused by catalyst degradation during successive recycling. Consequently, more Nb_2O_5 becomes exposed on the surface. These findings align with a previous study [671], which reported similar binding energies for the Nb3d line, consisting of two peaks representing pentavalent Nb^{5+}, and the O 1s line, with two peaks at 529.7 and 531.3 eV corresponding to oxygen in the Nb–OH and Nb–O–P moieties, respectively.

Despite a lower intensity or slightly reduced amount of phosphorus in the reused carbon cryogel, a sharp peak was observed (**Figure 9.4e**), influenced by calcination at 100℃ for each recycling cycle. The P2p line comprised $P2p_{3/2}$ and $P2p_{1/2}$ at binding energies of 131.3 and 132.2 eV, respectively, corresponding to the pentavalent tetra-coordinated phosphorus P^{5+}. Changes in phosphorus binding states during the recycling process also contribute to sharper peaks. According to Jalil *et* al., the broadening peak in the reused carbon cryogel

spectrum suggests the deterioration of surface crystallinity, resulting from the destruction of the Keggin structure of $H_3PW_{12}O_{40}$ molecules and an apparent enrichment of the surface with phosphorus [658].

Interestingly, thiol groups (SO_3H) at 165.8 eV were also observed in this study (**Figure 9.4f**), possibly due to the presence of sulphur in the used alkaline lignin for carbon cryogel formation. The broadening of the thiol group peak could also suggest the reduction of sulphur species when interacting with water during hydrolysis. The introduction of water may induce reductive processes, converting sulphur-containing groups to lower oxidation states and lower energy level to 161.0 eV. The observed shifts in metal sulphate peak may be indicative of the catalytic effects on the hydrolysis reaction. SO_3H functionalised group has become the co-catalyst sites for the acid treated catalysts that can enhance the conversion of biomass to LA despite alterations in the chemical compositions.

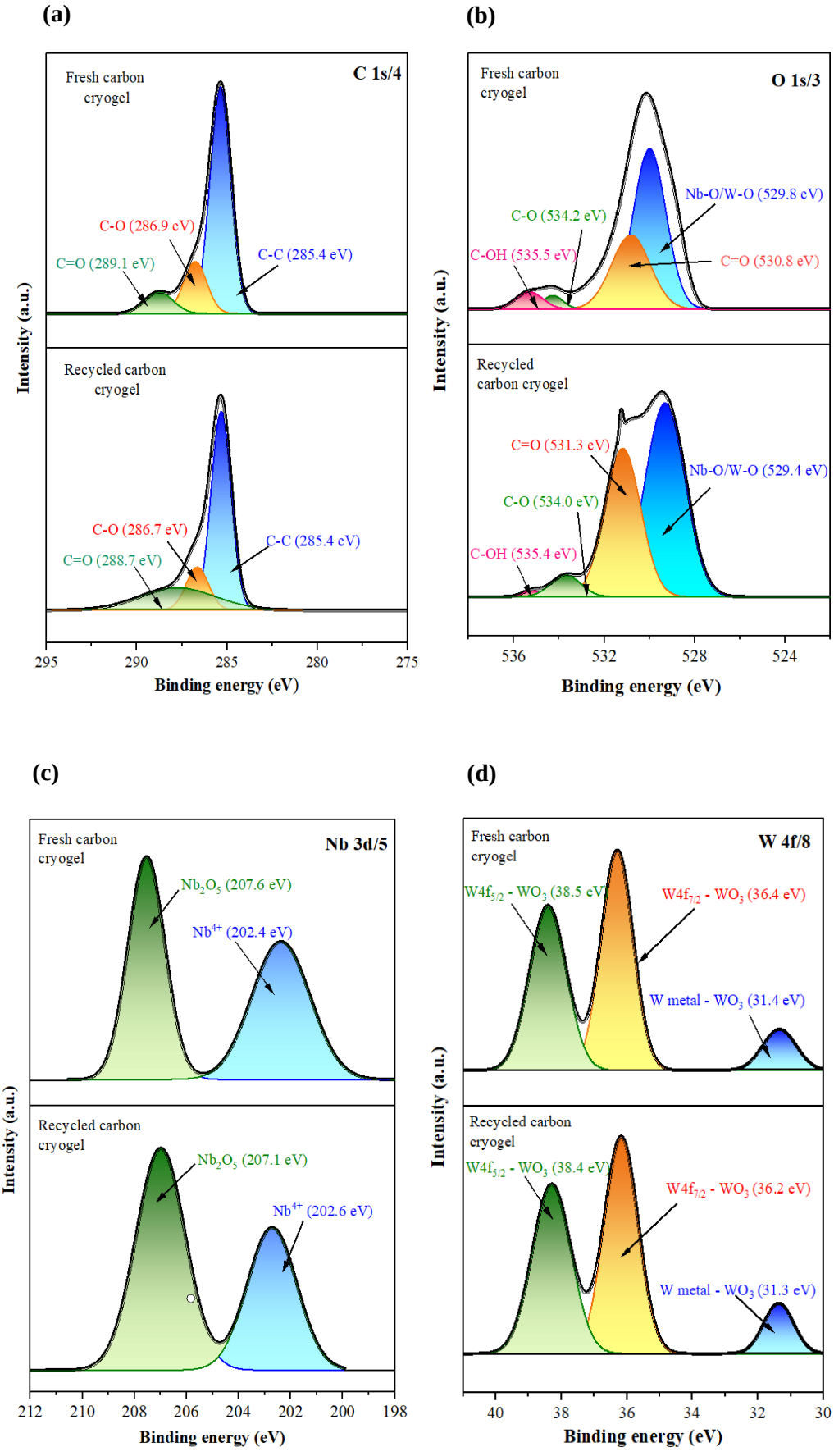
(a)
Fresh carbon cryogel
C 1s/4
C-O (286.9 eV)
C=O (289.1 eV)
C-C (285.4 eV)
Recycled carbon cryogel
C-O (286.7 eV)
C=O (288.7 eV)
C-C (285.4 eV)
Intensity (a.u.)
295 290 285 280 275
Binding energy (eV)
(b)
Fresh carbon cryogel
O 1s/3
Nb-O/W-O (529.8 eV)
C-O (534.2 eV)
C-OH (535.5 eV)
C=O (530.8 eV)
Recycled carbon cryogel
C=O (531.3 eV)
Nb-O/W-O (529.4 eV)
C-O (534.0 eV)
C-OH (535.4 eV)
Intensity (a.u.)
536 532 528 524
Binding energy (eV)
(c)
Fresh carbon cryogel
Nb 3d/5
Nb2O5 (207.6 eV)
Nb4+ (202.4 eV)
Recycled carbon cryogel
Nb2O5 (207.1 eV)
Nb4+ (202.6 eV)
Intensity (a.u.)
212 210 208 206 204 202 200 198
Binding energy (eV)
(d)
Fresh carbon cryogel
W 4f/8
W4f5/2 - WO3 (38.5 eV)
W4f7/2 - WO3 (36.4 eV)
W metal - WO3 (31.4 eV)
Recycled carbon cryogel
W4f5/2 - WO3 (38.4 eV)
W4f7/2 - WO3 (36.2 eV)
W metal - WO3 (31.3 eV)
Intensity (a.u.)
40 38 36 34 32 30
Binding energy (eV)

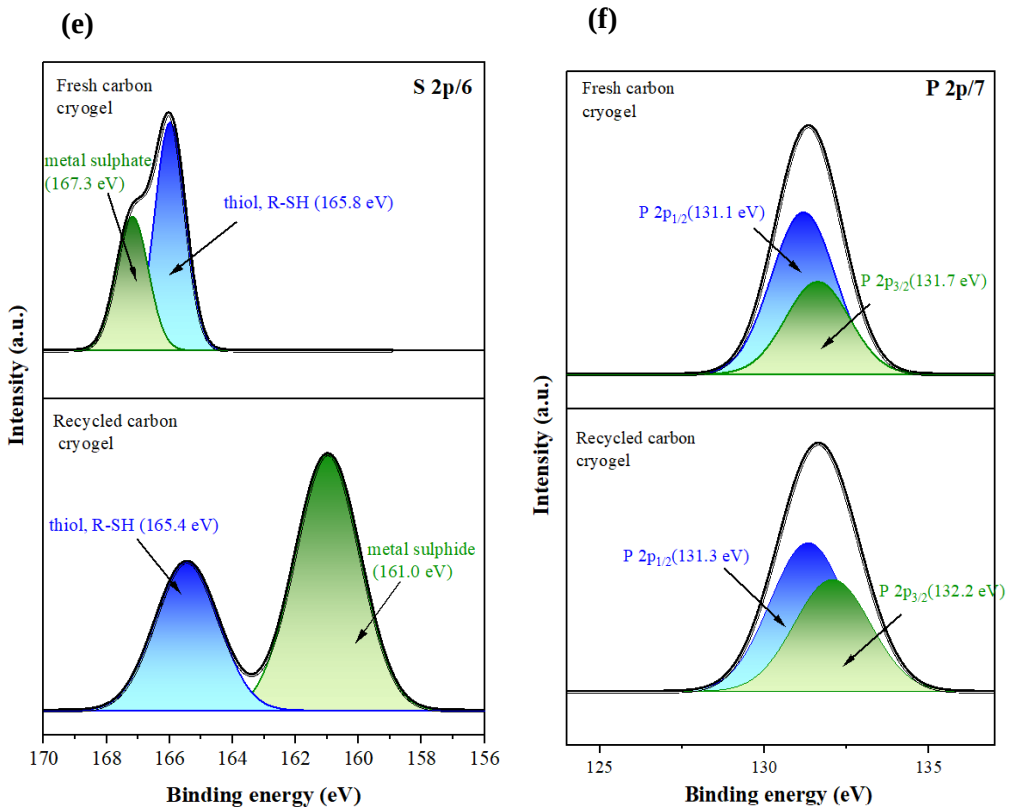

Figure 9.4 The XPS spectra of carbon cryogels, with peaks representing the elements (a) carbon; (b) oxygen; (c) niobium; (d) tungsten; (e) phosphorus and (f) sulphur.

Figure 9.5 presents the FTIR spectra of both fresh and used carbon cryogels, revealing a slight shift in the stretching frequencies. Notably, the decreasing C–O–C stretching at 1041 cm^{-1} (associated with glycosidic linkages) and the C–O stretching related to ether or ester groups at 1132 cm^{-1} in recycled carbon cryogels indicate possible catalyst leaching. Despite this, the catalyst retains a degree of stability—there is no significant shift in the FTIR stretching frequencies. The FTIR data suggests that the structural integrity of the catalyst's active sites remains largely intact, indicative of stability [672].

Additionally, a new bond vibration stretching was observed in **Figure 9.5** at the absorption peak 3750 cm^{-1}. This may indicate the presence of an O–H functional group from alcohol compounds like cetyl alcohol (as mentioned in

Chapter 8, Section 8.2), co-produced at low concentrations during the conversion process. Interestingly, the 1670 cm^{-1} peak, typically indicative of glucose-derived humins, was not observed for both fresh and recycled carbon cryogels. Instead, the appearance of 1702 cm^{-1} stretching could possibly be attributed to carbonyls in saturated aliphatic ketones, supporting the catalyst's selectivity to transform to HMF intermediate and then LA rather than forming humins [652].

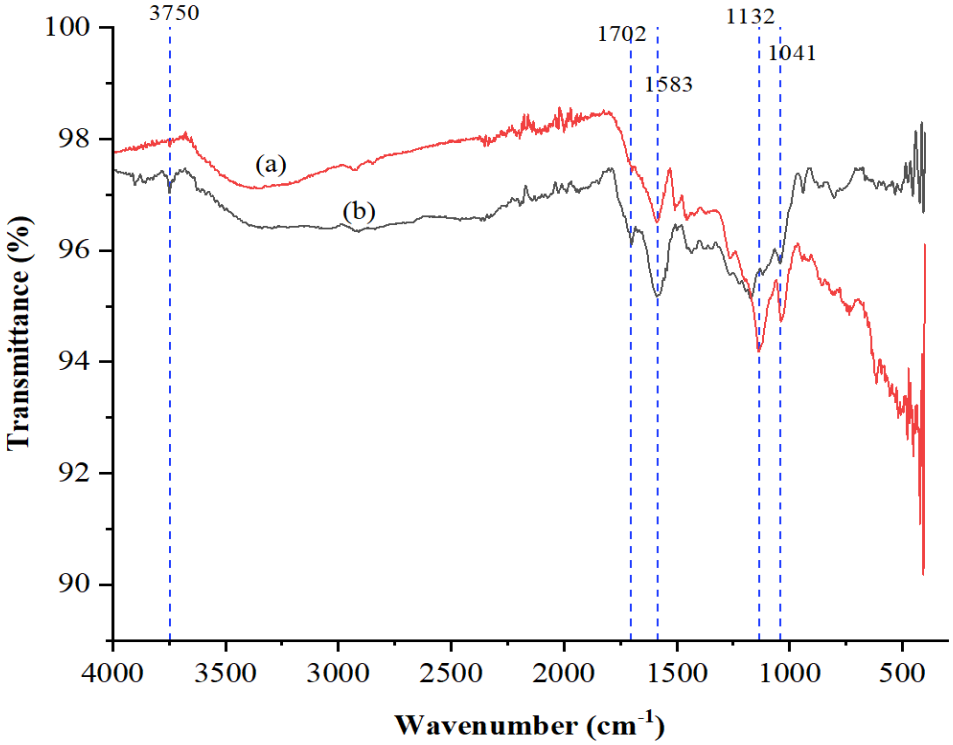

Figure 9.5 FTIR spectra of carbon cryogels (a) pre-recycling and (b) post recycling after 8th cycles.

However, a small amount of humin may still be presumed to be deposited at the surface of the catalyst as some active sites are leaching. The changes in vibrational behaviour will slightly alter the composition and rearrangement of C and O. This aligns with the EDX mapping in **Figure 9.6**, which shows the difference in C and O distribution within the carbon cryogel. Specifically, there

was an agglomeration of C and O in a specific area where certain locations on the catalyst had increased C and O concentrations, potentially creating a conducive environment for humin formation. The EDX reveals that the C and O content in recycled carbon cryogel was 66.00% and 23.31%, respectively, compared to fresh carbon cryogel, which contained 53.89% C and 24.41% O, confirming humin formation. Overall, the slight reduction in oxygen content could be attributed to the removal of surface-adsorbed oxygen during the post-calcination process for each recycling step.

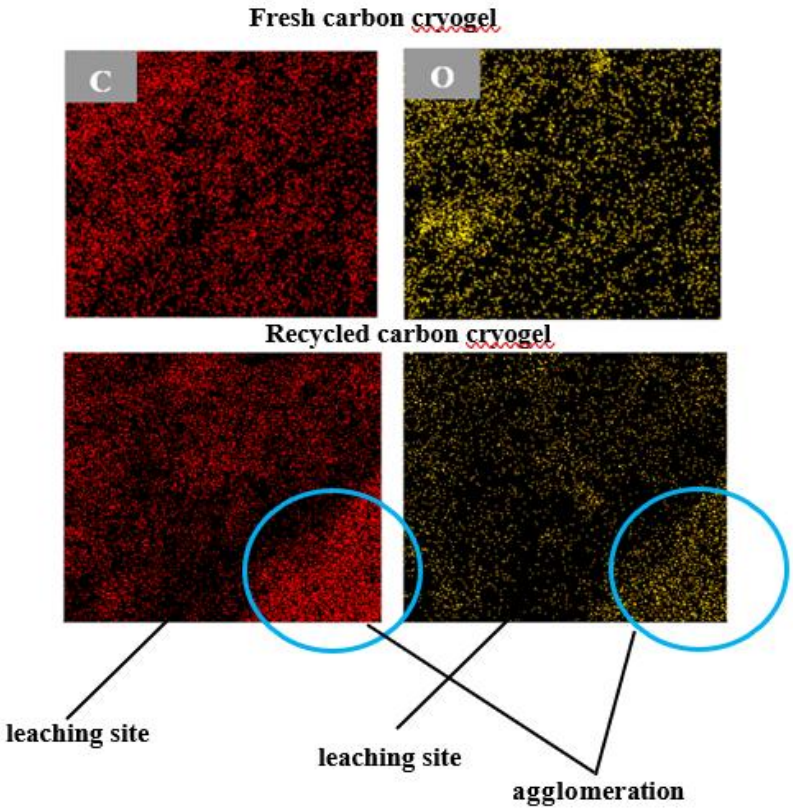

Figure 9.6 EDX mapping for C and O elements in carbon cryogel before and after recycling.

Furthermore, although humin formation may occur in small amounts from HMF-derived humin, it is promoted by sufficient acidity of Brønsted acid sites [673]. This is evident from the vibration stretching of C=C at 1583 cm^{-1},

comparable to the findings achieved by Tsilomelekis *et* al. [652], who found C=C stretching at 1525 cm^{-1} when carbohydrates were used as substrates. These results from FTIR align with the product analysis obtained from HPLC-VWD, where HMF was not observed in some samples, probably due to high microwave power suppressing HMF formation to LA and humins.

While humins can be oxidatively converted to low-molecular-weight carboxylic acids using polyoxometalate catalysts [674], the potential of phosphotungstic acid from this acid group is evident in this study. The main products of this oxidative valorisation are acetic acid, formic acid, and CO_2 [674]. This is supported by the potential products found in preceding chapters, indicating the derivatives of acetic acid that form acetate esters. Additionally, the use of GVL as a polar aprotic solvent could help stabilise the carbonyl group against nucleophilic attack, thus selectively favouring LA formation over humins. Zandvoort *et* al. postulated that humin nanoparticles may form in the presence of polar aprotic solvents like DMSO, but the growth of humin nanoparticles is further retarded, resulting in smaller humin sizes (~200 nm) [675].

Table 9.1, derived from XRF analysis, illustrates the diminishing composition of oxide compounds in carbon cryogel before and after eight cycles of recycling, consistent with the findings from XPS analysis. **Figure 9.7** visually represents the elemental distributions within the carbon cryogel before and after the recycling process. The XRF results reveal minimal impurities in the carbon cryogel, likely originating from alkaline lignin and xanthan gum raw materials; however, all impurities are deemed negligible, constituting trace elements present in amounts less than 0.1%.

Table 9.1 Oxide components in carbon cryogels.

Compound	Mass percentage (%)	
	Fresh carbon cryogel	**Recycled carbon cryogel**
Nb_2O_5	8.7	2.2
WO_3	64.6	58.4
P_2O_5	1.25	0.51
SO_3	19.3	14.6

Despite changes in the elemental composition, the Raman spectra presented in **Figure 9.8** highlight consistent features in both the fresh carbon cryogel and the recycled carbon cryogel. These features manifest as two distinct peaks at 1350 cm^{-1} (D band) and 1576 cm^{-1} (G band) [676]. The broad D band signals the presence of a significant number of defects [677]. An insightful metric for assessing the degree of disorder or defects in carbonaceous materials is the intensity ratio of the D band (disorder-induced band) to the G band (graphitic band), denoted as I_D/I_G.

The I_D band originates from disorder-induced phonon modes, indicating the existence of defects, disorder, or structural imperfections in the carbon material. In contrast, the I_G band is associated with the in-plane stretching of sp^2-hybridised carbon atoms, reflecting an ordered, graphitic structure. A higher I_D/I_G ratio implies a greater level of disorder or defects in the carbon structure.

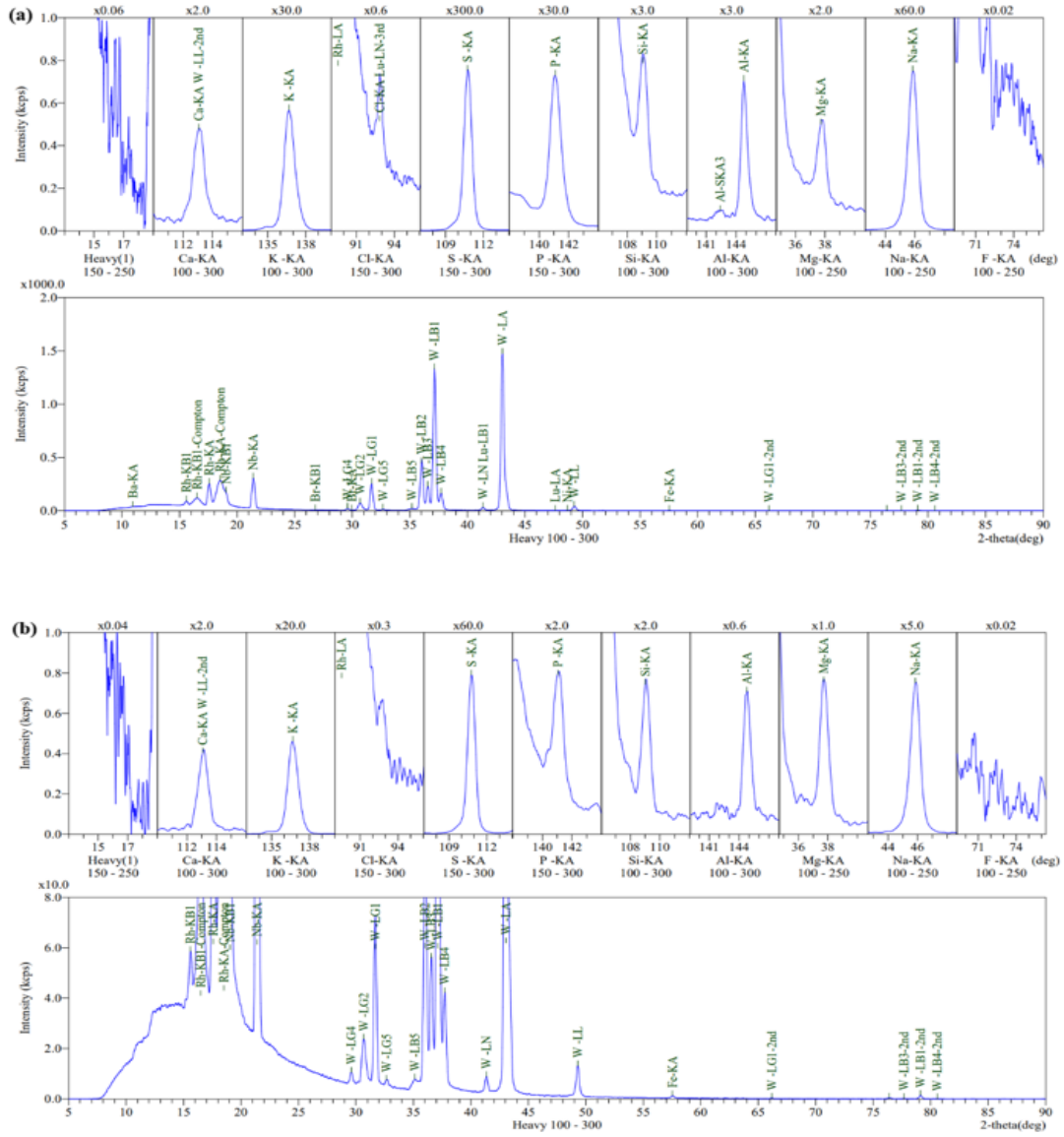

Figure 9.7 The distribution of elements based on XRF analysis in (a) fresh carbon cryogel and (b) recycled carbon cryogel.

In this investigation, both the fresh carbon cryogel and the recycled carbon cryogel exhibited I_D/I_G ratios of 0.54 and 0.58, respectively. These values, comparable to the I_D/I_G of carbon cryogel reported by Liang *et* al. in the range of 0.8–0.9 [678], suggest a consistent structural characteristic. The minor increase in defects (0.04) observed in the recycled carbon cryogel after eight cycles indicates the potential of the carbon cryogel as an efficient catalytic system for biomass conversion to LA.

This slight increase in defects may be attributed to the accumulation of defects in the carbon structure during the washing and regeneration processes of the catalyst. The recycling of the carbon cryogel could potentially introduce new defect sites; however, these changes are not significant enough to compromise the overall efficiency of the catalytic system.

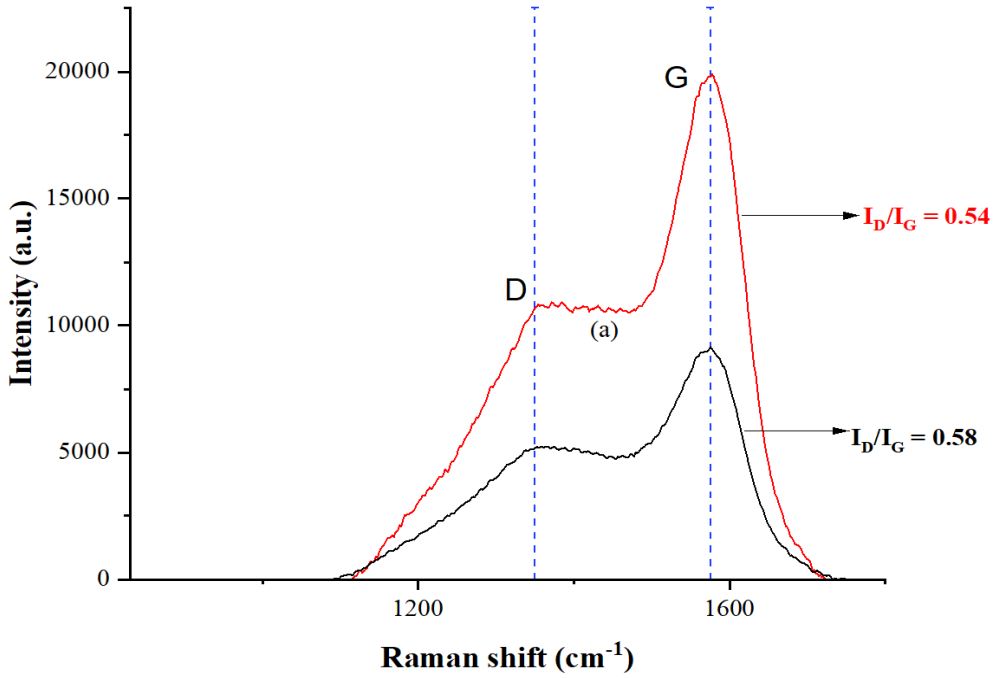

Figure 9.8 Raman spectra of **(**a) fresh carbon cryogel and (b) recycled carbon cryogel.

9.4 Comparison with alternative catalysts

Table 9.2 provides a comprehensive overview of acid catalysts utilised for multiple cycles in the production of LA across various feedstocks and catalytic types. The recyclability of these catalysts is crucial for achieving cost-effective LA production using solid acid catalysts. The application of carbon cryogel in biomass conversion to LA aligns with findings in other studies (refer to **Table 9.2**).

While some catalyst loss was anticipated due to active site leaching into the medium during hydrolysis, the carbon cryogel efficiency remained above 83% in producing LA after the first three cycles, in contrast to 97.4% in the fresh cycle. Catalyst regeneration was measured at approximately 90%. The catalyst efficiency for LA production gradually declined to 52.8% after eight cycles, indicating economic potential for repeated use, with a 12% LA yield. Tiong *et* al. reported a similar loss of catalytic sites (25%) after six cycles using ionic liquid, resulting in a 7% of final LA yield [679]. While Liu *et* al. assessed the reusability of Fe-NbP under optimal reaction conditions (0.056 M glucose, 32.3 mol% Fe-NbP, 10 mL deionised water; 3 h, and 180 °C). Following the catalytic reaction, the LA yield experienced a slight decrease from 64.2% to 54.8% over four consecutive cycles. Notably, this decrease of less than 10% in LA yield after four cycles is comparable to the findings in this study, where the LA yield decreased by less than 5% after the same number of cycles [211].

Hurst *et* al. suggested catalyst recovery through calcination at 450 °C, achieving a 63% recovery rate (excluding 12% due to catalyst contamination) [38]. The non-calcined SZR catalyst exhibited a substantial drop in LA yields to 25.5% in the third cycle, compared to a 42.3% yield with the calcined catalyst. Recycled catalysts analysed via EDX revealed that the uncalcined catalyst surface had a higher surface carbon content (28.6 wt.%) than the calcined catalyst (20.4 wt.%). This increase suggests the adsorption of humins and other thermally stable carbonaceous residues at 450 °C. Higher-temperature calcination may further reduce the carbon content; however, studies indicate that synthetic humins remain thermally robust at higher temperatures, with only 66 wt.% decomposition at 1000 °C.

Table 9.2 Comparisons for different recycling methods for various catalyst types.

Ref.	Catalyst	Method of recycling	Number of recycling	First Cycle	Last cycle	Catalyst loss
[635]	Dicationic ionic liquids	Liquid-liquid extraction	4	48.2	47.4	5%
[38]	Sulphated Zirconia—HCl		3	63.8	42.3	< 0.1%
[32]	CP-SO3H-1.69	Filtration, washing and oven-dried at 80°C overnight	4	45	12	< 1
[531]	20% Nb/Al oxide	–	5	20.0	14.7	No significant loss
[554]	Carbon foam-supported $H_5AlW_{12}O_{40}$	Oven-dried at 80°C for 12 h	5	60.9	50.6	–
[653]	Superacid	Filtration, calcination at 580°C for 5 h	3	67.0	11.1	–
[680]	Acidic ionic liquid ([SMIM][$FeCl_4$])	Liquid-liquid extraction	5	68	24.8	No significant loss
[679]	$InCl_3$-[HMIM][HSO_4]	Liquid-liquid extraction	5	18.4	3.7	25%
[681]	[C_4SO_3Hmim][HSO_4]	Liquid-liquid extraction	4	63	65	–

9.5 Concluding remarks

The use of carbon cryogel as a catalyst for biomass conversion, despite undergoing slight chemical changes over multiple cycles, demonstrates promising reusability. Analyses using XPS, FTIR, and XRF reveal alterations in the C–C, C–O, and C=O bonds, as well as changes in the elemental composition, particularly in phosphorus (P), niobium (Nb), and tungsten (W). The pronounced phosphorus peak observed in XPS spectra post-recycling suggests that calcination at 100 ℃ effectively preserves the structural stability of the catalyst.

Although minor leaching of catalyst components is noted, the overall efficiency of the reused carbon cryogel remains relatively high, decreasing from 97.4% to 52.8% over eight cycles. This marginal decrease is attributed to the loss of W and P, which corroborates findings from previous studies. Despite these changes, the carbon cryogel proves to be a robust and potentially reusable catalyst, offering advantages over the raw catalyst in biomass conversion processes.

The subsequent chapter will delve into the economic value of microwave conversion of OPMF to LA using the carbon cryogel catalytic system. This assessment will include a detailed cost analysis that justifies the role of this system in sustainable LA production. By linking recycling studies to cost analysis, the chapter aims to demonstrate how maintaining catalyst efficiency over multiple cycles can optimise production costs and enhance the economic feasibility of this catalytic process. Understanding these financial implications is crucial for scaling up the technology for industrial applications, ensuring that the advances in catalyst reusability translate into tangible economic benefits.

Chapter 10

Cost Analysis of Microwave Conversion of Oil Palm Mesocarp Fibre to Levulinic Acid Using Lignin-Derived Cryogel Incorporated with $H_3PW_{12}O_{40}$-Nb_2O_5

10.1 Introduction

The global market for LA is poised for significant growth in the coming years, driven by escalating demand for sustainable and renewable chemicals. As of 2021, the cost of LA was estimated to be approximately $3–$5 per pound (equivalent to $7–$11 per kilogram), although this figure can vary based on several factors. Notably, ongoing advancements in production technology and economies of scale may lead to a decline in LA production costs, making LA a promising and cost-effective alternative to traditional petrochemicals.

Two primary technologies dominate the global LA market: the Biofine Process and acid hydrolysis. The Biofine Process, patented by Biofine Renewables LLC, has been successfully demonstrated at pilot scale [96]. This innovative process involves the hydrolysis of lignocellulose using dilute sulphuric acid (H_2SO_4) to produce LA, furfural, formic acid (FA), and lignin char [682]. Operating within a continuous two-stage reactor system under optimal conditions, the Biofine Process achieves LA yields of 70–80%, corresponding to a 50% mass yield based on C6 sugars [683]. Additionally, FA constitutes 20% of the mass yield, while water-insoluble humins account for the remaining product mass [47]. The popularity of the Biofine Process stems from its superior production efficiency [96]. However, concerns about the use of toxic

and non-recyclable mineral acids in commercial production necessitate the transition to a greener, renewable, and cost-effective catalyst that maintains product efficiency and selectivity [683].

Building on the insights gained in Chapter 9, Chapter 10 evaluates both the economic and environmental feasibility of catalysts used in LA production. This chapter specifically examines the innovative lignin carbon cryogel incorporated with $H_3PW_{12}O_{40}$-Nb_2O_5, comparing its costs and sustainability against conventional systems. The analysis highlights the potential of these advanced catalysts to reduce production costs and environmental impact, emphasising the necessity for sustainable practices in the chemical industry.

Sustainable catalysts are crucial for scaling operations to an industrial level without compromising environmental integrity. As production scales, demands for raw materials and energy increase, potentially elevating costs and environmental footprints. Catalysts like the lignin carbon cryogel with $H_3PW_{12}O_{40}$-Nb_2O_5 address these challenges by enhancing resource efficiency and reducing waste. Their ability to maintain high activity and selectivity over multiple cycles ensures consistent production quality and reduces the need for frequent catalyst replacement, thereby lowering long-term operational costs. Moreover, the use of eco-friendly catalysts aligns with global sustainability goals, promoting a greener chemical industry capable of meeting market demands while adhering to environmental regulations. This alignment is essential for gaining consumer trust and securing regulatory approvals, ultimately facilitating successful large-scale adoption of innovative catalytic processes.

10.2 Economic feasibility analysis

Table 10.1 presents a cost analysis for manufacturing carbon cryogel catalysts using the Design-to-Cost (DtC) and Activity-Based Costing (ABC) methods. This analysis focuses exclusively on direct material costs, omitting labour and other non-material expenses, to provide preliminary insights into economic feasibility. Excluding labour costs simplifies the initial estimation, allowing for a quick assessment of cost feasibility. This approach highlights potential savings through material selection and usage while integrating cost considerations into the design process to ensure the final product meets cost targets. The ABC method further aids in allocating overhead costs, such as electricity, to specific cost-driving activities, thus improving understanding of the true production costs.

The costs associated with catalyst procurement, synthesis, and reactor operation for biomass conversion to LA are detailed in **Table 10.1**. The upstream cost related to feedstock acquisition is negligible due to the abundant, low-cost availability of OPMF, a byproduct of the palm oil industry. At the lab scale, producing a carbon cryogel catalyst costs RM 20.90 for 4 grams, equating to RM 5.23 per gram. This low cost is achieved by using environmentally friendly materials like lignin, xanthan gum, phosphotungstic acid, and niobium oxide. Under optimised conditions (**Chapter 6, Section 6.6, Table 6.16**), only 0.13 g of catalyst is needed for biomass conversion, with a cost of RM 0.68 for eight cycles.

Table 10.2 predicts a product yield of 29.4 g L^{-1} over eight cycles, comparable to literature values referenced in **Chapter 2, Section 2.3.3**. The cost of microwave conversion is RM 9.04 per fresh cycle and RM 8.36 per recycling

cycle, saving approximately 7.5% per recycling run. This system is cost-effective compared to conventional heating methods, which require longer durations (at least 2 h) and higher power consumption that eventually increase the overall cost of LA production [581, 684]. While the cost of GVL is currently high due to its commercial sourcing, it could become cost-competitive if derived from biomass through efficient conversion technologies.

For every 1 gram of carbon cryogel (costing RM 5.23), approximately 0.9 g of LA can be produced. To produce 50 g of LA, around 56 g of carbon cryogel is necessary, costing about RM 293. This preliminary cost is slightly lower than the commercial price of LA (RM 354 per 50 g from Sigma Aldrich). However, this estimate represents only a preliminary economic feasibility analysis, as it does not include other upstream and downstream costs such as transportation, packaging, waste management, and more. Despite these omissions, the lower estimated cost of carbon cryogel serves as a crucial baseline for preventing resource wastage on impractical or overly expensive options, and thereby guiding the selection of economically viable catalysts for potential scaling from laboratory to industrial production. The challenges of scaling up this production include maintaining consistent performance, addressing dynamic changes in mass and heat transfer, managing increased equipment and energy costs, ensuring quality control, and adhering to environmental and safety standards. Strategies to overcome these challenges involve rigorous intermediary testing, process optimisation with advanced simulation tools, the integration of scalability metrics, real-time monitoring, risk assessment, and compliance with environmental regulations. By implementing these practices, the goal is to ensure that scaled-up production not only meets desired

performance and cost targets but also successfully contributes to industrial applications.

Table 10.1 The overall cost of materials and process involved in the synthesis of carbon cryogel.

Cost breakdown	Condition	Power rating (kW)	Electricity cost (RM/kWh)	Price (RM)	Assumption
Raw material					
Lignin	2 g	–	–	1.40	8.49
Xanthan gum	0.8 g	–	–	3.38	
Phosphotungstic acid	0.468 g	–	–	1.93	
Niobium oxide	0.014 g	–	–	0.06	
t-butanol	20 mL	–	–	1.72	
Process					
Stirring	5.25 h	0.6	0.32	1.00	12.41
Hydrothermal	1 h, 180 °C	1.1	0.32	0.35	
Freezing	12 h, -20 °C	1.2	0.32	4.61	
Freeze drying	12 h, -40 °C	0.8	0.32	3.09	
Calcination	5 h, 300 °C	2.1	0.32	3.36	
Total[a]	4 g of carbon cryogel was produced				20.90
Total[a]	1 g of carbon cryogel was produced				5.23

[a]Estimated total cost of carbon cryogel produced during a single synthesis process.
[b]Estimated total cost of carbon cryogel for every 1 gram.

Table 10.2 The overall cost for microwave process for biomass conversion to LA.

Cost breakdown	Condition	Power rating (kW)	Price (RM)	Product (LA yield)		
				Cycle	Mass (%)	Concentration (g L^{-1})
Microwave conversion biomass to LA						
0.13 g carbon cryogel	Use for eight cycles	–	0.68	Fresh	22.1	4.6
				1st	20.5	3.6
				2nd	19.9	3.7
GVL	Use 4.916 mL for every cycle	–	8.31	3rd	19.0	3.4
				4th	17.7	4.2
				5th	15.8	2.7
Power	5 min heating up 5 min run 1 min residence time	1.15	0.05	6th	14.6	2.5
				7th	13.8	2.6
				8th	12.0	2.1
Total	Fresh cycle Recycling cycle		9.04 8.36		29.4 [a]	

[a]Total LA yield in concentration after 8th cycles.

10.3 Comparative cost analysis

Researchers are continually exploring innovative catalysts to enhance biomass conversion processes, focusing on improving efficiency, selectivity, and sustainability. These catalysts, which include homogeneous, heterogeneous, and ionic liquids, are essential for developing ecologically sound and economically viable methods for producing LA from biomass. However, determining their exact cost-effectiveness is complex due to various technical, economic, and environmental considerations. Key factors influencing costs include the quantity of catalyst needed, particularly during the transition from laboratory to industrial scale, as catalysts may exhibit different behaviours across scales. Despite their

potential, the economic viability of these emerging catalysts remains uncertain until they are proven at industrial scales.

Evaluating the economic viability of advanced catalysts in the biomass-to-levulinic acid process involves several critical considerations as represented in **Table 10.3**. While sulphuric acid offers a low cost of RM 5.23 per 100 g, the carbon cryogel, priced at RM 523 for the same quantity, appears significantly more expensive initially. However, this higher upfront cost is offset by the long-term benefits and cost savings associated with the carbon cryogel's reusability and efficiency.

Despite its higher initial cost, the carbon cryogel stands out due to its ability to be reused over eight cycles while maintaining a 52% LA efficiency, even in the final cycle. This reusability significantly offsets the initial investment, making the carbon cryogel a more sustainable and economically viable choice in the long run. In contrast, sulphuric acid is typically single-use and requires complex recycling processes, which can increase overall costs and environmental impact. The carbon cryogel's reduced environmental footprint further enhances its appeal. Unlike sulphuric acid, which is toxic and corrosive, the carbon cryogel aligns with industry shifts towards greener chemistry solutions, supporting sustainable biomass conversion. Safety concerns associated with catalyst handling and processing also favour the carbon cryogel, as it poses fewer risks compared to more hazardous alternatives.

When evaluating advanced catalysts, a total cost of ownership approach is crucial. This includes considering all costs from purchase to disposal, ensuring a comprehensive understanding of the catalyst's economic viability. By factoring in the carbon cryogel's long-term cost savings, environmental benefits, and

reusability, it becomes a compelling option for industries aiming to enhance sustainability and performance. In conclusion, while the initial cost of carbon cryogel is higher than conventional options, its efficiency, reusability, and reduced environmental impact present a strong case for adoption in the biomass-to-LA conversion process. This thorough evaluation highlights the importance of considering both immediate costs and long-term benefits when selecting catalysts for industrial applications.

Table 10.3 Key aspects for determining the economic viability of the catalyst.

Ref	Catalyst	Initial cost (RM/100 g)	Reusability	Cost per cycle (RM)	Efficiency (LA yield)[a]	Environmental impact	Safety concerns	Total cost of ownership (TCO)
[685]	Sulphuric acid	5.23	Single use	5.23	69.4%	Toxic, corrosive	Severe burns, harmful	High due to disposal costs
This study	Carbon cryogel	523.00	8 cycles	65.38	97.4%	Eco-friendly, less toxic	Lower risk, safer	Lower due to reusability
[686]	Ionic liquid ([SMIM][$FeCl_4$])	412.00	5 cycles	82.40	77.3%	Moderate environmental impact	Mildly corrosive	Moderate due to limited use
[687]	Hydrochloric acid	5.00	Single use	5.00	54.5%	Toxic, corrosive	Severe burns, harmful	High due to disposal costs
[653]	Solid superacid (S_2O_{82}−/ZrO_2−SiO_2-Sm_2O_3)	500.00	3 cycles	166.67	70.0%	Low environmental impact	Low risk, safer	Lower due to reusability
[688]	Cr/HY zeolite	480.00	4 cycles	120.00	66.1%	Moderate environmental impact	Toxic, requires careful handling	Moderate due to limited reuse
[689]	Fe/HY zeolite	460.00	5 cycles	92.00	54.8	Low environmental impact	Low risk, safer	Moderate due to limited reuse
[690]	[C_4MIM] [HSO_4]	470.00	5 cycles	94.00	66.7%	Low environmental impact	Mildly corrosive	Moderate due to limited reuse

[a]Efficiency is based on the actual LA yield over the theoretical LA yield in the fresh cycle of the catalytic system.

10.4 Sustainability and environmental considerations

In the pursuit of sustainable industrial processes, selecting catalysts that are both economically viable and environmentally friendly is crucial. Carbon cryogel stands out as a promising candidate when compared to traditional mineral acids like sulphuric acid, offering a balance of efficiency, safety, and sustainability. The increasing emphasis on sustainable practices necessitates the careful evaluation of catalysts that not only enhance productivity but also minimise environmental impact.

To facilitate informed decision-making in risk assessment, the National Fire Protection Association (NFPA) provides a standardised rating system. This system aids organisations in evaluating the hazards associated with materials and processes by employing colour codes (**Figure 10.1**) and numerical ratings to assess various risks, including health hazards, flammability, instability, carcinogenicity, and toxicity (**Table 10.4**). Such a systematic approach is essential for prioritising risks and ensuring safety in industrial applications.

One of the key advantages of carbon cryogel is its significantly lower toxicity compared to sulphuric acid. The latter, characterised by a low LD_{50} value, poses substantial risks through oral ingestion, skin contact, and inhalation, leading to severe burns and other hazards. The LD_{50}, or median lethal dose, represents the quantity of a substance that results in the death of 50% of a test population, with lower LD_{50} values indicating higher toxicity. Meanwhile, the LC_{50} value refers to the concentration of a substance in air (or water) expected to result in death within 14 days for 50% of exposed test animals. Among the safety data sheets reviewed from Merck, Fisher Scientific, and TCI America,

sulphuric acid is the only chemical clearly associated with inhalation exposure. This raises concerns about its environmental sustainability compared to other chemicals with no documented inhalation risks. In contrast, carbon cryogel presents a safer alternative, exhibiting minimal acute toxicity and lower inhalation risks. Its synthesis utilises less aggressive chemicals, which further reduces potential exposure to harmful substances, making it a more desirable option from a safety perspective.

A risk assessment matrix (**Table 10.5**) comparing the chemicals involved in the synthesis of carbon cryogel and sulphuric acid reveals stark differences in their risk profiles. The risks are assessed based on two key parameters: **Severity** (the impact if the risk occurs) and **Likelihood** (the probability of the risk occurring). The analysis reveals varying risk levels, highlighting that sulphuric acid poses significant threats due to its corrosive nature, while phosphotungstic acid also presents a notable risk but is less hazardous. The risks associated with phosphotungstic acid can be reduced by implementing mitigation strategies focusing on proper handling procedures and the use of personal protective equipment (PPE).

On the bright side, carbon cryogel's lower environmental footprint aligns with the goals of sustainable production and promotes greener chemistry solutions. Furthermore, the incorporation of biomass-derived materials in the formulation of carbon cryogel enhances its eco-friendly profile, making it a more attractive choice for industrial applications.

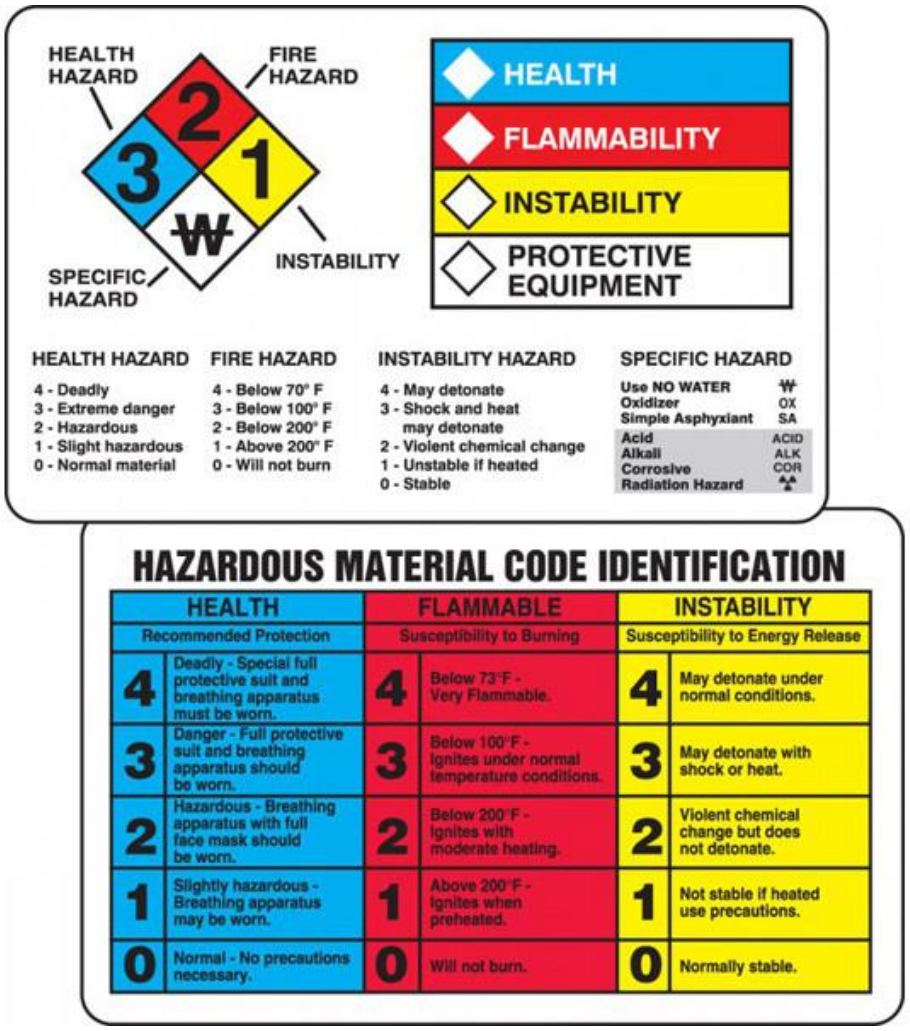

Figure 10.1 NFPA safety data sheet.

Table 10.4 NFPA rating for raw materials used for carbon cryogel synthesis.

Materials	**NFPA rating**				**Carcinogenicity**		**Acute toxicity**		
	Health	**Flammability**	**Instability**	**Physical**	**IARC**	**NTP**	**LD_{50} Oral (mg kg^{-1})**	**LD_{50} Dermal (mg kg^{-1})**	**LC_{50} Inhalation (mg L^{-1})**
Sulphuric acid	3	0	2	W	Group 1	Known	2140	> 2000	0.375
Phosphotungstic acid	3	1	0	N/A	Not listed	Not listed	3300	Not listed	Not listed
Niobium (V) oxide	0	0	0	N/A	Not listed	Not listed	4000	Not listed	Not listed
Xanthan gum	0	0	0	N/A	Not listed	Not listed	Not listed	Not listed	Not listed
Alkaline lignin	0	0	0	N/A	Not listed	Not listed	6030	Not listed	Not listed

*Note: IARC (International Agency for Research on Cancer), NTP (National Toxicity Program), Group 1 (Carcinogenic to humans), Known (Known carcinogen)

Table 10.5 Risk assessment matrix for chemicals used in the synthesis of carbon cryogel compared to conventional sulphuric acid.

Chemical	Risk factor	Severity (1-5)[a]	Likelihood (1-5)[b]	Risk level[c]
Alkaline lignin	Dust inhalation causing respiratory issues	3	2	6
	Skin irritation upon contact	2	3	6
	Environmental impact if not disposed properly	4	2	8
Xanthan gum	Allergic reactions in sensitive individuals	2	2	4
	Inhalation as dust causing minor irritation	1	2	2
	Viscosity alteration in mixtures	2	3	6
Phosphotungstic acid	Corrosive to skin and eyes	4	3	12
	Toxic if ingested	5	1	5
	Environmental hazard in water bodies	4	2	8
Niobium oxide	Respiratory tract irritation as dust	3	2	6
	Skin irritation upon prolonged exposure	2	2	4
	Potential environmental accumulation	3	2	6
Sulphuric acid	Severe burns on skin and eyes	5	3	15
	Toxic fumes causing respiratory issues	4	3	12
	Reactive with water causing splattering	4	2	8

[a] Severity Scale: 1 = Insignificant, 2 = Minor, 3 = Moderate, 4 = Major, 5 = Critical
[b]Likelihood Scale: 1 = Rare, 2 = Unlikely, 3 = Possible, 4 = Likely, 5 = Almost Certain
[c]Risk level is equal to severity multiplied by likelihood, Scale: 1-4 = Low Risk, 5-12 = Medium Risk, 13-20 = High Risk, 21-25 = Critical Risk

10.5 Concluding remarks

In the biomass conversion process, catalysts play a crucial role by accelerating reaction steps, enhancing selectivity, and increasing yields. Selecting a robust catalyst is essential as it directly impacts process efficiency, product yield, and overall cost-effectiveness. However, the development of catalysts carries inherent risks, prompting the need to consider sustainability factors to address potential economic, environmental, and social uncertainties.

Compared to conventional sulphuric acid, the carbon cryogel incorporated with $H_3PW_{12}O_{40}$-Nb_2O_5 currently has higher production costs at the laboratory scale. This is primarily due to the specialised materials and processes required for its synthesis. Nonetheless, its high recyclability, durability, and stability over multiple cycles make it a potentially cost-effective option in the long term. As production scales up from laboratory to industrial levels, economies of scale may offset these costs. Increased production volumes typically lead to a decrease in average cost per unit, driven by factors such as bulk purchasing, improved operational efficiency, and the distribution of fixed costs across a larger output.

The emerging carbon cryogel is designed to minimise energy consumption, waste generation, and harmful emissions, aligning with modern environmental standards. Unlike sulphuric acid, which can emit sulphur oxides and hydrogen during combustion, the phosphotungstic acid and niobium oxide incorporated in carbon cryogel are not reported to produce hazardous combustion products. This characteristic not only reduces the environmental footprint but also enhances workplace safety by mitigating exposure to harmful

substances. Additionally, carbon cryogel aligns with social well-being and safety indicators, as evidenced by its higher LD_{50} and LC_{50} values, indicating lower toxicity and risk to humans and wildlife. This alignment is essential for gaining consumer trust and securing regulatory approvals, as well as fostering a socially responsible image for producers.

Balancing the efficiency and cost-effectiveness of carbon cryogel with economic, environmental, and societal concerns is crucial for sustainable production of LA. This balanced approach supports the achievement of several United Nations SDGs, including:

- **SDG 7: Affordable and Clean Energy**: By reducing energy consumption and promoting cleaner production methods, carbon cryogel contributes to more sustainable energy practices.
- **SDG 12: Responsible Consumption and Production**: The use of OPMF, lignin carbon cryogel and GVL supports resource efficiency and waste reduction, key aspects of responsible production.
- **SDG 13: Climate Action**: By minimising emissions and environmental impacts, the carbon cryogel supports efforts to mitigate climate change.

In conclusion, while the initial costs of carbon cryogel at the laboratory scale are higher than conventional catalysts, its long-term benefits in terms of recyclability, environmental impact, and alignment with global sustainability goals make it a promising candidate for large-scale industrial applications. This approach ensures that advancements in catalyst technology not only drive economic growth but also promote a greener and more sustainable chemical industry.

Chapter 11

Conclusions and Recommendations

11.1 Conclusions

In this groundbreaking study, the remarkable potential of lignin-derived carbon cryogels incorporated with $H_3PW_{12}O_{40}$-Nb_2O_5 as a novel carbon-based catalyst was explored. This catalyst demonstrates exceptional efficiency in converting biomass to LA, achieving an impressive 97.3% conversion rate and yielding 22.1% LA out of 22.7% of the theoretical LA yield from cellulose conversion, using oil palm mesocarp fibre as the feedstock.

Recognising the critical importance of tailoring the catalyst to desired properties, the sol-gel method was adopted to enhance catalyst features. By anchoring $H_3PW_{12}O_{40}$ and Nb_2O_5 onto a robust lignin-based support, sustainability and resilience were achieved, ensuring efficient hydrolysis of biomass under mild conditions.

At the outset, the study delves into the unique characteristics of biomass. By testing solvent properties, the aim was to enhance the deconstruction of biomass into cellulose. The efficiency of cellulose hydrolysis hinges on successfully removing lignin and hemicellulose. The investigation reveals promising results: GVL achieved a fair yield of lignin and hemicellulose removal at 90% and 55%, respectively, with the highest percentage recovery of cellulose reaching 64%, hence facilitating direct conversion of cellulose to LA.

Despite the catalyst's selectivity playing a pivotal role in enhancing glucose dehydration to LA, solid acid catalysts often encounter recycling challenges. Here, an intriguing trade-off emerges:

- **$H_3PW_{12}O_{40}$**, despite its high Brønsted acidity and efficacy in catalysing biomass hydrolysis, glucose dehydration, and HMF formation (yielding LA at 7.45 mmol g^{-1}), raises concerns about leaching due to its solubility in water.
- **Nb_2O_5**, as a water-tolerant Lewis acid, facilitates glucose isomerisation to fructose—an essential step for further LA conversion. However, its fine powder form complicates the recycling process.

To develop an efficient catalytic system, striking a balance between product selectivity, yield, and environmental impact is always challenging. While microwave treatment efficiently transfers energy to reactants, catalyst efficiency remains crucial for lowering activation energy. Designing a catalyst that meets microwave conditions—reducing pore sizes to enhance thermal conductivity while optimising activity and stability—is a challenge. In this study, a well-designed catalyst balances micropores, mesopores, and macropores, ensuring efficient binding with biomass. The dominant mesopores distribution resulted in optimised carbon cryogel properties (surface area of 57.41 $m^2 g^{-1}$ and pore volume of 0.156 $cm^3 g^{-1}$), leading to the optimum LA yield. Achieving an acidity of 12.50 $mmol g^{-1}$ with a Brønsted -to-Lewis acid catalyst ratio of 1.48, this present catalytic system exhibits a synergy factor of 2.15—a testament to the carbon cryogel's prowess in one-pot biomass conversion.

In the pursuit of developing a sustainable catalytic system, the cost of the catalyst is crucial, even alongside considerations of efficiency and selectivity.

The production cost of carbon cryogel stands at RM 5.23 per gram. Notably, the overall synthesis cost of carbon cryogel incorporated with $H_3PW_{12}O_{40}$-Nb_2O_5 remains relatively low due to the use of cost-effective raw materials, including lignin, xanthan gum, niobium oxide, and phosphotungstic acid. These materials are also environmentally friendly, providing an additional advantage, as evidenced by its stability to allow for 8 recycling times with 95% catalyst recovery in the first cycle decreasing to 68% recovery in the last cycle, signifying the robust carbon cryogel as a catalyst support.

Despite the promising results, it is important to acknowledge several limitations that could affect the broader application and economic viability of this catalytic system. The optimisation of recycling and regeneration conditions for the catalyst was not conducted, which could impact long-term efficiency and sustainability. Additionally, the quantification of humin byproducts, which are inevitable during the process, was not addressed. This leaves a gap in understanding the complete environmental impact. Furthermore, detailed upstream and downstream costs, such as transportation, waste management, and packaging expenses, were not included in this analysis. These factors are crucial for assessing the economic viability of large-scale applications and could significantly influence the feasibility of implementing this technology in industry settings.

While this study unveils a sustainable and efficient catalyst, these limitations highlight the need for further research to fully understand and enhance the economic and environmental effectiveness of the system. Addressing these limitations will be crucial for evaluating the scalability of this innovative catalytic process. By overcoming these challenges, we could pave the

way for more sustainable and efficient biomass conversion technologies. The findings of this study open promising avenues for LA production and resource sustainability. Future research should concentrate on resolving these issues to improve the practical applicability and environmental advantages of this catalytic system.

11.2 Recommendations

Several recommendations have been proposed to improve the carbon cryogel catalytic system for converting biomass to LA. Despite numerous efforts to increase LA yield, the overall cost of processing—from upstream to downstream—continues to pose a significant barrier to large-scale production through hydrolysis. Notably, downstream processing alone represents 50–70% of the total LA production cost, highlighting the urgent need for detailed cost analysis. Further studies should be conducted to evaluate the specific cost drivers associated with downstream processing. This analysis can inform strategies to optimise these costs, potentially leading to more economically viable production methods.

The high solubility of LA in water complicates its separation. GVL can assist in extracting LA from the final product solution, but its commercial use may be cost-prohibitive for large-scale production. Therefore, further investigation into producing GVL within the carbon cryogel catalytic system is recommended. Considering its presence in product analysis, this approach could allow for recycling the GVL solvent, thereby reducing the need for large volumes of extraction solvents and lowering manufacturing costs.

Detailing the surface acidity of the catalyst by identifying specific surface groups such as SO_3H, COOH, and OH is suggested. This analysis can confirm the dominant species contributing to the high acidity of the carbon cryogel and help control catalytic activity. Sulphur in alkaline lignin could enhance the system's activity, promoting the transformation of saccharides into glucose and HMF. Additionally, the presence of the SO_3H group as a co-catalyst could lead to the development of better multi-functional catalysts without needing mineral acid activation, such as H_2SO_4. An elemental analyser is proposed for evaluating hydrogen distribution within the catalyst structure, supplementing information from XPS and EDX analysis.

The formation of humins in acid water solutions necessitates finding economically and environmentally friendly applications for these byproducts in the biomass hydrolysis industry. Solid acid catalysts capable of degrading humin residue into levulinate esters are worth considering, given initial GC-MS screenings suggesting potential ester production. Humins, primarily used for heat generation due to their carbon-rich nature, could be transformed into valuable levulinate esters like methyl levulinate, ethyl levulinate, and butyl levulinate. These short-chain fatty esters share properties with biodiesel fatty acid methyl esters and can be used as gasoline additives and diesel transportation fuel due to their non-toxicity, high lubricity, flashpoint stability, and improved cold flow properties. Conducting a mass balance check to identify the proportion of LA and other valuable by-products that can be sustainably produced is crucial. NMR analysis is also necessary to confirm changes in product analysis and validate chemical structures.

Evaluating the hydrophobicity index of the carbon cryogel through contact angle measurement and adsorption studies can identify the proportion of hydrophobic and hydrophilic groups within the material. Strong hydrophobic characteristics boost catalytic applications for biomass upgrading processes, as carbon surfaces efficiently prevent the leaching of the active phase during catalytic reactions, enhancing catalyst recyclability—a critical benchmark for industrial applications. Meanwhile, assessing the hydrophilic nature of the carbon cryogel is important for verifying hydrothermal stability and potential deactivation due to crystalline structure deterioration in water.

The key to catalyst design lies in precisely controlling the activity of active sites and tuning the microenvironments around these sites, which requires a fundamental understanding of the reaction mechanism. Computational chemistry can provide insights into how catalysts function at a molecular level, enabling precise manipulation of the microenvironment to achieve desired catalytic performance.

References

[1] O. Ali Qamar *et al.*, “Feasibility-to-applications of value-added products from biomass: Current trends, challenges, and prospects,” *Chem. Eng. J.*, vol. 454, p. 140240, 2023.

[2] G. C. Hayes and C. R. Becer, “Levulinic acid: a sustainable platform chemical for novel polymer architectures,” *Polym. Chem.*, vol. 11, pp. 4068–4077, 2020.

[3] S. Kang, J. Fu, and G. Zhang, “From lignocellulosic biomass to levulinic acid: A review on acid-catalyzed hydrolysis,” *Renew. Sust. Energ. Rev.*, vol. 94, pp. 340–362, 2018.

[4] A. Mukherjee, M.-J. Dumont, and V. Raghavan, “Review: Sustainable production of hydroxymethylfurfural and levulinic acid: Challenges and opportunities,” *Biomass Bioenergy*, vol. 72, pp. 143–183, 2015.

[5] Mordor Intelligence, “Levulinic Acid Market Size & Share Analysis - Growth Trends & Forecasts (2024 - 2029)”, Hyderabad. Accessed: Nov. 20, 2024. [Online]. Available: Source: https://www.mordorintelligence.com/industry-reports/levulinic-acid-market

[6] J. J. Bozell *et al.*, “Production of levulinic acid and use as a platform chemical for derived products,” *Resour. Conserv. Recycl.*, vol. 28, pp. 227–239, 2000.

[7] D. J. Hayes, J. Ross, M. H. B. Hayes, and S. Fitzpatrick, “The Biofine Process: Production of Levulinic Acid, Furfural and Formic Acid from Lignocellulosic Feedstocks,” in *Biorefineries-Industrial Processes and Products: Status Quo and Future Directions*, Wiley VCH, 2008.

[8] P. Kahar *et al.*, ‘An integrated biorefinery strategy for the utilization of palm-oil P. Kahar *et al.*, “An integrated biorefinery strategy for the utilization of palm-oil wastes”, *Bioresour. Technol.*, vol. 344, p. 126266, 2022.

[9] Ahmad Parveez Ghulam Kadir, “Malaysian Palm Oil’s Key Role In Global Food Security”, Malaysian Palm Oil Council (MPOC).

[10] N. Abdullah and F. Sulaiman, “The Oil Palm Wastes in Malaysia”, in *Biomass Now: Sustainable Growth and Use*, M. D. Matovic, Ed., Rijeka, Croatia: InTech, 2013, pp. 75–99.

[11] M. F. Awalludin, O. Sulaiman, R. Hashim, and W. N. A. W. Nadhari, "An overview of the oil palm industry in Malaysia and its waste utilization through thermochemical conversion, specifically via liquefaction," *Renew. Sust. Energ. Rev.*, vol. 50, pp. 1469–1484, 2015.

[12] Malaysian Palm Oil Board, "Tapping biomass potential", *New Straits Times*, 2024.

[13] X. Chen, Z. Zhang, B. Yuan, F. Yu, C. Xie, and S. Yu, "Lignin-based sulfonated carbon as an efficient biomass catalyst for clean benzylation of benzene ring compounds," *J. Ind. Eng. Chem.*, vol. 111, pp. 369–379, 2022.

[14] R. Kupila, K. Lappalainen, T. Hu, H. Romar, and U. Lassi, "Lignin-based activated carbon-supported metal oxide catalysts in lactic acid production from glucose," *Appl. Catal. A Gen.*, vol. 612, p. 118011, 2021.

[15] A. A. Mekkaoui, A. Aberkouks, L. Fkhar, M. Ait Ali, L. El Firdoussi, and S. El Houssame, "Novel palladium nanoparticles supported on mesoporous natural phosphate: Catalytic ability for the preparation of aromatic hydrocarbons from natural terpenes," *Appl. Organomet. Chem.*, vol. 34, e6917, 2020.

[16] V. B. Kumar, I. N. Pulidindi, and A. Gedanken, "Selective conversion of starch to glucose using carbon based solid acid catalyst," *Renew. Energy*, vol. 78, pp. 141–145, 2015.

[17] X. Yu, L. Peng, X. Gao, L. He, and K. Chen, "One-step fabrication of carbonaceous solid acid derived from lignosulfonate for the synthesis of biobased furan derivatives', *RSC Adv*, vol. 8, pp. 15762–15772, 2018.

[18] M. Hara *et al.*, "A Carbon Material as a Strong Protonic Acid," *Angew. Chem. Int. Ed.*, vol. 43, pp. 2955–2958, 2004.

[19] S. Suganuma *et al.*, "Hydrolysis of Cellulose by Amorphous Carbon Bearing SO_3 H, COOH, and OH Groups," *J. Am. Chem. Soc.*, vol. 130, pp. 12787–12793, 2008.

[20] S. Xiong, Y. Guan, C. Luo, L. Zhu, and S. Wang, "Critical Review on the Preparation of Platform Compounds from Biomass or Saccharides via Hydrothermal Conversion over Carbon-Based Solid Acid Catalysts," *Energy Fuels*, vol. 35, pp. 14462–14483, 2021.

[21] Y. Han, L. Ye, X. Gu, P. Zhu, and X. Lu, "Lignin-based solid acid catalyst for the conversion of cellulose to levulinic acid using γ-valerolactone as solvent," *Ind. Crops Prod.*, vol. 127, pp. 88–93, 2019.

[22] M. R. A. Helmi, D. U. C. Rahayu, A. P. Pratama, I. Khatrin, A. N. Ramadhani, and Y. K. Krisnandi, “Comparative study of microwave-assisted versus conventional heated reactions of biomass conversion into levulinic acid over hierarchical Mn_3O_4/ZSM-5 zeolite catalysts,” *Carbon Resour. Convers.*, vol. 6, pp. 245–252, 2023.

[23] R. Lou *et al.*, “Metal–Organic-Framework-Mediated Fast Self-Assembly 3D Interconnected Lignin-Based Cryogels in Deep Eutectic Solvent for Supercapacitor Applications,” *Polymers (Basel)*, vol. 15, p. 1824, 2023.

[24] M. M. Zainol, N. A. S. Amin, and M. Asmadi, “Synthesis and characterization of carbon cryogel microspheres from lignin–furfural mixtures for biodiesel production,” *Bioresour. Technol.*, vol. 190, pp. 44–50, 2015.

[25] S. Tabasso, D. Carnaroglio, E. Calcio Gaudino, and G. Cravotto, “Microwave, ultrasound and ball mill procedures for bio-waste valorisation,” *Green Chem.*, 17, pp. 684–693, 2015.

[26] S. Kang, R. Miao, J. Guo, and J. Fu, “Sustainable production of fuels and chemicals from biomass over niobium based catalysts: A review”, *Catal. Today*, vol. 374, pp. 61–76, 2021.

[27] R. S. de Carvalho, F. de A. Rodrigues, R. S. Monteiro, and W. L. da Silva Faria, “Optimization of Furfural Synthesis from Xylose Using Niobic Acid and Niobium Phosphate as Catalysts,” *Waste Biomass Valorization*, vol. 10, pp. 2673–2680, 2019.

[28] F. Wang, H.-Z. Wu, C.-L. Liu, R.-Z. Yang, and W.-S. Dong, “Catalytic dehydration of fructose to 5-hydroxymethylfurfural over Nb_2O_5 catalyst in organic solvent,” *Carbohydr. Res.*, vol. 368, pp. 78–83, 2013.

[29] Z. Chen, S. Zhang, B. Yan, Q. Cai, and S. Zhang, “Lignin-based solid acid catalyst for cellulose residue conversion into levulinic acid in biphasic system,” *Ind. Crops Prod.*, vol. 178, p. 114523, 2022.

[30] M. G. dos Santos, H. M. Fogarin, D. D. Virginio da Silva, and K. J. Dussán, “Bioprocess development for levulinic acid production using sugarcane biomass,” *Sustain. Chem. Pharm.*, vol. 33, p. 101085, 2023.

[31] N. S. M. Azlan, C. L. Yap, S. Gan, and M. B. A. Rahman, “Recent advances in the conversion of lignocellulosic biomass and its degraded products to levulinic acid: A synergy of Brønsted-Lowry acid and Lewis acid,” *Ind. Crops Prod.*, vol. 181, p. 114778, 2022.

[32] Y. Zuo, Y. Zhang, and Y. Fu, “Catalytic Conversion of Cellulose into Levulinic Acid by a Sulfonated Chloromethyl Polystyrene Solid Acid Catalyst,” *ChemCatChem*, vol. 6, pp. 753–757, 2014.

[33] D. W. Rackemann and W. O. Doherty, “The conversion of lignocellulosics to levulinic acid,” *Biofuel., Bioprod. Biorefin.*, vol. 5, pp. 198–214, 2011.

[34] F. Shen, R. L. Smith, L. Li, L. Yan, and X. Qi, “Eco-friendly Method for Efficient Conversion of Cellulose into Levulinic Acid in Pure Water with Cellulase-Mimetic Solid Acid Catalyst,” *ACS Sustain. Chem. Eng.*, vol. 5, pp. 2421–2427, 2017.

[35] K. Wang, J. Jiang, X. Liang, H. Wu, and J. Xu, “Direct Conversion of Cellulose to Levulinic Acid over Multifunctional Sulfonated Humins in Sulfolane–Water Solution,” *ACS Sustain. Chem. Eng.*, vol. 6, pp. 15092–15099, 2018.

[36] Y. K. Krisnandi *et al.*, “Hierarchical MnOx/ZSM-5 as Heterogeneous Catalysts in Conversion of Delignified Rice Husk to Levulinic Acid,” *Indonesian J. Chem.*, vol. 19, p. 115, 2019.

[37] Y. Chen, G. Li, F. Yang, and S-M. Zhang, “Mn/ZSM-5 participation in the degradation of cellulose under phosphoric acid media,” *Polym. Degradation Stability*, vol. 96, pp. 863–869, 2011.

[38] G. Hurst, J. M. González-Carballo, L. Tosheva, and S. Tedesco, “Synergistic Catalytic Effect of Sulphated Zirconia—HCl System for Levulinic Acid and Solid Residue Production Using Microwave Irradiation,” *Energies*, vol. 14, p. 1582, 2021.

[39] P. D. Muley, Y. Wang, J. Hu, and D. Shekhawat, “Microwave-assisted heterogeneous catalysis,” in *Catalysis*, Royal Society of Chemistry, 2021, pp. 1–37.

[40] A. Mukherjee and M.-J. Dumont, “Levulinic Acid Production from Starch Using Microwave and Oil Bath Heating: A Kinetic Modeling Approach,” *Ind. Eng. Chem. Res.*, vol. 55, pp. 8941–8949, 2016.

[41] J. Fan *et al.*, “Direct Microwave-Assisted Hydrothermal Depolymerization of Cellulose,” *J. Am. Chem. Soc.*, vol. 135, pp. 11728–11731, 2013.

[42] J. Tian, J. Wang, S. Zhao, C. Jiang, X. Zhang, and X. Wang, “Hydrolysis of cellulose by the heteropoly acid $H_3PW_{12}O_{40}$,” *Cellulose*, vol. 17, pp. 587–594, 2010.

[43] P. L. Dhepe and A. Fukuoka, “Cellulose Conversion under Heterogeneous Catalysis,” *ChemSusChem*, vol. 1, pp. 969–975, 2008.

[44] R. Rinaldi and F. Schüth, “Acid Hydrolysis of Cellulose as the Entry Point into Biorefinery Schemes,” *ChemSusChem*, vol. 2, pp. 1096–1107, 2009.

[45] X. Tong, Y. Ma, and Y. Li, “Biomass into chemicals: Conversion of sugars to furan derivatives by catalytic processes,” *Appl. Catal. A Gen.*, vol. 385, pp. 1–13, 2010.

[46] S. Van de Vyver, J. Geboers, P. A. Jacobs, and B. F. Sels, “Recent Advances in the Catalytic Conversion of Cellulose,” *ChemCatChem*, vol. 3, pp. 82–94, 2011.

[47] L. D. Mthembu, R. Gupta, and N. Deenadayalu, “Advances in Biomass-Based Levulinic Acid Production,” *Waste Biomass Valorization*, vol. 14, pp. 1–22, 2023.

[48] K. Shimizu and A. Satsuma, “Toward a rational control of solid acid catalysis for green synthesis and biomass conversion,” *Energy Environ. Sci.*, vol. 4, p. 3140, 2011.

[49] H. Danner and R. Braun, “Biotechnology for the production of commodity chemicals from biomass,” *Chem. Soc. Rev.*, vol. 28, pp. 395–405, 1999.

[50] Y. P. Zhang and L. R. Lynd, “Toward an aggregated understanding of enzymatic hydrolysis of cellulose: Noncomplexed cellulase systems,” *Biotechnol. Bioeng.*, vol. 88, pp. 797–824, 2004.

[51] D. Esposito and M. Antonietti, “Redefining biorefinery: the search for unconventional building blocks for materials,” *Chem. Soc. Rev.*, vol. 44, pp. 5821–5835, 2015.

[52] C. Li, X. Zhao, A. Wang, G. W. Huber, and T. Zhang, “Catalytic Transformation of Lignin for the Production of Chemicals and Fuels,” *Chem. Rev.*, vol. 115, pp. 11559–11624, 2015.

[53] M. Mennani *et al.*, “Current approaches, emerging developments and functional prospects for lignin-based catalysts – a review,” *Green Chem.*, vol. 25, pp. 2896–2929, 2023.

[54] L. T. Mika, E. Cséfalvay, and Á. Németh, “Catalytic Conversion of Carbohydrates to Initial Platform Chemicals: Chemistry and Sustainability,” *Chem. Rev.*, vol. 118, pp. 505–613, 2018.

[55] W. Schutyser, T. Renders, S. Van den Bosch, S.-F. Koelewijn, G. T. Beckham, and B. F. Sels, “Chemicals from lignin: an interplay of lignocellulose fractionation, depolymerisation, and upgrading,” *Chem. Soc. Rev.*, vol. 47, pp. 852–908, 2018.

[56] J. Zakzeski, P. C. A. Bruijnincx, A. L. Jongerius, and B. M. Weckhuysen, “The Catalytic Valorization of Lignin for the Production of Renewable Chemicals,” *Chem. Rev.*, vol. 110, pp. 3552–3599, 2010.

[57] Z. Zhang, J. Song, and B. Han, “Catalytic Transformation of Lignocellulose into Chemicals and Fuel Products in Ionic Liquids,” *Chem. Rev.*, vol. 117, pp. 6834–6880, 2017.

[58] T. W. Walker, A. H. Motagamwala, J. A. Dumesic, and G. W. Huber, “Fundamental catalytic challenges to design improved biomass conversion technologies,” *J Catal.*, vol. 369, pp. 518–525, 2019.

[59] L. Lin, X. Han, B. Han, and S. Yang, “Emerging heterogeneous catalysts for biomass conversion: studies of the reaction mechanism,” *Chem. Soc. Rev.*, vol. 50, pp. 11270–11292, 2021.

[60] P. Sudarsanam, R. Zhong, S. Van den Bosch, S. M. Coman, V. I. Parvulescu, and B. F. Sels, “Functionalised heterogeneous catalysts for sustainable biomass valorisation,” *Chem. Soc. Rev.*, vol. 47, pp. 8349–8402, 2018.

[61] M. Pagliaro, “Sol–gel catalysts for synthetic organic chemistry: milestones in 30 years of successful innovation”, *J Solgel Sci. Technol.*, vol. 95, pp. 551–561, 2020.

[62] C.-W. Wu, P.-H. Li, Y.-M. Wei, C. Yang, and W.-J. Wu, “Review on the preparation and application of lignin-based carbon,” *RSC Adv.*, vol. 12, pp. 10755–10765, 2022.

[63] S. Esposito, “Traditional Sol-Gel Chemistry as a Powerful Tool for the Preparation of Supported Metal and Metal Oxide Catalysts,”*Materials*, vol. 12, p. 668, 2019.

[64] N. A. S. Ramli and N. A. S. Amin, “Catalytic hydrolysis of cellulose and oil palm biomass in ionic liquid to reducing sugar for levulinic acid production,” *Fuel Process. Technol.*, vol. 128, pp. 490–498, 2014.

[65] T. Zhang *et al.*, “Catalytic conversion of xylose and corn stalk into furfural over carbon solid acid catalyst in γ-valerolactone,” *Bioresour. Technol.*, vol. 209, pp. 108–114, 2016.

[66] Y. Gao, J. Remón, and A. S. Matharu, “Microwave-assisted hydrothermal treatments for biomass valorisation: a critical review,” *Green Chem.*, vol. 23, pp. 3502–3525, 2021.

[67] A. Babin, C. Vaneeckhaute, and M. C. Iliuta, “Potential and challenges of bioenergy with carbon capture and storage as a carbon-negative energy source: A review,” *Biomass Bioenergy*, vol. 146, p. 105968, 2021.

[68] X. Lu *et al.*, “Gasification of coal and biomass as a net carbon-negative power source for environment-friendly electricity generation in China,” *Proc. Natl. Acad. Sci. U.S.A.*, vol. 116, pp. 8206–8213, 2019.

[69] D. E. Resasco, B. Wang, and D. Sabatini, “Distributed processes for biomass conversion could aid UN Sustainable Development Goals,” *Nat. Catal.*, vol. 1, pp. 731–735, 2018.

[70] Y. Wu, Y. Zhang, J. Zhou, and D. Gu, “Recent progress on functional mesoporous materials as catalysts in organic synthesis,” *Emergent Mater.*, vol. 3, pp. 247–266, 2020.

[71] N. R. Syed, B. Zhang, S. Mwenya, and A. S. Aldeen, “A Systematic Review on Biomass Treatment Using Microwave-Assisted Pyrolysis under PRISMA Guidelines,” *Molecules*, vol. 28, p. 5551, 2023.

[72] K. Martina, G. Cravotto, and R. S. Varma, “Impact of Microwaves on Organic Synthesis and Strategies toward Flow Processes and Scaling Up,” *J. Org. Chem.*, vol. 86, pp. 13857–13872, 2021.

[73] M. Morte, J. Dean, H. Kitajima, and B. Hascakir, “Increasing the Penetration Depth of Microwave Radiation Using Acoustic Stress to Trigger Piezoelectricity,” *Energy Fuels*, vol. 33, pp. 6327–6334, 2019.

[74] E. G. Fawaz, D. A. Salam, S. S. Rigolet, and T. J. Daou, “Hierarchical Zeolites as Catalysts for Biodiesel Production from Waste Frying Oils to Overcome Mass Transfer Limitations,” *Molecules*, vol. 26, p. 4879, 2021.

[75] Z. Yuan, J. Long, Y. Xia, X. Zhang, T. Wang, and L. Ma, “Production of Levulinic Acid from *Pennisetum alopecuroides* in the Presence of an Acid Catalyst,” *Bioresources*, vol. 11, pp. 3511–3523, 2016.

[76] NREL, Advances in Technology at the National Renewable Energy Laboratory, “Cellulose Conversion Key to Fuel of the Future -NREL Improving Key Step in Producing Ethanol from Biomass,” Available: Source: https://www.nrel.gov/.

[77] X. Hu, S. Jiang, L. Wu, S. Wang, and C.-Z. Li, “One-pot conversion of biomass-derived xylose and furfural into levulinate esters via acid catalysis,” *Chem. Commun.*, vol. 53, pp. 2938–2941, 2017.

[78] G. W. Huber and J. A. Dumesic, “An overview of aqueous-phase catalytic processes for production of hydrogen and alkanes in a biorefinery,” *Catal. Today*, vol. 111, pp. 119–132, 2006.

[79] Y. Román-Leshkov, C. J. Barrett, Z. Y. Liu, and J. A. Dumesic, “Production of dimethylfuran for liquid fuels from biomass-derived carbohydrates,” *Nature*, vol. 447, pp. 982–985, 2007.

[80] H. Zhao, J. E. Holladay, H. Brown, and Z. C. Zhang, “Metal Chlorides in Ionic Liquid Solvents Convert Sugars to 5-Hydroxymethylfurfural,” *Sci.*, vol. 316, pp. 1597–1600, 2007.

[81] A. Boisen *et al.*, “Process integration for the conversion of glucose to 2,5-furandicarboxylic acid,” *Chem. Eng. Res. Des.*, vol. 87, pp. 1318–1327, 2009.

[82] J. Lewkowski, “Synthesis, chemistry and applications of 5-hydroxymethyl-furfural and its derivatives,” *Arkivoc*, vol. 2001, pp. 17–54, 2001.

[83] S. Liu *et al.*, “High-Yield and High-Efficiency Conversion of HMF to Levulinic Acid in a Green and Facile Catalytic Process by a Dual-Function Brønsted-Lewis Acid $HScCl_4$ Catalyst,” *ACS Omega*, vol. 6, pp. 15940–15947, 2021.

[84] X. Yu and P. G. Pickup, “Recent advances in direct formic acid fuel cells (DFAFC),” *J. Power Sources*, vol. 182, pp. 124–132, 2008.

[85] B. Loges, A. Boddien, H. Junge, and M. Beller, “Controlled Generation of Hydrogen from Formic Acid Amine Adducts at Room Temperature and Application in H_2/O_2 Fuel Cells,” *Angew. Chem. Int. Ed.*, vol. 47, pp. 3962–3965, 2008.

[86] J. Q. Bond, D. M. Alonso, D. Wang, R. M. West, and J. A. Dumesic, “Integrated Catalytic Conversion of γ-Valerolactone to Liquid Alkenes for Transportation Fuels,” *Sci.*, vol. 327, pp. 1110–1114, 2010.

[87] H. Mehdi, V. Fábos, R. Tuba, A. Bodor, L. T. Mika, and I. T. Horváth, “Integration of Homogeneous and Heterogeneous Catalytic Processes for a Multi-step Conversion of Biomass: From Sucrose to Levulinic Acid, γ-valerolactone, 1,4-Pentanediol, 2-Methyl-tetrahydrofuran, and Alkanes,” *Top Catal.*, vol. 48, pp. 49–54, 2008.

[88] L. Deng, J. Li, D. Lai, Y. Fu, and Q. Guo, “Catalytic Conversion of Biomass-Derived Carbohydrates into γ-Valerolactone without Using an External H_2 Supply,” *Angew. Chem. Int. Ed.*, vol. 48, pp. 6529–6532, 2009.

[89] H. Heeres, R. Handana, D. Chunai, C. Borromeus Rasrendra, B. Girisuta, and H. Jan Heeres, “Combined dehydration/(transfer)-hydrogenation of C6-sugars (D-glucose and D-fructose) to γ-valerolactone using ruthenium catalysts,” *Green Chem.*, vol. 11, p. 1247, 2009.

[90] M. Signoretto, S. Taghavi, E. Ghedini, and F. Menegazzo, “Catalytic Production of Levulinic Acid (LA) from Actual Biomass,” *Molecules*, vol. 24, p. 2760, 2019.

[91] J. A. Conti Silva, L. M. Grilo, M. H. Vasconcelos, and T. M. Lacerda, “Levulinic acid: perspectives of its biobased production and most promising derivatives,” in *Production of Top 12 Biochemicals Selected by USDOE from Renewable Resources*, Elsevier, 2022, pp. 387–414.

[92] A. Morone, M. Apte, and R. A. Pandey, “Levulinic acid production from renewable waste resources: Bottlenecks, potential remedies, advancements and applications,” *Renew. Sust. Energ. Rev.*, vol. 51, pp. 548–565, 2015.

[93] S. Andersson-Engels, R. Berg, K. Svanberg, and S. Svanberg, “Multi-colour fluorescence imaging in connection with photodynamic therapy of δ-amino levulinic acid (ALA) sensitised skin malignancies,” *Bioimaging*, vol. 3, pp. 134–143, 1995.

[94] A. Kumar, D. Z. Shende, and K. L. Wasewar, “Production of levulinic acid: A promising building block material for pharmaceutical and food industry,” *Mater. Today. Proc.*, vol. 29, pp. 790–793, 2020.

[95] V. Ghorpade and M. Hanna, “Industrial Applications for Levulinic Acid,” in *Cereals*, Boston, MA: Springer US, 1997, pp. 49–55.

[96] D. J. Hayes, S. Fitzpatrick, M. H. B. Hayes, and J. R. H. Ross, “The Biofine Process – Production of Levulinic Acid, Furfural, and Formic Acid from Lignocellulosic Feedstocks,” in *Biorefineries-Industrial Processes and Products*, Wiley, 2005, pp. 139–164.

[97] J. Lange *et al.*, “Valeric Biofuels: A Platform of Cellulosic Transportation Fuels,” *Angew. Chem. Int. Ed.*, vol. 49, pp. 4479–4483, 2010.

[98] D. M. Alonso, J. Q. Bond, and J. A. Dumesic, “Catalytic conversion of biomass to biofuels,” *Green Chem.*, vol. 12, p. 1493, 2010.

[99] J. C. Serrano-Ruiz, D. Wang, and J. A. Dumesic, “Catalytic upgrading of levulinic acid to 5-nonanone,” *Green Chem.*, vol. 12, p. 574, 2010.

[100] T. J. Schwartz, A. R. P. van Heiningen, and M. C. Wheeler, “Energy densification of levulinic acid by thermal deoxygenation,” *Green Chem.*, vol. 12, p. 1353, 2010.

[101] S. Yaman, “Pyrolysis of biomass to produce fuels and chemical feedstocks,” *Energy Convers. Manag.*, vol. 45, pp. 651–671, 2004.

[102] M. Kircher, “The transition to a bio-economy: National perspectives,” *Biofuel. Bioprod. Biorefine.*, vol. 6, pp. 240–245, 2012.

[103] M. S. Umar, P. Jennings, and T. Urmee, “Generating renewable energy from oil palm biomass in Malaysia: The Feed-in Tariff policy framework,” *Biomass Bioenergy*, vol. 62, pp. 37–46, 2014.

[104] W. T. Tsai, M. K. Lee, and Y. M. Chang, “Fast pyrolysis of rice straw, sugarcane bagasse and coconut shell in an induction-heating reactor,” *J. Anal. Appl. Pyrolysis*, vol. 76, pp. 230–237, 2006.

[105] S. S. Kim, J. Kim, Y. H. Park, and Y. K. Park, “Pyrolysis kinetics and decomposition characteristics of pine trees,” *Bioresour. Technol.*, vol. 101, pp. 9797–9802, 2010.

[106] R. Hashim *et al.*, “Characterization of raw materials and manufactured binderless particleboard from oil palm biomass,” *Mater. Des.*, vol. 32, pp. 246–254, 2011.

[107] S. Nizamuddin, S. Shrestha, S. Athar, B. S. Ali, and M. A. Siddiqui,” A critical analysis on palm kernel shell from oil palm industry as a feedstock for solid char production,” *Rev. Chem. Eng.*, vol. 32, pp. 489–505, 2016.

[108] S. Asokapandian, S. Sreelakshmi, and G. Rajamanickam, “Lipids and Oils: An Overview,” in *Food biopolymers: Structural, functional and nutraceutical properties*, Cham: Springer International Publishing, 2021, pp. 389–411.

[109] M. Poletto, “Effect of extractive content on the thermal stability of two wood species from Brazil,” *Maderas. Ciencia y tecnología*, vol. 18, pp. 435–442, 2016.

[110] F. Abnisa, A. Arami-Niya, W. M. A. Wan Daud, J. N. Sahu, and I. M. Noor, “Utilization of oil palm tree residues to produce bio-oil and bio-

char via pyrolysis," *Energy Convers. Manag.*, vol. 76, pp. 1073–1082, 2013.

[111] R. Venderbosch and W. Prins, "Fast pyrolysis technology development," *Biofuel., Bioprod. Biorefin.*, vol. 4, pp. 178–208, 2010.

[112] J. Akhtar and N. A. S. Amin, "A review on process conditions for optimum bio-oil yield in hydrothermal liquefaction of biomass," *Renew. Sust. Energ. Rev.*, vol. 15, pp. 1615–1624, 2011.

[113] A. C. Goncalves, I. Malico, and A. M. O. Sousa, "Solid Biomass from Forest Trees to Energy: A review," in *Renewable Resources and Biorefineries*, IntechOpen, 2018, pp. 23–34.

[114] M. Antar, D. Lyu, M. Nazari, A. Shah, X. Zhou, and D. L. Smith, "Biomass for a sustainable bioeconomy: An overview of world biomass production and utilization," *Renew. Sust. Energ. Rev.*, vol. 139, p. 110691, 2021.

[115] S. A. Pasma, R. Daik, S. Ramli, M. Y. Maskat, and M. H. Zulfakar, "Enzymatic degradation of lignin extracted from oil palm empty fruit bunch using laccase and cutinase," *Bioresources*, vol. 14, pp. 8879–8891, 2019.

[116] J. Fan *et al.*, "Optimization of ethanol-extracted lignin from palm fiber by response surface methodology and preparation of activated carbon fiber for dehumidification," *Bioresour. Bioprocess*, vol. 9, p. 61, 2022.

[117] A. L. Sazali, S. K. Amran, M. R. Anuar, K. F. Pa'ee, and T.-L. K. Yong, "Lignin from oil palm biomass using deep eutectic solvent as carbon fibre precursor," *Biomass Convers. Biorefin.*, vol. 14, pp. 29451–29464, 2024.

[118] N. Saba, M. Jawaid, and M. T. H. Sultan, "Thermal properties of oil palm biomass based composites," in *Lignocellulosic Fibre and Biomass-Based Composite Materials*, Elsevier, 2017, pp. 95–122.

[119] A. Sharma and S. K. Kar, *Energy Sustainability Through Green Energy*. New Delhi: Springer India, 2015.

[120] A. Q. Nguyen and L. T. P. Trinh, "Thermochemical Conversion of Cellulose and Hemicellulose," in *Biomass Utilization: Conversion Strategies*, Cham: Springer International Publishing, 2022, pp. 107–131.

[121] C. G. Yoo, X. Meng, Y. Pu, and A. J. Ragauskas, "The critical role of lignin in lignocellulosic biomass conversion and recent pretreatment strategies: A comprehensive review," *Bioresour. Technol.*, vol. 301., p. 122784, 2020.

[122] S. Chaudhary, V. P. Jain, and G. Jaiswar, “The composition of polysaccharides: monosaccharides and binding, group decorating, polysaccharides chains,” in *Innovation in Nano-Polysaccharides for Eco-sustainability*, Elsevier, 2022, pp. 83–118.

[123] C. Miao and W. Y. Hamad, “Cellulose reinforced polymer composites and nanocomposites: A critical review,” *Cellulose*, vol. 20, pp. 2221–2262, 2013.

[124] D. L. Klass, “Photosynthesis of Biomass and Its Conversion-Related Properties,” in *Biomass for Renewable Energy, Fuels, and Chemicals*, Academic Press, 1998, pp. 51–88.

[125] Y. Habibi, L. A. Lucia, and O. J. Rojas, “Cellulose nanocrystals: Chemistry, self-assembly, and applications,” *Chem. Rev.*, vol. 110, pp. 3479–3500, 2010.

[126] D. Trache, M. H. Hussin, M. K. M. Haafiz, and V. K. Thakur, “Recent progress in cellulose nanocrystals: Sources and production,” *Nanoscale*, vol. 9, pp. 1763–1786, 2017.

[127] H. M. Ng *et al.*, “Extraction of cellulose nanocrystals from plant sources for application as reinforcing agent in polymers,” *Compos. B Eng.*, vol. 75, pp. 176–200, 2015.

[128] M. A. Millett and A. J. Stamm, “Molecular Properties of Hemicellulose Fractions,” *J. Phys. Chem.*, vol. 51, pp. 134–148, 1947.

[129] P. Ademark et al., “Softwood hemicellulose-degrading enzymes from *Aspergillus niger*: Purification and properties of a *β*-mannanase,” *J. Biotechnol.*, vol. 63, pp. 199–210, 1998.

[130] R. R. Mod, R. L. Ory, N. M. Morris, and F. L. Normand, “Chemical Properties and Interactions of Rice Hemicellulose with Trace Minerals in Vitro,” *J. Agric. Food Chem.*, vol. 29, 449–454, 1981.

[131] P. Kumar, D. M. Barrett, M. J. Delwiche, and P. Stroeve, “Methods for pretreatment of lignocellulosic biomass for efficient hydrolysis and biofuel production,” *Ind. Eng. Chem. Res.*, vol. 48, pp. 3713–3729, 2009.

[132] T.-A. Hsu, *Pretreatment of Biomass*, 1st edition. 1996.

[133] J. D. McMillan, “Pretreatment of Lignocellulosic Biomass,” in *Enzymatic Conversion of Biomass for Fuels Production*, ACS Publications, 1994, pp. 292–324.

[134] N. Mosier *et al.*, “Features of promising technologies for pretreatment of lignocellulosic biomass,” *Bioresour. Technol.*, vol. 96, pp. 673–686, 2005.

[135] Y. Sun and J. Cheng, “Hydrolysis of lignocellulosic materials for ethanol production: a review,” *Bioresour. Technol.*, vol. 83, pp. 1–11, 2002.

[136] L. Cadoche and G. D. López. “Assessment of Size Reduction as a Preliminary Step in the Production of Ethanol from Lignocellulosic Wastes,” *Biological Wastes*, vol. 30, pp. 153– 157.

[137] E. Takaâ Cs *et al.*, “Effect of combined gamma-irradiation and alkali treatment on cotton–cellulose,” *Radiat. Phys. Chem.*, vol. 57, pp. 399–403, 2000.

[138] M. Galbe and G. Zacchi, “Pretreatment of lignocellulosic materials for efficient bioethanol production,” *Adv. Biochem. Eng. Biotechnol.*, vol. 108, pp. 41–65, 2007.

[139] S. S. Hassan, G. A. Williams, and A. K. Jaiswal, “Emerging technologies for the pretreatment of lignocellulosic biomass,” *Bioresour. Technol.*, vol. 262, pp. 310–318, 2018.

[140] J. C. López-Linares, M. T. García-Cubero, S. Lucas, G. González-Benito, and M. Coca, “Microwave assisted hydrothermal as greener pretreatment of brewer’s spent grains for biobutanol production,” *Chem. Eng. J.*, vol. 368, pp. 1045–1055, 2019.

[141] L. N. Megashah, H. Ariffin, M. R. Zakaria, and Y. Ando, “Characteristics of cellulose from oil palm mesocarp fibres extracted by multi-step pretreatment methods,” *IOP Conf. Ser. Mater. Sci. Eng.*, vol. 368, p. 012001, 2018.

[142] V. Rigual, T. M. Santos, J. C. Domínguez, M. V. Alonso, M. Oliet, and F. Rodriguez, “Evaluation of hardwood and softwood fractionation using autohydrolysis and ionic liquid microwave pretreatment,” *Biomass Bioenergy*, vol. 117, pp. 190–197, 2018.

[143] E. barbary, M. Hassan and N. Shukry, “Polyhydric alcohol liquefaction of some lignocellulosic agricultural residues,” *Ind. Crops Prod.*, vol. 27, pp. 33–38, 2008.

[144] L. Lin, Y. Yao, M. Yoshioka, and N. Shiraishi, “Liquefaction mechanism of cellulose in the presence of phenol under acid catalysis,” *Carbohydr. Polym.*, vol. 57, pp. 123–129, 2004.

[145] Z. Liu and F. S. Zhang, “Effects of various solvents on the liquefaction of biomass to produce fuels and chemical feedstocks,” *Energy Convers. Manag.*, vol. 49, pp. 3498–3504, 2008.

[146] G. P. Gopalan, A. Suku, and S. Anas, “Nanostructured Cellulose: Extraction and Characterization,” in *Handbook of Biomass*, Singapore: Springer Nature Singapore, 2023, pp. 1–41.

[147] N. Shahi, B. Min, B. Sapkota, and V. K. Rangari, “Eco-Friendly Cellulose Nanofiber Extraction from Sugarcane Bagasse and Film Fabrication,” *Sustainability*, vol. 12, p. 6015, 2020.

[148] A. Leroy, X. Falourd, L. Foucat, V. Méchin, F. Guillon, and G. Paës, “Evaluating polymer interplay after hot water pretreatment to investigate maize stem internode recalcitrance,” *Biotechnol. Biofuels*, vol. 14, p. 164, 2021.

[149] R. Aguado, A. F. Lourenço, P. J. T. Ferreira, A. Moral, and A. Tijero, “The relevance of the pretreatment on the chemical modification of cellulosic fibers,” *Cellulose*, vol. 26, pp. 5925–5936, 2019.

[150] D. Li, J. Henschen, and M. Ek, “Esterification and hydrolysis of cellulose using oxalic acid dihydrate in a solvent-free reaction suitable for preparation of surface-functionalised cellulose nanocrystals with high yield,” *Green Chem.*, vol. 19, pp. 5564–5567, 2017.

[151] O. Manaenkov *et al.*, “Kinetic Modeling for the “One-Pot” Hydrogenolysis of Cellulose to Glycols over Ru@Fe_3O_4/Polymer Catalyst,” *Reactions*, vol. 3, pp. 1–11, 2021.

[152] M. Zheng, A. Wang, J. Pang, N. Li, and T. Zhang, “Mechanism and Kinetic Analysis of the Hydrogenolysis of Cellulose to Polyols,” in *Reaction Pathways and Mechanisms in Thermocatalytic Biomass Conversion*, Springer, 2016, pp. 227–260.

[153] L.-W. Lai and A. Idris, “Disruption of Oil Palm Trunks and Fronds by Microwave-Alkali Pretreatment,” *Bioresources*, vol. 8, pp. 2792–2804, 2013.

[154] S. M. Nomanbhay, R. Hussain, and K. Palanisamy, “Microwave-Assisted Alkaline Pretreatment and Microwave Assisted Enzymatic Saccharification of Oil Palm Empty Fruit Bunch Fiber for Enhanced Fermentable Sugar Yield,” *J Sustain. Bioenergy Syst.*, vol. 3, pp. 7–17, 2013.

[155] J. Akhtar, C. Loong Teo, L. W. Lai, N. Hassan, A. Idris, and R. A. Aziz, “Factors Affecting Delignification of Oil Palm Empty Fruit Bunch by

Microwave-assisted Dilute Acid/Alkali Pretreatment," *Bioresources*, vol. 10, pp. 588–596, 2015.

[156] N. Md Rahim, E. Fazlina Hashim, and J. Akhtar, "Study on Composition, Structural and Property Changes of Oil Palm Frond Biomass Under Different Pretreatments," *Cellul. Chem. Technol.*, vol. 50, pp. 951–959, 2016.

[157] W. Fatriasari, S. H. Anita, and L. Risanto, "Microwave Assisted Acid Pretreatment of Oil Palm Empty Fruit Bunches (EFB) to Enhance Its Fermentable Sugar Production," *Waste Biomass Valorization*, vol. 8, pp. 379–391, 2017.

[158] N. N. Solihat *et al.*, "Disruption of oil palm empty fruit bunches by microwave-assisted oxalic acid pretreatment," *J. Math. Fundam. Sci.*, vol. 49, pp. 244–257, 2017.

[159] S. H. Anita *et al.*, "Optimization of Microwave-Assisted Oxalic Acid Pretreatment of Oil Palm Empty Fruit Bunch for Production of Fermentable Sugars," *Waste Biomass Valorization*, vol. 11, pp. 2673–2687, 2020.

[160] S. S. Joshi, A. D. Zodge, K. V. Pandare, and B. D. Kulkarni, "Efficient conversion of cellulose to levulinic acid by hydrothermal treatment using zirconium dioxide as a recyclable solid acid catalyst," *Ind. Eng. Chem. Res.*, vol. 53, pp. 18796–18805, 2014.

[161] S. Kang and J. Yu, "Effect of Methanol on Formation of Levulinates from Cellulosic Biomass," *Ind. Eng. Chem. Res.*, vol. 54, pp. 11552–11559, 2015.

[162] J. Shen and C. E. Wyman, "Hydrochloric acid-catalyzed levulinic acid formation from cellulose: data and kinetic model to maximize yields," *AIChE J.*, vol. 58, pp. 236–246, 2012.

[163] X. Zheng, Z. Zhi, X. Gu, X. Li, R. Zhang, and X. Lu, "Kinetic study of levulinic acid production from corn stalk at mild temperature using $FeCl_3$ as catalyst," *Fuel*, vol. 187, pp. 261–267, 2017.

[164] M. M. Zainol, N. A. S. Amin, and M. Asmadi, "Synthesis and characterization of porous microspherical ionic liquid carbon cryogel catalyst for ethyl levulinate production," *Diam. Relat. Mater.*, vol. 95, pp. 154–165, 2019.

[165] B. Kim, J. Yang, M. Kim, and J. W. Lee, "One-pot selective production of levulinic acid and formic acid from spent coffee grounds in a catalyst-free biphasic system," *Bioresour. Technol.*, vol. 303, p. 122898, 2020.

[166] W. Weiqi and W. Shubin, “Experimental and kinetic study of glucose conversion to levulinic acid catalyzed by synergy of Lewis and Brønsted acids,” *Chem. Eng. J.*, vol. 307, pp. 389–398, 2017.

[167] X. Zhang, X. Zhang, N. Sun, S. Wang, X. Wang, and Z. Jiang, “High production of levulinic acid from cellulosic feedstocks being catalyzed by temperature-responsive transition metal substituted heteropolyacids,” *Renew. Energy*, vol. 141, pp. 802–813, 2019.

[168] K. C. Badgujar, L. D. Wilson, and B. M. Bhanage, “Recent advances for sustainable production of levulinic acid in ionic liquids from biomass: Current scenario, opportunities and challenges,” *Renew. Sustain. Energy Rev.*, vol. 102, pp. 266–284, 2019.

[169] M. S. Rahaman *et al.*, “Cooperative Brønsted-Lewis acid sites created by phosphotungstic acid encapsulated metal–organic frameworks for selective glucose conversion to 5-hydroxymethylfurfural,” *Fuel*, vol. 310, p. 122459, Feb. 2022.

[170] Ch. Ramesh Kumar, P. S. Sai Prasad, and N. Lingaiah, “Aluminium exchanged heteropoly tungstate supported on titania catalysts: The generation of Lewis acidity and its role for benzylation reaction,” *J. Mol. Catal. A Chem.*, vol. 350, pp. 83–90, 2011.

[171] Ch. Ramesh Kumar, K. T. V. Rao, P. S. Sai Prasad, and N. Lingaiah, “Tin exchanged heteropoly tungstate: An efficient catalyst for benzylation of arenes with benzyl alcohol,” *J. Mol. Catal. A Chem.*, vol. 337, pp. 17–24, 2011.

[172] K. Shimizu, H. Furukawa, N. Kobayashi, Y. Itaya, and A. Satsuma, “Effects of Brønsted and Lewis acidities on activity and selectivity of heteropolyacid-based catalysts for hydrolysis of cellobiose and cellulose,” *Green Chem.*, vol. 11, p. 1627, 2009.

[173] Ch. R. Kumar, P. S. S. Prasad, and N. Lingaiah, “Heteropoly tungstate supported on tin oxide catalysts for liquid phase benzylation of anisole with benzyl alcohol,” *Appl. Catal. A Gen.*, vol. 384, pp. 101–106, 2010.

[174] L. L. Name *et al.*, “Phosphotungstic acid impregnated niobium coated superparamagnetic iron oxide nanoparticles as recyclable catalyst for selective isomerization of terpenes,” *RSC Adv.*, vol. 11, pp. 14203–14212, 2021.

[175] H. Firouzabadi, N. Iranpoor, and F. Nowrouzi, “Aluminum dodecatungstophosphate ($AlPW_{12}O_{40}$) as a non-hygroscopic Lewis acid catalyst for the efficient Friedel-Crafts acylation of aromatic compounds

under solvent-less conditions," *Tetrahedron*, vol. 60, pp. 10843–10850, 2004.

[176] H. Firouzabadi, N. Iranpoor, and A. A. Jafari, "Aluminumdodecatungstophosphate ($AlPW_{12}O_{40}$), a versatile and a highly water tolerant green Lewis acid catalyzes efficient preparation of indole derivatives," *J. Mol. Catal. A Chem.*, vol. 244, pp. 168–172, 2006.

[177] H. Firouzabadi, N. Iranpoor, A. A. Jafari, and S. Makarem, "Aluminumdodecatungstophosphate ($AlPW_{12}O_{40}$) as a reusable Lewis acid catalyst. Facile regioselective ring opening of epoxides with alcohols, acetic acid and thiols," *J. Mol. Catal. A Chem.*, vol. 250, pp. 237–242, 2006.

[178] K. Srilatha, N. Lingaiah, B. L. A. P. Devi, R. B. N. Prasad, S. Venkateswar, and P. S. S. Prasad, "Esterification of free fatty acids for biodiesel production over heteropoly tungstate supported on niobia catalysts," *Appl. Catal. A Gen.*, vol. 365, pp. 28–33, 2009.

[179] N. Lingaiah, N. S. Babu, K. M. Reddy, P. S. S. Prasad, and I. Suryanarayana, "An efficient reusable silver-exchanged tungstophosphoric acid heterogeneous catalyst for solvent-free intermolecular hydroamination of alkynes," *Chem. Commun.*, pp. 278–279, 2007.

[180] T. Baba, H. Watanabe, and Y. Ono, "Generation of acidic sites in metal salts of heteropoly acids," *J. Phys. Chem.*, vol. 87, pp. 2406–2411, 1983.

[181] A. Ghosh, "Acidity of heteropoly compounds," *J. Catal.*, vol. 101, pp. 238–245, 1986.

[182] T. Baba, J. Sakai, and Y. Ono, "The Conversion of Methanol into Hydrocarbons over Metal Salts of Heteropolyacids," *Chem. Soc. Japan*, vol. 55, pp. 2657– 2658, 1982.

[183] K. ichi Shimizu, K. Niimi, and A. Satsuma, "Polyvalent-metal salts of heteropolyacid as efficient heterogeneous catalysts for Friedel-Crafts acylation of arenes with carboxylic acids," *Catal. Commun.*, vol. 9, pp. 980–983, 2008.

[184] K. ichi Shimizu, K. Niimi, and A. Satsuma, "Polyvalent-metal salts of heteropolyacid as catalyst for Friedel-Crafts alkylation reactions," *Appl. Catal. A Gen.*, vol. 349, pp. 1–5, 2008.

[185] M. Cheng, T. Shi, H. Guan, S. Wang, X. Wang, and Z. Jiang, "Clean production of glucose from polysaccharides using a micellar

heteropolyacid as a heterogeneous catalyst," *Appl. Catal. B*, vol. 107, pp. 104–109, 2011.

[186] Z. Sun *et al.*, "One-pot depolymerization of cellulose into glucose and levulinic acid by heteropolyacid ionic liquid catalysis," *RSC Adv.*, vol. 2, p. 9058, 2012.

[187] Z. Sun, L. Xue, S. Wang, X. Wang, and J. Shi, "Single step conversion of cellulose to levulinic acid using temperature-responsive dodeca-aluminotungstic acid catalysts," *Green Chem.*, vol. 18, pp. 742–752, 2016.

[188] X. Li *et al.*, "Efficient catalytic production of biomass-derived levulinic acid over phosphotungstic acid in deep eutectic solvent," *Ind. Crops Prod.*, vol. 145, p. 112154, 2020.

[189] V. B. Kumar, I. N. Pulidindi, R. K. Mishra, and A. Gedanken, "Development of Ga Salt of Molybdophosphoric Acid for Biomass Conversion to Levulinic Acid," *Energy Fuels*, vol. 30, pp. 10583–10591, 2016.

[190] F. Chambon, F. Rataboul, C. Pinel, A. Cabiac, E. Guillon, and N. Essayem, "Cellulose hydrothermal conversion promoted by heterogeneous Brønsted and Lewis acids: Remarkable efficiency of solid Lewis acids to produce lactic acid," *Appl. Catal. B*, vol. 105, pp. 171–181, 2011.

[191] M. N. Catrinck *et al.*, "One-step process to produce furfural from sugarcane bagasse over niobium-based solid acid catalysts in a water medium," *Fuel Process. Technol.*, vol. 207, p. 106482, 2020.

[192] M. N. Catrinck, E. S. Ribeiro, R. S. Monteiro, R. M. Ribas, M. H. P. Barbosa, and R. F. Teófilo, "Direct conversion of glucose to 5-hydroxymethylfurfural using a mixture of niobic acid and niobium phosphate as a solid acid catalyst," *Fuel*, vol. 210, pp. 67–74, 2017.

[193] K. Nakajima *et al.*, "$Nb_2O_5 \cdot nH_2O$ as a Heterogeneous Catalyst with Water-Tolerant Lewis Acid Sites," *J. Am. Chem. Soc.*, vol. 133, pp. 4224–4227, 2011.

[194] L. Zhu *et al.*, "Preparation of the Nb-P/SBA-15 catalyst and its performance in the dehydration of fructose to 5-hydroxymethylfurfural," *J. Fuel Chem. Technol.*, vol. 45, pp. 651–659, 2017.

[195] P. Carniti, A. Gervasini, S. Biella, and A. Auroux, "Niobic acid and niobium phosphate as highly acidic viable catalysts in aqueous medium:

Fructose dehydration reaction," *Catal. Today*, vol. 118, pp. 373–378, 2006.

[196] M. J. C. Molina, M. L. Granados, A. Gervasini, and P. Carniti, "Exploitment of niobium oxide effective acidity for xylose dehydration to furfural," *Catal. Today*, vol. 254, pp. 90–98, 2015.

[197] Y. Zhang *et al.*, "Mesoporous niobium phosphate: an excellent solid acid for the dehydration of fructose to 5-hydroxymethylfurfural in water," *Catal. Sci. Technol.*, vol. 2, p. 2485, 2012.

[198] M. B. Pinto, A. L. Soares, A. Mella Orellana, H. A. Duarte, and H. A. De Abreu, "Structural, Electronic, and Thermodynamic Properties of the T and B Phases of Niobia: First-Principle Calculations," *J. Phys. Chem. A*, vol. 121, pp. 2399–2409, 2017.

[199] R. Wojcieszak, A. Jasik, S. Monteverdi, M. Ziolek, and M. M. Bettahar, "Nickel niobia interaction in non-classical Ni/Nb_2O_5 catalysts," *J. Mol. Catal. A Chem.*, vol. 256, pp. 225–233, 2006.

[200] C. Nico, T. Monteiro, and M. P. F. Graça, "Niobium oxides and niobates physical properties: Review and prospects," *Prog. Mater. Sci.*, vol. 80, pp. 1–37, 2016.

[201] C. Valencia-Balvín, S. Pérez-Walton, G. M. Dalpian, and J. M. Osorio-Guillén, "First-principles equation of state and phase stability of niobium pentoxide," *Comput. Mater. Sci.*, vol. 81, pp. 133–140, 2014.

[202] I. Nowak and M. Ziolek, "Niobium Compounds: Preparation, Characterization, and Application in Heterogeneous Catalysis," *Chem. Rev.*, vol. 99, pp. 3603–3624, 1999.

[203] G. F. Leal *et al.*, "Design of Nickel Supported on Water-Tolerant Nb_2O_5 Catalysts for the Hydrotreating of Lignin Streams Obtained from Lignin-First Biorefining," *iScience*, vol. 15, pp. 467–488, 2019.

[204] A. M. Barrios *et al.*, "Hydrodeoxygenation of phenol over niobia supported Pd catalyst," *Catal. Today*, vol. 302, pp. 115–124, 2018.

[205] L. Dong *et al.*, "Comparison of two multifunctional catalysts [M/Nb_2O_5 (M = Pd, Pt)] for one-pot hydrodeoxygenation of lignin," *Catal. Sci. Technol.*, vol. 8, pp. 6129–6136, 2018.

[206] W. Guan, X. Chen, S. Jin, C. Li, C.-W. Tsang, and C. Liang, "Highly Stable Nb_2O_5 –Al_2O_3 Composites Supported Pt Catalysts for Hydrodeoxygenation of Diphenyl Ether," *Ind. Eng. Chem. Res.*, vol. 56, pp. 14034–14042, 2017.

[207] W. Guan *et al.*, “Catalytic hydrogenolysis of lignin β-O-4 aryl ether compound and lignin to aromatics over Rh/Nb_2O_5 under low H_2 pressure,” *Fuel Process. Technol.*, vol. 203, p. 106392, 2020.

[208] Y. Shao *et al.*, “Selective production of arenes via direct lignin upgrading over a niobium-based catalyst,” *Nat. Commun.*, vol. 8, p. 16104, 2017.

[209] M. Lin *et al.*, “Features of Nb_2O_5 as a metal oxide support of Pt and Pd catalysts for selective catalytic oxidation of NH_3 with high N_2 selectivity,” *J. Catal.*, vol. 389, pp. 366–374, 2020.

[210] E. Z. Kurmaev *et* al., “Electronic structure of niobium oxides,” *J. Alloys Compd.*, vol. 347, pp. 213–218, 2002.

[211] Y. Liu, H. Li, J. He, W. Zhao, T. Yang, and S. Yang, “Catalytic conversion of carbohydrates to levulinic acid with mesoporous niobium-containing oxides,” *Catal. Commun.*, vol. 93, pp. 20–24, 2017.

[212] F. Yang, X. Tong, F. Xia, C. Zheng, L. Qin, and X. Jiang, “Efficient Hydroxymethylfurfural Production over Phosphoric Carbon Solid Acids,” *Catal. Letters*, vol. 148, pp. 1848–1855, 2018.

[213] J.-L. Gao, S. Gao, C.-L. Liu, Z.-T. Liu, and W.-S. Dong, “Synthesis, characterization, and catalytic application of ordered mesoporous carbon–niobium oxide composites,” *Mater. Res. Bull.*, vol. 59, pp. 131–136, 2014.

[214] C. García-Sancho, I. Agirrezabal-Telleria, M. B. Güemez, and P. Maireles-Torres, “Dehydration of d-xylose to furfural using different supported niobia catalysts,” *Appl. Catal. B*, vol. 152–153, pp. 1–10, 2014.

[215] D. Ballesteros-Plata *et al.*, “Bimetallic Niobium-Based Catalysts Supported on SBA-15 for Hydrodeoxygenation of Anisole,” *Ind. Eng. Chem. Res.*, vol. 60, pp. 18831–18840, 2021.

[216] S. Kannan, P. Arumugam, and G. Govindasamy, “SBA-15 and carbon supported nickel, heteropoly acid catalysts for the hydrodeoxygenation of lignin derived trans-anethole to sustainable aviation fuel,” *J. Porous Mater.*, vol. 30, pp. 639–653, 2023.

[217] P. P. Upare *et al.*, “Chemical conversion of biomass-derived hexose sugars to levulinic acid over sulfonic acid-functionalized graphene oxide catalysts,” *Green Chem.*, vol. 15, p. 2935, 2013.

[218] N. H. H. Phuc *et al.*, “A Review of Bifunctional Catalysts for Zinc-Air Batteries,” *Nanoenergy Adv.*, vol. 3, pp. 13–47, 2023.

[219] K. B. Tan, G. Zhan, D. Sun, J. Huang, and Q. Li, “The development of bifunctional catalysts for carbon dioxide hydrogenation to hydrocarbons *via* the methanol route: from single component to integrated components,” *J. Mater. Chem. A*, vol. 9, pp. 5197–5231, 2021.

[220] D. Xue, H. Xia, W. Yan, J. Zhang, and S. Mu, “Defect Engineering on Carbon-Based Catalysts for Electrocatalytic CO_2 Reduction,” *Nanomicro Lett.*, vol. 13, p. 5, 2021.

[221] S. Yadav and D. Chattopadhyay, “Lignin: the Building Block of Defense Responses to Stress in Plants,” *J. Plant Growth Regul.*, vol. 42, pp. 6652–6666, 2023.

[222] C. Yang, S. Maldonado, and C. R. J. Stephenson, “Electrocatalytic Lignin Oxidation,” *ACS Catal.*, vol. 11, pp. 10104–10114, 2021.

[223] R. A. Perkins and G. H. Meier, “The oxidation behavior and protection of niobium,” *JOM*, vol. 42, pp. 17–21, 1990.

[224] E. Zhu *et al.*, “Study on the Effect of Niobium on the High Temperature Oxidation Resistance of Ferritic Stainless Steel,” *Metals (Basel)*, vol. 14, p. 25, 2023.

[225] Z. Ling *et al.*, “Freeze-drying for sustainable synthesis of nitrogen doped porous carbon cryogel with enhanced supercapacitor and lithium ion storage performance,” *Nanotechnology*, vol. 26, p. 374003, 2015.

[226] M. Mennani *et al.*, “Effects of direct sulfonation on the catalytic activity and recyclability of novel lignin-based solid acid catalysts from agri-food waste,” *Int. J. Biol. Macromol.*, vol. 230, p. 123242, 2023.

[227] M. Nasrollahzadeh, M. Ghasemzadeh, H. Gharoubi, and Z. Nezafat, “Progresses in polysaccharide and lignin-based ionic liquids: Catalytic applications and environmental remediation,” *J. Mol. Liq.*, vol. 342, p. 117559, 2021.

[228] S. Zhu *et al.*, “Catalytic transformation of cellulose into short rod-like cellulose nanofibers and platform chemicals over lignin-based solid acid,” *Appl. Catal. B*, vol. 268, p. 118732, 2020.

[229] F. Kong and M. Wang, “Preparation of Sulfur-Modulated Nickel/Carbon Composites from Lignosulfonate for the Electrocatalytic Oxidation of 5-Hydroxymethylfurfural to 2,5-Furandicarboxylic Acid,” *ACS Appl. Energy Mater.*, vol. 4, pp. 1182–1188, 2021.

[230] X. Li, Y. Lv, and D. Pan, “Pt catalysts supported on lignin-based carbon dots for methanol electro-oxidation,” *Colloids Surf. A Physicochem. Eng. Asp.*, vol. 569, pp. 110–118, 2019.

[231] R. Mohami, A. Shakeri, and M. Nasrollahzadeh, “Mannich-mediated synthesis of a recyclable magnetic kraft lignin-coated copper nanostructure as an efficient catalyst for treatment of environmental contaminants in aqueous media,” *Sep. Purif. Technol.*, vol. 285, p. 120373, 2022.

[232] N. Sarki *et al.*, “Lignin Residue-Derived Carbon-Supported Nanoscale Iron Catalyst for the Selective Hydrogenation of Nitroarenes and Aromatic Aldehydes,” *ACS Omega*, vol. 7, pp. 19804–19815, 2022.

[233] S. Chen, G. Wang, W. Sui, A. M. Parvez, L. Dai, and C. Si, “Novel lignin-based phenolic nanosphere supported palladium nanoparticles with highly efficient catalytic performance and good reusability,” *Ind. Crops Prod.*, vol. 145, p. 112164, 2020.

[234] Y. Qi *et al.*, “Novel lignin-based single atom catalysts as peroxymonosulfate activator for pollutants degradation: Role of single cobalt and electron transfer pathway,” *Appl. Catal. B*, vol. 286, p. 119910, 2021.

[235] M. Wang, X. Zhang, H. Li, J. Lu, M. Liu, and F. Wang, “Carbon Modification of Nickel Catalyst for Depolymerization of Oxidized Lignin to Aromatics,” *ACS Catal.*, vol. 8, pp. 1614–1620, 2018.

[236] J. Zhuang *et al.*, “Lignin-based carbon dots as high-performance support of Pt single atoms for photocatalytic H_2 evolution,” *Chem. Eng. J.*, vol. 446, p. 136873, 2022.

[237] B. Matović *et al.*, “Carbon cryogel preparation and characterization,” *Diam. Relat. Mater.*, vol. 121, p. 108727, 2022.

[238] R. W. Pekala, “Organic aerogels from the polycondensation of resorcinol with formaldehyde,” *J. Mater. Sci.*, vol. 24, pp. 3221–3227, 1989.

[239] B. Babić, B. Kaluđerović, Lj. Vračar, and N. Krstajić, “Characterization of carbon cryogel synthesized by sol–gel polycondensation and freeze-drying,” *Carbon*, vol. 42, pp. 2617–2624, 2004.

[240] A. Kalijadis *et al.*, “Composition, structure and potential energy application of nitrogen doped carbon cryogels,” *Mater. Chem. Phys.*, vol. 239, p. 122120, 2020.

[241] C. Moreno-Castilla and F. J. Maldonado-Hódar, “Carbon aerogels for catalysis applications: An overview,” *Carbon*, vol. 43, pp. 455–465, 2005.

[242] F. Rodríguez-reinoso, “The role of carbon materials in heterogeneous catalysis,” *Carbon*, vol. 36, pp. 159–175, 1998.

[243] M. M. Zainol, N. A. S. Amin, and M. Asmadi, “Kinetics and thermodynamic analysis of levulinic acid esterification using lignin-furfural carbon cryogel catalyst,” *Renew. Energy*, vol. 130, pp. 547–557, 2019.

[244] M. M. Zainol, M. Asmadi, P. Iskandar, W. A. N. Wan Ahmad, N. A. S. Amin, and T. T. Hoe, “Ethyl levulinate synthesis from biomass derivative chemicals using iron doped sulfonated carbon cryogel catalyst,” *J. Clean. Prod.*, vol. 281, p. 124686, 2021.

[245] M. M. Zainol, N. A. S. Amin, and M. Asmadi, “Effects of thermal treatment on carbon cryogel preparation for catalytic esterification of levulinic acid to ethyl levulinate,” *Fuel Process. Technol.*, vol. 167, pp. 431–441, 2017.

[246] C. Lin and J. A. Ritter, “Effect of synthesis pH on the structure of carbon xerogels,” *Carbon*, vol. 35, pp. 1271–1278, 1997.

[247] C. Paul, Hiemenz, and P. L. Timothy, *Polymer Chemistry*, 3rd ed. Taylor and Francis Group, 2020.

[248] Y. Guo, J. Bae, Z. Fang, P. Li, F. Zhao, and G. Yu, “Hydrogels and Hydrogel-Derived Materials for Energy and Water Sustainability,” *Chem. Rev.*, vol. 120, pp. 7642–7707, 2020.

[249] A. Beaucamp *et al.*, “Lignin for energy applications – state of the art, life cycle, technoeconomic analysis and future trends,” *Green Chem.*, vol. 24, pp. 8193–8226, 2022.

[250] J. J. Liao, N. H. A. Latif, D. Trache, N. Brosse, and M. H. Hussin, “Current advancement on the isolation, characterization and application of lignin,” *Int. J. Biol. Macromol.*, vol. 162, pp. 985–1024, 2020.

[251] A. Tribot *et al.*, “Wood-lignin: Supply, extraction processes and use as bio-based material,” *Eur. Polym. J.*, vol. 112, pp. 228–240, 2019.

[252] H. de Baynast *et al.*, “Effects of Kraft lignin and corn cob agro-residue on the properties of injected-moulded biocomposites,” *Ind. Crops Prod.*, vol. 177, p. 114421, 2022.

[253] M. R. Ridho *et al.*, “Lignin as Green Filler in Polymer Composites: Development Methods, Characteristics, and Potential Applications,” *Adv. Mater. Sci. Eng.*, vol. 2022, pp. 1–33, 2022.

[254] M. N. Mohamad Ibrahim, N. Zakaria, C. S. Sipaut, O. Sulaiman, and R. Hashim, “Chemical and thermal properties of lignins from oil palm biomass as a substitute for phenol in a phenol formaldehyde resin production,” *Carbohydr. Polym.*, vol. 86, pp. 112–119, 2011.

[255] A. U. Buranov and G. Mazza, “Lignin in straw of herbaceous crops,” *Ind. Crops Prod.*, vol. 28, pp. 237–259, 2008.

[256] J. L. Espinoza-Acosta, P. I. Torres-Chávez, E. Carvajal-Millán, B. Ramírez-Wong, L. A. Bello-Pérez, and B. Montaño-Leyva, “Ionic Liquids and Organic Solvents for Recovering Lignin from Lignocellulosic Biomass,” *Bioresources*, vol. 9, pp. 3660–3687, 2014.

[257] C. Chio, M. Sain, and W. Qin, “Lignin utilization: A review of lignin depolymerization from various aspects,” *Renew. Sust. Energ. Rev.*, vol. 107, pp. 232–249, 2019.

[258] C. A. Cateto, M. F. Barreiro, and A. E. Rodrigues, “Monitoring of lignin-based polyurethane synthesis by FTIR-ATR,” *Ind. Crops Prod.*, vol. 27, pp. 168–174, 2008.

[259] A. Arshanitsa, L. Krumina, G. Telysheva, and T. Dizhbite, “Exploring the application potential of incompletely soluble organosolv lignin as a macromonomer for polyurethane synthesis,” *Ind. Crops Prod.*, vol. 92, pp. 1–12, 2016.

[260] N. Mahmood, Z. Yuan, J. Schmidt, and C. (Charles) Xu, “Depolymerization of lignins and their applications for the preparation of polyols and rigid polyurethane foams: A review,” *Renew. Sust. Energ. Rev.*, vol. 60, pp. 317–329, 2016.

[261] W. O. S. Doherty, P. Mousavioun, and C. M. Fellows, “Value-adding to cellulosic ethanol: Lignin polymers,” *Ind. Crops Prod.*, vol. 33, pp. 259–276, 2011.

[262] B. M. Upton and A. M. Kasko, “Strategies for the Conversion of Lignin to High-Value Polymeric Materials: Review and Perspective,” *Chem. Rev.*, vol. 116, pp. 2275–2306, 2015.

[263] E. Gazo Hanna, K. Younes, S. Amine, and R. Roufayel, “Exploring Gel-Point Identification in Epoxy Resin Using Rheology and Unsupervised Learning,” *Gels*, vol. 9, p. 828, 2023.

[264] P. Polanowski and A. Sikorski, “The Influence of Constraints on Gelation in a Controlling/Living Copolymerization Process,” *Int. J. Mol. Sci.*, vol. 24, p. 2701, 2023.

[265] X. Liu, J. Zhang, M. Liu, X. Han, and H. Liu, “Hydrophilicity–hydrophobicity adjustable polymer-modified surfaces from one-step dip-coating method,” *J. Coat Technol. Res.*, 2024.

[266] J. Tan, Y. Zhao, J. L. Hedrick, and Y. Y. Yang, “Effects of Hydrophobicity on Antimicrobial Activity, Selectivity, and Functional Mechanism of Guanidinium-Functionalized Polymers,” *Adv. Healthc. Mater.*, vol. 11, p. 2100482, 2022.

[267] J. L. Ifkovits and J. A. Burdick, “Review: Photopolymerizable and Degradable Biomaterials for Tissue Engineering Applications,” *Tissue Eng.*, vol. 13, pp. 2369–2385, 2007.

[268] E. Caló and V. V. Khutoryanskiy, “Biomedical applications of hydrogels: A review of patents and commercial products,” *Eur. Polym. J.*, vol. 65, pp. 252–267, 2015.

[269] N. Singh *et al.*, “Synthesis of a Double-Network Supramolecular Hydrogel by Having One Network Catalyse the Formation of the Second,” *Chem. Eur. J.*, vol. 23, pp. 2018–2021, 2017.

[270] X. Wang, Z. Zhou, X. Guo, Q. He, C. Hao, and C. Ge, “Ultrasonic-assisted synthesis of sodium lignosulfonate-grafted poly(acrylic acid-co-poly(vinyl pyrrolidone)) hydrogel for drug delivery,” *RSC Adv.*, vol. 6, pp. 35550–35558, 2016.

[271] D. F. Coutinho *et al.*, “Modified Gellan Gum hydrogels with tunable physical and mechanical properties,” *Biomaterials*, vol. 31, pp. 7494–7502, 2010.

[272] Z. Bao, C. Xian, Q. Yuan, G. Liu, and J. Wu, “Natural Polymer-Based Hydrogels with Enhanced Mechanical Performances: Preparation, Structure, and Property,” *Adv. Healthc. Mater.*, vol. 8, p. 1900670, 2019.

[273] C. C. Ahrens, M. E. Welch, L. G. Griffith, and P. T. Hammond, “Uncharged Helical Modular Polypeptide Hydrogels for Cellular Scaffolds,” *Biomacromolecules*, vol. 16, pp. 3774–3783, 2015.

[274] H. Cui, X. Zhuang, C. He, Y. Wei, and X. Chen, “High performance and reversible ionic polypeptide hydrogel based on charge-driven assembly for biomedical applications,” *Acta Biomater.*, vol. 11, pp. 183–190, 2015.

[275] M. Ishihara *et al.*, “Photocrosslinkable chitosan as a dressing for wound occlusion and accelerator in healing process,” *Biomaterials*, vol. 23, pp. 833–840, 2002.

[276] D. D. Lane, A. K. Fessler, S. Goo, D. L. Williams, and R. J. Stewart, "Sustained tobramycin release from polyphosphate double network hydrogels," *Acta Biomater.*, vol. 50, pp. 484–492, 2017.

[277] C. M. Madl, L. M. Katz, and S. C. Heilshorn, "Bio-Orthogonally Crosslinked, Engineered Protein Hydrogels with Tunable Mechanics and Biochemistry for Cell Encapsulation," *Adv. Funct. Mater.*, vol. 26, pp. 3612–3620, 2016.

[278] J. Wu, X. Zhao, D. Wu, and C.-C. Chu, "Development of a biocompatible and biodegradable hybrid hydrogel platform for sustained release of ionic drugs," *J. Mater. Chem. B*, vol. 2, pp. 6660–6668, 2014.

[279] Y. Alinejad, A. Adoungotchodo, E. Hui, F. Zehtabi, and S. Lerouge, "An injectable chitosan/chondroitin sulfate hydrogel with tunable mechanical properties for cell therapy/tissue engineering," *Int. J. Biol. Macromol.*, vol. 113, pp. 132–141, 2018.

[280] X. Gou *et al.*, "Mechanical property of PEG hydrogel and the 3D red blood cell microstructures fabricated by two-photon polymerization," *Appl. Surf. Sci*, vol. 416, pp. 273–280, 2017.

[281] C. Yang *et al.*, "Reduced Graphene Oxide-Containing Smart Hydrogels with Excellent Electro-Response and Mechanical Properties for Soft Actuators," *ACS Appl. Mater. Interfaces*, vol. 9, pp. 15758–15767, 2017.

[282] E. Sanmartín-Masiá, S. Poveda-Reyes, and G. Gallego Ferrer, "Extracellular matrix–inspired gelatin/hyaluronic acid injectable hydrogels," *Int. J. Polym. Mater. PO*, vol. 66, pp. 280–288, 2017.

[283] J. M. Zuidema, M. M. Pap, D. B. Jaroch, F. A. Morrison, and R. J. Gilbert, "Fabrication and characterization of tunable polysaccharide hydrogel blends for neural repair," *Acta Biomater.*, vol. 7, pp. 1634–1643, 2011.

[284] J. Li, Z. Suo, and J. J. Vlassak, "Stiff, strong, and tough hydrogels with good chemical stability," *J. Mater. Chem. B*, vol. 2, pp. 6708–6713, 2014.

[285] S. Lin, C. Cao, Q. Wang, M. Gonzalez, J. E. Dolbow, and X. Zhao, "Design of stiff, tough and stretchy hydrogel composites via nanoscale hybrid crosslinking and macroscale fiber reinforcement," *Soft Matter.*, vol. 10, pp. 7519–7527, 2014.

[286] R. E. Webber, C. Creton, H. R. Brown, and J. P. Gong, "Large Strain Hysteresis and Mullins Effect of Tough Double-Network Hydrogels," *Macromolecules*, vol. 40, pp. 2919–2927, 2007.

[287] X. Zhao, “Multi-scale multi-mechanism design of tough hydrogels: building dissipation into stretchy networks,” *Soft Matter.*, vol. 10, pp. 672–687, 2014.

[288] R. Y. Lochhead, “The Use of Polymers in Cosmetic Products,” in *Cosmetic Science and Technology*, Elsevier, 2017, pp. 171–221.

[289] M. J. N. Amaldoss and Reeta, “Gum-based nanoparticles in cancer therapy,” in *Micro- and Nanoengineered Gum-Based Biomaterials for Drug Delivery and Biomedical Applications*, Elsevier, 2022, pp. 183–225.

[290] M. Nasrollahzadeh, M. Sajjadi, Z. Nezafat, and N. Shafiei, “Polysaccharide biopolymer chemistry,” in *Biopolymer-Based Metal Nanoparticle Chemistry for Sustainable Applications*, Elsevier, 2021, pp. 45–105.

[291] M. Milas and M. Rinaudo, “Conformational investigation on the bacterial polysaccharide xanthan,” *Carbohydr. Res.*, vol. 76, pp. 189–196, 1979.

[292] S. Bratskaya *et al.*, “Chitosan Gels and Cryogels Cross-Linked with Diglycidyl Ethers of Ethylene Glycol and Polyethylene Glycol in Acidic Media,” *Biomacromolecules*, vol. 20, pp. 1635–1643, 2019.

[293] C. Oelschlaeger, F. Bossler, and N. Willenbacher, “Synthesis, Structural and Micromechanical Properties of 3D Hyaluronic Acid-Based Cryogel Scaffolds,” *Biomacromolecules*, vol. 17, pp. 580–589, 2016.

[294] H.-W. Leung, “Polyethylene Glycol,” in *Encyclopedia of Toxicology*, Elsevier, 2014, pp. 1043–1044.

[295] J. K. Fink, “Furan Resins,” in *Reactive Polymers Fundamentals and Applications*, Elsevier, 2005, pp. 203–215.

[296] M. Xiang, J. Liu, W. Fu, T. Tang, and D. Wu, “Improved Activity for Cellulose Conversion to Levulinic Acid through Hierarchization of ETS-10 Zeolite,” *ACS Sustain. Chem. Eng.*, vol. 5, pp. 5800–5809, 2017.

[297] A. Eldridge and A. Fam, “Durability of Concrete Cylinders Wrapped with GFRP Made from Furfuryl Alcohol Bioresin,” *J. Compos. Constr.*, vol. 18, p. 04014013, 2014.

[298] H. Fujii *et al.*, “Fabrication of Fe-Based Metallic Glass Particle Reinforced Al-Based Composite Materials by Friction Stir Processing,” *Mater. Trans.*, vol. 52, pp. 1634–1640, 2011.

[299] A. M. Orlova, “Furfural-based Binder for Composite Construction Materials,” *Procedia Eng.*, vol. 153, pp. 527–530, 2016.

[300] S. Sun *et al.*, “Simultaneous and Efficient Production of Furfural and Subsequent Glucose in MTHF/H_2O Biphasic System via Parameter Regulation,” *Polymers*, vol. 12, p. 557, 2020.

[301] N. Sweygers, J. Harrer, R. Dewil, and L. Appels, “A microwave-assisted process for the in-situ production of 5-hydroxymethylfurfural and furfural from lignocellulosic polysaccharides in a biphasic reaction system,” *J. Clean. Prod.*, vol. 187, pp. 1014–1024, 2018.

[302] C. Wu *et al.*, “Conversion of Xylose into Furfural Using Lignosulfonic Acid as Catalyst in Ionic Liquid,” *J. Agric. Food Chem.*, vol. 62, pp. 7430–7435, 2014.

[303] S. Zhao, W. J. Malfait, N. Guerrero-Alburquerque, M. M. Koebel, and G. Nyström, “Biopolymer Aerogels and Foams: Chemistry, Properties, and Applications,” *Angew. Chem. Int. Ed.*, vol. 57, pp. 7580–7608, 2018.

[304] Z. Zhao *et al.*, “Effects of Sulfuric Acid on the Curing Behavior and Bonding Performance of Tannin–Sucrose Adhesive,” *Polymers*, vol. 10, p. 651, 2018.

[305] Y. Cheng and G. Sui, “Synthesis and regulation mechanism of bio-oil–glucose phenolic resin using furfural as cross-linking agent,” *Iran. Polym. J.*, vol. 31, pp. 619–628, 2022.

[306] J. Zhang *et al.*, “Preparation of a starch-based adhesive cross-linked with furfural, furfuryl alcohol and epoxy resin,” *Int. J. Adhes. Adhes.*, vol. 110, p. 102958, 2021.

[307] J. P. Gong, Y. Katsuyama, T. Kurokawa, and Y. Osada, “Double-Network Hydrogels with Extremely High Mechanical Strength,” *Adv. Mater.*, vol. 15, pp. 1155–1158, 2003.

[308] Y. Tanaka, J. P. Gong, and Y. Osada, “Novel hydrogels with excellent mechanical performance,” *Prog. Polym. Sci.*, vol. 30, pp. 1–9, 2005.

[309] E. C. Muniz and G. Geuskens, “Polyacrylamide Hydrogels and Semi-Interpenetrating Networks (IPNs) with Poly(N-Isopropylacrylamide): Mechanical Properties by Measure of Compressive Elastic Modulus,” *J. Mater. Sci. Mater. Med.*, vol. 12, pp. 879–881, 2001.

[310] N. Mazloom, R. Khorassani, G. H. Zohuri, H. Emami, and J. Whalen, “Development and Characterization of Lignin-Based Hydrogel for Use

in Agricultural Soils: Preliminary Evidence," *Clean*, vol. 47, p. 1900101, 2019.

[311] Wahyudiono, M. Sasaki, and M. Goto, "Recovery of phenolic compounds through the decomposition of lignin in near and supercritical water," *Chem. Eng. Process.: Process Intensif.*, vol. 47, pp. 1609–1619, 2008.

[312] P. K. Mishra and A. Ekielski, "The Self-Assembly of Lignin and Its Application in Nanoparticle Synthesis: A Short Review," *Nanomaterials*, vol. 9, p. 243, 2019.

[313] C. Zhang, A. Aung, L. Liao, and S. Varghese, "A novel single precursor-based biodegradable hydrogel with enhanced mechanical properties," *Soft Matter.*, vol. 5, p. 3831, 2009.

[314] L. Hossain, V. S. Raghuwanshi, J. Tanner, and G. Garnier, "Modulating nanocellulose hydrogels and cryogels strength by crosslinking and blending," *Colloids Surf. A Physicochem. Eng. Asp.*, vol. 630, p. 127608, 2021.

[315] J. E. Peñaranda A. and M. A. Sabino, "Effect of the presence of lignin or peat in IPN hydrogels on the sorption of heavy metals," *Polym. Bull.*, vol. 65, pp. 495–508, 2010.

[316] F. Oveissi, S. Naficy, T. Y. L. Le, D. F. Fletcher, and F. Dehghani, "Tough and Processable Hydrogels Based on Lignin and Hydrophilic Polyurethane," *ACS Appl. Bio. Mater.*, vol. 1, pp. 2073–2081, 2018.

[317] S. Huang *et al.*, "Facile fabrication and characterization of highly stretchable lignin-based hydroxyethyl cellulose self-healing hydrogel," *Carbohydr. Polym.*, vol. 223, p. 115080, 2019.

[318] K. Ravishankar *et al.*, "Biocompatible hydrogels of chitosan-alkali lignin for potential wound healing applications," *Mater. Sci. Eng.: C*, vol. 102, pp. 447–457, 2019.

[319] L. I. Grishechko, G. Amaral-Labat, A. Szczurek, V. Fierro, B. N. Kuznetsov, and A. Celzard, "Lignin–phenol–formaldehyde aerogels and cryogels," *Microporous Mesoporous Mater.*, vol. 168, pp. 19–29, 2013.

[320] F. Chen, M. Xu, L. Wang, and J. Li, "Preparation and characterization of organic aerogels by the lignin-resorcinol-formaldehyde copolymer," *Bioresources*, vol. 6, pp. 1262–1272, 2011.

[321] Q. Yin, W. Yang, C. Sun, and M. Di, "Preparation and properties of lignin-epoxy resin composite," *Bioresources*, vol. 7, pp. 5737–5748, 2012.

[322] T. Lindström and L. Westman, “The colloidal behaviour of kraft lignin Part IV: Syneresis and hysteresis in swelling of kraft lignin gels,” *Colloid Polym. Sci.*, vol. 260, pp. 594–598, 1982.

[323] D. Ciolacu, A. M. Oprea, N. Anghel, G. Cazacu, and M. Cazacu, “New cellulose–lignin hydrogels and their application in controlled release of polyphenols,” *Mater. Sci. Eng.: C*, vol. 32, pp. 452–463, 2012.

[324] L. Dai, W. Zhu, J. Lu, F. Kong, C. Si, and Y. Ni, “A lignin-containing cellulose hydrogel for lignin fractionation,” *Green Chem.*, vol. 21, pp. 5222–5230, 2019.

[325] D. Ciolacu and G. Cazacu, “New Green Hydrogels Based on Lignin,” *J. Nanosci. Nanotechnol.*, vol. 18, pp. 2811–2822, 2018.

[326] L. Wu, S. Huang, J. Zheng, Z. Qiu, X. Lin, and Y. Qin, “Synthesis and characterization of biomass lignin-based PVA super-absorbent hydrogel,” *Int. J. Biol. Macromol.*, vol. 140, pp. 538–545, 2019.

[327] M. Nishida, Y. Uraki, and Y. Sano, “Lignin gel with unique swelling property,” *Bioresour. Technol*, vol. 88, pp. 81–83, 2003.

[328] J. H. Park, H. H. Rana, J. Y. Lee, and H. S. Park, “Renewable flexible supercapacitors based on all-lignin-based hydrogel electrolytes and nanofiber electrodes,” *J. Mater. Chem. A Mater.*, vol. 7, pp. 16962–16968, 2019.

[329] L. Passauer *et al.*, “Dynamic Moisture Sorption Characteristics of Xerogels from Water-Swellable Oligo(oxyethylene) Lignin Derivatives,” *ACS Appl. Mater. Interfaces*, vol. 4, pp. 5852–5862, 2012.

[330] W. K. El-Zawawy, “Preparation of hydrogel from green polymer,” *Polym. Adv. Technol.*, vol. 16, pp. 48–54, 2005.

[331] W. K. El-Zawawy and M. M. Ibrahim, “Preparation and characterization of novel polymer hydrogel from industrial waste and copolymerization of poly(vinyl alcohol) and polyacrylamide,” *J. Appl. Polym. Sci.*, vol. 124, pp. 4362–4370, 2012.

[332] I. E. Raschip, G. E. Hitruc, C. Vasile, and M.-C. Popescu, “Effect of the lignin type on the morphology and thermal properties of the xanthan/lignin hydrogels,” *Int. J. Biol. Macromol.*, vol. 54, pp. 230–237, 2013.

[333] Y. Zhang *et al.*, “Novel lignin–chitosan–PVA composite hydrogel for wound dressing,” *Mater. Sci. Eng.: C*, vol. 104, p. 110002, 2019.

[334] M. Li, X. Jiang, D. Wang, Z. Xu, and M. Yang, “In situ reduction of silver nanoparticles in the lignin based hydrogel for enhanced antibacterial application,” *Colloids Surf. B Biointerfaces*, vol. 177, pp. 370–376, 2019.

[335] Z. Jin, Y. Yu, S. Shao, J. Ye, L. Lin, and K. Iiyama, “Lignin as a cross-linker of acrylic acid-grafted carboxymethyl lignocellulose,” *J. Wood Sci.*, vol. 56, pp. 470–476, 2010.

[336] X.-F. Sun, Y. Hao, Y. Cao, and Q. Zeng, “Superadsorbent hydrogel based on lignin and montmorillonite for Cu(II) ions removal from aqueous solution,” *Int. J. Biol. Macromol.*, vol. 127, pp. 511–519, 2019.

[337] P. Jiang *et al.*, “Preparation and characterization of thermo-sensitive gel with phenolated alkali lignin,” *Sci. Rep.*, vol. 8, p. 14450, 2018.

[338] J. Domínguez-Robles, M. S. Peresin, T. Tamminen, A. Rodríguez, E. Larrañeta, and A.-S. Jääskeläinen, “Lignin-based hydrogels with ‘super-swelling’ capacities for dye removal,” *Int. J. Biol. Macromol.*, vol. 115, pp. 1249–1259, 2018.

[339] E. Larrañeta *et al.*, “Synthesis and Characterization of Lignin Hydrogels for Potential Applications as Drug Eluting Antimicrobial Coatings for Medical Materials,” *ACS Sustain. Chem. Eng.*, vol. 6, pp. 9037–9046, 2018.

[340] J. Maitra and V. K. Shukla, “Cross-linking in Hydrogels - A Review,” *Am. J. Polym. Sci.*, vol. 4, pp. 25–31, 2014.

[341] M. W. Tibbitt, A. M. Kloxin, L. A. Sawicki, and K. S. Anseth, “Mechanical Properties and Degradation of Chain and Step-Polymerized Photodegradable Hydrogels,” *Macromolecules*, vol. 46, pp. 2785–2792, 2013.

[342] S. Lee, X. Tong, and F. Yang, “Effects of the poly(ethylene glycol) hydrogel crosslinking mechanism on protein release,” *Biomater. Sci.*, vol. 4, pp. 405–411, 2016.

[343] C. Hachimi Alaoui, G. Réthoré, P. Weiss, and A. Fatimi, “Sustainable Biomass Lignin-Based Hydrogels: A Review on Properties, Formulation, and Biomedical Applications,” *Int. J. Mol. Sci.*, vol. 24, p. 13493, 2023.

[344] L. L. Hench and J. K. West, “The sol-gel process,” *Chem. Rev.*, vol. 90, pp. 33–72, 1990.

[345] Z. Wang, Q. Liu, J. Yu, T. Wu, and G. Wang, “Surface structure and catalytic behavior of silica-supported copper catalysts prepared by

impregnation and sol–gel methods," *Appl. Catal. A Gen.*, vol. 239, pp. 87–94, 2003.

[346] R. Takahashi, S. Sato, T. Sodesawa, M. Kato, and S. Yoshida, "Preparation of Cu/SiO_2 catalyst by solution exchange of wet silica gel," *J. Solgel Sci. Technol.*, vol. 19, pp. 715–718, 2000.

[347] D. Monti, N. W. Cant, D. L. Trimm, and M. S. Wainwright, "Hydrogenolysis of methyl formate over copper on silica: I. Study of surface species by in situ infrared spectroscopy," *J. Catal.*, vol. 100, pp. 17–27, 1986.

[348] Y. Zhu, Z. Li, and J. Chen, "Applications of lignin-derived catalysts for green synthesis," *Green Energy Environ.*, vol. 4, pp. 210–244, 2019.

[349] D. Chen *et al.*, "Sustainable utilization of lignocellulose: Preparation of furan derivatives from carbohydrate biomass by bifunctional lignosulfonate-based catalysts," *Catal. Commun.*, vol. 84, pp. 159–162, 2016.

[350] M. A. Cauqui and J. M. Rodríguez-Izquierdo, "Application of the sol-gel methods to catalyst preparation," *J. Non Cryst. Solids*, vol. 147–148, pp. 724–738, 1992.

[351] G. M. Pajonk, "Aerogel catalysts," *Appl. Catal.*, vol. 72, pp. 217–266, 1991.

[352] M. Schneider and A. Baiker, "Aerogels in Catalysis," *Catal. Rev.*, vol. 37, pp. 515–556, 1995.

[353] C. M. Fierro, J. Górka, J. A. Zazo, J. J. Rodriguez, J. Ludwinowicz, and M. Jaroniec, "Colloidal templating synthesis and adsorption characteristics of microporous–mesoporous carbons from Kraft lignin," *Carbon N Y*, vol. 62, pp. 233–239, 2013.

[354] J. Yan, A. M. Buckley, and M. Greenblatt, "The preparation and characterization of silica gels doped with copper complexes," *J. Non Cryst. Solids*, vol. 180, pp. 180–190, 1995.

[355] Y. Mizushima and M. Hori, "Alumina aerogel for support of a methane combustion catalyst," *Appl. Catal. A Gen.*, vol. 88, pp. 137–148, 1992.

[356] E. D. Guerreiro, O. F. Gorriz, J. B. Rivarola, and L. A. Arrúa, "Characterization of Cu/SiO_2 catalysts prepared by ion exchange for methanol dehydrogenation," *Appl. Catal. A Gen.*, vol. 165, pp. 259–271, 1997.

[357] M. Kohler, “The structure of Cu/SiO_2 catalysts prepared by the ion-exchange technique,” *J. Catal.*, vol. 108, pp. 323–333, 1987.

[358] Z. Li *et al.*, “Comparative study of sol–gel-hydrothermal and sol–gel synthesis of titania–silica composite nanoparticles,” *J. Solid State Chem.*, vol. 178, pp. 1395–1405, 2005.

[359] D. Rico-García, L. Ruiz-Rubio, L. Pérez-Alvarez, S. L. Hernández-Olmos, G. L. Guerrero-Ramírez, and J. L. Vilas-Vilela, “Lignin-Based Hydrogels: Synthesis and Applications,” *Polymers*, vol. 12, p. 81, 2020.

[360] K.-T. Lin *et al.*, “Deep Eutectic Solvent Assisted Facile Synthesis of Lignin-Based Cryogel,” *Macromolecules*, vol. 52, pp. 227–235, 2019.

[361] X. Xu *et al.*, “Flexible, Highly Graphitized Carbon Aerogels Based on Bacterial Cellulose/Lignin: Catalyst-Free Synthesis and its Application in Energy Storage Devices,” *Adv. Funct. Mater.*, vol. 25, pp. 3193–3202, 2015.

[362] D. Moreau, C. Chauvet, F. Etienne, F. P. Rannou, and L. Corté, “Hydrogel films and coatings by swelling-induced gelation,” *Proc. Natl. Acad. Sci. U.S.A.*, vol. 113, pp. 13295–13300, 2016.

[363] X. Zhao, M. Li, and X. Lou, “Sol–gel assisted hydrothermal synthesis of ZnO microstructures: Morphology control and photocatalytic activity,” *Adv. Powder Technol.*, vol. 25, pp. 372–378, 2014.

[364] D. O. Costa, S. J. Dixon, and A. S. Rizkalla, “One- and Three-Dimensional Growth of Hydroxyapatite Nanowires during Sol–Gel–Hydrothermal Synthesis,” *ACS Appl. Mater. Interfaces*, vol. 4, pp. 1490–1499, 2012.

[365] I. N. Savina, G. C. Ingavle, A. B. Cundy, and S. V. Mikhalovsky, “A simple method for the production of large volume 3D macroporous hydrogels for advanced biotechnological, medical and environmental applications,” *Sci. Rep.*, vol. 6, p. 21154, 2016.

[366] V. K. Thakur and M. K. Thakur, “Recent advances in green hydrogels from lignin: a review,” *Int. J. Biol. Macromol.*, vol. 72, pp. 834–847, 2015.

[367] F. I. G. Rawlins, “Elasticity, Plasticity and Structure of Matter,” *Nature*, vol. 141, pp. 810–810, 1938.

[368] R. W. Pekala, C. T. Alviso, F. M. Kong, and S. S. Hulsey, “Aerogels derived from multifunctional organic monomers,” *J. Non Cryst. Solids*, vol. 145, pp. 90–98, 1992.

[369] R. W. Pekala *et al.*, “Carbon aerogels for electrochemical applications,” *J. Non Cryst. Solids*, vol. 225, pp. 74–80, 1998.

[370] S. A. Al-Muhtaseb and J. A. Ritter, “Preparation and Properties of Resorcinol–Formaldehyde Organic and Carbon Gels,” *Adv. Mater.*, vol. 15, pp. 101–114, 2003.

[371] H. Liu and H. Chung, “Lignin-based polymers via graft copolymerization,” *J. Polym. Sci. A Polym. Chem.*, vol. 55, pp. 3515–3528, 2017.

[372] K. Kraiwattanawong, N. Sano, and H. Tamon, “Capacitive performance of binder-free carbon/carbon composite cryogels,” *Microporous Mesoporous Mater.*, vol. 165, pp. 228–233, 2013.

[373] K. Kraiwattanawong, N. Sano, and H. Tamon, “Carbon tunnels formed in carbon/carbon composite cryogels,” *Microporous Mesoporous Mater.*, vol. 153, pp. 47–54, 2012.

[374] E. Frackowiak and F. Béguin, “Carbon materials for the electrochemical storage of energy in capacitors,” *Carbon*, vol. 39, pp. 937–950, 2001.

[375] H. Wang, Q. Gao, and J. Hu, “High Hydrogen Storage Capacity of Porous Carbons Prepared by Using Activated Carbon,” *J. Am. Chem. Soc.*, vol. 131, pp. 7016–7022, 2009.

[376] T. Yamamoto, T. Nishimura, T. Suzuki, and H. Tamon, “Effect of drying conditions on mesoporosity of carbon precursors prepared by sol–gel polycondensation and freeze drying,” *Carbon*, vol. 39, pp. 2374–2376, 2001.

[377] C. Lin and J. A. Ritter, “Carbonization and activation of sol–gel derived carbon xerogels,” *Carbon*, vol. 38, pp. 849–861, 2000.

[378] R. Petričević, M. Glora, and J. Fricke, “Planar fibre reinforced carbon aerogels for application in PEM fuel cells,” *Carbon*, vol. 39, pp. 857–867, 2001.

[379] S. Berthon *et al.*, “DLS and SAXS investigations of organic gels and aerogels,” *J. Non Cryst. Solids*, vol. 285, pp. 154–161, 2001.

[380] S. Y. Kim, D. H. Yeo, J. W. Lim, K.-P. Yoo, K. H. Lee, and H. Kim, “Synthesis and Characterization of Resorcinol-Formaldehyde Organic Aerogel,” *J. Chem. Eng. Japan*, vol. 34, pp. 216–220, 2001.

[381] E. J. Zanto, S. A. Al-Muhtaseb, and J. A. Ritter, “Sol−Gel-Derived Carbon Aerogels and Xerogels: Design of Experiments Approach to

Materials Synthesis," *Ind. Eng. Chem. Res.*, vol. 41, pp. 3151–3162, 2002.

[382] F. Despetis, K. Barral, L. Kocon, and J. Phalippou, "Effect of Aging on Mechanical Properties of Resorcinol-Formaldehyde Gels," *J. Sol-Gel Sci. Technol.*, vol. 19, pp. 829–831, 2000.

[383] C. Liang, G. Sha, and S. Guo, "Resorcinol–formaldehyde aerogels prepared by supercritical acetone drying," *J Non Cryst. Solids*, vol. 271, pp. 167–170, 2000.

[384] J. Phalippou, M. Prassas, and J. Zarzycki, "Crystallization of gels and glasses made from hot-pressed gels," *J Non Cryst. Solids*, vol. 48, pp. 17–30, 1982.

[385] G. Orcel, J. Phalippou, and L. Hench, "Structural evolution at low temperature of formamide modified silica xerogels," *J Non Cryst. Solids*, vol. 104, pp. 170–180, 1988.

[386] T. Yamamoto, T. Sugimoto, T. Suzuki, S. R. Mukai, and H. Tamon, "Preparation and characterization of carbon cryogel microspheres," *Carbon*, vol. 40, pp. 1345–1351, 2002.

[387] R. Kocklenberg *et al.*, "Texture control of freeze-dried resorcinol–formaldehyde gels," *J. Non Cryst. Solids*, vol. 225, pp. 8–13, 1998.

[388] G. Qin and S. Guo, "Preparation of RF organic aerogels and carbon aerogels by alcoholic sol–gel process," *Carbon*, vol. 39, pp. 1935–1937, 2001.

[389] J. Kuhn, R. Brandt, H. Mehling, R. Petričević, and J. Fricke, "In situ infrared observation of the pyrolysis process of carbon aerogels," *J. Non Cryst. Solids*, vol. 225, pp. 58–63, 1998.

[390] H. Tamon, H. Ishizaka, M. Mikami, and M. Okazaki, "Porous structure of organic and carbon aerogels synthesized by sol-gel polycondensation of resorcinol with formaldehyde," *Carbon*, vol. 35, pp. 791–796, 1997.

[391] S. Q. Zhang *et al.*, "The investigation of the adsorption character of carbon aerogels," *Nanostructured Materials*, vol. 11, pp. 375–381, 1999.

[392] T. Yamamoto, T. Nishimura, T. Suzuki, and H. Tamon, "Control of mesoporosity of carbon gels prepared by sol–gel polycondensation and freeze drying," *J. Non Cryst. Solids*, vol. 288, pp. 46–55, 2001.

[393] R. Saliger, V. Bock, R. Petricevic, T. Tillotson, S. Geis, and J. Fricke, "Carbon aerogels from dilute catalysis of resorcinol with formaldehyde," *J. Non Cryst. Solids*, vol. 221, pp. 144–150, 1997.

[394] M. Glora, M. Wiener, R. Petričević, H. Pröbstle, and J. Fricke, "Integration of carbon aerogels in PEM fuel cells," *J. Non Cryst. Solids*, vol. 285, pp. 283–287, 2001.

[395] T. Komolwanich *et al.*, "Comparative potentiality of Kans grass (*Saccharum spontaneum*) and Giant reed (*Arundo donax*) as lignocellulosic feedstocks for the release of monomeric sugars by microwave/chemical pretreatment," *Cellulose*, vol. 21, pp. 1327–1340, 2014.

[396] S. Ethaib, R. Omar, S. M. M. Kamal, D. R. A. Biak, "Microwave-assisted pretreatment of lignocellulosic biomass: A review," *J. Eng. Sci Technol.*, vol. 10, pp. 97–109, 2015.

[397] W. Fatriasari, R. Raniya, M. Oktaviani, and E. Hermiati, "The Improvement of Sugar and Bioethanol Production of Oil Palm Empty Fruit Bunches (*Elaeis guineensis Jacq*) through Microwave-Assisted Maleic Acid Pretreatment," *Bioresources*, vol. 13, pp. 4378–4403, 2018.

[398] J.-W. Lee, R. C. L. B. Rodrigues, H. J. Kim, I.-G. Choi, and T. W. Jeffries, "The roles of xylan and lignin in oxalic acid pretreated corncob during separate enzymatic hydrolysis and ethanol fermentation," *Bioresour. Technol.*, vol. 101, pp. 4379–4385, 2010.

[399] Y. Yan *et al.*, "Microwave-Assisted Oxalic Acid Pretreatment for the Enhancing of Enzyme Hydrolysis in the Production of Xylose and Arabinose from Bagasse," *Molecules*, vol. 23, p. 862, 2018.

[400] J. J. Shah and K. Mohanraj, "Comparison of Conventional and Microwave-assisted Synthesis of Benzotriazole Derivatives," *Indian J. Pharm. Sci.*, vol. 76, pp. 46–53, 2014.

[401] S. Tsubaki, K. Oono, A. Onda, K. Yanagisawa, and J. Azuma, "Comparative decomposition kinetics of neutral monosaccharides by microwave and induction heating treatments," *Carbohydr. Res.*, vol. 375, pp. 1–4, 2013.

[402] S. Haghighi Mood *et al.*, "Lignocellulosic biomass to bioethanol, a comprehensive review with a focus on pretreatment," *Renew. Sust. Energ. Rev.*, vol. 27, pp. 77–93, 2013.

[403] P. Lidström, J. Tierney, B. Wathey, and J. Westman, "Microwave assisted organic synthesis—a review," *Tetrahedron*, vol. 57, pp. 9225–9283, 2001.

[404] F. Mushtaq, R. Mat, and F. N. Ani, “A review on microwave assisted pyrolysis of coal and biomass for fuel production,” *Renew. Sust. Energ. Rev.*, vol. 39, pp. 555–574, 2014.

[405] A. A. Salema, F. N. Ani, J. Mouris, and R. Hutcheon, “Microwave dielectric properties of Malaysian palm oil and agricultural industrial biomass and biochar during pyrolysis process,” *Fuel Process. Technol.*, vol. 166, pp. 164–173, 2017.

[406] A. Bichot *et al.*, “Decoupling thermal and non-thermal effects of the microwaves for lignocellulosic biomass pretreatment,” *Energy Convers. Manag.*, vol. 203, p. 112220, 2020.

[407] F. Motasemi and M. T. Afzal, “A review on the microwave-assisted pyrolysis technique,” *Renew. Sust. Energ. Rev.*, vol. 28, pp. 317–330, 2013.

[408] D. Dallinger and C. O. Kappe, “Microwave-Assisted Synthesis in Water as Solvent,” *Chem. Rev.*, vol. 107, pp. 2563–2591, 2007.

[409] B. Yang and C. E. Wyman, “Effect of xylan and lignin removal by batch and flowthrough pretreatment on the enzymatic digestibility of corn stover cellulose,” *Biotechnol. Bioeng.*, vol. 86, pp. 88–98, 2004.

[410] B. Basak *et al.*, “Advances in physicochemical pretreatment strategies for lignocellulose biomass and their effectiveness in bioconversion for biofuel production,” *Bioresour. Technol.*, vol. 369, p. 128413, 2023.

[411] A. Maria *et al.*, “Levulinic acid production from waste biomass,” *Bioresources*, vol. 7, pp. 1824–1835, 2012.

[412] Y. Wang, F. Delbecq, W. Kwapinski, and C. Len, “Application of sulfonated carbon-based catalyst for the furfural production from d - xylose and xylan in a microwave-assisted biphasic reaction,” *Molecular Catalysis*, vol. 438, pp. 167–172, 2017.

[413] D. Duan *et al.*, “Microwave-assisted acid pretreatment of alkali lignin: Effect on characteristics and pyrolysis behavior,” *Bioresour. Technol.*, vol. 251, pp. 57–62, 2018.

[414] C. Gabriel, S. Gabriel, E. H. Grant, E. H. Grant, B. S. J. Halstead, and D. Michael P. Mingos, “Dielectric parameters relevant to microwave dielectric heating,” *Chem. Soc. Rev.*, vol. 27, p. 213, 1998.

[415] F. Langa, P. de la Cruz, A. de la Hoz, A. Díaz-Ortiz, and E. Díez-Barra, “Microwave irradiation: more than just a method for accelerating reactions,” *Contemp. Org. Synth.*, vol. 4, pp. 373–386, 1997.

[416] K. Aliko, K. Doudin, A. Osatiashtiani, J. Wang, P. D. Topham, and E. Theodosiou, “Microwave-assisted synthesis of levulinic acid from low-cost, sustainable feedstocks using organic acids as green catalysts,” *J. Chem. Technol. Biotechnol.*, vol. 95, pp. 2110–2119, 2020.

[417] G. Kłosowski, D. Mikulski, and A. Menka, “Microwave-Assisted One-Step Conversion of Wood Wastes into Levulinic Acid,” *Catalysts*, vol. 9, p. 753, 2019.

[418] V. B. Kumar, I. N. Pulidindi, and A. Gedanken, “Synergistic catalytic effect of the $ZnBr_2$ –HCl system for levulinic acid production using microwave irradiation,” *RSC Adv.*, vol. 5, pp. 11043–11048, 2015.

[419] K. Lappalainen *et al.*, “Microwave-assisted conversion of novel biomass materials into levulinic acid,” *Biomass Convers. Biorefin.*, vol. 8, pp. 965–970, 2018.

[420] H. Ren, Y. Zhou, and L. Liu, “Selective conversion of cellulose to levulinic acid via microwave-assisted synthesis in ionic liquids,” *Bioresour. Technol.*, vol. 129, pp. 616–619, 2013.

[421] N. Sweygers, R. Dewil, and L. Appels, “Production of Levulinic Acid and Furfural by Microwave-Assisted Hydrolysis from Model Compounds: Effect of Temperature, Acid Concentration and Reaction Time,” *Waste Biomass Valorization*, vol. 9, pp. 343–355, 2018.

[422] Á. Szabolcs, M. Molnár, G. Dibó, and L. T. Mika, “Microwave-assisted conversion of carbohydrates to levulinic acid: an essential step in biomass conversion,” *Green Chem.*, vol. 15, pp. 439–445, 2013.

[423] J. M. Tukacs *et al.*, “Microwave-Assisted Valorization of Biowastes to Levulinic Acid,” *ChemistrySelect*, vol. 2, pp. 1375–1380, 2017.

[424] J. A. Dean, *Lange’s Handbook of Chemistry*, 13th ed. New York, 1985.

[425] S. A. Galema, “Microwave chemistry,” *Chem. Soc. Rev.*, vol. 26, p. 233, 1997.

[426] T. Welton, “Room-Temperature Ionic Liquids. Solvents for Synthesis and Catalysis,” *Chem. Rev.*, vol. 99, pp. 2071–2083, 1999.

[427] R. Diyanilla, T. S. Hamidon, L. Suryanegara, and M. Hazwan Hussin, “Overview of Pretreatment Methods Employed on Oil Palm Biomass in Producing Value-added Products: A Review,” *Bioresources*, vol. 15, pp. 9935–9997, 2020.

[428] C. Chiappe *et al.*, “Exploring and exploiting different catalytic systems for the direct conversion of cellulose into levulinic acid,” *New J. Chem.*, vol. 42, pp. 1845–1852, 2018.

[429] D. M. Alonso, S. G. Wettstein, and J. A. Dumesic, “Gamma-valerolactone, a sustainable platform molecule derived from lignocellulosic biomass,” *Green Chem.*, vol. 15, p. 584, 2013.

[430] S. M. Bruce *et al.*, “Small pore zeolite catalysts for furfural synthesis from xylose and switchgrass in a γ-valerolactone/water solvent,” *J. Mol. Catal. A Chem.*, vol. 422, pp. 18–22, 2016.

[431] J. Hegner, K. C. Pereira, B. DeBoef, and B. L. Lucht, “Conversion of cellulose to glucose and levulinic acid via solid-supported acid catalysis,” *Tetrahedron Lett.*, vol. 51, pp. 2356–2358, 2010.

[432] D. M. Alonso, J. M. R. Gallo, M. A. Mellmer, S. G. Wettstein, and J. A. Dumesic, “Direct conversion of cellulose to levulinic acid and gamma-valerolactone using solid acid catalysts,” *Catal. Sci. Technol.*, vol. 3, pp. 927–931, 2013.

[433] W. E. S. Hart, J. B. Harper, and L. Aldous, “The effect of changing the components of an ionic liquid upon the solubility of lignin,” *Green Chem.*, vol. 17, pp. 214–218, 2015.

[434] M. Mora-Pale, L. Meli, T. V. Doherty, R. J. Linhardt, and J. S. Dordick, “Room temperature ionic liquids as emerging solvents for the pretreatment of lignocellulosic biomass,” *Biotechnol. Bioeng.*, vol. 108, pp. 1229–1245, 2011.

[435] S. S. Y. Tan *et al.*, “Extraction of lignin from lignocellulose at atmospheric pressure using alkylbenzenesulfonate ionic liquid,” *Green Chem.*, vol. 11, p. 339, 2009.

[436] Y. Wang *et al.*, “Lignin dissolution in dialkylimidazolium-based ionic liquid–water mixtures,” *Bioresour. Technol.*, vol. 170, pp. 499–505, 2014.

[437] Z. Strassberger, P. Prinsen, F. van der Klis, D. S. van Es, S. Tanase, and G. Rothenberg, “Lignin solubilisation and gentle fractionation in liquid ammonia,” *Green Chem.*, vol. 17, pp. 325–334, 2015.

[438] F. Jiang, Q. Zhu, D. Ma, X. Liu, and X. Han, “Direct conversion and NMR observation of cellulose to glucose and 5-hydroxymethylfurfural (HMF) catalyzed by the acidic ionic liquids,” *J. Mol. Catal. A Chem.*, vol. 334, pp. 8–12, 2011.

[439] S. Hu, Z. Zhang, J. Song, Y. Zhou, and B. Han, “Efficient conversion of glucose into 5-hydroxymethylfurfural catalyzed by a common Lewis acid $SnCl_4$ in an ionic liquid,” *Green Chem.*, vol. 11, p. 1746, 2009.

[440] Y. Zhang, E. A. Pidko, and E. J. M. Hensen, “Molecular Aspects of Glucose Dehydration by Chromium Chlorides in Ionic Liquids,” *Chem. Eur. J.*, vol. 17, pp. 5281–5288, 2011.

[441] A. Brandt, M. J. Ray, T. Q. To, D. J. Leak, R. J. Murphy, and T. Welton, “Ionic liquid pretreatment of lignocellulosic biomass with ionic liquid–water mixtures,” *Green Chem.*, vol. 13, p. 2489, 2011.

[442] C. Li, Q. Wang, and Z. K. Zhao, “Acid in ionic liquid: An efficient system for hydrolysis of lignocellulose,” *Green Chem.*, vol. 10, pp. 177–182, 2008.

[443] M. Mazza, D.-A. Catana, C. Vaca-Garcia, and C. Cecutti, “Influence of water on the dissolution of cellulose in selected ionic liquids,” *Cellulose*, vol. 16, pp. 207–215, 2009.

[444] Y. Cao and T. Mu, “Comprehensive Investigation on the Thermal Stability of 66 Ionic Liquids by Thermogravimetric Analysis,” *Ind. Eng. Chem. Res.*, vol. 53, pp. 8651–8664, 2014.

[445] F. G. Calvo-Flores and J. A. Dobado, “Lignin as Renewable Raw Material,” *ChemSusChem*, vol. 3, pp. 1227–1235, 2010.

[446] S. Constant *et al.*, “New insights into the structure and composition of technical lignins: a comparative characterisation study,” *Green Chem.*, vol. 18, pp. 2651–2665, 2016.

[447] R. Shu *et al.*, “Investigation on the structural effect of lignin during the hydrogenolysis process,” *Bioresour. Technol.*, vol. 200, pp. 14–22, 2016.

[448] I. T. Horváth, “Solvents from nature,” *Green Chem.*, vol. 10, p. 1024, 2008.

[449] W. Luo *et al.*, “High performing and stable supported nano-alloys for the catalytic hydrogenation of levulinic acid to γ-valerolactone,” *Nat. Commun.*, vol. 6, p. 6540, 2015.

[450] J. Song *et al.*, “Porous Zirconium–Phytic Acid Hybrid: a Highly Efficient Catalyst for Meerwein–Ponndorf–Verley Reductions,” *Angew. Chem. Int. Ed.*, vol. 54, pp. 9399–9403, 2015.

[451] Z. Xue, X. Zhao, R. Sun, and T. Mu, “Biomass-Derived γ-Valerolactone-Based Solvent Systems for Highly Efficient Dissolution

of Various Lignins: Dissolution Behavior and Mechanism Study," *ACS Sustain. Chem. Eng.*, vol. 4, pp. 3864–3870, 2016.

[452] L. Faba, D. Garcés, E. Díaz, and S. Ordóñez, "Carbon Materials as Phase-Transfer Promoters for Obtaining 5-Hydroxymethylfurfural from Cellulose in a Biphasic System," *ChemSusChem*, vol. 12, pp. 3769–3777, 2019.

[453] S. Tulaphol *et al.*, "Direct Production of Levulinic Acid in One Pot from Hemp Hurd by Dilute Acid in Ionic Liquids," *Energy Fuels*, vol. 34, pp. 1764–1772, 2020.

[454] F. N. D. C. Gomes, F. M. T. Mendes, and M. M. V. M. Souza, "Synthesis of 5-hydroxymethylfurfural from fructose catalyzed by phosphotungstic acid," *Catal. Today*, vol. 279, pp. 296–304, 2017.

[455] W. Li *et al.*, "Enhanced furfural production from raw corn stover employing a novel heterogeneous acid catalyst," *Bioresour. Technol.*, vol. 245, pp. 258–265, 2017.

[456] T. Yang, W. Li, A. T. Ogunbiyi, and S. An, "Efficient catalytic conversion of corn stover to furfural and 5-hydromethylfurfural using glucosamine hydrochloride derived carbon solid acid in γ-valerolactone," *Ind. Crops Prod.*, vol. 161, p. 113173, 2021.

[457] A. Deng *et al.*, "A feasible process for furfural production from the pre-hydrolysis liquor of corncob via biochar catalysts in a new biphasic system," *Bioresour. Technol.*, vol. 216, pp. 754–760, 2016.

[458] P. K. Khatri, N. Karanwal, S. Kaul, and S. L. Jain, "Sulfonated polymer impregnated carbon composite as a solid acid catalyst for the selective synthesis of furfural from xylose," *Tetrahedron Lett.*, vol. 56, pp. 1203–1206, 2015.

[459] D. Scholz, O. Kröcher, and F. Vogel, "Deactivation and Regeneration of Sulfonated Carbon Catalysts in Hydrothermal Reaction Environments," *ChemSusChem*, vol. 11, pp. 2189–2201, 2018.

[460] B. Chieng, S. Lee, N. Ibrahim, Y. Then, and Y. Loo, "Isolation and Characterization of Cellulose Nanocrystals from Oil Palm Mesocarp Fiber," *Polymers*, vol. 9, p. 355, 2017.

[461] S. S. Mohtar *et al.*, "Extraction and characterization of lignin from oil palm biomass via ionic liquid dissolution and non-toxic aluminium potassium sulfate dodecahydrate precipitation processes," *Bioresour. Technol.*, vol. 192, pp. 212–218, 2015.

[462] W. Lan, C.-F. Liu, and R.-C. Sun, “Fractionation of Bagasse into Cellulose, Hemicelluloses, and Lignin with Ionic Liquid Treatment Followed by Alkaline Extraction,” *J. Agric. Food Chem.*, vol. 59, pp. 8691–8701, 2011.

[463] F. Monteil-Rivera, G. H. Huang, L. Paquet, S. Deschamps, C. Beaulieu, and J. Hawari, “Microwave-assisted extraction of lignin from triticale straw: Optimization and microwave effects,” *Bioresour. Technol.*, vol. 104, pp. 775–782, 2012.

[464] K. Song, X. Zhu, W. Zhu, and X. Li, “Preparation and characterization of cellulose nanocrystal extracted from *Calotropis procera* biomass,” *Bioresour. Bioprocess*, vol. 6, pp. 1–8, 2019.

[465] P. Selvakumar *et al.*, “Optimization of binary acids pretreatment of corncob biomass for enhanced recovery of cellulose to produce bioethanol,” *Fuel*, vol. 321, p. 124060, 2022.

[466] W. Namchot, N. Panyacharay, W. Jonglertjunya, and C. Sakdaronnarong, “Hydrolysis of delignified sugarcane bagasse using hydrothermal technique catalyzed by carbonaceous acid catalysts,” *Fuel*, vol. 116, pp. 608–616, 2014.

[467] E. Kolvari, N. Koukabi, and M. M. Hosseini, “Perlite: A cheap natural support for immobilization of sulfonic acid as a heterogeneous solid acid catalyst for the heterocyclic multicomponent reaction,” *J. Mol. Catal. A Chem.*, vol. 397, pp. 68–75, 2015.

[468] “NIST Tandem Mass Spectral Libraries”. Accessed: May 31, 2024. [Online]. Available: https://chemdata.nist.gov/

[469] T. Rashid, N. Gnanasundaram, A. Appusamy, C. F. Kait, and M. Thanabalan, “Enhanced lignin extraction from different species of oil palm biomass: Kinetics and optimization of extraction conditions,” *Ind. Crops Prod.*, vol. 116, pp. 122–136, 2018.

[470] N. Lubis, S. Gea, Tamrin, and J. Tarigan, “Lignocellulosic analysis from oil palm empty fruit bunches and crystallinity index analysis of cellulose nanofibers isolated via high pressure steam explosion,” *AIP Conf. Proc.*, vol. 2626, p. 040006, 2023.

[471] J. Rao, Z. Lv, G. Chen, and F. Peng, “Hemicellulose: Structure, chemical modification, and application,” *Prog. Polym. Sci.*, vol. 140, p. 101675, 2023.

[472] N. I. A. Ahamd Nordin *et* al., "Modification of Oil Palm Mesocarp Fiber Characteristics Using Superheated Steam Treatment," *Molecules*, vol. 18, pp. 9132–9146, 2013.

[473] N. I. Iberahim, J. M. Jahim, S. Harun, M. T. M. Nor, and O. Hassan, "Sodium Hydroxide Pretreatment and Enzymatic Hydrolysis of Oil Palm Mesocarp Fiber," *Int. J. Chem. Eng. Appl.*, vol. 4, pp. 101–105, 2013.

[474] N. Ahmad Rizal, M. Ibrahim, M. Zakaria, E. Kamal Bahrin, S. Abd-Aziz, and M. Hassan, "Combination of Superheated Steam with Laccase Pretreatment Together with Size Reduction to Enhance Enzymatic Hydrolysis of Oil Palm Biomass," *Molecules*, vol. 23, p. 811, 2018.

[475] T. A. T. Yasim-Anuar, H. Ariffin, M. N. F. Norrrahim, and M. A. Hassan, "Factors affecting spinnability of oil palm mesocarp fiber cellulose solution for the production of microfiber," *Bioresources*, vol. 12, pp. 715–734, 2017.

[476] M. R. Zakaria, S. Fujimoto, S. Hirata, and M. A. Hassan, "Ball Milling Pretreatment of Oil Palm Biomass for Enhancing Enzymatic Hydrolysis," *Appl. Biochem. Biotechnol.*, vol. 173, pp. 1778–1789, 2014.

[477] J. Long, X. Li, B. Guo, L. Wang, and N. Zhang, "Catalytic delignification of sugarcane bagasse in the presence of acidic ionic liquids," *Catal. Today*, vol. 200, pp. 99–105, 2013.

[478] Y. Yuan *et al.*, "Recent advances in understanding the effects of lignin structural characteristics on enzymatic hydrolysis," *Biotechnol. Biofuels*, vol. 14, p. 205, 2021.

[479] J. Sun *et al.*, "Rapid room temperature solubilization and depolymerization of polymeric lignin at high loadings," *Green Chem.*, vol. 18, pp. 6012–6020, 2016.

[480] Z. Yinghuai, K. Tang, and N. S., "Applications of Ionic Liquids in Lignin Chemistry," in *Ionic Liquids - New Aspects for the Future*, InTech, 2013.

[481] N. Zhou, W. P. D. W. Thilakarathna, Q. S. He, and H. P. V. Rupasinghe, "A Review: Depolymerization of Lignin to Generate High-Value Bio-Products: Opportunities, Challenges, and Prospects," *Front. Energy Res.*, vol. 9, p. 758744, 2022.

[482] E. M. Jincy and K. S. Femina, "Heteropolymer in Biomass: Hemicellulose Extraction and Modifications," in *Handbook of Biomass*, Singapore: Springer Nature Singapore, 2023, pp. 1–32.

[483] Y. Lu, Q. He, G. Fan, Q. Cheng, and G. Song, “Extraction and modification of hemicellulose from lignocellulosic biomass: A review,” *Green Process. Synthesis*, vol. 10, pp. 779–804, 2021.

[484] F. L. Shimizu, G. O. de Azevedo, L. F. Coelho, F. C. Pagnocca, and M. Brienzo, “Minimum Lignin and Xylan Removal to Improve Cellulose Accessibility,” *Bioenergy Res.*, vol. 13, pp. 775–785, 2020.

[485] B. R. Prasad, R. K. Padhi, and G. Ghosh, “A review on key pretreatment approaches for lignocellulosic biomass to produce biofuel and value-added products,” *Int. J. Environ. Sci. Technol.*, vol. 20, pp. 6929–6944, 2023.

[486] Rajesh Banu J *et al.*, “Lignocellulosic Biomass Pretreatment for Enhanced Bioenergy Recovery: Effect of Lignocelluloses Recalcitrance and Enhancement Strategies,” *Front. Energy Res.*, vol. 9, p. 646057, 2021.

[487] A. Laca, A. Laca, and M. Díaz, “Hydrolysis: From cellulose and hemicellulose to simple sugars,” in *Second and Third Generation of Feedstocks*, Elsevier, 2019, pp. 213–240.

[488] L. Shuai and J. Luterbacher, “Organic Solvent Effects in Biomass Conversion Reactions,” *ChemSusChem*, vol. 9, pp. 133–155, 2016.

[489] S. G. Wettstein, D. M. Alonso, Y. Chong, and J. A. Dumesic, “Production of levulinic acid and gamma-valerolactone (GVL) from cellulose using GVL as a solvent in biphasic systems,” *Energy Environ. Sci.*, vol. 5, p. 8199, 2012.

[490] A. Pinkert, K. N. Marsh, and S. Pang, “Reflections on the Solubility of Cellulose,” *Ind. Eng. Chem. Res.*, vol. 49, pp. 11121–11130, 2010.

[491] J. G. Huddleston *et al.*, “Characterization and comparison of hydrophilic and hydrophobic room temperature ionic liquids incorporating the imidazolium cation,” *Green Chem.*, vol. 3, pp. 156–164, 2001.

[492] C. S. M. Pereira, V. M. T. M. Silva, and A. E. Rodrigues, “Ethyl lactate as a solvent: Properties, applications and production processes – a review,” *Green Chem.*, vol. 13, pp. 2658–2671, 2011.

[493] D. R. Chiou, S. Y. Chen, and L. J. Chen, “Density, viscosity, and refractive index for water + 2-butoxyethanol and + 2-(2-butoxyethoxy)ethanol at various temperatures,” *J. Chem. Eng. Data*, vol. 55, pp. 1012–1016, 2010.

[494] C. Wohlfarth, *Viscosity of Pure Organic Liquids and Binary Liquid Mixtures*. Berlin, Heidelberg: Springer Berlin Heidelberg, 2017.

[495] R. M. Pires, H. F. Costa, A. G. M. Ferreira, and I. M. A. Fonseca, "Viscosity and density of water + ethyl acetate + ethanol mixtures at 298.15 and 318.15 K and atmospheric pressure," *J. Chem. Eng. Data*, vol. 52, pp. 1240–1245, 2007.

[496] J. Byun and J. Han, "Catalytic conversion of corn stover for γ-valerolactone production by two different solvent strategies: Techno-economic assessment," *Energy*, vol. 175, pp. 546–553, 2019.

[497] H. Q. Lê, H. Sixta, and M. Hummel, "Ionic liquids and gamma-valerolactone as case studies for green solvents in the deconstruction and refining of biomass," *Curr. Opin. Green Sustain. Chem.*, vol. 18, pp. 20–24, 2019.

[498] D. Díez, A. Urueña, R. Piñero, A. Barrio, and T. Tamminen, "Determination of Hemicellulose, Cellulose, and Lignin Content in Different Types of Biomasses by Thermogravimetric Analysis and Pseudocomponent Kinetic Model (TGA-PKM Method)," *Processes*, vol. 8, p. 1048, 2020.

[499] R. Moriana, F. Vilaplana, and M. Ek, "Cellulose Nanocrystals from Forest Residues as Reinforcing Agents for Composites: A Study from Macro- to Nano-Dimensions," *Carbohydr. Polym.*, vol. 139, pp. 139–149, 2016.

[500] X. Meng *et al.*, "Effects of the advanced organosolv pretreatment strategies on structural properties of woody biomass," *Ind. Crops Prod.*, vol. 146, p. 112144, 2020.

[501] F. M. Kuswa, H. P. Putra, Prabowo, A. Darmawan, M. Aziz, and H. Hariana, "Investigation of the combustion and ash deposition characteristics of oil palm waste biomasses," *Biomass Convers. Biorefin.*, vol. 14, pp. 24375–24395, 2024.

[502] N. I. A. Ahamd Nordin *et* al., "Modification of Oil Palm Mesocarp Fiber Characteristics Using Superheated Steam Treatment," *Molecules*, vol. 18, pp. 9132–9146, 2013.

[503] S. Park, J. O. Baker, M. E. Himmel, P. A. Parilla, and D. K. Johnson, "Cellulose crystallinity index: measurement techniques and their impact on interpreting cellulase performance," *Biotechnol. Biofuels*, vol. 3, p. 10, 2010.

[504] S. M. Ajayi, S. O. Olusanya, A. E. Didunyemi, S. F. Abimbade, E. G. Olumayede, and C. O. Akintayo, "Physicochemical properties of oil palm biomass waste fibres and its cellulose for engineering applications: a review," *Biomass Convers. Biorefin.*, 2024.

[505] W. Yao, Y. Weng, and J. M. Catchmark," Improved cellulose X-ray diffraction analysis using Fourier series modelling," *Cellulose*, vol. 27, pp. 5563–5579, 2020.

[506] C. K. Saurabh *et al.*, "Palm frond nanowhiskers," *Bioresources*, vol. 11, pp. 6742–6755, 2016.

[507] S. Kubo and J. F. Kadla, "Hydrogen Bonding in Lignin: A Fourier Transform Infrared Model Compound Study," *Biomacromolecules*, vol. 6, pp. 2815–2821, 2005.

[508] J. Patel, B. Maji, N. S. H. N. Moorthy, and S. Maiti, "Xanthan gum derivatives: review of synthesis, properties and diverse applications," *RSC Adv.*, vol. 10, pp. 27103–27136, 2020.

[509] L. Shi *et al.*, "Effects of polyethylene glycol on the surface of nanoparticles for targeted drug delivery," *Nanoscale*, vol. 13, pp. 10748–10764, 2021.

[510] R. H. Cunha, M. Nele, and M. L. Dias, "Reaction and thermal behavior of vitrimer-like polyhydroxy esters based on polyethylene glycol diglycidyl ether," *J. Appl. Polym. Sci.*, vol. 137, p. 49329, 2020.

[511] Q. Xu *et al.*, "Cross-polymerisation between furfural and the phenolics of varied molecular structure in bio-oil," *Bioresour. Technol. Rep.*, vol. 8, p. 100324, 2019.

[512] A. E. Kazzaz, Z. H. Feizi, and P. Fatehi, "Grafting strategies for hydroxy groups of lignin for producing materials," *Green Chem.*, vol. 21, p. 5714, 2019.

[513] K. M. Salleh, S. Zakaria, M. S. Sajab, S. Gan, and H. Kaco, "Superabsorbent hydrogel from oil palm empty fruit bunch cellulose and sodium carboxymethylcellulose," *Int. J. Biol. Macromol.*, vol. 131, pp. 50–59, 2019.

[514] K. Zheng and A. R. Boccaccini, "Sol-gel processing of bioactive glass nanoparticles: A review," *Adv. Colloid Interface Sci.*, vol. 249, pp. 363–373, 2017.

[515] Z. Mohammadhashemi, M. J. Zohuriaan-Mehr, and R. Jahanmardi, "Antibacterial activity induction into superabsorbent hydrogel via Schiff-base-metal coordination modification," *Polym. Bull.*, vol. 80, pp. 8045–8065, 2023.

[516] J. Luo and Q. Fu, "Aldehyde-Directed C(sp^2)−H Functionalization under Transition-Metal Catalysis," *Adv. Synth. Catal.*, vol. 363, pp. 3868–3878, 2021.

[517] S. Huang *et al.*, “Facile preparation of biomass lignin-based hydroxyethyl cellulose super-absorbent hydrogel for dye pollutant removal,” *Int. J. Biol. Macromol.*, vol. 137, pp. 939–947, 2019.

[518] C. Campana, R. Leger, R. Sonnier, L. Ferry, and P. Ienny, “Effect of post curing temperature on mechanical properties of a flax fiber reinforced epoxy composite,” *Compos. Part A Appl. Sci. Manuf.*, vol. 107, pp. 171–179, 2018.

[519] Y. Jia *et al.*, “Gas-carrying enhances the combustion temperature of the biomass particles,” *Energy*, vol. 239, p. 121956, 2022.

[520] C. Bao *et al.*, “Microwave-associated chemistry in environmental catalysis for air pollution remediation: A review,” *Chem. Eng. J.*, vol. 466, p. 142902, 2023.

[521] T. Caykara, M. Bulut, N. Dilsiz, and Y. Akyüz, “Macroporous Poly(Acrylamide) Hydrogels: Swelling and Shrinking Behaviors,” *J. Macromol. Sci. Part A*, vol. 43, pp. 889–897, 2007.

[522] D. Hua, S. Gao, M. Zhang, W. Ma, and C. Huang, “A novel xanthan gum-based conductive hydrogel with excellent mechanical, biocompatible, and self-healing performances,” *Carbohydr. Polym.*, vol. 247, p. 116743, 2020.

[523] I. M. Bhat, S. M. Wani, S. A. Mir, and F. A. Masoodi, “Advances in xanthan gum production, modifications and its applications,” *Biocatal. Agric. Biotechnol.*, vol. 42, p. 102328, 2022.

[524] A. Alam *et al.*, “Electrically conductive, mechanically robust, pH-sensitive graphene/polymer composite hydrogels,” *Compos. Sci. Technol.*, vol. 127, pp. 119–126, 2016.

[525] N. S. M. Azlan, C. L. Yap, Y. W. Tiong, S. Gan, and M. B. A. Rahman, “The Interplay of Brønsted-Lowry and Lewis Acid Sites in Bifunctional Catalyst for the Biomass Conversion to Levulinic Acid,” *J. Biomimetics, Biomater. Biomed. Eng.*, vol. 61, pp. 71–76, 2023.

[526] M. M. Zainol, N. A. S. Amin, M. Asmadi, and N. A. S. Ramli, “Esterification of Levulinic Acid to Ethyl Levulinate Using Liquefied Oil Palm Frond-Based Carbon Cryogel Catalyst,” *Bioenergy Res.*, vol. 12, pp. 359–369, 2019.

[527] W. H. Arnawtee *et al.*, “Lignin valorization: Facile synthesis, characterization and catalytic activity of multiwalled carbon nanotubes/kraft lignin/Pd nanocomposite for environmental remediation,” *Sep. Purif. Technol.*, vol. 290, p. 120793, 2022.

[528] P. Puligundla, S.-E. Oh, and C. Mok, “Microwave-assisted pretreatment technologies for the conversion of lignocellulosic biomass to sugars and ethanol: a review,” *Carbon Lett.*, vol. 17, pp. 1–10, 2016.

[529] A. Aguilar-Reynosa *et al.*, “Microwave heating processing as alternative of pretreatment in second-generation biorefinery: An overview,” *Energy Convers. Manag.*, vol. 136, pp. 50–65, 2017.

[530] B. K. Ozsel, D. Ozturk, and B. Nis, “One-pot hydrothermal conversion of different residues to value-added chemicals usıng new acidic carbonaceous catalyst,” *Bioresour. Technol.*, vol. 289, p. 121627, 2019.

[531] R. Wang *et al.*, “Facile and Low-Cost Preparation of Nb/Al Oxide Catalyst with High Performance for the Conversion of Kiwifruit Waste Residue to Levulinic Acid,” *Catalysts*, vol. 5, pp. 1636–1648, 2015.

[532] S. S. Chen *et al.*, “Valorization of cellulosic food waste into levulinic acid catalyzed by heterogeneous Brønsted acids: Temperature and solvent effects,” *Chem. Eng. J.*, vol. 327, pp. 328–335, 2017.

[533] K. Ingtipi, B. J. Choudhury, and V. S. Moholkar, “Development of NaOH-borax crosslinked PVA-xanthan gum-lignin hydrogel as green fire retardant coating,” *Prog. Org. Coat.*, vol. 174, p. 107268, 2023.

[534] Y. Liu, H. Wang, G. Yu, Q. Yu, B. Li, and X. Mu, “A novel approach for the preparation of nanocrystalline cellulose by using phosphotungstic acid,” *Carbohydr. Polym.*, vol. 110, pp. 415–422, 2014.

[535] B. Chamnankid, C. Ratanatawanate, and K. Faungnawakij, “Conversion of xylose to levulinic acid over modified acid functions of alkaline-treated zeolite Y in hot-compressed water,” *Chem. Eng. J.*, vol. 258, pp. 341–347, 2014.

[536] H. Mochizuki, T. Yokoi, H. Imai, S. Namba, J. N. Kondo, and T. Tatsumi, “Effect of desilication of H-ZSM-5 by alkali treatment on catalytic performance in hexane cracking,” *Appl. Catal. A Gen.*, vol. 449, pp. 188–197, 2012.

[537] N. Katada, T. Tsubaki, and M. Niwa, “Measurements of number and strength distribution of Brønsted and Lewis acid sites on sulfated zirconia by ammonia IRMS–TPD method,” *Appl. Catal. A Gen.*, vol. 340, pp. 76–86, 2008.

[538] N. A. S. Ramli and N. A. S. Amin, “Fe/HY zeolite as an effective catalyst for levulinic acid production from glucose: Characterization and catalytic performance,” *Appl. Catal. B*, vol. 163, pp. 487–498, 2015.

[539] Z. Zhang *et al.*, “Selective catalytic conversion of Kraft lignin into monoaromatic hydrocarbons over niobium oxide catalysts,” *Fuel Process. Technol.*, vol. 235, p. 107382, 2022.

[540] K. Lu, Y. Wang, L. Zhu, B. Xing, and S. Wang, “Efficient Conversion of Biomass-Derived Saccharides to Levulinic Acid Using Silicotungstic Acid,” *Energy Fuels*, vol. 37, pp. 6642–6650, 2023.

[541] S. Hu, F. Jiang, and Y.-L. Hsieh, “1D Lignin-Based Solid Acid Catalysts for Cellulose Hydrolysis to Glucose and Nanocellulose,” *ACS Sustain. Chem. Eng.*, vol. 3, pp. 2566–2574, 2015.

[542] A. Zhu, Q. Li, L. Li, and J. Wang, “One-pot synthesis of 3,4-dihydro-2(H)-pyrimidinones catalyzed by reusable acidic choline-based ionic liquids,” *Catal. Letters*, vol. 143, pp. 463–468, 2013.

[543] T. Kitano, T. Shishido, K. Teramura, and T. Tanaka, “Brønsted Acid Property of Alumina-Supported Niobium Oxide Calcined at High Temperatures: Characterization by Acid-Catalyzed Reactions and Spectroscopic Methods,” *J. Phys. Chem. C*, vol. 116, pp. 11615–11625, 2012.

[544] D. Lopez, K. Suwannakarn, D. Bruce, and J. Goodwinjr, “Esterification and transesterification on tungstated zirconia: Effect of calcination temperature,” *J Catal.*, vol. 247, pp. 43–50, 2007.

[545] E. Iglesia *et al.*, “Selective isomerization of alkanes on supported tungsten oxide acids,” *Stud. Surf. Sci Catal.*, vol. 101, pp. 533–542, 1996.

[546] D. P. Serrano, R. A. García, M. Linares, and B. Gil, “Influence of the calcination treatment on the catalytic properties of hierarchical ZSM-5,” *Catal. Today*, vol. 179, pp. 91–101, 2012.

[547] S. Brunauer, L. S. Deming, W. E. Deming, and E. Teller, “On a Theory of the van der Waals Adsorption of Gases,” *J. Am. Chem. Soc.*, vol. 62, pp. 1723–1732, 1940.

[548] M. Thommes *et al.*, “Physisorption of gases, with special reference to the evaluation of surface area and pore size distribution (IUPAC Technical Report),” *Pure Appl. Chem.*, vol. 87, pp. 1051–1069, 2015.

[549] M. A. Al-Ghouti and D. A. Da’ana, “Guidelines for the use and interpretation of adsorption isotherm models: A review,” *J. Hazard Mater.*, vol. 393, p. 122383, 2020.

[550] A. Kaur and D. Sud, “Thionyl Chloride Facilitated Polymerization of Xanthan Gum Grafted Copolymers for Wastewater Remediation by

Exclusion of Synthetic Dyes," *J. Polym. Environ.*, vol. 30, pp. 4978–4998, 2022.

[551] P. Pang, H. Han, L. Hu, C. Guo, Y. Gao, and Y. Xie, "The calculations of pore structure parameters from gas adsorption experiments of shales: Which models are better?," *J. Nat. Gas. Sci. Eng.*, vol. 94, p. 104060, 2021.

[552] Z. Y. Zakaria, J. Linnekoski, and N. A. S. Amin, "Catalyst screening for conversion of glycerol to light olefins," *Chem. Eng. J.*, vol. 207–208, pp. 803–813, 2012.

[553] P. K. Kumari, B. S. Rao, D. Dhana Lakshmi, N. R. Sai Paramesh, C. Sumana, and N. Lingaiah, "Tungstophosphoric acid supported on mesoporouus niobiumoxophosphate: an efficient solid acid catalyst for etherification of 5-hydroxymethylfurfural to 5-ethoxymethylfurfural," *Catal. Today*, vol. 325, pp. 53–60, 2019.

[554] X. Xu *et al.*, "Direct and efficient conversion of cellulose to levulinic acid catalyzed by carbon foam-supported heteropolyacid with Brønsted–Lewis dual-acidic sites," *Bioresour. Technol.*, vol. 387, p. 129600, 2023.

[555] J. S. Kruger, V. Nikolakis, and D. G. Vlachos, "Carbohydrate dehydration using porous catalysts," *Curr. Opin. Chem. Eng.*, vol. 1, pp. 312–320, 2012.

[556] W. Zeng, D. Cheng, H. Zhang, F. Chen, and X. Zhan, "Dehydration of glucose to levulinic acid over MFI-type zeolite in subcritical water at moderate conditions," *React. Kinet., Mech. Catal.*, vol. 100, pp. 377–384, 2010.

[557] N. Ya'aini, N. A. S. Amin, and S. Endud, "Characterization and performance of hybrid catalysts for levulinic acid production from glucose," *Microporous Mesoporous Mater.*, vol. 171, pp. 14–23, 2013.

[558] D. Verboekend and J. Pérez-Ramírez, "Design of hierarchical zeolite catalysts by desilication," *Catal. Sci. Technol.*, vol. 1, p. 879, 2011.

[559] F. Thibault-Starzyk *et al.*, "Quantification of enhanced acid site accessibility in hierarchical zeolites – The accessibility index," *J. Catal.*, vol. 264, pp. 11–14, 2009.

[560] J. Zheng, R. Orentas, X. Yan, and H. Liu, "Humoral immune response induced by an engineered cell-based neuroblastoma vaccine with or without CD25 blockade," *Acta Biochim. Biophys. Sin.*, vol. 43, pp. 124–132, 2011.

[561] H. E. van der Bij and B. M. Weckhuysen, “Phosphorus promotion and poisoning in zeolite-based materials: synthesis, characterisation and catalysis,” *Chem. Soc. Rev.*, vol. 44, pp. 7406–7428, 2015.

[562] N. Y. Chen, W. W. Kaeding, and F. G. Dwyer, “Para-directed aromatic reactions over shape-selective molecular sieve zeolite catalysts,” *J. Am. Chem. Soc.*, vol. 101, pp. 6783–6784, 1979.

[563] H. L. Janardhan, G. V. Shanbhag, and A. B. Halgeri, “Shape-selective catalysis by phosphate modified ZSM-5: Generation of new acid sites with pore narrowing,” *Appl. Catal. A Gen.*, vol. 471, pp. 12–18, 2014.

[564] G. Seo, “^{31}P, ^{27}Al, and ^{129}Xe NMR study of phosphorus-impregnated HZSM-5 zeolite catalysts,” *J. Catal.*, vol. 124, pp. 224–230, 1990.

[565] B. S. Rao, P. K. Kumari, D. Dhanalakshmi, and N. Lingaiah, “Selective conversion of furfuryl alcohol into butyl levulinate over zinc exchanged heteropoly tungstate supported on niobia catalysts,” *Mol. Catal.*, vol. 427, pp. 80–86, 2017.

[566] F. A. Dawodu, O. Ayodele, J. Xin, S. Zhang, and D. Yan, “Effective conversion of non-edible oil with high free fatty acid into biodiesel by sulphonated carbon catalyst,” *Appl. Energy*, vol. 114, pp. 819–826, 2014.

[567] M. Hara, “Biodiesel Production by Amorphous Carbon Bearing SO_3H, COOH and Phenolic OH Groups, a Solid Brønsted Acid Catalyst,” *Top. Catal.*, vol. 53, pp. 805–810, 2010.

[568] M. H. A. Elella, R. R. Mohamed, E. A. ElHafeez, and M. W. Sabaa, “Synthesis of novel biodegradable antibacterial grafted xanthan gum,” *Carbohydr. Polym.*, vol. 173, pp. 305–311, 2017.

[569] M. W. Sabaa, D. H. Hanna, M. H. Abu Elella, and R. R. Mohamed, “Encapsulation of bovine serum albumin within novel xanthan gum based hydrogel for protein delivery,” *Mater. Sci. Eng. C*, vol. 94, pp. 1044–1055, 2019.

[570] J. A. Sirviö, M. Visanko, and H. Liimatainen, “Deep eutectic solvent system based on choline chloride-urea as a pre-treatment for nanofibrillation of wood cellulose,” *Green Chem.*, vol. 17, pp. 3401–3406, 2015.

[571] Y. Wu *et al.*, “Microwave-assisted hydrolysis of crystalline cellulose catalyzed by biomass char sulfonic acids,” *Green Chem.*, vol. 12, p. 696, 2010.

[572] F. Su, L. Ma, D. Song, X. Zhang, and Y. Guo, “Design of a highly ordered mesoporous $H_3PW_{12}O_{40}/ZrO_2$–Si(Ph)Si hybrid catalyst for methyl levulinate synthesis,” *Green Chem.*, vol. 15, p. 885, 2013.

[573] L. Hu *et al.*, “Catalytic conversion of carbohydrates into 5-hydroxymethylfurfural over cellulose-derived carbonaceous catalyst in ionic liquid,” *Bioresour. Technol.*, vol. 148, pp. 501–507, 2013.

[574] C. M. Cai, N. Nagane, R. Kumar, and C. E. Wyman, “Coupling metal halides with a co-solvent to produce furfural and 5-HMF at high yields directly from lignocellulosic biomass as an integrated biofuels strategy,” *Green Chem.*, vol. 16, pp. 3819–3829, 2014.

[575] C. Liang, Y. Hu, L. Guo, L. Wu, and W. Zhang, “Kinetic study of acid hydrolysis of corncobs to levulinic acid,” *Bioresources*, vol. 12, pp. 4049–4061, 2017.

[576] X. Li, Y. Jiang, L. Wang, L. Meng, W. Wang, and X. Mu, “Effective low-temperature hydrolysis of cellulose catalyzed by concentrated $H_3PW_{12}O_{40}$ under microwave irradiation,” *RSC Adv.*, vol. 2, p. 6921, 2012.

[577] M. Larhed, C. Moberg, and A. Hallberg, “Microwave-Accelerated Homogeneous Catalysis in Organic Chemistry,” *Acc. Chem. Res.*, vol. 35, pp. 717–727, 2002.

[578] P. Mazo, D. Estenoz, M. Sponton, and L. Rios, “Kinetics of the Transesterification of Castor Oil with Maleic Anhydride Using Conventional and Microwave Heating,” *J. Am. Oil Chem. Soc.*, vol. 89, pp. 1355–1361, 2012.

[579] K. Adavi, A. Amini, M. Latifi, J. Shabanian, and J. Chaouki, “Kinetic study of multiphase reactions under microwave irradiation: A mini-review,” *Front. Chem. Eng.*, vol. 4, pp. 1–8, 2022.

[580] X. Zhang, X. Ma, Z. Yu, and G. Shen, “Effect of microwave pretreatment on pyrolysis of chili straw: thermodynamics, activation energy, and solid reaction mechanism,” *Environ. Sci. Pollut. Res.*, vol. 31, pp. 15759–15769, 2024.

[581] S. Morales-delaRosa, J. M. Campos-Martin, and J. L. G. Fierro, “Optimization of the process of chemical hydrolysis of cellulose to glucose,” *Cellulose*, vol. 21, pp. 2397–2407, 2014.

[582] B. Girisuta, K. Dussan, D. Haverty, J. J. Leahy, and M. H. B. Hayes, “A kinetic study of acid catalysed hydrolysis of sugar cane bagasse to levulinic acid,” *Chem. Eng. J.*, vol. 217, pp. 61–70, 2013.

[583] A. L. Cardoso, R. Augusti, and M. J. Da Silva, “Investigation on the Esterification of Fatty Acids Catalyzed by the $H_3PW_{12}O_{40}$ heteropolyacid,” *J. Am. Oil Chem. Soc.*, vol. 85, pp. 555–560, 2008.

[584] W. Deng, M. Liu, Q. Zhang, X. Tan, and Y. Wang, “Acid-catalysed direct transformation of cellulose into methyl glucosides in methanol at moderate temperatures,” *Chem. Commun.*, vol. 46, p. 2668, 2010.

[585] V. I. Kovalenko, “Crystalline cellulose: structure and hydrogen bonds,” *Russ. Chem. Rev.*, vol. 79, pp. 231–241, 2010.

[586] J. F. Matthews *et al.*, “High-Temperature Behavior of Cellulose I,” *J. Phys. Chem. B*, vol. 115, pp. 2155–2166, 2011.

[587] C. O. Kappe, B. Pieber, and D. Dallinger, “Microwave Effects in Organic Synthesis: Myth or Reality?,” *Angew. Chem. Int. Ed.*, vol. 52, pp. 1088–1094, 2013.

[588] P. Hirunsit, T. Toyao, S. M. A. H. Siddiki, K. Shimizu, and M. Ehara, “Origin of Nb_2O_5 Lewis Acid Catalysis for Activation of Carboxylic Acids in the Presence of a Hard Base,” *ChemPhysChem*, vol. 19, pp. 2848–2857, 2018.

[589] L. Prati, A. Jouve, and A. Villa, “Production and Upgrading of γ-Valerolactone with Bifunctional Catalytic Processes,” in *Production of Biofuels and Chemicals with Bifunctional Catalysts*, Springer, 2017, pp. 221–237.

[590] N. A. S. Ramli and N. A. S. Amin, “Kinetic study of glucose conversion to levulinic acid over Fe/HY zeolite catalyst,” *Chem. Eng. J.*, vol. 283, pp. 150–159, 2016.

[591] C. Chang, X. Ma, and P. Cen, “Kinetic Studies on Wheat Straw Hydrolysis to Levulinic Acid,” *Chin. J. Chem. Eng.*, vol. 17, pp. 835–839, 2009.

[592] B. Girisuta, B. Danon, R. Manurung, L. P. B. M. Janssen, and H. J. Heeres, “Experimental and kinetic modelling studies on the acid-catalysed hydrolysis of the water hyacinth plant to levulinic acid,” *Bioresour. Technol.*, vol. 99, pp. 8367–8375, 2008.

[593] H. Ren, B. Girisuta, Y. Zhou, and L. Liu, “Selective and recyclable depolymerization of cellulose to levulinic acid catalyzed by acidic ionic liquid,” *Carbohydr. Polym.*, vol. 117, pp. 569–576, 2015.

[594] M. Sasaki *et al.*, “Cellulose hydrolysis in subcritical and supercritical water,” *J. Supercrit. Fluids*, vol. 13, pp. 261–268, 1998.

[595] M. Sasaki, Z. Fang, Y. Fukushima, T. Adschiri, and K. Arai, "Dissolution and Hydrolysis of Cellulose in Subcritical and Supercritical Water," *Ind. Eng. Chem. Res.*, vol. 39, pp. 2883–2890, 2000.

[596] S. Karwa, V. M. Gajiwala, J. Heltzel, S. K. R. Patil, and C. R. F. Lund, "Reactivity of levulinic acid during aqueous, acid-catalyzed HMF hydration," *Catal. Today*, vol. 263, pp. 16–21, 2016.

[597] K. Dussan, B. Girisuta, D. Haverty, J. J. Leahy, and M. H. B. Hayes, "Kinetics of levulinic acid and furfural production from *Miscanthus×giganteus*," *Bioresour. Technol.*, vol. 149, pp. 216–224, 2013.

[598] Q. Liu, F. Yang, H. Yin, and Y. Du, "Conversion of saccharides into levulinic acid and 5-hydroxymethylfurfural over WO_3 –Ta_2O_5 catalysts," *RSC Adv.*, vol. 6, pp. 49760–49763, 2016.

[599] Q. Jing and X. Lü, "Kinetics of Non-catalyzed Decomposition of Glucose in High-temperature Liquid Water," *Chin. J. Chem. Eng.*, vol. 16, pp. 890–894, 2008.

[600] L. Yan, A. A. Greenwood, A. Hossain, and B. Yang, "A comprehensive mechanistic kinetic model for dilute acid hydrolysis of switchgrass cellulose to glucose, 5-HMF and levulinic acid," *RSC Adv.*, vol. 4, p. 23492, 2014.

[601] Z. Zhi, N. Li, Y. Qiao, X. Zheng, H. Wang, and X. Lu, "Kinetic study of levulinic acid production from corn stalk at relatively high temperature using $FeCl_3$ as catalyst: A simplified model evaluated," *Ind. Crops Prod.*, vol. 76, pp. 672–680, 2015.

[602] O. Akin and A. Yuksel, "Novel hybrid process for the conversion of microcrystalline cellulose to value-added chemicals: part 1: process optimization," *Cellulose*, vol. 23, pp. 3475–3493, 2016.

[603] G. Yang, E. A. Pidko, and E. J. M. Hensen, "Mechanism of Brønsted acid-catalyzed conversion of carbohydrates," *J. Catal.*, vol. 295, pp. 122–132, 2012.

[604] R. S. Assary, P. C. Redfern, J. R. Hammond, J. Greeley, and L. A. Curtiss, "Computational Studies of the Thermochemistry for Conversion of Glucose to Levulinic Acid," *J. Phys. Chem. B*, vol. 114, pp. 9002–9009, 2010.

[605] D. Garcés, E. Díaz, and S. Ordóñez, "Aqueous Phase Conversion of Hexoses into 5-Hydroxymethylfurfural and Levulinic Acid in the

Presence of Hydrochloric Acid: Mechanism and Kinetics," *Ind. Eng. Chem. Res.*, vol. 56, pp. 5221–5230, 2017.

[606] B. Girisuta, L. P. B. M. Janssen, and H. J. Heeres, "Kinetic Study on the Acid-Catalyzed Hydrolysis of Cellulose to Levulinic Acid," *Ind. Eng. Chem. Res.*, vol. 46, pp. 1696–1708, 2007.

[607] X. Luo *et al.*, "Heteropoly Acid-Based Catalysts for Hydrolytic Depolymerization of Cellulosic Biomass," *Front. Chem.* vol. 8, p. 580146, 2020.

[608] X. Cheng *et al.*, "Kinetics for glucose conversion to levulinic acid over solid acid catalyst in γ-valerolactone solution," *Biochem. Eng. J.*, vol. 180, p. 108360, 2022.

[609] B. Song, Y. Yu, and H. Wu, "Tuning glucose decomposition in hot-compressed gamma-valerolactone/water mixtures: From isomerization to dehydration reactions," *Fuel*, vol. 238, pp. 225–231, 2019.

[610] L. Qi *et al.*, "Operando Solid-State NMR Observation of Solvent-Mediated Adsorption-Reaction of Carbohydrates in Zeolites," *ACS Catal.*, vol. 7, pp. 3489–3500, 2017.

[611] Y. W. Tiong, C. L. Yap, S. Gan, and W. S. P. Yap, "Kinetic and thermodynamic studies of oil palm mesocarp fiber cellulose conversion to levulinic acid and upgrading to ethyl levulinate via indium trichloride-ionic liquids," *Renew. Energy*, vol. 146, pp. 932–943, 2020.

[612] Q. Qing, Q. Guo, P. Wang, H. Qian, X. Gao, and Y. Zhang, "Kinetics study of levulinic acid production from corncobs by tin tetrachloride as catalyst," *Bioresour. Technol.*, vol. 260, pp. 150–156, 2018.

[613] A. Paajanen, A. Rinta-Paavola, and J. Vaari, "High-temperature decomposition of amorphous and crystalline cellulose: reactive molecular simulations," *Cellulose*, vol. 28, pp. 8987–9005, 2021.

[614] R. D. S. Bezerra, P. R. S. Teixeira, A. S. N. M. Teixeira, C. Eiras, J. A. Osajima, and E. C. S. Filho, "Chemical Functionalization of Cellulosic Materials — Main Reactions and Applications in the Contaminants Removal of Aqueous Medium," in *Cellulose - Fundamental Aspects and Current Trends*, InTech, 2015.

[615] A. Paajanen and J. Vaari, "High-temperature decomposition of the cellulose molecule: a stochastic molecular dynamics study," *Cellulose*, vol. 24, pp. 2713–2725, 2017.

[616] K. R. Spacino, D. Borsato, G. M. Buosi, and L. T. Chendynski, "Determination of kinetic and thermodynamic parameters of the B100

biodiesel oxidation process in mixtures with natural antioxidants," *Fuel Process. Technol.*, vol. 137, pp. 366–370, 2015.

[617] T. Lonhienne, C. Gerday, and G. Feller, "Psychrophilic enzymes: revisiting the thermodynamic parameters of activation may explain local flexibility," *Biochim. et Biophys. Acta Prot. Struct. Mol. Enzymol.*, vol. 1543, pp. 1–10, 2000.

[618] N. A. S. Ramli and N. A. S. Amin, "Thermo-kinetic assessment of glucose decomposition to 5-hydroxymethyl furfural and levulinic acid over acidic functionalized ionic liquid," *Chem. Eng. J.*, vol. 335, pp. 221–230, 2018.

[619] W. Deng, Q. Zhang, and Y. Wang, "Catalytic transformations of cellulose and its derived carbohydrates into 5-hydroxymethylfurfural, levulinic acid, and lactic acid," *Sci. China Chem.*, vol. 58, pp. 29–46, 2015.

[620] R. Weingarten, J. Cho, R. Xing, W. C. Conner, and G. W. Huber, "Kinetics and Reaction Engineering of Levulinic Acid Production from Aqueous Glucose Solutions," *ChemSusChem*, vol. 5, pp. 1280–1290, 2012.

[621] Y. Liu and F. M. Kerton, "Mechanistic studies on the formation of 5-hydroxymethylfurfural from the sugars fructose and glucose," *Pure Appl. Chem.*, vol. 93, pp. 463–478, 2021.

[622] L. Liu, "Structure and Formation Mechanism of 5-Hydroxymethylfurfural (HMF)-Derived Humins," in *Biomass-Derived Humins*, Singapore: Springer Nature Singapore, 2023, pp. 7–21.

[623] S. K. Singh, Y. Kumar, and S. Sasmal, "One-Step method for the production of 5-HMF from catalytic conversion of microalgal biomass," *Biomass Convers. Biorefin.*, 2023.

[624] I. Agirrezabal-Telleria, I. Gandarias, and P. L. Arias, "Heterogeneous acid-catalysts for the production of furan-derived compounds (furfural and hydroxymethylfurfural) from renewable carbohydrates: A review," *Catal. Today*, vol. 234, pp. 42–58, 2014.

[625] J. Jow, G. L. Rorrer, M. C. Hawley, and D. T. A. Lamport, "Dehydration of d-fructose to levulinic acid over LZY zeolite catalyst," *Biomass*, vol. 14, pp. 185–194, 1987.

[626] K. Lourvanij and G. L. Rorrer, "Reactions of aqueous glucose solutions over solid-acid Y-zeolite catalyst at 110-160 °C," *Ind. Eng. Chem. Res.*, vol. 32, pp. 11–19, 1993.

[627] T. Wang, J. A. Glasper, and B. H. Shanks, “Kinetics of glucose dehydration catalyzed by homogeneous Lewis acidic metal salts in water,” *Appl. Catal. A Gen.*, vol. 498, pp. 214–221, 2015.

[628] C. Megías-Sayago, S. Navarro-Jaén, F. Drault, and S. Ivanova, “Recent Advances in the Brønsted/Lewis Acid Catalyzed Conversion of Glucose to HMF and Lactic Acid: Pathways toward Bio-Based Plastics,” *Catalysts*, vol. 11, p. 1395, 2021.

[629] C. M. Bohn, “Transformation of Biomass Carbohydrates by Transition Metal Catalysts,” Thesis Dissertation, Purdue University, 2014.

[630] Q. Xiang, Y. Y. Lee, and R. W. Torget, “Kinetics of Glucose Decomposition During Dilute-Acid Hydrolysis of Lignocellulosic Biomass,” *Appl. Biochem. Biotechnol.*, vol. 115, pp. 1127–1138, 2004.

[631] C. N. Hamelinck, G. van Hooijdonk, and A. P. Faaij, “Ethanol from lignocellulosic biomass: techno-economic performance in short-, middle- and long-term,” *Biomass Bioenergy*, vol. 28, pp. 384–410, 2005.

[632] E. S. Kim, S. Liu, M. M. Abu-Omar, and N. S. Mosier, “Selective Conversion of Biomass Hemicellulose to Furfural Using Maleic Acid with Microwave Heating,” *Energy Fuels*, vol. 26, pp. 1298–1304, 2012.

[633] X. Hu, S. Wang, L. Wu, D. Dong, M. Mahmudul Hasan, and C.-Z. Li, “Acid-treatment of C5 and C6 sugar monomers/oligomers: Insight into their interactions,” *Fuel Process. Technol.*, vol. 126, pp. 315–323, 2014.

[634] D. W. Rackemann, J. P. Bartley, and W. O. S. Doherty, “Methanesulfonic acid-catalyzed conversion of glucose and xylose mixtures to levulinic acid and furfural,” *Ind. Crops Prod.*, vol. 52, pp. 46–57, 2014.

[635] A. S. Khan *et al.*, “Efficient conversion of lignocellulosic biomass to levulinic acid using acidic ionic liquids,” *Carbohydr. Polym.*, vol. 181, pp. 208–214, 2018.

[636] T. Runge and C. Zhang, “Two-Stage Acid-Catalyzed Conversion of Carbohydrates into Levulinic Acid,” *Ind. Eng. Chem. Res.*, vol. 51, pp. 3265–3270, 2012.

[637] Y. Yang, C. Hu, and M. M. Abu-Omar, “Conversion of glucose into furans in the presence of $AlCl_3$ in an ethanol–water solvent system,” *Bioresour. Technol.*, vol. 116, pp. 190–194, 2012.

[638] P. T. M. Do, J. R. McAtee, D. A. Watson, and R. F. Lobo, “Elucidation of Diels–Alder Reaction Network of 2,5-Dimethylfuran and Ethylene on HY Zeolite Catalyst,” *ACS Catal.*, vol. 3, pp. 41–46, 2013.

[639] Y.-P. Li, M. Head-Gordon, and A. T. Bell, “Computational Study of *p* -Xylene Synthesis from Ethylene and 2,5-Dimethylfuran Catalyzed by H-BEA,” *J. Phys. Chem. C*, vol. 118, pp. 22090–22095, 2014.

[640] Y. Yang *et al.*, “Hydrogenolysis of 5-Hydroxymethylfurfural to 2,5-Dimethylfuran under Mild Conditions without Any Additive,” *ACS Sustain. Chem. Eng.*, vol. 7, pp. 5711–5716, 2019.

[641] E. Tarasova *et al.*, “Effect of green co-solvents on properties and synthesis of cellulose esters in superbase ionic liquid,” *Cellulose*, vol. 31, pp. 4911–4927, 2024.

[642] S. Van de Vyver *et al.*, “Catalytic production of levulinic acid from cellulose and other biomass-derived carbohydrates with sulfonated hyperbranched poly(arylene oxindole)s,” *Energy Environ. Sci.*, vol. 4, p. 3601, 2011.

[643] C. S. Julie Chandra, S. Sasi, T. K. Bindu Sharmila, and J. R. Varghese, “Modern Biomass Conversion Technologies,” in *Handbook of Biomass*, Singapore: Springer Nature Singapore, 2023, pp. 1–31.

[644] Y. J. Pagán-Torres, T. Wang, J. M. R. Gallo, B. H. Shanks, and J. A. Dumesic, “Production of 5-Hydroxymethylfurfural from Glucose Using a Combination of Lewis and Brønsted Acid Catalysts in Water in a Biphasic Reactor with an Alkylphenol Solvent,” *ACS Catal.*, vol. 2, pp. 930–934, 2012.

[645] G. Yang, E. A. Pidko, and E. J. M. Hensen, “The Mechanism of Glucose Isomerization to Fructose over Sn-BEA Zeolite: A Periodic Density Functional Theory Study,” *ChemSusChem*, vol. 6, pp. 1688–1696, 2013.

[646] C. Yue, G. Li, E. A. Pidko, J. J. Wiesfeld, M. Rigutto, and E. J. M. Hensen, “Dehydration of Glucose to 5-Hydroxymethylfurfural Using Nb-doped Tungstite,” *ChemSusChem*, vol. 9, pp. 2421–2429, 2016.

[647] L. Bayne, R. V. Ulijn, and P. J. Halling, “Effect of pore size on the performance of immobilised enzymes,” *Chem. Soc. Rev.*, vol. 42, p. 9000, 2013.

[648] S. Taghavi *et al.*, “Levulinic Acid Production: Comparative Assessment of Al-Rich Ordered Mesoporous Silica and Microporous Zeolite,” *Catal. Letters*, vol. 153, pp. 41–53, 2023.

[649] K. Kraiwattanawong, S. R. Mukai, H. Tamon, and A. W. Lothongkum, “Control of mesoporous properties of carbon cryogels prepared from wattle tannin and furfural,” *J. Porous Mater.*, vol. 15, pp. 695–703, 2008.

[650] G. Wang *et al.*, “Recent Progress in Using Mesoporous Carbon Materials as Catalyst Support for Proton Exchange Membrane Fuel Cells,” *Nanomaterials*, vol. 13, p. 2818, 2023.

[651] S. Taghavi *et al.*, “Levulinic Acid Production: Comparative Assessment of Al-Rich Ordered Mesoporous Silica and Microporous Zeolite,” *Catal. Letters*, vol. 153, pp. 41–53, 2023.

[652] G. Tsilomelekis *et al.*, “Molecular structure, morphology and growth mechanisms and rates of 5-hydroxymethyl furfural (HMF) derived humins,” *Green Chem.*, vol. 18, pp. 1983–1993, 2016.

[653] H. Chen, B. Yu, and S. Jin, “Production of levulinic acid from steam exploded rice straw via solid superacid,” *Bioresour. Technol.*, vol. 102, pp. 3568–3570, 2011.

[654] Y. Jian, Y. Meng, and H. Li, “Selectivity Control of C-O Bond Cleavage for Catalytic Biomass Valorization,” *Front. Energy Res.*, vol. 9, p. 827680, 2022.

[655] A. A. Tortosa Masiá, B. J. P. Buhre, R. P. Gupta, and T. F. Wall, “Characterising ash of biomass and waste,” *Fuel Process. Technol.*, vol. 88, pp. 1071–1081, 2007.

[656] S. V. Vassilev, D. Baxter, L. K. Andersen, and C. G. Vassileva, “An overview of the chemical composition of biomass,” *Fuel*, vol. 89, pp. 913–933, 2010.

[657] J. Guo, Y. L. Ma, J. Y. Yu, Y. J. Gao, N. X. Ma, and X. Y. Wu, “Highly selective cleavage C–O ether bond of lignin model compounds over Ni/CaO–H-ZSM-5 in ethanol,” *BMC Chem.*, vol. 13, pp. 1–15, 2019.

[658] P. A. Jalil, M. Faiz, N. Tabet, N. M. Hamdan, and Z. Hussain, “A study of the stability of tungstophosphoric acid, $H_3PW_{12}O_{40}$, using synchrotron XPS, XANES, hexane cracking, XRD, and IR spectroscopy,” *J Catal.*, vol. 217, pp. 292–297, 2003.

[659] J. Horvat, B. Klaić, B. Metelko, and V. Šunjić, “Mechanism of levulinic acid formation,” *Tetrahedron Lett.*, vol. 26, pp. 2111–2114, 1985.

[660] R. K. P. Purushothaman, J. van Haveren, A. Mayoral, I. Melián-Cabrera, and H. J. Heeres, “Exploratory Catalyst Screening Studies on the Base Free Conversion of Glycerol to Lactic Acid and Glyceric Acid in Water Using Bimetallic Au–Pt Nanoparticles on Acidic Zeolites,” *Top. Catal.*, vol. 57, pp. 1445–1453, 2014.

[661] J. Ahlkvist, J. Wärnå, T. Salmi, and J.-P. Mikkola, “Heterogeneously catalyzed conversion of nordic pulp to levulinic and formic acids,” *React. Kinet. Mech. Catal.*, vol. 119, pp. 415–427, 2016.

[662] S. Kang and J. Yu, “An intensified reaction technology for high levulinic acid concentration from lignocellulosic biomass,” *Biomass Bioenergy*, vol. 95, pp. 214–220, 2016.

[663] K. Yan, C. Jarvis, J. Gu, and Y. Yan, “Production and catalytic transformation of levulinic acid: A platform for speciality chemicals and fuels,” *Renew. Sust. Energ. Rev.*, vol. 51, pp. 986–997, 2015.

[664] T. M. Aida *et al.*, “Dehydration of d-glucose in high temperature water at pressures up to 80MPa,” *J. Supercrit. Fluids*, vol. 40, pp. 381–388, 2007.

[665] M. Dabiri and S. Bashiribod, “Phosphotungstic Acid: An Efficient, Cost-effective and Recyclable Catalyst for the Synthesis of Polysubstituted Quinolines,” *Molecules*, vol. 14, pp. 1126–1133, 2009.

[666] Z. Fehér, D. Richter, G. Dargó, and J. Kupai, “Factors influencing the performance of organocatalysts immobilised on solid supports: A review,” *Beilstein J. Org. Chem.*, vol. 20, pp. 2129–2142, 2024.

[667] L. Liu, “Humins Valorization’, in *Biomass-Derived Humins*, Singapore: Springer Nature Singapore, 2023, pp. 131–147.

[668] J. C. Velasco Calderón, J. S. Arora, and S. H. Mushrif, “Mechanistic Investigation into the Formation of Humins in Acid-Catalyzed Biomass Reactions,” *ACS Omega*, vol. 7, pp. 44786–44795, 2022.

[669] J. Halim *et al.*, “X-ray photoelectron spectroscopy of select multi-layered transition metal carbides (MXenes),” *Appl. Surf. Sci.*, vol. 362, pp. 406–417, 2016.

[670] M. T. Marques, A. M. Ferraria, J. B. Correia, A. M. B. do Rego, and R. Vilar, “XRD, XPS and SEM characterisation of Cu–NbC nanocomposite produced by mechanical alloying,” *Mater. Chem. Phys.*, vol. 109, pp. 174–180, 2008.

[671] D.-M. Gao *et al.*, “Synthesis of a hierarchically porous niobium phosphate monolith by a sol–gel method for fructose dehydration to 5-hydroxymethylfurfural,” *Catal. Sci. Technol.*, vol. 8, pp. 3675–3685, 2018.

[672] S. Liu, M. Zhu, and M. Iqbal, “Research Progress on Stability of Solid Acid Catalysts,” *Catal. Surv. from Asia*, vol. 24, pp. 196–206, 2020.

[673] Z. Xu, Y. Yang, P. Yan, Z. Xia, X. Liu, and Z. C. Zhang, “Mechanistic understanding of humin formation in the conversion of glucose and fructose to 5-hydroxymethylfurfural in [BMIM]Cl ionic liquid,” *RSC Adv.*, vol. 10, pp. 34732–34737, 2020.

[674] T. Esser, A. Wassenberg, D. Voß, and J. Albert, “Selective catalytic oxidation of humins to carboxylic acids using the $H_4[PVMo_{11}O_{40}]$ Keggin-type polyoxometalate enhanced by alcohol doping and solubilizer,” *React. Chem. Eng.*, 2024.

[675] I. van Zandvoort, E. J. Koers, M. Weingarth, P. C. A. Bruijnincx, M. Baldus, and B. M. Weckhuysen, “Structural characterization of ^{13}C-enriched humins and alkali-treated ^{13}C humins by 2D solid-state NMR,” *Green Chem.*, vol. 17, pp. 4383–4392, 2015.

[676] N. Wang, W. Ma, Z. Ren, Y. Du, P. Xu, and X. Han, “Prussian blue analogues derived porous nitrogen-doped carbon microspheres as high-performance metal-free peroxymonosulfate activators for non-radical-dominated degradation of organic pollutants,” *J. Mater. Chem. A Mater.*, vol. 6, pp. 884–895, 2018.

[677] W. Peng, S. Liu, H. Sun, Y. Yao, L. Zhi, and S. Wang, “Synthesis of porous reduced graphene oxide as metal-free carbon for adsorption and catalytic oxidation of organics in water,” *J. Mater. Chem. A Mater.*, vol. 1, p. 5854, 2013.

[678] L. Liang, M. Zhou, W. Yang, and L. Jiang, “Enhanced activation of persulfate by carbohydrate-derived carbon cryogels for effective removal of organic pollutants,” *Chem. Eng. Journal*, vol. 352, pp. 673–681, 2018.

[679] Y. W. Tiong, C. L. Yap, S. Gan, and W. S. P. Yap, “One-pot conversion of oil palm empty fruit bunch and mesocarp fiber biomass to levulinic acid and upgrading to ethyl levulinate via indium trichloride-ionic liquids,” *J. Clean Prod.*, vol. 168, pp. 1251–1261, 2017.

[680] N. A. S. Ramli and N. A. S. Amin, “A new functionalized ionic liquid for efficient glucose conversion to 5-hydroxymethyl furfural and levulinic acid,” *J. Mol. Catal. A Chem.*, vol. 407, pp. 113–121, 2015.

[681] X.-Y. Tian, Y.-P. Du, X.-P. Zheng, Y. Chai, Y.-C. Zhang, and Y.-Z. Zheng, “One-pot directly conversion of passion fruit husk to levulinic acid using highly efficient and recyclable SO_3H-functionalized ionic liquids,” *Fuel Process. Technol.*, vol. 253, p. 108025, 2024.

[682] B. Girisuta and H. J. Heeres, “Levulinic Acid from Biomass: Synthesis and Applications,” in: Fang, Z., Smith, Jr., R., Qi, X. (eds) Production of

Platform Chemicals from Sustainable Resources. Biofuels and Biorefineries. Springer, Singapore, 2017, pp. 143–169.

[683] C. Antonetti, D. Licursi, S. Fulignati, G. Valentini, and A. Raspolli Galletti, “New Frontiers in the Catalytic Synthesis of Levulinic Acid: From Sugars to Raw and Waste Biomass as Starting Feedstock,” *Catalysts*, vol. 6, p. 196, 2016.

[684] A. M. Raspolli Galletti *et al.*, “Sustainable Exploitation of Residual *Cynara cardunculus L.* to Levulinic Acid and n-Butyl Levulinate,” *Catalysts*, vol. 11, p. 1082, 2021.

[685] C. Chang, P. Cen, and X. Ma, “Levulinic acid production from wheat straw,” *Bioresour. Technol.*, vol. 98, pp. 1448–1453, 2007.

[686] N. A. S. Ramli and N. A. S. Amin, “Optimization of Biomass Conversion to Levulinic Acid in Acidic Ionic Liquid and Upgrading of Levulinic Acid to Ethyl Levulinate,” *Bioenergy Res.*, vol. 10, pp. 50–63, 2017.

[687] D. B. Bevilaqua, M. K. D. Rambo, T. M. Rizzetti, A. L. Cardoso, and A. F. Martins, “Cleaner production: levulinic acid from rice husks,” *J. Clean Prod.*, vol. 47, pp. 96–101, 2013.

[688] N. Ya’aini, N. A. S. Amin, and M. Asmadi, “Optimization of levulinic acid from lignocellulosic biomass using a new hybrid catalyst,” *Bioresour. Technol.*, vol. 116, pp. 58–65, 2012.

[689] N. A. S. Ramli and N. A. S. Amin, “Optimization of renewable levulinic acid production from glucose conversion catalyzed by Fe/HY zeolite catalyst in aqueous medium,” *Energy Convers. Manag.*, vol. 95, pp. 10–19, 2015.

[690] C. Zhou, X. Yu, H. Ma, R. He, and S. Vittayapadung, “Optimization on the Conversion of Bamboo Shoot Shell to Levulinic Acid with Environmentally Benign Acidic Ionic Liquid and Response Surface Analysis,” *Chin. J. Chem. Eng.*, vol. 21, pp. 544–550, 2013.

[691] M. J. Valero-Romero, E. M. Márquez-Franco, J. Bedia, J. Rodríguez-Mirasol, and T. Cordero, “Hierarchical porous carbons by liquid phase impregnation of zeolite templates with lignin solution,” *Microporous Mesoporous Mater.*, vol. 196, pp. 68–78, 2014.

[692] F. Pua, Z. Fang, S. Zakaria, F. Guo, and C. Chia, “Direct production of biodiesel from high-acid value Jatrophaoil with solid acid catalyst derived from lignin,” *Biotechnol. Biofuels*, vol. 4, p. 56, 2011.

[693] F. Guo, Z.-L. Xiu, and Z.-X. Liang, “Synthesis of biodiesel from acidified soybean soapstock using a lignin-derived carbonaceous catalyst,” *Appl. Energy*, vol. 98, pp. 47–52, 2012.

[694] F. Liang, Y. Song, C. Huang, J. Zhang, and B. Chen, “Preparation and performance evaluation of a lignin-based solid acid from acid hydrolysis lignin,” *Catal. Commun.*, vol. 40, pp. 93–97, 2013.

[695] F. Guo, Z. Fang, and T.-J. Zhou, “Conversion of fructose and glucose into 5-hydroxymethylfurfural with lignin-derived carbonaceous catalyst under microwave irradiation in dimethyl sulfoxide–ionic liquid mixtures,” *Bioresour. Technol.*, vol. 112, pp. 313–318, 2012.

[696] S. Kang, J. Ye, Y. Zhang, and J. Chang, “Preparation of biomass hydrochar derived sulfonated catalysts and their catalytic effects for 5-hydroxymethylfurfural production,” *RSC Adv.*, vol. 3, p. 7360, 2013.

[697] L. Hu *et al.*, “Magnetic lignin-derived carbonaceous catalyst for the dehydration of fructose into 5-hydroxymethylfurfural in dimethylsulfoxide,” *Chem. Eng. J.*, vol. 263, pp. 299–308, 2015.

[698] X. Zhang, Z. Zhang, F. Wang, Y. Wang, Q. Song, and J. Xu, “Lignosulfonate-based heterogeneous sulfonic acid catalyst for hydrolyzing glycosidic bonds of polysaccharides,” *J. Mol. Catal. A Chem.*, vol. 377, pp. 102–107, 2013.

[699] H. Tamon, H. Ishizaka, T. Yamamoto, and T. Suzuki, “Preparation of mesoporous carbon by freeze drying,” *Carbon*, vol. 37, pp. 2049–2055, 1999.

[700] H. Tamon, H. Ishizaka, T. Yamamoto, and T. Suzuki, “Influence of freeze-drying conditions on the mesoporosity of organic gels as carbon precursors,” *Carbon*, vol. 38, pp. 1099–1105, 2000.

[701] N. Job *et al.*, “Carbon aerogels, cryogels and xerogels: Influence of the drying method on the textural properties of porous carbon materials,” *Carbon*, vol. 43, pp. 2481–2494, 2005.

[702] Y. Teramoto, S.-H. Lee, and T. Endo, “Cost reduction and feedstock diversity for sulfuric acid-free ethanol cooking of lignocellulosic biomass as a pretreatment to enzymatic saccharification,” *Bioresour. Technol.*, vol. 100, pp. 4783–4789, 2009.

Appendices

Appendix 1

Table A.1 Synthesis of lignin-based catalysts via different conditions, which influence textural properties of lignin.

Lignin type	Product/Solid acid	Activation (Template/Acid Condition	Calcination/ Carbonisation	Textural properties			Ref.
		T (°C)/t (h)	T (°C)/t (h)	A_{BET} ($m^2 g^{-1}$)	V_{mic} ($cm^3 g^{-1}$)/ V_{mes} ($cm^3 g^{-1}$)	$–SO_3H$ (mmol g^{-1})	
Commercial lignin	Carbon cryogel microspheres	90/0.5	500/5.0	330.4	–/–	<14.73	[24]
Kraft lignin	Activated carbon (20 nm silicon colloids) [a]	80/2.0	850/2.0	200.0	0.02/0.53	–	[353]
Kraft lignin	Activated carbon (13 nm silicon colloids) [a]	80/2.0	850/2.0	360.0	0.09/0.31	–	[353]
Alcell lignin	Template carbon materials (500 nm Zeolite Y)	25/1.0	700/2.0	952.0	0.35/0.15	–	[691]
Alcell lignin	Template carbon materials (17 nm Zeolite *β*)	25/1.0	700/2.0	864.0	0.321/0.958	–	[691]

Alcell lignin	Template carbon materials (120 nm ZSM-5)	25/1.0	700/2.0	619.0	0.249/0.132	–	[691]
Alcell lignin	Template carbon materials (170 nm mordenite)	25/1.0	700/2.0	682.0	0.275/0.098	–	[691]
Kraft lignin	Solid acid	200/2.0	400/1.0	54.8	–/–	2.10	[692]
Residual lignin	Lignin-derived solid acid catalyst	150/0.5	400/1.0	4.7	–/–	0.86	[693]
Sulphuric acid lignin	Solid acid	30/24.0	–/–	12.7	–/–	0.37	[694]
Black liquor	Lignin-derived solid acid catalyst	200/5.0	400/1.0	–	–/–	1.34	[695]
Dealkali lignin	Carbon-based sulphonated catalyst (L225-SO_3H)	150/12.0	225/–	<2.0	–/–	0.87	[696]
Enzymatic hydrolysis lignin	Magnetic lignin-derived amorphous carbon (MLC-SO_3H)	150/10.0	400/1.0	234.6	–/–	0.77	[697]
Lignosulphonate	Lignosulphonate-based catalyst (LF-A) [b]	–/2.0	–/–	25.0	–/–	1.00	[698]
Lignosulphonate	Lignosulphonate-based catalyst (LF-B) [c]	–/2.0	–/–	53.0	–/–	1.01	[698]
Lignosulphonate	Lignosulphonate-based catalyst (LF-C) [d]	–/2.0	–/–	107.0	–/–	1.03	[698]

Alkali lignin	Carbon-based solid catalyst	100/18.0	–/–	7.6	0.002/–	1.30	[466]
Alkali lignin	Sulphonated carbon fibre (HTSACFs) [e]	150/20.0	900/0.5	475.0	0.08/–	0.56	[541]

Note:

[a] Catalyst was prepared via microwave-irradiation.

[b] Lignosulphonate-based catalyst was prepared without silica balls.

[c] Silica balls (diameters of 15–17 nm) were added to the catalyst.

[d] Silica balls (diameters of 200–300 nm) were added to the catalyst.

[e] Solid acid catalyst was treated via hydrothermal.

Appendix 2

Table A.2 Different conditions for sol-gel process.

R/C molar ratio	R/W or dilution ratio (D)	Gelation and curing	Solvent exchange	Pyrolysis	BET surface area	Mesopore area or volume	Total pore volume	Average or peak pore size	Ref.
25, 200	R/W = 0.125, 0.250 g cm^{-3}	Curing one day at 298 K, one day at 323 K, and three days at 363 K	t-butanol, water	1273 K using nitrogen	800-1200 $m^2 g^{-1}$	V_{meso} =1.39–1.54 $cm^3 g^{-1}$	V_{mac} = 0.26–2.61 $cm^3 g^{-1}$	Peak radius 2.5–6.5 nm	[699]
200	R/W= 0.250 g cm^{-3}	Curing one day at 25 °C, one day at 50 °C, and three days at 90 °C	t-butanol, water	1000 °C under nitrogen flow	908 $m^2 g^{-1}$ with t-butanol and 915 $m^2 g^{-1}$ with water	549 $m^2 g^{-1}$ and 0.18 $cm^3 g^{-1}$ with t-butanol to 605 $m^2 g^{-1}$ and 0.2 $cm^3 g^{-1}$ V_{meso} =1.39 $cm^3 g^{-1}$ with t-butanol and 1.84 $cm^3 g^{-1}$ with water	-	Peak radius 5.5 nm with t-butanol and 8.1 nm with water	[700]

50, 75, 100, 200	R/W = 0.125, 0.25. 0.3775. 0.5 g cm^{-3}	Curing one day at 298 K, one day at 323 K, and three days at 363 K	t-butanol	1273 K using nitrogen	388–754 $m^2 g^{-1}$	V_{meso} = 0.12–1.29 $cm^3 g^{-1}$	-	Peak radius 1.4–7 nm	[392]
50, 500, 1000	D = 5.7, 20	Gelation at 85 °C for 7 days	Immersion in liquid nitrogen	1050 °C under nitrogen flow	275–740 $m^2 g^{-1}$	-	0.5-6.3 $cm^3 g^{-1}$, reported using Hg porosimetry	Maximum pore diameter 4–100 nm	[701]
50, 100, 200	R/W = 0.125, 0.25. 0.5 g cm^{-3}	One day at 25 °C, one day at 50 °C, and three days at 85 °C	1000 °C under nitrogen flow	TBA	8–1230 $m^2 g^{-1}$	-	Up to 2.01 $cm^3 g^{-1}$	Peak radius up to 11.8 nm	[372], [373]

Appendix 3

Holocellulose, which is the combined content of hemicellulose and cellulose, was analysed following the method outlined by Teramoto *et* al. [702]. The procedure involved treating the biomass sample with deionised water containing acetic acid and $NaClO_2$ at 75 ºC for 1 h. Subsequently, 0.04 ml of acetic acid and 0.2 g of $NaClO_2$ were added to the mixture every hour for a total of 3 h. The resulting residue was then filtered, washed, and dried overnight until a constant weight was achieved. The holocellulose content was determined based on the weight of the solid residues obtained.

To determine the cellulose content, 0.2 g of the previously obtained holocellulose was shaken in a flask with 5 ml of 17.5% NaOH aqueous solution at 30 ºC for 40 min using a water bath shaker. Afterward, 5 ml of deionised water was added to the mixture and shaken for an additional 5 min before filtration. The remaining residue was washed with 8 ml of 10% acetic acid and boiling water. Finally, the cellulose residue was dried overnight and weighed.

The hemicellulose content was calculated as the difference between the holocellulose and cellulose contents.

Appendix 4

To establish a calibration curve and confirm the appearance of the targeted compounds in the HPLC chromatogram, working and calibration standards were prepared using a mixed standard solution containing glucose, fructose, HMF, LA, FA and 2-methoxyethanol (as internal standard). The standards encompassed with a two series of concentrations: 1) 25, 50, 75, 100, 125, 150 mg L^{-1} and 2) 300, 450, 600, 750, and 900 mg L^{-1}.

Quality assurance and quality control measures were executed to monitor each analytical procedure. Analyses were carried out in triplicate and injected with the internal standard to monitor the performance of external standard (LA, glucose, fructose, FA and HMF). The mean concentration for each compound was calculated by dividing the concentration obtained from the calibration curve by the internal standard. This value was then used as the final analytical result. Each sample was injected twice to ensure the stability of the compound peaks in the chromatogram. Every 5 samples, the instrument was run with a blank to avoid carry-over or column contamination. The analysis of method was subsequently validated via several parameters, including precision, linearity, and sensitivity, which included limit of detection (LOD) and limit of quantification (LOQ).

Both LOD and LOQ were measured using the calibration curve technique. The LOD and LOQ were measured from S_{res} as the residual standard deviation of the calibration curve regression line shown in **Eq. A.1**, where *SE* is the standard error of the intercept, and *N* is the number of samples. The S_{res} values were then substituted into **Eq. A.2** and **A.3** to determine the respective values of LOD and LOQ, with *s* representing the slope.

$$S_{res} = SE \times \sqrt{N} \quad \text{(A.1)}$$

$$\text{LOD} = 3.3 \times (S_{res}/s) \quad \text{(A.2)}$$

$$\text{LOQ} = 10 \times (S_{res}/s) \quad \text{(A.3)}$$

LOD and LOQ for each compound are represented in **Table A.3**. The correlation coefficient of the calibration curve for each compound (**Figure A.1**) indicated good linearity. The variations in the compound concentrations were 99% explained by the linear model of the calibration curve. The precision of the method was computed as the dispersion sets of data using RSD. Intraday repeatability (**Table A.4 and A.5**) and interday reproducibility (**Table A.6 and A.7**) of the mixed calibration standards achieved low RSD (0.04–5.41%), with all values <10%, far below the acceptable limit of RSD (20%).

Table A.3 LOD and LOQ of targeted compounds.

Compound	**LOD (mg L^{-1})**	**LOQ (mg L^{-1})**
Glucose	1.185	3.591
Fructose	1.115	3.378
Levulinic acid	1.701	5.154
Formic acid	1.506	4.565
HMF	1.177	3.567

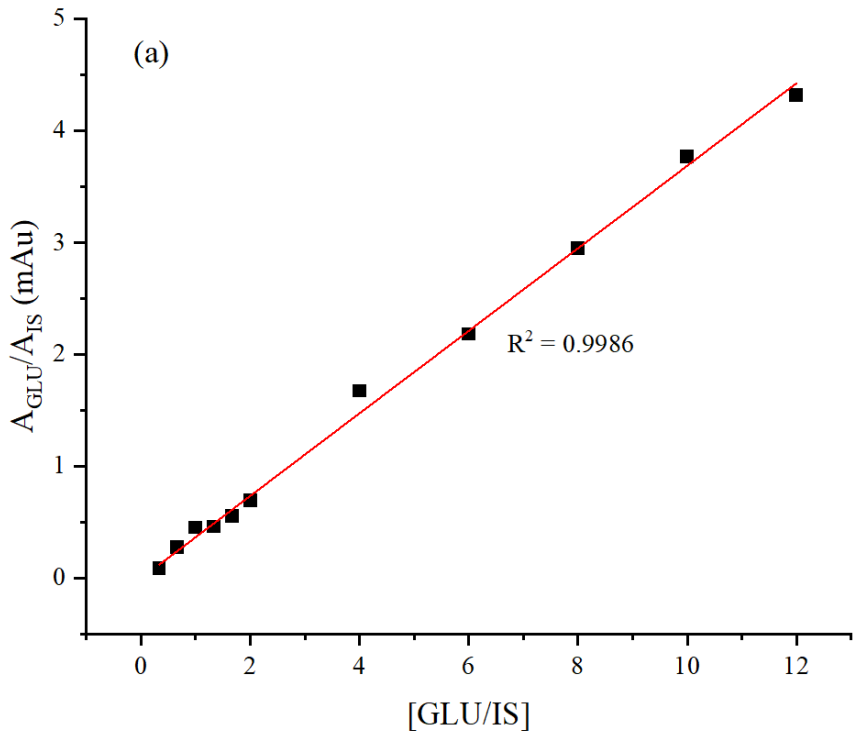
(a)
A_{GLU}/A_{IS} (mAu)
[GLU/IS]
R^2 = 0.9986
0
1
2
3
4
5
0
2
4
6
8
10
12

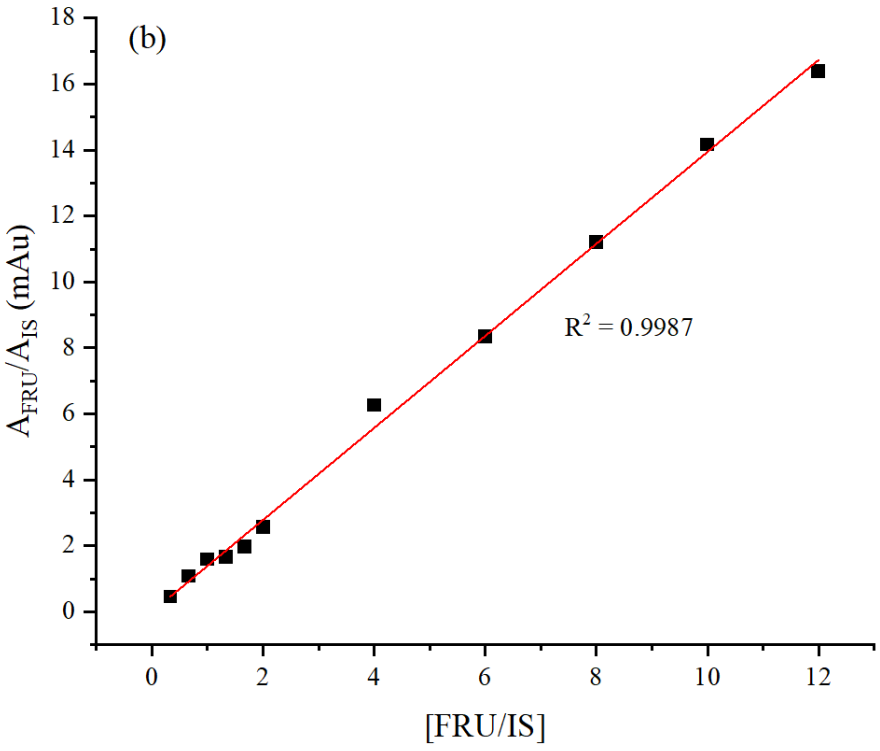
(b)
A_{FRU}/A_{IS} (mAu)
[FRU/IS]
R^2 = 0.9987
0
2
4
6
8
10
12
14
16
18
0
2
4
6
8
10
12

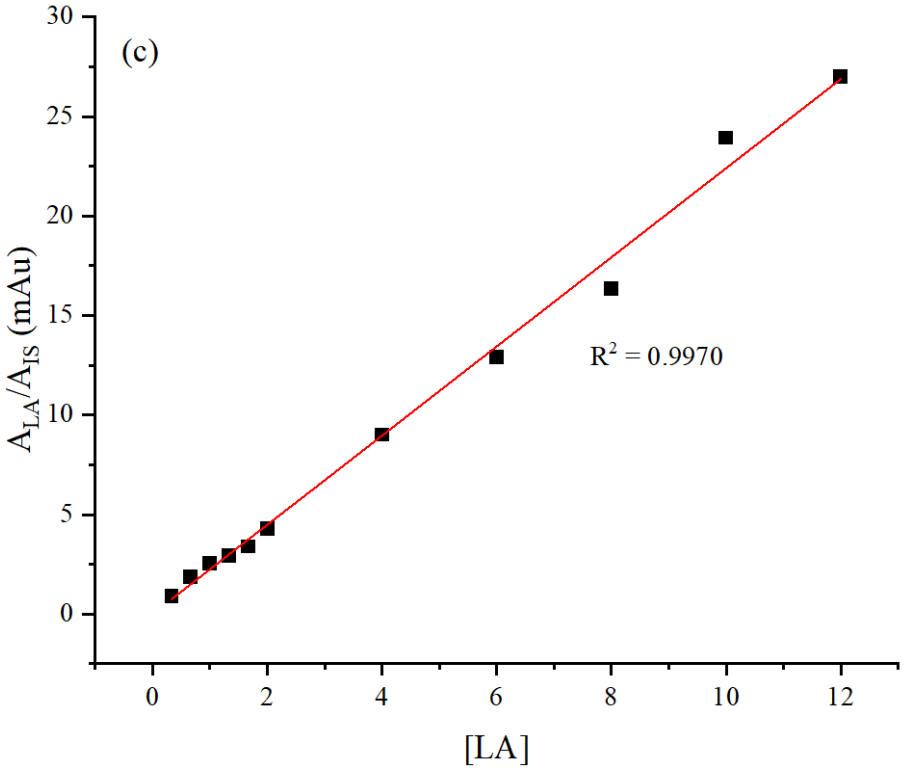
(c)
A_{LA}/A_{IS} (mAu)
[LA]
R^2 = 0.9970

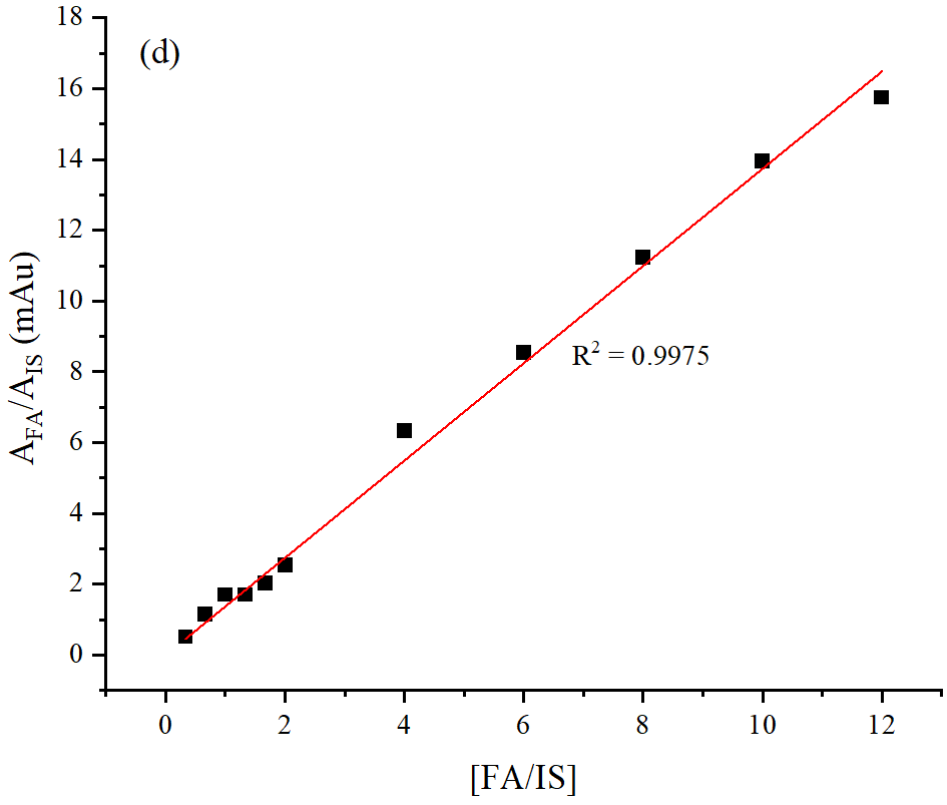
(d)
A_{FA}/A_{IS} (mAu)
[FA/IS]
R^2 = 0.9975

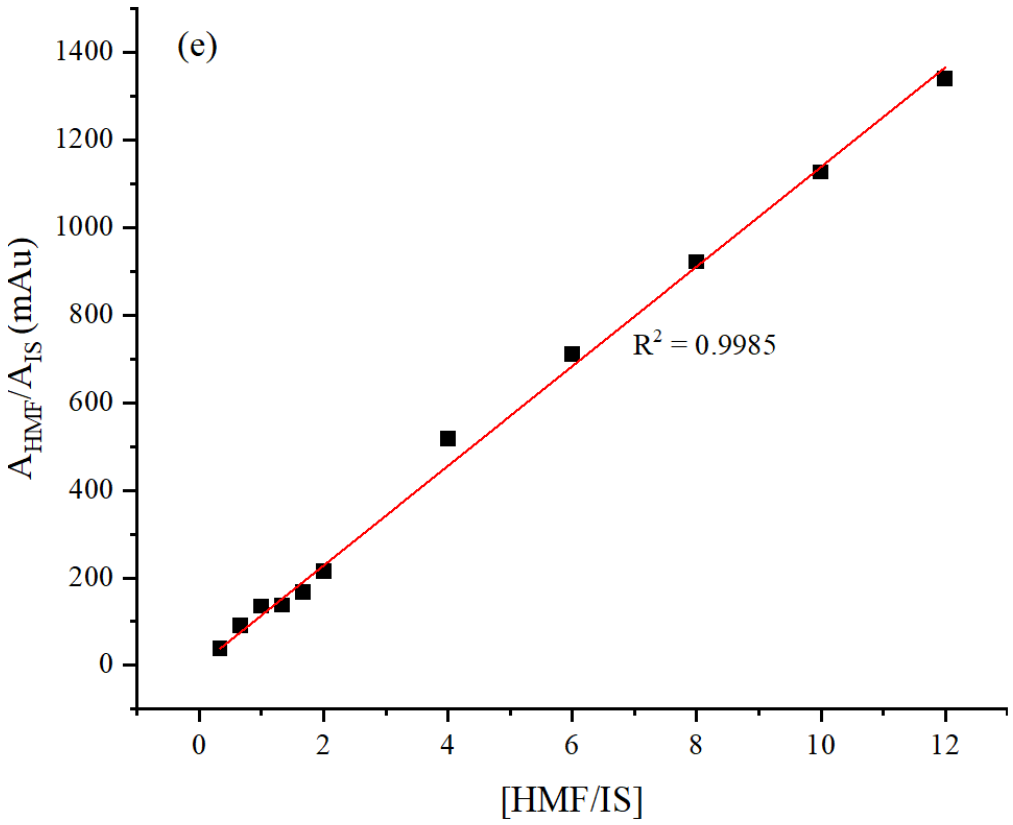

Figure A.1 The calibration curve represents concentrations ranging from 25 to 900 mgL^{-1} for the following substances: (a) glucose; (b) fructose; (c) LA; (d) FA and (e) HMF.

Table A.4 Intraday repeatability was assessed for mixed standards ranging from 25–150 mgL^{-1}, with measurements normalised to an internal standard.

Compound	**Retention time, t (min)**		**Peak area (mAu)**											
			25 mg L^{-1}		**50 mg L^{-1}**		**75 mg L^{-1}**		**100 mg L^{-1}**		**125 mg L^{-1}**		**150 m gL^{-1}**	
	Avg (SD)	**RSD**	**Avg (SD)**	**RSD**	**Avg (SD)**	**RSD**	**Avg (SD)**	**RSD**	**Avg (SD)**	**RSD**	**Avg (SD)**	**RSD**	**Avg (SD)**	**RSD**
Glucose	8.3 (0.004)	0.04	0.0976 (0.0053)	5.41	0.2730 (0.0046)	1.69	0.4623 (0.0084)	1.81	0.4701 (0.0084)	1.78	0.5583 (0.0047)	0.83	0.6927 (0.0053)	0.76
Fructose	9.4 (0.004)	0.04	0.4631 (0.0064)	1.37	1.0777 (0.0031)	0.29	1.5904 (0.0041)	0.25	1.6703 (0.0064)	0.39	1.9681 (0.0159)	0.81	2.5183 (0.0641)	2.54
Formic acid	15.3 (0.006)	0.04	0.5245 (0.0096)	1.82	1.1566 (0.0269)	2.32	1.7058 (0.0070)	0.41	1.7180 (0.0122)	0.71	2.0876 (0.0832)	3.98	2.5724 (0.0288)	1.12
Levulinic acid	16.2 (0.009)	0.06	0.8904 (0.0052)	0.58	1.8528 (0.0111)	0.60	2.5673 (0.0488)	1.90	2.9457 (0.0411)	1.39	3.4606 (0.0800)	2.31	4.2836 (0.0135)	0.31
HMF	31.5 (0.022)	0.07	38.2564 (0.5214)	1.36	89.1986 (0.5726)	0.64	135.0578 (0.3506)	0.26	138.0093 (0.7817)	0.57	166.9399 (0.6142)	0.37	215.1785 (0.9481)	0.44

Table A.5 Intraday repeatability was assessed for mixed standards ranging from 300–900 mgL^{-1}, with measurements normalised to an internal standard.

Compound	**Retention time, t (min)**		**Peak area (mAu)**									
			300 mg L^{-1}		**450 mg L^{-1}**		**600 mg L^{-1}**		**750 mg L^{-1}**		**900 mg L^{-1}**	
	Avg (SD)	**RSD**	**Avg (SD)**	**RSD**	**Avg (SD)**	**RSD**	**Avg (SD)**	**RSD**	**Avg (SD)**	**RSD**	**Avg (SD)**	**RSD**
Glucose	8.3 (0.004)	0.04	1.7021 (0.0283)	1.66	2.2136 (0.0319)	1.44	3.0147 (0.0758)	2.52	3.7660 (0.0206)	0.55	4.394 (0.0626)	1.43
Fructose	9.4 (0.004)	0.04	6.2551 (0.0104)	0.17	8.4157 (0.0601)	0.71	11.3343 (0.1244)	1.10	14.2090 (0.0424)	0.30	16.5256 (0.1356)	0.82
Formic acid	15.3 (0.006)	0.04	6.3612 (0.0380)	0.60	8.5691 (0.0470)	0.55	11.5594 (0.3194)	2.76	13.9041 (0.0442)	0.32	15.8100 (0.0682)	0.43
Levulinic acid	16.2 (0.009)	0.06	9.0346 (0.0329)	0.36	12.9515 (0.0478)	0.37	16.3354 (0.0118)	0.07	23.9159 (0.0195)	0.08	26.8420 (0.2381)	0.89
HMF	31.5 (0.022)	0.07	517.9296 (0.5463)	0.11	710.3831 (0.6327)	0.09	922.0959 (0.8234)	0.09	1127.0630 (0.4658)	0.04	1342.6210 (2.5341)	0.19

Table A.6 Interday reproducibility was assessed for mixed standards ranging from 25–150 mgL^{-1}, with measurements normalised to an internal standard.

Compound	**Retention time, t (min)**		**Peak area (mAu)**											
			25 mg L^{-1}		**50 mg L^{-1}**		**75 mg L^{-1}**		**100 mg L^{-1}**		**125 mg L^{-1}**		**150 mg L^{-1}**	
	Avg (SD)	**RSD**	**Avg (SD)**	**RSD**	**Avg (SD)**	**RSD**	**Avg (SD)**	**RSD**	**Avg (SD)**	**RSD**	**Avg (SD)**	**RSD**	**Avg (SD)**	**RSD**
Glucose	8.3 (0.004)	0.02	0.0951 (0.0035)	3.71	0.2756 (0.0085)	3.09	0.4618 (0.0129)	2.79	0.4815 (0.0175)	3.63	0.5591 (0.0038)	0.68	0.7001 (0.0030)	0.42
Fructose	9.4 (0.004)	0.02	0.4521 (0.0161)	3.56	1.0731 (0.0067)	0.63	1.6068 (0.0135)	0.84	1.6699 (0.0078)	0.47	1.9750 (0.0136)	0.69	2.5500 (0.0472)	1.85
Formic acid	15.3 (0.006)	0.03	0. 5310 (0.0145)	2.74	1.1529 (0.0317)	2.75	1.6827 (0.0327)	1.94	1.7149 (0.0166)	0.97	2.0941 (0.0602)	2.87	2.6914 (0.0606)	2.25
Levulinic acid	16.2 (0.009)	0.04	0.8876 (0.0030)	0.33	1.8613 (0.0171)	0.92	2.5631 (0.0270)	1.05	2.9753 (0.0611)	2.05	3.3835 (0.0603)	1.78	4.3503 (0.0687)	1.58
HMF	31.5 (0.022)	0.08	38.2564 (0.5994)	1.57	89.1986 (0.7416)	0.83	134.5245 (0.2849)	0.21	137.6392 (0.7172)	0.52	167.1499 (0.8335)	0.50	214.3678 (0.2927)	0.14

Table A.7 Interday reproducibility was assessed for mixed standards ranging from 300–900 mg L^{-1}, with measurements normalised to an internal standard.

Compound	**Retention time, t (min)**		**Peak area (mAu)**									
			300 mg L^{-1}		**450 mg L^{-1}**		**600 mg L^{-1}**		**750 mg L^{-1}**		**900 mg L^{-1}**	
	Avg (SD)	**RSD**	**Avg (SD)**	**RSD**	**Avg (SD)**	**RSD**	**Avg (SD)**	**RSD**	**Avg (SD)**	**RSD**	**Avg (SD)**	**RSD**
Glucose	8.3 (0.004)	0.02	1.6725 (0.0171)	1.02	2.2087 (0.0330)	1.50	2.9346 (0.0612)	2.09	3.7856 (0.0177)	0.47	4.4148 (0.1324)	3.00
Fructose	9.4 (0.004)	0.02	6.2342 (0.1196)	1.92	8.3818 (0.0439)	0.52	11.3977 (0.1736)	1.52	14.4241 (0.3039)	2.11	16.4657 (0.1814)	1.10
Formic acid	15.3 (0.006)	0.03	6.3680 (0.0869)	1.36	8.5329 (0.1058)	1.24	11.3928 (0.1708)	1.50	13.9708 (0.0139)	0.10	15.8542 (0.1170)	0.74
Levulinic acid	16.2 (0.009)	0.04	9.0287 (0.0247)	0.27	12.8667 (0.1261)	0.98	16.2687 (0.0467)	0.29	23.7641 (0.1986)	0.84	26.8438 (0.1187)	0.44
HMF	31.5 (0.022)	0.08	517.4928 (0.3735)	0.07	710.4174 (0.6569)	0.09	922.4639 (1.2648)	0.14	1127.0630 (1.1050)	0.10	1342.9540 (2.6516)	0.20

Appendix 5

Table A.8 Vibrational frequency chart for IR spectra.

Type of vibration		Wavenumber (cm^{-1})	Intensity
Alcohol	O–H	3400–3650	Medium broad
	C–O	1050–1150	Medium
Alkane	C=C stretching	1200	
	$–CH_3$ bending	1375	
	C–H stretching	3000–2840	Medium
Alkene	C=C stretching	1640–1680	Medium
	= C–H	3020–3100	Medium
Arene	C–H	3030	Weak
	C=C stretching	1660–2000	Weak
		1450–1600	Medium
Aromatic	C=C stretching	1600, 1500,1450	Medium
	=C–H bending	Below 900	
Alkynes	≡C–H stretching	3300	Strong
	C≡C stretching	2100	Medium to weak
	≡C–H bending	700–600	
Carboxylic acid	O–H	2500–3100	Strong, broad
	C=O	1710	Strong
Ester	C=O	1735	Strong
Ester sp^2	C–O	1200–1250	Strong
Ester sp^3	C–O	1000–1100	Strong
Aldehyde	C=O	1730	Strong
	C–H	2720	Weak
Amide	C=O	1690	Strong
	–N–H bending	3200, 3400	Medium
Amine	–N–H bending	3500–3300	Medium, broad
	C–N stretching	1350–1000	Medium
Ketone	C=O	1715	Strong
Nitriles	C≡N	2250	Medium
Imines	C=N	1690–1640	Medium
Nitro group (NO_2)	N=O	1550(As), 1350(s)	Strong
Alkyl halide (C–X)	C–Cl	750	Strong
	C–Br, C–I	<660	Strong

Appendix 6

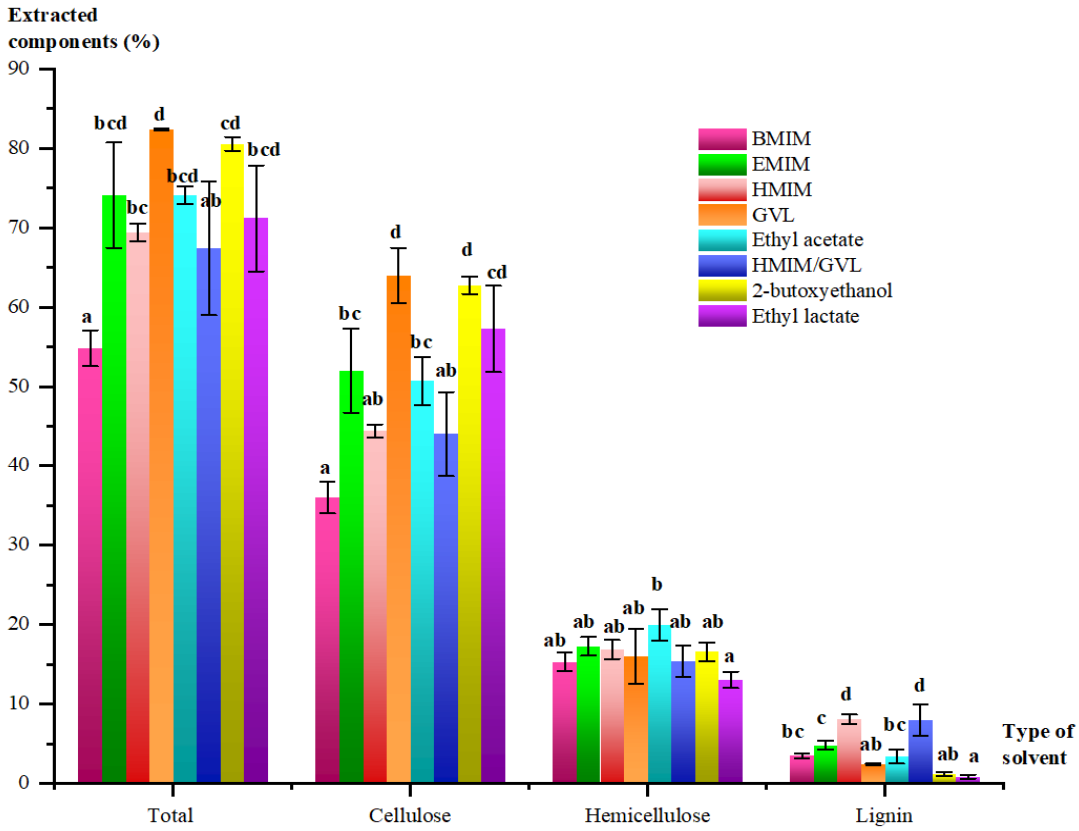

Figure A.2 Percentage of lignocellulosic components extracted from different solvents. Standard error bars were calculated from the standard deviation of triplicate samples. One-way ANOVA followed by Tukey's post hoc test was carried out for each fraction. Means followed by same letter (a,b,c,d) are not significantly different from each other (p-value>0.05).

Appendix 7

To calculate the percentage purity of cellulose in a sample using a Differential Thermogravimetric (DTG) curve, a thermogravimetric analysis (TGA) was performed to obtain the DTG curve, which shows the rate of weight loss as a function of temperature. The peak corresponding to the decomposition of cellulose, typically occurring between 300°C and 400°C, was observed. The weight loss associated with this peak was measured by integrating the area under the DTG curve. Next, the total weight loss of the sample from the TGA data was determined, which includes all decomposition events up to the final temperature. Finally, the percentage purity of cellulose was calculated using the formula:

Percentage Purity = (Weight Loss due to Cellulose / Total Weight Loss) × 100

Table A.9 The purity of cellulose, based on the DTG curve, corresponds to an original weight loss of 5.4 mg.

Sample	**Cellulose weight (mg)**	**Percentage purity (%)**
Extracted cellulose by GVL	4.5	83.3
OPMF	2.3	40.7
DOPMF	2.5	46.3

Appendix 8

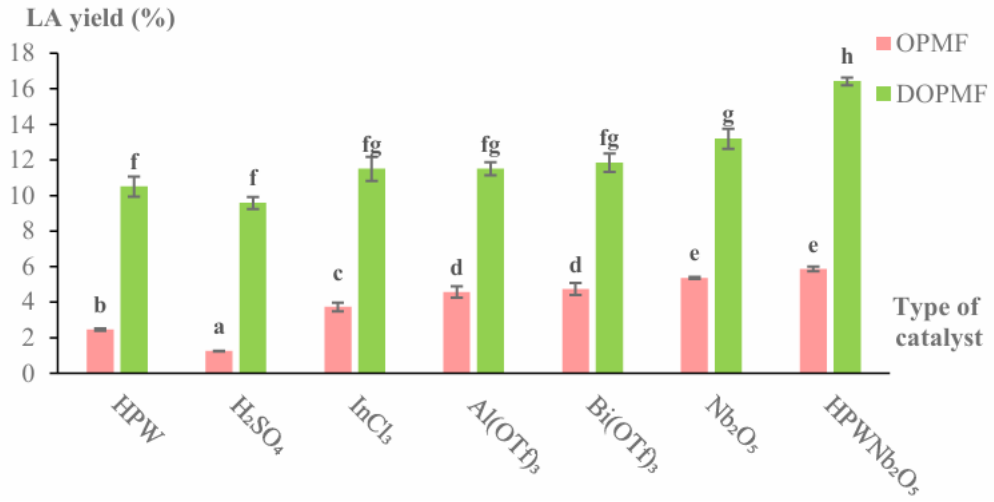

Figure A.3 Production of LA by a single functional or bifunctional catalyst via direct conversion of biomass to LA in a one-pot reaction. Different letters of a, b, c, d, and e indicate there is a significant difference between catalyst groups for OPMF conversion, while f, g, and h represent DOPMF conversion.

Appendix 9

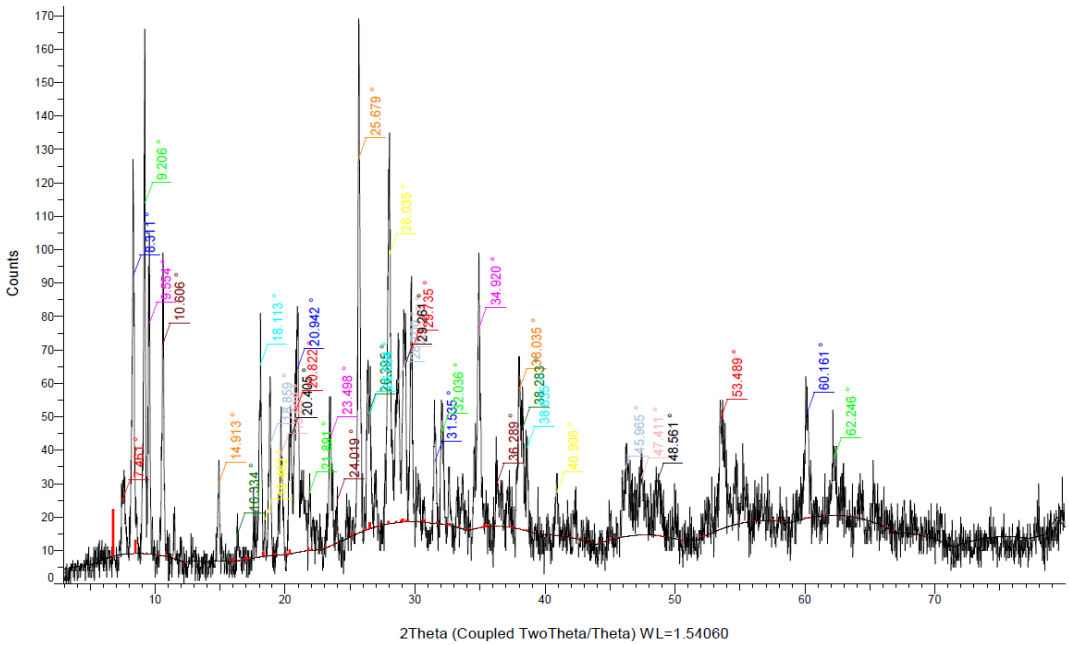

Figure A.4 XRD pattern for phosphotungstic acid.

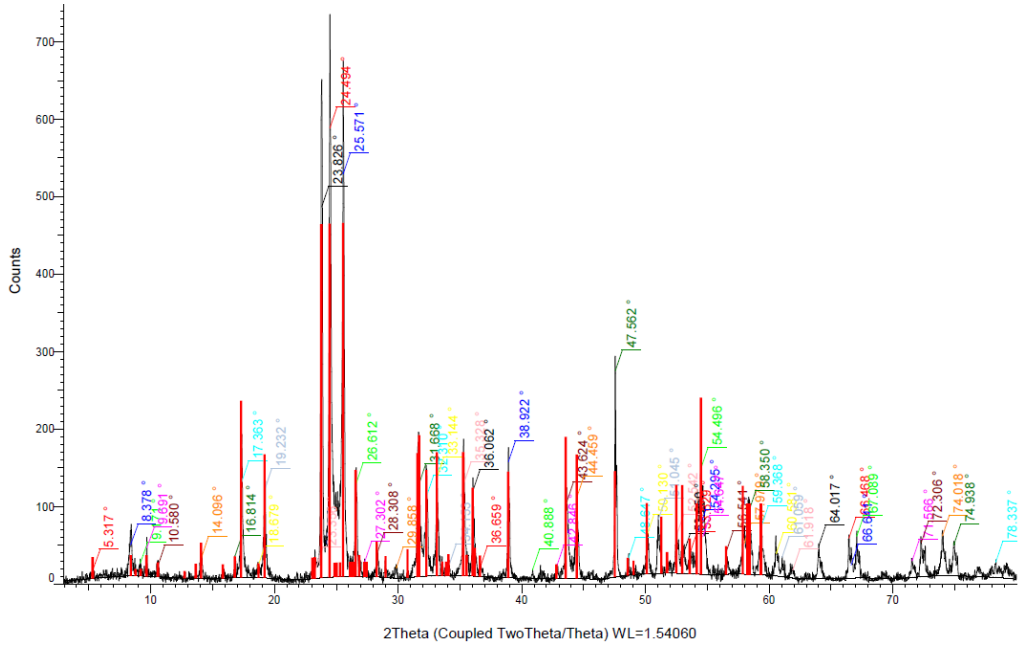

Figure A.5 XRD pattern for niobium oxide.

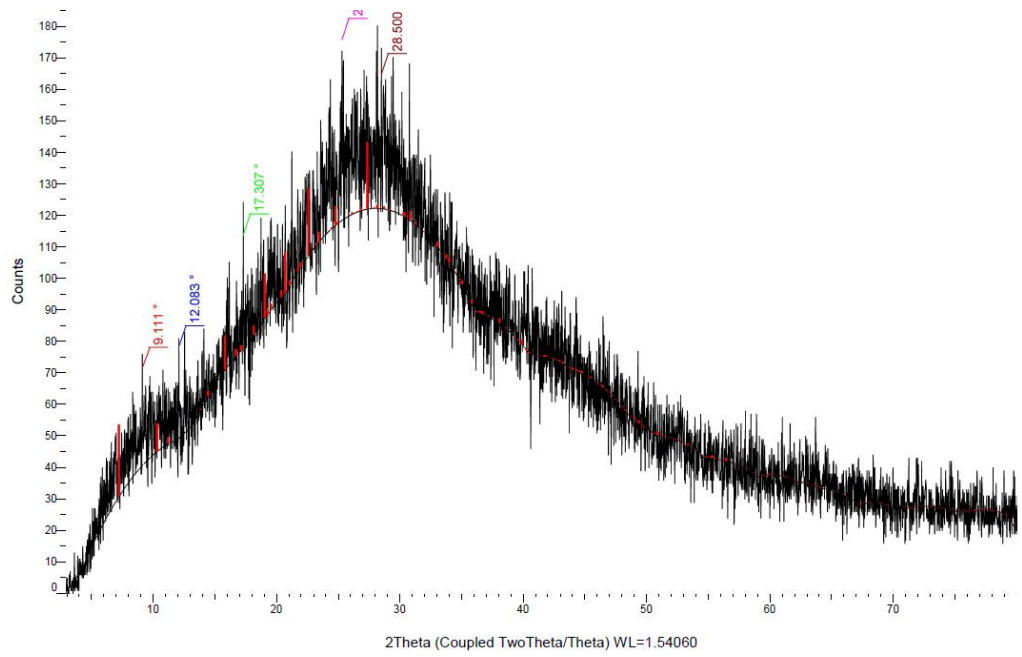

Figure A.6 XRD pattern for xanthan gum-lignin hydrogel

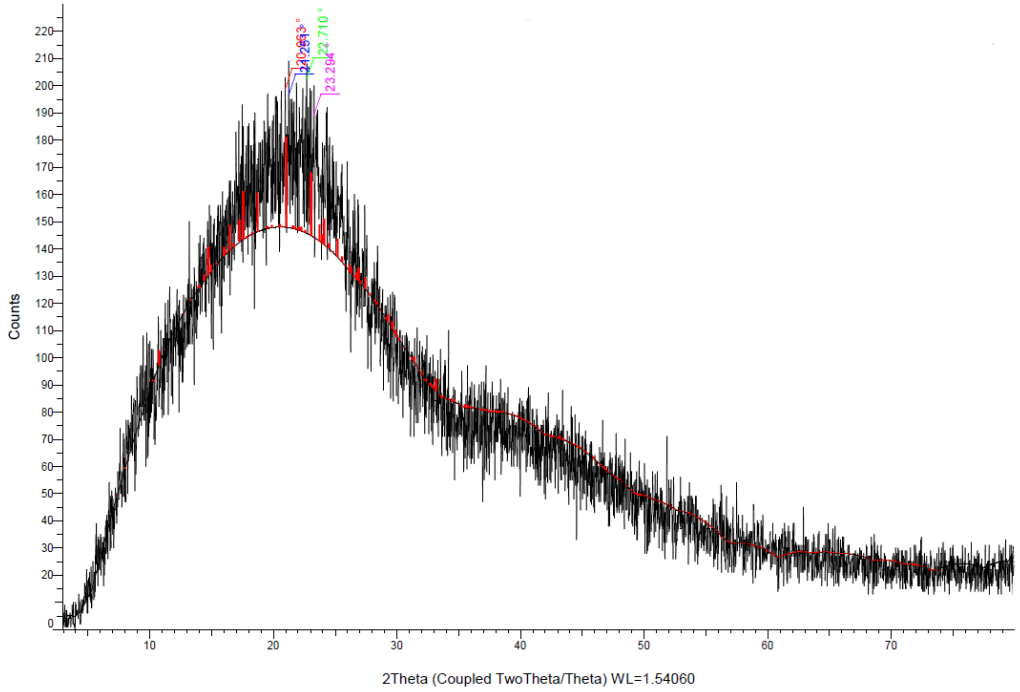

Figure A.7 XRD pattern for raw lignin.

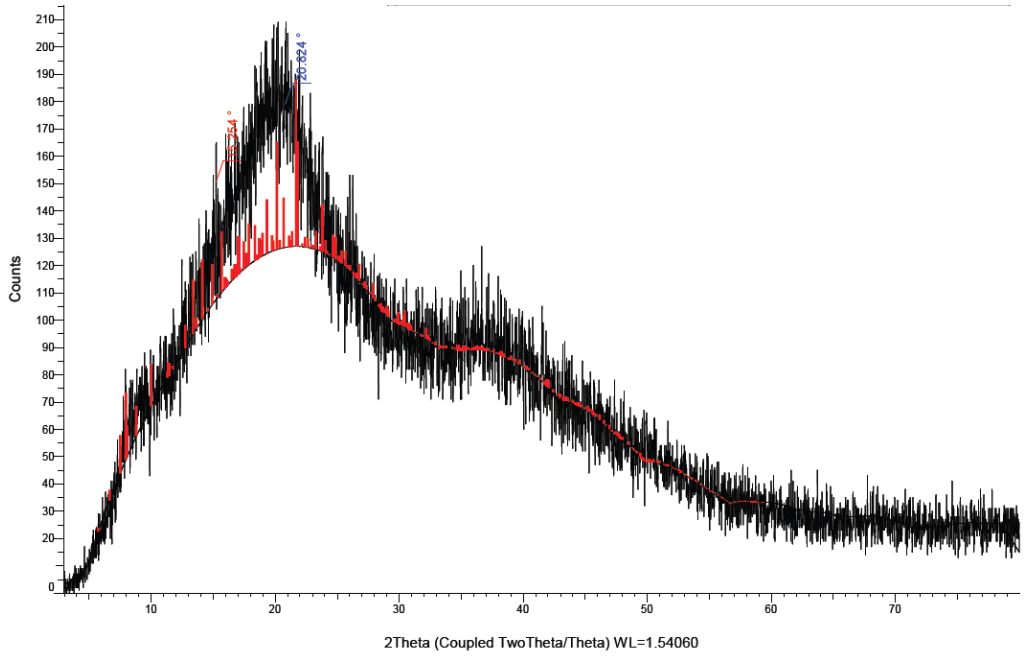

Figure A.8 XRD pattern for raw xantham gum